SEPTEMBER 2020

AJNR

VOLUME 41 • PP 1541–1757

AJNR
AMERICAN JOURNAL OF NEURORADIOLOGY

SEPTEMBER 2020
VOLUME 41
NUMBER 9
WWW.AJNR.ORG

THE JOURNAL OF DIAGNOSTIC AND INTERVENTIONAL NEURORADIOLOGY

Deep learning for pediatric posterior fossa tumor detection
MRS as an aid to diagnose malignant transformation in low-grade gliomas
Neurovascular complications in COVID-19
Fusion image guidance for supra-aortic vessel catheterization

Official Journal ASNR • ASFNR • ASHNR • ASPNR • ASSR

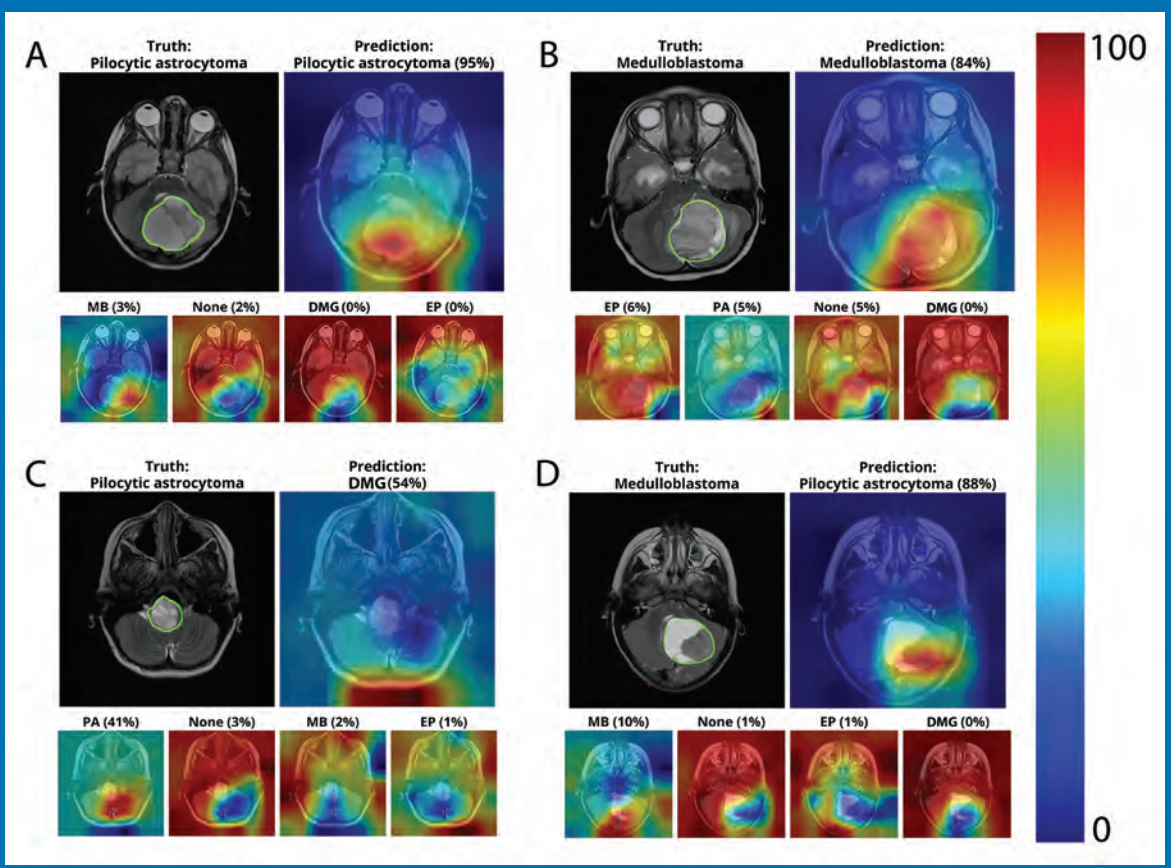

FRED™

Flow **R**e-**D**irection
Endoluminal **D**evice

FLOW DIVERSION.

SIMPLIFIED.

MicroVention™
TERUMO

MicroVention Worldwide Innovation Center
35 Enterprise
Aliso Viejo, CA 92656 USA
PH +1 714.247.8000

MicroVention UK Limted
PH +1 44 (0) 191 258 6777

MicroVention Europe S.A.R.L.
PH +33 (1) 39 21 77 46

MicroVention Deutschland GmbH
PH +49 211 210 798-0

Web
microvention.com

The New Standard of **Ease and Simplicity** in Flow Diversion Treatment.

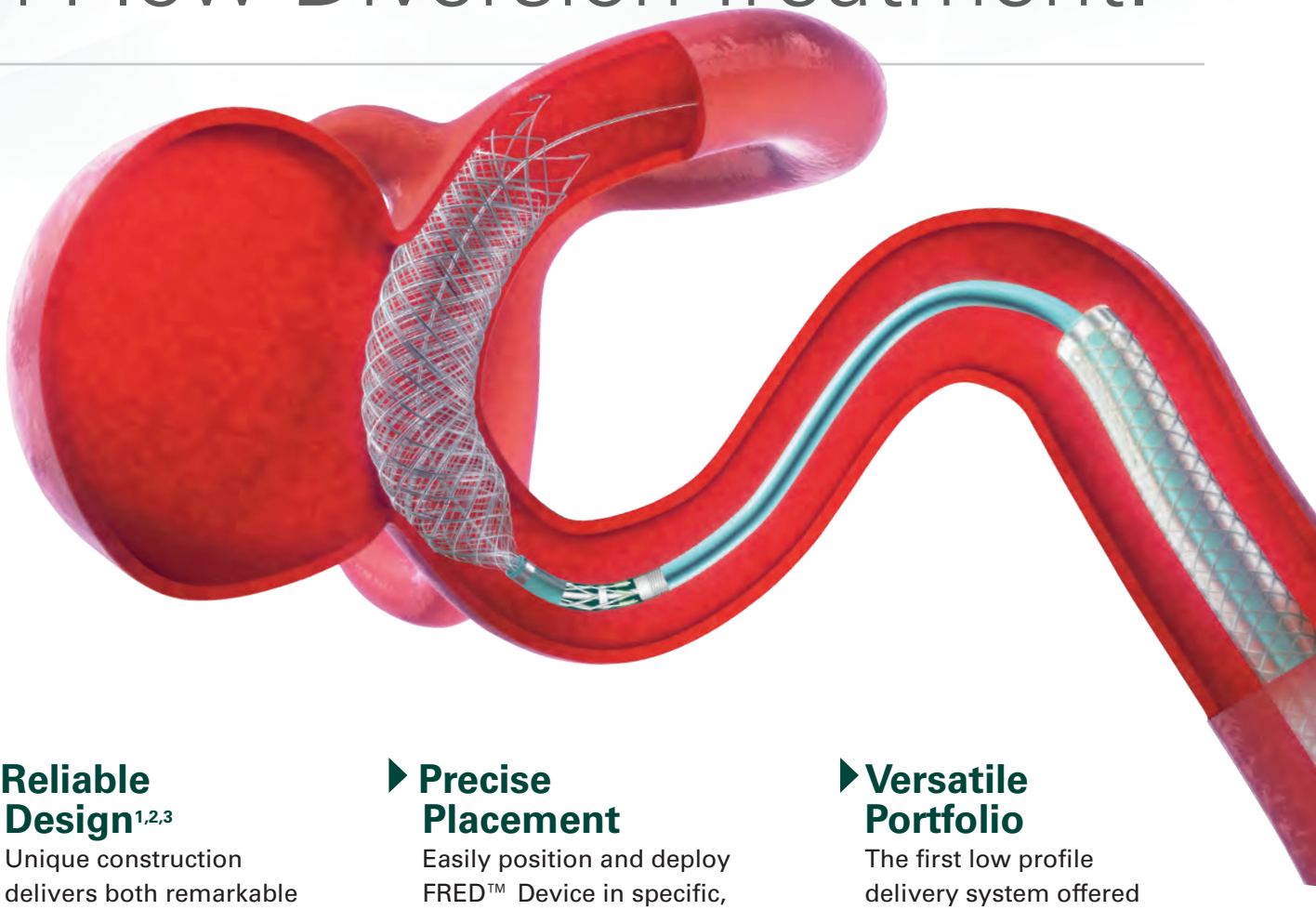

Reliable Design[1,2,3]

Unique construction delivers both remarkable ease of use and excellent flow diversion[1,2,3]

Precise Placement

Easily position and deploy FRED™ Device in specific, targeted locations[4,5,6]

Versatile Portfolio

The first low profile delivery system offered in combination with large diameter and long length options

References:
1. TR11-211 2. TR13-171 3. TR15-055 4. TR13-192 5. TR15-072 6. TR19-145

The Flow Re-Direction Endoluminal Device (FRED™) System is indicated for use in the internal carotid artery from the petrous segment to the terminus for the endovascular treatment of adult patients (22 years of age or older) with wide-necked (neck width ≥ 4 mm or dome-to-neck ratio < 2) saccular or fusiform intracranial aneurysms arising from a parent vessel with a diameter ≥ 2.0 mm and ≤ 5.0 mm.

Use of the FRED™ System is contraindicated under these circumstances: Patients in whom anticoagulant, anti-platelet therapy, or thrombolytic drugs are contraindicated. Patients with known hypersensitivity to metal such as nickel-titanium and metal jewelry. Patients with anatomy that does not permit passage or deployment of the FRED™ System. Patients with an active bacterial infection. Patients with a pre-existing stent in place at the target aneurysm. Patients in whom the parent vessel size does not fall within the indicated range. Patients who have not received dual anti-platelet agents prior to the procedure. For complete indications, contraindications, potential complications, warnings, precautions, and instructions, see instructions for use (IFU provided in the device).

RX Only: Federal (United States) law restricts this device to sale by or on the order of a physician.

MICROVENTION™ and FRED™ are registered trademarks of MicroVention, Inc. in the United States and other jurisdictions. © 2020 MicroVention, Inc. 04/2020.

Simplify
the MOC Process

Manage
your CME Credits Online

CMEgateway.org

Available to Members of Participating Societies

- American Board of Radiology (ABR)
- American College of Radiology (ACR)
- American Roentgen Ray Society (ARRS)
- American Society of Neuroradiology (ASNR)
- Commnission on Accreditation of Medical Physics Educational Programs, Inc. (CAMPEP)
- Radiological Society of North America (RSNA)
- Society of Interventional Radiology (SIR)
- SNM
- The Society for Pediatric Radiology (SPR)

It's Easy and Free!

Log on to CME Gateway to:

- View or print reports of your CME credits from multiple societies from a single access point.
- Print an aggregated report or certificate from each participating organization.
- Link to SAMs and other tools to help with maintenance of certification.

American Board of Radiology (ABR) participation!

By activating ABR in your organizational profile, your MOC–fulfilling CME and SAM credits can be transferred to your own personalized database on the ABR Web site.

Sign Up Today!

go to CMEgateway.org

AJNR

AMERICAN JOURNAL OF NEURORADIOLOGY

SEPTEMBER 2020
VOLUME 41
NUMBER 9
WWW.AJNR.ORG

Publication Preview at www.ajnr.org features articles released in advance of print. Visit www.ajnrblog.org to comment on AJNR content and chat with colleagues and AJNR's News Digest at http://ajnrdigest.org to read the stories behind the latest research in neuroimaging.

1541 **PERSPECTIVES** *G. Sparacia*

REVIEW ARTICLES

1542 **Radiologically Isolated Syndrome: A Review for Neuroradiologists** *M. Hosseiny, et al.* — ADULT BRAIN

1550 **Diagnostic Performance of PET and Perfusion-Weighted Imaging in Differentiating Tumor Recurrence or Progression from Radiation Necrosis in Posttreatment Gliomas: A Review of Literature** *N. Soni, et al.* — ADULT BRAIN

1558 **Neuroimaging Advances in Deep Brain Stimulation: Review of Indications, Anatomy, and Brain Connectomics** *E.H. Middlebrooks, et al.* — ADULT BRAIN

GENERAL CONTENTS

1569 **Manganese-Enhanced MRI in Patients with Multiple Sclerosis** *D.J. Suto, et al.* — ADULT BRAIN FUNCTIONAL

1577 **Disability Improvement Is Associated with Less Brain Atrophy Development in Multiple Sclerosis** *E. Ghione, et al.* — ADULT BRAIN FUNCTIONAL

1584 **Patterning Chronic Active Demyelination in Slowly Expanding/Evolving White Matter MS Lesions** *C. Elliott, et al.* — ADULT BRAIN FUNCTIONAL

1592 **MRS as an Aid to Diagnose Malignant Transformation in Low-Grade Gliomas with Increasing Contrast Enhancement** *C.H. Toh, et al.* — ADULT BRAIN FUNCTIONAL

1599 **Thin-Section MR Imaging for Carotid Cavernous Fistula** *D. Kim, et al.* — ADULT BRAIN

1606 **Lack of Baseline Intracranial Aneurysm Wall Enhancement Predicts Future Stability: A Systematic Review and Meta-Analysis of Longitudinal Studies** *A.S. Larson, et al.* — ADULT BRAIN

1611 **Assessment of Ischemic Volumes by Using Relative Filling Time Delay on CTP Source Image in Patients with Acute Stroke with Anterior Circulation Large Vessel Occlusions** *W. Cao, et al.* — ADULT BRAIN FUNCTIONAL

1618 **Myelin and Axonal Damage in Normal-Appearing White Matter in Patients with Moyamoya Disease** *S. Hara, et al.* — ADULT BRAIN FUNCTIONAL

1625 **COVID-19 and Involvement of the Corpus Callosum: Potential Effect of the Cytokine Storm?** *C. Rasmussen, et al.* — ADULT BRAIN

1629 **MR Susceptibility Imaging with a Short TE (MR-SISET): A Clinically Feasible Technique to Resolve Thalamic Nuclei** *S. Chung, et al.* — ADULT BRAIN

AJNR (Am J Neuroradiol ISSN 0195–6108) is a journal published monthly, owned and published by the American Society of Neuroradiology (ASNR), 800 Enterprise Drive, Suite 205, Oak Brook, IL 60523. Annual dues for the ASNR include approximately 21% for a journal subscription. The journal is printed by Cadmus Journal Services, 5457 Twin Knolls Road, Suite 200, Columbia, MD 21045; Periodicals postage paid at Oak Brook, IL and additional mailing offices. Printed in the U.S.A. POSTMASTER: Please send address changes to American Journal of Neuroradiology, P.O. Box 3000, Denville, NJ 07834, U.S.A. Subscription rates: nonmember $410 ($480 foreign) print and online, $320 online only; institutions $470 ($540 foreign) print and basic online, $935 ($1000 foreign) print and extended online, $380 online only (basic), $825 online only (extended); single copies are $35 each ($40 foreign). Indexed by PubMed/MEDLINE, BIOSIS Previews, Current Contents (Clinical Medicine and Life Sciences), EMBASE, Google Scholar, HighWire Press, Q-Sensei, RefSeek, Science Citation Index, SCI Expanded, Meta/CZI, ReadCube, and Semantic Scholar. Copyright © American Society of Neuroradiology.

1632 **Neurovascular Complications in COVID-19 Infection: Case Series** *A.M. Franceschi, et al.* — ADULT BRAIN

1641 **Leukoencephalopathy Associated with Severe COVID-19 Infection: Sequela of Hypoxemia?** *M. Lang, et al.* — ADULT BRAIN

1646 ***Commentary*** **Level of Evidence during the COVID-19 Pandemic: Making the Case for Case Series and Case Reports** *I. Ikuta*

1647 **Emergent Premedication for Contrast Allergy Prior to Endovascular Treatment of Acute Ischemic Stroke** *D.A. Tonetti, et al.* — INTERVENTIONAL

1652 **Shape Modification is Common in Woven EndoBridge–Treated Intracranial Aneurysms: A Longitudinal Quantitative Analysis Study** *J. Rosskopf, et al.* — INTERVENTIONAL

1657 **The Distribution and Role of M1 and M2 Macrophages in Aneurysm Healing after Platinum Coil Embolization** *Z. Khashim, et al.* — INTERVENTIONAL

1663 **Fusion Image Guidance for Supra-Aortic Vessel Catheterization in Neurointerventions: A Feasibility Study** *A. Feddal, et al.* — INTERVENTIONAL

1670 **Predictors of Favorable Outcome after Endovascular Thrombectomy in MRI: Selected Patients with Acute Basilar Artery Occlusion** *M. Mahmoudi, et al.* — INTERVENTIONAL

1677 **Intraluminal Carotid Artery Thrombus in COVID-19: Another Danger of Cytokine Storm?** *A.Y. Mohamud, et al.* — EXTRACRANIAL VASCULAR

1683 **MRI Findings of Immune Checkpoint Inhibitor–Induced Hypophysitis: Possible Association with Fibrosis** *R. Kurokawa, et al.* — HEAD & NECK

1690 **A Simple Formula to Estimate Parathyroid Weight on 4D-CT, Predict Pathologic Weight, and Diagnose Parathyroid Adenoma in Patients with Primary Hyperparathyroidism** *R. Yeh, et al.* — HEAD & NECK

1698 **Diagnostic Accuracy of MRI-Based Morphometric Parameters for Detecting Olfactory Nerve Dysfunction** *M.K. Lee, et al.* — HEAD & NECK

1703 **Anosmia in COVID-19 Associated with Injury to the Olfactory Bulbs Evident on MRI** *M.F.V.V. Aragão, et al.* — HEAD & NECK

1707 **COVID-19–Associated Bifacial Weakness with Paresthesia Subtype of Guillain-Barré Syndrome** *K.L. Hutchins, et al.* — HEAD & NECK

1712 **Internal Auditory Canal Diverticula among Pediatric Patients: Prevalence and Assessment for Hearing Loss and Anatomic Associations** *P.M. Bunch, et al.* — PEDIATRICS

1718 **Deep Learning for Pediatric Posterior Fossa Tumor Detection and Classification: A Multi-Institutional Study** *J.L. Quon, et al.* — PEDIATRICS FUNCTIONAL

1726 **Assessment of Maturational Changes in White Matter Anisotropy and Volume in Children: A DTI Study** *G. Coll, et al.* — PEDIATRICS FUNCTIONAL

1733 **Focal Areas of High Signal Intensity in Children with Neurofibromatosis Type 1: Expected Evolution on MRI** *S. Calvez, et al.* — PEDIATRICS

1740 **Neuroimaging Appearance of Cerebral Malignant Epithelioid Glioneuronal Tumors in Children** *G. Orman, et al.* — PEDIATRICS

1745 **The Evaluation and Prediction of Laminoplasty Surgery Outcome in Patients with Degenerative Cervical Myelopathy Using Diffusion Tensor MRI** *X. Han, et al.* — SPINE

1754 **Respiratory Phase Affects the Conspicuity of CSF–Venous Fistulas in Spontaneous Intracranial Hypotension** *T.J. Amrhein, et al.* — SPINE

1757 35 YEARS AGO IN AJNR

ONLINE FEATURES

LETTERS

E73 **Missed Medium-Vessel Occlusions on CT Angiography: Make It Easier . . . Easily!** *J.M. Ospel, et al.*

E75 ***Reply*** *B.A. Fasen, et al.*

E76 **CT Fluid-Blood Levels in COVID-19 Intracranial Hemorrhage** *N.K. Wee, et al.*

E78 **Neuro-Thoracic Radiologists "Corner": Incidental Pulmonary Findings on a Neck MRI Leading to the Diagnosis of COVID-19** *P. Smith, et al.*

E80 **The Development of Subcortical Gray Matter Atrophy in Multiple Sclerosis: One Size Does Not Fit All** *G. Pontillo, et al.*

E82 **Possible Acute Disseminated Encephalomyelitis Related to Severe Acute Respiratory Syndrome Coronavirus 2 Infection** *P.S. Utukuri, et al.*

E84 **Erratum**

BOOK REVIEWS *R.M. Quencer, Section Editor*

Please visit www.ajnrblog.org to read and comment on Book Reviews.

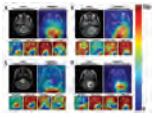

Class activation maps showing the areas of the input slice that the model preferentially emphasizes when predicting tumor subtype on individual scans. The upper row of each subpanel shows representative T2 tumor areas manually denoted (*upper left*) and map overlay of the most confident prediction (*upper right*). The lower row of each panel shows less confident predictions. Examples of correct predictions (*A* and *B*) and incorrect predictions of (*C* and *D*) are shown.

Indicates Editor's Choices selection

Indicates Fellows' Journal Club selection

Indicates open access to non-subscribers at www.ajnr.org

Indicates article with supplemental on-line table

Indicates article with supplemental on-line photo

Indicates article with supplemental on-line video

Evidence-Based Medicine Level 1

Evidence-Based Medicine Level 2

AJNR

AMERICAN JOURNAL OF NEURORADIOLOGY

Publication Preview at www.ajnr.org features articles released in advance of print. Visit www.ajnrblog.org to comment on AJNR content and chat with colleagues and AJNR's News Digest at http://ajnrdigest.org to read the stories behind the latest research in neuroimaging.

SEPTEMBER 2020 • VOLUME 41 • NUMBER 9 • WWW.AJNR.ORG

EDITOR-IN-CHIEF

Jeffrey S. Ross, MD
Professor of Radiology, Department of Radiology, Mayo Clinic College of Medicine, Phoenix, AZ

SENIOR EDITORS

Harry J. Cloft, MD, PhD
Professor of Radiology and Neurosurgery, Department of Radiology, Mayo Clinic College of Medicine, Rochester, MN

Christopher G. Filippi, MD
Professor and Vice Chair of Biomedical and Translational Science, Donald and Barbara Zucker School of Medicine at Hofstra/Northwell, Lenox Hill Hospital and Greenwich Village Healthplex, New York, NY

Thierry A.G.M. Huisman, MD
Radiologist-in-Chief, Texas Children's Hospital, Houston, TX

Yvonne W. Lui, MD
Associate Professor of Radiology, Chief of Neuroradiology, New York University School of Medicine, New York, NY

C.D. Phillips, MD, FACR
Professor of Radiology, Weill Cornell Medical College, Director of Head and Neck Imaging, New York-Presbyterian Hospital, New York, NY

Lubdha M. Shah, MD, MS
Professor of Radiology and Director of Spine Imaging, University of Utah Department of Radiology and Imaging Sciences, Salt Lake City, UT

Charles M. Strother, MD
Professor of Radiology, Emeritus, University of Wisconsin, Madison, WI

STATISTICAL SENIOR EDITOR

Bryan A. Comstock, MS
Senior Biostatistician, Department of Biostatistics, University of Washington, Seattle, WA

ARTIFICIAL INTELLIGENCE DEPUTY EDITOR

Peter D. Chang, MD
Assistant Professor-in-Residence, Departments of Radiological Sciences, Computer Sciences, and Pathology, Director, Center for Artificial Intelligence in Diagnostic Medicine (CAIDM), University of California, Irvine, Irvine, CA

EDITORIAL BOARD

Ashley H. Aiken, *Atlanta, GA*
Lea M. Alhilali, *Phoenix, AZ*
Mohammed A. Almekhlafi, *Calgary, Alberta, Canada*
Joachim Berkefeld, *Frankfurt, Germany*
Aashim Bhatia, *Pittsburgh, PA*
Waleed Brinjikji, *Rochester, MN*
Judah Burns, *New York, NY*
Danielle Byrne, *Dublin, Ireland*
Federico Cagnazzo, *Montpellier, France*
J. Levi Chazen, *New York, NY*
James Y. Chen, *San Diego, CA*
Gloria C. Chiang, *New York, NY*
Daniel Chow, *Irvine, CA*
Kars C.J. Compagne, *Rotterdam, The Netherlands*
Arturo Consoli, *Suresnes, France*
Seena Dehkharghani, *New York, NY*
Nilesh K. Desai, *Houston, TX*
Yonghong Ding, *Rochester, MN*
Birgit Ertl-Wagner, *Toronto, Ontario, Canada*
Clifford J. Eskey, *Hanover, NH*
Massimo Filippi, *Milan, Italy*
Nils D. Forkert, *Calgary, Alberta, Canada*
Ana M. Franceschi, *New York, NY*
Frank Gaillard, *Melbourne, Australia*
Joseph J. Gemmete, *Ann Arbor, Michigan*
Wende N. Gibbs, *Phoenix, AZ*
Philipp Gölitz, *Erlangen, Germany*
Brent Griffith, *Detroit, MI*
Raymond Y. Huang, *Boston, MA*
Gábor Janiga, *Magdeburg, Germany*
Joseph M. Hoxworth, *Phoenix, Arizona*
Christof Karmonik, *Houston, TX*
Timothy J. Kaufmann, *Rochester, MN*
Hillary R. Kelly, *Boston, MA*
Toshibumi Kinoshita, *Akita, Japan*
Stephen F. Kralik, *Houston, TX*
Alexander W. Korutz, *Chicago, IL*
Alexander Lerner, *Los Angeles, CA*
Yinsheng Li, *Madison, WI*
Franklin A. Marden, *Chicago, IL*
Markus A. Möhlenbruch, *Heidelberg, Germany*
Kambiz Nael, *Los Angeles, CA*
Renato Hoffmann Nunes, *Sao Paulo, Brazil*
Sasan Partovi, *Cleveland, OH*
Johannes A.R. Pfaff, *Heidelberg, Germany*
Laurent Pierot, *Reims, France*
Alireza Radmanesh, *New York, NY*
Prashant Raghavan, *Baltmore, MD*
Eytan Raz, *New York, NY*
Paul M. Ruggieri, *Cleveland, OH*
Sebastian Schafer, *Madison, WI*
Maksim Shapiro, *New York, NY*
Timothy Shepherd, *New York, NY*
James Shin, *New York, NY*
Mark S. Shiroishi, *Los Angeles, CA*
Bruno P. Soares, *Baltimore, MD*
Jason F. Talbott, *San Francisco, CA*
Ruth Thiex, *Everett, Washington*
Vincent Thijs, *Melbourne, Victoria, Australia*
Fabio Triulzi, *Milan, Italy*
Anderanik Tomasian, *Los Angeles, CA*
Anja G. van der Kolk, *Utrecht, the Netherlands*
Arastoo Vossough, *Philadelphia, PA*
Elysa Widjaja, *Toronto, Ontario, Canada*
Leonard Yeo, *Singapore*
Woong Yoon, *Gwangju, South Korea*
David M. Yousem, *Evergreen, CO*
Carlos Zamora, *Chapel Hill, NC*
Chengcheng Zhu, *Seattle, WA*

EDITORIAL FELLOW

Matthew D. Alvin, *Baltimore, MD*

SPECIAL CONSULTANTS TO THE EDITOR

AJNR Blog Editor
Neil Lall, *Denver, CO*
Case of the Month Editor
Nicholas Stence, *Aurora, CO*
Case of the Week Editors
Juan Pablo Cruz, *Santiago, Chile*
Matylda Machnowska, *Toronto, Ontario, Canada*
Sapna Rawal, *Toronto, Ontario, Canada*
Classic Case Editor
Sandy Cheng-Yu Chen, *Taipei, Taiwan*
Health Care and Socioeconomics Editor
Pina C. Sanelli, *New York, NY*
Physics Editor
Greg Zaharchuk, *Stanford, CA*
Podcast Editor
Wende N. Gibbs, *Phoenix, AZ*
Twitter Editor
Roger Jordan, *Houston, TX*

Official Journal:

American Society of Neuroradiology
American Society of Functional Neuroradiology
American Society of Head and Neck Radiology
American Society of Pediatric Neuroradiology
American Society of Spine Radiology

Founding Editor
Juan M. Taveras
Editors Emeriti
Mauricio Castillo, Robert I. Grossman, Michael S. Huckman, Robert M. Quencer

Managing Editor
Karen Halm
Assistant Managing Editor
Laura Wilhelm
Editorial Assistant
Margaret B. Sabato
Executive Director, ASNR
Mary Beth Hepp

ASNR 59th Annual Meeting

CALL FOR ABSTRACTS

Join us May 22-26, 2021, in San Francisco to present the best scientific research in Neuroradiology.

SUBMISSION DEADLINE:

Monday, November 2, 2020 (11:59 PM ET)
Submit online at asnr.org/annualmeeting

Acceptance notifications will be sent on or before January 15, 2021 upon conclusion of peer review.

ABSTRACT SUBMISSION INFORMATION

1. **IMPORTANT**: All oral presenters should be prepared to submit electronic versions of their presentations for our virtual audience, in addition to presenting to the live audience in San Francisco. Virtual presentation ability will be offered during the live meeting to those oral presenters impacted by governmental and institutional travel restrictions. For more information on ASNR21 and COVID-19 contingency planning, please visit www.asnr.org/annualmeeting.
2. Presenters of accepted abstracts **must register at their own expense** for the ASNR Annual Meeting.
3. Submission topic areas include: **Adult Brain, Spine, Head & Neck, Pediatrics, Functional/Advanced Imaging, Interventional, Health Policy, and AI/Informatics**.
4. Submit each abstract in **one** category only.
5. The *American Journal of Neuroradiology (AJNR)* encourages presenters to submit manuscripts based on their work to *AJNR* before considering other journals.
6. Maximum length: **2,500 characters, not including title, authors, images, figures**.
7. Submission site allows uploading of files into the system.
8. Changes can be made to submitted abstracts until the deadline.
9. Available awards include the Cornelius Dyke Memorial Award, Outstanding Oral Presentation Awards, and Educational Exhibit Awards.

FOR EACH ABSTRACT

- All authors must have disclosure on file in the submission system. Remove authors with missing disclosures prior to submitting abstracts. Email **education@asnr.org** to add authors after the submission deadline.
- At least one reference is required, and up to five references may be included. References should be formatted according to *AJNR* author instructions.
- The use of charts, tables and graphics are encouraged if relevant to the research submitted.
- Only one graphic file with a maximum of four images is permitted.
- Required graphic file resolution is 300 dpi or greater (e.g. 900 pixel width by 900 pixel height for a 3-inch by 3-inch image).
- Maximum file size of 100 megabytes.
- Only .jpg and .gif formats are accepted.

SUBMISSION CATEGORIES

ORAL PRESENTATION (With additional electronic version)

- 6-minute presentation plus shared session discussion that summarizes details of original investigative research.
- Additional electronic poster required (single PowerPoint slide, summarizing details of the oral presentation).
- Required abstract format: Purpose, Materials and Methods, Results, Conclusion.

ELECTRONIC SCIENTIFIC POSTER (Single PowerPoint Slide)

- Visual presentation summarizing details of original investigative research.
- Required abstract format: Purpose, Materials and Methods, Results, Conclusion.

ELECTRONIC EDUCATIONAL EXHIBIT (Multislide PowerPoint Presentation)

- A visually oriented educational presentation. Electronic Educational Exhibits highlight the unique didactic advantages of the computer format and focus on its interactive potential.
- Required abstract format: summary of the planned presentation and list of educational objectives. Consider use of Purpose, Materials/Methods, Results and Conclusion when appropriate.
- Live presentation time for select abstracts.

EDUCATIONAL EXHIBIT POSTER (Printed Poster; additional PDF version required for awards consideration)

- A visual presentation/display featuring cutting-edge material or instructional review of a topic.
- Required abstract format: summary of the planned presentation and list of educational objectives. Consider use of Purpose, Materials/Methods, Results and Conclusion when appropriate.
- Live presentation time for select abstracts.

Questions?
Contact the ASNR Education Department at **education@asnr.org**.

ASNR
American Society of Neuroradiology

AJNR go green

AJNR urges American Society of Neuroradiology members to reduce their environmental footprint by voluntarily suspending their print subscription.

The savings in paper, printing, transportation, and postage directly fund new electronic enhancements and expanded content.

The digital edition of *AJNR* presents the print version in its entirety, along with extra features including:

- **Publication Preview**
- **Case Collection**
- **Podcasts**
- **The *AJNR* News Digest**
- **The *AJNR* Blog**

It also reaches subscribers much faster than print. An electronic table of contents will be sent directly to your mailbox to notify you as soon as it publishes.

Readers can search, reference, and bookmark current and archived content 24 hours a day on www.ajnr.org.

ASNR members who wish to opt out of print can do so by using the AJNR Go Green link on the *AJNR* Website (http://www.ajnr.org/content/subscriber-help-and-services). Just type your name in the email form to stop print and spare our ecosystem.

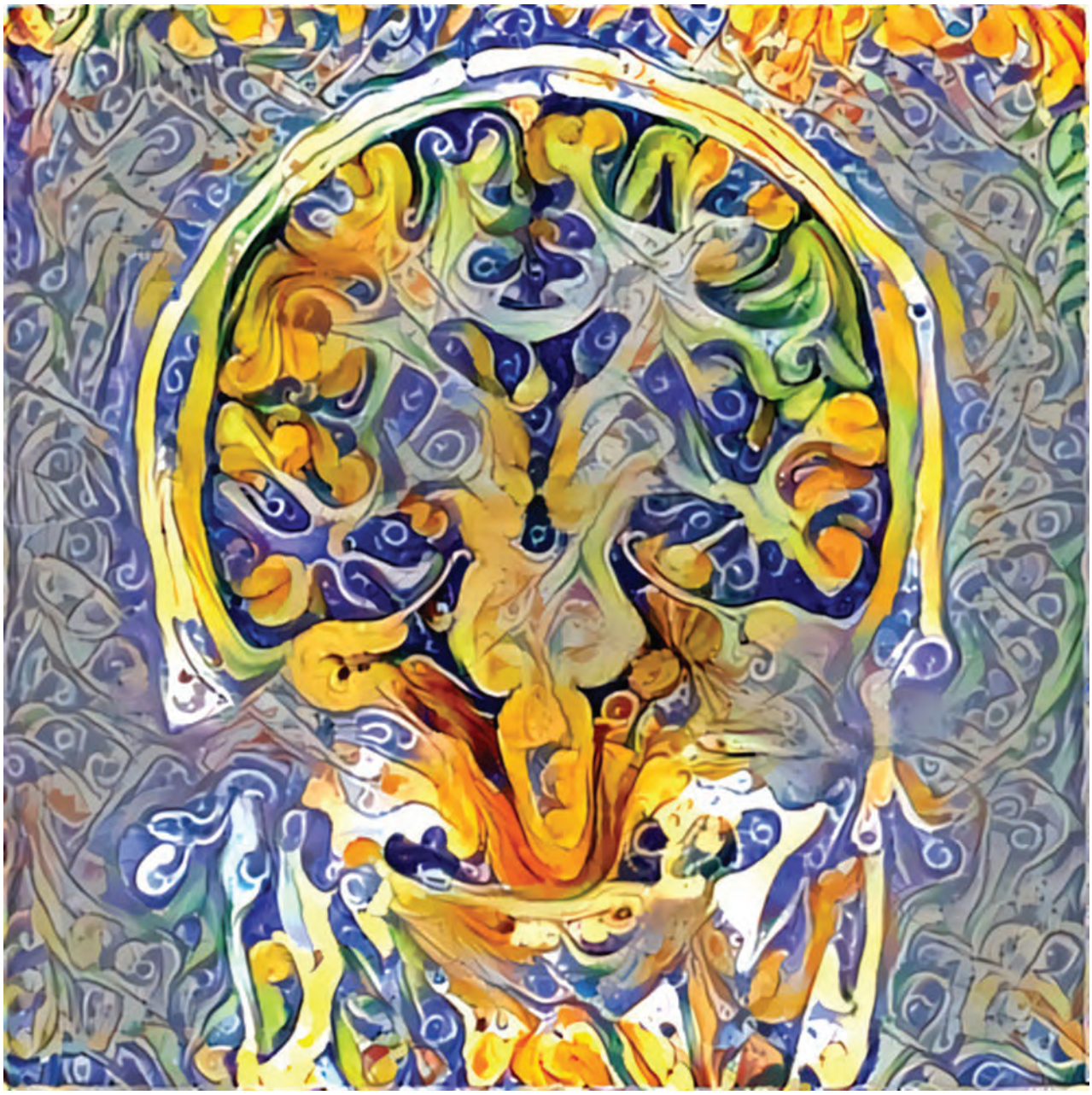

Title: Machine learning (artificial intelligence) artistic postprocessed brain coronal MRI remapped with a typical Sicilian maiolica ceramics texture. The machine learning postprocessing technique was applied to remap the brain structures extracted from a brain MRI and blend them with a ceramic tile design by using a neural texture transfer technique.

Gianvincenzo Sparacia, MD, Neuroradiologist, IRCCS-ISMETT–University of Pittsburgh Medical Center, Palermo, Italy

Radiologically Isolated Syndrome: A Review for Neuroradiologists

M. Hosseiny, S.D. Newsome, and D.M. Yousem

ABSTRACT

SUMMARY: Radiologically isolated syndrome refers to an entity in which white matter lesions fulfilling the criteria for multiple sclerosis occur in individuals without a history of a clinical demyelinating attack or alternative etiology. Since its introduction in 2009, the diagnostic criteria of radiologically isolated syndrome and its clinical relevance have been widely debated by neurologists and radiologists. The aim of the present study was to review the following: 1) historical evolution of radiologically isolated syndrome criteria, 2) clinical and imaging findings in adults and children with radiologically isolated syndrome, 3) imaging features of patients with radiologically isolated syndrome at high risk for conversion to MS, and 4) challenges and controversies for work-up, management, and therapeutic interventions of patients with radiologically isolated syndrome.

ABBREVIATIONS: CIS = clinically isolated syndrome; DIS = dissemination in space; DIT = dissemination in time; MAGNIMS = Magnetic Resonance Imaging in MS; RIS = radiologically isolated syndrome; RRMS = relapsing-remitting multiple sclerosis; CADASIL = cerebral autosomal dominant arteriopathy with subcortical infarcts and leukoencephalopathy; ADEM = acute disseminated encephalomyelitis

Radiologically isolated syndrome (RIS) refers to an entity in which brain or spine MR imaging or both demonstrate incidental white matter lesions that are characteristic in morphology and location of a demyelinating disease, fulfilling the revised 2017 McDonald Criteria for dissemination in space (DIS) (On-line Table),[1] but without a clinical history of demyelinating attacks or ongoing neurologic deterioration or other alternative causes of the white matter lesions such as those from vascular, infectious, toxic, and drug-related pathology.[2] Some might argue that RIS is not truly a clinical diagnosis and instead is part of a continuum from health to disease that cannot currently be distinguished on the basis of imaging and clinical features.

The widespread use of brain MR imaging in multiple settings has led to frequent reporting of such incidental lesions on T2-weighted and FLAIR pulse sequences.[3] In most cases of RIS, patients are being evaluated for headache, trauma, or nonspecific dizziness, symptoms that are not characteristically attributed to MS, and they have not had prior clinical episodes of neurologic deficits.

While the prevalence of RIS remains unknown, incidentally found white matter lesions resembling demyelination occur in 0.1%–0.7% of the general population.[4] The incidence of RIS has been estimated at 0.8 per 100,000 person-years in a Swedish cohort consisting of 1907 patients, compared with the 10.2 per 100,000 person-year incidence of MS.[5] The prevalence of RIS is known to be increased in healthy relatives of patients with MS. Gabelic et al[6] found that the prevalence of RIS was 2.9% in the healthy relatives of patients with MS in contrast to the prevalence of 2.4% in nonfamilial healthy controls. Liu et al[7] assessed T2 hyperintensities in 326 consecutive patients 10–55 years of age presenting with headache and found that the Barkhof and 2010 McDonald criteria for DIS were met in 2.4%–7.1% and 24.4%–34.5%, respectively. These reported figures, however, far exceed the prevalence of MS. Overall, on the basis of postmortem studies, the prevalence of RIS seems to fall within 0.06%–0.7%.[8]

Since RIS was first defined in 2009,[9] the implications of these imaging findings have been widely investigated. The conversion rate of RIS to MS and the debate over whether to start MS disease-modifying therapies (with their potentially serious side effects) in RIS are subjects of intense scrutiny, summarized herein.[10]

Received April 10, 2020; accepted after revision May 4.

From the Department of Radiological Sciences (M.H.), David Geffen School of Medicine at the University of California, Los Angeles, Los Angeles, California; Department of Neurology (S.D.N.), Johns Hopkins University School of Medicine, Baltimore, Maryland; and Russell H. Morgan Department of Radiology and Radiological Sciences (D.M.Y.), Johns Hopkins Medical Institution, Baltimore, Maryland.

Please address correspondence to David M. Yousem, MD, MBA, Johns Hopkins Medical Institution, 600 North Wolfe St, Phipps B112D, Baltimore, MD 21287; e-mail: dyousem1@jhu.edu; @dyousem1

Indicates open access to non-subscribers at www.ajnr.org

Indicates article with supplemental on-line table.

http://dx.doi.org/10.3174/ajnr.A6649

Table 1: Proposed diagnostic criteria for RIS by Okuda et al[9]

Inclusion Criteria	Exclusion Criteria
CNS white matter lesions on MR imaging that are ovoid, well-circumscribed, >3 mm, and homogeneously hyperintense on T2-weighted images with or without involvement of the corpus callosum	CNS lesions in a vascular pattern
CNS lesions fulfill 3 of 4 Barkof criteria	Historical accounts of remitting clinical symptoms consistent with neurologic dysfunction
1) One gadolinium-enhancing lesion or 9 T2-hyperintense lesions if no gadolinium-enhancing lesions	MR imaging anomalies can be explained by the direct physiologic effects of substances (recreational drug abuse, toxic exposure) or a medical condition
2) At least 1 infratentorial lesion	MR imaging phenotypes suggestive of leukoaraiosis (small-vessel ischemic disease) or extensive white matter pathology lacking involvement of the corpus callosum
3) At least 1 juxtacortical lesion, and	White matter lesions are better accounted for by another medical condition
4) At least 3 periventricular lesions	
MR imaging anomalies do not account for clinically apparent impairment in social, occupational, or generalized areas of functioning	

History

Okuda et al[9] first described RIS as showing T2-hyperintence, ovoid, homogeneous, well-defined lesions on MR imaging that fulfilled at least 3 of 4 Barkhof criteria (Table 1) for DIS in individuals without a history of symptoms consistent with a central nervous system demyelinating disorder, toxic conditions, or other disease processes that might lead to such imaging findings. Development of clinically isolated syndrome (CIS) or clinically definite MS was noted in the longitudinal follow-up of 10 of 30 patients for which such data were available. The mean time to the first clinically defining neurologic event was 5.4 years.[9]

Nine articles on the topic were written in 2009 after the article by Okuda et al.[9] Since then, the literature has expanded with 16 articles on the topic written in 2014 and 27 in 2019. However, there has not been a review of the imaging findings of RIS in a radiology-based scientific journal to date.

Criteria Evolution

The diagnosis of RIS has relied on the imaging criteria used to make the diagnosis of MS. The 2010 McDonald Criteria simplified the DIS criteria for the diagnosis of MS by focusing on the distribution of the demyelinating lesions (juxtacortical, periventricular, infratentorial, and spinal cord) rather than the total number of lesions.[11] The 2010 and 2017 revised McDonald criteria did not address the RIS entity because of the paucity of longitudinal data surrounding RIS. However, in 2017, the Magnetic Resonance Imaging in MS (MAGNIMS) European group tried to better define the imaging criteria for RIS. The MAGNIMS consensus group did not propose a strict recommendation on diagnosing and treating RIS; however, they suggested that identical MR imaging criteria for DIS and dissemination in time (DIT) should be used for RIS and MS (Table 2).[1]

In other words, instead of using the Barkhof criteria as proposed in Okuda et al,[9] the revised 2017 McDonald and/or MAGNIMS criteria should be applied (On-line Table). On the basis of the new guidelines, DIS in RIS is based on the presence of T2/FLAIR hyperintense lesions in at least 2 of the following topographies: cortical or juxtacortical white matter, periventricular white matter, spinal cord, and the infratentorial (brain stem and/or cerebellum) compartment (Fig 1).

A detailed clinical history and a meticulous neurologic examination are essential to rule out any clinical evidence of MS before labeling the patient as fulfilling the definition of RIS. The criteria used for diagnosing clinically definite MS require the presence of clinical relapses (relapsing-onset MS) or ongoing neurologic deterioration from the start (progressive onset).[2] MAGNIMS opined and the 2017 McDonald Criteria Panel agreed that if a clinical episode occurs in a subject positive for RIS-DIS/DIT then a diagnosis of MS can be made.

Imaging Findings

In the article of Okuda et al[9] on RIS, 10 of 41 (24%) patients with periventricular, juxtacortical, spinal, or infratentorial white matter lesions had ≥1 enhancing plaque at the time of RIS presentation. Of these 41 patients, MR imaging progression (the presence of new T2 foci, new gadolinium enhancement, or enlargement of pre-existing lesions) on longitudinal MR imaging, fulfilling the DIT criteria, was identified in 59% of the cohort (24/41). In a subsequent multicenter cohort of 456 patients with RIS, the frequency of periventricular, juxtacortical, spinal cord, and infratentorial lesions was 98.7%, 90.1%, 35.2%, and 30.4%, respectively.[12] Gadolinium-enhancing lesions were found in 82.3% of this study cohort (Fig 2).[12] In a study of 19 patients with RIS and 20 individuals with relapsing-remitting MS (RRMS), no significant difference was found between the

Table 2: Modified criteria for the diagnosis of RIS[2]

Inclusion Criteria	Exclusion Criteria
≥1 T2-hyperintense lesions on T2-weighted scans involving at least 2 of the following 4 locations:	Neurologic dysfunction suggestive of MS based on historical symptoms and/or objective signs
1. Periventricular white matter	MR imaging abnormalities explained by other disease processes, especially considering age, vascular, toxins, or drug-related abnormalities
2. Cortical/juxtacortical	
3. Spinal cord	
4. Infratentorial	

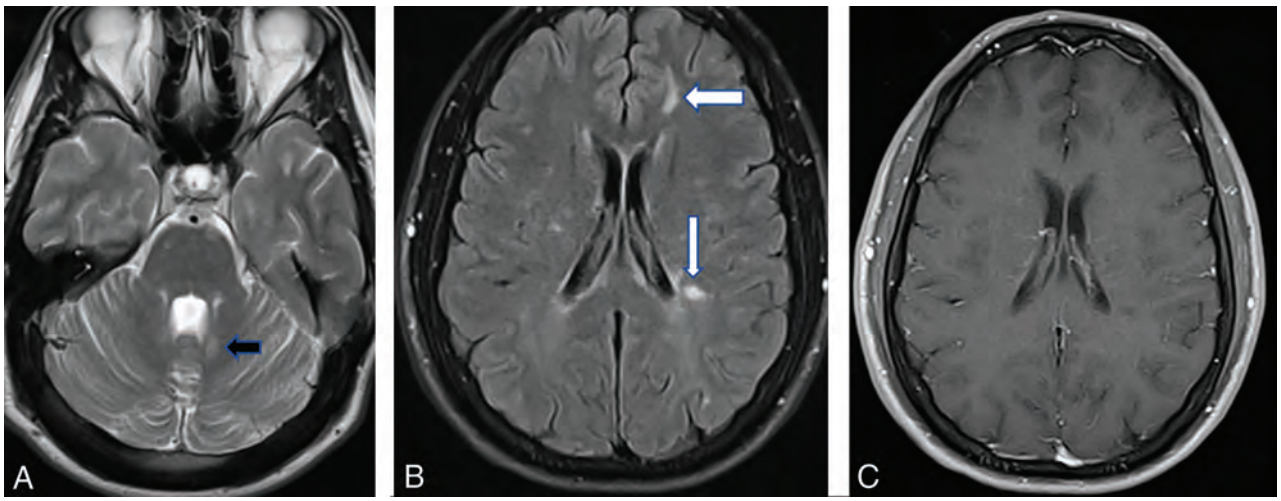

FIG 1. *A*, Axial T2-weighted image in a 21-year-old patient presenting to the emergency department with the worst headache of her life shows left periventricular posterior fossa lesions (*arrow*). *B*, The FLAIR scan demonstrates periventricular (Dawson fingers-like) and juxtacortical lesions (*arrows*). *C*, None of the lesions show gadolinium enhancement.

groups in T1-weighted and T2-weighted lesion volume or frequency and distribution of lesions.[13] In addition to white matter lesions, cortical lesions have been described in 40% of patients with RIS in a study by Giorgio et al.[14] The authors found that these cortical lesions involved the frontotemporal lobes most commonly and were more frequent in patients with RIS with the following: 1) oligoclonal bands in the CSF, 2) DIT on follow-up, and 3) coexistent cervical cord lesions. The unanswered question remains as to whether patients with RIS with cortical lesions have a higher MS conversion rate.

The perivenular distribution of the lesions is a key feature in distinguishing RIS from other mimickers (eg, migraines, strokes, synovitis-acne-pustulosis-hyperostosis-osteitis syndrome). A high percentage of RIS lesions show the central vein sign, specifically when higher magnetic fields and susceptibility-weighted sequences are used.[15,16] The paramagnetic rim sign refers to the signal drop (ie, susceptibility artifact) at the edge of the white matter lesions in chronic demyelination. A study of 15 individuals with RIS reported the central vein sign and paramagnetic rim sign in 93% and 73% of the study population, respectively.[17]

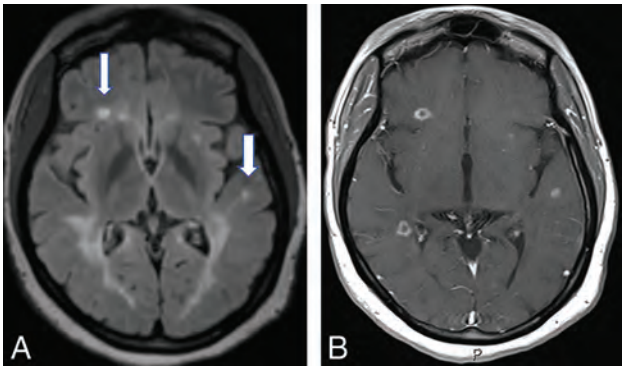

FIG 2. *A*, A 32-year-old woman being evaluated for benign positional vertigo. The FLAIR scans have severe confluent periventricular disease and a few juxtacortical foci (*arrows*) of high signal. *B*, On postgadolinium scanning, numerous ring-enhancing demyelinating lesions are present, both periventricular-periatrial on the right and juxtacortical bilaterally.

Advanced Imaging

On 3D quantitative volumetric studies, normalized whole-brain volume, normalized cerebral cortical volume,[18] and normalized cerebellar white matter volume[19] have been found to be significantly lower in patients with RIS compared with healthy individuals. In addition, on MR spectroscopy studies, decreased *N*-acetyl-aspartate/creatine levels in lesional regions, normal-appearing white matter, and cortical gray matter have been found in patients with RIS compared with healthy controls, suggestive of early neuronal damage.[20]

Studies using DTI have described microstructural changes in the brain MR imaging of individuals with RIS, which are confined to the lesional area; this finding is in contrast to the altered white matter integrity in both lesions and normal-appearing white matter in RRMS. De Stefano et al[13] examined brain MRIs of 19 individuals with RIS compared with 20 with RRMS and 20 healthy controls. They found lesional magnetization transfer to be significantly lower in those with RIS than in healthy controls, but significantly higher than in those with RRMS. Normal-appearing white matter magnetization transfer values were similar in patients with RIS and healthy controls but significantly higher than normal-appearing white matter in patients with RRMS.

Giogrio et al[21] identified lower fractional anisotropy values in white matter tracts with lesions in patients with RIS compared with healthy controls. In addition, the study compared the functional connectivity in individuals with RRMS and RIS versus healthy controls. There was no difference in resting-state network connectivity among those with RIS, RRMS, and controls; however, patients with RIS had significantly lower functional connectivity in sensorimotor and working memory subnetworks than patients with RRMS.

Similar changes were reported in advanced MR imaging of the spinal cord in RIS. In a study[22] of 3T spinal cord MR imaging in 24 individuals with RIS and 14 healthy controls, the spinal

cord magnetization transfer ratios were lower in patients with RIS. By contrast, there were no significant differences in the DTI metrics (fractional anisotropy and mean, perpendicular, and parallel diffusivity) between individuals with RIS and healthy controls.

Evolution to MS

A number of clinical and paraclinical features have been studied in RIS to help identify whether markers exist that portend early clinical conversion to MS. These predictors may help identify patients with high-risk RIS who might benefit from early treatment with MS disease-modifying therapies, though treatment is controversial at this juncture in time.

In a multicenter study of 451 individuals with RIS, approximately two-thirds of individuals developed new lesions on longitudinal MR imaging, while one-third of them developed CIS within 5 years of the index MR imaging.[12] Since this publication in 2014, it has been accepted that RIS with DIS and DIT plus CIS implies a diagnosis of MS.[2] Approximately 10% of the entire cohort eventually developed primary-progressive MS.

Patients with spinal cord lesions appear to be at particular risk of conversion, with 56% converting to MS.[23] In 1 study of patients with RIS, 84% of individuals who had cervical cord lesions converted to MS, while only 7% of those without cervical cord lesions converted.[24] Similarly, thoracic cord lesions, though occurring more rarely, place patients with RIS at higher risk of conversion to MS (hazard ratio, 2.23 versus 2.02 for cervical cord lesions).[4]

In contrast to spinal lesions, periventricular and juxtacortical lesions were not found to be predictive of clinical conversion.[12,25] Additionally, the number of lesions and their location in the brain are not a strong predictor of clinical conversion.[26] A few studies have found the presence of infratentorial lesions to be predictive of clinical conversion,[24,27] while others have not.[12,25,28]

Lebrun et al[28] suggested that the criteria for high-risk RIS should include younger age, the presence of gadolinium-enhancing lesions, and abnormal visual-evoked potentials. According to the multinational study mentioned above[12] that included 451 individuals with RIS (78.5% females; mean age, 37.2 years), younger age (hazard ratio, 0.98; 95% CI, 0.96–0.99), male sex (hazard ratio, 1.93; 95% CI, 1.24–2.99), and the presence of lesions within the cervical or thoracic spinal cord (hazard ratio, 3.08; 95% CI, 2.06–4.62) were identified in the multivariate analysis as the most significant predictors for the development of MS. The presence of contrast enhancement on baseline MR imaging, the location of the lesions in the brain, a family history of MS, and the CSF profile were not strong predictors of clinical conversion in this model. Older men with spinal cord lesions and RIS had a higher rate of conversion to primary-progressive MS.[29]

CSF biomarkers have also been studied in patients with RIS. Oligoclonal bands have been the most important CSF biomarker to predict clinical conversion to MS.[26] In the 2017 McDonald MS criteria, oligoclonal bands can replace DIT.[1] Smaller cohorts have shown a higher risk if patients have elevated interleukin 8,[30] neurofilament light chain,[31] and immunoglobulin G indexes[23] in the spinal fluid.

Lebrun et al[32] also found a higher rate of clinical conversion to MS in pregnant patients with a significantly shorter mean conversion time.

Overall, the presence of spinal cord lesions, oligoclonal bands in CSF, and younger age is the most important predictor for conversion. Whether the presence of contrast-enhancing lesions can be a predictor of clinical conversion is controversial.

Relationship to Clinically Isolated Syndrome

Patients are considered to have CIS when they present with their first clinical symptom suggestive of CNS demyelination and do not fulfill the McDonald criteria for clinically definite MS. The neurologic event might involve the optic nerve, spinal cord, brain stem, cerebellum, or cerebral hemispheres. The clinical event needs to persist in a constant fashion for at least 24 hours and occur in the absence of fever or infection to be called a demyelinating attack.[1] In a study of 156 individuals with CIS with a median follow-up of 7 years, 42% converted to clinically definite MS.[33] The rate of conversion of CIS to MS appears to be higher than that in individuals with RIS. MR imaging is the most helpful tool to predict conversion to MS in patients with CIS. MR imaging abnormalities suggestive of demyelinating disease are seen in 50%–70% of individuals with CIS.[34] The risk of conversion to clinically definite MS is approximately 60%–82% in those with abnormal MR imaging findings, in contrast to 8%–25% in those with a normal MR imaging findings.[35] In individuals with RIS who develop CIS, the presence of DIT (eg, the presence of both gadolinium-enhancing and nonenhancing lesions) on MR imaging will fulfill the criteria for a diagnosis of MS. Several MR imaging features have been associated with a higher risk of conversion of CIS to MS, including the involvement of white matter tracts attributed to motor function, the involvement of tracts near the corpus callosum,[36] the presence of spinal cord lesions,[37] the development of new brain lesions, and lateral ventricle enlargement.[38]

Differential Diagnosis

As stated in the original article of Okuda et al,[9] the label of RIS can be applied only after excluding other causes of white matter lesions. Okuda et al added, as part of these criteria (see Table 1), "The MR imaging anomalies are not due to the direct physiologic effects of substances (recreational drug abuse, toxic exposure) or a medical condition" and "Exclusion of individuals with MR imaging phenotypes suggestive of leukoaraiosis or extensive white matter pathology lacking involvement of the corpus callosum." Similarly, the MAGNIMS 2018 statement lists as exclusion criteria "MR imaging abnormalities explained by any other disease process, with particular attention to aging or vascular-related abnormalities, and those due to exposure to toxins or drugs."[2] These statements are included because an age limit has not been defined for RIS. Therefore, an elderly patient with small-vessel ischemic disease with lesions in the posterior fossa and periventricular region who develops a new ischemic focus may fulfill the McDonald 2017 and the RIS imaging criteria of Okuda et al.

When one considers the causes of white matter lesions that may mimic the RIS pattern, the list spans several entities

Table 3: Selected entities often mistaken for RIS

Entity	Distinguishing Clinical Features	Distinguishing Imaging Features	Important Keys to Diagnosis
Toxins/drug-related	Altered mental status changes during intoxication, history of substance abuse	Deep gray matter frequently involved, symmetric lesions	Urine and serum toxicology tests
Age-related leukoaraiosis	Older individual, cardiovascular risk factors	Small (<3 mm), nonenhancing lesions in periventricular and deep white matter, coexistent striatocapsular lacunar disease, absence of callososeptal lesions/ Dawson fingers–type lesions	Lacunar disease and atypical white matter lesions for RIS in an older individual
Migraines	Headache or aura predominates	Predominantly subcortical white matter lesions that are small (<3 mm) and do not enhance, few periventricular lesions	Headache history and lack of typical imaging features consistent with RIS
Vasculitis	Episodic neurologic symptoms with superimposed strokes	Gray and white matter lesions coexist, may have enhancing vessel wall and/or leptomeningeal enhancement, MRA with stenoses	Systemic symptoms present, elevated erythrocyte sedimentation rate and/or C-reactive protein level, extra-/intracranial vessels abnormal, brain biopsy
CADASIL	Strokelike episodes, family history of similar clinical syndrome	White matter disease favoring anterior temporal tip subcortical regions, external capsule, presence of lacunar infarcts	Genetic testing diagnostic
Collagen vascular diseases	Clinical history of arthritis, long-standing chronic disease, episodic	Gray and white matter lesions ± vasculitis, occasional encephalitis	Clinical symptoms of a systemic disorder and presence of serologic autoantibodies/ inflammatory markers
ADEM	Encephalitis, seizures, children > adults, history of viral/ vaccine prodrome	Gray matter disease predominates, more diffuse enhancement, may have positive findings on DWI	History of prodromal virus infection or vaccination, encephalopathic
Posttraumatic	History of ≥1 traumatic, sports-related event	Favors gray-white matter junction, hemorrhagic products present, classic tears in splenium-brain stem deep gray matter	Hemorrhage and stereotypical locations of disease at shearing sites

Note:—ADEM indicates acute disseminated encephalomyelitis.

including vascular (migraine changes, vasculitis, CADASIL, neonatal hypoxic-ischemic injuries, anoxic episodes, and small-vessel ischemic disease), inflammatory/infectious entities (sarcoidosis, lupus, acute disseminated encephalomyelitis, progressive multifocal leukoencephalopathy, synovitis-acne-pustulosis-hyperostosis-osteitis syndrome), posttraumatic changes (remote clinical and subclinical trauma, sports-related, ie, boxers), drug-related (splenial demyelination in seizure medications versus causes of posterior reversible encephalopathy syndrome), and idiopathic (Table 3).[39] Two series[40,41] of "misdiagnosed MS" reported the most common final diagnoses to be migraine, fibromyalgia, psychiatric/psychogenic disease, nonspecific white matter abnormalities, small-vessel ischemic disease, and neuromyelitis optica spectrum disorders. As opposed to these entities described above, which have overt signs and symptoms, patients with RIS are, by definition, asymptomatic.

Despite this very broad differential diagnosis, subspecialty-trained neuroradiologists have been shown to be very accurate in recognizing the pattern of white matter lesions suggestive of MS and therefore RIS. In a study performed at a large academic center,[42] the order in which MS was suggested in a differential diagnosis of the neuroradiologist's report determined the likelihood of a final diagnosis in patients who did not previously have a diagnosis of MS. When MS was listed as the only diagnosis, the neuroradiologists were correct in the final diagnosis in 22/24 cases (92.3%). When "demyelinating disorder" only was listed, they were correct in 43/51 cases (84.3%), and when MS was listed as the first potential diagnosis in a list of differentials, the final diagnosis was proved to be MS in 38% (3/8) of cases. The final diagnoses in those patients inaccurately reported as "likely MS" included migraines ($n = 9$), peripheral neuropathy ($n = 4$), postconcussive lesions ($n = 3$), substance abuse ($n = 2$), cerebrovascular disease ($n = 2$), and no diagnosis ($n = 5$).[42]

The imaging findings that are more suggestive of RIS than other entities include the central vein sign of demyelination around a vein and involvement of the corpus callosum (corpus callosum–septum pellucidum interface). The original RIS diagnostic criteria of Okuda et al[9] excluded patients if they were "lacking involvement of the corpus callosum." Moreover, spinal involvement also helps to practically exclude diagnoses like migraines, posterior reversible encephalopathy syndrome, progressive multifocal leukoencephalopathy, and so forth. A good review of the accuracy of MR imaging for MS alone and in combination with clinical findings, serologic tests, and CSF markers can be found in the study by Schaffler et al.[43]

Clinical Approach to RIS

Despite RIS being described more than a decade ago, there are no specific, universally adopted guidelines for the monitoring and treatment of this evolving entity. This issue is mostly secondary to a paucity of available longitudinal studies and lack of expert consensus[1] on how one should approach such patients. Hence, clinicians are left with relying on short studies, review articles, and their anecdotal experiences.

An initial pragmatic approach that many clinicians take after an individual fulfills the criteria for RIS is similar to how clinicians evaluate and monitor patients with suspected CIS and MS. First, a detailed history and physical examination by an experienced neurology clinician are recommended to ensure that a patient truly has RIS, especially because treatment is recommended for most patients with CIS and MS. The emphasis, therefore, is to discover prior or current neurologic signs and symptoms that might fulfill the CIS or MS criteria. At this juncture, most clinicians[44-46] are hesitant to start patients with RIS on prophylactic disease-modifying therapies because a substantial number of patients with RIS will not develop MS and there are potential serious risks associated with MS therapies.

Obtaining paraclinical testing beyond an MR imaging is also extremely important because this can help stratify patients with RIS into low-risk (eg, no spine lesions, normal lumbar puncture) or high-risk (eg, spine lesions, presence of CSF-restricted oligoclonal bands)[12,47] for conversion to MS. Hence, most neurology clinicians will recommend a lumbar puncture to assess markers of autoimmunity and inflammation, including CSF pleocytosis, an elevated immunoglobulin G index, and/or CSF-restricted oligoclonal bands. In addition, just like with MS, serologic testing is necessary for ruling out mimickers of demyelinating disorders (systemic/rheumatic disorders, nutritional deficiencies, infectious diseases, and so forth) and for identifying conditions that have a stronger propensity to cause disabling neurologic attacks (eg, seropositive neuromyelitis optica spectrum disorders, anti-myelin oligodendrocyte glycoprotein–associated disorders, and so forth).

Other tests that are commonly performed that may be associated with the prognosis of patients with RIS include visual-evoked potential testing and optical coherence tomography.[28,48,49] Electromyography, nerve conduction studies, and other ancillary studies are typically not performed unless there are "red flags" in the history and/or examination suggesting an alternative diagnosis (eg, peripheral neuropathy).

Most clinicians will also obtain a total serum 25-hydroxyvitamin D level on their patients because chronic vitamin D deficiency is associated with a risk of developing MS.[50] If a patient with RIS has low vitamin D, vitamin D supplementation is recommended.

After the initial assessment and work-up for RIS is completed, clinicians are then challenged by how patients with RIS should be monitored across time. Currently, there is a paucity of data that help guide clinicians on when surveillance imaging should be performed in RIS, especially as it relates to assessing evidence of DIT.[2,51] The MAGNIMS group and the Consortium of Multiple Sclerosis Centers MR Imaging Task Force have published expert consensus guidelines that can be followed.[2,51] Future and ongoing prospective longitudinal studies will help refine these guidelines along with the advent of newer imaging techniques (central vein sign, paramagnetic rim sign) and other biomarkers (eg, neurofilament light chain).

At this time, the treatment approach for patients with RIS is controversial. As previously highlighted, a substantial number of patients with RIS will not develop CIS or MS, especially those who are considered to have low-risk RIS. A recent comprehensive review article[52] on RIS discussed the importance of clinical trials in RIS because data are lacking establishing the benefit of starting treatment in RIS. Hence, treatment is not recommended for most upfront, though if new inflammatory activity (ie, gadolinium-enhancing lesions) is seen on follow-up MR imaging, many neurologists would strongly consider starting therapy.

In 1 retrospective study in which a small cohort of patients with RIS received MS disease-modifying therapies, the 5-year risk of developing an MS-defining clinical event was 45% (33/73 patients) in those receiving disease-modifying therapies versus 31% (117/378) in those who did not receive disease-modifying therapies.[12] There are several RIS randomized clinical trials ongoing that are evaluating whether starting dimethyl fumarate or teriflunomide will prevent or delay conversion to clinically definite MS versus a placebo.

RIS in Pediatrics

There are limited data on the prevalence and clinical significance of RIS in children. In a review of brain MRIs in 3966 pediatric patients,[53] only 1 patient (0.03%) was identified as fulfilling the RIS criteria. In a longitudinal multicenter study[54] of 38 pediatric patients with a median age of 15 years who were diagnosed with RIS based on the McDonald 2010 DIS criteria, 42% experienced a first clinical neurologic attack with a median interval of 2 years. In addition, radiologic progression was reported in 61% of the study cohort. These reported numbers are very similar to those of RIS in adult patients; however, the study found that clinical conversion to MS occurs after a shorter interval in pediatric patients compared with adults. Most important, the authors also reported that the presence of ≥2 CSF-related oligoclonal bands or spinal cord lesions was a significant predictor of clinical conversion.[55] The conventional MR imaging findings in children are not different from those seen in adult patients with RIS. Because there are sparse data available on RIS in children, there is not sufficient evidence to conclude that these patients could potentially benefit from early disease-modifying treatment.[56]

CONCLUSIONS

There are patients without a defined neurologic event who have MR imaging findings that fulfill the imaging criteria for MS. After an extensive work-up to exclude other neurologic, systemic, or iatrogenic etiologies, these patients are labeled as fulfilling the criteria for RIS. At baseline and in follow-up, the presence of imaging factors (spinal lesions, enhancing lesions, corpus callosum lesions), demographic characteristics (men, pregnant women, younger age, relative of a patient with MS), and/or CSF markers (oligoclonal bands) incurs a higher risk of subsequent conversion to MS. Radiologists who identify patients with classic MS-like lesions in the appropriate clinical and patient group settings should suggest

the RIS entity. The surveillance of patients with RIS, the agent and extent of treatment, and long-term outcomes are subjects of ongoing debate and clinical trials. More studies are also needed with advanced MR imaging techniques to investigate whether novel technologies being developed will help identify which patients with RIS are at greatest risk for conversion to clinically definite MS.

Disclosures: Scott D. Newsome—*UNRELATED*: *Consultancy*: Biogen, Genentech, Celgene, EMD Serono, *Comments*: attended scientific advisory board meetings; *Grants/Grants Pending*: Biogen, Novartis, Genentech, National Multiple Sclerosis Society, Department of Defense, and Patient-Centered Outcomes Research Institute*; *Other*: Gerson Lehrman Group, BioIncept, and MedDay Pharmaceuticals, *Comments*: advisor for Gerson Lehrman Group and BioIncept and a clinical adjudication committee member for a MedDay Pharmaceuticals clinical trial. David M. Yousem—*UNRELATED*: *Board Membership*: mrionline.com, *Comments*: unpaid board member; *Expert Testimony*: medicolegal reviews; *Payment for Lectures Including Service on Speakers Bureaus*: mrionline.com, American College of Radiology speaker; *Royalties*: Elsevier for 5 books, informational analytics for peer review program; *Payment for Development of Educational Presentations*: mrionline.com. *Money paid to the institution.

REFERENCES

1. Thompson AJ, Banwell BL, Barkhof F, et al. **Diagnosis of multiple sclerosis: 2017 revisions of the McDonald criteria.** *Lancet Neurol* 2018;17:162–73 CrossRef Medline
2. De Stefano N, Giorgio A, Tintoré M, et al; MAGNIMS study group. **Radiologically isolated syndrome or subclinical multiple sclerosis: MAGNIMS consensus recommendations.** *Mult Scler* 2018;24:214–21 CrossRef Medline
3. Morris Z, Whiteley WN, Longstreth WT Jr, et al. **Incidental findings on brain magnetic resonance imaging: systematic review and meta-analysis.** *BMJ* 2009;339:b3016 CrossRef Medline
4. Yamout B, Al Khawajah M. **Radiologically isolated syndrome and multiple sclerosis.** *Mult Scler Relat Disord* 2017;17:234–37 CrossRef Medline
5. Forslin Y, Granberg T, Jumah AA, et al. **Incidence of radiologically isolated syndrome: a population-based study.** *AJNR Am J Neuroradiol* 2016;37:1017–22 CrossRef Medline
6. Gabelic T, Ramasamy DP, Weinstock-Guttman B, et al. **Prevalence of radiologically isolated syndrome and white matter signal abnormalities in healthy relatives of patients with multiple sclerosis.** *AJNR Am J Neuroradiol* 2014;35:106–12 CrossRef Medline
7. Liu S, Kullnat J, Bourdette D, et al. **Prevalence of brain magnetic resonance imaging meeting Barkhof and McDonald criteria for dissemination in space among headache patients.** *Mult Scler* 2013;19:1101–05 CrossRef Medline
8. Granberg T, Martola J, Kristoffersen-Wiberg M, et al. **Radiologically isolated syndrome–incidental magnetic resonance imaging findings suggestive of multiple sclerosis, a systematic review.** *Mult Scler* 2013;19:271–80 CrossRef Medline
9. Okuda DT, Mowry EM, Beheshtian A, et al. **Incidental MRI anomalies suggestive of multiple sclerosis: the radiologically isolated syndrome.** *Neurology* 2009;72:800–05 CrossRef Medline
10. Lebrun C. **The radiologically isolated syndrome.** *Rev Neurol (Paris)* 2015;171:698–706 CrossRef Medline
11. Polman CH, Reingold SC, Banwell B, et al. **Diagnostic criteria for multiple sclerosis: 2010 revisions to the McDonald criteria.** *Ann Neurol* 2011;69:292–302 CrossRef Medline
12. Okuda DT, Siva A, Kantarci O, et al; Radiologically Isolated Syndrome Consortium (RISC) and Club Francophone de la Sclérose en Plaques (CFSEP). **Radiologically isolated syndrome: 5-year risk for an initial clinical event.** *PLoS One* 2014;9:e90509 CrossRef Medline
13. De Stefano N, Stromillo ML, Rossi F, et al. **Improving the characterization of radiologically isolated syndrome suggestive of multiple sclerosis.** *PLoS One* 2011;6:e19452 CrossRef Medline
14. Giorgio A, Stromillo ML, Rossi F, et al. **Cortical lesions in radiologically isolated syndrome.** *Neurology* 2011;77:1896–99 CrossRef Medline
15. Sati P, Oh J, Constable RT, et al; NAIMS Cooperative. **The central vein sign and its clinical evaluation for the diagnosis of multiple sclerosis: a consensus statement from the North American Imaging in Multiple Sclerosis Cooperative.** *Nat Rev Neurol* 2016;12:714–22 CrossRef Medline
16. Suthiphosuwan S, Sati P, Guenette M, et al. **The central vein sign in radiologically isolated syndrome.** *AJNR Am J Neuroradiol* 2019;40:776–83 CrossRef Medline
17. Oh JS, Guenette S, Absinta M, et al. **The central vein sign and paramagnetic rim sign in white matter lesions of radiologically isolated syndrome (S6.003).** *Neurology* 2019;92:(15 Suppl):S6.003
18. Rojas JI, Patrucco L, Miguez J, et al. **Brain atrophy in radiologically isolated syndromes.** *J Neuroimaging* 2015;25:68–71 CrossRef Medline
19. George IC, El Mendili MM, Inglese M, et al. **Cerebellar volume loss in radiologically isolated syndrome.** *Mult Scler* 2019 Nov 4. [Epub ahead of Print] CrossRef Medline
20. Stromillo ML, Giorgio A, Rossi F, et al. **Brain metabolic changes suggestive of axonal damage in radiologically isolated syndrome.** *Neurology* 2013;80:2090–94 CrossRef Medline
21. Giorgio A, Stromillo ML, De Leucio A, et al. **Appraisal of brain connectivity in radiologically isolated syndrome by modeling imaging measures.** *J Neurosci* 2015;35:550–58 CrossRef Medline
22. Alcaide-Leon P, Cybulsky K, Sankar S, et al. **Quantitative spinal cord MRI in radiologically isolated syndrome.** *Neurol Neuroimmunol Neuroinflamm* 2018;5:e436 CrossRef Medline
23. Thouvenot E, Hinsinger G, Demattei C, et al. **Cerebrospinal fluid chitinase-3-like protein 1 level is not an independent predictive factor for the risk of clinical conversion in radiologically isolated syndrome.** *Mult Scler* 2019;25:669–677 CrossRef Medline
24. Okuda DT, Mowry EM, Cree BA, et al. **Asymptomatic spinal cord lesions predict disease progression in radiologically isolated syndrome.** *Neurology* 2011;76:686–92 CrossRef Medline
25. Etemadifar M, Janghorbani M, Koushki MM, et al. **Conversion from radiologically isolated syndrome to multiple sclerosis.** *Int J Prev Med* 2014;5:1379–86 Medline
26. Bisulca J, De Lury A, Coyle PK, et al. **MRI features associated with high likelihood of conversion of radiologically isolated syndrome to multiple sclerosis.** *Mult Scler Relat Disord* 2019;36:101381 CrossRef Medline
27. Maia AC Jr, Rocha AJ, Barros BR, et al. **Incidental demyelinating inflammatory lesions in asymptomatic patients: a Brazilian cohort with radiologically isolated syndrome and a critical review of current literature.** *Arq Neuropsiquiatr* 2012;70:5–11 CrossRef Medline
28. Lebrun C, Bensa C, Debouverie M, et al; Club Francophone de la Sclérose en Plaques. **Association between clinical conversion to multiple sclerosis in radiologically isolated syndrome and magnetic resonance imaging, cerebrospinal fluid, and visual evoked potential: follow-up of 70 patients.** *Arch Neurol* 2009;66:841–46 CrossRef Medline
29. Kantarci OH, Lebrun C, Siva A, et al. **Primary progressive multiple sclerosis evolving from radiologically isolated syndrome.** *Ann Neurol* 2016;79:288–94 CrossRef Medline
30. Rossi S, Motta C, Studer V, et al. **Subclinical central inflammation is risk for RIS and CIS conversion to MS.** *Mult Scler* 2015;21:1443–52 CrossRef Medline
31. Matute-Blanch C, Villar LM, Alvarez-Cermeno JC, et al. **Neurofilament light chain and oligoclonal bands are prognostic biomarkers in radiologically isolated syndrome.** *Brain* 2018;141:1085–93 CrossRef Medline
32. Lebrun C, Le Page E, Kantarci O, et al; Club Francophone de la Sclerose en Plaques (CFSEP) and the Radiologically Isolated Syndrome Consortium (RISC) Group. **Impact of pregnancy on conversion to clinically isolated syndrome in a radiologically isolated syndrome cohort.** *Mult Scler* 2012;18:1297–1302 CrossRef Medline
33. Tintore M, Rovira A, Rio J, et al. **Baseline MRI predicts future attacks and disability in clinically isolated syndromes.** *Neurology* 2006;67:968–72 CrossRef Medline
34. Miller DH, Chard DT, Ciccarelli O. **Clinically isolated syndromes.** *Lancet Neurol* 2012;11:157–69 CrossRef Medline

35. Brownlee WJ, Miller DH. **Clinically isolated syndromes and the relationship to multiple sclerosis.** *J Clin Neurosci* 2014;21:2065–71 CrossRef Medline
36. Giorgio A, Battaglini M, Rocca MA, et al; MAGNIMS Study Group. **Location of brain lesions predicts conversion of clinically isolated syndromes to multiple sclerosis.** *Neurology* 2013;80:234–41 CrossRef Medline
37. Sombekke MH, Wattjes MP, Balk LJ, et al. **Spinal cord lesions in patients with clinically isolated syndrome: a powerful tool in diagnosis and prognosis.** *Neurology* 2013;80:69–75 CrossRef Medline
38. Uher T, Horakova D, Bergsland N, et al. **MRI correlates of disability progression in patients with CIS over 48 months.** *Neuroimage Clinical* 2014;6:312–19 CrossRef Medline
39. Miller DH, Weinshenker BG, Filippi M, et al. **Differential diagnosis of suspected multiple sclerosis: a consensus approach.** *Mult Scler* 2008;14:1157–74 CrossRef Medline
40. Solomon AJ, Klein EP, Bourdette D. "**Undiagnosing" multiple sclerosis: the challenge of misdiagnosis in MS.** *Neurology* 2012;78:1986–91 CrossRef Medline
41. Solomon AJ, Bourdette DN, Cross AH, et al. **The contemporary spectrum of multiple sclerosis misdiagnosis: a multicenter study.** *Neurology* 2016;87:1393–99 CrossRef Medline
42. Pakpoor J, Saylor D, Izbudak I, et al. **Follow-up of emergency department MRI scans suggesting new diagnosis of CNS demyelination.** *AJR Am J Roentgenol* 2017;209:171–75 CrossRef Medline
43. Schaffler N, Kopke S, Winkler L, et al. **Accuracy of diagnostic tests in multiple sclerosis: a systematic review.** *Acta Neurol Scand* 2011;124:151–64 CrossRef Medline
44. Tornatore C, Phillips JT, Khan O, et al. **Consensus opinion of US neurologists on practice patterns in RIS, CIS, and RRMS: evolution of treatment practices.** *Neurol Clin Pract* 2016;6:329–38 CrossRef Medline
45. Fernandez O, Delvecchio M, Edan G, et al. **Survey of diagnostic and treatment practices for multiple sclerosis in Europe.** *Eur J Neurol* 2017;24:516–22 CrossRef Medline
46. Carnero Contentti E, Pettinicchi JP, Caride A, et al. **Decision-making on radiologically isolated syndrome among Argentinean neurologists: a survey based on clinical experience.** *Mult Scler Relat Disord* 2019;27:61–64 CrossRef Medline
47. Boyko A. **Radiologically isolated syndrome with oligoclonal bands in CSF (RIS + OCB) can be classified as high MS risk group**. *Mult Scler* 2020;26:869–70 CrossRef Medline
48. Filippatou A, Shoemaker T, Esch M, et al. **Spinal cord and infratentorial lesions in radiologically isolated syndrome are associated with decreased retinal ganglion cell/inner plexiform layer thickness.** *Mult Scler* 2019;25:1878–87 CrossRef Medline
49. Vural A, Okar S, Kurne A, et al. **Retinal degeneration is associated with brain volume reduction and prognosis in radiologically isolated syndrome.** *Mult Scler* 2020;26:38–47 CrossRef Medline
50. Pierrot-Deseilligny C, Souberbielle JC. **Vitamin D and multiple sclerosis: an update.** *Mult Scler Relat Disord* 2017;14:35–45 CrossRef Medline
51. Traboulsee A, Simon JH, Stone L, et al. **Revised Recommendations of the Consortium of MS Centers Task Force for a Standardized MRI Protocol and Clinical Guidelines for the Diagnosis and Follow-Up of Multiple Sclerosis.** *AJNR Am J Neuroradiol* 2016;37:394–401 CrossRef Medline
52. Makhani N. **Treatment considerations in the radiologically isolated syndrome.** *Curr Treat Options Neurol* 2020;22:3 CrossRef Medline
53. Jansen PR, Dremmen M, van den Berg A, et al. **Incidental findings on brain imaging in the general pediatric population.** *N Engl J Med* 2017;377:1593–95 CrossRef Medline
54. Makhani N. **The radiologically isolated syndrome: an opportunity to prevent multiple sclerosis in children.** *Pediatr Neurol* 2018;85:13–15 CrossRef Medline
55. Makhani N, Lebrun C, Siva A, et al; Observatoire Francophone de la Sclérose en Plaques (OFSEP), Société Francophone de la Sclérose en Plaques (SFSEP), the Radiologically Isolated Syndrome Consortium (RISC) and the Pediatric Radiologically Isolated Syndrome Consortium (PARIS). **Oligoclonal bands increase the specificity of MRI criteria to predict multiple sclerosis in children with radiologically isolated syndrome.** *Mult Scler J Exp Transl Clin* 2019;5:2055217319836664 CrossRef Medline
56. Wilbur C, Yeh EA. **Radiologically isolated syndrome in children: current knowledge and future directions.** *Mult Scler Relat Disord* 2018;24:79–84 CrossRef Medline
57. Barkhof F, Filippi M, Miller DH, et al. **Comparison of MRI criteria at first presentation to predict conversion to clinically definite multiple sclerosis.** *Brain* 1997;120:2059–69 CrossRef Medline
58. McDonald WI, Compston A, Edan G, et al. **Recommended diagnostic criteria for multiple sclerosis: guidelines from the International Panel on the Diagnosis of Multiple Sclerosis.** *Ann Neurol* 2001;50:121–27 CrossRef Medline
59. Swanton JK, Fernando K, Dalton CM, et al. **Modification of MRI criteria for multiple sclerosis in patients with clinically isolated syndromes.** *J Neurol Neurosurg Psychiatry* 2006;77:830–33 CrossRef Medline
60. Filippi M, Rocca MA, Ciccarelli O, et al. **MRI criteria for the diagnosis of multiple sclerosis: MAGNIMS consensus guidelines.** *Lancet Neurol* 2016;15:292–303 CrossRef Medline

Diagnostic Performance of PET and Perfusion-Weighted Imaging in Differentiating Tumor Recurrence or Progression from Radiation Necrosis in Posttreatment Gliomas: A Review of Literature

N. Soni, M. Ora, N. Mohindra, Y. Menda, and G. Bathla

ABSTRACT

SUMMARY: Tumor resection followed by chemoradiation remains the current criterion standard treatment for high-grade gliomas. Regardless of aggressive treatment, tumor recurrence and radiation necrosis are 2 different outcomes. Differentiation of tumor recurrence from radiation necrosis remains a critical problem in these patients because of considerable overlap in clinical and imaging presentations. Contrast-enhanced MR imaging is the universal imaging technique for diagnosis, treatment evaluation, and detection of recurrence of high-grade gliomas. PWI and PET with novel radiotracers have an evolving role for monitoring treatment response in high-grade gliomas. In the literature, there is no clear consensus on the superiority of either technique or their complementary information. This review aims to elucidate the diagnostic performance of individual and combined use of functional (PWI) and metabolic (PET) imaging modalities to distinguish recurrence from posttreatment changes in gliomas.

ABBREVIATIONS: AAT = amino acid tracer; ASL = arterial spin-labeling; AUC = area under the curve; ^{11}C-MET = ^{11}C-methionine; DCE = dynamic contrast-enhanced; FDOPA = 6-[^{18}F]fluoro-L-dopa; FET = [^{18}F]fluoroethyl-L-tyrosine; FLT = ^{18}F-fluorothymidine; HGG = high-grade glioma; K^{trans} = volume transfer constant; rCBV = relative cerebral blood volume; RN = radiation necrosis; TBR = tumor-to-background ratio; TR = tumor recurrence; Ve = volume of tissue; Vp = plasma volume

Gliomas are primary brain tumors with an incidence of 5–6 per 100,000 population. Glioblastoma is the most common and aggressive subtype with a median survival period of <15 months and a 5-year survival rate of <10%.[1] The current criterion standard treatment for high-grade gliomas (HGGs) is maximum tumor resection followed by radiation therapy with concurrent and adjuvant temozolomide-based chemotherapy, which has shown improved survival. Despite advances in imaging and multidisciplinary treatment, glioblastoma carries a dismal prognosis. Chemoradiation may induce new enhancement and edema that may mimic tumor recurrence (TR) or progression on follow-up imaging. TR is inevitable after a median survival time of 32–36 weeks.[2] Radiation necrosis (RN) may also manifest as new or increased enhancement caused by disruption of the BBB from detrimental effects of radiation on the surrounding healthy tissue. RN usually manifests 3–12 months after radiation therapy with an incidence of 3%–24% depending on radiation dose.[3] Apart from RN, pseudoprogression and pseudoresponse are 2 new posttreatment entities that have been recognized during follow-up. Pseudoprogression may constitute an overresponse to effective treatment with a reported incidence of 10%–30% and usually occurs within the first 3 months after completing radiation therapy with or without temozolomide. Pseudoresponse refers to a transient rapid decrease in lesion enhancement and surrounding edema after antiangiogenic treatment (ie, bevacizumab) by normalizing the BBB and mimicking favorable tumor response while the actual tumor remains viable or progresses.[2,4,5]

Contrast-enhanced MR imaging remains the primary imaging technique in HGG follow-up because of its widespread availability and excellent soft-tissue and contrast resolution. A recent meta-analysis of glioblastoma with enhancing lesions on posttreatment MR imaging revealed true progression in 60% and treatment-related changes in 36% of patients.[6] Posttreatment evaluation is generally based on Response Assessment in Neuro-Oncology criteria that rely on clinical condition, lesion size, and enhancement.[7] Recently, The Response Assessment in Neuro-Oncology working group recommended PET using radio-labeled amino acids as an additional tool in the diagnostic assessment of brain tumors.[8] Differentiation of "tumor progression/recurrence"

Received January 8, 2020; accepted after revision May 29.

From the Department of Radiology (N.S., Y.M., G.B.), University of Iowa Hospitals and Clinics, Iowa City, Iowa; and Department of Radiodiagnosis (M.O., N.M.), Sanjay Gandhi Post Graduate Institute of Medical Sciences, Institute of Nuclear Medicine, Lucknow, India.

Neetu Soni and Manish Ora share first authorship.

Please address correspondence to Neetu Soni, MD, Department of Nuclear Medicine, University of Iowa Hospitals and Clinics, 200 Hawkins Dr, Iowa City, IA 52242; e-mail: neetu-soni@uiowa.edu; @NeetuSo27437480

Indicates open access to non-subscribers at www.ajnr.org

Indicates article with supplemental on-line tables.

http://dx.doi.org/10.3174/ajnr.A6685

and "treatment-related changes" is still challenging, and to date, no single technique provides a reliable detection of glioma recurrence. Biopsy remains the criterion standard to give immediate therapy decisions compared with clinical follow-up. However, as an invasive procedure, it is associated with morbidity and mortality rates of 1%–5% and 0%–2.3%, respectively.[9] It is also important for pathologists to be aware of tumor heterogeneity while analyzing biopsy samples in these cases.[5]

There is no standard management for recurrent glioblastoma, and patients may undergo reoperation, re-radiation, or chemotherapy with progression-free survival and overall survival of 10 and 30 weeks, respectively.[10] Thus, accurate and timely diagnosis of recurrent tumor is necessary to reduce the surgical risk and health care cost and improve the quality of life. Limitations of conventional imaging in evaluating posttreatment changes have encouraged the use of advanced MR imaging techniques (perfusion, diffusion-weighted, and spectroscopy) and PET imaging with novel radiopharmaceuticals. Both imaging modalities have their advantages and limitations at the expense of time and cost burden.

PWI is commonly used for the primary diagnosis and posttreatment glioma surveillance. The 3 most frequently used MR perfusion techniques are T2*-based dynamic susceptibility contrast (DSC); T1-weighted dynamic contrast-enhanced (DCE), which uses exogenous contrast; and arterial spin-labeling (ASL) based on arterial endogenous tracer.[11,12] Because PET is a functional technique, it may provide additional insight beyond MR imaging into the biology of gliomas, which may have a potential role in the noninvasive grading, tumor delineation, radiation therapy planning, and posttreatment response evaluation.[13] Use of [^{18}F] FDG is widespread in clinical nuclear medicine and is of relatively low cost. Because of the low tracer uptake in gray matter, amino acid tracers (AATs) are very helpful in differentiating TR from treatment-induced changes. ^{11}C-methionine (^{11}C-MET) is the most studied and validated AAT.[8] With the advent of integrated PET/MR imaging in clinical practice, studies have shown a strong correlation between these 2 modalities by providing complete anatomic, functional, and metabolic information of tumors at a single point of time. This review summarizes the current role, limitations, and challenges of perfusion MR imaging and PET imaging to differentiate TR or progression from RN in gliomas.

Literature Search

We searched PubMed to collect relevant published articles (up to October 2019) aiming to provide independent or comparative results of these 2 imaging modalities in differentiating TR or progression from RN in gliomas. Eligible studied fulfilled the following criteria: 1) pathologically proved glioma (grades II–IV); 2) newly enhancing lesions on imaging, with diagnoses of TR or RN on PET, PWI, or both; 3) definitive diagnosis based on histopathology and/or clinical and imaging follow-up; 4) sample size $\geq$20 for individual technique and $\geq$10 for combined studies; and 5) full-text articles in English. We followed a nonquantitative approach and extracted the relevant information from each article.

Perfusion-Weighted Imaging

Parameters derived from perfusion MR imaging indirectly evaluate tumor neoangiogenesis by assessing blood volume, blood flow, and permeability. Whereas TR reflects hyperperfusion caused by associated neoangiogenesis, RN shows hypoperfusion caused by coagulative necrosis. DSC is the most widely used PWI because of the short acquisition time and widely available user-friendly postprocessing software. However, DSC has susceptibility artifacts and effects of contrast leakage. DCE provides better spatial resolution, is less prone to susceptibility artifacts, and evaluates both blood volume and permeability. However, the complex pharmacokinetic compartment models and nonavailability of user-friendly or vendor-based standardized software limit the use of DCE-PWI. Relative cerebral blood volume (rCBV) is the most validated perfusion parameter for evaluation of brain tumors that can be assessed both qualitatively and quantitatively.[11,12] ASL is a noninvasive perfusion technique that uses magnetically labeled arterial blood as an endogenous tracer, so it is less prone to susceptibility artifacts. ASL provides absolute quantification of CBF that is reliable and reproducible and correlates with other perfusion techniques.[11] Several studies have shown the usefulness of DSC, DCE, and ASL to distinguish TR from RN in gliomas (On-line Table 1).[14-27]

A few studies have compared DSC and DCE perfusion techniques for differentiating TR from RN (On-line Table 1).[22,23,25] A recent meta-analysis including 28 articles demonstrated a pooled sensitivity and specificity of 90% and 88% for DSC and 89% and 85% for DCE, respectively.[28] Another meta-analysis also verified similar results, with a pooled sensitivity and specificity of 87% and 86% for DSC and 92% and 85% for DCE, respectively. The study reported a wide range of optimal rCBV cutoff values (range, 0.71–3.7) to reliably distinguish TR from RN because of technical issues such as vascular leak.[29] Kim et al,[30] in their large retrospective study, reported the added value of either DSC or DCE-PWI to the routine MR imaging in significantly improving the prediction of recurrent glioblastoma. Using a mean rCBV threshold of 1.8, Young et al[15] found 100% sensitivity and 75% specificity in identifying TR. Nael et al[22] found 80% sensitivity and 92% specificity by using a mean rCBV threshold of 2.2. Di Costanzo et al[16] also found significantly higher rCBV values in recurrent glioma than in RN and reported similar diagnostic accuracy (86%) as in the literature. Wang et al[18] used maximum rCBV instead of rCBV mean values and reported 62% sensitivity and 80% specificity at a cutoff of 4.4. In many cases, TR coexists with RN, leading to overlap of the rCBV ratios.[19] Blasel et al[19] also reported superior diagnostic accuracy of maximum rCBV (sensitivity, 78%; specificity, 86%) compared with rCBVmean (sensitivity, 65%; specificity, 71%), which reflects tumor heterogeneity and regional perfusion differences.

A recent meta-analysis by van Dijken et al[29] showed higher diagnostic accuracy of DCE compared with DSC, but another meta-analysis by Patel et al,[28] showed equal diagnostic accuracy of both in differentiating TR from RN. DCE-derived parameters include volume transfer constant (K^{trans}), extravascular extracellular space per unit volume of tissue (Ve), and plasma volume (Vp).[4,29] Yun et al[21] found mean K^{trans} as the most promising parameter in differentiating true progression from pseudo-

progression (sensitivity, 59%; specificity, 94%) compared with Vp. On the contrary, Thomas et al[20] found higher area under curve (AUC) for Vp compared with K^{trans} in differentiating pseudoprogression (Vp cutoff, <3.7; sensitivity, 85%; specificity, 79%) from true progression (mean K^{trans} >3.6; sensitivity, 69%; specificity, 79%). The increased permeability may confound K^{trans} because of radiation-induced endothelial damage. Zakhari et al[23] reported DSC-derived rCBV measurement as more accurate than DCE in differentiating TR from RN. They argued against the routine use of DCE perfusion in posttreatment evaluation of HGGs. Seeger et al[25] also reported similar results and found better diagnostic performance of rCBV compared with K^{trans}. On the contrary, Shin et al[31] showed statistically significant differences in K^{trans} and rCBV and suggested that DCE is more accurate than DSC in posttreatment evaluation of HGGs. Few studies discuss the role of ASL to differentiate TR from posttreatment evaluation of HGGs (On-line Table 1).[24-27] A meta-analysis identified low diagnostic accuracy of ASL with pooled sensitivity of 52%–79% and specificity of 64%–82%.[29] Ye et al[24] found a close linear correlation between ASL and DSC PWI in the differentiation of TR from RN. ASL could be an ideal imaging technique for the long-term follow-up of gliomas after treatment, including those with renal dysfunction.[24]

PET with Novel Radiotracers

PET/CT provides clinically invaluable information about detection, grading, biopsy site selection, and assessing treatment response of tumors.[13] On-line Table 2 summarizes the various PET radiotracers and their uptake mechanism, half-life, availability, and uptake in the healthy brain. We will discuss the most commonly used FDG,[32-37] and other various radio-labeled AATs such as ^{11}C-MET),[32,36,38-42] 6[^{18}F]fluoro-L-dopa (FDOPA),[43-45] and [^{18}F]fluoroethyl-L-tyrosine (FET),[46-51] as well as ^{18}F-fluorothymidine (FLT),[50,52] which evaluates DNA syntheses (On-line Table 3).

Glucose Metabolism: FDG-PET

[^{18}F]-FDG is a glucose analog that is actively transported into the cells by glucose transporter proteins and phosphorylated to FDG-6-phosphate. In cancer cells, increased mitosis, anaerobic glycolysis, glucose transporter proteins level, and glycolytic enzymes contribute to the higher uptake of FDG. Patronas et al[53] first, in 1982, used [^{18}F]-FDG to evaluate posttreatment changes in gliomas. After that, several studies have shown FDG-PET as a useful diagnostic tool to distinguish TR from RN with variable sensitivity (71%–86%) and specificity (62%–100%).[32,35-37,43,54,55] Gómez-Río et al[37] reported higher sensitivity (78%) and specificity (95%) of FDG-PET compared with ^{201}Tl SPECT in differentiating TR from RN. A meta-analysis including 16 studies reported a pooled sensitivity and specificity of 77% and 78%, respectively.[56] Another meta-analysis also confirmed similar results.[52] Few FDG-PET studies have shown comparable results to MR imaging and suggested that simultaneous PET/MR imaging offers a synergistic multiparametric assessment of recurrence with improved diagnostic accuracy.[54,55] FDG-PET has inherent limitations of high physiologic uptake in the healthy brain and inflammatory tissue. Hence, the use of various AATs has been proposed.[32,33,36,52]

Amino Acid Transport and Protein Synthesis

PET with AAT-^{11}C-MET,[32,36,39,40,42] [^{18}F] FET,[46-50] and [^{18}F] FDOPA[33,43-45] has shown remarkable results in evaluating posttreatment changes of gliomas. Radiolabeled AATs show high tumor-to-background ratio (TBR) in gliomas because of increased cell proliferation and extracellular matrix production.

^{11}C-MET is the most studied and validated AAT. Several studies have reported variable sensitivities (66%–91%) and specificities (60%–100%) to differentiate between TR and RN.[32,36,39-42] Semiquantitative analysis of ^{11}C-MET provided an early diagnosis with high diagnostic accuracy even for small lesions.[41] Qualitative visual interpretation of the images has also shown adequate results for the TR diagnosis.[40] A meta-analysis of ^{11}C-MET, including 7 studies, reported a pooled sensitivity of 70% and specificity of 93% for detection of recurrence in HGGs.[56] ^{11}C-MET-PET has shown good correlation with MR imaging, and simultaneous PET/MR imaging could achieve higher diagnostic accuracy.[38,39]

FET-PET has been also reported to be reliable in differentiating posttherapeutic benign changes from TR.[46,47] FET-PET has shown diagnostic performance similar to FLT and ^{11}C-MET.[49,50] In a meta-analysis, [^{18}F] FET had good diagnostic accuracy in differentiating TR from RN with pooled sensitivity and specificity of 82% and 80%, respectively.[57] In a recent systematic review, [^{18}F] FET reported better diagnostic performance than FDG and ^{11}C-MET.[58]

[^{18}F] FDOPA is an ideal radiotracer with a longer half-life that shows high uptake in gliomas with low background signal. A number of studies have shown better results with [^{18}F] FDOPA in evaluating posttreatment changes in gliomas (On-line Table 3). FDOPA-PET has shown superior diagnostic performance (sensitivity, specificity, and accuracy of 100%, 85.7%, and 96.4%, respectively) compared with FDG (sensitivity, specificity, and accuracy of 47.6%, 100%, and 60.7%, respectively) in differentiating TR from RN.[33] In a recent meta-analysis of 48 studies, [^{18}F] FDOPA has shown a significant advantage in the diagnosis of glioma recurrence in comparison with [^{18}F] FET (AUC values, 0.9691 versus 0.9124; P = .015), though both exhibited moderate overall accuracy in diagnosing TR from RN.[57]

Cell Proliferation and Membrane Biosynthesis

Cell proliferation and DNA replication are characteristic of malignant transformation. The pyrimidine analog 3′-deoxy-3′-FLT acts as a marker of tumor proliferation, and its uptake in the brain depends on the BBB permeability, thus providing high tumor-to-background contrast in brain tumors.[59] PET using FLT is found to be an excellent technique for gliomas, with a reported sensitivity of 83%–95% and specificity of 72%–100% for detecting TR.[33,44,45] A meta-analysis including 24 studies (799 patients) concluded moderately better accuracy of FLT in comparison with FDG for diagnosing TR.[52] FLT uptake is a function of the plasma input function and its transport rate across the BBB. Therefore, a kinetic model of [^{18}F] FLT uptake, transport, and metabolism is required to quantify DNA synthesis in tumors.[60] The assumption

that [^{18}F] FLT reflects the DNA synthesis may be misleading without a kinetic model.[61] However, in contrast to the FET, no significant advantage was found for FLT.[50] Choline is a precursor for phosphatidylcholine and other phospholipids biosynthesis, which are essential components of the cell membrane and increases in cell proliferation.[62] A recent meta-analysis revealed high diagnostic accuracy for the identification of TR from the RN with pooled sensitivity and specificity of 87% and 82%, respectively.[63] But the number of patients in these studies was relatively small, so no reliable conclusion could not be drawn.

Apart from visual analysis, various parameters have been developed to evaluate the PET images. TBR is helpful in the primary diagnosis and is of paramount importance in follow-up for the posttreatment response evaluation of tumors. Metabolic tumor volume measurement correlates with the overall survival. Recently, a few studies have also shown the feasibility and the added advantage of dynamic PET over static PET acquisition.[48,64] For static images, the most commonly used parameters are tumor to normal uptake (T/N), standardized uptake values, and metabolic tumor volume. Higher T/N ratios are found associated with poor prognosis for overall survival and progression-free survival in patients with brain tumors.[65]

Dynamic imaging is increasingly used in PET/CT to evaluate brain tumors. After dynamic acquisition, tumors are delineated by using region of interest or volume of interest on all time frames of the dynamic PET data, and time-activity curves are extracted. Time-activity curves are then categorized by various shapes into different time-activity curve patterns, such as increasing plateau or decreasing uptake.[48] Other parameters such as maximal TBR and minimal time-to-peak could also be derived.[66]

Combined Use of PET and Perfusion MR Imaging

We have observed the individual roles of PET and PWI in posttreatment evaluation of gliomas. In this section, we include studies that simultaneously used both modalities (either by using hybrid PET/MR imaging or individual PET and MR imaging) in similar groups of patients to distinguish TR from RN. A total of 14 studies were found, including [^{18}F] FDG ($n = 6$),[54,55,67-70] [^{18}F] FET ($n = 4$),[51,71-73] ^{11}C-MET ($n = 2$),[38,74] FDOPA ($n = 1$),[75] and combined FDG with ^{11}C-MET ($n = 1$)[36] (On-line Table 4). Hybrid PET/MR imaging improved the overall diagnostic accuracy either by simultaneously or sequentially acquiring the morphologic and functional information in a single short acquisition time.[76] Kim et al[36] first analyzed the combined use of [^{18}F] FDG, ^{11}C-MET-PET, and DSC PWI in a small cohort of 10 HGGs. DSC showed statistically insignificant superior results over PET in distinguishing TR from RN. Subsequently, several studies have reported better diagnostic accuracy by simultaneous use of PET and PWI (On-line Table 4).[36,38,51,54,55,67-75] In a pilot study of 30 HGGs, ASL provided better results than DSC and FDG in detecting TR. However, DSC provided better spatial resolution with improved sensitivity when predominant TR with superimposed regions of predominant mixed RN were excluded while ASL sensitivity remained unchanged.[54] Although DSC is the most commonly used PWI, DCE has also shown promising results. Hatzoglou et al[68] validated the superior performance of the DCE imaging over FDG in assessing the TR in a heterogeneous cohort of 53 patients (29 gliomas and 24 metastases). DCE (AUC = 0.87) outperformed FDG-PET (AUC = 0.75), and the Vp ratio alone yielded higher predictive value compared with combination of K^{trans} and the standard uptake value ratio.[68] In a recent study by Seligman et al,[70] FDG-PET and DCE MR imaging showed comparable accuracy and sensitivity in identifying tumor progression, but DCE MR imaging had better specificity. The authors also found the effect of genetic mutations on perfusion–metabolism mismatch for 11 patients with HGGs. Tumors with receptor tyrosine kinase mutations showed less permeability, and tumors with *IDH* mutations showed lower FDG avidity. Other mutations (RB, p53, and *MGMT*) were not associated with any perfusion–metabolism discordance.[70] The authors concluded that a combination of FDG-PET and DCE MR imaging cutoff parameters provides the best diagnostic utility in distinguishing TR from RN. Both modalities achieved high sensitivities, but DCE MR imaging had better specificity.[70]

Integrated PET/MR imaging simultaneously acquires functional and structural parameters, which might have the potential to impact patient management by timely and accurate recognition of TR.[55,71,72] AATs show superior contrast to that of FDG because of low uptake in the normal brain tissue. [^{18}F] FET provides valuable information for re-radiation treatment planning of HGGs by differentiating metabolically active tumor from normal brain tissue.[66] Jena et al[51] in their multiple receiver operating characteristic analysis found FET uptake, the Cho/Cr ratio, and rCBVmean to be the most useful parameters to distinguish glioma recurrence from RN. The accuracy of rCBVmean improved after adding maximal TBR or the Cho/Cr ratio. TBR with the Cho/Cr ratio yielded the highest accuracy of 97%. In another retrospective study, a combination of rCBVmean, ADCmean, and Cho/Cr resulted in an AUC of 0.91, and a combination of FDG TBR further increased diagnostic accuracy (AUC $>$ 0.93).[55] Among all individual parameters, the Cho/Cr ratio and FET or FDG TBRmean were the most significant discriminators for the prediction of recurrence.[51,55] The same group also demonstrated a moderate positive correlation between the FET uptake and rCBV mean, which mirrored the coupled vascularity and amino acid uptake with endothelial proliferation and mitotic activity of the tumor. The diagnostic accuracy, sensitivity, and specificity for recurrence detection by using all MR imaging parameters were 93.75%, 96%, and 85.7%, respectively, which further improved to 96.87%, 100%, and 85.7%, respectively, on addition of FET TBR.[71] Recently, a few studies tested the feasibility of dynamic FET-PET and have shown further improvement in the already remarkable diagnostic accuracy of static PET.[48,64,72] In a large heterogeneous cohort ($n = 124$) of gliomas with different grades and histologies, Galldiks et al[48] found a sensitivity of 93% and specificity of 100% in differentiating TR from benign treatment-related changes by combining static and dynamic FET-PET. Pyka et al[72] performed dynamic FET, PWI, and DWI for glioma recurrence. The accuracy of combined multiparametric analysis was higher (AUC = –0.89) for recurrent gliomas, especially when high specificity was demanded (AUC for static PET = 0.86, dynamic PET = 0.73, DWI = 0.73, and PWI = 0.70).[72] TR often occurs in the primary tumor bed. Lundemann et al[77] have explored the use of pretreatment FET, FDG-PET, and DCE MR

imaging parameters to predict recurrence location in posttreatment glioblastoma by using voxel analysis. In TR, voxels showed increased FET uptake and elevated vascular permeability (Ki) and Ve. They suggested that subclinical neovascularization already exists at the time of radiation therapy, which later may manifest as visible TR.[77]

^{11}C-MET-PET has proved a useful imaging biomarker for glioma recurrence, with less interobserver variability than FDG. D'Souza et al[74] demonstrated the high combined diagnostic performance of ^{11}C-MET-PET and DSC PWI in the identification of glioma recurrence in which ^{11}C-MET seemed to be more sensitive (95% versus 84%) and DSC more specific (90% versus 80%). Qiao et al[38] also reported similar results and increased diagnostic performance in a combined multiparametric evaluation of the ^{11}C-MET and DSC (AUC = 0.953; sensitivity = 84%; and specificity = 100%). [^{18}F] FDOPA was more sensitive and specific for evaluating TR than FDG-PET, especially low-grade glioma recurrence without striatum involvement.[33] Volumetric and active metabolic tumor parameters have been seen closely associated with clinical outcomes and overall survival of patients with gliomas. [^{18}F] FDOPA identified larger active metabolic tumor volume with significantly higher TBR than DSC rCBV in recurrent gliomas. Larger tumor volume with FDOPA correlated better with real tumor extent, though no targeted biopsies were obtained to assess the discrepancies.[75] Similar results have also been identified by using ^{11}C-MET-PET compared with contrast-enhanced MR imaging.[48,74]

Despite inherent technical and biologic differences between these 2 imaging modalities, several authors have claimed that the diagnostic information provided by amino acid PET is comparable with or even superior to that obtained by PWI and vice versa.[65] The increasing use of advanced MR imaging techniques and the availability of hybrid PET/MR imaging systems will facilitate the optimal use of both modalities in neuro-oncologic applications. Multiparametric analysis of both modalities may improve the overall diagnostic accuracy in the posttreatment evaluation of gliomas.

Challenges and Future Directions

Despite the advantages, widespread clinical implementation of PET/MR imaging is still limited because of the availability of integrated PET/MR imaging systems and considerable heterogeneities in methodologies. DSC MR imaging and PET with FDG, ^{11}C-MET, or FET are the commonly used imaging methods with good quantitative agreement in posttreatment evaluation of gliomas. Overall, DSC and DCE PWI showed comparable high diagnostic accuracy for TR from RN compared with ASL.[28,29] PWI has the advantage of being less expensive and less time-consuming because these patients generally undergo follow-up MR imaging. Amino acid PET, with a short half-life such as ^{11}C-MET, presents logistic difficulties and requires a local cyclotron. Among the available AATs, no significant differences exist in terms of the tumor-to-background uptake, though variations have been seen in tracer distribution and the time-activity curves of the tracer. However, the number of patients in these studies was too small to show reliable conclusions. Other novel promising PET tracers such as FLT and FDOPA are still under investigation.

Hybrid systems allow simultaneous acquisition of PET with perfusion. However, there are technical challenges such as PET attenuation correction, which affects quantitative reliability and its integration into routine clinical workflow. MR imaging–based approaches on the segmentation of Dixon water and fat separation and ultrashort TE sequences have been reported to be inaccurate for attenuation correction and underestimate the tracer uptake in the brain. The recently developed novel Region specific optimization of continuous linear attenuation coefficients based on UTE (RESOLUTE) method for attenuation correction is a clinically acceptable measure that needs further clinical validation.[78] Another major problem in hybrid PET/MR imaging is movement artifacts, which compromise both MR imaging and PET image quality.[79]

Technical advancements in PET techniques and the ever-evolving field of radiopharmaceuticals have opened a new domain in glioma imaging. Apart from the usual qualitative uptake parameters, various novel parameters such as shape and uptake heterogeneity may provide additional information on the biologic profile of tumor.[80] Furthermore, with the introduction of theranostics, which uses the same radiopharmaceuticals for diagnosis and therapy of tumors, better patient management is anticipated. It is achieved by exchanging the radionuclide, that is, short-lived positron emitter ^{68}Ga used for PET with the longer-lived β-emitters such as yttrium-90 or lutetium-177 for therapy purposes. Research has shown a possible role of new tracers such as ^{68}Ga PSMA-11, ^{68}Ga-labeled peptides (arginylglycylaspartic acid peptides and substance P), and ^{64}Cu chloride in patients with suspected glioma recurrence.[81]

Limitations

HGG is a relatively rare tumor with a dismal prognosis. Several PET/MR imaging studies using multiparametric evaluation have been undertaken to identify glioma recurrences. However, most studies are retrospective, include a limited number of patients, and use heterogeneous imaging protocols and methods. Histopathologic confirmation of the RN is not available in many patients. In general, most RN diagnoses were established if the lesion remained unchanged or shrank or disappeared on subsequent imaging or clinical follow-up. The PET/MR imaging parameter cutoff values are not standardized. The diagnostic accuracies were variable secondary to the differences in methods, perfusion and PET techniques, radiotracers, and reference standards (histopathology versus clinical follow-up). These limitations need consideration when analyzing the study results.

CONCLUSIONS

Advanced PET/MR imaging techniques noninvasively examine the biologic properties of the tumor and complement the MR imaging alone. With the available clinical literature, it is apparent that combined use of amino acid PET and perfusion MR imaging improves the overall diagnostic accuracy for earlier detection of recurrence, but more research is needed to identify the most optimal use. Currently, this field is held back by a lack of a clear consensus because of the use of heterogeneous protocols and

interpretative criteria. Therefore, large prospective, multi-institutional studies using a homogeneous protocol are needed to investigate and validate these results.

Disclosures: Girish Bathla—*UNRELATED: Grants/Grants Pending*: research grant with Siemens.

REFERENCES

1. Auffinger B, Thaci B, Nigam P, et al. **New therapeutic approaches for malignant glioma: in search of the Rosetta stone.** *F1000 Med Rep* 2012;4:18 CrossRef Medline
2. Roy S, Lahiri D, Maji T, et al. **Recurrent glioblastoma: where we stand.** *South Asian J Cancer* 2015;4:163–73 CrossRef Medline
3. Verma N, Cowperthwaite MC, Burnett MG, et al. **Differentiating tumor recurrence from treatment necrosis: a review of neuro-oncologic imaging strategies.** *Neuro-oncology* 2013;15:515–34 CrossRef Medline
4. van Dijken BRJ, van Laar PJ, Smits M, et al. **Perfusion MRI in treatment evaluation of glioblastomas: clinical relevance of current and future techniques.** *J Magn Reson Imaging* 2019;49:11–22 CrossRef Medline
5. Zikou A, Sioka C, Alexiou GA, et al. **Radiation necrosis, pseudoprogression, pseudoresponse, and tumor recurrence: imaging challenges for the evaluation of treated gliomas.** *Contrast Media Mol Imaging* 2018;2018:6828396 CrossRef Medline
6. Abbasi AW, Westerlaan HE, Holtman GA, et al. **Incidence of tumour progression and pseudoprogression in high-grade gliomas: a systematic review and meta-analysis.** *Clin Neuroradiol* 2018; 28:401–11 CrossRef Medline
7. Bahrami N, Piccioni D, Karunamuni R, et al. **Edge contrast of the FLAIR hyperintense region predicts survival in patients with high-grade gliomas following treatment with bevacizumab.** *AJNR Am J Neuroradiol* 2018;39:1017–24 CrossRef Medline
8. Verger A, Arbizu J, Law I. **Role of amino-acid PET in high-grade gliomas: limitations and perspectives.** *Q J Nucl Med Mol Imaging* 2018;62:254–66 CrossRef Medline
9. Kreth F, Muacevic A, Medele R, et al. **The risk of haemorrhage after image guided stereotactic biopsy of intra-axial brain tumours: a prospective study.** *Acta Neurochir (Wien)* 2001;143:539–46 CrossRef Medline
10. Gallego O. **Nonsurgical treatment of recurrent glioblastoma.** *Curr Oncol* 2015;22:e273–81 CrossRef Medline
11. Essig M, Shiroishi MS, Nguyen TB, et al. **Perfusion MRI: the five most frequently asked technical questions.** *AJR Am J Roentgenol* 2013;200:24–34 CrossRef Medline
12. Welker K, Boxerman J, Kalnin A, et al. **ASFNR recommendations for clinical performance of MR dynamic susceptibility contrast perfusion imaging of the brain.** *AJNR Am J Neuroradiol* 2015;36: E41–51 CrossRef Medline
13. la Fougère C, Suchorska B, Bartenstein P, et al. **Molecular imaging of gliomas with PET: opportunities and limitations.** *Neuro Oncol* 2011;13:806–19 CrossRef Medline
14. Barajas RF, Jr., Chang JS, Segal MR, et al. **Differentiation of recurrent glioblastoma multiforme from radiation necrosis after external beam radiation therapy with dynamic susceptibility-weighted contrast-enhanced perfusion MR imaging.** *Radiology* 2009;253:486–96 CrossRef Medline
15. Young RJ, Gupta A, Shah AD, et al. **MRI perfusion in determining pseudoprogression in patients with glioblastoma.** *Clin Imaging* 2013;37:41–49 CrossRef Medline
16. Di Costanzo A, Scarabino T, Trojsi F, et al. **Recurrent glioblastoma multiforme versus radiation injury: a multiparametric 3-T MR approach.** *Radiol Med* 2014;119:616–24 CrossRef Medline
17. Prager AJ, Martinez N, Beal K, et al. **Diffusion and perfusion MRI to differentiate treatment-related changes including pseudoprogression from recurrent tumors in high-grade gliomas with histopathologic evidence.** *AJNR Am J Neuroradiol* 2015;36:877–85 CrossRef Medline
18. Wang S, Martinez-Lage M, Sakai Y, et al. **Differentiating tumor progression from pseudoprogression in patients with glioblastomas using diffusion tensor imaging and dynamic susceptibility contrast MRI.** *AJNR Am J Neuroradiol* 2016;37:28–36 CrossRef Medline
19. Blasel S, Zagorcic A, Jurcoane A, et al. **Perfusion MRI in the evaluation of suspected glioblastoma recurrence.** *J Neuroimaging* 2016; 26:116–23 CrossRef Medline
20. Thomas AA, Arevalo-Perez J, Kaley T, et al. **Dynamic contrast enhanced T1 MRI perfusion differentiates pseudoprogression from recurrent glioblastoma.** *J Neurooncol* 2015;125:183–90 CrossRef Medline
21. Yun TJ, Park CK, Kim TM, et al. **Glioblastoma treated with concurrent radiation therapy and temozolomide chemotherapy: differentiation of true progression from pseudoprogression with quantitative dynamic contrast-enhanced MR imaging.** *Radiology* 2015;274:830–40 CrossRef Medline
22. Nael K, Bauer AH, Hormigo A, et al. **Multiparametric MRI for differentiation of radiation necrosis from recurrent tumor in patients with treated glioblastoma.** *AJR Am J Roentgenol* 2018;210:18–23 CrossRef Medline
23. Zakhari N, Taccone MS, Torres CH, et al. **Prospective comparative diagnostic accuracy evaluation of dynamic contrast-enhanced (DCE) vs. dynamic susceptibility contrast (DSC) MR perfusion in differentiating tumor recurrence from radiation necrosis in treated high-grade gliomas.** *J Magn Reson Imaging* 2019;50:573–82 CrossRef Medline
24. Ye J, Bhagat SK, Li H, et al. **Differentiation between recurrent gliomas and radiation necrosis using arterial spin labeling perfusion imaging.** *Exp Ther Med* 2016;11:2432–36 CrossRef Medline
25. Seeger A, Braun C, Skardelly M, et al. **Comparison of three different MR perfusion techniques and MR spectroscopy for multiparametric assessment in distinguishing recurrent high-grade gliomas from stable disease.** *Acad Radiology* 2013;20:1557–65 CrossRef Medline
26. Nyberg E, Honce J, Kleinschmidt-DeMasters BK, et al. **Arterial spin labeling: pathologically proven superiority over conventional MRI for detection of high-grade glioma progression after treatment.** *Neuroradiol J* 2016;29:377–83 CrossRef Medline
27. Razek A, El-Serougy L, Abdelsalam M, et al. **Differentiation of residual/recurrent gliomas from postradiation necrosis with arterial spin labeling and diffusion tensor magnetic resonance imaging-derived metrics.** *Neuroradiology* 2018;60:169–77 CrossRef Medline
28. Patel P, Baradaran H, Delgado D, et al. **MR perfusion-weighted imaging in the evaluation of high-grade gliomas after treatment: a systematic review and meta-analysis.** *Neuro Oncol* 2017;19:118–27 CrossRef Medline
29. van Dijken BRJ, van Laar PJ, Holtman GA, et al. **Diagnostic accuracy of magnetic resonance imaging techniques for treatment response evaluation in patients with high-grade glioma, a systematic review and meta-analysis.** *Eur Radiology* 2017;27:4129–44 CrossRef Medline
30. Kim HS, Goh MJ, Kim N, et al. **Which combination of MR imaging modalities is best for predicting recurrent glioblastoma? Study of diagnostic accuracy and reproducibility.** *Radiology* 2014;273:831–43 CrossRef Medline
31. Shin KE, Ahn KJ, Choi HS, et al. **DCE and DSC MR perfusion imaging in the differentiation of recurrent tumour from treatment-related changes in patients with glioma.** *Clin Radiol* 2014;69:e264–72 CrossRef Medline
32. Takenaka S, Asano Y, Shinoda J, et al. **Comparison of (11)C-methionine, (11)C-choline, and (18)F-fluorodeoxyglucose-PET for distinguishing glioma recurrence from radiation necrosis.** *Neurol Med Chir(Tokyo)* 2014;54:280–89 CrossRef Medline
33. Karunanithi S, Sharma P, Kumar A, et al. **18F-FDOPA PET/CT for detection of recurrence in patients with glioma: prospective**

comparison with 18F-FDG PET/CT. *Eur J Nucl Med Mol Imaging* 2013;40:1025–35 CrossRef Medline
34. Santra A, Kumar R, Sharma P, et al. **F-18 FDG PET-CT in patients with recurrent glioma: comparison with contrast enhanced MRI.** *Eur J Radiology* 2012;81:508–13 CrossRef Medline
35. Tan H, Chen L, Guan Y, et al. **Comparison of MRI, F-18 FDG, and 11C-choline PET/CT for their potentials in differentiating brain tumor recurrence from brain tumor necrosis following radiotherapy.** *Clin Nucl Med* 2011;36:978– 81CrossRef Medline
36. Kim YH, Oh SW, Lim YJ, et al. **Differentiating radiation necrosis from tumor recurrence in high-grade gliomas: assessing the efficacy of 18F-FDG PET, 11C-methionine PET and perfusion MRI.** *Clin Neurol Neurosurg* 2010;112:758–65 CrossRef Medline
37. Gómez-Río M, Rodríguez-Fernández A, Ramos-Font C, et al. **Diagnostic accuracy of 201Thallium-SPECT and 18F-FDG-PET in the clinical assessment of glioma recurrence.** *Eur J Nucl Med Mol Imaging* 2008;35:966–75 CrossRef Medline
38. Qiao Z, Zhao X, Wang K, et al. **Utility of dynamic susceptibility contrast perfusion-weighted MR imaging and (11)C-methionine PET/CT for differentiation of tumor recurrence from radiation injury in patients with high-grade gliomas.** *AJNR Am J Neuroradiol* 2019;40:253–59 CrossRef Medline
39. Deuschl C, Kirchner J, Poeppel TD, et al. **11C-MET PET/MRI for detection of recurrent glioma.** *Eur J Nucl Med Mol Imaging* 2018; 45:593–601 CrossRef Medline
40. Minamimoto R, Saginoya T, Kondo C, et al. **Differentiation of brain tumor recurrence from post-radiotherapy necrosis with 11C-methionine PET: visual assessment versus quantitative assessment.** *PLoS One* 2015;10:e0132515 CrossRef Medline
41. Okamoto S, Shiga T, Hattori N, et al. **Semiquantitative analysis of C-11 methionine PET may distinguish brain tumor recurrence from radiation necrosis even in small lesions.** *Ann Nucl Med* 2011;25:213–20 CrossRef Medline
42. Terakawa Y, Tsuyuguchi N, Iwai Y, et al. **Diagnostic accuracy of 11C-methionine PET for differentiation of recurrent brain tumors from radiation necrosis after radiotherapy.** *J Nucl Med* 2008;49: 694–99 CrossRef Medline
43. Karunanithi S, Sharma P, Kumar A, et al. **Comparative diagnostic accuracy of contrast-enhanced MRI and 18F-FDOPA PET-CT in recurrent glioma.** *Eur Radiol* 2013;23:2628–35 CrossRef Medline
44. Rossi Espagnet MC, Romano A, Mancuso V, et al. **Multiparametric evaluation of low grade gliomas at follow-up: comparison between diffusion and perfusion MR with (18)F-FDOPA PET.** *Br J Radiol* 2016;89:20160476 CrossRef Medline
45. Herrmann K, Czernin J, Cloughesy T, et al. **Comparison of visual and semiquantitative analysis of 18F-FDOPA-PET/CT for recurrence detection in glioblastoma patients.** *Neuro-Oncology* 2014;16: 603–09 CrossRef Medline
46. Rachinger W, Goetz C, Pöpperl G, et al. **Positron emission tomography with O-(2-[18F]fluoroethyl)-l-tyrosine versus magnetic resonance imaging in the diagnosis of recurrent gliomas.** *Neurosurgery* 2005;57:505–11; discussion 505-11 CrossRef Medline
47. Pöpperl G, Götz C, Rachinger W, et al. **Value of O-(2-[18F]fluoroethyl)- L-tyrosine PET for the diagnosis of recurrent glioma.** *Eur J Nucl Med Mol Imaging* 2004;31:1464–70 CrossRef Medline
48. Galldiks N, Stoffels G, Filss C, et al. **The use of dynamic O-(2-18F-fluoroethyl)-l-tyrosine PET in the diagnosis of patients with progressive and recurrent glioma.** *Neuro-Oncology* 2015;17:1293–1300 CrossRef Medline
49. Grosu A-L, Astner ST, Riedel E, et al. **An interindividual comparison of O-(2-[18F]fluoroethyl)-L-tyrosine (FET)- and L-[methyl-11C]methionine (MET)-PET in patients with brain gliomas and metastases.** *Int J Radiat Oncol Biol Phys* 2011;81:1049–58 CrossRef Medline
50. Jeong SY, Lee TH, Rhee CH, et al. **3′-Deoxy-3′-[18F]fluorothymidine and O-(2-[18F]fluoroethyl)-L-tyrosine PET in patients with suspicious recurrence of glioma after multimodal treatment: initial results of a retrospective comparative study.** *Nucl Med Mol Imaging* 2010;44:45–54 CrossRef Medline
51. Jena A, Taneja S, Gambhir A, et al. **Glioma recurrence versus radiation necrosis: single-session multiparametric approach using simultaneous O-(2-18F-fluoroethyl)-L-tyrosine PET/MRI.** *Clin Nucl Med* 2016;41:e228–36 CrossRef Medline
52. Li Z, Yu Y, Zhang H, et al. **A meta-analysis comparing 18F-FLT PET with 18F-FDG PET for assessment of brain tumor recurrence.** *Nucl Med Commun* 2015;36:695–701 CrossRef Medline
53. Patronas N, Di Chiro G, Brooks R, et al. **Work in progress: [18F] fluorodeoxyglucose and positron emission tomography in the evaluation of radiation necrosis of the brain.** *Radiology* 1982;144:885–89 CrossRef Medline
54. Ozsunar Y, Mullins ME, Kwong K, et al. **Glioma recurrence versus radiation necrosis? A pilot comparison of arterial spin-labeled, dynamic susceptibility contrast enhanced MRI, and FDG-PET imaging.** *Acad Radiol* 2010;17:282–90 CrossRef Medline
55. Jena A, Taneja S, Jha A, et al. **Multiparametric evaluation in differentiating glioma recurrence from treatment-induced necrosis using simultaneous (18)F-FDG-PET/MRI: a single-institution retrospective study.** *AJNR Am J Neuroradiol* 2017;38:899–907 CrossRef Medline
56. Nihashi T, Dahabreh IJ, Terasawa T. **Diagnostic accuracy of PET for recurrent glioma diagnosis: a meta-analysis.** *AJNR Am J Neuroradiol* 2013;34:944–950 CrossRef Medline
57. Yu J, Zheng J, Xu W, et al. **Accuracy of (18)F-FDOPA positron emission tomography and (18)F-FET positron emission tomography for differentiating radiation necrosis from brain tumor recurrence.** *World Neurosurg* 2018;114:e1211–24 CrossRef Medline
58. Furuse M, Nonoguchi N, Yamada K, et al. **Radiological diagnosis of brain radiation necrosis after cranial irradiation for brain tumor: a systematic review.** *Radiat Oncol* 2019;14:28 CrossRef Medline
59. Herholz K. **Brain tumors: an update on clinical PET research in gliomas.** *Semin Nucl Med* 2017;47:5–17 CrossRef Medline
60. Ullrich R, Backes H, Li H, et al. **Glioma proliferation as assessed by 3'-fluoro-3'-deoxy-L-thymidine positron emission tomography in patients with newly diagnosed high-grade glioma.** *Clin Cancer Res* 2008;14:2049–55 CrossRef Medline
61. Peck M, Pollack HA, Friesen A, et al. **Applications of PET imaging with the proliferation marker [18F]-FLT.** *Q J Nucl Med Mol Imaging* 2015;59:95–104 Medline
62. Zeisel SH. **Dietary choline: biochemistry, physiology, and pharmacology.** *Annu Rev Nutr* 1981;1:95–121 CrossRef Medline
63. Gao L, Xu W, Li T, et al. **Accuracy of 11C-choline positron emission tomography in differentiating glioma recurrence from radiation necrosis: a systematic review and meta-analysis.** *Medicine (Baltimore)* 2018;97:e11556 CrossRef Medline
64. Pyka T, Gempt J, Ringel F, et al. **Prediction of glioma recurrence using dynamic ^{18}F-fluoroethyltyrosine PET.** *AJNR Am J Neuroradiol* 2014;35:1924–29 CrossRef Medline
65. Zhang Q, Gao X, Wei G, et al. **Prognostic value of MTV, SUVmax and the T/N ratio of PET/CT in patients with glioma: a systematic review and meta-analysis.** *J Cancer* 2019;10:1707–16 CrossRef Medline
66. Fleischmann DF, Unterrainer M, Corradini S, et al. **Report of first recurrent glioma patients examined with PET-MRI prior to re-irradiation.** *PLoS One* 2019;14:e0216111 CrossRef Medline
67. Prat R, Galeano I, Lucas A, et al. **Relative value of magnetic resonance spectroscopy, magnetic resonance perfusion, and 2-(18F) fluoro-2-deoxy-D-glucose positron emission tomography for detection of recurrence or grade increase in gliomas.** *J Clin Neurosci* 2010;17:50–53 CrossRef Medline
68. Hatzoglou V, Yang TJ, Omuro A, et al. **A prospective trial of dynamic contrast-enhanced MRI perfusion and fluorine-18 FDG PET-CT in differentiating brain tumor progression from radiation injury after cranial irradiation.** *Neuro Oncol* 2016;18:873–80 CrossRef Medline

69. Hojjati M, Badve C, Garg V, et al. **Role of FDG-PET/MRI, FDG-PET/CT, and dynamic susceptibility contrast perfusion MRI in differentiating radiation necrosis from tumor recurrence in glioblastomas.** *J Neuroimaging* 2018;28:118–25 CrossRef Medline
70. Seligman L, Kovanlikaya I, Pisapia DJ, et al. **Integrated PET-MRI for glioma surveillance: perfusion-metabolism discordance rate and association with molecular profiling.** *AJR Am J Roentgenol* 2019; 212:883–91 CrossRef Medline
71. Sogani SK, Jena A, Taneja S, et al. **Potential for differentiation of glioma recurrence from radionecrosis using integrated (18)F-fluoroethyl-L-tyrosine (FET) positron emission tomography/magnetic resonance imaging: a prospective evaluation.** *Neurol India* 2017; 65:293–301 CrossRef Medline
72. Pyka T, Hiob D, Preibisch C, et al. **Diagnosis of glioma recurrence using multiparametric dynamic 18F-fluoroethyl-tyrosine PET-MRI.** *Eur J Radiol* 2018;103:32–37 CrossRef Medline
73. Verger A, Filss CP, Lohmann P, et al. **Comparison of O-(2-(18)F-Fluoroethyl)-L-tyrosine positron emission tomography and perfusion-weighted magnetic resonance imaging in the diagnosis of patients with progressive and recurrent glioma: a hybrid positron emission tomography/magnetic resonance study.** *World Neurosurg* 2018;113:e727–37 CrossRef Medline
74. D'Souza MM, Sharma R, Jaimini A, et al. **11C-MET PET/CT and advanced MRI in the evaluation of tumor recurrence in high-grade gliomas.** *Clin Nucl Med* 2014;39:791–98 CrossRef Medline
75. Cicone F, Filss CP, Minniti G, et al. **Volumetric assessment of recurrent or progressive gliomas: comparison between F-DOPA PET and perfusion-weighted MRI.** *Eur J Nucl Med Mol Imaging* 2015;42:905–15 CrossRef Medline
76. Yang Y, He MZ, Li T, et al. **MRI combined with PET-CT of different tracers to improve the accuracy of glioma diagnosis: a systematic review and meta-analysis.** *Neurosurg Rev* 2019;42: 185–95 CrossRef Medline
77. Lundemann M, Munck Af Rosenschold P, Muhic A, et al. **Feasibility of multi-parametric PET and MRI for prediction of tumour recurrence in patients with glioblastoma.** *Eur J Nucl Med Mol Imaging* 2019;46:603–13 CrossRef Medline
78. Ladefoged CN, Andersen FL, Kjaer A, et al. **RESOLUTE PET/MRI attenuation correction for O-(2-(18)F-fluoroethyl)-L-tyrosine (FET) in brain tumor patients with metal implants.** *Front Neurosci* 2017;11:453 CrossRef Medline
79. Marner L, Henriksen OM, Lundemann M, et al. **Clinical PET/MRI in neurooncology: opportunities and challenges from a single-institution perspective.** *Clin Transl Imaging* 2017;5:135–49 CrossRef Medline
80. Jung JH, Ahn BC. **Current radiopharmaceuticals for positron emission tomography of brain tumors.** *Brain Tumor Res Treat* 2018;6: 47–53 CrossRef Medline
81. Bailly C, Vidal A, Bonnemaire C, et al. **Potential for nuclear medicine therapy for glioblastoma treatment.** *Front Pharmacol* 2019;10: 772–72 CrossRef Medline

Neuroimaging Advances in Deep Brain Stimulation: Review of Indications, Anatomy, and Brain Connectomics

E.H. Middlebrooks, R.A. Domingo, T. Vivas-Buitrago, L. Okromelidze, T. Tsuboi, J.K. Wong, R.S. Eisinger, L. Almeida, M.R. Burns, A. Horn, R.J. Uitti, R.E. Wharen Jr, V.M. Holanda, and S.S. Grewal

ABSTRACT

SUMMARY: Deep brain stimulation is an established therapy for multiple brain disorders, with rapidly expanding potential indications. Neuroimaging has advanced the field of deep brain stimulation through improvements in delineation of anatomy, and, more recently, application of brain connectomics. Older lesion-derived, localizationist theories of these conditions have evolved to newer, network-based "circuitopathies," aided by the ability to directly assess these brain circuits in vivo through the use of advanced neuroimaging techniques, such as diffusion tractography and fMRI. In this review, we use a combination of ultra-high-field MR imaging and diffusion tractography to highlight relevant anatomy for the currently approved indications for deep brain stimulation in the United States: essential tremor, Parkinson disease, drug-resistant epilepsy, dystonia, and obsessive-compulsive disorder. We also review the literature regarding the use of fMRI and diffusion tractography in understanding the role of deep brain stimulation in these disorders, as well as their potential use in both surgical targeting and device programming.

ABBREVIATIONS: AL = ansa lenticularis; ALIC = anterior limb of the internal capsule; ANT = anterior nucleus of the thalamus; AS = ansa subthalamica; ATR = anterior thalamic radiations; DBS = deep brain stimulation; DRTT = dentatorubrothalamic tract; ET = essential tremor; FGATIR = fast gray matter acquisition TI inversion recovery; FL = fasciculus lenticularis; FS = fasciculus subthalamicus; GPe = globus pallidus externus; GPi = globus pallidus internus; MFB = medial forebrain bundle; MMT = mammillothalamic tract; OCD = obsessive-compulsive disorder; PD = Parkinson disease; slMFB = superolateral branch of the medial forebrain bundle; STN = subthalamic; TF = thalamic fasciculus; VIM = ventral intermedius nucleus; VO = ventralis oralis; ZI = zona incerta

The use of deep brain stimulation (DBS) for treatment of multiple movement and psychiatric disorders has been both beneficial and safe.[1] Currently, there are 5 indications for DBS recognized by the United States FDA: essential tremor (ET), Parkinson disease (PD), and drug-resistant epilepsy, with dystonia and obsessive-compulsive disorder (OCD) carrying a humanitarian device exemption. The relevant brain targets include the ventral intermedius nucleus (VIM) of the thalamus, subthalamic nucleus (STN), globus pallidus internus (GPi), anterior nucleus of the thalamus (ANT), and anterior limb of the internal capsule (ALIC). While their pathophysiology may be different, these disorders share 1 unifying feature: They represent brain network disorders, or "circuitopathies."[2] Additionally, no anatomic correlates (viewed on neuroimaging) can be found that code for various clinical signs of these conditions. Consequently, there has been a shift from traditional localizationist models of the brain to a "connectomic" approach (considering function more distributed within brain networks) to study mechanisms of and responses to DBS and other forms of functional neurosurgery. Reimagining the role of neuroimaging in directing such treatments is of paramount importance.

Historically, neurosurgical targeting was performed by use of a coordinate system referenced to readily identifiable landmarks ("indirect targeting"), for example, the anterior/posterior commissure line. Initial targeting was further refined during awake surgery by use of microelectrode neurophysiologic recordings and macrostimulation. Unfortunately, every pass of a microelectrode increases the risk of complication, as well as the possibility of inducing a transient "microlesion" effect that can further limit or complicate intraoperative testing and interpretation. Surgical targeting and stimulation programming rapidly evolved in conjunction with improvements in MR imaging technology. Improved direct visualization of targets with high-field MR imaging and volumetric, high-

Received April 22, 2020; accepted after revision June 3.

From the Departments of Radiology (E.H.M., L.O.), Neurosurgery (E.H.M., R.A.D., T.V.-B., R.E.W., S.S.G.), and Neurology (R.J.U.), Mayo Clinic, Jacksonville, Florida; Department of Neurology (T.T., J.K.W., R.S.E., L.A., M.R.B.), Norman Fixel Institute for Neurological Diseases, University of Florida, Gainesville, Florida; Department of Neurology (T.T.), Nagoya University Graduate School of Medicine, Nagoya, Japan; Department for Neurology (A.H.), Charité, University Medicine Berlin, Berlin, Germany; and Center of Neurology and Neurosurgery Associates (V.M.H.), BP–A Beneficência Portuguesa de São Paulo, São Paulo, Brazil.

Please address correspondence to Erik H. Middlebrooks, MD, Departments of Radiology and Neurosurgery, Mayo Clinic, 4500 San Pablo Rd, Jacksonville, FL 32224; email: middlebrooks.erik@mayo.edu; @EMiddlebrooksMD

Indicates open access to non-subscribers at www.ajnr.org

Indicates article with supplemental on-line photo.

http://dx.doi.org/10.3174/ajnr.A6693

Summary of key anatomic tracts and structures

Structure	Figure	Regions Connected	Relevant Disorders	Hypothesized Effects of Stimulation
AL	Fig 4*B*, -*D* (yellow)	GPi, VOa	PD and dystonia	Improve dystonia and dyskinesia
AS	Fig 4*B*, -*C* (purple); Fig 3*B*, -*C* (blue)	STN, GPi	PD and dystonia	Direct stimulation effect unknown
ATR	Fig 5*A*, -*B* (red)	Thalamus, prefrontal cortex	OCD	Improve OCD
DRTT	Fig 1*C*, -*D* (red and green); Fig 4*D* (green)	DN, RN, VIM/VOp, M1	ET and tremor-predominant PD	Improve tremor, worsen ataxia
FL	Fig 2*A*; Fig 4*D* (red)	GPi, VOa	PD and dystonia	Improve dystonia and parkinsonism
FS	Fig 3*B*, -*C* (Pink); Fig 4*B*, -*C* (red)	STN, GPe	PD and dystonia	Direct stimulation effect unknown
Hyperdirect pathway (limbic/associative)	Fig 3*A* (cyan, yellow)	STN, broad limbic and associative regions	OCD	Improve OCD
Hyperdirect pathway (motor)	Fig 3*A* (orange)	STN, motor cortex	PD	Improve parkinsonism
MMT	Fig 6*C* (green)	Mammillary body, ANT	Epilepsy	Decrease seizures
MFB	Fig 5*A*, -*B* (cyan)	VTA, nucleus accumbens and olfactory cortex	Depression (off-label use)	Possibly worsens OCD
TF	Fig 2*A*	Combination of FL, AL, and DRTT, thalamus	PD, dystonia, ET	Improve tremor
vtaPP (formerly slMFB)[a]	Fig 5*A*, -*B* (green)	DN, VTA, SFG, MFG, and lateral OFC	OCD	Possibly improve OCD
ANT	Fig 6*A*–*C*		Epilepsy	Decrease seizures
VIM	Fig 1*A*–*C*; Fig 4*D*		ET and tremor-predominant PD	Improve tremor, worsen ataxia, dysarthria
VOa/VOp	Fig 1*A*, -*B*; Fig 4*D*		ET and tremor-predominant PD	Improve tremor, dystonia, worsen ataxia
ZI	Fig 1*C*; Fig 2*A*		ET and tremor-predominant PD	Improve tremor, worsen ataxia

Note:—DN indicates dentate nucleus; M1, primary motor cortex; MFG, middle frontal gyrus; OFC, orbitofrontal cortex; RN, red nucleus; SFG, superior frontal gyrus; VOa, ventralis oralis anterior; VOp, ventralis oralis posterior; VTA, ventral tegmental area; vtaPP, projection pathway from the ventral tegmental area.
[a] vtaPP (slMFB) likely represents misidentification of the limbic/associative hyperdirect pathway.

resolution imaging allowed "direct targeting" of some structures. However, other targets remain poorly resolved, such as the nuclei of the thalamus. More recently, the field of brain connectomics (fMRI and diffusion tractography) has shown great promise in elucidating the mechanisms of DBS and providing patient-specific functional targets that cannot otherwise be defined noninvasively.

In this review, we discuss the FDA-approved indications of DBS, including relevant connectomic and structural anatomy (summarized in the Table), as well as commonly employed MR imaging sequences. A combination of diffusion tractography and postmortem examination and an ultra-high-resolution 7T FLASH MR imaging[3] open-source image set (https://datadryad.org/stash/dataset/doi:10.5061/dryad.119f80q) is used throughout to highlight relevant anatomy. For tractography, a group-averaged dataset[4] based on 1021 subjects from the Human Connectome Project (https://www.humanconnectome.org) open-source data base, normalized to Montreal Neurological Institute template space and reconstructed by using a q-space diffeomorphic reconstruction,[5] was utilized to obtain the spin distribution function.[6] Tractography was then generated in DSI Studio (http://dsi-studio.labsolver.org) by using a combination of manual regions of interest, as well as from the DBS Intrinsic Template Atlas[7] and Horn et al.[8] Tractography was displayed in Lead-DBS software (http://www.lead-dbs.org).[9] The generated tract atlas will be released as open-source data, and is currently available in the latest release of the Lead DBS software package.

Essential Tremor

ET was 1 of 2 initially approved indications for DBS in 1997 (along with severe tremor in PD), targeting the VIM nucleus of the thalamus. Multiple clinical trials have demonstrated the efficacy of VIM stimulation in the treatment of medical-refractory ET.[10] Since the approval of VIM as a treatment target, more recent studies have questioned the ideal target location for treatment of tremor. In particular, there has been increasing interest in the posterior subthalamic area, which encompasses the caudal zona incerta (ZI).[11] Long-term studies, however, have shown that while there is a more pronounced improvement, initially, with caudal ZI stimulation, the VIM target has produced better long-term tremor relief.[12] Last, the ventralis oralis (VO) nucleus of the thalamus has also been explored as a potential target for tremor, but has not been extensively studied.[13]

Anatomy. The ventral thalamus contains multiple nuclei that function in the sensorimotor network. The ventral caudal nucleus, a relay nucleus for proprioception, vibration, and fine touch via the medial lemniscus pathway, lies in the posterior

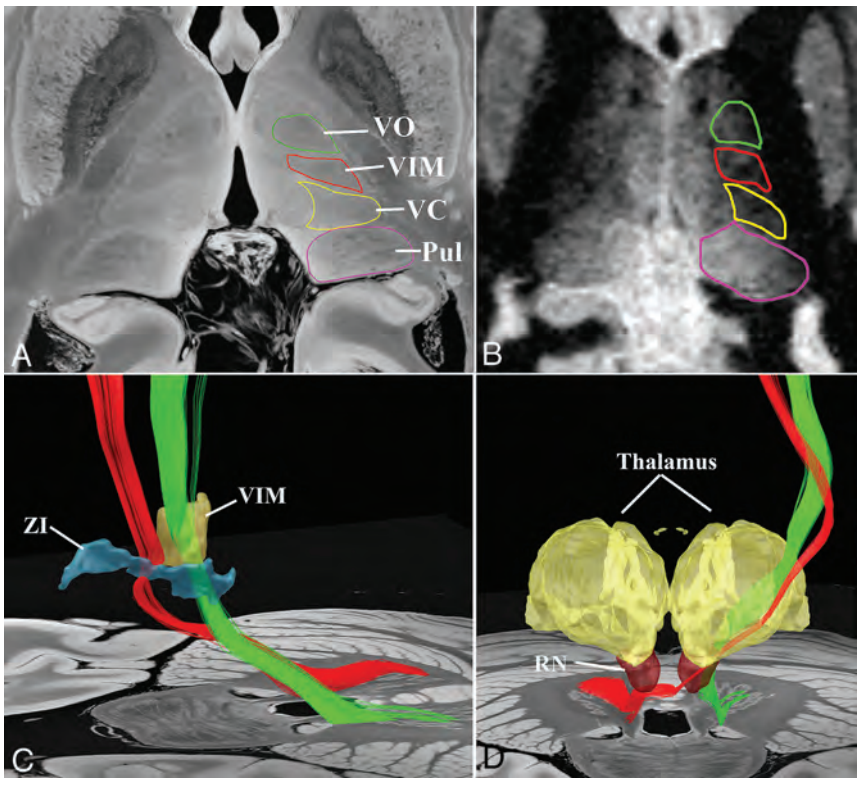

FIG 1. Axial 7T image (*A*) and axial 3T FGATIR image (*B*) illustrating the internal architecture of the ventral thalamus with key ventral nuclei outlined, including the ventral caudal (VC), VIM, and VO nuclei lying anterior to the pulvinar (Pul). Sagittal oblique (*C*) and coronal (*D*) images showing the relationship of the decussating (red) and nondecussating (green) tracts of the left DRTT and their relationship to the VIM nucleus and ZI (blue). The decussating fibers can be seen along the anterior border of the VIM in the location of the posterior VO. The DRTT extends from the dentate nucleus through the superior cerebellar peduncle, with part of the tract decussating in the midbrain and part continuing ipsilateral to the level of the red nucleus (RN), through the posterior subthalamic region and ZI, thalamus, and terminating in the primary motor cortex.

ventral thalamus.[14] Anterior to the ventral caudal nucleus is the VIM (Fig 1*A*, -*B*; images without outlines in On-line Figure), and anterior to the VIM is the VO nucleus, which is divided into a posterior and anterior portion, which receives pallidofugal fibers from the pallidum (discussed later).[15] The VIM and ventralis oralis posterior largely receive fibers of the dentatorubrothalamic tract (DRTT).[14,16] The DRTT courses from the dentate nucleus of the cerebellum through the ipsilateral superior cerebellar peduncle and then partially decussates in the midbrain (Fig 1*C*, -*D*).[17] Most fibers cross to the contralateral red nucleus and ascend through the posterior subthalamic area, VIM, and ventralis oralis posterior and finally terminate within the primary motor cortex. A small subset (20%–30%) does not decussate but rather courses to the ipsilateral red nucleus and follows a similar path to the ipsilateral primary motor cortex.[17]

The outer boundaries of the thalamus are generally well-defined on high-resolution, T1-weighted gradient recalled-echo sequences (eg, MPRAGE). Contrast can be enhanced by application of 2 TIs in MPRAGE to create MP2RAGE images.[18] The application of white matter suppression can also help delineate the thalamic boundaries and has the added advantage of revealing internal architecture of the thalamic nuclei (Fig 1*B*).[19] Susceptibility-weighted imaging can also reveal internal details of the thalamic nuclei; however, this has been primarily shown at ultra-high-field (7T).[20]

Connectomics. Multiple studies have examined the role of connectomics in the treatment of tremor targeting the VIM/posterior subthalamic area region. Early studies examining the segmentation of the thalamus based on the diffusion tractography connectivity profile showed that diffusion tractography was an independent predictor of tremor improvement.[21-25] Based on diffusion tractography results, a common hypothesis has emerged that both VIM and caudal ZI stimulation exert their effect through stimulation of the DRTT, which traverses both targets (Fig 1*D*).[26]

Other studies examined segmentation of the thalamus using diffusion tractography, which revealed similar segregation of the ventral thalamus as described by histologic atlases.[25,27] Using this approach, Middlebrooks et al[28] showed substantial variability in structural connectivity in a cohort of subjects using a fixed anterior/posterior commissure targeting point, highlighting the need for more patient-specific, network-based targeting. By using this approach, several studies found that such segmentation was predictive of improvement in tremor, particularly, connectivity with nodes in the motor network.[21-24]

More recent studies focused on the DRTT, with several showing improvement in tremor associated with overlap of stimulation volume with the DRTT.[25,29] Al-Fatly et al[29] used atlas-based connectivity measures, in contrast to previous studies using patient data,[21,25] and found stimulation volumes in the posterior subthalamic area closely associated with the DRTT correlated with greater tremor control. Importantly, many European datasets have focused more on the posterior subthalamic area region compared with United States datasets targeting the ventral thalamus, which has led to difficulty in fully understanding the role of local structures (such as the VIM, ventralis oralis posterior, and caudal ZI) versus the white matter tracts traversing these regions.[30] It is likely that influencing the DRTT plays a major role in tremor reduction, but the role of local stimulation effects in these different gray matter regions may be important given the variability in outcomes targeting the posterior subthalamic area versus the ventral thalamus, particularly the incidence of stimulation-induced adverse effects.

In control subjects, fMRI has been used to localize the thalamic region corresponding to the thalamic motor network by using resting-state connectivity.[31,32] Unfortunately, lengthy acquisition times currently limit application to the clinical setting. Using group-averaged normative data, however, Al-Fatly et al[29]

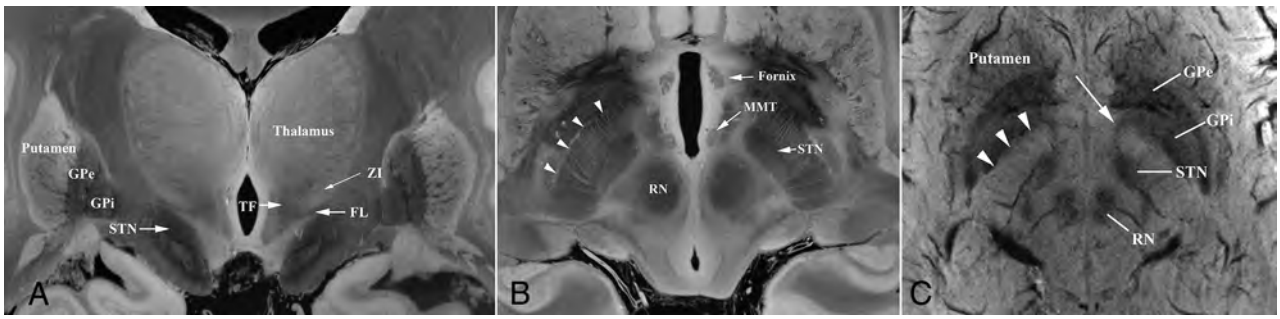

FIG 2. Coronal (*A*) and axial 7T MR imaging (*B*) showing the relationship of structures of the basal ganglia and subthalamic area. The ZI is bordered inferiorly by the FL and superiorly by the TF as it inserts into the thalamus. The Edinger comb system can be seen as *dark lines* traversing the internal capsule perpendicularly (*arrowheads*) composed of the pallidofugal tracts, fasciculus subthalamicus, and FL. Axial susceptibility-weighted MR imaging (*C*) shows similar anatomy including the Edinger comb (*arrowheads*) and the ansa subthalamica (*arrow*). RN indicates red nucleus.

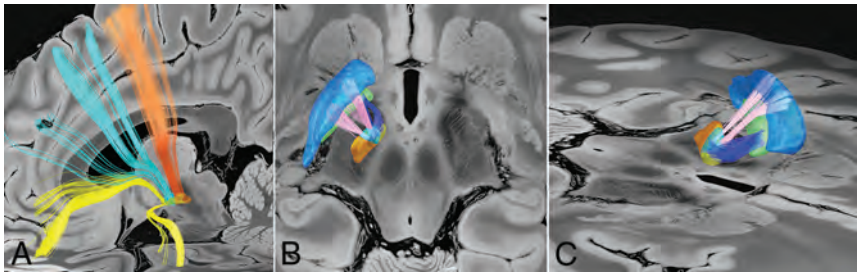

FIG 3. Sagittal view of the tripartite division of the STN (*A*) and corresponding hyperdirect fibers (orange = posterolateral sensorimotor STN; cyan = middle associative STN; yellow = anteromedial limbic STN). Axial (*B*) and oblique coronal views (*C*) show the course of the AS (blue fibers) extending from the anteroventral pole of the globus pallidus internus (green region) and curving into the anterior pole of the limbic division of the STN (yellow region), while the FS (pink fibers) traverses the Edinger comb system extending from the globus pallidus externus (light blue region) to the middle associative STN (cyan).

reported correlation between tremor improvement and functional connectivity similar to that seen with the structural connectivity, namely cerebellothalamocortical motor network connectivity. Gibson et al[33] used active VIM stimulation to assess blood oxygen level–dependent signal changes in a cohort of patients with ET. Activation in sensorimotor, supplementary motor area, cerebellar, brain stem, and thalamic regions correlated with greater improvement in tremor. Interestingly, stimulation-induced adverse effects were more associated with precentral, postcentral, and subcentral region activation, which could support the lower incidence of adverse effects, such as ataxia, with more anterior VIM/ventralis oralis posterior stimulation.[21,30,33]

Parkinson Disease

Along with ET, the FDA approved VIM DBS for severe tremor in PD. In 2002, the FDA expanded its indications, approving DBS use in both the STN and GPi for advanced PD cases. Both targets have been shown as safe and effective, with comparable outcomes in motor symptom improvement.[34] Both GPi and STN DBS have pros and cons, and target selection should be based on patient-by-patient considerations.[34]

Anatomy. The STN is a small, almond-shaped subthalamic structure that lies anterolateral to the red nucleus, superior to the substantia nigra, and inferior to the ZI (Fig 2).[35] The STN is positioned in close proximity to multiple critical white matter tracts, including the corticospinal tract ventrolaterally, medial lemniscus posterolaterally, and the optic tract inferolaterally.[35] The STN is considered to be functionally divided into 3 zones that do not have a clear anatomic distinction. This tripartite division consists of a posterolateral motor division, middle associative division, and anteromedial limbic division.[36] These subdivisions are of critical importance when considering DBS programming due to the possibility of off-target adverse effects. Likely, the divisions are implemented as a gradient, rather than in the form of clear compartments. Given that the STN receives direct input from a wide array of frontal regions, this gradient is largely informed by a similar functional gradient in the frontal cortex. Thus, functional zones of the nucleus can be defined by their structural and functional connectivity, as described next.

The STN has broad cortical and subcortical connections, including the caudate, putamen, pedunculopontine nucleus, globus pallidus externus (GPe), GPi, substantia nigra, substantia innominata, hypothalamus, olfactory tubercle, and mamillary body.[35] These broad connections follow the tripartite function in motor, associative, and limbic processes, eg, limbic regions predominantly interact with limbic regions of the striatum or thalamus (Fig 3*A*). With regard to DBS, several key tracts warrant discussion. The fasciculus subthalamicus (FS) and ansa subthalamica (AS) are 2 of the 4 primary pallidofugal tracts (passing out of the pallidum) and connect the GPe and the GPi with the STN, respectively (Figs 3*B*-, *C*).[35,37] The FS courses from the GPe lateral to the genu and ALIC to insert along the anterolateral aspect of the STN.[35] The AS is a less described pathway that courses from the anteroventral pole of the GPi, intimately associated with the ansa lenticularis (AL), tracking anteriorly to curve around the internal capsule, and descend inferiorly to the anterovental STN (both limbic).[37] Both connections likely contribute to the effect of STN DBS, in particular in treatment of dystonia.[35]

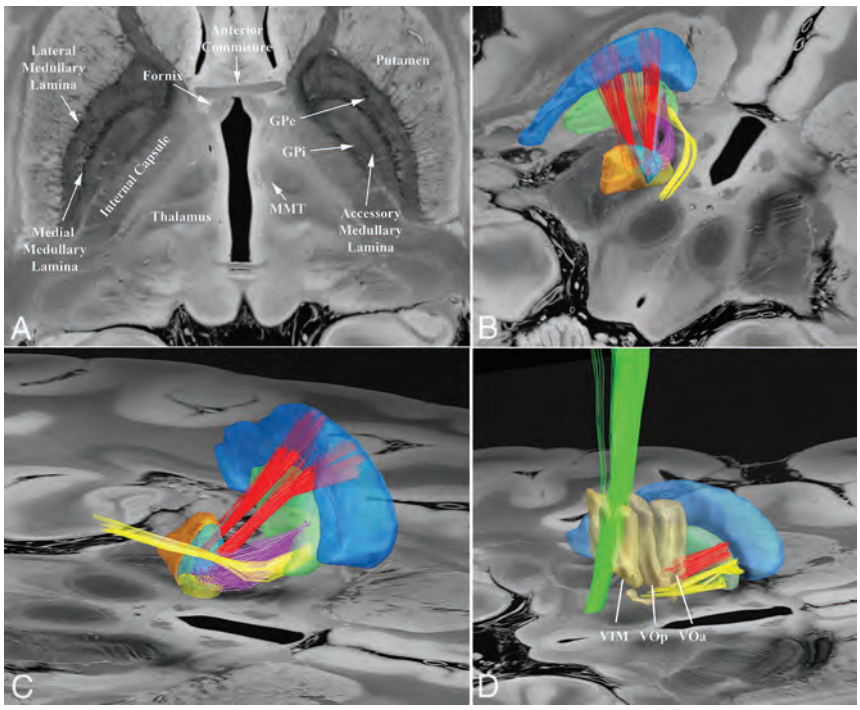

FIG 4. Axial 7T MR imaging (*A*) showing the anatomy of the pallidum and adjacent structures. Posterior oblique (*B*) and anterior oblique views (*C*) highlight the relationship of the AL (yellow fibers) that originates from the anteroventral pole of the globus pallidus internus near the origin of the AS (purple fibers) but courses more dorsal to the AS. The FS is shown as red fibers. Sagittal view (*D*) shows the components of the thalamic fasciculus: dentatorubrothalamic tract (green), AL (yellow), and FL (red) associated with the VIM, ventralis oralis posterior (VOp), and ventralis oralis anterior (VOa) nuclei, respectively.

Although it is not part of the original rate model of the basal ganglia, the more recently described hyperdirect pathway consists of direct connections from the cortex to the STN (Fig 3*A*).[38,39] In keeping with the tripartite division of the STN, hyperdirect connections extend to the motor cortex from the posterior STN, associative cortex from the mid-STN, and limbic regions from the anterior STN. The hyperdirect pathway has been implicated in symptomatology of PD and associated with motor improvement seen with STN DBS in PD using diffusion tractography.[35]

The dorsal pallidum consists of the GPi and GPe, which are separated by the thin internal medial medullary lamina (Fig 4*A*). The external lateral medullary lamina separates the GPe from the adjacent putamen. An accessory lamina further subdivides the GPi into medial and lateral subcomponents. The internal capsule forms the medial border of the globus pallidus. The dorsal pallidum plays a major role in the motor network and is a common treatment target for multiple movement disorders. Similar to the STN, the pallidum has also been described as having a tripartite division.[40]

The GPi primarily connects to the thalamus, putamen, pedunculopontine nucleus, GPe, STN, substantia nigra, habenula, and amygdala.[35] Also reported are direct corticopallidal connections to both GPi and GPe using diffusion tractography,[16,40] but the existence and role of these fibers are yet to be fully elucidated. Further complicating the issue, in the macaque, a peripallidal neuronal network composed of large acetylcholinesterase-containing cells related to the nucleus basalis has been shown to project diffusely to neocortex.[41] This could mean that direct connections between cortex and GPi, as seen in diffusion tractography, are projections to the cortex that originate from a peripallidal cell mass, or even false-positive connections, isolated due to the close proximity of the GPi to the internal capsule.[42]

Of primary importance to DBS, the pallidofugal pathways are generally divided into the AL, fasciculus lenticularis (FL), FS, and AS (Fig 4*B*, -*C*). The FS and AS have been discussed above. The FL and AL, or pallidothalamic connections, ultimately join together with the cerebellothalamic fibers (DRTT) to form the thalamic fasciculus (TF) before inserting in the ventral thalamus (Fig 4*D*).[35] The pallidofugal fibers of the FS and FL traverse the internal capsule at a perpendicular angle, creating the Edinger comb system, which can be readily seen on susceptibility-weighted imaging (Fig 2*C*). The AL courses from the inferomedial border along the anterior pole of the GPi, extends anteriorly and medially to cross the internal capsule, passes anteriorly to the STN, and then joins the FL.[35] The FL extends from the GPi medial border, extends directly through the internal capsule, and then lies dorsal to the STN and ventral to the ZI, separating these 2 structures before joining the AL to form the TF (Fig 2*A*).[35] The TF then courses dorsal to the ZI and inserts into the ventral thalamus with most fibers from the DRTT entering the VIM, the AL into the ventralis oralis posterior, and the FL into the ventralis oralis anterior (Fig 4*D*). The ZI is bordered inferiorly by the FL and superiorly by the TF. The relationship of these tracts is crucial, as they likely serve a major therapeutic role in DBS for movement disorders, for instance, DRTT/TF stimulation in alleviating tremor in caudal ZI DBS and reduction of dyskinesia with more dorsal STN stimulation (likely affecting the AL).[43]

Connectomics. Support for the functional zones of the STN has been illustrated by several studies. Using diffusion tractography data with local field potential recordings in the STN, high connectivity to the motor and premotor cortices was found in the dorsolateral STN, while the ventral STN showed connectivity to limbic regions, such as the amygdala, hippocampus, and medial temporal regions.[44] Connectivity profiles have illustrated the variability in brain networks affected by DBS in treating specific symptoms of PD. Akram et al[45] used stimulation modeling combined with diffusion tractography in patients with STN DBS with PD to explore structural connectivity patterns associated with improvement in bradykinesia, rigidity, and tremor. Greater connectivity to the prefrontal cortex and supplemental motor area

were more beneficial for rigidity, while connectivity to the supplemental motor area only was associated with improved bradykinesia.[45] As may be expected from previously discussed tremor networks, connectivity to the primary motor cortex was associated with greatest benefit in tremor.[45]

To determine if connectivity measures alone could be used to predict improvement across a cohort, Horn et al[46] used group-level resting-state fMRI and diffusion tractography data from existing cohorts to predict improvement in Unified Parkinson's Disease Rating Scale Part III motor scores in a group of patients with PD. By employing a group of stimulation volumes to generate structural and functional connectivity maps associated with Unified Parkinson's Disease Rating Scale Part III outcomes, models were formulated to predict individual patient outcomes.[46] On the basis of solely connectivity data, they were able to predict postoperative motor scores within 15%, highlighting the potential power of connectomics in predicting patient outcomes associated with specific DBS programming settings.[46] Similarly, Lin et al[47] used machine learning to examine connectivity profiles associated with effective-versus-ineffective electrode contacts and predicted, with 84.9% accuracy, which electrode contacts would be effective in reducing motor symptoms. Additionally, their study illustrated the potential of connectomics to reduce the burden on DBS programmers in the performance of tedious permutation surveys of multiple DBS contacts to determine optimal effectiveness.

The role of connectomics in GPi DBS has been less explored; however, it could potentially offer even greater benefit to programming and targeting than the STN due to the larger size of the GPi. Middlebrooks et al[15] evaluated the role of diffusion tractography in predicting outcomes from GPi DBS and found that the changes in Unified Parkinson's Disease Rating Scale Part III motor scores in PD correlated primarily with connectivity to the M1 region, followed by the supplemental motor area/premotor cortex.

Dystonia

Dystonia manifests in the form of muscle contractions that can be intermittent or sustained, resulting in phasic or repetitive movements and/or abnormal posture.[48] DBS has been used to treat various forms of dystonia, from focal (predominantly cervical) to generalized dystonia. DBS for dystonia targeting the bilateral GPi received a humanitarian device exemption by the FDA in 2003. Multiple clinical trials[49–51] have established the efficacy of GPi DBS in primary generalized dystonia, finding that those having the *DYT1* gene mutation have a better response to DBS.[52]

Anatomy. Relevant anatomy and imaging considerations of the sensorimotor portion of the GPi have been previously discussed (see PD section).

Connectomics. Connectivity in DBS for dystonia has not been extensively studied. Okromelidze et al[53] have recently shown that stimulation volumes with structural and functional connectivity to motor regions of the cerebellum, thalamus, and sensorimotor cortex were correlated with greater improvement in primary generalized dystonia. Similarly, by using diffusion tractography analysis of ventral and dorsal contacts in focal dystonia, Rozanski et al[54] found that connections from the more efficacious ventral contacts had greater connectivity to the primary sensorimotor regions, while less efficacious dorsal contacts had greater connectivity to premotor and supplementary motor areas.

Unfortunately, the combination of the heterogeneity of patients with dystonia as well as the relatively low number of patients treated with DBS compared with PD and ET has resulted in greater gaps in understanding connectivity in DBS for dystonia. However, connectomics stands to potentially benefit dystonia more than ET or PD given the lack of reliable, immediate (at the time of stimulation onset) clinical or physiologic markers, which limits confidence in both targeting and subsequent programming. As opposed to the near-immediate change in motor symptoms seen with ET and PD DBS, the effect of DBS in dystonia may take days to weeks to manifest and may change from month to month, resulting in frustrating, unpredictable, and suboptimal clinical outcomes.[55] An imaging biomarker, therefore, may result in more successful targeting and programming, greatly benefiting dystonia DBS outcomes.

OCD

The last target to receive humanitarian device exemption by the FDA was the ALIC for treatment of OCD in 2009.[56] A multinational, multicenter study by Greenberg et al[57] reported symptom reduction and functional improvement in >60% of the patient population, with overall reduction of illness changing from severe at baseline to moderate with DBS treatment. Furthermore, 38% showed clinical remission, according to their Yale-Brown Obsessive Compulsive Scale score.[57] Like dystonia, the lack of an immediate biophysical marker of treatment effect makes DBS targeting and programming challenging; therefore, identifying useful imaging biomarkers stands to benefit OCD outcomes.

Anatomy. Underlying pathophysiology of OCD is commonly thought to involve frontostriatal dysfunction and abnormal cortico-striato-thalamo-cortical tracts.[58] As such, multiple DBS targets have been utilized, including the nucleus accumbens, ventral striatum, and ALIC. Within the FDA-approved target of the ALIC, 2 primary fiber tracts have been discussed with regard to OCD DBS, the anterior thalamic radiations (ATR) and the medial forebrain bundle (MFB), namely what has been described as the superolateral branch (slMFB). The ATR connects the thalamus to the frontal lobe, particularly to the dorsolateral prefrontal cortex (Fig 5). The classic MFB connects the ventral tegmental area to the nucleus accumbens and olfactory cortex and does not lie within the ALIC but is more ventral in location. The slMFB DBS target, as described by Coenen et al,[59] connects the dentate nucleus, ventral tegmental areas, superior and middle frontal gyri, and lateral orbitofrontal cortex. However, this tract has only been described by DTI, and no other confirmation of its existence has been found (see Discussion below). Anatomically, the ATR is described as lying medial to slMFB within ALIC.[59]

Connectomics. One of the first DBS connectivity studies in OCD showed that connectivity to the right middle frontal gyrus (dorsolateral prefrontal cortex) was greater in positive responders, whereas connectivity to the lateral orbitofrontal cortex and

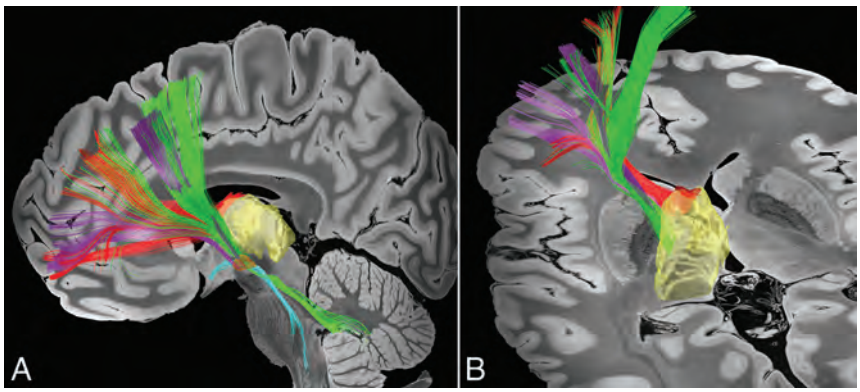

FIG 5. Sagittal (*A*) and posterior oblique views (*B*) showing the relationship of tracts associated with deep brain stimulation of the ALIC for treatment of OCD. The ATR (Red) extend anteriorly from the thalamus (yellow). The MFB (cyan) connects the ventral tegmental area with the nucleus accumbens and olfactory cortex. The MFB does not traverse the ALIC, but, rather, lies ventral and medial to ALIC. The tracts described as a superolateral branch of the MFB (green) mirror the position of the frontal connections of the anteromedial subthalamic nucleus (purple fibers) within the ALIC—both lying lateral to the ATR. These fibers of the subthalamic nucleus may account for the tractography findings previously reported as the superolateral branch of the MFB (more recently referred to as the projection pathway from the ventral tegmental [vtaPP] area). The subthalamic nucleus is shown in orange.

ventrolateral prefrontal cortex was associated with nonresponse.[60] Similarly, Baldermann et al[61] found stimulation of the ATR region, with connection to the medial and lateral prefrontal cortex and right middle frontal gyrus to correlate with greater improvement. Their results showed connectivity with the anatomically correct MFB to be associated with nonresponse. Together, these studies suggest the ATR as a stimulation target within the ALIC.

Others, however, have reported seemingly contradictory findings. Coenen et al[62] performed an observational study of direct targeting of the slMFB, employing diffusion tractography in 2 patients, and both showed some benefit with DBS, but this study did not compare stimulation of the ATR. Liebrand et al[63] used diffusion tractography of the slMFB and ATR to show greater symptom improvement with stimulation closer to the slMFB. The authors reported "a distinct media-lateral organization of, respectively, the ATR and MFB within the vALIC [ventral ALIC]"; however, the MFB does not traverse the ALIC and is ventral to ATR, not lateral (Fig 5).[63,64] Given the described anatomy of the slMFB and DBS response, it is possible that these fibers within the ALIC and lateral to the ATR represent connections of the anteromedial STN, which has also been shown to be an effective DBS target for OCD.[65] Here, we show that these fibers of the anteromedial STN that connect the STN to the anterior cingulate cortex, lateral orbitofrontal cortex, and dorsolateral prefrontal cortex[65] share a similar course to what has been described as the slMFB (Fig 5).[62]

In summary, the effect of ALIC DBS in OCD is likely mediated through the ATR or connections of the anteromedial STN to the frontal lobe. There is limited anatomic evidence of the slMFB, short of diffusion tractography, but the anatomic description of this fiber tract, seemingly, corresponds to connections between the anteromedial STN and frontal lobe. Because the MFB does not traverse within the ALIC, it is likely that studies reporting stimulation of the slMFB in ALIC DBS are not utilizing accepted anatomic structures or nomenclature. Due to this conflicting nomenclature, the slMFB fibers have more recently been referred to as the projection pathway from the ventral tegmental area; however, further studies are needed to demonstrate these as a novel pathway versus misidentification of normal anteromedial STN cortical connections.

Epilepsy

Epilepsy is a common disorder (> 1% prevalence in most populations) with drug-resistant epilepsy cases comprising approximately 20%–40% of all patients with epilepsy. Patients who are not candidates for surgical resection or lesioning, such as those with generalized onset, poor localization, or eloquent brain onset, previously had limited treatment options. More recently, several forms of neuromodulation have provided new treatment options, including vagus nerve stimulation, responsive neural stimulation, and DBS. Unfortunately, these technologies are in their infancy, and a thorough understanding of their mechanism and ideal patient selection is not well-known. The most recent of these to be approved by the FDA (in 2018) is bilateral DBS of the ANT. Efficacy and safety of ANT DBS was shown in the Stimulation of the Anterior Nucleus of the Thalamus in Epilepsy (SANTE) trial, which found a 68% responder rate at 5 years.[66] While effective in many patients, substantial variability in outcomes was reported.[66] Also of note, stimulation-induced adverse effects, including depression and memory impairment, were found, the mechanism of which is not entirely understood.[66] Outcome variability was likely related to multiple factors, including differing surgical approaches; variation in patient population; lack of reliable, direct targeting; and challenges in identifying the optimal stimulation settings, because epilepsy DBS lacks an immediate physiologic biomarker seen in other applications (eg, immediate cessation of tremor in movement disorders).[67-70]

Anatomy. Much like other applications in DBS, indirect targeting of the ANT was the most widely used method in early studies. Unfortunately, epilepsy is known to be associated with regional thalamic atrophy,[71] which questions the utility of employing such indirect targeting in the brain of a patient with long-standing epilepsy. Grewal et al[72] have shown that indirect targeting of the ANT produced a wide range of inaccuracies compared with direct ANT targeting in a cohort of patients with epilepsy, which was dependent on the degree of thalamic atrophy. Grewal et al[69] showed the utility of fast gray matter acquisition T1 inversion recovery (FGATIR) MR imaging in direct visualization of the ANT

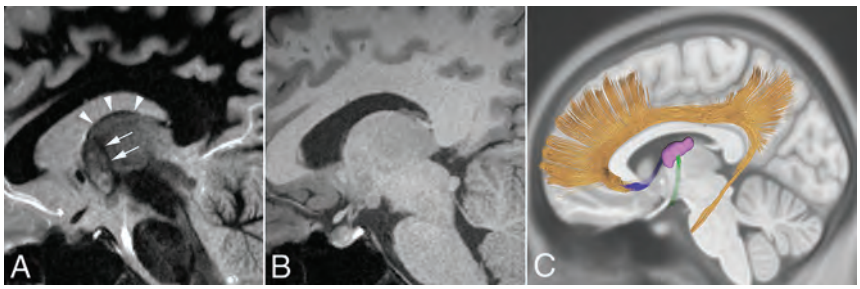

FIG 6. Sagittal 3T FGATIR MR imaging (*A*) compared with MPRAGE (*B*) in the same patient. The FGATIR more clearly highlights the course of the mammillothalamic tract (*arrow*) seen as a dark band extending from the mammillary body, through the thalamus, and terminating at the base of the anterior ANT (*outlined by arrowheads*). Sagittal view of the main connections of the ANT (purple region) (*C*). The mammillothalamic tract (green) connects the mamillary body to the ANT. Tracts (blue) then connect the ANT (through the stria terminalis) with the anterior cingulate and cingulate bundle (orange).

(Fig 6*A*, -*B*), which is currently the most utilized sequence for direct targeting of ANT.

The mammillothalamic tract (MMT) is a component of the limbic circuit that connects the mammillary body to the ANT (Fig 6*C*).[73] MMT arises from the anteromedial mammillary body traversing posterior to the insertion of the fornix and extending superiorly within the substance of the thalamus.[69,73] The termination of the MMT corresponds to the inferior boundary of the ANT. The continuation of the limbic circuit connects the ANT to the anterior cingulate cortex, traditionally thought to course through the ALIC, but more recent evidence suggests connections extending through the stria terminalis, septal area, and subgenual cingulate (Fig 6*C*).[74] Importantly, recent studies have shown that the greatest response to ANT DBS was with stimulation volumes near the termination of the MMT and into the anterior ANT, which suggests modulation of this circuit that enters via the MMT and exits the anterior pole of the ANT as the biologic basis of seizure control.[75,76]

Connectomics. Diffusion tractography of MMT has been previously reported. An initial study[77] utilized lengthy diffusion acquisition, replicated with >50% reduction in time in a subsequent study.[69] Nevertheless, given the acquisition times, postprocessing, technical knowledge, and management of substantial distortions present in echo-planar imaging, diffusion tractography has not been shown to be of added value to the clear visualization of the MMT present on FGATIR imaging.

The mechanism of ANT DBS is not understood, but fMRI provides valuable insights into the connectivity pattern associated with ANT DBS response. Middlebrooks et al[78] used atlas-based resting-state fMRI to show that responders had greater connectivity to multiple nodes of the default mode network compared with nonresponders. Additionally, they showed that anticorrelation of connectivity to the hippocampus was greater in DBS responders.[78] These findings are in line with prior animal studies that revealed elevated γ-aminobutyric acid levels in the hippocampus after ANT stimulation, supporting the inhibitory nature of anticorrelated resting-state connectivity. If such connectivity is a predictor of ANT DBS response, this could aid in understanding treatment failure in some patients—for instance, in a small cohort, patients with mesial temporal sclerosis were shown to have impairment of evoked potentials in the hippocampus after ANT stimulation and were all nonresponders.[79] If network damage due to epilepsy limits transmission of DBS stimulus within these networks identified by fMRI, treatment may, therefore, be ineffective.

Last, the lack of timely, reliable, clinical biophysical markers of optimal DBS programming may give fMRI the potential to provide a useful in vivo biomarker for device programming. The feasibility of using fMRI to directly visualize areas of the brain affected by stimulation, by using a block design fMRI under the conditions of DBS ON versus DBS OFF, as has been recently shown, produced similar activation patterns within the default mode network and several other areas of the brain.[80] While more studies are required to understand the ideal patterns of activation associated with optimal clinical outcomes, fMRI has the potential to be used as a patient-specific in vivo biomarker to select optimal stimulation settings.

CONCLUSIONS

Brain connectomics has led to advances in the understanding of DBS and will continue to shape surgical targeting and programming. The potential for improvements in patient safety and treatment outcomes suggests that the role of neuroimaging in DBS management will only continue to increase. A thorough understanding of relevant functional and structural anatomy is critical to providing neuroradiologic guidance for DBS.

ACKNOWLEDGMENTS

The authors acknowledge the assistance of Lucy Bahn, PhD, in the preparation of this article.

Disclosures: Erik H. Middlebrooks—*UNRELATED: Grants/Grants Pending:* Boston Scientific Corp, Varian Medical Systems, *Comments*: Research grant support.* Tito Vivas-Buitrago—*UNRELATED: Employment:* Mayo Clinic. Joshua K. Wong—*UNRELATED: Grants/Grants Pending:* National Institutes of Health, 1R25NS108939.* Robert S. Eisinger—*UNRELATED: Other:* National Institutes of Health, *Comments*: I am supported by the National Institute of Neurological Disorders and Stroke of the National Institutes of Health under Award Number F30NS111841. Leonardo Almeida—*UNRELATED: Consultancy:* Medtronic/Boston Scientific. Matthew R. Burns—*RELATED: Grant:* Parkinson's Foundation, *Comments*: I receive salary support through the Parkinson's Foundation; *UNRELATED: Grants/Grants Pending:* American Parkinson's Disease Association, *Comments*: I have an early career grant pending with the American Parkinson's Disease Association. Andreas Horn—*UNRELATED: Grants/Grants Pending:* Deutsche Forschungsgesellschaft. Vanessa M. Holanda—*UNRELATED: Payment for Development of Educational Presentations:* Boston Scientific, Abbott, Medicicor, Gusmed.* *Money paid to the institution.

REFERENCES

1. Franzini A, Cordella R, Messina G, et al. **Targeting the brain: considerations in 332 consecutive patients treated by deep brain stimulation**

(DBS) for severe neurological diseases. *Neurol Sci* 2012;33:1285–1303 CrossRef Medline
2. DeLong MR, Wichmann T. **Basal ganglia circuits as targets for neuromodulation in Parkinson's disease.** *JAMA Neurol* 2015;72:1354–60 CrossRef Medline
3. Edlow BL, Mareyam A, Horn A, et al. **7 Tesla MRI of the ex vivo human brain at 100 micron resolution.** *Sci Data* 2019;6:244 CrossRef Medline
4. Yeh FC, Panesar S, Fernandes D, et al. **Population-averaged atlas of the macroscale human structural connectome and its network topology.** *Neuroimage* 2018;178:57–68 CrossRef Medline
5. Yeh FC, Tseng WY. **NTU-90: a high angular resolution brain atlas constructed by q-space diffeomorphic reconstruction.** *Neuroimage* 2011;58:91–99 CrossRef Medline
6. Yeh FC, Wedeen VJ, Tseng WY. **Generalized q-sampling imaging.** *IEEE Trans Med Imaging* 2010;29:1626–35 CrossRef Medline
7. Ewert S, Plettig P, Li N, et al. **Toward defining deep brain stimulation targets in MNI space: a subcortical atlas based on multimodal MRI, histology and structural connectivity.** *Neuroimage* 2018;170:271–82 CrossRef Medline
8. Horn A, Wenzel G, Irmen F, et al. **Deep brain stimulation induced normalization of the human functional connectome in Parkinson's disease.** *Brain* 2019;142:3129–43 CrossRef Medline
9. Horn A, Li N, Dembek TA, et al. **Lead-DBS v2: Towards a comprehensive pipeline for deep brain stimulation imaging.** *Neuroimage* 2019;184:293–316 CrossRef Medline
10. Flora ED, Perera CL, Cameron AL, et al. **Deep brain stimulation for essential tremor: a systematic review.** *Mov Disord* 2010;25:1550–59 CrossRef Medline
11. Blomstedt P, Stenmark Persson R, Hariz GM, et al. **Deep brain stimulation in the caudal zona incerta versus best medical treatment in patients with Parkinson's disease: a randomised blinded evaluation.** *J Neurol Neurosurg Psychiatry* 2018;89:710–16 CrossRef Medline
12. Eisinger RS, Wong J, Almeida L, et al. **Ventral intermediate nucleus versus zona incerta region deep brain stimulation in essential tremor.** *Mov Disord Clin Pract* 2018;5:75–82 CrossRef
13. Foote KD, Okun MS. **Ventralis intermedius plus ventralis oralis anterior and posterior deep brain stimulation for posttraumatic Holmes tremor: two leads may be better than one: technical note.** *Neurosurgery* 2005;56:E445 CrossRef Medline
14. Sammartino F, Krishna V, King NK, et al. **Tractography-based ventral intermediate nucleus targeting: novel methodology and intraoperative validation.** *Mov Disord* 2016;31:1217–25 CrossRef Medline
15. Middlebrooks E, Tuna I, Grewal S, et al. **Segmentation of the globus pallidus internus using probabilistic diffusion tractography for deep brain stimulation targeting in Parkinson's disease.** *AJNR Am J Neuroradiol* 2018;39:1127–34 CrossRef Medline
16. Schlaier J, Anthofer J, Steib K, et al. **Deep brain stimulation for essential tremor: targeting the dentato-rubro-thalamic tract?** *Neuromodulation* 2015;18:105–12 CrossRef Medline
17. Meola A, Comert A, Yeh FC, et al. **The nondecussating pathway of the dentatorubrothalamic tract in humans: human connectome-based tractographic study and microdissection validation.** *J Neurosurg* 2016;124:1406–12 CrossRef Medline
18. Marques JP, Kober T, Krueger G, et al. **MP2RAGE, a self bias-field corrected sequence for improved segmentation and T1-mapping at high field.** *Neuroimage* 2010;49:1271–81 CrossRef Medline
19. Tourdias T, Saranathan M, Levesque IR, et al. **Visualization of intra-thalamic nuclei with optimized white-matter-nulled MPRAGE at 7T.** *Neuroimage* 2014;84:534–45 CrossRef Medline
20. Jorge J, Gretsch F, Najdenovska E, et al. **Improved susceptibility-weighted imaging for high contrast and resolution thalamic nuclei mapping at 7T.** *Magn Reson Med* 2020;84:1218–34 CrossRef Medline
21. Middlebrooks EH, Tuna IS, Almeida L, et al. **Structural connectivity-based segmentation of the thalamus and prediction of tremor improvement following thalamic deep brain stimulation of the ventral intermediate nucleus.** *Neuroimage Clin* 2018;20:1266–73 CrossRef Medline
22. Kim W, Sharim J, Tenn S, et al. **Diffusion tractography imaging-guided frameless linear accelerator stereotactic radiosurgical thalamotomy for tremor: case report.** *J Neurosurg* 2018;128:215–21 CrossRef Medline
23. Pouratian N, Zheng Z, Bari AA, et al. **Multi-institutional evaluation of deep brain stimulation targeting using probabilistic connectivity-based thalamic segmentation.** *J Neurosurg* 2011;115:995–1004 CrossRef Medline
24. Tsolaki E, Downes A, Speier W, et al. **The potential value of probabilistic tractography-based for MR-guided focused ultrasound thalamotomy for essential tremor.** *Neuroimage Clin* 2018;17:1019–27 CrossRef Medline
25. Akram H, Dayal V, Mahlknecht P, et al. **Connectivity derived thalamic segmentation in deep brain stimulation for tremor.** *Neuroimage Clin* 2018;18:130–42 CrossRef Medline
26. Calabrese E, Hickey P, Hulette C, et al. **Postmortem diffusion MRI of the human brainstem and thalamus for deep brain stimulator electrode localization.** *Hum Brain Mapp* 2015;36:3167–78 CrossRef Medline
27. Behrens TE, Johansen-Berg H, Woolrich MW, et al. **Non-invasive mapping of connections between human thalamus and cortex using diffusion imaging.** *Nat Neurosci* 2003;6:750–57 CrossRef Medline
28. Middlebrooks EH, Holanda VM, Tuna IS, et al. **A method for preoperative single-subject thalamic segmentation based on probabilistic tractography for essential tremor deep brain stimulation.** *Neuroradiology* 2018;60:303–09 CrossRef Medline
29. Al-Fatly B, Ewert S, Kubler D, et al. **Connectivity profile of thalamic deep brain stimulation to effectively treat essential tremor.** *Brain* 2019;142:3086–98 CrossRef Medline
30. Middlebrooks EH, Grewal SS, Holanda VM. **Complexities of connectivity-based DBS targeting: rebirth of the debate on thalamic and subthalamic treatment of tremor.** *Neuroimage Clin* 2019;22:101761 CrossRef Medline
31. Anderson JS, Dhatt HS, Ferguson MA, et al. **Functional connectivity targeting for deep brain stimulation in essential tremor.** *AJNR Am J Neuroradiol* 2011;32:1963–68 CrossRef Medline
32. Greene DJ, Marek S, Gordon EM, et al. **Integrative and network-specific connectivity of the basal ganglia and thalamus defined in individuals.** *Neuron* 2020;105:742–58.e6 CrossRef Medline
33. Gibson WS, Jo HJ, Testini P, et al. **Functional correlates of the therapeutic and adverse effects evoked by thalamic stimulation for essential tremor.** *Brain* 2016;139:2198–210 CrossRef Medline
34. Ramirez-Zamora A, Ostrem JL. **Globus pallidus interna or subthalamic nucleus deep brain stimulation for Parkinson's disease: a review.** *JAMA Neurol* 2018;75:367–72 CrossRef Medline
35. Holanda VM, Okun MS, Middlebrooks EH, et al. **Postmortem dissections of common targets for lesion and deep brain stimulation surgeries.** *Neurosurgery* 2020;86:860–72 CrossRef Medline
36. Parent A, Hazrati L-N. **Functional anatomy of the basal ganglia. II. The place of subthalamic nucleus and external pallidium in basal ganglia circuitry.** *Brain Res Rev* 1995;20:128–54 CrossRef Medline
37. Alho EJL, Alho A, Horn A, et al. **The ansa subthalamica: a neglected fiber tract.** *Mov Disord* 2020;35:75–80 CrossRef Medline
38. Petersen MV, Mlakar J, Haber SN, et al. **Holographic reconstruction of axonal pathways in the human brain.** *Neuron* 2019;104:1056–64 CrossRef Medline
39. Eisinger RS, Cernera S, Gittis A, et al. **A review of basal ganglia circuits and physiology: application to deep brain stimulation.** *Parkinsonism Relat Disord* 2019;59:9–20 CrossRef Medline
40. Grewal SS, Holanda VM, Middlebrooks EH. **Corticopallidal connectome of the globus pallidus externus in humans: an exploratory study of structural connectivity using probabilistic diffusion tractography.** *AJNR Am J Neuroradiol* 2018;39:2120–25 CrossRef Medline

41. Parent A, De Bellefeuille L. **Organization of efferent projections from the internal segment of globus pallidus in primate as revealed by flourescence retrograde labeling method.** *Brain Res* 1982;245:201–13 CrossRef Medline
42. Maier-Hein KH, Neher PF, Houde JC, et al. **The challenge of mapping the human connectome based on diffusion tractography.** *Nat Commun* 2017;8:1349 CrossRef Medline
43. Aquino CC, Duffley G, Hedges DM, et al. **Interleaved deep brain stimulation for dyskinesia management in Parkinson's disease.** *Mov Disord* 2019;34:1722–27 CrossRef Medline
44. Accolla EA, Herrojo Ruiz M, Horn A, et al. **Brain networks modulated by subthalamic nucleus deep brain stimulation.** *Brain* 2016;139:2503–15 CrossRef Medline
45. Akram H, Sotiropoulos SN, Jbabdi S, et al. **Subthalamic deep brain stimulation sweet spots and hyperdirect cortical connectivity in Parkinson's disease.** *Neuroimage* 2017;158:332–45 CrossRef Medline
46. Horn A, Reich M, Vorwerk J, et al. **Connectivity predicts deep brain stimulation outcome in Parkinson disease.** *Ann Neurol* 2017;82:67–78 CrossRef Medline
47. Lin H, Na P, Zhang D, et al. **Brain connectivity markers for the identification of effective contacts in subthalamic nucleus deep brain stimulation.** *Hum Brain Mapp* 2020;41:2028–36 CrossRef Medline
48. Albanese A, Bhatia K, Bressman SB, et al. **Phenomenology and classification of dystonia: a consensus update.** *Mov Disord* 2013;28:863–73 CrossRef Medline
49. Vidailhet M, Vercueil L, Houeto JL, et al. **Bilateral deep-brain stimulation of the globus pallidus in primary generalized dystonia.** *N Engl J Med* 2005;352:459–67 CrossRef Medline
50. Vidailhet M, French SPIDY Study Group, Vercueil L, Houeto JL, et al. **Bilateral, pallidal, deep-brain stimulation in primary generalised dystonia: a prospective 3 year follow-up study.** *Lancet Neurol* 2007;6:223–29 CrossRef Medline
51. Kupsch A, Benecke R, Muller J, et al. **Pallidal deep-brain stimulation in primary generalized or segmental dystonia.** *N Engl J Med* 2006;355:1978–90 CrossRef Medline
52. Artusi CA, Dwivedi A, Romagnolo A, et al. **Differential response to pallidal deep brain stimulation among monogenic dystonias: systematic review and meta-analysis.** *J Neurol Neurosurg Psychiatry* 2020;91:426–33 CrossRef Medline
53. Okromelidze L, Tsuboi T, Eisinger RS, et al. **Functional and structural connectivity patterns associated with clinical outcomes in deep brain stimulation of the globus pallidus internus for generalized dystonia.** *AJNR Am J Neuroradiol* 2020;41:508–14 CrossRef Medline
54. Rozanski VE, Vollmar C, Cunha JP, et al. **Connectivity patterns of pallidal DBS electrodes in focal dystonia: a diffusion tensor tractography study.** *Neuroimage* 2014;84:435–42 CrossRef Medline
55. Reese R, Volkmann J. **Deep brain stimulation for the dystonias: evidence, knowledge gaps, and practical considerations.** *Mov Disord Clin Pract* 2017;4:486–94 CrossRef Medline
56. Tastevin M, Spatola G, Régis J, et al. **Deep brain stimulation in the treatment of obsessive-compulsive disorder: current perspectives.** *Neuropsychiatr Dis Treat* 2019;15:1259–72 CrossRef Medline
57. Greenberg BD, Gabriels LA, Malone DA, Jr, et al. **Deep brain stimulation of the ventral internal capsule/ventral striatum for obsessive-compulsive disorder: worldwide experience.** *Mol Psychiatry* 2010;15:64–79 CrossRef Medline
58. Ahmari SE, Spellman T, Douglass NL, et al. **Repeated cortico-striatal stimulation generates persistent OCD-like behavior.** *Science* 2013;340:1234–39 CrossRef Medline
59. Coenen VA, Panksepp J, Hurwitz TA, et al. **Human medial forebrain bundle (MFB) and anterior thalamic radiation (ATR): imaging of two major subcortical pathways and the dynamic balance of opposite affects in understanding depression.** *J Neuropsychiatry Clin Neurosci* 2012;24:223–36 CrossRef Medline
60. Hartmann CJ, Lujan JL, Chaturvedi A, et al. **Tractography activation patterns in dorsolateral prefrontal cortex suggest better clinical responses in OCD DBS.** *Front Neurosci* 2015;9:519 CrossRef Medline
61. Baldermann JC, Melzer C, Zapf A, et al. **Connectivity profile predictive of effective deep brain stimulation in obsessive-compulsive disorder.** *Biol Psychiatry* 2019;85:735–43 CrossRef Medline
62. Coenen VA, Schlaepfer TE, Goll P, et al. **The medial forebrain bundle as a target for deep brain stimulation for obsessive-compulsive disorder.** *CNS Spectr* 2017;22:282–89 CrossRef Medline
63. Liebrand LC, Caan MWA, Schuurman PR, et al. **Individual white matter bundle trajectories are associated with deep brain stimulation response in obsessive-compulsive disorder.** *Brain Stimul* 2019;12:353–60 CrossRef Medline
64. Ding SL, Royall JJ, Sunkin SM, et al. **Comprehensive cellular-resolution atlas of the adult human brain.** *J Comp Neurol* 2016;524:3127–481 CrossRef Medline
65. Tyagi H, Apergis-Schoute AM, Akram H, et al. **A randomized trial directly comparing ventral capsule and anteromedial subthalamic nucleus stimulation in obsessive-compulsive disorder: clinical and imaging evidence for dissociable effects.** *Biol Psychiatry* 2019;85:726–34 CrossRef Medline
66. Salanova V, Witt T, Worth R, et al. **Long-term efficacy and safety of thalamic stimulation for drug-resistant partial epilepsy.** *Neurology* 2015;84:1017–25 CrossRef Medline
67. Lehtimaki K, Coenen VA, Goncalves Ferreira A, et al. **The surgical approach to the anterior nucleus of thalamus in patients with refractory epilepsy: experience from the international multicenter registry (MORE).** *Neurosurgery* 2019;84:141–50 CrossRef Medline
68. Wu C, D'Haese P-F, Pallavaram S, et al. **Variations in thalamic anatomy affect targeting in deep brain stimulation for epilepsy.** *Stereotact Funct Neurosurg* 2016;94:387–96 CrossRef Medline
69. Grewal SS, Middlebrooks EH, Kaufmann TJ, et al. **Fast gray matter acquisition T1 inversion recovery MRI to delineate the mammillothalamic tract for preoperative direct targeting of the anterior nucleus of the thalamus for deep brain stimulation in epilepsy.** *Neurosurg Focus* 2018;45:E6 CrossRef Medline
70. Wang YC, Grewal SS, Middlebrooks EH, et al. **Targeting analysis of a novel parietal approach for deep brain stimulation of the anterior nucleus of the thalamus for epilepsy.** *Epilepsy Res* 2019;153:1–6 CrossRef Medline
71. Yang L, Li H, Zhu L, et al. **Localized shape abnormalities in the thalamus and pallidum are associated with secondarily generalized seizures in mesial temporal lobe epilepsy.** *Epilepsy Behav* 2017;70:259–64 CrossRef Medline
72. Grewal SS, Middlebrooks EH, Okromelidze L, et al. **Variability between direct and indirect targeting of the anterior nucleus of the thalamus.** *World Neurosurg* 2020 Apr 14. [Epub ahead of print] CrossRef Medline
73. Baydin S, Gungor A, Tanriover N, et al. **Fiber tracts of the medial and inferior surfaces of the cerebrum.** *World Neurosurg* 2017;98:34–49 CrossRef Medline
74. Choi SH, Kim YB, Paek SH, et al. **Papez circuit observed by in vivo human brain with 7.0T MRI super-resolution track density imaging and track tracing.** *Front Neuroanat* 2019;13:17 CrossRef Medline
75. Guo W, Koo BB, Kim JH, et al. **Defining the optimal target for anterior thalamic deep brain stimulation in patients with drug-refractory epilepsy.** *J Neurosurg* 2020;1–10 CrossRef Medline
76. Schaper F, Plantinga BR, Colon AJ, et al. **Deep brain stimulation in epilepsy: a role for modulation of the mammillothalamic tract in seizure control?** *Neurosurgery* 2020 May 18. [Epub ahead of print] CrossRef Medline
77. Kamali A, Zhang CC, Riascos RF, et al. **Diffusion tensor tractography of the mammillothalamic tract in the human brain using**

a high spatial resolution DTI technique. *Sci Rep* 2018;8:5229 CrossRef Medline

78. Middlebrooks EH, Grewal SS, Stead M, et al. **Differences in functional connectivity profiles as a predictor of response to anterior thalamic nucleus deep brain stimulation for epilepsy: a hypothesis for the mechanism of action and a potential biomarker for outcomes.** *Neurosurg Focus* 2018;45:E7 CrossRef Medline
79. Wang YC, Kremen V, Brinkmann BH, et al. **Probing circuit of Papez with stimulation of anterior nucleus of the thalamus and hippocampal evoked potentials.** *Epilepsy Res* 2020;159:106248 CrossRef Medline
80. Middlebrooks EH, Lin C, Okromelidze L, et al. **Functional activation patterns of deep brain stimulation of the anterior nucleus of the thalamus.** *World Neurosurg* 2020;136:357–63 CrossRef Medline

Manganese-Enhanced MRI in Patients with Multiple Sclerosis

D.J. Suto, G. Nair, D.M. Sudarshana, S.U. Steele, J. Dwyer, E.S. Beck, J. Ohayon, H. McFarland, A.P. Koretsky, I.C.M. Cortese, and D.S. Reich

ABSTRACT

BACKGROUND AND PURPOSE: Cellular uptake of the manganese ion, when administered as a contrast agent for MR imaging, can noninvasively highlight cellular activity and disease processes in both animals and humans. The purpose of this study was to explore the enhancement profile of manganese in patients with multiple sclerosis.

MATERIALS AND METHODS: Mangafodipir is a manganese chelate that was clinically approved for MR imaging of liver lesions. We present a case series of 6 adults with multiple sclerosis who were scanned at baseline with gadolinium, then injected with mangafodipir, and followed at variable time points thereafter.

RESULTS: Fourteen new lesions formed during or shortly before the study, of which 10 demonstrated manganese enhancement of varying intensity, timing, and spatial pattern. One gadolinium-enhancing extra-axial mass, presumably a meningioma, also demonstrated enhancement with manganese. Most interesting, manganese enhancement was detected in lesions that formed in the days after mangafodipir injection, and this enhancement persisted for several weeks, consistent with contrast coming from intracellular uptake of manganese. Some lesions demonstrated a diffuse pattern of manganese enhancement in an area larger than that of both gadolinium enhancement and T2-FLAIR signal abnormality.

CONCLUSIONS: This work demonstrates the first use of a manganese-based contrast agent to enhance MS lesions on MR imaging. Multiple sclerosis lesions were enhanced with a temporal and spatial profile distinct from that of gadolinium. Further experiments are necessary to uncover the mechanism of manganese contrast enhancement as well as cell-specific uptake.

ABBREVIATION: RRMS = relapsing-remitting MS

Multiple sclerosis causes focal inflammatory demyelinating lesions in the central nervous system, with variable axonal destruction and remyelination.[1] MR imaging is commonly used in MS to monitor disease activity and response to treatment, but MR imaging can also be used to investigate lesion pathophysiology.[2] Contrast-enhanced MR imaging is the criterion standard for the detection of acute disease activity. Gadolinium chelates are the most commonly used MR imaging contrast agents to detect new lesions when the BBB is disrupted, resulting in leakage of gadolinium into the parenchyma. However, exploration of other contrast agents with different mechanisms of action offers the potential for additional insights into disease pathophysiology.

MS lesions are believed to form in a complicated series of immune cell interactions that combine to cause demyelination and cell death.[3] Blood-derived macrophages play a key role in this process and have been shown by histopathologic techniques to be abundant in early lesions.[4] Despite our evolving understanding of the cellular and biochemical stages of an MS lesion, current imaging techniques lack the ability to finely monitor this development.[3] Additionally, gadolinium chelates, which are confined to the intravascular and interstitial compartments, are limited to detecting changes in vascular permeability and are unable to directly probe intracellular processes.

Received March 15, 2020; accepted after revision May 31.

From the National Institute of Neurological Disorders and Stroke, National Institutes of Health, Bethesda, Maryland.

This study was supported by the Intramural Research Program of the National Institute of Neurological Disorders and Stroke (Z01 NS003119).

Paper previously presented as an oral presentation at: Congress of the European Committee for Treatment and Research in Multiple Sclerosis, September 11–13, 2019; Stockholm, Sweden.

Please address correspondence to Daniel S. Reich, MD, PhD, Translational Neuroradiology Section, National Institute of Neurological Disorders and Stroke/National Institutes of Health, 10 Center Dr, MSC 1400, Building 10, Room 5C103, Bethesda, MD 20892; e-mail: daniel.reich@nih.gov

Indicates open access to non-subscribers at www.ajnr.org

Indicates article with supplemental on-line table.

Indicates article with supplemental on-line photos.

http://dx.doi.org/10.3174/ajnr.A6665

Clinical and demographic data

Participant	Age (yr)	Sex	MS Phenotype	Current Disease-Modifying Therapy	EDSS	Years Since Symptom Onset
1	38	M	RRMS	None	1	<1
2	42	F	RRMS	Dimethyl fumarate	1.5	5
3	32	F	RRMS	None	0	<1
4	40	F	RRMS	Interferon β-1a	3	6
5	33	F	RRMS	Daclizumab	2	15
6	39	M	SPMS	Autologous stem cell transplant, conditioning with cyclophosphamide and rituximab	6	13

Note:—SPMS indicates secondary-progressive MS; EDSS, Expanded Disability Status Scale.

Manganese ions (Mn^{2+}) are paramagnetic and shorten the T1 relaxation time, allowing the metal to be used as an MR imaging contrast agent. Additionally, manganese acts as a calcium analog and can enter cells through calcium channels.[5] Due to these dual properties, manganese has been explored in animal models as a surrogate marker for neuroanatomy, cell activity and viability, and neuronal transport. Additionally, like calcium, manganese can be trafficked through axons, released at synapses, and taken up by postsynaptic neurons, allowing tract tracing in animal studies.[6-10] Despite the focus of the field on neuronal import of manganese, uptake by other cell types is likely, given the ubiquity of calcium channels.

In humans, manganese-enhanced MR imaging has been limited by concerns about free manganese toxicity to cardiac muscle cells.[11] Mangafodipir, a chelate of manganese and an organic ligand dipyridoxyl diphosphate, was therefore developed to allow safe and tolerable release of manganese via transmetallation with zinc in plasma to lower the risk of cardiotoxicity relative to infusion of manganese salts.[12] Mangafodipir was approved by the FDA in 1997 as a contrast agent for imaging lesions in the liver and pancreas. However, mangafodipir-enhanced brain MR imaging in humans has received little attention. In a recent study, we described a typical pattern of enhancement of manganese in the choroid plexus, anterior pituitary gland, and exocrine glands (including lacrimal, submandibular, and parotid glands) in healthy people.[13] We found no evidence on MR imaging of manganese enhancement within the brain parenchyma in these subjects, suggesting that mangafodipir is unable to cross the BBB. We established a peak of enhancement in the anterior pituitary gland between 1 and 24 hours and a peak of choroid plexus enhancement at 1.5 hours. Both the spatial and the temporal enhancement profiles of these structures are consistent with studies that infused manganese salts into animals, suggesting that the contrast seen was due to released manganese.[14]

The intracellular uptake characteristics of manganese, as gleaned from animal studies, offer the potential to expand our understanding of cellular activity and viability in active, demyelinating lesions in vivo. Thus, using a 1-time, single-dose injection of mangafodipir, we explored manganese enhancement of lesions in the brain in adults with MS.

MATERIALS AND METHODS

Six adults with MS (4 women) were recruited under an institutional review board–approved protocol (NCT01326715) from April 2015 to February 2019, after confirming no stated history of excessive manganese exposure, inadequate hepatic or biliary function, or contraindications to MR imaging. The average age was 37 ± 3.9 years; the median Expanded Disability Status Scale score was 2 (range, 0–6), and median years since MS symptom onset was 7 (range, 0–15) (Table).

MR Imaging Acquisition and Mangafodipir Administration

All prospective participants were imaged at baseline with gadolinium (gadobutrol, 0.1 mmol/kg) no more than 1 week before mangafodipir injection to assess evidence of a disrupted BBB and to exclude individuals with >5 enhancing lesions (a prespecified safety measure). Mangafodipir was reformulated from a clinical-grade stock under an FDA investigational new drug application, because commercial mangafodipir is no longer produced or marketed. For 1 minute, 5 μmol/kg of mangafodipir was administered intravenously. Five of the 6 participants were imaged within 4 hours of mangafodipir injection; one was first scanned 3 days after injection. Subsequent scans were obtained at variable points within the days to weeks after injection, on the basis of our initial experience in healthy volunteers, participant availability, and an intention to sample a range of postinjection time points in this pilot study. Because manganese (unlike gadolinium) enters cells, we expected slower washout than with gadolinium. All participants underwent a 1-month post-mangafodipir injection MR imaging to assess for persistent signal change in the brain; if found, monthly scans were obtained until residual enhancement resolved.

Images were acquired on a 3T Magnetom Skyra (Siemens) scanner with a 32-channel head coil. Several T1- and T2-weighted sequences were acquired, including a 3D T1 sampling perfection with application-optimized contrasts by using different flip angle evolution (SPACE sequence; Siemens) (0.67-mm isotropic resolution, TR = 700 ms, TE = 26 ms, FOV = 256 mm, turbo factor = 96, fat suppression = SPectral Attenuated Inversion Recovery), a 3D-T1-weighted gradient-echo sequence (1 mm isotropic, TR = 7.8 ms, TE = 3ms, FOV = 256 mm, flip angle = 18°), and a 3D-T2-FLAIR sequence (1-mm isotropic resolution, TR = 4800 ms, TE = 353 ms, FOV = 256 mm). No dynamic image series was acquired during postmangafodipir acquisitions.

MR Imaging Processing

Images from all postmangafodipir time points were cross-sectionally and then longitudinally registered to the baseline T1-gradient-echo sequence using 3dAllineate (afni.nimh.nih.gov). Image processing also included inhomogeneity correction with N4 Bias Field Correction (https://simpleitk.readthedocs.io/en/master/link_N4BiasFieldCorrection_docs.html).[15] Intensity normalization was

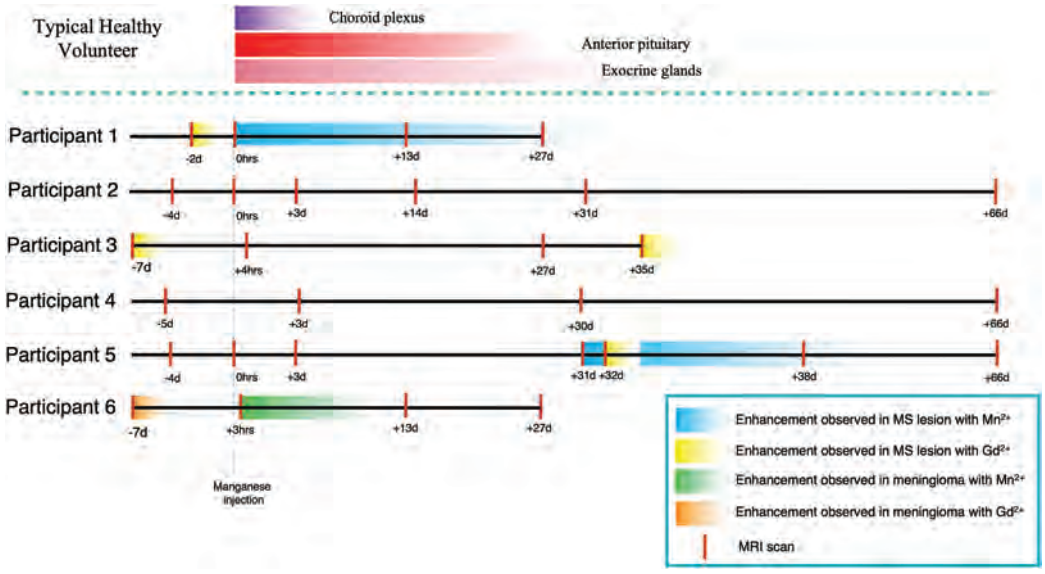

FIG 1. Summary of MR imaging time points and contrast enhancement. Participants were imaged at baseline, shortly after injection, and in the days to months after injection. *Red vertical lines* indicate MR imaging scans; *blue bars*, enhancement of MS lesions due to mangafodipir injection; *yellow bars*, gadolinium enhancement of MS lesions; the *green bar*, enhancement of a meningioma due to mangafodipir injection; and the *orange bar*, gadolinium enhancement of a meningioma. Gradients suggest decay of signal between time points but are not intended to be quantitative because temporal granularity is limited by infrequent imaging time points. D indicates days; Gd^{2+}, gadolinium ion.

achieved by normalizing the whole brain to the median intensity of the skull-stripped brain and subsequently scaling by the maximum intensity. Subtraction images were generated by voxelwise subtraction of the registered, uniformity-corrected, and intensity-normalized T1-SPACE baseline scans from the respective post-mangafodipir T1-SPACE images.

RESULTS

Findings in All Participants

All participants demonstrated a typical pattern of enhancement in the choroid plexus, anterior pituitary, and exocrine glands, including lacrimal, submandibular, and parotid glands, similar to that in healthy volunteers.[13]

Findings in Specific Participants

Findings in individual lesions are summarized in Fig 1 and the On-line Table.

Participant 1

Participant 1 was a 38-year-old man with mild lesion burden and minimally prominent CSF spaces. On baseline MR imaging, there was a large, gadolinium-enhancing lesion in the left periventricular white matter (the lesion that was responsible for his initial MS presentation). Two days later, he was imaged before and within 1 hour after infusion with mangafodipir. This scan demonstrated subtle manganese enhancement in the same lesion (Fig 2*C*). Central enhancement in this lesion resolved by day 13. No other brain lesions enhanced with mangafodipir. In scans obtained 13 and 27 days postmangafodipir, faint and diffuse enhancement was noted caudal to the lesion border (Fig 2*I, -J, -L, -M*).

Participant 2

Participant 2 was a 42-year-old woman with relapsing-remitting MS (RRMS), minimally prominent CSF spaces, and a moderate lesion burden. The baseline MR imaging showed no evidence of parenchymal gadolinium enhancement. Images acquired approximately 30 minutes after injection of mangafodipir demonstrated no abnormal enhancement in the brain and no enhancement of previously visualized MS lesions (On-line Fig 1*A–C*). Hyperintense T1-weighted signal had resolved in the choroid plexus by 14 days post-mangafodipir injection, similar to prior work on healthy volunteers. All typical manganese-related enhancement had resolved by 38 days postinjection. No new lesions formed during this period.

Participant 3

Participant 3 was a 32-year-old woman with moderate lesion burden and minimally prominent CSF spaces. Baseline MR imaging 1 week before mangafodipir injection demonstrated 2 small lesions on T2-FLAIR, measuring approximately 4 × 2 and 3 × 2 mm in-plane and enhancing faintly with gadolinium. Four hours post-mangafodipir injection, manganese enhancement was not apparent in any MS lesion, regardless of gadolinium enhancement status (On-line Fig 1*D–F*). Typical mangafodipir-related enhancement in the exocrine glands and choroid plexus resolved by day 27 postmangafodipir. At this time point, the 2 small, previously gadolinium-enhancing lesions were no longer visible on T2-FLAIR. A small new T2-FLAIR lesion had formed, but this did not demonstrate T1-hyperintensity indicative of manganese enhancement. Follow-up imaging 8 days later (35 days post-mangafodipir injection) showed gadolinium enhancement of this new lesion.

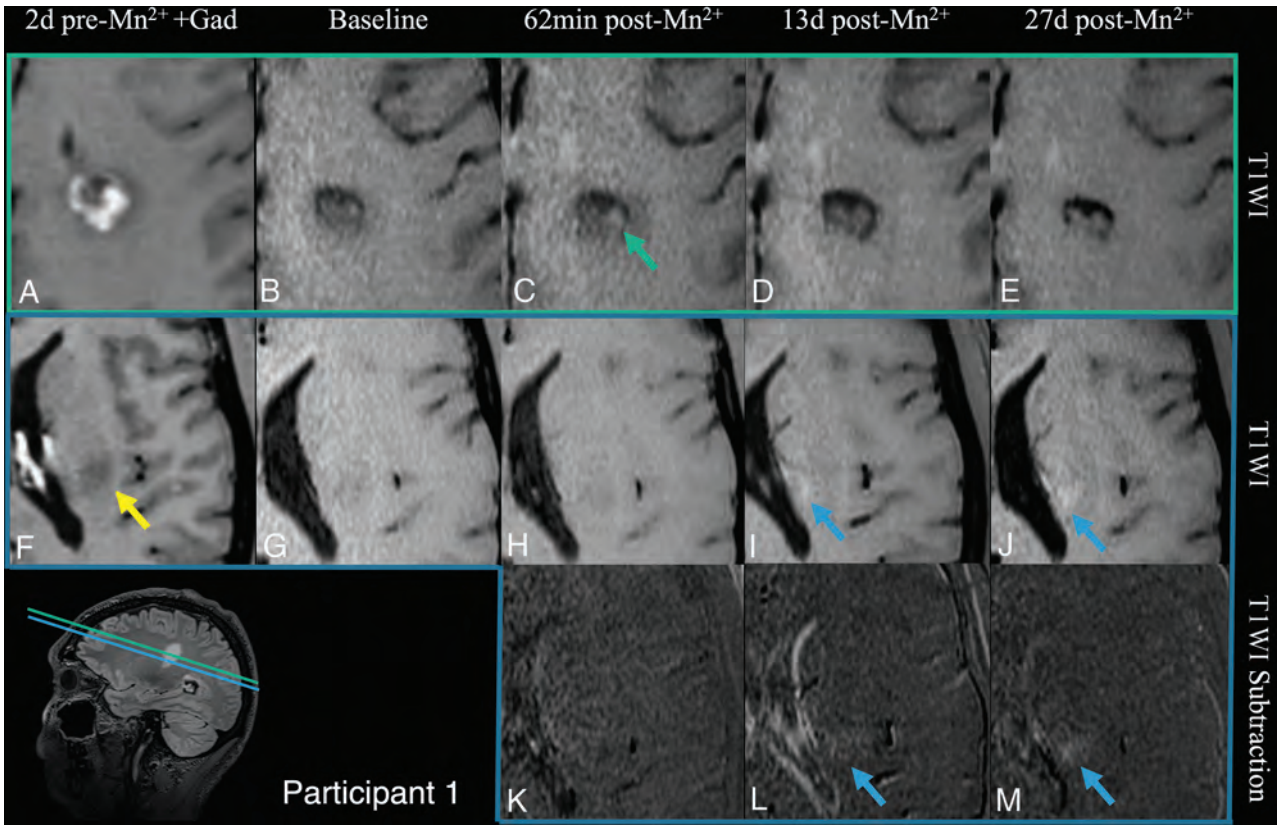

FIG 2. Mangafodipir enhancement of an active gadolinium-enhancing lesion (participant 1). At screening, this lesion enhanced with gadolinium on T1-SPACE (*A*) with caudal edema visible on T1 (*F*, *yellow arrow*). At the center of the lesion (*green plane*, *A–E*), faint manganese enhancement is noted at 62 minutes (*C*) and resolved 13 days after injection (*D*). Caudal to the lesion (*blue plane*, *F–M*), manganese enhancement was noted outside the lesion border at 13 days (*I*, *blue arrow*) and on subtraction images (*L*). This enhancement persisted at 27 days (*J* and *M*, *blue arrow*). Additionally, ventricular narrowing, which commonly fluctuates,[16] was noted on day 13 postmangafodipir in reference to the baseline (*L*); this appeared to resolve by day 27 postmangafodipir.

Participant 4

Participant 4 was a 40-year-old woman with moderately prominent CSF spaces and moderate lesion burden. The baseline scan showed no abnormal enhancement with gadolinium. On the first postmangafodipir scan 3 days after mangafodipir injection, there was no evidence of enhancement within the brain parenchyma, including in MS lesions. No new lesions developed during the study. All typical manganese enhancement that persisted through 30 days postmangafodipir had resolved by 66 days after mangafodipir injection.

Participant 5

Participant 5 was a 33-year-old woman with severe lesion burden and moderately prominent CSF spaces. The baseline scan showed no abnormal enhancement with gadolinium. Immediately after mangafodipir injection, there was no abnormal manganese enhancement in the brain and no enhancement of previously visualized MS lesions. MR imaging was repeated 3 days postmangafodipir injection, no new T2-FLAIR lesions had formed, and there was no manganese enhancement in the brain. At 31 days postinjection, 8 new T2-FLAIR lesions were noted. Of these lesions, all were T1-hyperintense, which was not typical of new MS lesions visualized previously in this individual; this finding suggests that the lesions had taken up Mn^{2+} between imaging time points. Three of the lesions demonstrated blush-like enhancement, characterized by a faint and diffuse enhancement pattern covering an area approximately 4 times larger than the T2 lesion (Fig 3, upper part). Five lesions demonstrated a punctate pattern of enhancement. A follow-up scan the next day (32 days postinjection) demonstrated nodular gadolinium enhancement in 5 of the 8 total lesions (Fig 3, middle and lower parts), and the area of gadolinium enhancement was contained within the T2-FLAIR lesion area. At 38 days post-mangafodipir injection, 2 additional new T2-FLAIR lesions had formed. All of this participant's manganese-enhancing lesions are shown in On-line Fig 2. Retrospective review of the day 31 scan showed T1-hyperintense signal in 1 of these lesions (On-line Fig 2, lesion 13), suggestive of manganese uptake before lesion detection on T2-FLAIR.

Participant 6

Participant 6 was a 39-year-old man with secondary-progressive MS, a moderate lesion burden, and minimally prominent CSF spaces. There were no gadolinium-enhancing MS lesions on baseline MR imaging; however, there was a long-standing extra-axial, dural-based mass anterior to the left temporal lobe, characteristic of meningioma, that was gadolinium-enhancing (Fig 4*B*, *-F*). He was imaged before and 3 hours after mangafodipir injection. The mass enhanced with mangafodipir (Fig 4*C*, *-G*), but none of the

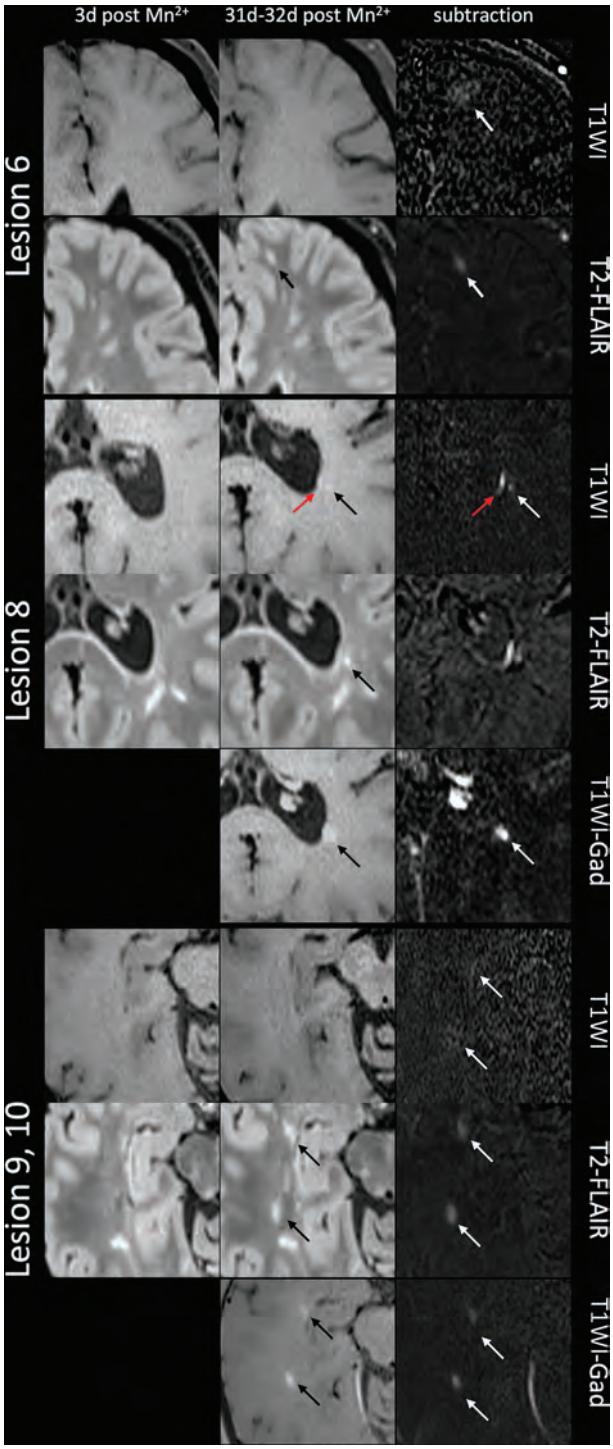

FIG 3. Mangafodipir enhancement of MS lesions (participant 5). *Upper part,* Lesion 6 showed blush-like mangafodipir enhancement in a T2 lesion that formed between days 3 and 31 post-mangafodipir injection. There is subtle TI-hyperintense signal visible only on subtraction, suggesting manganese enhancement, in an area larger than the T2-FLAIR lesion. This lesion did not enhance with gadolinium on day 32 post-mangafodipir injection. *Middle, lower part,* Several lesions that formed between day 3 and day 31 post-mangafodipir injection enhanced with both manganese and gadolinium. Lesion 8 (*middle*) demonstrates nodular (*black arrow*) and ependymal (*red arrow*) enhancement with manganese but only nodular enhancement with gadolinium. Lesions 9 and 10 (*lower part*) demonstrate blush-like enhancement with manganese, visible on subtraction images, and nodular enhancement with gadolinium. Gad indicates gadolinium.

MS lesions enhanced. Enhancement in the mass had resolved by the next scan, 13 days post-mangafodipir injection (Fig 4*D, -H*).

DISCUSSION

In this report, we describe the use of a manganese-based contrast agent (mangafodipir) in a series of adults with MS and report that active MS plaques enhance with manganese in patterns distinct from those of gadolinium enhancement in the same lesions. Although variable delays between mangafodipir infusion and imaging limit direct comparison across the participants in our study, several patterns emerged. Similar to healthy volunteers,[13] we found a characteristic pattern of manganese enhancement in the anterior pituitary gland, exocrine glands, and choroid plexus shortly after injection. We did not observe manganese enhancement in chronic MS lesions. One MS lesion that was gadolinium-enhancing 2 days before mangafodipir administration also demonstrated manganese enhancement. Most interesting, some lesions that formed in the days to weeks after mangafodipir injection also enhanced, evident in delayed scans.

With respect to the manganese enhancement pattern, 4 active lesions demonstrated diffuse, blush-like enhancement that encompassed a much larger volume than was hyperintense on either T2-FLAIR or postgadolinium T1 (Fig 3). Considering that we never observed manganese enhancement in areas with intact BBBs, this observation suggests that the manganese ion or mangafodipir entered the brain parenchyma within the lesions, was taken up by local cells or cell processes, and subsequently spread outside the T2-FLAIR area. We cannot resolve whether such uptake was within axons, glia, invading immune cells, or some combination.

In addition to distinct enhancement patterns, the kinetics of manganese enhancement also differ from that of gadolinium. In participant 5, manganese enhancement occurred during a much longer time window than gadolinium enhancement: Lesions newly visible on T2-FLAIR even 38 days after injection demonstrated manganese enhancement. Lesion 13, which was not visible on T2-FLAIR 31 days postinjection, showed faint enhancement with manganese at that timepoint. Additionally, this lesion demonstrated gadolinium enhancement the following day, with no T2-FLAIR correlate. This result is consistent with published data suggesting that demyelination, which causes hyperintense signal on T2-weighted images, is preceded by other pathologic processes in both MS[17,18] and experimental autoimmune encephalomyelitis[3,19] lesions and that these processes are not entirely invisible to MR imaging. It also suggests that the manganese that is injected with mangafodipir may be retained in various stores within the body (possibly in the liver, kidney, and exocrine/endocrine glands), subsequently re-entering the circulation at low-but-steady levels. This characteristic would allow manganese accumulation within the intracellular compartments in newly forming lesions with damaged BBBs.

Observations in participant 3 further illustrate that manganese enhancement of MS lesions must be interpreted differently from gadolinium enhancement. This participant had 2 small lesions that enhanced with gadolinium at baseline, as well as a newly formed and later gadolinium-enhancing lesion. However, none of these lesions demonstrated evidence of enhancement after mangafodipir.

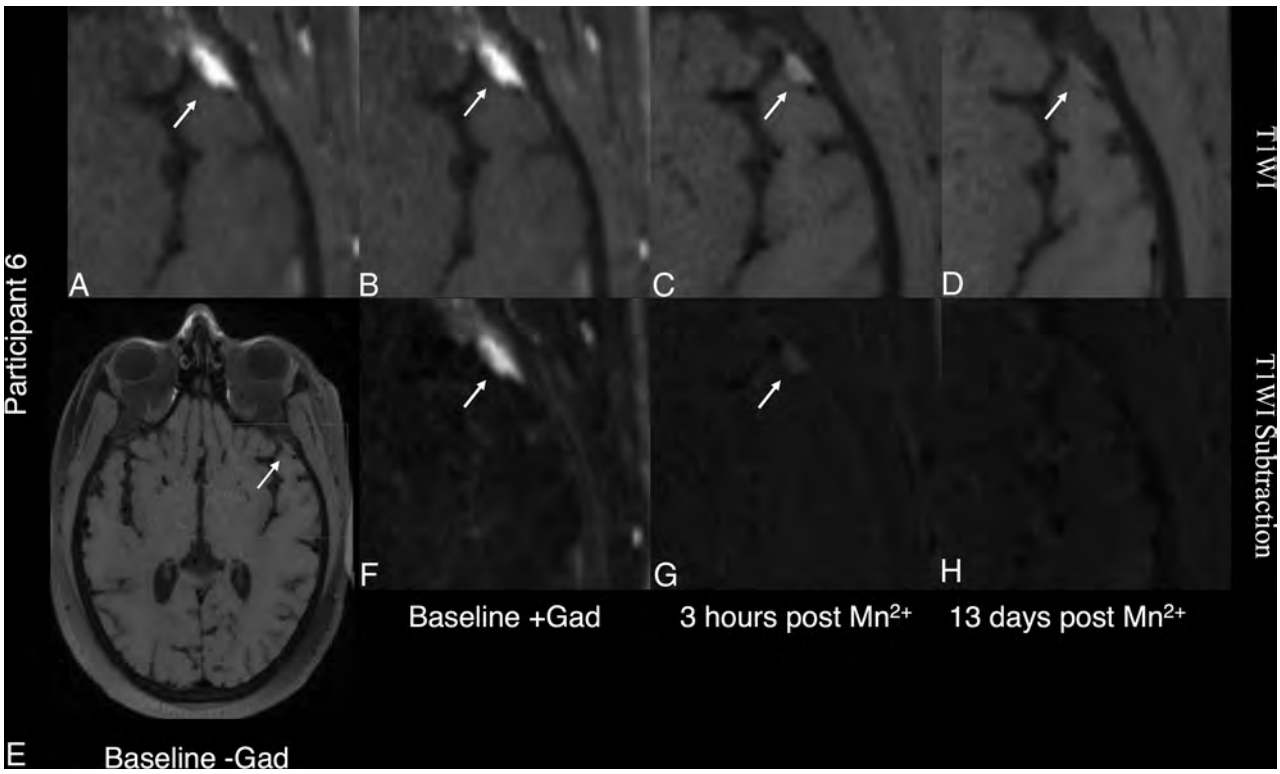

FIG 4. Manganese enhancement of a presumed meningioma in participant 6, a 39-year-old man with secondary-progressive MS. The mass (*arrow*) is visible on precontrast T1-weighted images (*A* and *E*) with vivid gadolinium enhancement (gadolinium [Gad]) visible on both T1-weighted (*B*) and T1 gadolinium subtraction (*F*) images. Mangafodipir enhancement is visible within the mass 3 hours after mangafodipir (*C* and *G*) and had resolved by 13 days postinjection (*D* and *H*).

It is possible that the small size and faint gadolinium enhancement of these lesions at baseline were below detectability with mangafodipir at the dose we used, but it could also suggest that these lesions were at a late active stage. Additionally, a lesion in this participant that formed after mangafodipir injection did not visibly take up manganese, potentially because the time between manganese injection and lesion formation was too long.

A key difference between manganese and gadolinium in animal studies is the ability of manganese to be imported into cells and, in neurons, transported within axons and across synapses.[20] The enhancement patterns we observed in MS lesions, though, appear different from those demonstrated in animal models, with no obvious linear enhancement along white matter tracts.[21,22] It is possible that tract-restricted manganese enhancement was too faint at the FDA-approved dose, which delivers a much lower manganese load than is typically given in animal experiments.[11,23] PET imaging with manganese-52 (Mn^{2+}) might overcome this limitation at the expense of spatial resolution.[24]

In addition to the observed manganese enhancement in MS lesions, participant 6 had a presumed meningioma that enhanced 3 hours following mangafodipir injection. The meningioma also avidly enhanced with gadolinium, but unlike with gadolinium, mangafodipir enhancement was not masked by nearby vascular enhancement. Manganese enhancement had resolved by the next scan 13 days later. Although mangafodipir has been previously shown to be equal or better at detecting liver lesions and metastases than contrast-enhanced CT and ferucarbotran-enhanced MR imaging, its use in meningiomas has not been reported.[25-28] One study reported that manganese retention in hepatocellular carcinoma correlates with tumor staging and prognosis,[29] and it is possible that patterns of manganese enhancement could also provide useful clinical information about intracranial tumors.

CONCLUSIONS

This is the first study to evaluate enhancement dynamics of manganese within MS lesions. Our data show that manganese ions enable visualization of the acute inflammatory demyelination that occurs in active MS lesions. Furthermore, the intracellular capability of manganese is consistent with diffuse enhancement in an area larger than that of the T2-FLAIR lesion days after injection. From the results in this small cohort, we cannot comment on differences in enhancement patterns that may be induced by disease-modifying therapies. Most important, we cannot distinguish between enhancement due to Mn^{2+} ions and mangafodipir at early time points because these may generate similar enhancement profiles. However, transmetallation of mangafodipir increases the likelihood that enhancement at later time points is due to the ion

itself. While mangafodipir used at the dose in this study does not fully recapitulate the ability of gadolinium to vividly and immediately mark active MS lesions, use of mangafodipir in MS imaging offers the possibility of following lesion formation in a longer window than gadolinium and may provide new insights into the pathophysiology of lesion formation.

ACKNOWLEDGMENTS

We thank the National Institute of Neurological Disorders and Stroke Neuroimmunology Clinic and the Clinical Trials Unit (in particular Rosalind Hayden, Rosemarie Cuento, and Sandra Martin), National Institutes of Health Pharmaceutical Development Section (especially Gopal Potti and Judith Starling), Dzung Pham, John Olson, and the Functional MR Imaging Facility for their assistance.

Disclosures: Daniel J. Suto—*RELATED*: *Grant*: National Institutes of Health Internal Funding, *Comments*: National Institute of Neurological Disorders and Stroke Z01 NS003119*; *Support for Travel to Meetings for the Study or Other Purposes*: Congress of the European Committee for Treatment and Research in Multiple Sclerosis; *Provision of Writing Assistance, Medicines, Equipment, or Administrative Support*: National Institute of Neurological Disorders and Stroke Z01 NS003119*; *UNRELATED*: *Employment*: National Institutes of Health, *Comments*: National Institutes of Health Postbaccalaureate Program.* Erin S. Beck—*RELATED*: *Grant*: National Multiple Sclerosis Society, *Comments*: fellowship grant to support my salary.* Henry McFarland—*UNRELATED*: *Employment*: Scientific Director of the Cummings Foundation, *Comments*: not-for-profit educational foundation; *Royalties*: daclizumab (Biogen through the National Institutes of Health), *Comments*: <$100 in 2019. Alan P. Koretsky—*RELATED*: *Grant*: I am an Intramural Investigator at the National Institute of Neurological Disorders and Stroke, National Institutes of Health; Congress allocated money to the National Institute of Neurological Disorders and Stroke that was used to support this work; however, we do not refer to this support as a grant; *UNRELATED*: *Patents (Planned, Pending or Issued)*: The National Institute of Neurological Disorders and Stroke supports patents for intramural investigators. I do have some patents pending, but there is no money to me or the National Institutes of Health; these are not related in any way to the submitted work; *Travel/Accommodations/Meeting Expenses Unrelated to Activities Listed*: Typically, travel is reimbursed when Intramural Investigators give academic presentations at universities or relevant meetings. No money is paid to me or the National Institutes of Health for these presentations. In addition, I serve on a couple of advisory committees (no compensation to me or the National Institutes of Health), for which travel is paid. Daniel S. Reich—*UNRELATED*: *Expert testimony*: Leventhal and Puga LLC, Bounds Law Group LLC; *Grants/Grants Pending*: Vertex Pharmaceuticals.* *Money paid to the institution.

REFERENCES

1. Reich DS, Lucchinetti CF, Calabresi PA. **Multiple sclerosis.** *N Engl J Med* 2018;378:169–80 CrossRef Medline
2. Filippi M, Rocca MA, Barkhof F, et al; Attendees of the Correlation between Pathological MRI Findings in MS Workshop. **Association between pathological and MRI findings in multiple sclerosis.** *Lancet Neurol* 2012;11:349–60 CrossRef Medline
3. Absinta M, Sati P, Reich DS. **Advanced MRI and staging of multiple sclerosis lesions.** *Nat Rev Neurol* 2016;12:358–68 CrossRef Medline
4. Henderson AP, Barnett MH, Parratt JD, et al. **Multiple sclerosis: distribution of inflammatory cells in newly forming lesions.** *Ann Neurol* 2009;66:739–53 CrossRef Medline
5. Silva AC, Bock NA. **Manganese-enhanced MRI: an exceptional tool in translational neuroimaging.** *Schizophr Bull* 2008;34:595–604 CrossRef Medline
6. Stieltjes B, Schlüter M, Didinger B, et al. **Diffusion tensor imaging in primary brain tumors: reproducible quantitative analysis of corpus callosum infiltration and contralateral involvement using a probabilistic mixture model.** *Neuroimage* 2006;31:531–42 CrossRef Medline
7. Walder N, Petter-Puchner AH, Brejnikow M, et al. **Manganese enhanced magnetic resonance imaging in a contusion model of spinal cord injury in rats: correlation with motor function.** *Invest Radiol* 2008;43:277–83 CrossRef Medline
8. Lee JH, Silva AC, Merkle H, et al. **Manganese-enhanced magnetic resonance imaging of mouse brain after systemic administration of MnCl2: dose-dependent and temporal evolution of T1 contrast.** *Magn Reson Med* 2005;53:640–48 CrossRef Medline
9. Monosov IE, Leopold DA, Hikosaka O. **Neurons in the primate medial basal forebrain signal combined information about reward uncertainty, value, and punishment anticipation.** *J Neurosci* 2015;35:7443–59 CrossRef Medline
10. Van Meir V, Pavlova D, Verhoye M, et al. **In vivo MR imaging of the seasonal volumetric and functional plasticity of song control nuclei in relation to song output in a female songbird.** *Neuroimage* 2006;31:981–92 CrossRef Medline
11. Crossgrove J, Zheng W. **Manganese toxicity upon overexposure.** *NMR Biomed* 2004;17:544–53 CrossRef Medline
12. Toft KG, Hustvedt SO, Grant D, et al. **Metabolism and pharmacokinetics of MnDPDP in man.** *Acta Radiol* 1997;38(4 Pt 2):677–89 CrossRef Medline
13. Sudarshana DM, Nair G, Dwyer JT, et al. **Manganese-enhanced MRI of the brain in healthy volunteers.** *AJNR Am J Neuroradiol* 2019;40:1309–16 CrossRef Medline
14. Aoki I, Wu YJ, Silva AC, et al. **In vivo detection of neuroarchitecture in the rodent brain using manganese-enhanced MRI.** *Neuroimage* 2004;22:1046–59 CrossRef Medline
15. Tustison NJ, Avants BB, Cook PA, et al. **N4ITK: improved N3 Bias correction.** *IEEE Trans Med Imaging* 2010;29:1310–20 CrossRef Medline
16. Nakamura K, Brown RA, Narayanan S, et al. **Diurnal fluctuations in brain volume: statistical analyses of MRI from large populations.** *Neuroimage* 2015;118:126–32 CrossRef Medline
17. Absinta M, Nair G, Sati P, et al. **Direct MRI detection of impending plaque development in multiple sclerosis.** *Neurol Neuroimmunol Neuroinflamm* 2015;2:e145 CrossRef Medline
18. Goodkin DE, Rooney WD, Sloan R, et al. **A serial study of new MS lesions and the white matter from which they arise.** *Neurology* 1998;51:1689–97 CrossRef Medline
19. Maggi P, Macri SM, Gaitán MI, et al. **The formation of inflammatory demyelinated lesions in cerebral white matter.** *Ann Neurol* 2014;76:594–608 CrossRef Medline
20. Pautler RG. **In vivo, trans-synaptic tract-tracing utilizing manganese-enhanced magnetic resonance imaging (MEMRI).** *NMR Biomed* 2004;17:595–601 CrossRef Medline
21. Saleem KS, Pauls JM, Augath M, et al. **Magnetic resonance imaging of neuronal connections in the macaque monkey.** *Neuron* 2002;34:685–700 CrossRef Medline
22. Chuang KH, Lee JH, Silva AC, et al. **Manganese enhanced MRI reveals functional circuitry in response to odorant stimuli.** *Neuroimage* 2009;44:363–72 CrossRef Medline
23. Wolf GL, Baum L. **Cardiovascular toxicity and tissue proton T1 response to manganese injection in the dog and rabbit.** *AJR Am J Roentgenol* 1983;141:193–97 CrossRef Medline
24. Saar G, Millo C, Szajek L, et al. **Anatomy, functionality, and neuronal connectivity with manganese radiotracers for positron emission tomography.** *Mol Imaging Biol* 2018;20:562–74 CrossRef Medline
25. Kim HJ, Kim KW, Byun JH, et al. **Comparison of mangafodipir trisodium- and ferucarbotran-enhanced MRI for detection and characterization of hepatic metastases in colorectal cancer patients.** *AJR Am J Roentgenol* 2006;186:1059–66 CrossRef Medline
26. Oudkerk M, Torres CG, Song B, et al. **Characterization of liver lesions with mangafodipir trisodium-enhanced MR imaging:**

multicenter study comparing MR and dual-phase spiral CT. *Radiology* 2002;223:517–24 CrossRef Medline

27. Choi JY, Kim MJ, Kim JH, et al. **Detection of hepatic metastasis: manganese- and ferucarbotran-enhanced MR imaging** (in French). *Eur J Radiol* 2006;60:84–90 CrossRef Medline
28. Beziat C, Pilleul F, Yzebe D, et al. **Detection of liver metastases in colorectal cancer on chemotherapy: comparative study between MRI with Teslascan and computed tomography with intravenous contrast media.** *J Radiol* 2004;85:307–11 CrossRef Medline
29. Sutcliffe RP, Lewis D, Kane PA, et al. **Manganese-enhanced MRI predicts the histological grade of hepatocellular carcinoma in potential surgical candidates.** *Clin Radiol* 2011;66:237–43 CrossRef Medline

Disability Improvement Is Associated with Less Brain Atrophy Development in Multiple Sclerosis

E. Ghione, N. Bergsland, M.G. Dwyer, J. Hagemeier, D. Jakimovski, D.P. Ramasamy, D. Hojnacki, A.A. Lizarraga, C. Kolb, S. Eckert, B. Weinstock-Guttman, and R. Zivadinov

ABSTRACT

BACKGROUND AND PURPOSE: It is unknown whether deceleration of brain atrophy is associated with disability improvement in patients with MS. Our aim was to investigate whether patients with MS with disability improvement develop less brain atrophy compared with those who progress in disability or remain stable.

MATERIALS AND METHODS: We followed 980 patients with MS for a mean of 4.8 ± 2.4 years. Subjects were divided into 3 groups: progress in disability (n = 241, 24.6%), disability improvement (n = 101, 10.3%), and stable (n = 638, 65.1%) at follow-up. Disability improvement and progress in disability were defined on the basis of the Expanded Disability Status Scale score change using standardized guidelines. Stable was defined as nonoccurrence of progress in disability or disability improvement. Normalized whole-brain volume was calculated using SIENAX on 3D T1WI, whereas the lateral ventricle was measured using NeuroSTREAM on 2D-T2-FLAIR images. The percentage brain volume change and percentage lateral ventricle volume change were calculated using SIENA and NeuroSTREAM, respectively. Differences among groups were investigated using ANCOVA, adjusted for age at first MR imaging, race, T2 lesion volume, and corresponding baseline structural volume and the Expanded Disability Status Scale.

RESULTS: At first MR imaging, there were no differences among progress in disability, disability improvement, and the stable groups in whole-brain volume (P = .71) or lateral ventricle volume (P = .74). During follow-up, patients with disability improvement had the lowest annualized percentage lateral ventricle volume change (1.6% ± 2.7%) followed by patients who were stable (2.1% ± 3.7%) and had progress in disability (4.1% ± 5.5%), respectively (P < .001). The annualized percentage brain volume change values were −0.7% ± 0.7% for disability improvement, −0.8% ± 0.7% for stable, and −1.1% ± 1.1% for progress in disability (P = .001).

CONCLUSIONS: Patients with MS who improve in their clinical disability develop less brain atrophy across time compared with those who progress.

ABBREVIATIONS: DMT = disease-modifying therapies; EDSS = Expanded Disability Status Scale; LVV = lateral ventricle volume; PBVC = percentage brain volume change; PLVVC = percentage lateral ventricle volume change; PP = primary-progressive; RR = relapsing-remitting; SP = secondary-progressive; T2-LV = T2 lesion volume

MS is an autoimmune disease of the central nervous system characterized by focal and diffuse inflammation[1] and neurodegeneration that presents with central, peripheral, and regional brain atrophy.[2,3] Brain atrophy measurement is one of the key biomarkers in MS[4,5] because it can be assessed in vivo by MR imaging. Brain atrophy is accelerated in patients with MS,[6] persists during the course of the disease, and is clinically meaningful since the earliest disease stages.[7] Brain atrophy is related to short- and long-term physical and cognitive clinical deterioration, more robust than other measures of disease burden and lesion activity.[5,8,9]

Received November 24, 2019; accepted after revision June 1, 2020.

From the Department of Neurology (E.G., N.B., M.G.D., J.H., D.J., D.P.R., R.Z.), Buffalo Neuroimaging Analysis Center, and Department of Neurology (D.H., A.A.L., C.K., S.E., B.W.-G.), Jacobs Comprehensive MS Treatment and Research Center, Jacobs School of Medicine and Biomedical Sciences; and Center for Biomedical Imaging at the Clinical Translational Science Institute (M.G.D., R.Z.),University at Buffalo, State University of New York, Buffalo, New York; and and IRCCS (N.B.), Fondazione Don Carlo Gnocchi ONLUS, Milan, Italy.

Research reported in this publication was funded by the National Center for Advancing Translational Sciences of the National Institutes of Health under award No. UL1TR001412.

The content is solely the responsibility of the authors and does not necessarily represent the official views of the National Institutes of Health.

Please address correspondence to Robert Zivadinov, MD, PhD, Department of Neurology, Jacobs School of Medicine and Biomedical Sciences, Buffalo Neuroimaging Analysis Center, Center for Biomedical Imaging at Clinical Translational, Science Institute, University at Buffalo, 100 High St, Buffalo, NY 14203; e-mail: rzivadinov@bnac.net

Indicates open access to non-subscribers at www.ajnr.org
Indicates article with supplemental on-line tables.
Indicates article with supplemental on-line photo.
http://dx.doi.org/10.3174/ajnr.A6684

A modest-to-strong link between development of brain atrophy and worsening of disability progression has been established.[10-12] Consequently, all recent major Phase 3 clinical trials in MS now consider brain atrophy as one of the main neurodegenerative outcomes for evaluating the efficacy of disease-modifying therapies (DMT).[13-18]

It has been shown that some of the available DMT can not only slow radiologic and clinical progression but also improve clinical status in a substantial proportion of patients with MS in the mid- to long-term.[13,15,16,18,19] Nevertheless, only a few studies have explored the relationship between behavior of brain volume changes and improvement in clinical status,[20-22] and no studies examined this phenomenon in the clinical routine in a large population of patients with MS followed long term. Thus, it is unknown whether patients with MS who experience disability improvement have a decelerated brain atrophy trajectory, compared with those with stable disease or disability progression.

In the current study, we hypothesized that long-term deceleration of brain atrophy progression will be linked to disability improvement in patients followed in a clinical routine. Thus, we investigated whether patients with MS with disability improvement develop less brain atrophy compared with those who either progress in their disease or remain stable.

MATERIALS AND METHODS

Subjects

This retrospective study included 980 patients with MS, who were prospectively followed in a single MS center (Jacobs Comprehensive MS Treatment and Research Center) between 2006 and 2016.

The inclusion criteria for this study were the following: 1) being diagnosed with MS according to the McDonald criteria,[23] 2) availability of both 2D-T2WI-FLAIR and 3D-T1WI sequences at every MR imaging examination, 3) the presence of 1 follow-up MR imaging examination in the same subject during ≥6 months after baseline examination, and 4) the availability of demographic (race was also included for completeness of the data reporting) and clinical information at baseline and follow-up examinations. Exclusion criteria were the following: 1) having a relapse or steroid treatment in the 30 days preceding the MR imaging examination, 2) pre-existing medical conditions known to be associated with brain pathology (cerebrovascular disease, positive history of alcohol abuse), and 3) pregnancy. The selection of subjects, according to the inclusion and exclusion criteria, is shown in the On-line Figure.

The study was approved by the local institutional review board, and due to the retrospective nature of the study, the requirement for obtaining informed consent was waived.

MR Imaging Acquisition and Analysis

The MR imaging examinations used in the present study were obtained on 1.5T and 3T Signa Excite HD 12.0 Twin Speed 8-channel scanners (GE Healthcare) with head and neck coils (HDNV; GE Healthcare), which did not undergo any hardware or software changes during the study period. The 3T MR imaging sequences used in this study were the following: 1) an axial 2D-T2WI-FLAIR sequence with TE/TI/TR of 120/2100/8500 ms, flip angle of 75°, FOV of 265 × 192, acquisition matrix of 1 × 1 × 3 mm; and 2) a 3D-T1WI sequence with TR/TI/TE of 2.8/900/5.9 ms, flip angle of 10°, FOV of 265 × 192, acquisition matrix of 1 × 1 × 1 mm. Similarly, the 1.5T sequences used TE/TI/TR of 120/2000/8000 ms and TE/TI/TR of 3.7/900/7.7 ms for the 2D-T2WI-FLAIR and 3D T1WI, respectively.

MR imaging analysis and quality control were performed in a fully blinded manner. The 3D-T1WI was preprocessed using an inpainting technique to avoid tissue misclassification of T1-hypointense lesions.[24] At baseline, normalized whole-brain volume was calculated using FSL SIENA or SIENAX (SIENAX; http://fsl.fmrib.ox.ac.uk/fsl/fslwiki/SIENA),[25] whereas for follow-up changes, the SIENA percentage brain volume change (PBVC) method was used.[25]

The Neurologic Software Tool for REliable Atrophy Measurement (NeuroSTREAM; http://www.neurostream.us/) was used to assess baseline lateral ventricle volume (LVV) and percentage LVV change (PLVVC) across time on 2D-T2-FLAIR images.[26]

Cross-sectionally, LVV and whole-brain volume values at the first available MR imaging examination were calculated. Changes between baseline and follow-up examinations were calculated determining PLVVC and PBVC and were subsequently annualized.

In addition, we calculated T2-lesion volume (T2-LV), using a semiautomated approach.[27]

Clinical Outcomes

Disability progression was defined as an increase from the baseline Expanded Disability Status Scale (EDSS) score of at least 1.0 point or 0.5 if the baseline EDSS score was >5.5. Disability improvement was defined as a reduction from the baseline EDSS score of at least 1.0 point if the baseline score was 2.0–5.5, or 0.5 if the baseline score was >5.5, as previously reported.[16,28] Stable disability status was defined as nonoccurrence of the disability progression or disability improvement.

Patients were also classified as having benign MS at baseline if the EDSS was ≤3.0 and disease duration was ≥15 years.[29]

Statistical Analysis

Analyses were performed using the Statistical Package for the Social Sciences, 24.0 (IBM). Differences between groups were analyzed using the χ^2 test, Kruskal-Wallis test, and 1-way ANOVA as appropriate.

Three different models assessed the PLVVC and PBVC differences among disability status groups using ANCOVA, adjusted for the following: 1) age at first MR imaging and race; 2) age at first MR imaging, race, T2-LV, and corresponding baseline structural volume; and 3) age at first MR imaging, race, T2-LV corresponding baseline structural volume, and EDSS. Additional pair-wise comparisons between groups were performed by Bonferroni-adjusted post hoc analyses, and adjusted estimated means with 95% confidence intervals were presented. The Cohen d measure of effect size was also calculated.

Secondary analyses of only patients with a follow-up time of ≤2 years used the same statistical approach. The effects of changes in MR imaging scanner strength on the follow-up,

changes of PLVVC, and PBVC were determined using mixed-effect modeling.

For all analyses, a nominal P value of $\leq .05$ was considered significant using 2-tailed tests. The P values presented hereafter are based on the third ANCOVA model.

RESULTS

Demographic and Clinical Characteristics of the Study Cohort

Nine hundred eighty patients with MS who met the inclusion criteria were enrolled in this study (On-line Table 1 and On-line Fig 1). Of those, 241 (24.6%) developed disability progression, 101 (10.3%) had disability improvement, and 638 (65.1%) remained stable during the follow-up period. The mean interval between baseline and follow-up was 4.8 ± 2.4 years for disability progression,
4.7 ± 2.4 years for disability improvement, and 4.8 ± 2.4 years for stable status ($P = .887$).

The study population consisted of 75.7% females, and their age in years at baseline was 47.1 ± 9.8 for DP, 44.7 ± 9.9 for DI and 45.4 ± 11.2 for Stable (P = .07) groups. The mean age at disease onset was 33.3 ± 9.6 years for disability progression, 31.3 ± 9.8 years for disability improvement, and 33.2 ± 10.4 years for stable status ($P = .2$). The mean disease duration at baseline was 13.3 ± 9.6 years for disability progression, 12.8 ± 9.5 years for disability improvement, and 11.8 ± 9.5 years for stable status ($P = .1$).

The median (interquartile range) EDSS at baseline was 3.0 (3.0) for disability progression, 3.5 (3.0) for disability improvement, and 2.5 (2.5) for stable status ($P < .001$). The median (interquartile range) EDSS at follow-up was 6.0 (3.0) for disability progression, 2.5 (2.5) for disability improvement, and 2.5 (2.5) for stable status ($P < .001$). The mean annualized relapse rate during the follow-up was 0.25 ± 0.55 for disability progression, 0.28 ± 0.69 for disability improvement, and 0.18 ± 0.37 for stable status ($P = .02$).

In the disability progression/disability improvement/stable categories at baseline, 182 (75.5%), 85 (84.2%), and 527 (82.6%) had relapsing-remitting (RR); 49 (20.3%), 14 (13.9%), and 100 (15.7%) had secondary-progressive (SP); and 10 (4.1%), 2 (2%), and 11 (1.7%) had primary-progressive (PP) MS disease subtypes ($P = .29$). The number of patients classified as having benign MS at baseline was 45 (18.7%) in disability progression, 8 (7.9%) in disability improvement, and 97 (15.2%) in stable groups ($P = .04$).

There was no significant difference in type of DMTs between the three disability groups at baseline ($P = .15$), but was at follow-up (0.03). However, more MS patients in the DP group started or switched DMT over the follow-up compared to the DI and Stable groups ($P = .02$) to: No significant differences occurred in DMT status over the follow-up (P = .2).

MR Imaging Characteristics at Baseline and during Follow-Up

In total, 527 patients had no change in MR imaging findings and 453 did. There were no significant differences in the proportion of patients with disability progression/disability improvement/stable status that either changed or remained the same on MR imaging during the follow-up (126/343/58 versus 115/295/43, $P = .42$).

The mean T2-LV at baseline was 21.9 ± 18.0 mL for disability progression, 17.2 ± 15.9 mL for disability improvement, and 16.8 ± 14.9 mL for stable status ($P < .001$). At baseline, LVV was available in all 980 (100%) subjects, and whole-brain volume, in 873 (89.1%) subjects. At follow-up, the PLVVC was available in all 980 (100%), and PBVC, in 612 (62.4%) patients. The whole-brain volume (107, 10.9%) at baseline and PBVC (368, 37.6%) during follow-up was not obtained because these measures did not pass quality control related to the use of a different scanner-strength field between baseline and follow-up, poor scan quality, and artifacts that affected calculation of these outcomes.

On-line Table 2 shows PLVVC and PBVC in disability progression, disability improvement, and stable groups. Figures 1 and 2 show representative changes of PLVVC and PBVC in disability progression and disability improvement in individual patients during follow-up, respectively. At baseline, there were no significant LVV and whole-brain volume differences among patients with MS in the disability progression, disability improvement, and stable groups.

During the follow-up period, the annualized PLVVC was 1.6% ± 2.7% in disability improvement, 2.1% ± 3.7% in stable status, and 4.1% ± 5.5% in disability progression groups (adjusted $P < .001$). Both disability improvement and stable groups had significantly lower total and annualized PLVVC compared with the disability progression group (adjusted $P < .001$). The disability improvement group did not show a significant difference in total (adjusted $P = .6$) or annualized (adjusted $P = .92$) PLVVC compared with the stable group. The estimated means and 95% confidence intervals for the analyses are shown in On-line Table 3.

The annualized PBVC was −0.7% ± 0.7% in the disability improvement, −0.8% ± 0.7% in stable, and −1.1% ± 1.1% in disability progression groups (adjusted $P = .001$). The disability improvement group had significantly lower total (adjusted $P = .01$) and annualized (adjusted $P = .02$) PBVC compared with the disability progression group. The stable group had significantly lower total (adjusted $P < .001$) and annualized PBVC compared with the disability progression group (adjusted $P = .01$). The disability improvement group did not show a significant difference in total (adjusted $P = 1.0$) or annualized PBVC (adjusted $P = 1.0$) compared with the stable group. The estimated means and 95% confidence intervals for the analyses are shown in On-line Table 3.

Although not significant, the data trends were seen within the smaller population of patients who were followed for ≤2 years (On-line Table 4). Similarly, the estimated means and 95% CI are shown in On-line Table 5.

MR Imaging Field Strength Effects on MR Imaging Brain Volume Changes

The main and interaction effects of the study variables on the changes in NeuroSTREAM-based PLVVC and SIENA-based PBVC were investigated. The change in MR imaging strength and time interaction was not significantly associated with PLVVC ($P = .97$), contributing to an opposite effect of 0.01%

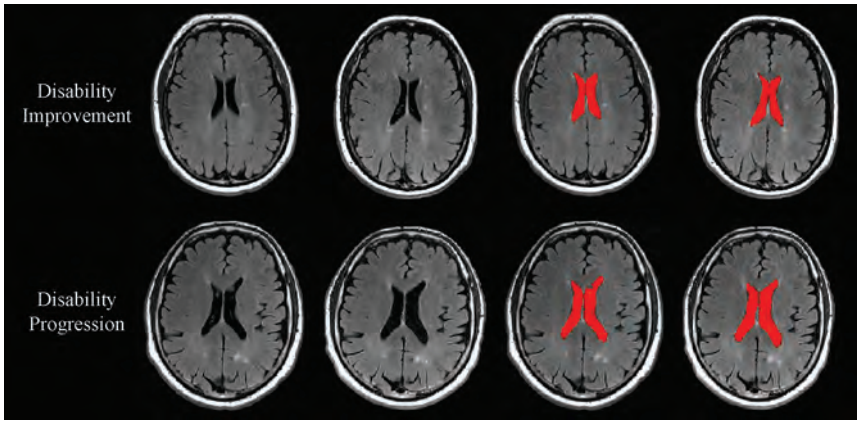

FIG 1. Change in lateral ventricle volume in patients with MS disability progression and disability improvement. In the *upper* and *lower rows* are shown in patients with MS with disability improvement and disability progression, respectively. From *left* to *right* are baseline and followup T2-FLAIR images and images of NeuroSTREAM LVV (highlighted in red) segmentation at baseline and at follow-up. Please note higher annualized percentage LVV change in patients with MS with disability progression (5.7%) compared with disability improvement (1.1%).

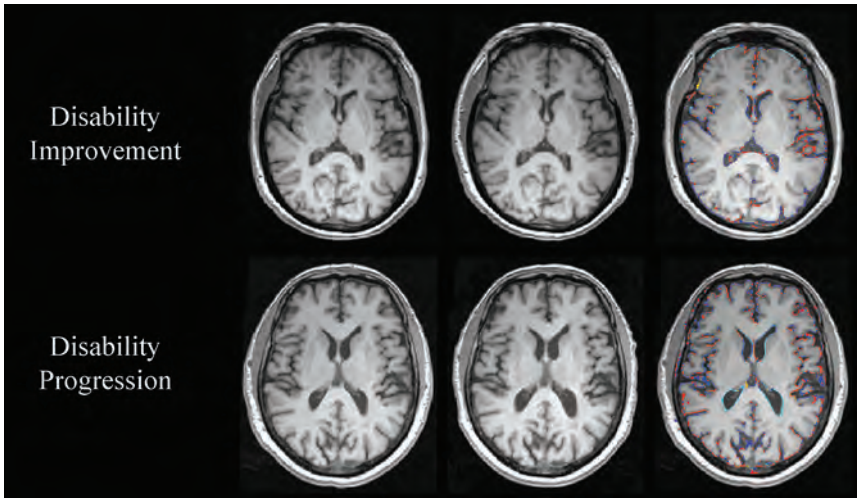

FIG 2. Change in whole-brain volume in patients with MS with disability improvement and disability progression. In the *upper and lower rows* are shown patients with MS with disability improvement and disability progression, respectively. From *left* to *right* are baseline and follow-up 3D-T1WI, and a SIENA brain volume change edge map showing areas of atrophy (in blue-light blue) and growth (in red-yellow). Please note the higher annualized PBVC rate in disability progressed (−2.4%) compared with disability improved (−0.5%).

during the same amount of follow-up time. Similar analysis for PBVC showed a significant effect of the change in MR imaging strength and time interaction ($P = .03$), contributing to an opposite effect of 0.16% during the same amount of follow-up time.

DISCUSSION

The present study provides additional insight into understanding the relationship between the development of brain atrophy in patients with MS who improve in disability compared with those who remain stable or progress. Data were retrospectively evaluated from a large cohort of patients with MS prospectively collected on a routine clinical basis during 10 years. The study included about 1000 patients with MS who were selected retrospectively, according to the inclusion and exclusion criteria, from a larger pool of >2000 subjects and were followed with MR imaging and clinical examinations for a mean time of almost 5 years. To our knowledge, research studies, especially those including routine clinical data that explore brain atrophy trajectories related specifically to the improvement of disability in patients with MS, are scarce. Therefore, the present study is one of the first longitudinal studies investigating this issue to date.

We used 2 different measures of brain atrophy in this study, LVV and whole-brain volume . It has been shown that LVV correlates with disability progression and cognitive impairment,[10-12] and due to its feasibility, it could represent a more adequate marker of MS-related brain atrophy to be applied in the clinical routine.[30,31] In fact, it was reported recently that changes in LVV act as a proxy for whole-brain volume and correlate with progression of GM and cortical atrophy in the 10-year period.[12] Moreover, LVV is located in the center of the brain, an area that is relatively immune to artifacts due to imprecise positioning, gradient distortions, incomplete head coverage, and wraparound artifacts.[26] We confirmed in this study, as in previous studies,[30,32] that LVV measurement was feasible in patients with MS and was not affected by changes in MR imaging strength and time interaction during follow-up. In addition, the PBVC is one of the most accepted methods for quantifying neurodegeneration in MS.[10] PBVC correlates with measures of central atrophy, such as LVV and GM atrophy; however, it is more difficult to obtain on routine clinical scans due to inherent changes in field strength, scanner type, software, and protocol among serial MR imaging examinations; this issue represents a difficult barrier to its adaptation for use in clinical settings.[12] This was confirmed in this study because 37.6% of the patients were excluded during the follow-up because PBVC did not pass quality control related to changes in MR imaging strength, poor scan quality, and artifacts.

PBVC was significantly affected by changes in MR imaging strength and time interaction during follow-up. In the present

study, we found that at baseline, there were no significant LVV or whole-brain volume differences among patients with MS with disability progression, disability improvement, and stable progression. During the follow-up period, the total and annualized PLVVC and PBVC were significantly lower for disability improvement compared with disability progression groups (all $P \leq .001$). Similar trends were seen within the smaller sample of patients who were followed for ≤2 years, indicating that brain atrophy trajectory differences can be detected in the first 2 years of follow-up among patients with MS with disability progression, disability improvement, and stable status. The disability improvement group did not show a significantly different total or annualized PLVVC and PBVC compared with the stable group.

A recent study compared brain atrophy data of 1514 patients with MS, 137 patients with clinically isolated syndrome, and 164 healthy subjects collected retrospectively during 5 years. The data reported for the annualized PLVVC and PBVC for healthy individuals were 1.6% and −0.4%, respectively, using the same scanners and protocols as in the present study.[30] Comparing the results from this and the previous studies,[30,32] we found that the annualized PLVVC was similar and the annualized PBVC was higher compared with those observed in healthy individuals. We could therefore hypothesize that patients with disability improvement and healthy subjects undergo a similar degree of central brain atrophy and a higher degree of whole-brain atrophy accumulation. Our results also corroborate a recent study that demonstrated that the degree of brain atrophy is the lowest in stable nonrelapsing/nonworsening RRMS, greater in relapsing/nonworsening and nonrelapsing/worsening RRMS, and the highest in relapsing and worsening RRMS.[33] Last, baseline whole-brain volume was the only predictor of disability progression in a recent study from the Serially Unified Multicenter MS Investigation consortium.[34]

Because it was shown that the rate of brain atrophy is slower in patients with MS with benign disease[35] and to avoid a potential bias within the 3 disability status groups, we calculated the proportion of patients with benign MS according to the definition based on EDSS and disease duration (EDSS ≤3.0 and disease duration ≥15 years).[29] Surprisingly, we found that the disability progression group had a larger proportion of patients with MS with benign disease at baseline (18.7%) compared with 7.9% of patients with MS with benign disease in the disability improvement and 15.2% in the stable groups, respectively. Because the disability improvement group had a significantly lower proportion of patients with MS with benign disease at baseline, a potential selection bias in the disability improvement sample is unlikely.

The use of DMT in our study population could have influenced disability progression or disability improvement status. In the present study, the use of DMT was present in 180 (74.7%) patients with disability progression, 79 (78.2%) with disability improvement, and 518 (81.2%) with stable status at baseline. No significant differences in the type of DMT at baseline or at follow-up among the 3 disability groups were detected. However, significantly more patients with MS in the disability progression group started or switched DMT during the follow-up, compared with patients with disability improvement or stable disease, indicating potentially more active or breakthrough disease characteristics. Given the heterogeneous status of the DMT in the disability status groups examined, we did not investigate the effect of specific DMT on the development of brain atrophy and disability progression/disability improvement/stable status during follow-up. However, our findings could be important for the design of future studies that will include a more homogeneous patient sample using specific DMT to explore disability status improvement in relation to brain atrophy trajectory changes.

A recent study showed that disability progression was associated with an annualized PBVC of 21.9% ($P < .001$) and a 33% increase in LVV ($P = .004$) in patients with MS.[30] A meta-analysis of 13 clinical trials, which included >13,500 patients with RRMS and used PBVC as the brain volume measurement method of choice, showed that disability progression during 2 years correlated with both brain atrophy ($P = .001$) and T2-LV ($P < .001$).[36] We used baseline T2-LV only as a covariate in this study because we did not aim to explore the effect of T2-LV on disability progression/disability improvement/stable status during the follow-up. Previous studies reported less accrual of T2-LV in patients with disability improvement, compared with those with disability progression.[13,15,16,18,19]

In the Comparison of Alemtuzumab and Rebif Efficacy in Multiple Sclerosis (CARE) MS-I and II[3,37] randomized, controlled, 2-year studies of alemtuzumab for patients with RRMS versus patients treated with high-dose high-frequency interferon-β-1a, disability improvement was detected in a significantly higher proportion of the patients treated with alemtuzumab. There was also a significant reduction in brain volume loss in alemtuzumab compared with interferon-β-1a-treated patients. In OPERA I and II clinical trials,[16] 821 and 835 patients with RRMS received intravenous ocrelizumab, 600 mg (anti-CD20 humanized antibody) versus high-dose high-frequency interferon-β-1a for 96 weeks, respectively. The ocrelizumab arm showed a 33% higher proportion of disability improvement (secondary end point), which reached statistical significance compared with interferon-β-1a (pooled data). Patients receiving ocrelizumab also showed significantly lower brain volume loss compared with interferon-β-1a. However, the relationship between disability improvement and slowing down of brain volume loss in the above-mentioned studies was not explored.

The present study had some limitations. First, we did not take into consideration biologic confounding factors that may have an impact on brain atrophy, such as dehydration, diurnal brain volume changes, menstrual cycle, pseudoatrophy due to use of various DMT, and cardiovascular, environmental, and genetic risk factors and comorbidities.[10,38] However, we hypothesize that due to the size and patient composition of the sample, such confounders are mitigated when assessing group effects. Another limitation is that we had to restrict disability status determination to the 5-year EDSS score change, without the 3- or 6-month confirmation of sustained effect. However, it is unlikely that true prevalence of disability progression or disability improvement was skewed by this assessment, especially because we excluded patients who had disease activity in the 30 days before clinical

and MR imaging examinations. Another limitation could be related to the absence of spinal cord atrophy assessment. Therefore, future prospective, multicenter studies should confirm our preliminary findings and explore various other conventional and nonconventional MR imaging techniques in relation to development of disability improvement.

CONCLUSIONS

This is one of the first longitudinal studies to evaluate the evolution of brain atrophy in those patients with MS who improve in disability, compared with those who remain stable or progress, in a large cohort of patients followed for several years in a clinical routine. Our results suggest that there is significantly less brain atrophy development in those patients with MS who improve with time, compared with those who progress in their disability.

ACKNOWLEDGMENTS

The authors would like to thank all the subjects who participated in this study.

Disclosures: Michael G. Dwyer—*UNRELATED*: *Consultancy*: EMD Serono; *Grants/Grants Pending*: Novartis, Celgene, Keystone Heart, Genentech, money paid to the individual. David Hojnacki—*UNRELATED*: *Consultancy*: Biogen, Genentech, EMD Serono, Bristol Myers Squibb; *Payment for Lectures Including Service on Speakers Bureaus*: Biogen, Genentech, EMD Serono, Bristol Myers Squibb. Channa Kolb—*UNRELATED*: *Payment for Lectures Including Service on Speakers Bureaus*: I served on speakers bureaus for Teva Pharmaceutical Industries, Biogen, EMD Serono, Alexion, Novartis, and Mallinckrodt. Bianca Weinstock-Guttman—*UNRELATED*: *Board Membership*: Biogen, Genentech; *Consultancy*: Biogen, Novartis, Genentech, Mallinckrodt, EMD Serono, Celgene; *Grants/Grants Pending*: Biogen, Novartis, Genentech, Celgene*; *Payment for Lectures Including Service on Speakers Bureaus*: Biogen, Novartis, Genentech, EMD Serono. Robert Zivadinov—*UNRELATED*: *Consultancy*: Celgene, Novartis, Sanofi, Immunic; *Grants/Grants Pending*: Celgene, Novartis, Sanofi, Mapi Pharma, Keystone Heart, V-Wave Medical, Protembis, Boston Scientific*; *Payment for Lectures Including Service on Speakers Bureaus*: Celgene, Novartis, Sanofi, EMD Serono. *Money paid to the institution.

REFERENCES

1. Frohman EM, Racke MK, Raine CS. **Multiple sclerosis: the plaque and its pathogenesis.** *N Engl J Med* 2006;354:942–55 CrossRef Medline
2. Calabrese M, Reynolds R, Magliozzi R, et al. **Regional distribution and evolution of gray matter damage in different populations of multiple sclerosis patients.** *PLoS One* 2015;10:e0135428 CrossRef Medline
3. Fisher E, Lee JC, Nakamura K, et al. **Gray matter atrophy in multiple sclerosis: a longitudinal study.** *Ann Neurol* 2008;64:255–65 CrossRef Medline
4. De Stefano N, Giorgio A, Battaglini M, et al. **Assessing brain atrophy rates in a large population of untreated multiple sclerosis subtypes.** *Neurology* 2010;74:1868–76 CrossRef Medline
5. Zivadinov R, Sepcic J, Nasuelli D, et al. **A longitudinal study of brain atrophy and cognitive disturbances in the early phase of relapsing-remitting multiple sclerosis.** *J Neurol Neurosurg Psychiatry* 2001;70:773–80 CrossRef Medline
6. Miller DH, Barkhof F, Frank JA, et al. **Measurement of atrophy in multiple sclerosis: pathological basis, methodological aspects and clinical relevance.** *Brain* 2002;125:1676–95 CrossRef Medline
7. Uher T, Horakova D, Kalincik T, et al. **Early magnetic resonance imaging predictors of clinical progression after 48 months in clinically isolated syndrome patients treated with intramuscular interferon beta-1a.** *Eur J Neurol* 2015;22:1113–23 CrossRef Medline
8. Lukas C, Minneboo A, de Groot V, et al. **Early central atrophy rate predicts 5-year clinical outcome in multiple sclerosis.** *J Neurol Neurosurg Psychiatry* 2010;81:1351–56 CrossRef Medline
9. Minneboo A, Jasperse B, Barkhof F, et al. **Predicting short-term disability progression in early multiple sclerosis: added value of MRI parameters.** *J Neurol Neurosurg Psychiatry* 2008;79:917–23 CrossRef Medline
10. Sanai SA, Saini V, Benedict RH, et al. **Aging and multiple sclerosis.** *Mult Scler* 2016;22:717–25 CrossRef Medline
11. Sastre-Garriga J, Pareto D, Rovira A. **Brain atrophy in multiple sclerosis: clinical relevance and technical aspects.** *Neuroimaging Clin N Am* 2017;27:289–300 CrossRef Medline
12. Zivadinov R, Uher T, Hagemeier J, et al. **A serial 10-year follow-up study of brain atrophy and disability progression in RRMS patients.** *Mult Scler* 2016;22:1709–18 CrossRef Medline
13. Coles AJ, Twyman CL, Arnold DL, et al. **Alemtuzumab for patients with relapsing multiple sclerosis after disease-modifying therapy: a randomised controlled phase 3 trial.** *Lancet* 2012;380:1829–39 CrossRef Medline
14. Calabresi PA, Radue EW, Goodin D, et al. **Safety and efficacy of fingolimod in patients with relapsing-remitting multiple sclerosis (FREEDOMS II): a double-blind, randomised, placebo-controlled, Phase 3 trial.** *Lancet Neurol* 2014;13:545–56 CrossRef Medline
15. Montalban X, Hauser SL, Kappos L, et al; ORATORIO Clinical Investigators. **Ocrelizumab versus placebo in primary progressive multiple sclerosis.** *N Engl J Med* 2017;376:209–20 CrossRef Medline
16. Hauser SL, Bar-Or A, Comi G, et al; OPERA I and OPERA II Clinical Investigators. **Ocrelizumab versus interferon beta-1a in relapsing multiple sclerosis.** *N Engl J Med* 2017;376:221–34 CrossRef Medline
17. O'Connor P, Wolinsky JS, Confavreux C, et al; TEMSO Trial Group. **Randomized trial of oral teriflunomide for relapsing multiple sclerosis.** *N Engl J Med* 2011;365:1293–1303 CrossRef Medline
18. Borges IT, Shea CD, Ohayon J, et al. **The effect of daclizumab on brain atrophy in relapsing-remitting multiple sclerosis.** *Mult Scler Relat Disord* 2013;2:133–40 CrossRef Medline
19. Giovannoni G, Comi G, Cook S, et al; CLARITY Study Group. **A placebo-controlled trial of oral cladribine for relapsing multiple sclerosis.** *N Engl J Med* 2010;362:416–26 CrossRef Medline
20. Chen JT, Collins DL, Atkins HL; Canadian MS BMT Study Group. **Brain atrophy after immunoablation and stem cell transplantation in multiple sclerosis.** *Neurology* 2006;66:1935–37 CrossRef Medline
21. Sicotte NL, Giesser BS, Tandon V, et al. **Testosterone treatment in multiple sclerosis: a pilot study.** *Arch Neurol* 2007;64:683–88 CrossRef Medline
22. Uher T, Horakova D, Bergsland N, et al. **MRI correlates of disability progression in patients with CIS over 48 months.** *Neuroimage Clin* 2014;6:312–19 CrossRef Medline
23. Polman CH, Reingold SC, Banwell B, et al. **Diagnostic criteria for multiple sclerosis: 2010 revisions to the McDonald criteria.** *Ann Neurol* 2011;69:292–302 CrossRef Medline
24. Gelineau-Morel R, Tomassini V, Jenkinson M, et al. **The effect of hypointense white matter lesions on automated gray matter segmentation in multiple sclerosis.** *Hum Brain Mapp* 2012;33:2802–14 CrossRef Medline
25. Smith SM, Zhang Y, Jenkinson M, et al. **Accurate, robust, and automated longitudinal and cross-sectional brain change analysis.** *Neuroimage* 2002;17:479–89 CrossRef Medline
26. Dwyer MG, Silva D, Bergsland N, et al. **Neurological software tool for reliable atrophy measurement (NeuroSTREAM) of the lateral ventricles on clinical-quality T2-FLAIR MRI scans in multiple sclerosis.** *Neuroimage Clin* 2017;15:769–79 CrossRef Medline
27. Zivadinov R, Rudick RA, De Masi R, et al. **Effects of IV methylprednisolone on brain atrophy in relapsing-remitting MS.** *Neurology* 2001;57:1239–47 CrossRef Medline

28. Coles AJ, Cohen JA, Fox EJ, et al; CARE-MS II and CAMMS03409 Investigators. **Alemtuzumab CARE-MS II 5-year follow-up: efficacy and safety findings.** *Neurology* 2017;89:1117–26 CrossRef Medline
29. Correale J, Peirano I, Romano L. **Benign multiple sclerosis: a new definition of this entity is needed.** *Mult Scler* 2012;18:210–18 CrossRef Medline
30. Ghione E, Bergsland N, Dwyer MG, et al. **Brain atrophy is associated with disability progression in patients with MS followed in a clinical routine.** *AJNR Am J Neuroradiol* 2018;39:2237–42 CrossRef Medline
31. Zivadinov R, Bergsland N, Korn JR, et al; MS-MRIUS Study Group. **Feasibility of brain atrophy measurement in clinical routine without prior standardization of the MRI protocol: results from MS-MRIUS, a longitudinal observational, multicenter real-world outcome study in patients with relapsing-remitting MS.** *AJNR Am J Neuroradiol* 2018;39:289–95 CrossRef Medline
32. Ghione E, Bergsland N, Dwyer MG, et al. **Aging and brain atrophy in multiple sclerosis.** *J Neuroimaging* 2019;29:527–35 CrossRef Medline
33. Cree BA, Hollenbach JA, Bove R, et al; University of California, San Francisco MS-EPIC Team. **Silent progression in disease activity-free relapsing multiple sclerosis.** *Ann Neurol* 2019;85:653–66 CrossRef Medline
34. Bakshi R, Healy BC, Dupuy SL, et al; SUMMIT consortium. **Brain MRI predicts worsening multiple sclerosis disability over 5 years in the SUMMIT Study.** *J Neuroimaging* 2020;30:212–18 CrossRef Medline
35. Gauthier SA, Berger AM, Liptak Z, et al. **Rate of brain atrophy in benign vs early multiple sclerosis.** *Arch Neurol* 2009;66:234–37 CrossRef Medline
36. Sormani MP, Arnold DL, De Stefano N. **Treatment effect on brain atrophy correlates with treatment effect on disability in multiple sclerosis.** *Ann Neurol* 2014;75:43–49 CrossRef Medline
37. Cohen JA, Coles AJ, Arnold DL, et al. **Alemtuzumab versus interferon beta 1a as first-line treatment for patients with relapsing-remitting multiple sclerosis: a randomised controlled Phase 3 trial.** *Lancet* 2012;380:1819–28 CrossRef Medline
38. Jakimovski D, Gandhi S, Paunkoski I, et al. **Hypertension and heart disease are associated with development of brain atrophy in multiple sclerosis: a 5-year longitudinal study.** *Eur J Neurol* 2019;26:87–88 CrossRef Medline

Patterning Chronic Active Demyelination in Slowly Expanding/Evolving White Matter MS Lesions

C. Elliott, D.L. Arnold, H. Chen, C. Ke, L. Zhu, I. Chang, E. Cahir-McFarland, E. Fisher, B. Zhu, S. Gheuens, M. Scaramozza, V. Beynon, N. Franchimont, D.P. Bradley, and S. Belachew

ABSTRACT

BACKGROUND AND PURPOSE: Slowly expanding/evolving lesions measured by conventional T1-weighted/T2-weighted brain MR imaging may contribute to progressive disability accumulation in MS. We evaluated the longitudinal change in myelin and axonal tissue integrity in white matter slowly expanding/evolving lesions by means of the magnetization transfer ratio and DTI radial diffusivity.

MATERIALS AND METHODS: Slowly expanding/evolving lesions were detected within the Study to Assess the Efficacy, Safety, Tolerability, and Pharmacokinetics of BIIB033 in Participants With Relapsing Forms of Multiple Sclerosis When Used Concurrently With Avonex (SYNERGY) Phase 2 clinical trial dataset (NCT01864148), comprising patients with relapsing-remitting and secondary-progressive MS ($n = 299$) with T1-weighted/T2-weighted MR imaging at all trial time points (baseline to week 72).

RESULTS: Compared with non-slowly expanding/evolving lesions (areas not classified as slowly expanding/evolving lesion) of baseline nonenhancing T2 lesions, slowly expanding/evolving lesions had a lower normalized magnetization transfer ratio and greater DTI radial diffusivity, both in patients with relapsing-remitting MS ($n = 242$) and secondary-progressive MS ($n = 57$, $P < .001$ for all). Although the changes with time in both the normalized magnetization transfer ratio and DTI radial diffusivity between slowly expanding/evolving lesions and non-slowly expanding/evolving lesions were positively correlated ($P < .001$), a decrease in the normalized magnetization transfer ratio and a greater increase in DTI radial diffusivity were observed in slowly expanding/evolving lesions versus non-slowly expanding/evolving lesions from baseline to week 72 in relapsing-remitting MS and secondary-progressive MS ($P < .001$ for all).

CONCLUSIONS: Patterns of longitudinal change in the normalized magnetization transfer ratio and DTI radial diffusivity in slowly expanding/evolving lesions were consistent with progressive demyelination and tissue loss, as seen in smoldering white matter MS plaques.

ABBREVIATIONS: MT = magnetization transfer; MTR = magnetization transfer ratio; nMTR = normalized MTR; nT1 = normalized T1; RD = radial diffusivity; RRMS = relapsing-remitting multiple sclerosis; SEL = slowly expanding/evolving lesion; SPMS = secondary-progressive multiple sclerosis

Chronic active lesions, or smoldering plaques, are a neuropathologic hallmark of chronic inflammation in MS[1] and are not found in neuromyelitis optica spectrum disorders[2] or chronic cerebrovascular diseases.[3]

Pathologically, chronic active lesions are typified by a "rim" of activated microglia and/or macrophages that may contain iron; they have altered morphology, sparse T- and B-cells at the core, and a slow rate of ongoing demyelination and axonal loss.[1,4-7] Susceptibility-based MR imaging methods have identified a hypointense paramagnetic rim that may reflect activity associated with iron accumulation and other MS-related pathology in the periphery of those chronic active white matter MS lesions.[4,8-11]

A method for automatic detection of slowly expanding/evolving lesions (SELs) on conventional T1-weighted/T2-weighted brain MR imaging was recently developed as a potential readout

Received February 26, 2020; accepted after revision May 31.

From NeuroRx Research (C.E., D.L.A.) Montreal, Quebec, Canada; Department of Neurology and Neurosurgery (D.L.A.), McGill University, Montreal, Quebec, Canada; and Biogen (H.C., C.K., L.Z., I.C., E.C.-M., E.F., B.Z., S.G., M.S., V.B., N.F., D.P.B., S.B.), Cambridge, Massachusetts.

This research was funded by Biogen, Cambridge, Massachusetts.

Please address correspondence to Colm Elliott, PhD, NeuroRx Research, Montreal, QC, Canada, 3575 Parc Ave, Suite 5322, Montreal, QC, H2X 3P9, Canada; e-mail: celliott@neurorx.com

Indicates open access to non-subscribers at www.ajnr.org
Indicates article with supplemental on-line appendix.
Indicates article with supplemental on-line photo.
Indicates article with supplemental on-line video.

http://dx.doi.org/10.3174/ajnr.A6742

of smoldering or chronic active plaques.[12] SELs are defined as contiguous regions of pre-existing T2 lesions showing constant and concentric local expansion, as assessed by the Jacobian determinant of the nonlinear deformation between reference and follow-up scans.[12] Furthermore, T1-weighted intensity-based measures of chronic white matter lesion tissue damage in SELs predict clinical progression in primary-progressive MS and may qualify as longitudinal in vivo neuroimaging correlates of progressive MS pathology.[13]

Practical guidelines recommend either paramagnetic rim identification on high-resolution T2* and phase MR imaging (7T or even 3T) or longitudinal T1-weighted/T2-weighted SEL detection for in vivo assessment of chronic active or smoldering lesions.[11] Paramagnetic rim lesion identification is a promising pathologic biomarker of iron/zinc accumulation in chronic active lesions.[14,15] In clinical trials and routine clinical practice settings, SEL detection may be more suitable for delivering quantitative measures of overall and lesion-level longitudinal change in tissue integrity associated with smoldering lesion inflammation, enabling the assessment of chronic lesion activity in datasets for which high-resolution T2* MR imaging is not available.

The magnetization transfer ratio (MTR) has previously been shown to associate strongly with myelin content,[16–19] especially in the absence of acute inflammation and edema. DTI can provide information about the orientation, size, and geometry of tissue integrity in white and gray matter in the brain and spinal cord.[20] DTI radial diffusivity (DTI-RD) has been proposed as a potential marker of overall myelination and/or tissue integrity in MS lesions.[21]

In this study, we used MTR and DTI-RD to evaluate longitudinal in vivo demyelination to further inform the pathologic understanding of chronic tissue damage in SELs of patients with relapsing-remitting MS (RRMS) and secondary-progressive MS (SPMS).[12]

MATERIALS AND METHODS

Trial Design, Patients, and MR Imaging Procedures

SELs[12] and non-SELs were determined in chronic white matter lesions of the pooled population (placebo and treatment groups) of the Study to Assess the Efficacy, Safety, Tolerability, and Pharmacokinetics of BIIB033 in Participants With Relapsing Forms of Multiple Sclerosis When Used Concurrently With Avonex (SYNERGY) trial (NCT01864148), a multicenter, randomized, double-blind, placebo-controlled, dose-ranging, parallel-group, Phase 2 study. Patients were randomly allocated in a 1:2:2:2:2 ratio to 1 of 5 parallel treatment groups of opicinumab (3, 10, 30, or 100 mg/kg) or placebo, once every 4 weeks for 72 weeks. Opicinumab is a human monoclonal antibody against LINGO-1, an inhibitor of oligodendrocyte differentiation and axonal regeneration.[22] All patients self-administered intramuscular interferon β-1a as a background anti-inflammatory treatment once a week, and approximately half of the population had not previously received MS disease-modifying therapies.[22] SYNERGY study details have been reported previously.[22] Eligible patients (18–58 years of age) had an Expanded Disability Status Scale score of 2–6 and relapsing MS, including RRMS and SPMS with relapses. Evidence of clinical or neuroimaging disease activity was required within 12 months before enrollment.[22]

Axial T1-weighted (3D spoiled gradient-echo, TR = 28–30 ms, TE = 511 ms, flip angle = 27°–30°, resolution = 1 × 1 × 3 mm), axial T2-weighted (2D fast spin-echo, TR = 4500–6200 ms, TE = 66–91 ms, resolution = 1 × 1 × 3 mm), axial MTR (2 consecutive 3D spoiled gradient-echo, TR = 32–62 ms, TE = 5–11 ms, flip angle = 10°–15°, resolution = 1 × 1 × 3 mm, with and without magnetization transfer pulse), and axial DTI (2D spin-echo echo-planar imaging sequence with a diffusion gradient, TR = 9800–16,000 ms, TE = 90–132 ms, b-values = 0 and 1000, 25–32 diffusion directions, resolution = 2.5 × 2.5 × 2.5 mm) were acquired at baseline and weeks 4, 8, 12, 16, 20, 24, 48, and 72.[22] Complete methods for brain MR imaging acquisitions are described in the On-line Appendix. The SEL analysis population ($n = 299$) represents the subset of the intention-to-treat population ($n = 418$) that had available T1-weighted and T2-weighted MR images at all aforementioned time points from baseline to week 72.

Identification of SELs

As previously described, SELs are detected as areas of T2 lesions, pre-existing at baseline, that show constant and concentric local expansion.[12] Before SEL detection, T2 lesions were identified in baseline scans using a semiautomated method,[23] in which a fully automated segmentation was subsequently manually reviewed and corrected by trained MR imaging readers. Identification of SELs is a 2-stage process. First, SEL candidates are identified as contiguous areas of pre-existing, nonenhancing T2 lesions that are ≥10 voxels in size and show local expansion from baseline to week 72; a minimum local expansion of 4% per year is used as a cutoff for determining SEL candidate boundaries, as in previous SEL analyses.[12] Local expansion is determined from the Jacobian determinant of the nonlinear deformation between the baseline and week 72 scans. Computation of the Jacobian is based on the pipeline proposed by Nakamura et al,[24] in which nonlinear registration is performed using the symmetric image normalization method,[25] and both T1-weighted and T2-weighted images are used for registration. The second stage of SEL detection scores each SEL candidate in turn, on the basis of the concentricity and constancy of expansion across time. Considering local expansion at all intermediate scans (weeks 4, 8, 12, 16, 20, 24, and 48) allows the identification of SEL candidates undergoing constant and gradual expansion across time; measuring concentricity allows identification of SEL candidates exhibiting inside-out radial expansion. Results pertaining to SEL analyses are presented for high-confidence SELs (with a heuristic score of ≥0).[12] Non-SELs are defined as complement regions from pre-existing, baseline, nonenhancing T2 lesions devoid of any SEL detection (irrespective of the heuristic score). SEL identification and all T1-weighted measures related to SELs and non-SELs were performed by NeuroRx Research staff, who remained blinded to all study patient-level information.

Normalization of T1-Weighted and MTR Signal Intensity

Before measuring T1-intensity change across time, T1WIs were normalized in a 2-stage process: 1) Least-trimmed squares normalized all serial T1WIs of a given patient to the baseline T1-

Baseline demographics and brain MR imaging characteristics of the SYNERGY SEL analysis population

	SEL Analysis Population[a]			Intention-to-Treat Population		
	RRMS	SPMS	All	RRMS	SPMS	All
No.	242	57	299	330	88	418
Median age (yr)	37.5	48.0	39.0	38.0	48.0	39.5
Female (%)	68	54	65	68	60	66
Mean (SD) number of T1 gadolinium-enhancing lesions	1.8 (4.7)	1.2 (3.7)	1.7 (4.5)	2.0 (4.7)	1.2 (3.3)	1.8 (4.4)
Patients with ≥1 T1 gadolinium-enhancing lesion (%)	45	30	42	46	31	43
Median nonenhancing T1-hypointense lesion volume (mL)	1.09	3.26	1.41	1.22	4.13	1.50
Median T2-hyperintense lesion volume (mL)	4.86	9.46	5.24	5.19	13.05	6.02
Median normalized brain volume (mL)	1447.9	1378.1	1426.1	1438.6	1367.0	1419.9
Median cortical gray matter volume (mL)	551.9	509.53	540.8	544.0	502.6	534.6

[a] The SEL analysis population ($n = 299$) represents the subset of the SYNERGY intention-to-treat population that had available T1-weighted and T2-weighted brain MR imaging scans at all time points from baseline to Week 72 (baseline and Weeks 4, 8, 12, 16, 20, 24, 48, and 72). For some time points, MTR and/or DTI-RD may not be available.

weighted scan, and 2) T1WIs for a given subject were linearly normalized by mapping the median gray matter T1 intensity at baseline to a value of zero and mapping the median normal-appearing white matter intensity at baseline to 1. Least-trimmed squares performs linear regression between coregistered sequential scans using the 50% of voxels whose least-squares fit has the smallest sum of squared residuals.[26] This process normalizes intensities within a given subject on the basis of only the subset of voxels that remain relatively unchanged with time. The first stage of normalization minimizes acquisition-related intensity variation across time for a given subject, whereas the second stage provides comparable measures of T1 intensity change across different subjects.

MTR intensities were calibrated by determining the median MTR values for both gray and white matter in a healthy control subject specific to each scanner. For each new-subject scan acquired in the same scanner, the MTR value corresponding to the median healthy control gray matter was mapped to zero, while the MTR value corresponding to the median healthy control white matter was mapped to 1. In normalized MTR images, a value of zero can thus be interpreted as corresponding to healthy (ie, non-MS) gray matter, while a value of 1 can be interpreted as corresponding to healthy white matter. DTI-RD is expressed in units of 10^{-3} mm^2/s and does not require normalization across scans.

Lesion-Level Visualization of Longitudinal Tissue Damage within a SEL Example

To display an example of lesion-level longitudinal tissue damage within discrete SELs, we modeled smooth voxel-based (linear fit) representations of normalized T1 (nT1), normalized MTR (nMTR), and DTI-RD intensity change across time in a high-confidence SEL. Heat map synthetic representations were produced that may represent biologic change and/or displacement. Linear models interpolating intensity change with time were used.

Statistical Analysis

The statistical analysis of SEL data was exploratory and included all patients from SYNERGY with no missing or nonevaluable T1-weighted and T2-weighted scans at any time point (baseline to week 72; SEL analysis population). No imputation of missing data was performed.

Continuous variables measuring tissue integrity (eg, MTR and DTI change from baseline in nMTR and DTI-RD) were compared between SELs and non-SELs using a Wilcoxon signed rank test, accounting for within-subject correlation of each variable. Change from baseline comparisons for continuous variables between patients with RRMS and SPMS were based on rank regression adjusted for covariates including baseline value, age, sex, and the baseline T2 volume category based on tertiles. Comparisons of baseline continuous variables between patients with RRMS and SPMS were based on rank regression, with MS type and covariates including age, sex, and baseline T2 volume category based on tertiles.

The Spearman rank correlation analysis was used to evaluate the association between change with time in continuous variables within SELs and non-SELs. Two-sided statistical tests were conducted at the 5% significance level without adjustment for multiplicity.

RESULTS

Baseline Demographics and Brain MR Imaging Characteristics of the SYNERGY SEL-Analysis Population

The baseline demographics and brain MR imaging characteristics of the SEL-analysis population from the SYNERGY dataset of patients with RRMS and SPMS are presented in the Table. The population was similar to the SYNERGY intention-to-treat population. In the SEL analysis population, patients with SPMS ($n = 57$) were ~10 years older and had a lower level of acute lesions as measured by the presence of gadolinium-enhancing T1 lesions and a 2-fold greater volume of baseline total T2 hyperintense lesions compared with patients with RRMS ($n = 242$). In addition, the baseline normalized brain volume and cortical gray matter volume were numerically lower, and a more balanced sex ratio was observed in the SPMS subgroup compared with patients with RRMS.

SEL Prevalence in RRMS versus SPMS

The proportion of patients with ≥1 SEL detected from baseline to week 72 was similar in patients with SPMS (89%) and RRMS (83%); a numerically greater proportion of patients with SPMS had >10 SELs (Fig 1*A*). Patients with SPMS had an overall greater number of SELs compared with patients with RRMS (median, 7.0 versus 4.0; Fig 1*B*), and an approximately 2-fold greater T2 volume of SELs (median at baseline, 718.2 versus 311.9 mm^3; Fig 1*C*); however, when accounting for differences in age, sex, and baseline total T2 hyperintense lesion volume, the differences

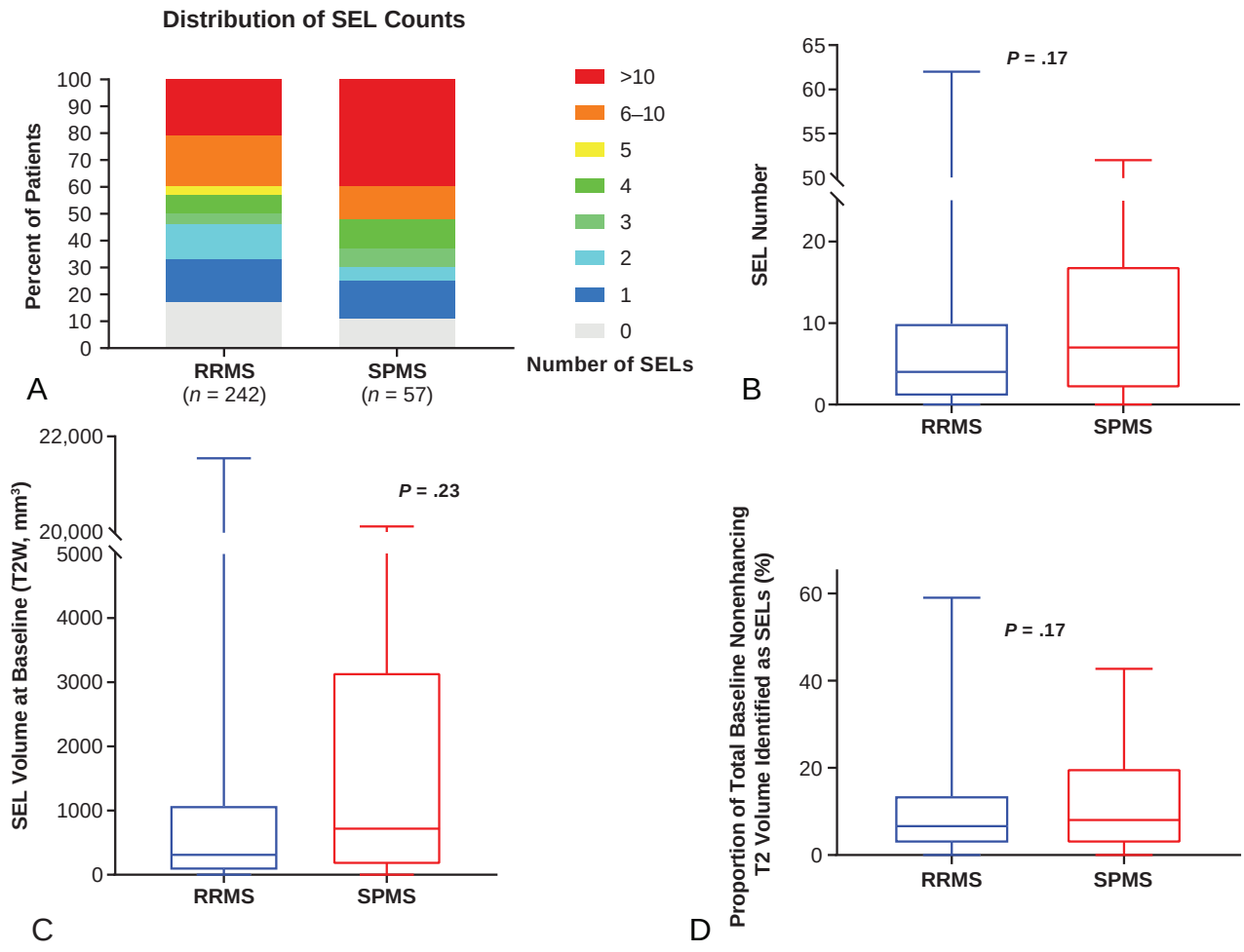

FIG 1. SEL prevalence in patients with RRMS and SPMS in SYNERGY. *A*, Frequency distribution (percentage) of patients with various levels of SEL counts. Boxplot representations of SEL number (*B*), SEL volume at baseline (*C*), and the proportion of total baseline nonenhancing T2 volume identified as SELs in SYNERGY in patients with RRMS ($n = 242$) and SPMS ($n = 57$) (*D*).

in the number of SELs and T2 volume of SELs between RRMS and SPMS were not significant ($P = .17$ and $P = .23$, respectively). The proportion of baseline total nonenhancing T2 lesion burden identified as SELs was similar between patients with RRMS and SPMS (Fig 1*D*).

Baseline Level and Longitudinal Change in Tissue Integrity in SELs and Non-SELs of Patients with RRMS and SPMS, as Measured by nMTR and DTI-RD

SELs at baseline had a lower nMTR (expressed as an nMTR unit) versus non-SELs in patients with RRMS and SPMS (median, −0.67 versus −0.46, $P < .001$, and median, −1.01 versus −0.62, $P < .001$, respectively; Fig 2*A*) and a greater DTI-RD (median, 0.98 versus 0.88×10^{-3} mm^2/s, $P < .001$, and median, 1.07 versus 0.96×10^{-3} mm^2/s, $P < .001$, respectively; Fig 3*A*); means and medians were computed at the patient level. Baseline nMTR and DTI-RD parameters were reflective of more severe alterations of tissue integrity in patients with SPMS compared with RRMS, both in SELs and non-SELs (Fig 2*A* and 3*A*).

An assessment of change from baseline to week 72 showed that SELs were affected by significantly more tissue damage across time compared with non-SELs, as measured by an nMTR decrease and DTI-RD increase in both MS types—RRMS ($P < .001$ for both; Fig 2*B*) and SPMS ($P < .001$ and $P < .001$, respectively; Fig 3*B*). Most important, the differences in change in nMTR and DTI-RD from baseline were significant between SELs and non-SELs as of week 24 in the pooled RRMS-SPMS population ($P < .001$ for both). However, despite this difference in the severity of longitudinal tissue damage with time, at the individual patient level, we observed a mild-to-moderate positive correlation between SELs and non-SELs with regard to changes in nMTR (Spearman correlation = 0.39, $P < .001$, pooled RRMS-SPMS population) and DTI-RD (Spearman correlation = 0.56, $P < .001$, pooled RRMS-SPMS population) from baseline to week 72.

Although tissue-integrity alteration was significantly more pronounced in SELs from patients with SPMS than RRMS at baseline, the longitudinal tissue damage, as indicated by an nMTR decrease and DTI-RD increase with time (baseline to week 72) was similar in SELs from patients with RRMS and SPMS (Figs 2*C* and 3*C*).

A subtle and similar increase in DTI-RD from baseline to week 72 in patients with RRMS and SPMS was observed in non-SELs of chronic white matter lesions (Fig 3*C*). In contrast, there were directionally opposite trends in changes from baseline in

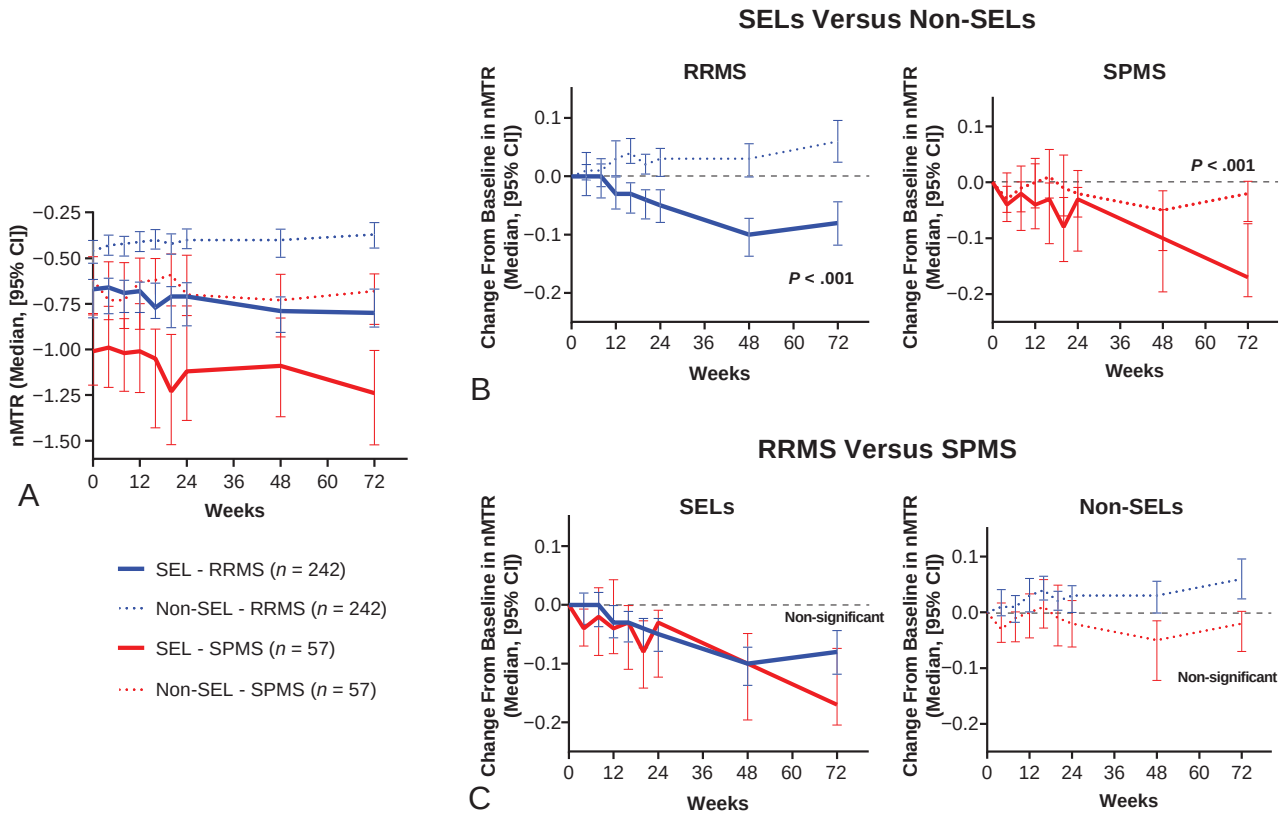

FIG 2. Change in nMTR in chronic white matter lesions. *A*, nMTR across time. *B*, Comparison of change from baseline in nMTR to week 72 between SELs and non-SELs in patients with RRMS and SPMS. *C*, Comparison of change from baseline in nMTR to week 72 between patients with RRMS and SPMS in SELs and non-SELs.

nMTR in non-SELs (albeit not statistically significant), with an increase in patients with RRMS and a decrease in patients with SPMS (Fig 2*C*). Overall, the findings from a comparison of baseline and longitudinal changes in nT1 intensity in SELs and non-SELs from patients with RRMS and SPMS were similar to aforementioned observations derived from the DTI-RD analysis (On-line Figure); these replicated previous findings that characterized T1-weighted normalized intensity changes in SELs versus non-SELs of chronic white matter lesions from patients with relapsing and primary-progressive forms of MS.[12]

An example of lesion-level chronic tissue damage, as measured by nT1 and nMTR intensity decrease and DTI-RD increase from baseline to week 72, is shown in Fig 4 and On-line Fig 2, where the longitudinal change with time can be visualized in a discrete SEL. Although a thorough analysis of spatial patterns of within-SEL intensity change was not conducted, examples of patterns consistent with ongoing demyelination at the lesion edge were observed.

DISCUSSION

This study further characterizes the nature of CNS tissue damage in chronic white matter MS lesions identified as SELs using serial conventional T1-weighted and T2-weighted MR imaging. Compared with non-SELs, SELs were previously shown to evolve independent of T1 gadolinium enhancement, demonstrate a lower T1 intensity at baseline, and exhibit a progressive decrease in T1 intensity with time, suggesting a progressive accumulation of neural tissue damage.[12]

We showed here that the longitudinal patterns of nMTR decrease and DTI-RD increase in SELs indicate a prominent contribution of chronic demyelination in those chronic active white matter MS lesions, though axonal loss may also be present. The overt consistency between longitudinal changes in nT1 intensity, nMTR, and DTI-RD in SELs and non-SELs with time provides evidence that nT1 intensity, though not a specific marker of myelin, could serve as a potential readout of chronic tissue damage in the absence of MTR and DTI acquisitions. Such nT1 intensity–based measures of CNS tissue integrity in SELs and non-SELs, separately, may provide value in clinical trials evaluating the effect of potential remyelination therapies.

The extent to which chronic demyelination in SELs evolves with an inside-out lesion-level pattern and its relationship to activated microglia/macrophage–mediated inflammatory processes on the lesion edge and/or to potential diffusible factors inherent to the scarce T- and B-cells (expected to populate the core of SELs within perivascular cuffs) need to be further investigated.[7] Quantitative susceptibility mapping imaging[27–31] should be used to assess the relation of SELs detected on MR imaging to the iron rim at the edge of chronic active lesions, as reported in pathologic studies, though only a subset of smoldering lesions appear to have iron/zinc rims.[14,15] The potential neuropathologic correlates of SELs warrant further investigation. However, the observed character of longitudinal nMTR, DTI-RD, and nT1 intensity features of change

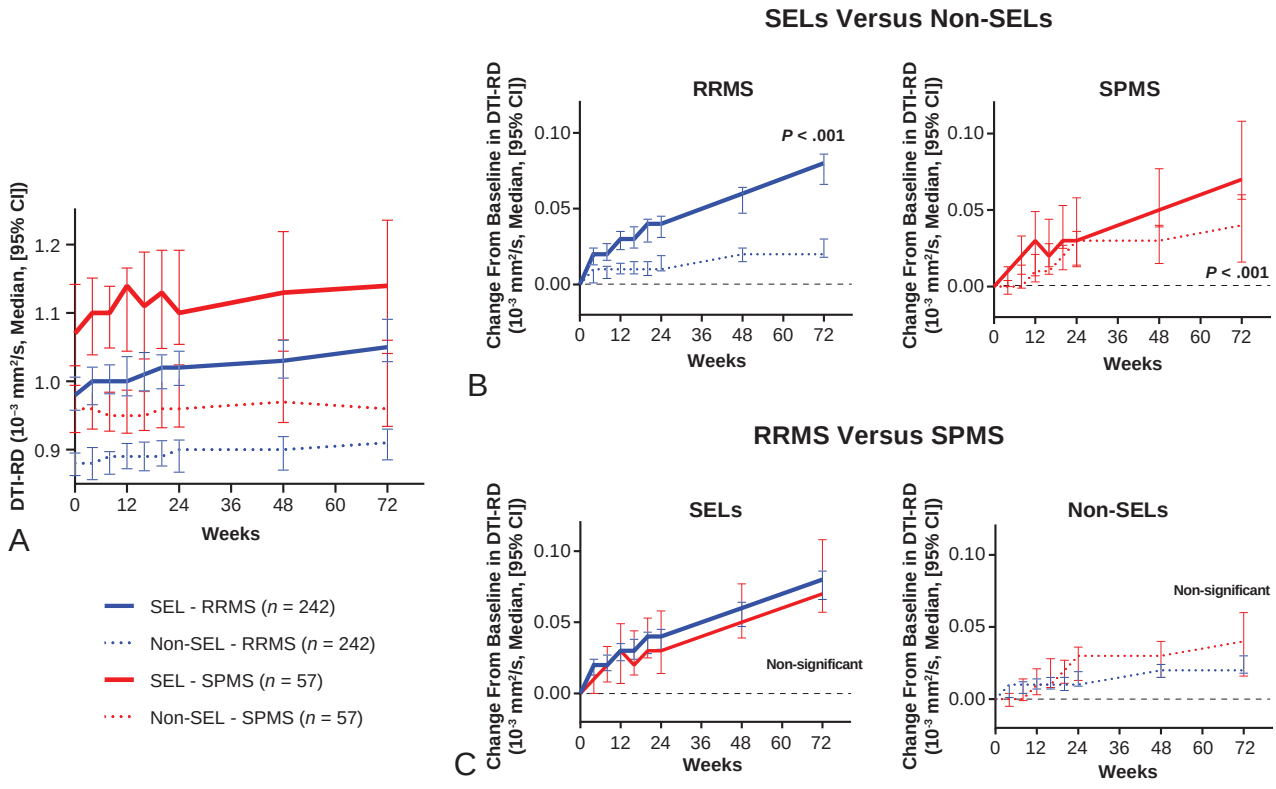

FIG 3. Change in DTI-RD in chronic white matter lesions. *A*, DTI-RD with time. *B*, Comparison of change from baseline in DTI-RD to week 72 between SELs and non-SELs in patients with RRMS and SPMS. *C*, Comparison of change from baseline in DTI-RD to week 72 between patients with RRMS and SPMS in SELs and non-SELs.

in tissue integrity in SELs may suggest that common mechanisms drive progressive demyelination in chronic white matter lesions across relapsing and progressive clinical presentations of the MS disease continuum. Furthermore, the correlation between the different rates of overall tissue demyelination observed in SELs and non-SELs, as measured by nMTR and DTI-RD, may indicate that a similar underlying pathology is diffusely at play throughout chronic white matter MS lesions, with maximal severity related to chronic lesion expansion in SELs.

The observed trend of nMTR increase in non-SELs of patients with RRMS suggests that remyelination may occur in chronic white matter lesions; however, a voxel-based approach would be needed to further address this hypothesis. Alternatively, the nMTR increase from baseline in non-SELs of patients with RRMS might be explained by the early resolution of inflammation and/or potential remyelination within foci of recent acute lesions, which might have formed before baseline but might still be a part of the baseline nonenhancing T2-hyperintense lesion tissue. In patients with radiologically isolated syndrome, acute and chronic demyelination may coexist from the onset of MS, irrespective of subsequent clinical phenotypes.[32] Although acute white matter MS lesions may be more amenable to remyelination owing to greater preservation of axons and lesser gliosis, spontaneous remyelination appears to be elusive in chronic active demyelinating lesions, which may represent a key driver of disability accumulation.[6,13,33] Further lesion-level spatiotemporal analyses of advanced and potentially multimodal brain MR imaging biomarkers of remyelination in SELs and non-SELs of chronic white matter lesions may help advance the understanding of putative associations between pathobiologic mechanisms of chronic demyelination, axonal loss, and remyelination failure.

The findings presented here have certain limitations. The current work did not investigate the potential impact of opicinumab versus placebo on chronic white matter lesion tissue integrity, which will be assessed more adequately in the Efficacy and Safety of BIIB033 (Opicinumab) as an Add-on Therapy to Disease-Modifying Therapies in Relapsing Multiple Sclerosis (AFFINITY) study (NCT03222973). Results should be interpreted with caution and may not fully reflect the natural history of changes in nMTR and DTI-RD in SELs and non-SELs of patients with RRMS and SPMS. The binary classification between SELs and non-SELs is somewhat artificial; longitudinal trajectories of tissue damage observed in non-SELs suggest that there may be a gradation of "activity" within chronic white matter MS lesions. Future work is needed to optimize SEL detection methods and further inform the understanding of spatiotemporal lesion-level patterns of tissue alteration in SELs by exploring alternative constancy/linearity and concentricity factor constraints of slow/chronic expansion detection criteria.

Furthermore, subsets of chronic active lesions that may shrink with time are not identified by the SEL detection method. The

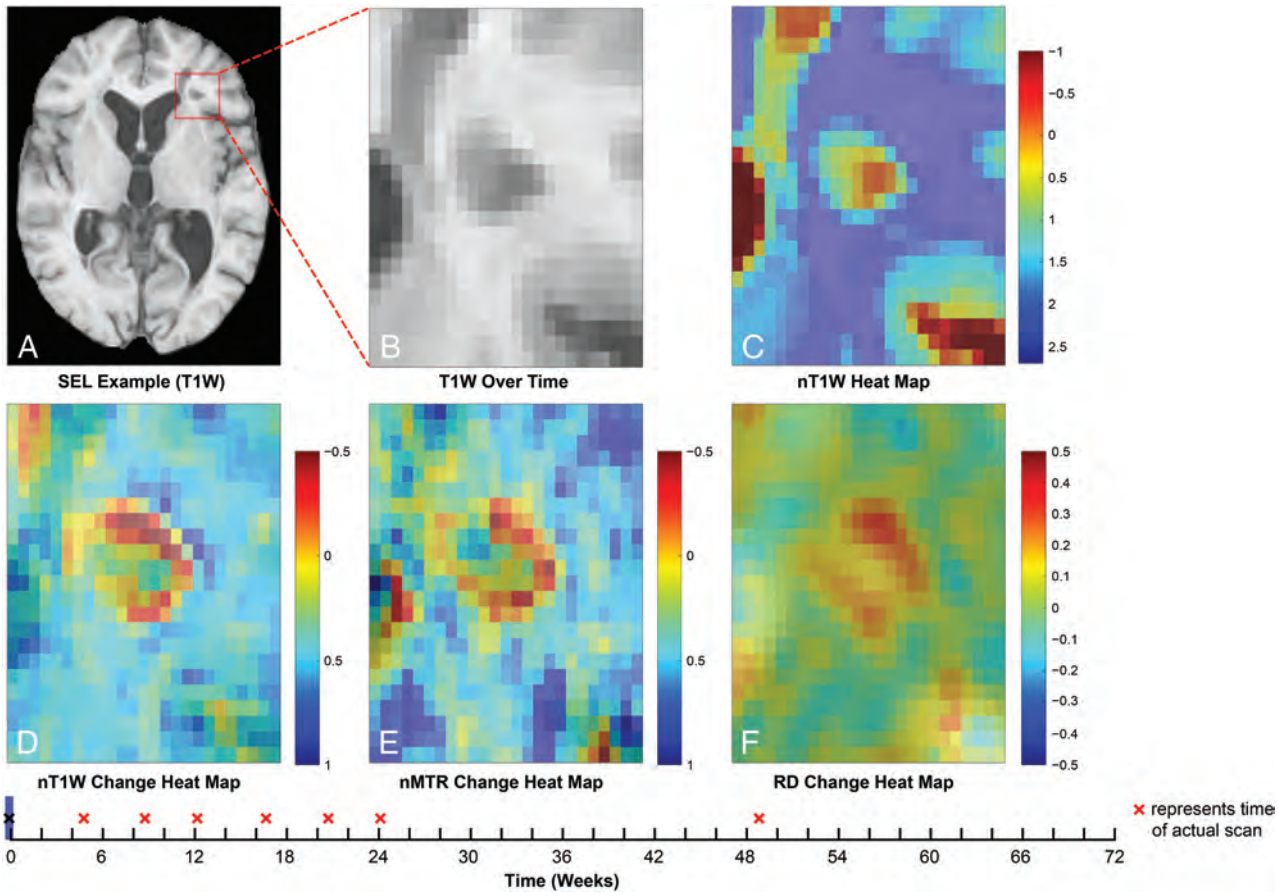

FIG 4. Example of lesion-level distribution of longitudinal tissue damage within SELs. Heat maps for normalized TIWI intensity and normalized TIWI (nTIWI), nMTR, and DTI-RD intensity change are based on linear modeling of intensity with time. Red "×" labels represent time of brain MR imaging scanning acquisitions. See On-line video for an animated version of this figure.

SEL quantification algorithm currently does not accommodate potential contraction at the lesion center across time, which is known to occur, especially in the longer term,[34] and underscores that the primary pathologic process in chronically evolving lesions (even those described by pathologists as "slowly expanding") is likely to include tissue loss. A recent study showed that chronic active lesions detected by the presence of a paramagnetic rim on high-field susceptibility-based MR imaging do not shrink slowly as other lesions do, but typically enlarge, similar to SELs, owing to ongoing demyelination (confirmed by pathologic assessment). Such chronic active/slowly expanding/smoldering MS lesions are associated with a more aggressive disease course[35] and disability progression[13] and should, therefore, be consistently assessed in MS clinical trials targeting chronic inflammation and remyelination.

CONCLUSIONS

Patterns of longitudinal change in nMTR and DTI-RD in SELs were consistent with progressive demyelination and tissue loss, as seen in smoldering white matter MS plaques. The consistency between longitudinal changes in nT1 intensity, nMTR, and DTI-RD in SELs and non-SELs with time suggests that nT1 intensity, though not a specific marker of myelin, could be a surrogate measure of chronic tissue damage in the absence of MTR and DTI acquisitions and may provide value in clinical trials evaluating the effect of potential remyelination and/or antiprogressive MS therapies.

ACKNOWLEDGMENTS

We thank all patients, their families, and the investigators who participated in SYNERGY. We also thank NeuroRx Research for evaluation of MR imaging scans. Editorial support for the preparation of this manuscript was provided by Excel Scientific Solutions.

Disclosures: Colm Elliott—*UNRELATED*: *Employment*: NeuroRx Research, *Comments*: full-time employee. Douglas L. Arnold—*UNRELATED*: *Personal Fees*: Acorda Therapeutics, Albert Charitable Trust, Biogen, Celgene, Roche, GeNeuro, Frequency Therapeutics, MedDay Pharma, Merck Serono, Novartis, Sanofi-Aventis, Wave Life Sciences; *Grant*: Biogen, Immunotec, Novartis; *Other:* NeuroRx Research, *Comments*: equity interest. Chunlei Ke—*UNRELATED*: *Employment*: Biogen; *Stock/Stock Options*: Biogen. Li Zhu—*UNRELATED*: *Employment*: Biogen; *Stock/Stock Options*: Biogen. Ih Chang—*UNRELATED*: former employee of and hold stock in Biogen. Ellen Cahir-McFarland—*UNRELATED*: *Other*: Biogen, *Comments*: employee who holds stock. Elizabeth Fisher—*UNRELATED*: *Employment*: Biogen, *Comments*: full-time employee; *Stock/Stock Options*: Biogen. Bing Zhu—*UNRELATED*: *Employment*: Biogen; *Stock/Stock Options*: Biogen. Sarah Gheuens—*UNRELATED*: former employee of and hold stock in Biogen; currently an employee of and hold stock in Agios Pharmaceuticals. Matthew Scaramozza—*UNRELATED*: *Employment*: Biogen, *Comments*: full-time salaried employee; *Stock/Stock Options*: Biogen, *Comments*: I received stock awards from Biogen as an employee and purchased stock under an employee stock purchase plan; *Travel/Accommodations/Meeting*

Expenses Unrelated to Activities Listed: Biogen, *Comments*: As an employee of Biogen, the company has paid for me to attend annual conferences in 2018 and 2019 (AAN and ECTRIMS). Nathalie Franchimont—*UNRELATED*: *Employment*: Biogen; *Stock/Stock Options*: Biogen, *Comments*: shareholder. Shibeshih Belachew—*UNRELATED*: *Employment*: Biogen; *Stock/Stock Options*: Biogen, *Comments*: shareholder. *Money paid to the institution.

REFERENCES

1. Frischer JM, Weigand SD, Guo Y, et al. **Clinical and pathological insights into the dynamic nature of the white matter multiple sclerosis plaque.** *Ann Neurol* 2015;78:710–21 CrossRef Medline
2. Chawla S, Kister I, Wuerfel J, et al. **Iron and non-iron-related characteristics of multiple sclerosis and neuromyelitis optica lesions at 7T MRI.** *AJNR Am J Neuroradiol* 2016;37:1223–30 CrossRef Medline
3. Kilsdonk ID, Wattjes MP, Lopez-Soriano A, et al. **Improved differentiation between MS and vascular brain lesions using FLAIR* at 7 Tesla.** *Eur Radiol* 2014;24:841–49 CrossRef Medline
4. Dal-Bianco A, Grabner G, Kronnerwetter C, et al. **Slow expansion of multiple sclerosis iron rim lesions: pathology and 7 T magnetic resonance imaging.** *Acta Neuropathol* 2017;133:25–42 CrossRef Medline
5. Kuhlmann T, Ludwin S, Prat A, et al. **An updated histological classification system for multiple sclerosis lesions.** *Acta Neuropathol* 2017;133:13–24 CrossRef Medline
6. Luchetti S, Fransen NL, van Eden CG, et al. **Progressive multiple sclerosis patients show substantial lesion activity that correlates with clinical disease severity and sex: a retrospective autopsy cohort analysis.** *Acta Neuropathol* 2018;135:511–28 CrossRef Medline
7. Machado-Santos J, Saji E, Tröscher AR, et al. **The compartmentalized inflammatory response in the multiple sclerosis brain is composed of tissue-resident CD8+ T lymphocytes and B cells**. *Brain* 2018;141:2066–82 CrossRef Medline
8. Filippi M, Rocca MA, Barkhof F, et al; Attendees of the Correlation between Pathological MRI Findings in MS Workshop. **Association between pathological and MRI findings in multiple sclerosis.** *Lancet Neurol* 2012;11:349–60 CrossRef Medline
9. Absinta M, Sati P, Reich DS. **Advanced MRI and staging of multiple sclerosis lesions.** *Nat Rev Neurol* 2016;12:358–68 CrossRef Medline
10. Absinta M, Sati P, Schindler M, et al. **Persistent 7-Tesla phase rim predicts poor outcome in new multiple sclerosis patient lesions.** *J Clin Invest* 2016;126:2597–609 CrossRef Medline
11. Filippi M, Preziosa P, Banwell BL, et al. **Assessment of lesions on magnetic resonance imaging in multiple sclerosis: practical guidelines.** *Brain* 2019;142:1858–75 CrossRef Medline
12. Elliott C, Wolinsky JS, Hauser SL, et al. **Slowly expanding/evolving lesions as a magnetic resonance imaging marker of chronic active multiple sclerosis lesions.** *Mult Scler* 2019;25:1915–25 CrossRef Medline
13. Elliott C, Belachew S, Wolinsky JS, et al. **Chronic white matter lesion activity predicts clinical progression in primary progressive multiple sclerosis.** *Brain* 2019;142:2787–99 CrossRef Medline
14. Haacke EM, Makki M, Ge Y, et al. **Characterizing iron deposition in multiple sclerosis lesions using susceptibility weighted imaging.** *J Magn Reson Imaging* 2009;29:537–44 CrossRef Medline
15. Popescu BF, Frischer JM, Webb SM, et al. **Pathogenic implications of distinct patterns of iron and zinc in chronic MS lesions.** *Acta Neuropathol* 2017;134:45–64 CrossRef Medline
16. Barkhof F, Brück W, De Groot CJ, et al. **Remyelinated lesions in multiple sclerosis: magnetic resonance image appearance.** *Arch Neurol* 2003;60:1073–81 CrossRef Medline
17. Schmierer K, Scaravilli F, Altmann DR, et al. **Magnetization transfer ratio and myelin in postmortem multiple sclerosis brain.** *Ann Neurol* 2004;56:407–15 CrossRef Medline
18. Merkler D, Boretius S, Stadelmann C, et al. **Multicontrast MRI of remyelination in the central nervous system.** *NMR Biomed* 2005;18:395–403 CrossRef Medline
19. Chen JT, Collins DL, Atkins HL, et al; Canadian MS/BMT Study Group. **Magnetization transfer ratio evolution with demyelination and remyelination in multiple sclerosis lesions.** *Ann Neurol* 2008;63:254–62 CrossRef Medline
20. Fox RJ, Cronin T, Lin J, et al. **Measuring myelin repair and axonal loss with diffusion tensor imaging.** *AJNR Am J Neuroradiol* 2011;32:85–91 CrossRef Medline
21. Klawiter EC, Schmidt RE, Trinkaus K, et al. **Radial diffusivity predicts demyelination in ex vivo multiple sclerosis spinal cords.** *Neuroimage* 2011;55:1454–60 CrossRef Medline
22. Cadavid D, Mellion M, Hupperts R, et al; SYNERGY Study Investigators. **Safety and efficacy of opicinumab in patients with relapsing multiple sclerosis (SYNERGY): a randomised, placebo-controlled, phase 2 trial.** *Lancet Neurol* 2019;18:845–56 CrossRef Medline
23. Francis SJ. ***Automatic Lesion Identification in MRI of Multiple Sclerosis Patients.*** Thesis. Division of Neuroscience, McGill University. 2004
24. Nakamura K, Guizard N, Fonov VS, et al. **Jacobian integration method increases the statistical power to measure gray matter atrophy in multiple sclerosis.** *Neuroimage Clin* 2014;4:10–17 CrossRef Medline
25. Avants BB, Epstein CL, Grossman M, et al. **Symmetric diffeomorphic image registration with cross-correlation: evaluating automated labeling of elderly and neurodegenerative brain.** *Med Image Anal* 2008;12:26–41 CrossRef Medline
26. Rousseeuw P, Van Driessen K. **Computing LTS regression for large data sets.** *Data Mining and Knowledge Discovery* 2006;12:29–45 CrossRef
27. Chen W, Gauthier SA, Gupta A, et al. **Quantitative susceptibility mapping of multiple sclerosis lesions at various ages.** *Radiology* 2014;271:183–92 CrossRef Medline
28. Wisnieff C, Ramanan S, Olesik J, et al. **Quantitative susceptibility mapping (QSM) of white matter multiple sclerosis lesions: interpreting positive susceptibility and the presence of iron.** *Magn Reson Med* 2015;74:564–70 CrossRef Medline
29. Deh K, Ponath GD, Molvi Z, et al. **Magnetic susceptibility increases as diamagnetic molecules breakdown: myelin digestion during multiple sclerosis lesion formation contributes to increase on QSM.** *J Magn Reson Imaging* 2018;48:1281–87 CrossRef Medline
30. Yao Y, Nguyen TD, Pandya S, et al. **Combining quantitative susceptibility mapping with automatic zero reference (QSM0) and myelin water fraction imaging to quantify iron-related myelin damage in chronic active MS lesions.** *AJNR Am J Neuroradiol* 2018;39:303–10 CrossRef Medline
31. Zhang S, Liu Z, Nguyen TD, et al. **Clinical feasibility of brain quantitative susceptibility mapping.** *Magn Reson Imaging* 2019;60:44–51 CrossRef Medline
32. Suthiphosuwan S, Sati P, Absinta M, et al. **Paramagnetic rim sign in radiologically isolated syndrome.** *JAMA Neurol* 2020;77:653 CrossRef Medline
33. Kaunzner UW, Kang Y, Zhang S, et al. **Quantitative susceptibility mapping identifies inflammation in a subset of chronic multiple sclerosis lesions.** *Brain* 2019;142:133–45 CrossRef Medline
34. Sethi V, Nair G, Absinta M, et al. **Slowly eroding lesions in multiple sclerosis.** *Mult Scler* 2017;23:464–72 CrossRef Medline
35. Absinta M, Sati P, Masuzzo F, et al. **Association of chronic active multiple sclerosis lesions with disability in vivo.** *JAMA Neurol* 2019;76:1474–83 CrossRef Medline

MRS as an Aid to Diagnose Malignant Transformation in Low-Grade Gliomas with Increasing Contrast Enhancement

C.H. Toh, M. Castillo, K.-C. Wei, and P.-Y. Chen

ABSTRACT

BACKGROUND AND PURPOSE: Increased contrast enhancement has been used as a marker of malignant transformation in low-grade gliomas. This marker has been found to have limited accuracy because many low-grade gliomas with increased contrast enhancement remain grade II. We aimed to investigate whether MR spectroscopy can contribute to the diagnosis of malignant transformation in low-grade gliomas with increased contrast enhancement.

MATERIALS AND METHODS: Patients with low-grade gliomas who had contemporaneous MR spectroscopy and histopathology for tumor regions with increased contrast enhancement between 2004 and 2015 were retrospectively reviewed. Clinical data collected were sex and age, Karnofsky Performance Scale, histologic subtypes, *isocitrate dehydrogenase 1* mutation status, disease duration, adjuvant therapy, and post-radiation therapy duration. Imaging data collected were contrast-enhancement size, whole-tumor size, MR spectroscopy metabolite ratios, and tumor grades of regions with increased contrast enhancement. Diagnostic values of these factors on malignant transformation of low-grade gliomas were statistically analyzed.

RESULTS: A total of 86 patients with 96 MR spectroscopy studies were included. Tumor grades associated with increased contrast enhancement were grade II ($n = 42$), grade III ($n = 27$), and grade IV ($n = 27$). On multivariate analysis, the NAA/Cho ratio was the only significant factor ($P < .001$; OR, 7.1; 95% CI, 3.2–16.1) diagnostic of malignant transformation. With 0.222 as the cutoff value, the sensitivity, specificity, and accuracy of NAA/Cho for diagnosing malignant transformation were 94.4%, 83.3%, and 89.6%, respectively.

CONCLUSIONS: MR spectroscopy complements conventional MR imaging in the diagnosis of malignant transformation in a subgroup of low-grade gliomas with increased contrast enhancement.

ABBREVIATIONS: LGG = low-grade glioma; MT = malignant transformation; WHO = World Health Organization

Low-grade gliomas (LGGs) are grade II World Health Organization (WHO) primary brain tumors, accounting for 14.6% of gliomas in population-based studies.[1] LGGs may remain clinically and radiographically stable for years after initial diagnosis and treatment. However, at an unpredictable time, some may show MR imaging features suggestive of disease progression, eg, enlargement of nonenhancing tumor and an increase of enhancement on postgadolinium T1-weighted images. At the time of imaging progression, the tumors may remain WHO grade II or may have progressed to WHO grade III or IV, ie, malignant transformation (MT). Definitive diagnosis of MT requires histopathologic examination, but due to potential surgical risk and costs, increased contrast enhancement is frequently used as a surrogate marker for MT in clinical practice, research studies, and clinical trials of LGG. In the widely used Response Assessment in Neuro-Oncology criteria,[2] an increase of enhancement is also regarded as MT, thus disease progression.

However, a recent study showed that up to 18% of LGGs with increased contrast enhancement remained WHO grade II.[3] Despite having a sensitivity of 92%, increased contrast enhancement had a specificity of 57% for the detection of MT. Besides, increased contrast enhancement may also be due to treatment-related changes.[4,5] In a consensus article recently published by

Received February 18, 2020; accepted after revision June 4.

From the Departments of Medical Imaging and Intervention (C.H.T.), and Neurosurgery (K.-C.W., P.-Y.C.), Chang Gung Memorial Hospital at Linkou and Chang Gung University College of Medicine, Tao-Yuan, Taiwan; and Department of Radiology (M.C.), University of North Carolina School of Medicine, Chapel Hill, North Carolina.

This work was supported, in part, by grants from the National Science Council Taiwan (NSC98-2314-B-182A-051-MY3 and NSC101-2314-B-182-084 to C.H.T.).

Please address correspondence to Cheng Hong Toh, MD, PhD, Department of Medical Imaging and Intervention, Chang Gung Memorial Hospital at Linkou, No. 5, Fuxing St, Guishan District, Taoyuan City 333, Taiwan (R.O.C.);
e-mail: eldomtoh@hotmail.com

Indicates open access to non-subscribers at www.ajnr.org

http://dx.doi.org/10.3174/ajnr.A6688

the Society for Neuro-Oncology and the European Association of Neuro-Oncology,[6] the limited accuracy of increased contrast enhancement as an indicator of MT in LGGs has also been recognized. Therefore, using increased contrast enhancement as a marker of MT may result in overtreatment of patients whose tumors remain low-grade, errors in the results of research studies, and misinterpretation of clinical benefits of new therapies. In light of the limited implications of increased contrast enhancement, it is crucial to search for imaging markers that can diagnose MT accurately.

Conventional MR imaging sequences such as T1WI, T2WI, FLAIR, and postcontrast T1WI provide only anatomic information. In contrast, proton MR spectroscopy (MRS) offers unique metabolic information of brain tumor biology and enables quantitative assessment of tissue metabolites such as Cho (a marker of cellular membrane turnover), Cr (a marker of energetic systems and intracellular metabolism), NAA (a marker of neuronal and axonal viability and density), lactate (a marker of anaerobic metabolism), and lipids (a marker of cellular breakdown or necrosis).[7] MR spectroscopy is used as an adjunct to conventional MR imaging because it helps in differentiating brain tumor from other lesions, identifies optimal biopsy sites in heterogeneous gliomas, monitors treatment response, and differentiates treatment-related changes and tumor recurrence.[8]

Previous studies have demonstrated the utility of MR spectroscopy in predicting or prognosticating MT and survival of those with LGGs.[9-15] To the best of our knowledge, the role of MR spectroscopy in diagnosing MT among LGGs with increased contrast enhancement has not been investigated. In the present study, using histopathology as the criterion standard, we aimed to determine the value of MR spectroscopy to diagnose MT in a group of patients who had a prior diagnosis of LGG and an increase in contrast enhancement on follow-up MR imaging.

MATERIALS AND METHODS

Patients

This retrospective study was performed after institutional review board approval (Chang Gung Memorial Hospital). Patients were retrospectively selected from the brain tumor database of our institution if they met all the following criteria: 1) prior pathologic diagnosis of LGG with follow-up MR imaging studies performed between 2004 and 2015 showing increased contrast enhancement; 2) having undergone surgery due to increased contrast enhancement with a pathologic diagnosis of grade II, III, or IV glioma; 3) availability of MR spectroscopy from brain regions with increased contrast enhancement; and 4) confirmed removal of the brain regions with increased contrast enhancement on follow-up MR imaging.

Increased contrast enhancement was defined as emergence of new contrast enhancement in previously nonenhancing tumors or regions thereof, new separate lesions with contrast enhancement, or at least a 25% increase in the size of enhancement for tumors with enhancement at baseline. Baseline referred to the first follow-up MR imaging after the last operation. Increased contrast enhancement was confirmed by neuroradiologists who compared the baseline MR imaging and the one before the next operation. Patients with multiple operations for separate instances of increased contrast enhancement were included as long as they had not already experienced MT and each event of increased contrast enhancement was treated independently.

Histopathologic diagnosis was made by a board-certified neuropathologist according to the 2000 WHO classification of CNS tumors before 2007 and thereafter based on the 2007 WHO classification. Patients younger than 18 years of age at initial diagnosis or with a diagnosis of radiation necrosis due to increased contrast enhancement were excluded. Patients were also excluded if their MR spectroscopy showed poor spectral resolution or inclusion of normal-appearing brain or edema in the VOIs.

Clinical and Imaging Information

Patient medical records were retrospectively reviewed to collect clinical information including sex, age and Karnofsky Performance Scale score at the time of increased contrast enhancement, histologic subtypes (diffuse astrocytoma, oligoastrocytoma, or oligodendroglioma), *isocitrate dehydrogenase 1* (*IDH-1*) mutation status, disease duration (time interval between first histopathologic diagnosis of LGG and increased contrast enhancement), adjuvant therapy received before increased contrast enhancement, post-radiation therapy duration (time interval between end of radiation therapy and increased contrast enhancement), and tumor grades associated with increased contrast enhancement.

The first follow-up MR imaging studies after the last operation were reviewed for baseline residual tumor. MR spectroscopy metabolites measured in brain regions with increased contrast enhancement were recorded. The size of the contrast enhancement was measured by determining the product of the largest diameter and its perpendicular length on single postcontrast transverse T1-weighted or MPRAGE images. The size of whole tumor, which included both enhancing and nonenhancing components, was measured on transverse FLAIR or T2-weighted images. If multiple lesions were present, the largest 3 were selected and their products were summed. Follow-up studies, either intraoperative or postoperative MR imaging, were reviewed to confirm removal of brain regions with increased contrast enhancement. All imaging reviews were performed by 2 neuroradiologists. Differences were resolved by consensus.

Conventional MR Imaging and MR Spectroscopy Protocols

Preoperative MR imaging and MR spectroscopy studies were performed on a single occasion using 1.5T (Magnetom Espree; Siemens) or 3T (Magnetom Tim Trio; Siemens) clinical MR imaging scanners. Intraoperative MR imaging studies were performed with a 1.5T unit (Magnetom Espree). Typical pulse sequences used included transverse T1WI (TR/TE, 250/2.46 ms; section thickness, 4 mm; gap, 1 mm; matrix, 256 × 256; and FOV, 220 × 220 mm), transverse T2WI (TR/TE, 4000/90 ms; section thickness, 4 mm; gap, 1; flip angle, 120°; echo-train length, 17; matrix, 512 × 358; and FOV, 220 × 220 mm), transverse and coronal FLAIR (TR/TE/TI, 8200/85/2500 ms; section thickness, 4 mm; gap, 1 mm; matrix, 320 × 256; and FOV, 220 × 220 mm), postcontrast T1WI in transverse, coronal, and sagittal planes as well as 3D-MPRAGE (TR/TE/TI, 2530/4.03/1100 ms; section

thickness, 1 mm; matrix, 256 × 256; and FOV, 256 × 224 mm) with intravenous administration of 0.1 mmol per kilogram of body weight gadopentetate dimeglumine (Magnevist; Bayer HealthCare Pharmaceuticals).

To better guide VOI placement, we performed all MR spectroscopy studies after contrast medium administration. Postcontrast T1WI or MPRAGE in axial, coronal, and sagittal planes was used to define VOIs. The location of the VOIs was carefully chosen by an on-site neuroradiologist to include as much of the enhancing regions as possible and avoid inclusion of necrosis, cysts, hemorrhage, edema, calcifications, and normal-appearing brain. Single-voxel MR spectroscopy studies were performed using a point-resolved spectroscopy sequence with automated shimming and water suppression. For MR spectroscopy performed on 3T machines, the acquisition parameters were the following: TR/TE, 2000/135 ms; flip angle, 90°; voxel size, 15 × 15 × 15 mm^3; average, 128. For MR spectroscopy performed on a 1.5T machine, the acquisition parameters were the following: TR/TE, 1500/135 ms; flip angle, 90°; voxel size, 16 × 18 × 20 mm^3; average, 192. The levels of metabolites in the VOIs were determined using the workstation software (Leonardo; Siemens). Peak integrals were obtained using a Levenberg-Marquardt fitting routine for principal peaks including lactate, NAA, Cr, and Cho at 1.33, 2.02, 3.02, and 3.22 ppm, respectively. The peak-area metabolite ratios Cho/Cr, NAA/Cr, NAA/Cho, and lactate/Cr were calculated. Because NAA was not detectable in some patients, the Cho/NAA ratio was not calculated.

Statistical Analysis

Clinical and imaging factors thought to be associated with MT were analyzed by univariate analysis. Categorical variables were tested with χ^2 analysis, and continuous variables were tested with the Student *t* test. Selected variables with *P* values < .05 by univariate analysis were subjected to multivariate analysis using logistic regression with a forward stepwise selection procedure. Odds ratios and 95% CIs were calculated to demonstrate the relative risk of each significant factor for MT. Areas under the curve and cutoff values of statistically significant variables were determined by receiver operating characteristic curve analysis. Cutoff values with the highest sensitivity and lowest false-positive rates were chosen for the calculation of sensitivity, specificity, and accuracy of each significant variable. A commercially available statistical software package (SPSS 22; IBM) was used for analysis, and *P* values < .05 were considered a statistically significant difference.

Table 1: Clinical and imaging data of patients with low-grade gliomas demonstrating increased contrast enhancement

Clinical Information	No. of Patients
Sex	
Female	33 (34.4%)
Male	63 (65.6%)
Age range (yr)	
20–39	35 (36.5%)
40–59	47 (49.0%)
Older than 60	14 (14.5%)
KPS	
≥90	74 (77.1%)
≤80	22 (22.9%)
Histologic subtype	
Diffuse astrocytoma	30 (31.3%)
Oligoastrocytoma	27 (28.1%)
Oligodendroglioma	39 (40.6%)
IDH1 mutation	
Wild-type	7 (7.3%)
Mutant	61 (63.5%)
Not available	28 (29.2%)
Baseline residual tumor	
Yes	81 (84.4%)
No	15 (15.6%)
Disease duration	
<2 years	10 (10.4%)
2–5 years	35 (36.5%)
5–10 years	25 (26.0%)
>10 years	26 (27.1%)
Adjuvant therapy	
RT	75 (78.1%)
Carmustine implant	9 (9.4%)
Temozolomide	16 (16.7%)
Post-RT duration	
<6 months	2 (2.7%)
6–12 months	5 (6.7%)
12–24 months	9 (12%)
>24 months	59 (78.6%)
Whole tumor size	
<4 cm^2	17 (17.7%)
4–16 cm^2	45 (46.9%)
>16 cm^2	34 (35.4%)
Contrast enhancement size	
<4 cm^2	37 (38.5%)
4–16 cm^2	36 (37.5%)
>16 cm^2	23 (24.0%)
Tumor grade	
II	42 (43.8%)
III	27 (28.1%
IV	27 (28.1%)

Note:—RT indicates radiation therapy; KPS, Karnofsky Performance Scale.

RESULTS

Between 2004 and 2015, a total of 222 patients with LGGs were regularly followed up in our institution after initial diagnosis and treatment. On follow-up MR imaging studies, 139 patients had 161 instances of increased contrast enhancement and proceeded to an operation. Six instances with a pathologic diagnosis of radiation necrosis were excluded. For the rest of the 155 instances, the pathologic diagnosis was grade II diffuse glioma ($n = 59$), grade III ($n = 53$), and grade IV ($n = 43$). MR spectroscopy was available in 47 of 57 grade II, 34 of 52 grade III, and 29 of 43 grade IV gliomas. Among the 110 MR spectroscopy studies, 14 were excluded due to poor spectral resolution (2 grade II, 5 grade III, and 2 grade IV), inclusion of normal brain in VOIs (1 grade II and 1 grade III), or brain regions with increased contrast enhancement that were not removed (2 grade II and 1 grade III). Successful removal of brain regions with increased contrast enhancement was confirmed in 33 instances with intraoperative MR imaging, in 30 with postoperative MR imaging performed within 1 week, and in 33 with postoperative MR imaging performed between 2 and 12 weeks. The final study population consisted of 86 patients with 96 MR spectroscopy studies (42 grade II, 27 grade III, and 27 grade IV). Seventy-five MR spectroscopy studies were performed on 3T MR imaging, and 21, on 1.5T.

Clinical and imaging data are shown in Table 1. Among these 96 instances, 63 (65.6%) occurred in male patients. The mean age

Table 2: Univariate analysis of factors associated with malignant transformation[a]

Factors	Malignant Transformation		*P* Value	OR	95% CI
	No	Yes			
Sex			.85	0.9	0.39–2.15
Male	28	35			
Female	14	19			
Age (yr)	49.1 ± 12.3	44.2 ± 12.6	.058	NA	–0.17–10.1
KPS	88.1 ± 11.9	90.7 ± 8.2	.202	NA	–6.73–1.44
Histologic subtype			.604	NA	NA
Diffuse astrocytoma	12	18			
Oligoastrocytoma	14	13			
Oligodendroglioma	16	23			
IDH1 mutation			.525	1.7	0.31–9.67
Yes	25	36			
No	2	5			
Mean disease duration (yr)	6.9 ± 5.1	7.1 ± 5.4	.818	NA	–2.42–1.92
Baseline residual tumor			.044	3.7	0.97–14.15
Yes	39	42			
No	3	12			
RT			.037	3.1	1.03–9.37
Yes	37	38			
No	5	16			
Post-RT duration (mo)	59.5 ± 48.7	75.6 ± 54.5	.182	NA	–39.9–7.71
Chemotherapy			.800	NA	NA
None	32	39			
Carmustine implant	3	6			
Temozolomide	7	9			
Whole-tumor size (cm^2)	10.8 ± 11.1	17.1 ± 11.1	.007	NA	–10.8 to –1.7
Contrast-enhancement size (cm^2)	6.1 ± 6.6	12.3 ± 11.1	.001	NA	–10.7 to –2.8
Cho/Cr	3.31 ± 4.26	5.60 ± 4.61	.015	NA	–4.1 to –0.5
NAA/Cho	0.41 ± 0.28	0.10 ± 0.07	<.001	NA	0.22–0.38
NAA/Cr	1.02 ± 1.19	0.58 ± 0.78	.033	NA	0.04–0.84
Lac/Cr	0.43 ± 1.41	0.77 ± 1.62	.285	NA	–0.96–0.28

Note:—NA indicates not applicable; Lac, lactate; RT, radiation therapy; KPS, Karnofsky Performance Scale.

[a] Data are mean ± SD for age, KPS, disease duration, post-RT duration, whole-tumor size, contrast enhancement size, and MR spectroscopy metabolite ratios.

and Karnofsky Performance Scale scores at the time of increased contrast enhancement were 46.3 years (range, 20–83) and 89.5 (range, 50–100), respectively. Initial histologic subtypes were diffuse astrocytoma ($n = 30$), oligoastrocytoma ($n = 27$), and oligodendroglioma ($n = 39$). Eighty-one instances had baseline residual tumors. *IDH1* mutation status was available in 68 (70.8%) instances with 61 (89.7%) being *IDH1*-mutant. Median disease duration was 5.2 years for those remaining with grade II, and 5.1 years for those with MT. Adjuvant therapy administered before an increase of contrast enhancement included radiation therapy ($n = 75$), Carmustine implants ($n = 9$), and temozolomide ($n = 16$). Median post-radiation therapy duration was 53.5 months (range, 3.5–206 months). NAA was not detectable in 3 instances of MT (1 grade III and 2 grade IV). Lactate was present in 14 (33.3%) instances that remained grade II and 21 (38.9%) of MT.

Table 2 illustrates the results of univariate analysis in which baseline residual tumor ($P = .044$) and previous adjuvant radiation therapy ($P = .037$) were associated with MT. LGGs with MT had significantly larger whole-tumor size ($P = .007$), larger contrast-enhancement size ($P = .001$), higher Cho/Cr ratio ($P = .015$), lower NAA/Cho ratio ($P < .001$), and lower NAA/Cr ratio ($P = .033$) compared with those without MT. Figures 1 and 2 illustrate measurements of metabolite levels in a LGG preserving grade II histology and an LGG with MT, respectively.

On multivariate analysis, the NAA/Cho ratio ($P < .001$; OR, 7.1, 95% CI, 3.2–16.1) was the only variable predictive of MT among LGGs with increased contrast enhancement. On receiver operating characteristic curve analysis (Fig 3), the discriminative power of NAA/Cho measured with an area under the curve was 0.922 ($P < .001$; 95% CI, 0.86–0.98). With 0.222 as the cutoff value, the sensitivity, specificity, and accuracy of NAA/Cho in diagnosing MT were 94.4%, 83.3%, and 89.6%, respectively.

DISCUSSION

Our study showed that among patients with a prior diagnosis of LGG, increased contrast enhancement on MR imaging can be seen in LGGs that remained grade II or those that underwent MT. NAA/Cho ratios measured in regions with increased contrast enhancement were significantly lower in LGGs with MT compared with those that remained grade II. Thus, the NAA/Cho ratio may diagnose MT among LGGs with increased contrast enhancement.

The median time to MT in the present study was 5.1 years, which correlates well with previous reports in which it ranged from 2.7 to 5.4 years.[16,17] Previously identified prognostic factors for MT include older age, male sex, multiple tumor locations, tumor size ≥5 cm, adjuvant temozolomide, presence of residual tumor, astrocytoma histology, and *IDH* wild-type.[16-18] However, in our study, none of these factors were helpful in making the diagnosis of MT. We speculate that this discrepancy could be due to different criteria for MT. In our study, MT was diagnosed with

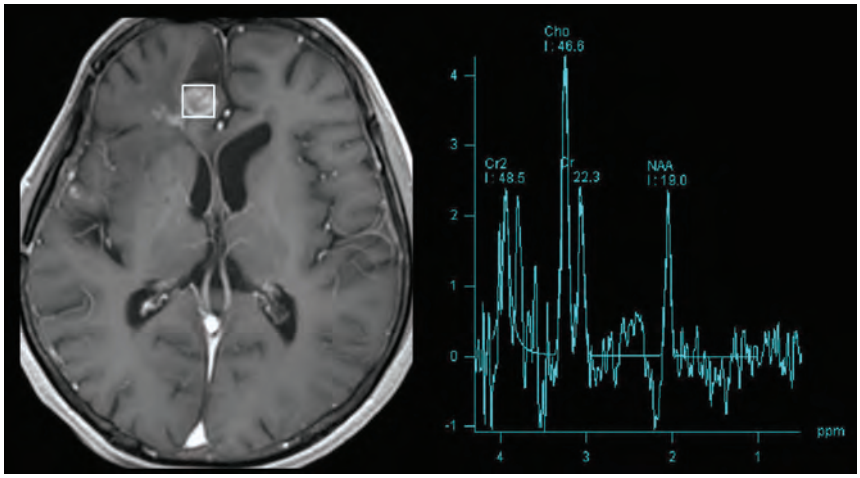

FIG 1. Measurement of metabolite levels using single-voxel MR spectroscopy in a low-grade glioma with increased contrast enhancement but preserved grade II histology. Transverse contrast-enhanced T1WI (left) shows an enhancing nodule in the right frontal lobe, posterior to the surgical cavity. A 15 × 15 × 15 cm^3 VOI was placed over the enhancing brain region. Spectrum (right) obtained with TE = 135 ms shows an increase in the Cho peak and a decrease in the NAA peak. The NAA/Cho ratio is 0.41.

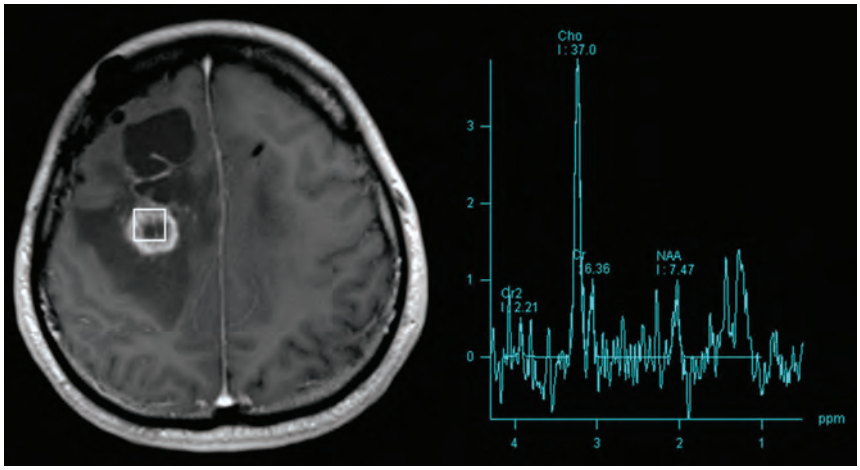

FIG 2. Measurement of metabolite levels using single-voxel MR spectroscopy in a low-grade glioma with increased contrast enhancement and malignant transformation. Transverse contrast-enhanced T1WI (left) shows an enhancing nodule in the right medial frontal lobe, posterior to the surgical cavity. A 15 × 15 × 15 cm^3 VOI was placed over the enhancing brain region. Spectrum (right) obtained with TE = 135 ms shows an increase in the Cho peak and a decrease in the NAA peak. The NAA/Cho ratio is 0.20.

histopathology, while in other studies, a significant proportion of MT cases were diagnosed with only MR imaging.

Increased contrast enhancement has been used as an indicator of MT in several clinical guidelines for LGG.[2,19,20] However, our results do not support this observation. In the present study, the percentage of LGGs that remained grade II despite having increased contrast enhancement was 37% (59 of 161), higher than the previously reported 18%.[3] In a recent study, the sensitivity and specificity of increased contrast enhancement for diagnosing MT were 92% and 57%, respectively.[3] Because of the low specificity, the authors suggested that histopathologic confirmation at the time of imaging progression should be attempted to guide subsequent therapy. However, an operation may not always be possible; therefore, noninvasive imaging markers play an important role in patient care. In our study, NAA/Cho was found to be diagnostic of MT and showed similar sensitivity (94.4%) but a higher specificity (83.3%).

Previous studies have tried to predict the outcome of LGG, particularly in the early course of the disease. Studies show that MR spectroscopy performed at baseline[9,10] or at recurrence[11,12] may predict progression-free survival and MT of LGG. MR spectroscopy may differentiate clinically stable LGGs from those that progress as a result of MT.[14,15] The NAA/Cho ratio was found to be the best MR spectroscopy marker for LGG progression, with a sensitivity of 53.9%.[13] The Cho/NAA ratio was shown to reliably differentiate recurrent glioma from post-radiation injury.[4,5] Those studies demonstrated the potential of MR spectroscopy in prognosticating or predicting survival of those with LGG. However, their diagnostic and therapeutic impact on patient care was limited due to inconsistent MR spectroscopy techniques and variable methods of choosing VOI locations, and most important, many MT cases were not histologically proved. In our study, we investigated the diagnostic performance at the time of increased contrast enhancement. With histology as the criterion standard, we found that MR spectroscopy could diagnose MT with high diagnostic performance (area under the curve = 0.924).

We found that MR spectroscopy was useful for diagnosing MT. There were several reasons for this finding, including the use of a single-voxel technique. Precise measurements of metabolite levels in brain regions with increased contrast enhancement were essential for differentiation between LGGs with preserved grade II histology and those with MT. Therefore, spectral contamination by adjacent normal brain, edema, and fat should be minimized because it could introduce significant measurement errors. Compared with multivoxel MR spectroscopy, single-voxel MR spectroscopy has a shorter acquisition time, better shimming, a higher signal-to-noise ratio, and better spectral quality. Moreover, it is less susceptible to contaminations from adjacent tissues. In our study, MR spectroscopy was performed after administration of a gadolinium contrast medium because increased contrast enhancement better guides VOI placement, allows consistency in choosing

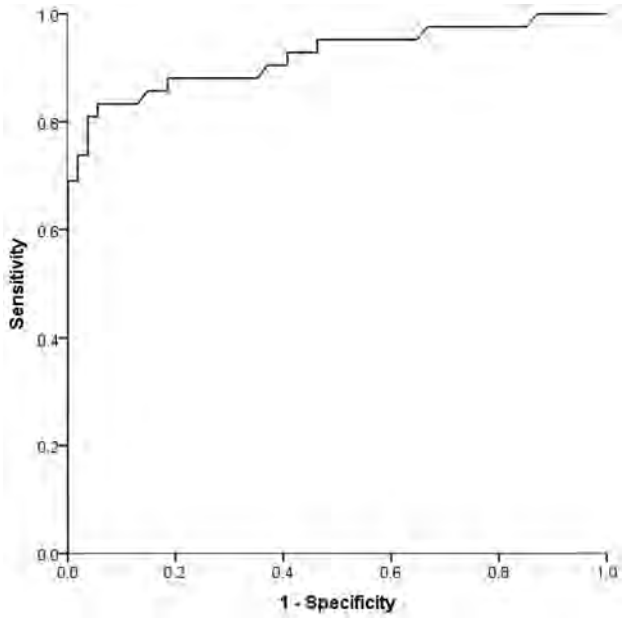

FIG 3. Receiver operating characteristic curve analysis of the diagnostic performance of the NAA/Cho ratio in differentiating LGG preserving grade II histology and LGG with MT.

the VOI location, and thus improves the reproducibility of metabolite measurements. Finally, locations of VOIs were decided by an on-site neuroradiologist, possibly helping to achieve good spectral quality.

In this study, patients with LGGs with increased contrast enhancement who did not proceed to an operation were excluded. Initially, this exclusion may appear as selection bias, but given the low specificity of increased contrast enhancement, this seeming limitation is actually the strength of our study. LGGs that progressed with only enlargement of nonenhancing tumors were not included in this study because they need different methods for choosing VOI location, and the MT rate for this group was 23%, much lower than the 82% for those with increased contrast enhancement.[3] Although we did not perform image-guided tissue sampling, we reviewed the intraoperative or postoperative MR imaging studies to confirm removal of brain regions with increased contrast enhancement. This step decreases the chances of tumor grade misclassification. A trend toward lower myo-inositol levels in high-grade gliomas compared with low-grade gliomas was reported.[21] Further studies using short-TE MR spectroscopy are needed to determine the utility of myo-inositol in diagnosing MT because our MR spectroscopy spectra obtained at a TE of 135 ms were not useful in demonstrating this metabolite. In the present study, NAA levels of LGGs with MT were lower than those that remained grade II. In some LGGs with MT, NAA was even undetectable. Therefore, NAA/Cho rather than Cho/NAA ratios were calculated. We speculate that a lower level or absence of NAA, which reflects more severe neuronal destruction, may be the principal metabolite change in MT. Further studies are needed to support our observations.

CONCLUSIONS

MR spectroscopy complements conventional MR imaging in the diagnosis of malignant transformation in a subgroup of low-grade gliomas with increased contrast enhancement. MR spectroscopy may reduce the need for an operation and help in clinical decision-making for low-grade gliomas with increased contrast enhancement.

Disclosures: Cheng Hong Toh—*RELATED*: *Grant*: National Science Council Taiwan, *Comments*: research grant.* *Money paid to institution.

REFERENCES

1. Ostrom QT, Cioffi G, Gittleman H, et al. **CBTRUS Statistical Report: Primary Brain and Other Central Nervous System Tumors Diagnosed in the United States in 2012-2016.** *Neuro Oncol* 2019;21:v1–100 CrossRef Medline
2. van den Bent MJ, Wefel JS, Schiff D, et al. **Response Assessment in Neuro-Oncology (a report of the RANO group): assessment of outcome in trials of diffuse low-grade gliomas.** *Lancet Oncol* 2011;12:583–93 CrossRef
3. Narang AK, Chaichana KL, Weingart JD, et al. **Progressive low-grade glioma: assessment of prognostic importance of histologic reassessment and MRI findings.** *World Neurosurg* 2017;99:751–57 CrossRef Medline
4. Fink JR, Carr RB, Matsusue E, et al. **Comparison of 3 Tesla proton MR spectroscopy, MR perfusion and MR diffusion for distinguishing glioma recurrence from posttreatment effects.** *J Magn Reson Imaging* 2012;35:56–63 CrossRef Medline
5. Matsusue E, Fink JR, Rockhill JK, et al. **Distinction between glioma progression and post-radiation change by combined physiologic MR imaging.** *Neuroradiology* 2010;52:297–306 CrossRef Medline
6. Schiff D, van den Bent M, Vogelbaum MA, et al. **Recent developments and future directions in adult lower-grade gliomas: Society for Neuro-Oncology (SNO) and European Association of Neuro-Oncology (EANO) Consensus.** *Neuro Oncol* 2019;21:837–53 CrossRef Medline
7. Bertholdo D, Watcharakorn A, Castillo M. **Brain proton magnetic resonance spectroscopy: introduction and overview.** *Neuroimaging Clin N Am* 2013;23:359–80 CrossRef Medline
8. Oz G, , Alger JR, Barker PB, et al; MRS Consensus Group. **Clinical proton MR spectroscopy in central nervous system disorders.** *Radiology* 2014;270:658–79 CrossRef Medline
9. Hattingen E, Raab P, Franz K, et al. **Prognostic value of choline and creatine in WHO grade II gliomas.** *Neuroradiology* 2008;50:759–67 CrossRef Medline
10. Bourdillon P, Hlaihel C, Guyotat J, et al. **Prediction of anaplastic transformation in low-grade oligodendrogliomas based on magnetic resonance spectroscopy and 1p/19q codeletion status.** *J Neurooncol* 2015;122:529–37 CrossRef Medline
11. Jalbert LE, Neill E, Phillips JJ, et al. **Magnetic resonance analysis of malignant transformation in recurrent glioma.** *Neuro Oncol* 2016;18:1169–79 CrossRef Medline
12. Neill E, Luks T, Dayal M, et al. **Quantitative multi-modal MR imaging as a non-invasive prognostic tool for patients with recurrent low-grade glioma.** *J Neurooncol* 2017;132:171–79 CrossRef Medline
13. Alimenti A, Delavelle J, Lazeyras F, et al. **Monovoxel 1H magnetic resonance spectroscopy in the progression of gliomas.** *Eur Neurol* 2007;58:198–209 CrossRef Medline
14. Tedeschi G, Lundbom N, Raman R, et al. **Increased choline signal coinciding with malignant degeneration of cerebral gliomas: a serial proton magnetic resonance spectroscopy imaging study.** *J Neurosurg* 1997;87:516–24 CrossRef Medline
15. Bobek-Billewicz B, Stasik-Pres G, Hebda A, et al. **Anaplastic transformation of low-grade gliomas (WHO II) on magnetic**

resonance imaging. *Folia Neuropathol* 2014;52:128–40 CrossRef Medline
16. Murphy ES, Leyrer CM, Parsons M, et al. **Risk factors for malignant transformation of low-grade glioma.** *Int J Radiat Oncol Biol Phys* 2018;100:965–71 CrossRef Medline
17. Tom MC, Park DYJ, Yang K, et al. **Malignant transformation of molecularly classified adult low-grade glioma.** *Int J Radiat Oncol Biol Phys* 2019;105:1106–12 CrossRef Medline
18. Chaichana KL, McGirt MJ, Laterra J, et al. **Recurrence and malignant degeneration after resection of adult hemispheric low-grade gliomas.** *J Neurosurg* 2010;112:10–17 CrossRef Medline
19. Soffietti R, Baumert BG, Bello L, et al; European Federation of Neurological Societies. **Guidelines on management of low-grade gliomas: report of an EFNS-EANO Task Force.** *Eur J Neurol* 2010;17:1124–33 CrossRef Medline
20. Sepulveda-Sanchez JM, Muñoz Langa J, Arráez MÁ, et al. **SEOM clinical guideline of diagnosis and management of low-grade glioma.** *Clin Transl Oncol 2018* 2017;20:3–15 CrossRef Medline
21. Castillo M, Smith JK, Kwock L. **Correlation of myo-inositol levels and grading of cerebral astrocytomas.** *AJNR Am J Neuroradiol* 2000;21:1645–49

Thin-Section MR Imaging for Carotid Cavernous Fistula

D. Kim, Y.J. Choi, Y. Song, S.R. Chung, J.H. Baek, and J.H. Lee

ABSTRACT

BACKGROUND AND PURPOSE: Carotid-cavernous fistulas are abnormal vascular shunts that can cause various neurologic or orbital symptoms. The purpose of this retrospective study was to evaluate the diagnostic performance of thin-section MR imaging for carotid cavernous fistula in patients with clinically suspected carotid cavernous fistula, and to identify possible imaging predictors of carotid cavernous fistula.

MATERIALS AND METHODS: A total of 98 patients who were clinically suspected of having carotid cavernous fistula (according to their symptoms and physical examinations) between January 2006 and September 2018 were included in this study. The patients underwent pretreatment thin-section MR imaging and DSA. Thin-section MR imaging consisted of 2D coronal T1- and T2WI with 3-mm thickness and 3D contrast-enhanced T1WI with 0.6 mm thickness. The diagnostic performance of thin-section MR imaging for carotid cavernous fistula was evaluated with the reference standard of DSA. Univariate logistic regression analysis was performed to determine possible imaging predictors of carotid cavernous fistula.

RESULTS: Among the 98 patients, DSA confirmed 38 as having carotid cavernous fistula. The overall accuracy, sensitivity, and specificity of thin-section MR imaging were 88.8%, 97.4%, and 83.3%, respectively. Possible imaging predictors on thin-section MR imaging included abnormal contour of the cavernous sinus (OR: 21.7), internal signal void of the cavernous sinus (OR: 15.3), prominent venous drainage flow (OR: 54.0), and orbital/periorbital soft tissue swelling (OR: 40.4).

CONCLUSIONS: Thin-section MR imaging provides high diagnostic performance and possible imaging predictors of carotid cavernous fistula in patients with clinically suspected carotid cavernous fistula. Thin-section MR imaging protocols could help decide appropriate management plans for patients with clinically suspected carotid cavernous fistula.

ABBREVIATION: CCF = carotid cavernous fistula

Carotid cavernous fistulas (CCFs) are abnormal vascular shunts connecting the carotid artery and cavernous sinus. The flow can originate either directly from the cavernous segment of the internal carotid artery (direct CCF), or indirectly through dural branches from the internal carotid artery or external carotid artery (indirect CCF or cavernous sinus dural arteriovenous fistula).[1] Common clinical symptoms of CCF include proptosis, conjunctival injection, chemosis, diplopia, headaches, subjective bruit, visual disturbance, and ocular pain.[2-5] The reference standard for the diagnosis and classification of CCF is DSA, which is also essential for management planning.[6,7] However, DSA is not routinely performed in all patients with suspected symptoms because of its semi-invasiveness. So, after consideration of clinical symptoms and imaging findings of CT, CTA, MR imaging, or MRA, physicians decide whether to perform DSA. DSA also presents limitations in the evaluation of structures other than vessels, such as orbital soft tissue and brain parenchyma.

CT, CTA, MR imaging, or MRA are usually used as the initial imaging technique for CCF.[8] The imaging findings on CT include proptosis, dilated superior ophthalmic veins, enlargement of extraocular muscles, orbital and periorbital soft tissue swelling, and focal bulging or diffuse distention of the cavernous sinus. Most CT findings are also visible on MR imaging.[9-18] Additionally, an abnormal signal void within the cavernous sinus due to increased flow may also be visible in patients with

Received March 10, 2020; accepted after revision May 26.

From the Department of Radiology and Research Institute of Radiology (D.K., Y.J.C., Y.S., S.R.C., J.H.B., J.H.L.), Asan Medical Center, University of Ulsan College of Medicine, Seoul, Republic of Korea; and Department of Radiology (D.K.), Busan Paik Hospital, Inje University College of Medicine, Busan, Republic of Korea.

Please address correspondence to Young Jun Choi, MD, PhD, Associate Professor, Department of Radiology and Research Institute of Radiology, University of Ulsan College of Medicine, Asan Medical Center, 86 Asanbyeongwon-gil, Songpa-gu, Seoul, 05505, Republic of Korea; e-mail: jehee23@gmail.com

Indicates article with supplemental on-line table.

http://dx.doi.org/10.3174/ajnr.A6757

CCF, though some studies described considerable numbers of false-positive and false-negative cases for this finding.[10,13] On MRA or CTA, visualization of flow signal or early contrast enhancement within the cavernous sinuses along with dilated draining veins can also be helpful for screening or diagnosing CCF.[19-24] Three-dimensional TOF MRA is known to be very sensitive in detecting CCF with some downside in the specificity.[19,22,25] More recent techniques to visualize CCF include 4D-CTA and arterial spin-labeled MR imaging.[26,27] With advances in MR imaging techniques, the resolution of MR imaging has notably increased over time and continues to do so. In head and neck imaging specifically, the fine structures of the cranial nerves and vascular anatomy have become more vivid owing to the introduction of thin-section MR imaging.[28-30] Due to its complex anatomy and relatively small size, the cavernous sinus is better depicted on thin-section MR imaging.[31] Additionally, subtle change of contour or signal change of cavernous sinus might be easily depicted on thin-section MR imaging. In the clinical setting, certain types of thin-section MR imaging for evaluating cranial nerve and orbit, are frequently used as the initial imaging technique for patients with orbital or cranial nerve symptoms. To the best of our knowledge, there is no published research on the diagnostic performance of thin-section MR imaging for CCF. Therefore, the purpose of our study was to evaluate the usefulness of thin-section MR imaging on a large cohort of patients with clinically suspected CCF.

MATERIALS AND METHODS

This retrospective study was approved by the review boards of our institution, and the requirement for informed consent for data evaluation was waived. The methods and reporting of the results are in accordance with the STROBE (Strengthening the Reporting of Observational Studies in Epidemiology) statement.[32] There was no external financial support for this study.

Study Population

The study population was obtained from a historical cohort of consecutive patients with clinically suspected CCF according to their symptoms and physical examinations, and who underwent pretreatment thin-section MR imaging and DSA between January 2006 and September 2018 at Asan Medical Center (2700 beds), an academic tertiary referral hospital in Seoul, Korea. The patients' symptoms included diplopia, eyeball pain, facial pain, ptosis, proptosis, periorbital swelling, eyeball injection, and visual disturbance. Patients were excluded from the study population if 1) they were under the age of 18, 2) the interval between thin-section MR imaging and DSA was more than 90 days, 3) thin-section MR imaging or DSA were obtained after treatment, and 4) the thin-section MR imaging or DSA image quality was poor. The patient selection procedure is summarized in Fig 1. Finally, 98 patients (32 men and 66 women) were enrolled. The age range of the patients was from 20 to 85 years, with a mean age of 54.6 years (standard deviation: 14.6 years).

Imaging Protocols

All patients underwent pretreatment thin-section MR imaging and DSA for evaluation of CCF. Because of the long study period, various MR imaging and DSA systems were used; however, most MR examinations were performed with a 3-T MR unit (Intera Achieva; Philips Medical Systems) by using a 16-element phased-array head coil. Two-dimensional coronal T1-weighted, T2-weighted (with and without fat suppression), and contrast-enhanced T1-weighted turbo spin-echo images were obtained at a 3-mm thickness. Contrast-enhanced 3D T1-turbo field echo images were obtained with a 0.6-mm thickness and reconstruction section thickness was 1.2 mm with an interslice distance of 0.6-mm. The scan range of the coronal and axial images covered the orbit and cavernous sinus. Detailed parameters for the thin-section MR imaging are summarized in On-line Table. Cerebral DSA images included both internal carotid arteriograms, both external carotid arteriograms, and both vertebral arteriograms.

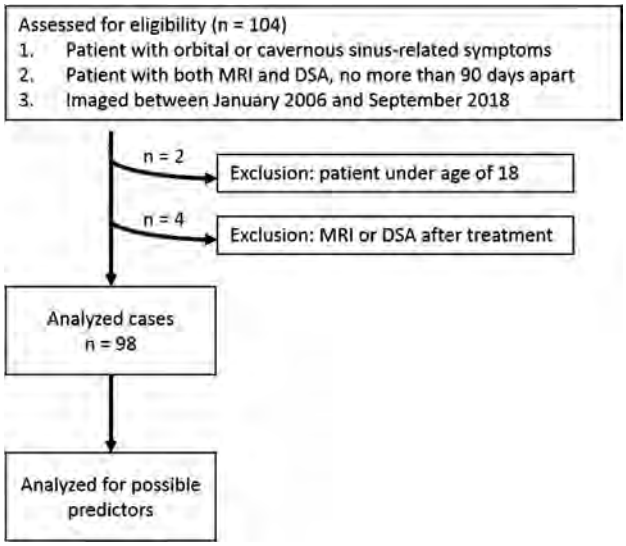

FIG 1. Flow diagram of the case selection procedure and case numbers in each subgroup.

Interpretation of Images

The thin-section MRIs of all patients were interpreted in consensus by 2 neuroradiologists (D.K. and Y.J.C., with 5 and 13 years of clinical experience in neuroradiology, respectively). Before evaluation, the 2 neuroradiologists completed a training session on imaging from 5 patients to help them reach a consensus on evaluation of the imaging findings. The 2 neuroradiologists were blinded to other radiologic imaging including the DSA, and to clinical information including symptoms, signs, and treatment given to the patients. The following possible imaging predictors for CCF on pretreatment thin-section MR imaging were analyzed: 1) abnormal contour of the cavernous sinus, 2) abnormal internal signal void of the cavernous sinus, 3) prominent venous drainage flow (anterior/lateral/posterior), and 4) orbital/periorbital soft tissue swelling.

Abnormal contour of the cavernous sinus was considered positive if the cavernous sinus was asymmetrically enlarged and the lateral wall of the cavernous sinus was outwardly convex or straight on the coronal view (Fig 2). Abnormal internal signal void of the cavernous sinus was considered positive if there was a signal void larger than 2 mm in the shortest diameter within or along the wall of the cavernous sinus on coronal imaging (Fig 3).

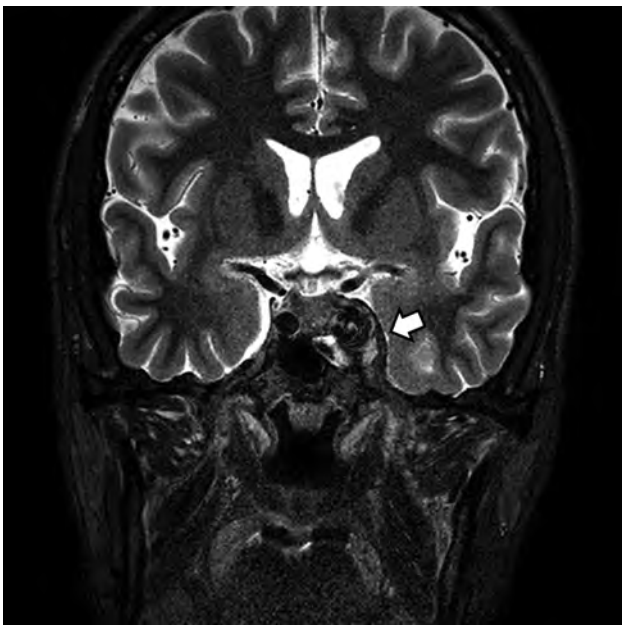

FIG 2. A CCF case with abnormal contour of the cavernous sinus. Coronal T2-weighted image of a patient with diplopia, confirmed to be left sixth cranial nerve palsy on neurologic examination. Note the abnormal contour bulging of the left cavernous sinus (*arrow*). An internal signal void was also noted on both T2-weighted (*arrow*) and T1-weighted imaging (not shown). The patient was confirmed as having a direct CCF on digital subtraction angiography.

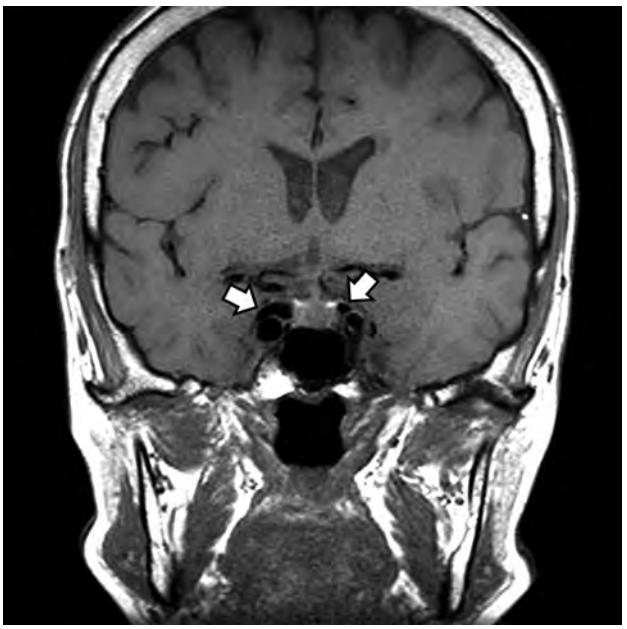

FIG 3. A CCF case with internal signal void of the cavernous sinuses. Coronal T1-weighted image of a patient with diplopia, confirmed to be right third cranial nerve palsy on neurologic examination. Note the internal signal void in both cavernous sinuses visible on T1-weighted image (*arrows*). The patient was confirmed to have an indirect CCF on digital subtraction angiography.

Signal void was evaluated on both T1- and T2-weighted MR imaging. Prominent venous drainage flow was considered positive if the superior or inferior ophthalmic vein (anterior), sphenoparietal sinus (lateral), or superior or inferior petrosal sinus (posterior) was prominently or asymmetrically enlarged with or without signal void (Figs 4 and 5). Orbital/periorbital soft tissue swelling was considered positive if there was high signal change and extraocular muscle thickening on T2-weighted MR imaging (Fig 6). The overall diagnosis (presence or absence of CCF) was also evaluated for each case, and the diagnostic performance of thin-section MR imaging was estimated.

The DSAs of all patients were reviewed by a neurointervention-dedicated neuroradiologist (Y.S, with 5 years of clinical experience in neuroradiology). The neuroradiologist was blinded to other radiologic images, including the thin-section MR imaging, and to clinical information, including symptoms and signs of the patient and treatment performed. The presence or absence of CCF on DSA was evaluated and considered as the reference standard. When present, the type of CCF (whether direct or indirect) was also evaluated. For patients with indirect CCF, a further classification according to Suh et al[33] (proliferative type, having numerous arterial feeders to the cavernous sinus; restrictive type, showing many delineable arterial feeders converging to the cavernous sinus; or late restrictive type, showing a few arterial feeders with sluggish retrograde venous flow) was determined.

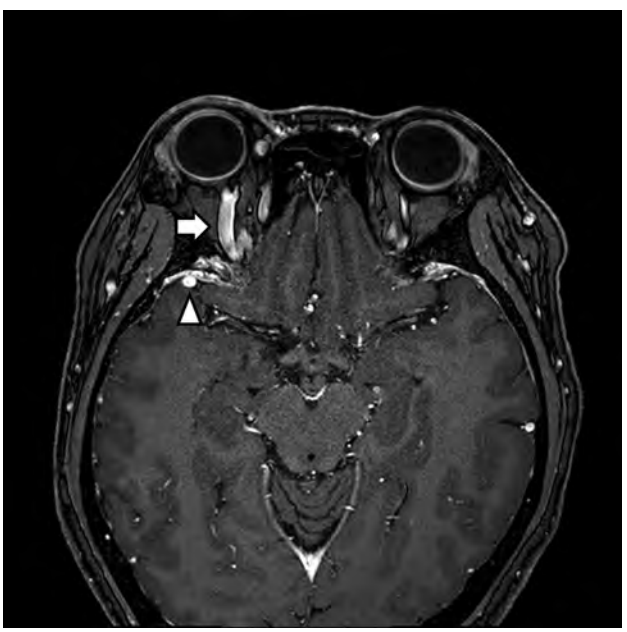

FIG 4. A CCF case with prominent venous drainage flow in the anterior and lateral venous structures. Axial contrast-enhanced T1-weighted image of a patient with right ocular pain and conjunctival injection. Note the enlarged right superior ophthalmic vein (anterior; *arrow*) and right sphenoparietal sinus (lateral; *arrowhead*). The patient was confirmed as having an indirect CCF on digital subtraction angiography.

Statistical Analysis

This study had 2 main outcomes. The primary outcome was the diagnostic performance of thin-section MR imaging for the diagnosis of CCF with the reference standard being DSA. The sensitivity, specificity, accuracy, positive and negative predictive values, and appropriate use criteria of the receiver operating characteristic curves of thin-section MR imaging for depicting the

FIG 5. A CCF case with prominent venous drainage flow in the posterior venous structure. Axial contrast-enhanced T1-weighted image of a patient with diplopia, confirmed to be right sixth cranial nerve palsy on neurologic examination. Note the enlarged right inferior petrosal sinus (posterior) with an internal signal void (*arrow*) indicating increased flow rate. The patient was confirmed as having an indirect CCF on digital subtraction angiography.

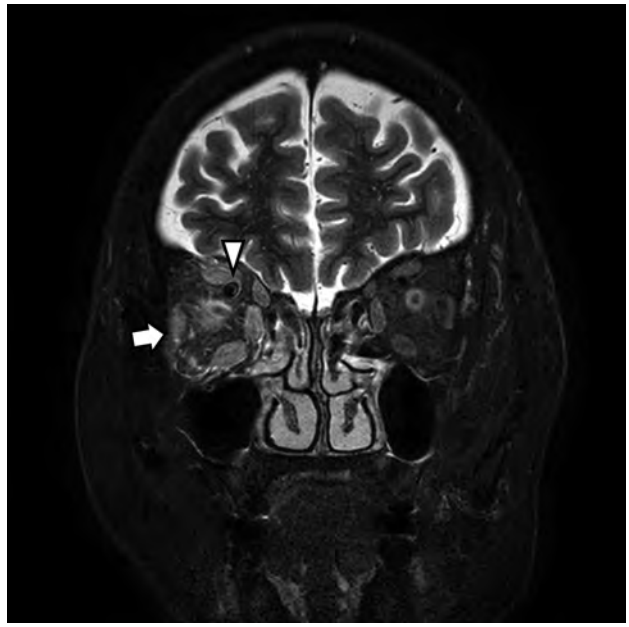

FIG 6. A CCF case with high signal change and orbital soft tissue thickening. Coronal T2-weighted image of a patient with periorbital swelling, conjunctival injection, ocular pain, and diplopia. Fat stranding and swelling of extraocular muscles (*arrow*) are noted. Prominent venous drainage flow in the superior ophthalmic vein is also noted (*arrowhead*). The patient was confirmed as having an indirect CCF on digital subtraction angiography.

presence of CCF were calculated. The secondary outcome was to determine possible imaging predictors for CCF on thin-section MR imaging. The Fisher exact test and univariable logistic regression analysis were used to determine possible predictors of CCF. The thin-section MR imaging characteristics of abnormal contour of the cavernous sinus, internal signal void of the cavernous sinus, prominent venous drainage flow (anterior/lateral/posterior), and orbital/periorbital soft tissue swelling were considered as potential adjustment variables. Statistical analyses were performed by using SPSS software (version 25.0; IBM), with statistical significance being defined as $P < .05$.

RESULTS

Among the 98 patients, 38 were confirmed as having CCF on DSA. Six patients had direct CCF, and 32 patients had indirect CCF. The baseline characteristics and clinical manifestations of the patients are summarized in Table 1. The overall diagnostic performance of thin-section MR imaging for diagnosing CCF was as follows: accuracy, sensitivity, and specificity were 88.8%, 97.4%, and 83.3%, respectively. There was 1 false-negative case (3.1%, 1/38) on thin-section MR imaging. Among the 32 indirect CCF cases, there were 10 proliferative type cases, 17 restrictive type cases, and 5 late restrictive type cases, while the single false-negative case was a late restrictive type. Among the 60 patients confirmed as CCF-negative on DSA, there were 10 false-positive cases on thin-section MR imaging (16.7%, 10/60).

In the univariable logistic regression, patients with CCF showed higher odds of an abnormal contour of the cavernous sinus (OR: 21.7), internal signal void of the cavernous sinus (OR: 15.3), prominent venous drainage flow in anterior, lateral, or posterior drainage venous structures (OR: 54.0), and orbital/periorbital soft tissue swelling (OR: 40.4) on thin-section MR imaging. The results of the univariable logistic regression are summarized in Table 2.

Radiologists do not usually rely on a single imaging feature to diagnose a disease; therefore, we analyzed various combinations of features to determine the best ones for diagnosis. Among the various feature combinations showing an accuracy above 85%, "any prominent venous drainage flow" and "internal signal void of the cavernous sinus" (combination 1) showed the highest accuracy (91.8%); "any prominent venous drainage flow" (anterior/lateral/posterior) and "orbital/periorbital soft tissue swelling" (combination 2) showed the highest specificity (96.7%) and positive likelihood ratio (23.7); and "prominent anterior venous drainage flow" or "orbital/periorbital soft tissue swelling" (combination 3) showed the highest sensitivity (92.1%) and the lowest negative likelihood ratio (0.097). The diagnostic performances of each feature and combination of features are summarized in Table 3.

DISCUSSION

In this study, we analyzed the diagnostic performance of thin-section MR imaging for CCF, and determined possible thin-section MR imaging predictors for CCF, by using a historical cohort of patients with clinically suspected CCF. The accuracy, sensitivity, and specificity of thin-section MR imaging for diagnosis of CCF were 88.8%, 97.4%, and 83.3%,

respectively. Patients with CCF showed a higher prevalence of abnormal contour of the cavernous sinus (OR: 21.7), internal signal void of the cavernous sinus (OR: 15.3), prominent venous drainage flow (OR: 54.0), and orbital/periorbital soft tissue swelling (OR: 40.4) on thin-section MR imaging.

Most of the research focusing on the MR imaging findings of CCF was conducted between the late 1980s and early 1990s.[9-13] The MR imaging findings of these studies included low or dark signal within the cavernous sinus, dilated superior ophthalmic vein, swelling of the extraocular muscles, and bulging of the lateral wall of the cavernous sinus. Uchino et al[12] analyzed 10 cases of indirect CCF and found that 9 out of 10 cases (90%) were positive for flow void within the cavernous sinus, and 8 out of 10 cases (80%) were positive for dilated superior ophthalmic vein on MR imaging. These findings correlate well with the results of our study, in which 92.1% of the CCF cases showed internal signal void within the cavernous sinus, and 78.9% showed prominent anterior venous drainage flow. However, most previous research covers case series studies in which the number of cases was less than or equal to 10. The study protocols used in previous studies mainly included non-3D T1-weighted, T2-weighted, and postcontrast T1-weighted imaging with section thickness ranging from 2 to 10 mm, acquired on scanners with magnetic fields equal to or less than 1.5T. To our knowledge, there has been no study on the diagnostic performance of MR imaging for CCF that has included a large number of cases. There was 1 false-negative case on thin-section MR imaging, which was an indirect CCF (late restrictive type). The late restrictive type CCF is characterized by a few arterial feeders and sluggish retrograde venous flow on DSA,[33] and these hemodynamic characteristics may be the cause for the incorrect diagnosis on thin-section MR imaging. There were 10 false-positive cases (16.7%) in terms of overall diagnostic performance in our study. In the false-positives, the common image findings were signal void in the cavernous sinus (10 cases), abnormal contour of cavernous sinus (9 cases), and prominent venous drainage flow in the lateral (4 cases) and posterior (4 cases) venous drainage structures. In most of our study cases, where fistulous or venous flow was not very slow, thin-section MR imaging showed satisfactory diagnostic performance in patients with clinically suspected CCF, with especially high sensitivity. Our study also focused on evaluating the possible imaging predictors for CCF on thin-section MR imaging. Abnormal contour of the cavernous sinus (OR: 21.7), internal signal void of the cavernous sinus (OR: 15.3), prominent venous drainage flow in anterior, lateral, or posterior drainage venous structures (OR: 54.0), and orbital/periorbital soft tissue swelling (OR: 40.4) on thin-section MR imaging were shown to be possible imaging predictors for CCF on thin-section MR imaging. Abnormal contour and signal void of the cavernous sinus were visible on coronal T1WI and T2WI with 3-mm thickness. Prominent venous drainage flows were best seen on the contrast-enhanced 3D T1WI with 0.6 mm thickness and axial reconstruction. Orbital/periorbital soft tissue swelling was well visualized on coronal images with 3-mm thickness, whereas it was not clearly visualized on contrast-enhanced 3D T1WI. It is evident that thin-section MR imaging is helpful in searching for these fine struc-

Table 1: Clinical characteristics of the study patients

	All Patients (n = 98)	CCF Positive Patients (n = 38)	CCF Negative Patients (n = 60)
Sex, *n*			
Male/Female	32/66	11/27	21/39
Age, years			
Mean (range)	54.6 (20–85)	66.0 (24–85)	51.4 (20–81)
Symptoms, *n* (%)			
Diplopia	54 (55.1)	20 (52.6)	34 (56.7)
Eyeball pain	27 (27.6)	14 (36.8)	13 (21.7)
Facial pain	2 (2.0)	1 (2.6)	1 (1.7)
Ptosis	30 (30.6)	8 (21.1)	22 (36.7)
Proptosis	14 (14.3)	9 (23.7)	5 (8.3)
Periorbital swelling	19 (19.4)	16 (42.1)	3 (5)
Conjunctival injection	23 (23.5)	16 (42.1)	7 (11.7)
Visual disturbance	18 (18.4)	7 (18.4)	11 (18.3)
Headache	40 (40.8)	14 (36.8)	26 (43.3)
Dizziness	13 (13.3)	5 (13.2)	8 (13.3)
Neurologic signs, *n* (%)			
Laterality			
Right	30 (30.6)	8 (21.1)	22 (36.7)
Left	22 (22.4)	6 (15.8)	16 (26.7)
3rd cranial neve palsy	26 (26.5)	4 (10.5)	22 (36.7)
4th cranial nerve palsy	5 (5.1)	2 (5.3)	3 (5)
6th cranial nerve palsy	22 (22.4)	8 (21.1)	14 (23.3)
Trauma history, *n* (%)	5 (5.1)	3 (7.9)	2 (3.3)

Table 2: Logistic regression of thin-section MR imaging predictors for CCF

Feature	Total	CCF Cases	Univariable Logistic Regression	
			OR (95% CI)	*P* Value
Abnormal contour of cavernous sinus	57.1% (56/98)	92.1% (35/38)	21.7 (6.0–78.9)	<.001
Signal void of cavernous sinus	73.5% (72/98)	92.1% (35/38)	15.3 (4.2–55.1)	<.001
Prominent venous drainage flow[a]	52.0% (51/98)	94.7% (36/38)	54.0 (11.6–251.7)	<.001
Anterior	36.7% (36/98)	78.9% (30/38)	33.8 (10.7–106.5)	<.001
Lateral	22.4% (22/98)	34.2% (13/38)	3.0 (1.1–7.8)	.030
Posterior	23.5% (23/98)	47.4% (18/38)	9.9 (3.3–30.2)	<.001
Orbital/periorbital soft tissue swelling	39.8% (39/98)	84.2% (32/38)	40.4 (12.5–130.8)	<.001

[a] Prominent venous drainage flow indicates the presence of prominent venous drainage flow in at least 1 of the anterior, lateral, and posterior prominent venous drainage flows.

Table 3: Diagnostic performance of each thin-section MR imaging feature and combination of imaging features for CCF[a]

	Accuracy	Sensitivity	Specificity	PLR	NLR
Abnormal contour of cavernous sinus	75.5% (65.8–83.6%)	92.1% (78.6–98.3)	65% (51.6–76.9)	2.6 (1.8–3.8)	0.1 (0.0–0.4)
Signal void of cavernous sinus	70.4% (60.7–78.5%)	92.1% (79.2–97.3)	56.7% (44.1–68.4)	2.1 (1.6–2.9)	0.1 (0.0–0.4)
Any prominent venous drainage flow	82.7% (74.0–88.9)	94.7% (82.7–98.5)	75% (62.8–84.2)	3.8 (2.4–5.9)	0.1 (0.0–0.3)
Prominent anterior venous drainage flow	85.7% (77.4–91.3)	79.0% (63.7–88.9)	90% (79.9–95.3)	7.9 (3.6–7.2)	0.2 (0.1–0.4)
Prominent lateral venous drainage flow	65.3% (55.0–74.6)	34.2% (19.6–51.2)	85% (73.4–92.9)	2.3 (1.1–4.8)	0.8 (0.6–1.0)
Prominent posterior venous drainage flow	74.5% (64.7–82.8)	47.4% (31.0–64.2)	91.7% (81.6–97.2)	5.7 (2.3–14.0)	0.6 (0.4–0.8)
Orbital/periorbital soft tissue swelling	86.7% (78.6–92.1)	84.2% (69.6–92.6)	88.3% (77.8–94.2)	7.2 (3.6–14.7)	0.2 (0.1–0.4)
Combination 1 (any prominent venous drainage flow AND internal signal void of cavernous sinus)	91.8% (84.7–95.8)	89.5% (75.9–95.8)	93.3% (84.1–97.4)	13.4 (5.2–34.8)	0.1 (0.0–0.3)
Combination 2 (any prominent venous drainage flow AND orbital/periorbital soft tissue swelling)	89.8% (82.2–94.4)	79.0% (63.7–88.9)	96.7% (88.6–99.1)	23.7 (6.0–93.4)	0.2 (0.1–0.4)
Combination 3 (prominent anterior venous drainage flow OR orbital/periorbital soft tissue swelling)	85.7% (77.4–91.3)	92.1% (79.2–97.3)	81.7% (70.1–89.4)	5.0 (2.9–8.6)	0.1 (0.0–0.3)

Note:—PLR indicates positive likelihood ratio; NLR, negative likelihood ratio.
[a] Data in parentheses are 95% confidence intervals.

tures and lesions, though determination of the optimal section thickness may require additional study.

There are several limitations to this study. First, the study was retrospective and patients were selected on the basis of their electronic medical records and the presence of certain radiologic examinations. This might have resulted in a selection bias. Furthermore, the MR imaging reviewers were aware that the patients had undergone DSA, and this might have induced some reader bias and might have affected diagnostic performance. Second, because this was a single-center study, the generalizability of these results may be limited, and a further prospective multicenter study may be needed. Third, there was a delay of up to 90 days between the MR imaging and DSA. However, in most cases the delay was less than 30 days (86.7%), and considering the slow-evolving natural course of CCF, this delay may be acceptable. Fourth, the comparison of thin-section MR imaging with CTA or MRA was not conducted. CTA and 3D TOF-MRA are also known as good modalities for screening CCF with high sensitivities. However, the case numbers of concurrent CTA with thin-section MR imaging and 3D TOF-MRA with thin-section MR imaging were too small to perform the comparative analysis in our study. Therefore, the results of this study do not justify the replacement of CTA or MRA to thin-section MR imaging in case of clinically suspected CCF. However, the results may be helpful in differentiating the cause of orbital or cranial nerve symptoms in patients who have undergone the thin-section MR imaging without CTA or MRA.

CONCLUSIONS

Thin-section MR imaging showed high performance for diagnosing CCF in patients with clinically suspected CCF. The possible imaging predictors for CCF on thin-section MR imaging included abnormal contour of the internal signal void in the cavernous sinus; prominent venous flow in the ophthalmic vein, sphenoparietal sinus, or petrosal sinus; and orbital/periorbital soft tissue swelling.

Disclosures: Jung Hwan Baek—*UNRELATED:* Consultancy: Radiofrequency ablation, *Comments:* STARmed and RF medical company from 2017.

REFERENCES

1. Barrow DL, Spector RH, Braun IF, et al. **Classification and treatment of spontaneous carotid-cavernous sinus fistulas.** *J Neurosurg* 1985;62:248–56 CrossRef Medline
2. Henderson AD, Miller NR. **Carotid-cavernous fistula: current concepts in aetiology, investigation, and management.** *Eye (Lond)* 2018;32:164–72 CrossRef Medline
3. Grumann AJ, Boivin-Faure L, Chapot R, et al. **Ophthalmologic outcome of direct and indirect carotid cavernous fistulas.** *Int Ophthalmol* 2012;32:153–59 CrossRef Medline
4. Keizer R. **Carotid-cavernous and orbital arteriovenous fistulas: ocular features, diagnostic and hemodynamic considerations in relation to visual impairment and morbidity.** *Orbit* 2003;22:121–42 CrossRef
5. Lasjaunias P, Chiu M, ter Brugge K, et al. **Neurological manifestations of intracranial dural arteriovenous malformations.** *J Neurosurg* 1986;64:724–30 CrossRef Medline
6. Modic MT, Berlin AJ, Weinstein MA. **The use of digital subtraction angiography in the evaluation of carotid cavernous sinus fistulas.** *Ophthalmology* 1982;89:441–44 CrossRef Medline
7. Debrun GM. **Angiographic workup of a carotid cavernous sinus fistula (CCF) or what information does the interventionalist need for treatment?** *Surg Neurol* 1995;44:75–79 CrossRef Medline
8. Dos Santos D, Monsignore LM, Nakiri GS, et al. **Imaging diagnosis of dural and direct cavernous carotid fistulae.** *Radiology Bras* 2014; 47:251–55 CrossRef Medline
9. Hirabuki N, Miura T, Mitomo M, et al. **MR imaging of dural arteriovenous malformations with ocular signs.** *Neuroradiology* 1988;30: 390–94 CrossRef Medline
10. Komiyama M, Fu Y, Yagura H, et al. **MR imaging of dural AV fistulas at the cavernous sinus.** *J Comput Assist Tomogr* 1990;14:397–401 CrossRef Medline
11. Elster AD, Chen MY, Richardson DN, et al. **Dilated intercavernous sinuses: an MR sign of carotid-cavernous and carotid-dural fistulas.** *AJNR Am J Neuroradiol* 1991;12:641–45
12. Uchino A, Hasuo K, Matsumoto S, et al. **MRI of dural carotid-cavernous fistulas. Comparisons with postcontrast CT.** *Clin Imaging* 1992;16:263–68 CrossRef Medline
13. Hirabuki N, Fujita N, Hashimoto T, et al. **Follow-up MRI in dural arteriovenous malformations involving the cavernous sinus:**

emphasis on detection of venous thrombosis. *Neuroradiology* 1992; 34:423–27 CrossRef Medline
14. Hirai T, Korogi Y, Hamatake S, et al. **Three-dimensional FISP imaging in the evaluation of carotid cavernous fistula: comparison with contrast-enhanced CT and spin-echo MR.** *AJNR Am J Neuroradiol* 1998;19:253–59
15. Kwon BJ, Han MH, Kang H-S, et al. **MR imaging findings of intracranial dural arteriovenous fistulas: relations with venous drainage patterns.** *AJNR Am J Neuroradiol* 2005;26:2500–07 Medline
16. Merrick R, Latchaw RE, Gold L. **Computerized tomography of the orbit in carotid-cavernous sinus fistulae.** *Comput Tomogr* 1980; 4:127–32 CrossRef Medline
17. Zilkha A, Daiz AS. **Computed tomography in carotid cavernous fistula.** *Surg Neurol* 1980;14:325–29 Medline
18. Ahmadi J, Teal JS, Segall HD, et al. **Computed tomography of carotid-cavernous fistula.** *AJNR Am J Neuroradiol* 1983;4:131–36 Medline
19. Ikawa F, Uozumi T, Kiya K, et al. **Diagnosis of carotid-cavernous fistulas with magnetic resonance angiography—demonstrating the draining veins utilizing 3-D time-of-flight and 3-D phase-contrast techniques.** *Neurosurg Rev* 1996;19:7–12 CrossRef Medline
20. Coskun O, Hamon M, Catroux G, et al. **Carotid-cavernous fistulas: diagnosis with spiral CT angiography.** *AJNR Am J Neuroradiol* 2000;21:712–16 Medline
21. Rucker JC, Biousse V, Newman NJ. **Magnetic resonance angiography source images in carotid cavernous fistulas.** *Br J Ophthalmol* 2004;88:311 CrossRef Medline
22. Chen CCC, Chang PT, Shy CG, et al. **CT angiography and MR angiography in the evaluation of carotid cavernous sinus fistula prior to embolization: a comparison of techniques.** *AJNR Am J Neuroradiol* 2005;26:2349–56
23. Akiba H, Tamakawa M, Hyodoh H, et al. **Assessment of dural arteriovenous fistulas of the cavernous sinuses on 3D dynamic MR angiography.** *AJNR Am J Neuroradiol* 2008;29:1652–57 CrossRef Medline
24. Lee JY, Jung C, Ihn YK, et al. **Multidetector CT angiography in the diagnosis and classification of carotid–cavernous fistula.** *Clinical Radiology* 2016;71:e64–71 CrossRef
25. Ouanounou S, Tomsick TA, Heitsman C, et al. **Cavernous sinus and inferior petrosal sinus flow signal on three-dimensional time-of-flight MR angiography.** *AJNR Am J Neuroradiol* 1999;20:1476–81 Medline
26. van Amerongen MJ, Pegge SAH, El Kandoussi M, et al. **The non-invasive search for the carotid-cavernous fistula: the added value of the 4D-CTA.** *Neuroradiology* 2017;59:835–37 CrossRef Medline
27. Yamamoto N, Yamamoto Y, Izumi Y, et al. **Dural arterivenous fistula at the cavernous sinus diagnosed by arterial spin-labeled imaging.** *Intern Med* 2018;57:1163–66 CrossRef Medline
28. Ettl A, Kramer J, Daxer A, et al. **High resolution magnetic resonance imaging of neurovascular orbital anatomy.** *Ophthalmology* 1997; 104:869–77 CrossRef Medline
29. Tanitame K, Sone T, Kiuchi Y, et al. **Clinical applications of high-resolution ocular magnetic resonance imaging.** *Jpn J Radiology* 2012; 30:695–705 CrossRef Medline
30. Lee JH, Cheng KL, Choi YJ, et al. **High-resolution imaging of neural anatomy and pathology of the neck.** *Korean J Radiology* 2017; 18:180–93 CrossRef Medline
31. Ettl A, Zwrtek K, Daxer A, et al. **Anatomy of the orbital apex and cavernous sinus on high-resolution magnetic resonance images.** *Surv Ophthalmol* 2000;44:303–23 CrossRef Medline
32. von EE, Altman DG, Egger M, et al. **Strengthening the reporting of observational studies in epidemiology (STROBE) statement: guidelines for reporting observational studies.** *BMJ* 2007;335:806–08 CrossRef Medline
33. Suh DC, Lee JH, Kim SJ, et al. **New concept in cavernous sinus dural arteriovenous fistula: correlation with presenting symptom and venous drainage patterns.** *Stroke* 2005;36:1134–39 CrossRef

Lack of Baseline Intracranial Aneurysm Wall Enhancement Predicts Future Stability: A Systematic Review and Meta-Analysis of Longitudinal Studies

A.S. Larson, V.T. Lehman, G. Lanzino, and W. Brinjikji

ABSTRACT

BACKGROUND: The utility of vessel wall MR imaging in identifying unstable intracranial aneurysms has been suggested but remains controversial.

PURPOSE: Our aim was to provide further insight into the potential relationship between aneurysm wall enhancement on initial vessel wall imaging and aneurysm instability at follow-up.

DATA SOURCES: Our sources were PubMed, Scopus, the Web of Science, and the Cochrane Central Register of Controlled Trials.

STUDY SELECTION: We searched for English language studies that reported the presence of vessel wall enhancement of unruptured intracranial aneurysms on baseline vessel wall imaging studies with longitudinal follow-up of aneurysm status.

DATA ANALYSIS: Aneurysms were grouped into "stable" and "unstable" groups at follow-up on the basis of growth, symptomatic manifestation, or rupture. The association of each group with aneurysm wall enhancement on initial vessel wall imaging was determined.

DATA SYNTHESIS: Three studies constituting 407 aneurysms were included. Aneurysms with wall enhancement were at higher risk of being unstable at follow-up (risk ratio = 3.6; 95% confidence interval, 1.7–7.5). The sensitivity of aneurysm wall enhancement on vessel wall imaging was 74.3% (95% CI, 56.7%–87.5%), specificity was 58.3% (95% CI, 53.1%–63.4%), positive predictive value was 14.4% (95% CI, 11.8%–17.4%), negative predictive value was 96.0% (95% CI, 93.2%–97.7%), and the overall accuracy of the test was 59.7% (95% CI, 54.8%–64.5%).

LIMITATIONS: Only 3 studies were identified for inclusion in this analysis. More longitudinal studies of vessel wall imaging and aneurysm progression are needed.

CONCLUSIONS: The lack of wall enhancement may be a predictor of aneurysm stability. The utility of vessel wall imaging in detecting unstable aneurysms requires more data.

ABBREVIATIONS: AWE = aneurysm wall enhancement; IA = intracranial aneurysm; VWI = vessel wall imaging

Intracranial saccular aneurysms (IAs) are common vascular lesions with an estimated prevalence of up to 3%.[1] In patients with unruptured IAs, it is challenging to know which IAs should be managed conservatively and which are at higher risk of rupture, thereby warranting intervention. Several patient-based factors and imaging features including size, aspect ratio, and irregular morphology have been shown to be risk factors for IA rupture.[2-6] Nevertheless, risk stratification of patients with unruptured IA remains inadequate; thus, the need for additional tools remains high in order to maximize our ability to appropriately select patients for intervention.

Inflammation within the vessel wall of the aneurysm is associated with IA instability and rupture.[7,8] With advances in imaging, aneurysm wall enhancement (AWE) on vessel wall imaging (VWI) is purported to be a marker of aneurysmal wall inflammation and, therefore, a potential marker for aneurysm growth and rupture.[9-11] Initial studies suggest that AWE is a marker of instability. However, authors have questioned the strength of the current evidence on several grounds. For example, there is some

Received April 6, 2020; accepted after revision June 5.

From the Departments of Radiology (A.S.L., V.T.L., G.L., W.B.) and Neurosurgery (A.S.L., G.L., W.B.), Mayo Clinic, Rochester, Minnesota.

Please address correspondence to Waleed Brinjikji, BS, Mayo Clinic, 200 1st St SW, Rochester MN, 55905; e-mail: Brinjikji.Waleed@mayo.edu; @TonyLarsonBS; @WBrinjikji

Indicates article with supplemental on-line appendix and tables.

http://dx.doi.org/10.3174/ajnr.A6690

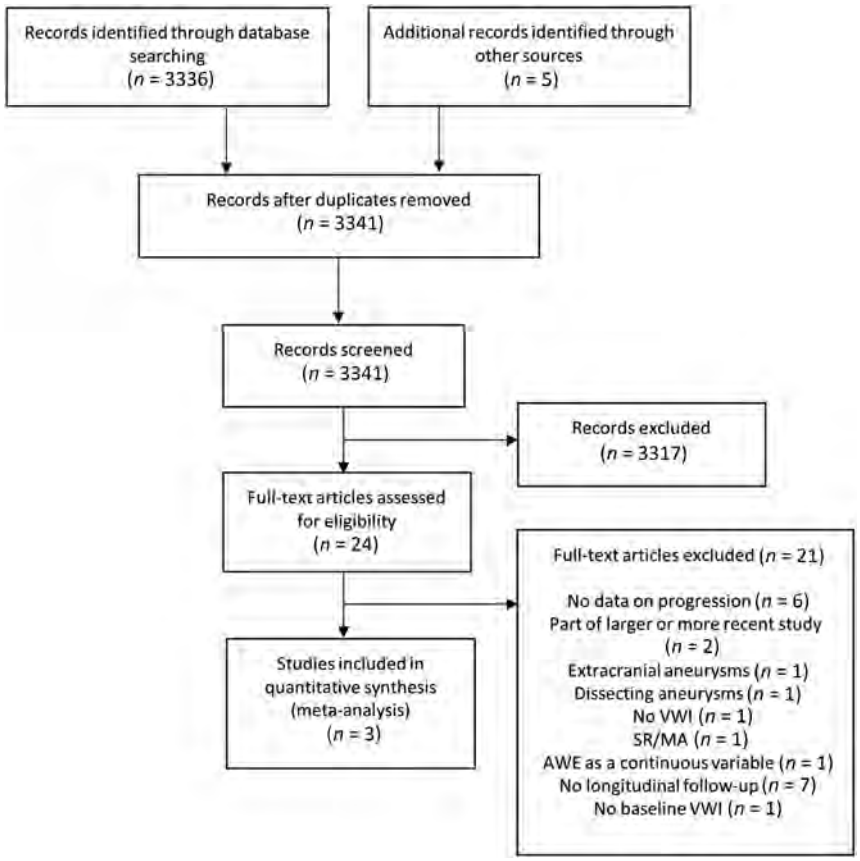

FIGURE. Literature review search strategy. SR/MA indicates systematic review/meta-analysis.

evidence that AWE can be caused by factors other than inflammation, such as slow blood flow near the aneurysm wall.[12] Additionally, the literature demonstrates grouping of types of unstable aneurysms in analyses, lack of robust histopathologic correlation, variability of methods, a possible association with increasing size, and, most important, limited long-term follow-up.[13,14] Until such prospective standardized long-term follow-up can be completed on a large number of patients, continued, periodic analysis of all available publications is important to characterize our best understanding of the current literature.

A prior meta-analysis demonstrated a robust relationship between AWE and aneurysm instability,[11] but only a single included study had data on longitudinal follow-up.[15] Since then, additional studies reporting longitudinal follow-up after initial VWI have been published; therefore, a separate analysis of these studies may shed more light on the clinical utility of VWI in detecting aneurysms at risk for progression.[16-19] Inclusion of ruptured aneurysms in unstable aneurysm subgroups likely plays a confounding role; therefore, ruptured aneurysms should be analyzed independently or not included in such analyses. With these ideas in mind, we performed a systematic review and meta-analysis of longitudinal studies to provide further insight into the controversial relationship between AWE on VWI and aneurysm instability.

MATERIALS AND METHODS

Search Strategy and Selection Criteria

Both the systematic review and meta-analysis were performed according to the Preferred Reporting Items for Systematic Reviews and Meta-Analyses guidelines.[20] A comprehensive search of several data bases from inception to March 10, 2020, limited to the English language and excluding animal studies, was conducted. The data bases included Ovid MEDLINE and Epub Ahead of Print, In-Process & Other Non-Indexed Citations, Ovid MEDLINE Daily, Ovid EMBASE, Ovid Cochrane Central Register of Controlled Trials, Ovid Cochrane Data Base of Systematic Reviews, and Scopus. The search strategy was designed and conducted by an experienced librarian with input from the principal investigator of the study. Controlled vocabulary supplemented with keywords was used to search for studies describing vessel wall imaging and intracranial aneurysms. The actual strategy listing all search terms used and how they are combined is available in the On-line Appendix.

Abstracts were reviewed for relevance, which included mention of intracranial aneurysms and vessel wall imaging. Abstracts without mention of both of these variables were excluded, and the full text was not reviewed. A study was considered eligible for this meta-analysis if it fulfilled the predefined inclusion criteria: Prospective and retrospective observational cohort analysis that compared the rates of AWE on initial VWI with longitudinal follow-up of aneurysm status. Our search strategy can be found in Fig 1.

Data Extraction and Aneurysm Classification

One reviewer (A.S.L.) independently extracted the relevant data from the eligible studies. Data extraction was performed for the following predefined variables: first author, year of publication, total number of patients, number of aneurysms demonstrating complete or partial AWE on initial vessel wall MR imaging, follow-up period, mean aneurysm size, and the number of stable and unstable intracranial saccular aneurysms as defined below. Also, data regarding the imaging sequences and field strength, interobserver agreement, and definition of wall enhancement were extracted. The primary end point of this meta-analysis was to compare complete or partial AWE as seen on initial vessel wall MR imaging studies between aneurysms that were stable or unstable at follow-up. In this regard, AWE was determined on a yes or no basis regardless of the degree or spatial pattern of enhancement. The definition of unstable saccular aneurysms included symptomatic, growing aneurysms on serial imaging or

those that ruptured at follow-up. Symptomatic aneurysms included intracranial aneurysms causing cranial nerve palsy or thunderclap headache without subarachnoid hemorrhage and after exclusion of other differential diagnoses.[16] The risk of bias assessment was performed with the Robins-I tool for nonrandomized studies (https://www.riskofbias.info/welcome/home).[21]

Statistical Synthesis and Analysis

Risk ratios with the corresponding 95% confidence intervals were used to report the outcomes. A P value $< .05$ was considered significant. We also calculated sensitivity, specificity, positive predictive value, negative predictive value, and accuracy of AWE in identifying unstable aneurysms at follow-up. STATA, Version 14.1 (StataCorp) was used as statistical software.

RESULTS

Search Results

The abstracts and titles from a total of 3341 records were reviewed for relevance. From this number, 3317 were excluded. Twenty-four full-text articles were reviewed, 21 of which were excluded for various reasons: Six were excluded because whether or not the aneurysm analyzed with VWI was growing or symptomatic was not mentioned in the text, 2 were excluded because they belonged to a larger or more recent study from the same group, 1 study was of extracranial aneurysms, 1 study was of dissecting aneurysms, 1 did not contain VWI studies of aneurysms, and 1 was a systematic review/meta-analysis. One study reported AWE as a continuous variable, which precluded our ability to consider AWE as a binary variable (with or without enhancement), and this study was therefore excluded.[22] Seven studies did not have longitudinal follow-up, and 1 did not have baseline VWI. Three studies satisfied the predetermined search criteria and were included in this meta-analysis as shown in the Preferred Reporting Items for Systematic Review and Meta-Analysis flow diagram (Figure).[16,18,19]

Characteristics of Studies and Aneurysms

All included studies in this meta-analysis were observational cohort analyses with longitudinal follow-up. In total, 407 saccular aneurysms with baseline VWI performed with follow-up analysis of aneurysm status (growth, symptom manifestation, or rupture) were included in this study. Detailed study characteristics are presented in On-line Table 1. Imaging characteristics are presented in On-line Table 2. All studies were determined to have a moderate risk of bias primarily attributable to their retrospective design and inherent risk of bias (On-line Table 3).

Vessel Wall Enhancement of Unstable-versus-Stable Intracranial Saccular Aneurysms

Aneurysms with AWE on initial VWI had a statistically significant higher risk of being unstable at follow-up (risk ratio = 3.6; 95% CI, 1.7–7.5) (Table 1). The sensitivity of AWE on VWI was 74.3% (95% CI, 56.7%–87.5%), specificity was 58.3% (95% CI, 53.1%–63.4%), positive predictive value was 14.4% (95% CI, 11.8%–17.4%), negative predictive value was 96.0% (95% CI, 93.2%–97.7%), and the overall accuracy of the test was 59.7% (95% CI, 54.8%–64.5%) (Table 2).

Table 1: Association of stable and unstable aneurysms with wall enhancement on initial VWI studies

	Unstable	Stable	Risk Ratio (95% CI)
Wall enhancement	26	155	3.6 (1.7–7.5)
No wall enhancement	9	217	

Table 2: Diagnostic statistics of aneurysm wall enhancement seen on VWI studies

Statistic	Value (95% CI)
Sensitivity	74.29% (56.7%–87.5%)
Specificity	58.3% (53.1%–63.4%)
Positive predictive value	14.4% (11.8%–17.4%)
Negative predictive value	96.0% (93.2%–97.7%)
Accuracy	59.7% (54.8%–64.5%)

DISCUSSION

Our meta-analysis of 407 saccular aneurysms that underwent baseline VWI with longitudinal follow-up demonstrated 2 primary findings: First, the high negative predictive value (96.0%) found here indicates that AWE on VWI may be a useful method of broadly screening aneurysms for stability in that those without AWE are exceptionally unlikely to progress. Second, the low positive predictive value of 14.4% suggests that a considerable number of IAs that demonstrate AWE may actually be stable.

We found a high negative predictive value of AWE for aneurysm instability. Other cross-sectional and longitudinal studies and a prior meta-analysis including predominantly cross-sectional data have found similar results. Edjlali et al[16] reported on 263 patients with a total of 333 aneurysms and found the negative predictive value of AWE to be 94.9%. Similar results were reported by Nagahata et al,[23] who found that strong or faint AWE was seen in only 4.8% and 13.3% of unruptured aneurysms, respectively. An aneurysm seen on high-resolution VWI without AWE would suggest that conservative management may be a more appropriate strategy.

In contrast, our study found a low positive predictive value of AWE and aneurysm instability (14.4%), indicating that less than one-sixth of aneurysms that demonstrate wall enhancement may actually be unstable. These findings suggest that for unruptured, incidental aneurysms, the presence of wall enhancement is not necessarily a marker of impending aneurysm instability. Ultimately, more studies with longitudinal follow-up are needed to determine the relevance of AWE and its relationship to aneurysm instability.

Several prior reports have indicated a role for VWI in screening aneurysms.[11,24] These findings must be carefully interpreted. "Instability" most commonly refers to aneurysms that have ruptured, are growing, or are symptomatic.[9,13] Ruptured aneurysms likely represent a distinct underlying mechanism of enhancement; moreover, their ruptured status likely already indicates that intervention is necessary. Similarly, aneurysms with symptomatic manifestations are detected by their symptomatic nature and typically warrant treatment as well. Because ruptured or symptomatic aneurysms already indicate that an aneurysm requires close follow-up and/or treatment, inclusion of such aneurysms into a

general group of unstable aneurysms may play a confounding role in determining the utility of VWI for detecting aneurysms at risk for growth/rupture. Grouped analyses of unstable aneurysms may, therefore, be less than ideal in determining the utility of VWI for detecting aneurysms at risk for progression/rupture. It is, thus, important that future analyses consist of explicit definitions of what is considered an unstable aneurysm to determine the utility of VWI in detecting at-risk aneurysms. Ideally, future longitudinal prospective studies with longer follow-up (≥3 years) should be pursued to interrogate growing-versus-nongrowing aneurysms in the context of AWE to further elucidate this potential relationship.

Although our results demonstrate that AWE on initial imaging studies is not necessarily a marker of impending instability, VWI may be important to establish a baseline level of AWE. In a recent study by Gariel et al,[25] increased AWE on follow-up imaging relative to baseline was predictive of aneurysm growth during a 2-year period. Furthermore, the specificity and positive predictive value for aneurysm growth of AWE was 100% and 96%, respectively. These results imply that increased AWE on follow-up imaging studies is a strong marker of instability and that such aneurysms likely warrant intervention. In this regard, although AWE on initial imaging studies may not be strongly predictive of future instability, obtaining VWI on initial MR imaging studies likely serves an important role in establishing a baseline degree of AWE for future comparisons. Of note, the study by Gariel et al was not included in our analysis because the included patients were a subgroup of a larger cohort studied in a separate report.[16]

The pathophysiologic process of aneurysm formation and progression is largely based on inflammation. Altered flow dynamics within the intracerebral vasculature results in inflammatory cell infiltration into the media and adventitia, which releases damaging proteinases and other biochemical signals that result in vessel wall weakening.[26] This, in turn, promotes aneurysmal formation, growth, and rupture. Aneurysm wall enhancement is thought secondary to vessel wall inflammation and vasa vasorum proliferation, though theoretically it may also be due to endothelial disruption of the aneurysm wall resulting in contrast permeation into the vessel.[10] Several studies have performed radiologic-pathologic correlation analyses, which support an inflammatory hypothesis.[27-29] However, the VWI protocols vary across studies, and most use low-resolution imaging. Furthermore, most studies also do not use additional flow-suppression sequences: It is well-understood that intra-aneurysmal slow flow adjacent to the aneurysm wall is associated with AWE, particularly in larger aneurysms in which higher degrees of flow disturbance are more likely to be encountered.[12] It is therefore possible that enhancement may actually represent slow flow adjacent to the aneurysm wall and not true enhancement of the wall itself. This possibility emphasizes the importance of using imaging protocols with flow suppression in future studies. The association between AWE and wall inflammation remains incompletely characterized.

Limitations

This meta-analysis included only 3 studies. However, with limited longitudinal data, performing periodic analyses such as this is important in order interrogate the utility of high-resolution VWI for aneurysm characterization. Of the included studies, there was heterogeneity in the type and spatial resolution of imaging sequences used as well as follow-up intervals. The use of a prepulse flow-suppression modification was not specified in the Methods of the included studies. There was also heterogeneity in the definition of AWE: Some studies included only aneurysms with circumferential wall enhancement, while other studies included aneurysms with any degree of AWE. Given the lack of patient-specific data, we could not adjust the analysis for potential confounders. Only 1 study reported the size of aneurysms with enhancement versus those without.[19]

CONCLUSIONS

With a high negative predictive value, lack of AWE strongly indicates longitudinal aneurysm stability with the previously mentioned limitations in mind. Further prospective, longitudinal studies with strict definitions of unstable aneurysms using prepulse flow-suppression protocols are required to draw more robust conclusions.

ACKNOWLEDGMENTS

The authors would like to thank Patricia Erwin, the Mayo Clinic librarian, for performing the literature search.

Disclosures: Giuseppe Lanzino–*UNRELATED: Board Membership:* Superior Medical Editing, Nested Knowledge.

REFERENCES

1. Vlak MH, Algra A, Brandenburg R, et al. **Prevalence of unruptured intracranial aneurysms, with emphasis on sex, age, comorbidity, country, and time period: a systematic review and meta-analysis.** *Lancet Neurol* 2011;10:626–36 CrossRef Medline
2. Backes D, Vergouwen MD, Velthuis BK, et al. **Difference in aneurysm characteristics between ruptured and unruptured aneurysms in patients with multiple intracranial aneurysms.** *Stroke* 2014;45:1299–1303 CrossRef Medline
3. Ujiie H, Tamano Y, Sasaki K, et al. **Is the aspect ratio a reliable index for predicting the rupture of a saccular aneurysm?** *Neurosurgery* 2001;48:495–502; discussion 502–03 CrossRef Medline
4. Greving JP, Wermer MJ, Brown RD, Jr, et al. **Development of the PHASES score for prediction of risk of rupture of intracranial aneurysms: a pooled analysis of six prospective cohort studies.** *Lancet Neurol* 2014;13:59–66 CrossRef Medline
5. Broderick JP, Viscoli CM, Brott T, et al; Hemorrhagic Stroke Project Investigators. **Major risk factors for aneurysmal subarachnoid hemorrhage in the young are modifiable.** *Stroke* 2003;34:1375–81 CrossRef Medline
6. Longstreth WT Jr, Nelson LM, Koepsell TD, et al. **Cigarette smoking, alcohol use, and subarachnoid hemorrhage.** *Stroke* 1992;23:1242–49 CrossRef Medline
7. FröSen J, Piippo A, Paetau A, et al. **Remodeling of saccular cerebral artery aneurysm wall is associated with rupture: histological analysis of 24 unruptured and 42 ruptured cases.** *Stroke* 2004;35:2287–93 CrossRef Medline
8. Kanematsu Y, Kanematsu M, Kurihara C, et al. **Critical roles of macrophages in the formation of intracranial aneurysm.** *Stroke* 2011;42:173–78 CrossRef
9. Hu P, Yang Q, Wang DD, et al. **Wall enhancement on high-resolution magnetic resonance imaging may predict an unsteady state of**

an intracranial saccular aneurysm. *Neuroradiology* 2016;58:979–85 CrossRef Medline
10. Omodaka S, Endo H, Niizuma K, et al. **Circumferential wall enhancement on magnetic resonance imaging is useful to identify rupture site in patients with multiple cerebral aneurysms.** *Neurosurgery* 2018;82:638–44 CrossRef Medline
11. Texakalidis P, Hilditch CA, Lehman V, et al. **Vessel wall imaging of intracranial aneurysms: systematic review and meta-analysis.** *World Neurosurg* 2018;117:453–58 CrossRef Medline
12. Cornelissen BM, Leemans EL, Coolen BF, et al. **Insufficient slow-flow suppression mimicking aneurysm wall enhancement in magnetic resonance vessel wall imaging: a phantom study.** *Neurosurg Focus* 2019;47:E19 CrossRef Medline
13. Lehman VT, Brinjikji W. **Vessel wall imaging of unruptured intracranial aneurysms: ready for prime time? Not so fast!** *AJNR Am J Neuroradiol* 2019;40:E26–29 CrossRef Medline
14. van den Berg R. **Intracranial aneurysm wall enhancement: fact or fiction?** *Neuroradiology* 2020;62:269–70 CrossRef Medline
15. Edjlali M, Gentric JC, Regent-Rodriguez C, et al. **Does aneurysmal wall enhancement on vessel wall MRI help to distinguish stable from unstable intracranial aneurysms?** *Stroke* 2014;45:3704–06 CrossRef Medline
16. Edjlali M, Guedon A, Ben Hassen W, et al. **Circumferential thick enhancement at vessel wall MRI has high specificity for intracranial aneurysm instability.** *Radiology* 2018;289:181–87 CrossRef Medline
17. Matsushige T, Shimonaga K, Ishii D, et al. **Vessel wall imaging of evolving unruptured intracranial aneurysms.** *Stroke* 2019;50:1891–94 CrossRef Medline
18. Tian B, Toossi S, Eisenmenger L, et al. **Visualizing wall enhancement over time in unruptured intracranial aneurysms using 3D vessel wall imaging.** *J Magn Reson Imaging* 2019;50:193–200 CrossRef Medline
19. Vergouwen MD, Backes D, van der Schaaf IC, et al. **Gadolinium enhancement of the aneurysm wall in unruptured intracranial aneurysms is associated with an increased risk of aneurysm instability: a follow-up study.** *AJNR Am J Neuroradiol* 2019;40:1112–16 CrossRef Medline
20. Moher D, Liberati A, Tetzlaff J, et al; PRISMA Group. **Preferred reporting items for systematic reviews and meta-analyses: the PRISMA statement.** *PLoS Med* 2009;6:e1000097 CrossRef Medline
21. Sterne JA, Hernan MA, Reeves BC, et al. **ROBINS-I: a tool for assessing risk of bias in non-randomised studies of interventions.** *BMJ* 2016;355:i4919 CrossRef Medline
22. Omodaka S, Endo H, Niizuma K, et al. **Circumferential wall enhancement in evolving intracranial aneurysms on magnetic resonance vessel wall imaging.** *J Neurosurg* 2018 Oct 1. [Epub ahead of print] CrossRef Medline
23. Nagahata S, Nagahata M, Obara M, et al. **Wall enhancement of the intracranial aneurysms revealed by magnetic resonance vessel wall imaging using three-dimensional turbo spin-echo sequence with motion-sensitized driven-equilibrium: a sign of ruptured aneurysm?** *Clin Neuroradiol* 2016;26:277–83 CrossRef Medline
24. Wang GX, Wen L, Lei S, et al. **Wall enhancement ratio and partial wall enhancement on MRI associated with the rupture of intracranial aneurysms.** *J Neurointerv Surg* 2018;10:566–70 CrossRef Medline
25. Gariel F, Ben Hassen W, Boulouis G, et al. **Increased wall enhancement during follow-up as a predictor of subsequent aneurysmal growth.** *Stroke* 2020;51:1868–72 CrossRef Medline
26. Zhang X, Ares WJ, Taussky P, et al. **Role of matrix metalloproteinases in the pathogenesis of intracranial aneurysms.** *Neurosurg Focus* 2019;47:E4 CrossRef Medline
27. Hudson JS, Zanaty M, Nakagawa D, et al. **Magnetic resonance vessel wall imaging in human intracranial aneurysms.** *Stroke* 2018 Dec 7. [Epub ahead of print] CrossRef Medline
28. Quan K, Song J, Yang Z, et al. **Validation of wall enhancement as a new imaging biomarker of unruptured cerebral aneurysm.** *Stroke* 2019;50:1570–73 CrossRef Medline
29. Shimonaga K, Matsushige T, Ishii D, et al. **Clinicopathological insights from vessel wall imaging of unruptured intracranial aneurysms.** *Stroke* 2018;49:2516–19 CrossRef Medline

Assessment of Ischemic Volumes by Using Relative Filling Time Delay on CTP Source Image in Patients with Acute Stroke with Anterior Circulation Large Vessel Occlusions

W. Cao, Y. Ling, L. Yang, F. Wu, X. Cheng, and Q. Dong

ABSTRACT

BACKGROUND AND PURPOSE: Thrombectomy up to 24 hours after stroke onset in patients with specific ischemic brain volumes remains a challenge, because many stroke centers do not apply specialized software to calculate ischemic volumes at advanced imaging. We aimed to establish the association between relative filling time delay on CTP source imaging and ischemic volume parameters and the infarct penumbra to core volume mismatch in patients with acute ischemic stroke.

MATERIALS AND METHODS: Consecutive patients with acute ischemic stroke and with M1 segment MCA with or without terminal ICA occlusions on baseline CTA and CTP within 24 hours of stroke symptom onset were included. Ischemic volumes were analyzed with software based on CTP maps. Relative filling time delay was classified into 4 grades—grade 0: relative filling time delay = 0 seconds; grade 1: relative filling time delay >0 to ≤4 seconds; grade 2: relative filling time delay >4 to ≤8 seconds; and grade 3: relative filling time delay > 8 seconds. Differences in ischemic volume parameters among relative filling time delay grades were tested.

RESULTS: We recruited 138 patients (median age, 69 years; 62.3% male). Different median volumes of the infarct core (grade 0, 7.3 mL; grade 1, 23.3 mL; grade 2, 45.7 mL; grade 3, 135 mL [$P < .001$]) and the penumbra (grade 0, 47.6 mL; grade 1, 90 mL; grade 2, 110 mL; grade 3, 92 mL [$P = .043$]) were observed among relative filling time delay grades. Target mismatch (defined by the criteria of the DEFUSE 3 trial) was identified in 71.7% of the patients (99/138). A relative filling time delay grade ≤ 1 independently predicted target mismatch, with a sensitivity of 0.79 (95% CI, 0.7–0.87) and a specificity of 0.66 (95% CI, 0.49–0.8).

CONCLUSIONS: Relative filling time delay grade based on CTP source imaging is a simple and effective parameter for evaluating ischemic volumes and target mismatch in patients with acute ischemic stroke. Further studies that compare relative filling time delay grade with clinical functional outcomes are necessary.

ABBREVIATIONS: DAWN = DWI or CTP Assessment with Clinical Mismatch in the Triage of Wake-Up and Late Presenting Strokes Undergoing Neurointervention with Trevo; DEFUSE 3 = Endovascular Therapy Following Imaging Evaluation for Ischemic Stroke 3; ICV = infarct core volume; rFTD = relative filling time delay; TMM = target mismatch

The importance of estimating the ischemic core volume through advanced imaging for endovascular treatment selection in an extended time window was immediately recognized with the success of the DAWN (DWI or CTP Assessment with Clinical Mismatch in the Triage of Wake-Up and Late Presenting Strokes Undergoing Neurointervention with Trevo) trial[1] and the DEFUSE 3 (Endovascular Therapy Following Imaging Evaluation for Ischemic Stroke 3) trial.[2] Surrogate parameters calculated by specialized software (RAPID; iSchemaView) based on CT perfusion or MR imaging are currently recommended for selecting candidates for endovascular treatment between 6 and 24 hours after last known well.

CTP has been used in stroke trials for the triage of patients for reperfusion treatment on the basis of the target mismatch (TMM) between the volume of salvageable tissue (penumbra) and unsalvageable tissue (core) according to perfusion thresholds.[3-5] However, to the best of our knowledge, only 10 of 982 stroke centers in China use RAPID. For those hospitals who have no application of RAPID or other specialized software, it is not possible to select patients with TMM for endovascular treatment between 6 to 24 hours time window after stroke onset.

Received February 4, 2020; accepted after revision June 10.

From the Department of Neurology and Institute of Neurology (W.C., Y.L., L.Y., F.W., X.C., Q.D.), Huashan Hospital, Fudan University, Shanghai, China; and State Key Laboratory of Medical Neurobiology (Q.D.), Fudan University, Shanghai, China.

Please address correspondence to Qiang Dong, PhD, Department of Neurology, Huashan Hospital, No. 12 Wulumuqi Zhong Rd, Shanghai, 200040, China; e-mail: dongqiang2222@gmail.com

Indicates article with supplemental on-line table.

http://dx.doi.org/10.3174/ajnr.A6718

The relative filling time delay (rFTD) based on CTP source imaging and assessed in the Sylvian fissures represents the abundance of leptomeningeal collateral supply and is a simple and reliable visual rating method to quantify cerebral collateral circulation. Cao et al[6] found that an rFTD ≤ 4 seconds independently predicted favorable clinical outcome and small infarction size after recanalization therapy (thrombolysis with or without thrombectomy) in patients with stroke with large vessel occlusion. Notably, rFTD is a visual method with no software requirement, which, in most hospitals, can be used by radiologists to quickly identify potential patientsfor thrombectomy. We aimed to establish the association of rFTD and ischemic volume parameters and infarct penumbra to core volume mismatch in patients with acute ischemic stroke.

MATERIALS AND METHODS

Patients

We identified patients with acute ischemic stroke from our prospectively recorded stroke data base who had presented to our institution between January 2012 and July 2019 within 24 hours of stroke symptom onset and received multimodal CT imaging before treatment. Patients with proximal MCA occlusion with or without ICA occlusion, in addition, were recruited for inclusion in our study. Demographic, clinical, and radiologic data were recorded and included age, sex, onset-to-CT time, blood pressure, and baseline NIHSS score. Risk factors, such as smoking history, hypertension, diabetes mellitus, hyperlipidemia, history of stroke or transient ischemic attack, and atrial fibrillation, were also recorded. The study was performed with the informed consent of the patients or their next of kin, and with ethics approval from the institutional review board of our institution.

CT Scanning and Image Processing

Whole-brain perfusion and angiography were performed at the time of the emergency before therapy by using a 256-section CT scanner (Brilliance iCT; Philips Healthcare) between January 2012 and March 2015, or by using a 64-section CT scanner (Discovery CT750 HD; GE Healthcare) between April 2015 and July 2019. A 40-mL bolus of nonionic contrast media was injected at a rate of 5 mL/s. CT scanning was initiated 5 seconds (Brilliance) or 7 seconds (Discovery) after a contrast agent bolus, as follows: Jog mode, 80 kVp/150 mAs (Brilliance) and shuttle mode, 80 kVp/220 mAs (Discovery); 13 cycles for 50 seconds (Brilliance) and 26 cycles for 34 seconds (Discovery); and 325 slices (Brilliance) or 312 slices (Discovery).

Imaging Analysis

CTA images were reviewed first to identify patients with complete occlusion of the MCA with or without ICA. For these patients, unprocessed CTP source imaging was reviewed on a standard PACS to identify the rFTD between the normal MCA Sylvian branches and the rFTD in the affected hemisphere. The rFTD was calculated as the time difference between the first appearance of contrast in each Sylvian fissure. The rFTD was divided into 4 grades—grade 0: rFTD = 0 seconds; grade 1: rFTD >0 to ≤4 seconds; grade 2: rFTD >4 to ≤8 seconds; grade 3: rFTD >8 seconds. Two raters (Y.L., L.Y.) were blinded to all clinical information and follow-up data at the time of reading the scans. Differences between the raters (Y.L., L.Y.) were reviewed by a senior neuroradiologist (W.C.) to determine consensus rFTD grade.

Ischemic volumes of the infarct core, penumbra, and hypoperfused lesion were calculated by commercial software MIStar (Apollo Medical Imaging Technology) based on CTP maps. The mismatch ratio was calculated as hypoperfused lesion volume to infarct core volume. "Target mismatch" was defined by using the imaging criteria of the DEFUSE 3 trial (hypoperfusion volume to infarct core volume [ICV] > 1.8, with an absolute ICV of <70 mL and absolute volume difference between the penumbra and the infarct core of >15 mL) (Fig 1).[2]

Statistics Analyses

Statistical analyses were performed by using SPSS, Version 23 (IBM). $P < .05$ was considered to indicate statistical significance. Differences in patient characteristics and ischemic volume parameters among the rFTD grades were tested by using the χ^2 test for categoric variables and the Kruskal-Wallis test for continuous variables. Receiver operating characteristic analysis was performed to determine the optimal threshold. Multivariate binary logistic regression was used to assess the association of rFTD grade ≤ 1 with TMM, ICV < 70 mL, and ICV < 51 mL. Predictors with $P <$ 0.1 were included in multivariate binary logistic regression, whereas at least 5 outcome events for every predictor in each of the 3 final models was required to avoid overfitting.[7] The area under the curve for each of the 3 multivariate models and for each of the 3 outcomes were calculated with receiver operating characteristic analysis. The agreement of rFTD grades between the observers was tested by using the intraclass correlation coefficient in total and by each CT scanner type. Differences in the intraclass correlation coefficients between the 2 CT scanner types were analyzed by using the Fisher *Z*-test.

RESULTS

Patient Characteristics

Between January 2012 and July 2019, 655 patients within 24 hours of stroke symptom onset received multimodal CT imaging before treatment. Of those, 138 patients (135 onset within 12 hours, 3 onset between 12 and ~24 hours) with acute occlusion identified in the MCA with or without ICA occlusion were recruited. The median age was 69 years (interquartile range, 59–76 years), with 62.3% male ($n = 86$). There were 44.2% patients ($n = 61$) who underwent CTP on a 256-section scanner between January 2012 and March 2015 and 55.8% ($n = 77$) who underwent CTP on a 64-section scanner between April 2015 and July 2019.

Comparison of Ischemic Volume Parameters among rFTD Grades

The characteristics of all the patients and patients stratified by rFTD grades are listed in Table 1. Different median ICVs (grade 0, 7.3 mL; grade 1, 23.3 mL; grade 2, 45.7 mL; grade 3, 135 mL [$P < .001$]), penumbra (grade 0, 47.6 mL; grade 1,

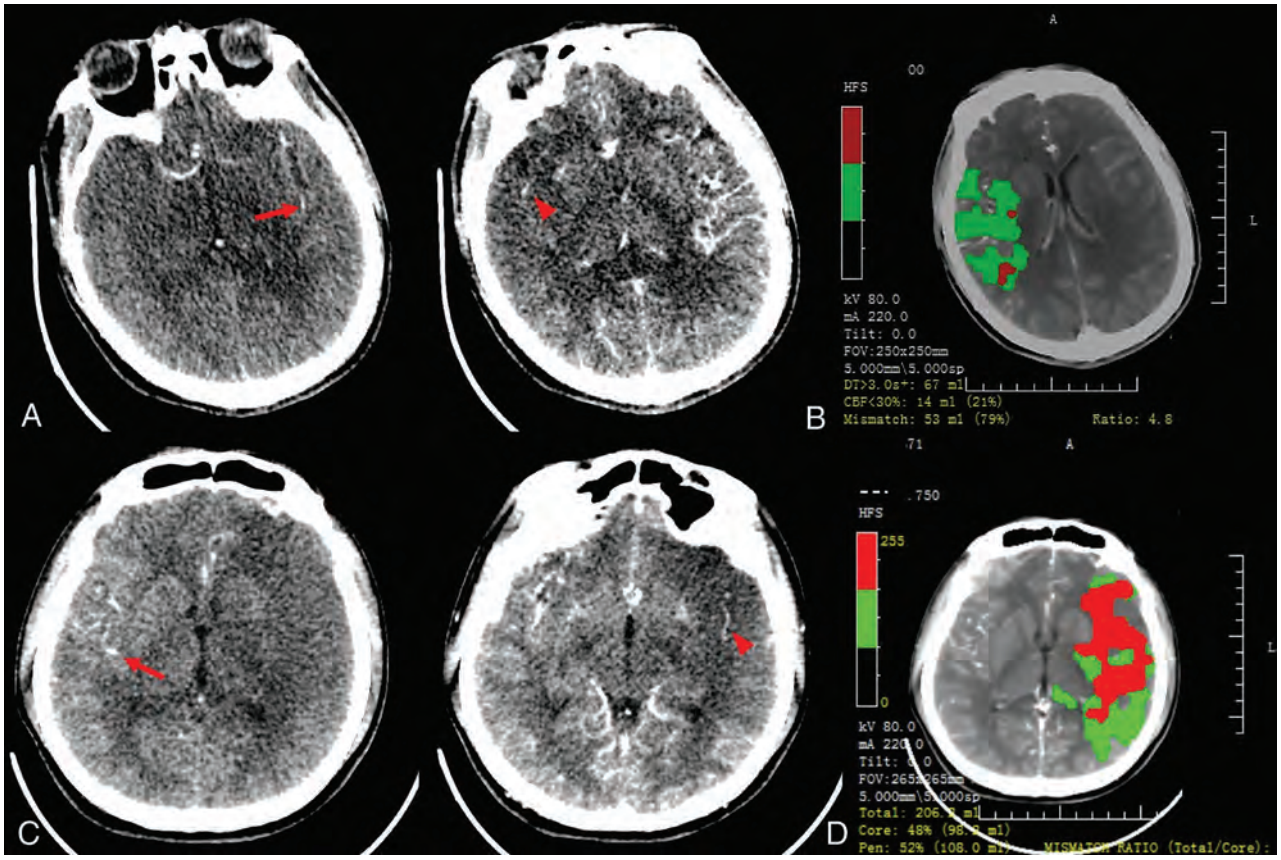

FIG 1. Case 1. A 46-year-old man with acute occlusion of the right MCA. CTP source imaging (SI) from a 256-section CT scanner showed that the first detection of contrast in the affected right hemisphere (*red arrowhead*) was delayed by 1 cycle (4 seconds for 1 cycle) after the first detection of contrast in the left Sylvian fissure (*red arrow*). The relative filling time delay (rFTD) was 4 seconds, which corresponds to a grade of 1 (*A*). Mismatch imaging calculated by software demonstrated a target mismatch between hypoperfusion volume (67 mL) and core volume (14 mL) (*B*). Case 2. A 24-year-old man with acute occlusion of the left MCA. CTP-SI from a 64-section CT scanner showed that the first detection of contrast in the affected left hemisphere (*red arrowhead*) was delayed by 5 cycles (1.3 seconds for 1 cycle) after the first detection of contrast in the right Sylvian fissure (*red arrow*). The rFTD was 6.5 seconds, which corresponded to a grade of 2 (*C*). Mismatch imaging showed a large core volume of 98 mL and no TMM (*D*).

90 mL; grade 2, 110 mL; grade 3, 92 mL [$P = .043$]), hypoperfused lesion (grade 0, 55.5 mL; grade 1, 121.6 mL; grade 2, 186.5 mL; grade 3, 242 mL [$P < .001$]), and mismatch ratio (grade 0, 5; grade 1, 5.4; grade 2, 2.6; grade 3, 1.8 [$P < .001$]) were observed among the rFTD grades (Fig 2). The percentages of TMM (grade 0, 64.3% [$n = 9$]; grade 1, 89.7% [$n = 70$]; grade 2, 54.5% [$n = 18$]; grade 3, 15.4% [$n = 2$] [$P < .001$]), ICV $<$ 70 mL (grade 0, 100% [$n = 14$]; grade 1, 91% [$n = 71$]; grade 2, 60.6% [$n = 20$]; grade 3, 23.1% [$n = 3$] [$P < .001$]), and ICV $<$ 51 mL (grade 0, 92.9% [$n = 13$]; grade 1, 79.5% [$n = 62$]; grade 2, 54.5% [$n = 18$]; grade 3, 0 [$n = 0$] [$P < .001$]) were different among the rFTD grades (Fig 3).

Predictive Value of rFTD for TMM and ICV

In the receiver operating characteristic analysis, rFTD grade was associated with TMM (area under the curve 0.71; 95% CI, 0.6–0.83; $P < .001$), ICV $<$70 mL (area under the curve 0.81; 95% CI, 0.72–0.9; $P < .001$), and ICV $<$51 mL (area under the curve 0.76; 95% CI, 0.67–0.85; $P < .001$). The optimal thresholds determined by the Youden index were grade 1 for TMM, ICV $<$ 70 mL, and ICV $<$ 51 mL.

The patients were then dichotomized into positive versus negative TMM, ICV $<$ 70 mL versus $\geq$ 70 mL, and ICV $<$ 51 mL versus $\geq$51 mL (On-line Table). The patients with TMM were associated with a lower baseline NIHSS score (12.5 versus 19; $P < .001$) and a higher proportion of rFTD grades $\leq$ 1 (79.8% versus 33.3% ; $P < .001$). Patients with ICV $<$ 70 mL were associated with a lower NIHSS score (13 versus 19; $P < .001$), a lower proportion of diabetes (27.8% versus 50%; $P = .022$), and a higher proportion of rFTD grades $\leq$ 1 (78.7% versus 23.3%; $P < .001$). The patients with ICV $<$ 51 mL were associated with less hypertension (60.2% versus 77.8%; $P = .041$), a lower NIHSS (13 versus 18; $P < .001$), and a higher proportion of rFTD grades $\leq$ 1 (80.6% versus 37.8%; $P < .001$). The distribution of the site of arterial occlusion was different between ICV $<$ 70 mL and ICV $\geq$ 70 mL (MCA, ICA, MCA + ICA: 70.4%, 25.9%, 3.7% versus 36.7%, 53.3%, 10%; $P = .003$) and between ICV $<$ 51 mL and ICV $\geq$ 51 mL (MCA, ICA, MCA + ICA: 72%, 25.8%, 2.2% versus 44.4%, 44.4%, 11.1%; $P = .003$).

Multivariate Regression Analysis for TMM, ICV $<$ 70 mL, and ICV $<$ 51 mL

Multivariate regression analyses, including rFTD grades $\leq$ 1 and variables with prespecified univariate values of $P \leq .1$, demonstrated

Table 1: Characteristics of all included patients and patients stratified by rFTD grade

Characteristic	Total	Grade 0	Grade 1	Grade 2	Grade 3	*P*
Patients, *n*	138	14	78	33	13	
Age, (median) (IQR) (yr)	69 (59, 76)	63.5 (55.25, 72.75)	66 (57, 75)	71 (59, 76.5)	75 (64, 79)	.169
Males, *n* (%)	86 (62.3)	7 (50)	48 (61.5)	21 (63.6)	10 (76.9)	.546
Clinical characteristics						
Onset-to-CT time (median) (IQR) (min)	119 (63, 201)	115.5 (70.25, 161.75)	120 (71.5, 224)	105 (52.75, 203)	123 (48.5, 174)	.845
Hypertension, *n* (%)	90 (65.9)	9 (64.3)	49 (62.8)	23 (69.7)	10 (76.9)	.738
Diabetes, *n* (%)	45 (32.6)	6 (42.9)	18 (23.1)	15 (45.5)	6 (46.2)	.059
Smoking, *n* (%)	53 (38.4)	6 (42.9)	30 (38.5)	11 (33.3)	6 (46.2)	.848
Previous stroke and/or TIA, *n* (%)	26 (18.8)	2 (14.3)	13 (16.7)	5 (15.2)	6 (46.2)	.07
Atrial fibrillation, *n* (%)	54 (39.1)	5 (35.7)	28 (35.9)	14 (42.4)	7 (53.8)	.627
Dyslipidemia, *n* (%)	24 (17.4)	2 (14.3)	14 (17.9)	6 (18.2)	2 (15.4)	.984
SBP (median) (IQR) (mm Hg)	147 (130, 162)	137 (124.5, 166.5)	145 (134.5, 160)	158 (128.5, 169.75)	147 (131, 172.5)	.508
DBP (median) (IQR) (mm Hg)	83 (80, 91)	82.5 (82.25, 89.5)	85 (80, 91.5)	85.5 (79.25, 99.75)	80 (69, 90.5)	.276
ABG (median) (IQR) (mol/L)	7.4 (6.1, 9.6)	7.15 (6.33, 8.89)	7 (5.7, 8.69)	8.05 (6.29, 10.2)	7.9 (7.2, 9.45)	.206
Baseline NIHSS score (median) (IQR)	16 (11, 19)	10.5 (4.75, 18.5)	14 (9, 17)	17.5 (12, 20)	19 (16.5, 22)	<.001
Occluded site, *n* (%)						.067
MCA	87 (63)	10 (71.4)	50 (64.1)	21 (63.6)	6 (46.2)	
ICA	44 (32.1)	3 (21.4)	25 (32.1)	12 (36.4)	4 (30.8)	
MCA + ICA	7 (5.1)	1 (7.1)	3 (3.8)	0 (0)	3 (23.1)	
Perfusion parameters						
Core (median) (IQR) (mL)	30.5 (10, 87, 61.25)	7.35 (0.13, 15.6)	23.3 (8.65, 43.8)	45.75 (25.17, 90.25)	135 (77.85, 185.5)	<.001
Penumbra (median) (IQR) (mL)	88.3 (52.75, 138.7)	47.65 (5, 113.37)	90 (54, 136)	110.05 (62.42, 155.02)	92 (50, 167.45)	.043
Low perfusion (median) (IQR) (mL)	132.3 (83.32, 213.25)	55.55 (14.5, 116.55)	121.6 (80.5, 195.5)	186.55 (141.55, 216.15)	242 (154, 309.85)	<.001
Mismatch ratio[a] (median) (IQR)	3.9 (2.4, 7.1)	5 (3.22, 21.85)	5.45 (2.24, 8.42)	2.6 (1.74, 7.5)	1.8 (1.4, 2.44)	<.001
TMM, *n* (%)	99 (71.7)	9 (64.3)	70 (89.7)	18 (54.5)	2 (15.4)	<.001
ICV <70 mL, *n* (%)	108 (78.3)	14 (100)	71 (91)	20 (60.6)	3 (23.1)	<.001
ICV <51 mL, *n* (%)	93 (67.4)	13 (92.9)	62 (79.5)	18 (54.5)	0 (0)	<.001

Note:—SBP indicates systolic blood pressure; DBP, diastolic blood pressure; ABG, admission blood glucose.
[a] Calculated by low perfusion volume to infarct core volume.

areas under the curve of 0.83, 0.88, and 0.84 for predicting TMM, ICV < 70 mL, and ICV < 51 mL, respectively. After adjustment for confounding variables, rFTD grade ≤ 1 was independently associated with TMM (OR 6.25; 95% CI, 2.48–15.72; $P < .001$), ICV < 70 mL (OR 9.73; 95% CI, 3.11–30.35; $P < .001$), and ICV < 51 mL (OR 5.84; 95% CI, 2.3–14.83; $P < .001$). The rFTD grade ≤ 1 predicted TMM with a sensitivity of 0.79 (95% CI, 0.7–0.87) and a specificity of 0.66 (95% CI, 0.49–0.8), predicted ICV < 70 mL with a sensitivity of 0.78 (95% CI, 0.69–0.86) and a specificity of 0.76 (95% CI, 0.57–0.9), and predicted ICV < 51 mL, with a sensitivity of 0.8 (95% CI, 0.71–0.88) and a specificity of 0.62 (95% CI, 0.42–0.72) (Table 2).

Reliability Assessment

The intraclass correlation coefficient of rFTD grades between the 2 observers was 0.83 in total, 0.92 in rFTD on 256-section and 0.76 on 64-section CT scanners, which represents excellent agreement.[8] The difference in intraclass correlation coefficient between 256-section and 64-section CT scanners was significant, with a $P < .001$.

DISCUSSION

Our study demonstrates that rFTD grade is associated with ischemic brain volumes, including infarct core, penumbra, and hypoperfusion tissue, in patients with acute ischemic stroke and with anterior circulation large cerebral artery occlusion. The rFTD grade ≤ 1 (rFTD ≤ 4 seconds) is a good marker in predicting TMM, ICV < 70 mL, and ICV < 51 mL, with high sensitivities and specificities.

It is now well known that poor baseline collaterals are associated with a larger ischemic core and worse functional outcomes. The DAWN trial used mismatches between clinical and imaging (estimated ischemic core volume by using CTP or DWI up to 50 mL) parameters to determine endovascular treatment candidacy between 6 and 24 hours from symptom onset. The DEFUSE 3 trial used perfusion-core mismatch and a maximum core size estimated up to 70 mL as imaging criteria to select patients with anterior circulation large vessel occlusion 6–16 hours from symptom onset. Our study established the associations between rFTD grade with 2 thresholds of ICV (<70 mL and <51 mL) and TMM (defined with the imaging criteria of the DEFUSE 3 trial). This assessment of rFTD grade on CTP source imaging can predict ICV and TMM without the need for dedicated software solutions while reducing the time required for computer data processing.

Automated CTP software is limited by the incidence of unreliable generation, for example, RAPID software was reported to fail to form perfusion maps in 3% to ~13% of patients.[9-11] Unreliable automated CTP maps are mainly due to

contrast bolus flow issues and motion artifacts. Dehkharghani et al[12] reported that 8.1% of patients had uninterpretable automated CTP maps strictly due to motion artifacts. However, assessing rFTD based on CTP source imaging is robust to motion in patients who are uncooperative. Because rFTD is normalized to contralateral delay, factors such as contrast injection and cardiac output, which affect the absolute delay to filling, are negated. These characteristics can make the assessment of rFTD feasible in patients with various conditions and can serve as an alternative solution when automated software fails to generate reliable CTP maps.

A previous study suggested that rFTD $\leq$ 4 seconds independently predicts a favorable clinical outcome and small size of the infarction after recanalization therapy.[6] However, thus far, few clinical trials have used this marker to evaluate collateral status before treatment. The association between ischemic volume parameters and rFTD $\leq$ 4 seconds is unclear. Thus, we analyzed the predictive power of rFTD grade $\leq$ 1 (equal to rFTD $\leq$ 4 seconds). We found that the sensitivities of rFTD grade $\leq$ 1 in predicting the 3 imaging criteria were very similar, whereas the specificity decreased (from high to low specificity) in the sequence of ICV $<$ 70 mL, TMM, and ICV $<$ 51 mL. Lower specificity of rFTD grade $\leq$ 1 for the prediction of TMM can be explained by the definition of TMM in the DEFUSE 3 trial, which required a mismatch ratio of $>$1.8 and an absolute volume between the penumbra and the infarct core $>$ 15 mL in addition to an ICV $<$ 70 mL. These criteria may potentially exclude patients who have excellent collateral flow, with very low ischemia tissue volume but are unable to achieve TMM.

Software packages can under- or overestimate ischemic volumes. A recent analysis of the accuracy of predicting final infarct volume by using RAPID demonstrated that RAPID corresponded to a median absolute error (9 mL) and overestimated the core volume in a few cases.[13] Core volume may be overestimated in cases of ultra-early reperfusion. In the International Stroke Perfusion Imaging (INSPIRE) registry, which relied on MIStar automated perfusion software, the optimal CTP threshold for estimating the ischemic core volume was different for patients treated by thrombectomy (regional cerebral blood flow [rCBF] $<$ 20%) versus patients treated with alteplase alone (rCBF $<$ 30%).[14] In addition, ischemic penumbra may be misclassified due to either technical or flow-related patterns. Most of the fully automated software packages do not have adequate postprocessing tools to subtract the miscalculated volumes, including skull base penumbral artifacts.[9] Tools are needed in the manual (nonautomated) versions of CTP when artifacts are recognized. As a visual method, rFTD can serve as a quick double-check when errors in processing are suspected and could, consequently, increase radiologist confidence.

The time for RAPID processing was constant for each site based on the exact acquisition protocol and hardware configuration, with a median across the range of scanner platforms at the 20 trial sites of 5 minutes 20 seconds (range, 3–10 min).[9] However, in our protocol,

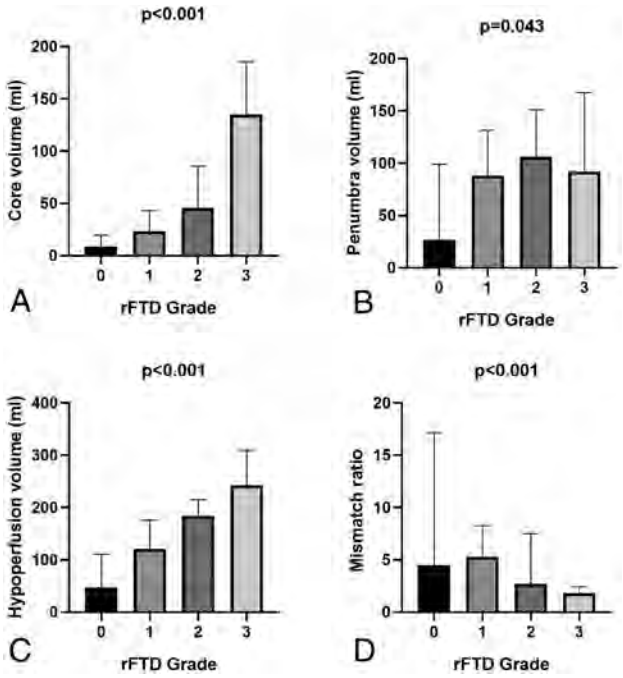

FIG 2. Comparison of ischemic volume parameters, including infarct core (*A*), penumbra (*B*), and hypoperfusion (*C*), and the mismatch ratio of hypoperfusion to core volume (*D*) among relative filling time delay grades.

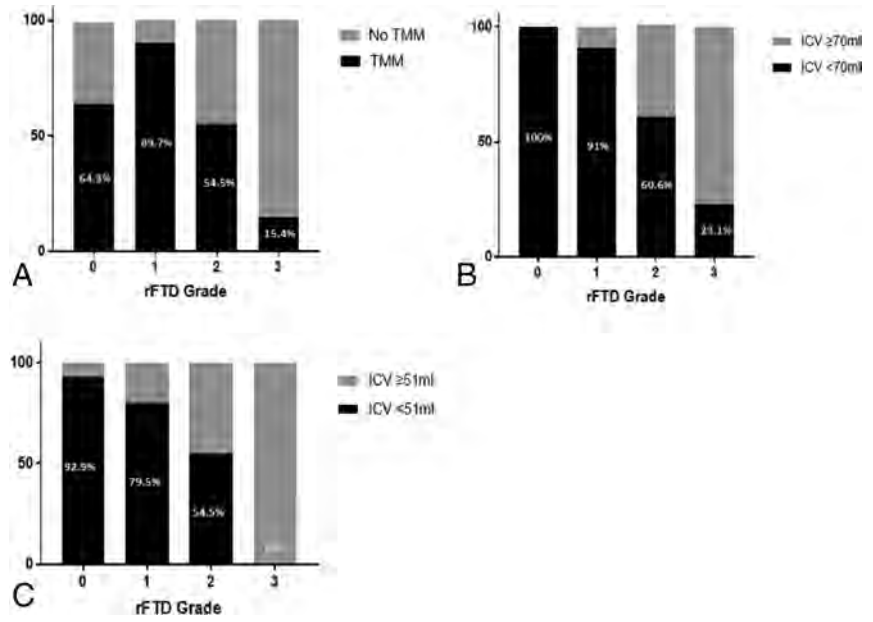

FIG 3. Percentages of target mismatch (*A*), infarct core volume $<$ 70 mL (*B*), and ICV $<$ 51 mL (*C*) among relative filling time delay grades.

Table 2: Multivariate regression analysis of the independent association between rFTD grade ≤ 1 and TMM, ICV < 70 mL, and ICV < 51 mL

Variable	adOR	95% CI	*P*	Sensitivity	Specificity
Prediction of TMM	6.25[a]	2.48–15.72	<.001	0.79	0.66
Prediction of ICV <70 mL	9.73[b]	3.11–30.35	<.001	0.78	0.76
Prediction of ICV <51 mL	5.84[c]	2.3–14.83	<.001	0.8	0.62

Note:—adOR indicates adjusted OR.
[a] Adjusted for dyslipidemia, baseline NIHSS score, and occluded site.
[b] Adjusted for diabetes, previous stroke and/or TIA, baseline NIHSS score, and occluded site.
[c] Adjusted for hypertension, diabetes, dyslipidemia, baseline NIHSS score, and occluded site.

rFTD requires no more than 1 minute of evaluation by a clinician, which reduces the time required for radiologic assessment.

There are several available clinical rating scales that have been designed to assess the collateral status of stroke while also predicting clinical outcome and infarct size. Multiphase CTA is an imaging tool that provides 3 time-resolved images of pial arterial filling, captured 8 seconds apart, over the whole brain. A previous study established the value of multiphase CTA in predicting ICV.[15] However, collateral flow filling with a relative delay time shorter than 8 seconds cannot be distinguished by using multiphase CTA. The rFTD grading that we derived is characterized by a range of 4 seconds between each grade, which allows more precise assessment of collateral flow.

In this study, we found that the interrater reliability of rFTD was impacted by the time of each scanning cycle according to different CT scanners and scanning modes. Jog mode on 256-section CT requires ~4 seconds per cycle (13 cycles for 50 seconds), whereas shuttle mode on 64-section CT requires only 1.3 seconds per cycle (26 cycles for 34 seconds). Shorter cycle times make it more challenging for observers to determine the earliest appearance of contrast filling in the Sylvan fissure and to rate the rFTD. For example, in our study, the raters had less confidence in determining whether the rFTD was 3.9 seconds (grade 1) or 5.2 seconds (grade 2) when using the shuttle mode of 64-section CT than in determining whether the rFTD was 4 seconds (grade 1) or 8 seconds (grade 2) when using the Jog mode of a 256-section CT scanner. Jog mode contributes to a higher interrater reliability of rFTD grade, though the precision of rFTD is lost. The rFTD cannot be assessed within the range of 4 seconds, which may cause more information pertaining to early collateral flow in acute stroke to be lost.

Our study is limited by the small and selected population of patients with ischemic stroke with large artery occlusion in the anterior circulation. In our study, most patients (135/138) exhibited onset within 12 hours, whereas only 3 patients exhibited onset between 12 and ~24 hours. The non-normal distribution of onset time among the included patients may potentially impact the result. Also, the agreement between the raters in grading rFTD could have been impacted by the scanning mode of CTP. A shorter scanning cycle time brings about more challenges for raters in determining the time point of the earliest contrast appearance in the Sylvan fissure.

CONCLUSIONS

The rFTD grade based on CTP source imaging is a simple and effective tool for evaluating ischemic volume parameters and TMM in patients with acute ischemic stroke without the need for any special software. Future studies are needed to evaluate the use of the rFTD grade for selecting patients in the appropriate time window for comparison with selection by specialized software and to prospectively study the clinical outcomes of these patients.

REFERENCES

1. Nogueira RG, Jadhav AP, Haussen DC, et al. **Thrombectomy 6 to 24 hours after stroke with a mismatch between deficit and infarct.** *N Engl J Med* 2018;378:11–21 CrossRef Medline
2. Albers GW, Marks MP, Kemp S, et al. **Thrombectomy for stroke at 6 to 16 hours with selection by perfusion imaging.** *N Engl J Med* 2018;378:708–18 CrossRef Medline
3. Hacke W, Furlan AJ, Al-Rawi Y, et al. **Intravenous desmoteplase in patients with acute ischaemic stroke selected by MRI perfusion-diffusion weighted imaging or perfusion CT (DIAS-2): a prospective, randomised, double-blind, placebo-controlled study.** *Lancet Neurol* 2009;8:141–50 CrossRef Medline
4. Parsons M, Spratt N, Bivard A, et al. **A randomized trial of tenecteplase versus alteplase for acute ischemic stroke.** *N Engl J Med* 2012; 366:1099–107 CrossRef Medline
5. Parsons MW. **Perfusion CT: is it clinically useful?.** *Int J Stroke* 2008;3:41–50 CrossRef Medline
6. Cao W, Campbell BCV, Dong Q, et al. **Relative filling time delay based on CT perfusion source imaging: a simple method to predict outcome in acute ischemic stroke.** *AJNR Am J Neuroradiol* 2014; 35:1683–87 CrossRef Medline
7. Vittinghoff E, McCulloch CE. **Relaxing the rule of ten events per variable in logistic and Cox regression.** *Am J Epidemiol* 2007; 165:710–18 CrossRef Medline
8. Koo TK, Li MY. **A guideline of selecting and reporting intraclass correlation coefficients for reliability research.** *J Chiropr Med* 2016; 15:155–63 CrossRef Medline
9. Campbell BC, Yassi N, Ma H, et al. **Imaging selection in ischemic stroke: feasibility of automated CT-perfusion analysis.** *Int J Stroke* 2015;10:51–54 CrossRef Medline
10. Xiong Y, Huang CC, Fisher M, et al. **Comparison of automated CT perfusion softwares in evaluation of acute ischemic stroke.** *J Stroke Cerebrovasc Dis* 2019;28:104392 CrossRef Medline
11. Bulwa Z, Dasenbrock H, Osteraas N, et al. **Incidence of unreliable automated computed tomography perfusion maps.** *J Stroke Cerebrovasc Dis* 2019;28:104471 CrossRef Medline
12. Dehkharghani S, Bammer R, Straka M, et al. **Performance and predictive value of a user-independent platform for CT perfusion analysis:**

threshold-derived automated systems outperform examiner-driven approaches in outcome prediction of acute ischemic stroke. *AJNR Am J Neuroradiol* 2015;36:1419–25 CrossRef Medline

13. Mokin M, Levy EI, Saver JL, et al. **Predictive value of RAPID assessed perfusion thresholds on final infarct volume in SWIFT PRIME (Solitaire With the Intention for Thrombectomy as Primary Endovascular Treatment).** *Stroke* 2017;48:932–38 CrossRef Medline
14. Bivard A, Kleinig T, Miteff F, et al. **Ischemic core thresholds change with time to reperfusion: a case control study.** *Ann Neurol* 2017;82:995–1003 CrossRef Medline
15. Menon BK, d'Esterre CD, Qazi EM, et al. **Multiphase CT angiography: a new tool for the imaging triage of patients with acute ischemic stroke.** *Radiology* 2015;275:510–20 CrossRef Medline

Myelin and Axonal Damage in Normal-Appearing White Matter in Patients with Moyamoya Disease

S. Hara, M. Hori, A. Hagiwara, Y. Tsurushima, Y. Tanaka, T. Maehara, S. Aoki, and T. Nariai

ABSTRACT

BACKGROUND AND PURPOSE: Although chronic ischemia is known to induce myelin and axonal damage in animal models, knowledge regarding patients with Moyamoya disease is limited. We aimed to investigate the presence of myelin and axonal damage in Moyamoya disease and their relationship with cognitive performance.

MATERIALS AND METHODS: Eighteen patients with Moyamoya disease (16–55 years of age) and 18 age- and sex-matched healthy controls were evaluated with myelin-sensitive MR imaging based on magnetization transfer saturation imaging and 2-shell diffusion MR imaging. The myelin volume fraction, which reflects the amount of myelin sheath; the g-ratio, which represents the ratio of the inner (axon) to the outer (axon plus myelin) diameter of the fiber; and the axon volume fraction, which reflects axonal components, were calculated and compared between the patients and controls. In the patients with Moyamoya disease, the relationship between these parameters and cognitive task–measuring performance speed was also evaluated.

RESULTS: Compared with the healthy controls, the patients with Moyamoya disease showed a significant decrease in the myelin and axon volume fractions ($P < .05$) in many WM regions, while the increases in the g-ratio values were not statistically significant. Correlations with cognitive performance were most frequently observed with the axon volume fraction ($r = 0.52–0.54$; $P < .03$ in the right middle and posterior cerebral artery areas) and were the strongest with the g-ratio values in the right posterior cerebral artery region ($r = 0.64$; $P = .004$).

CONCLUSIONS: Myelin-sensitive MR imaging and diffusion MR imaging revealed that myelin and axonal damage exist in patients with Moyamoya disease. The relationship with cognitive performance might be stronger with axonal damage than with myelin damage.

ABBREVIATIONS: ACA = anterior cerebral artery; AVF = axon volume fraction; GRAPPA = generalized autocalibrating partially parallel acquisition; MMD = Moyamoya disease; MVF = myelin volume fraction; MTsat = magnetization transfer saturation; PCA = posterior cerebral artery; V_{ic} = intracellular volume fraction; V_{iso} = isotropic volume fraction; TMT = Trail-Making Test; WAIS = Wechsler Adult Intelligence Scale

Chronic ischemia induced in animal models is known to damage the structure of myelin, which wraps around axons to provide the efficient conduction of neural signals, and axons.[1] Few previous studies have directly investigated whether chronic ischemia in humans also damages the myelin structure, such as in patients with Moyamoya disease (MMD).

MMD is a progressive cerebrovascular disease that mainly affects children and young adult patients in contrast to atherosclerotic cerebrovascular diseases,[2] which cause chronic hemodynamic impairment characterized by strong perfusion delay.[3,4] Previous diffusion MR imaging studies have suggested that in vivo microstructural damage might exist in this disease population and might be related to cognitive function.[5-7] However,

Received March 29, 2020; accepted after revision June 5.

From the Department of Neurosurgery (S.H., Y. Tanaka, T.M., T.N.), Tokyo Medical and Dental University, Tokyo, Japan; Department of Radiology (S.H., M.H., A.H., Y.T., S.A.), Juntendo University, Tokyo, Japan; Department of Diagnostic Radiology (M.H.), Toho University Omori Medical Center, Tokyo, Japan; and Department of Radiology (Y. Tsurushima), Kenshinkai Tokyo Medical Clinic, Tokyo, Japan.

This work was supported by Grants-in-Aid for Scientific Research "KAKENHI," the Japan Society for the Promotion of Science (grants 19K18406 and 16H06280), and a research grant (2017-2020) from the Japanese Society of Neuroradiology.

Preliminary results previously presented at: Annual Meeting of The Japanese Society of Neuroradiology, February 16–18, 2018; Tsukuba, Japan; and Joint Annual Meeting of the International Society for Magnetic Resonance in Medicine and the European Society for Magnetic Resonance in Medicine and Biology, June 16–18, 2018; Paris, France.

Please address correspondence to Shoko Hara, MD, Department of Neurosurgery, Tokyo Medical and Dental University, 1-5-45 Yushima, Bunkyo-ku, Tokyo 113-8519, Japan; e-mail: shara.nsrg@tmd.ac.jp

Indicates open access to non-subscribers at www.ajnr.org
Indicates article with supplemental on-line appendix and tables.
Indicates article with supplemental on-line photos.
http://dx.doi.org/10.3174/ajnr.A6708

because myelin contains few free water molecules and the water protons of macromolecules in the myelin sheath and water protons between the phospholipid bilayers have a short transverse relaxation time (T2 ≈ 10 ms), the signal is theoretically negligible in typical diffusion MR imaging acquisitions using long TEs (≈50–100 ms).[8] Hence, diffusion MR imaging cannot directly assess myelin damage, and the results of these studies provide indirect evidence of myelin damage in MMD. To the best of our knowledge, no previous studies, including postmortem case reports, have directly investigated whether myelin damage exists in patients with MMD.

We hypothesized that myelin damage exists in patients with MMD and is related to cognitive function. To investigate this hypothesis, we applied an MR imaging technique called magnetization transfer saturation (MTsat),[9] which sensitizes water molecules bound to macromolecules and enables the quantitative estimation of myelin in a clinically feasible scanning time. This technique has been shown to be clinically useful in patients with other neurologic disorders.[10,11] The relationship between the axon size and myelin thickness can be captured by a parameter called the myelin g-ratio, which is defined as the ratio of the inner (axon) to the outer (axon plus myelin) diameter of the nerve fiber (On-line Fig 1; see the illustration in the box).[8,12] Thus, we combined MTsat with diffusion MR imaging, which can evaluate the presence of axonal damage,[13] to calculate the g-ratio. Because the destruction of myelin could lead to a decrease in the nerve-conduction velocity,[14] we hypothesized that decreases in myelin and increases in the g-ratio correlated with reductions in processing speed.

MATERIALS AND METHODS

Study Protocol and Background of the Participants

This prospective observational study was approved by the ethics committees of Tokyo Medical and Dental University (M2000-2302) and Juntendo University (16–100), with registration to the University Hospital Medical Information Network Clinical Trials Registry (UMIN-CTR ID: 000027949). The inclusion criteria were patients diagnosed with MMD according to the diagnostic guidelines,[15] 16–64 years of age, who were able to undergo MR imaging without sedative agents and had no neurologic deficits affecting the scores of neurophysiological tests, with a modified Rankin Scale score of 0–2. The exclusion criteria were cortical or large (>10 mm) WM infarcts visible on routine MR imaging sequences.

Between May 2017 and December 2019, eighteen patients (4 males; 17–55 years of age; average, 36 years; all right-handed), including 9 postoperative patients, participated in this study (details are provided in On-line Table 1 and the On-line Appendix). All patients underwent a series of MR imaging scans and a cognitive battery within an interval of 0–20 days (7 days on average; On-line Table 2).

During the same period, 18 age- and sex-matched healthy subjects with no history of neurologic or systematic diseases (4 males; 16–44 years of age; average, 35 years) were recruited and evaluated by the same MR imaging protocol.

Cognitive Assessments

The cognitive battery (the details are provided in the On-line Appendix) included the Processing Speed Index and Trail-Making Test parts A and B (TMT-A and -B). The Processing Speed Index is an index measuring visual motor speed in the Wechsler Adult Intelligence Scale (WAIS-III). TMT-A and -B assess the speed of information processing and executive functioning, respectively. The results of TMT-A and -B were converted to z scores using the reported normal ranges of each age group.

MR Imaging Acquisition

All MR imaging data were acquired using a 3T system (Magnetom Skyra; Siemens) equipped with a 32-multichannel receiver head coil. The total acquisition time of the entire protocol, including T1WI, MRA, FLAIR, and SWI (acquisition parameters provided in the On-line Appendix), was approximately 30 minutes.

Three sagittal 3D multiecho fast low-angle shot sequences were performed with predominant magnetization transfer–, proton density-, and T1-weighting (TR = 24/24/10 ms, TE = 1.85/1.85/1.85 ms, flip angle = 5°/5°/13°, matrix = 128 × 128, section number = 128, parallel acquisition techniques = generalized autocalibrating partially parallel acquisition [GRAPPA] acceleration factor = 2, FOV = 200 mm, voxel size = 1.56 × 1.56 × 1.56 mm). For the magnetization transfer–weighted images, excitation was preceded by an off-resonance Gaussian-shaped radiofrequency pulse (frequency offset from water resonance = 1200 Hz, bandwidth = 192 Hz, pulse duration = 9.984 ms, and nominal flip angle = 500°). The acquisition times were 2 minutes 23 seconds, 2 minutes 23 seconds, and 1 minute. Two additional B_1 maps using coronal echo-planar imaging with nominal 10° and 20° flip angles were acquired within a short acquisition time (approximately 10 seconds each).

The diffusion-weighted images were acquired using a fat-saturated single-shot echo-planar imaging sequence along 30 and 60 motion-probing gradient directions with b values of 700 and 2850 s/mm^2, TR = 4500 ms, TE = 105 ms, flip angle = 90°, matrix = 100 × 90, number of slices = 90, voxel size = 2 × 2 × 2 mm, multiband factor = 2. Several volumes of non-diffusion-weighted images were also acquired with reversed phase-encoded blips, resulting in pairs of images with distortions along opposite directions. The acquisition times were approximately 8 minutes 38 seconds for the main images and 1 minute 37 seconds for the reversed phase-encoded blips.

Postprocessing of the MR Imaging Data

The postprocessing of the MR imaging data (On-line Fig 1) was conducted using Matlab 2014a (MathWorks). The data were exported from the scanner in DICOM format and converted to NIfTI format using dicm2nii (https://www.github.com/xiangruili/dicm2nii). Images with magnetization transfer–, proton density-, and T1-weighting were converted to the MTsat index using a previously described method,[9] while correcting for small higher order dependencies of the MTsat on the local radiofrequency transmit field using B_1 maps.[16] The MTsat index was multiplied by 0.1; this calibration calculated the myelin volume fraction (MVF), revealing that the amount of myelin sheath in the splenium of the corpus callosum in the healthy volunteers was 0.3–0.4 and that the g-ratio was 0.7–0.8, consistent with the

values reported in previous studies.[8,17,18] Values under 0 and above 1 were considered errors and changed to 0.

Based on the paired non-diffusion-weighted images (ie, $b = 0$ s/mm^2), the susceptibility-induced off-resonance field was estimated using a method similar to previously described procedures[19,20] implemented in the FMRIB Software Library (FSL; http://www.fmrib.ox.ac.uk/fsl)[21] to correct for susceptibility-induced distortions in the diffusion-weighted images. Then, the diffusion data were fitted to the neurite orientation dispersion and density imaging model using the NODDI Matlab toolbox, Version 0.9[13] (https://www.nitrc.org/projects/noddi_toolbox/) and converted to the intracellular volume fraction (V_{ic}) and isotropic volume fraction (V_{iso}). The axon volume fraction (AVF), which reflects the axonal components, and the g-ratio were calculated from MVF, V_{ic}, and V_{iso} using the following equations:[8,22]

$$\mathrm{AVF} = (1 - \mathrm{MVF}) \times (1 - V_{\mathrm{iso}}) \times V_{ic},$$

.

$$\mathrm{g-ratio} = \sqrt{\frac{\mathrm{AVF}}{\mathrm{MVF} + \mathrm{AVF}}}.$$

WM segmentation was performed on 3D-T1WI using the standard segmentation tool in SPM12 (http://www.fil.ion.ucl.ac.uk/spm/software/spm12/). WM masks with a probability threshold of 0.9 were created and applied to the MVF, AVF, and g-ratio maps to minimize partial volume effects. WM lesions visible on FLAIR and $b = 0$ s/mm^2 images were manually deleted from each map.

Calculation of Regional Values

The WM labels of the Harvard-Oxford cortical and subcortical probabilistic structural atlases (http://ftp.nmr.mgh.harvard.edu/pub/dist/freesurfer/tutorial_packages/centos6/fsl_507/doc/wiki/Atlases.html)[23] (threshold of 25%) distributed with FSL were divided into 6 vascular regions (anterior, middle, and posterior cerebral arteries [ACA, MCA, and PCA] of the right and left sides) using the vascular territorial atlas (https://figshare.com/articles/ATT_based_flow_territories/1488674) as a reference.[24] These labels were converted to each subject's space by linear (FLIRT; http://www.fmrib.ox.ac.uk/fsl/fslwiki/FLIRT) and nonlinear (FNIRT; http://fsl.fmrib.ox.ac.uk/fsl/fslwiki/FNIRT) Image Registration Tools implemented in FSL[21] and were used as ROIs to extract the MVF, AVF, and g-ratio values of each region (On-line Fig 1).

Statistical Analysis

Unpaired *t*-tests were used to compare the regional values of the MVF, AVF, and g-ratio between the patients with MMD and the healthy controls. Pearson correlation coefficients were calculated between regional metrics and cognitive scores in patients with MMD. The analyses were performed using JMP, Version 12.0.1 (SAS Institute), and $P < .05$ (with and without Bonferroni correction for comparison of 3 parameters) was regarded as statistically significant.

RESULTS

Representative cases are shown in Fig 1 and On-line Fig 2. As shown in Fig 1, a decreased MVF and decreased AVF were observed in the affected hemisphere, while the increase in the g-ratio was less prominent. As shown in On-line Fig 2, a decreased MVF was observed in the postoperative hemisphere as well, which had an improved hemodynamic condition at the time of the study. The decrease in AVF was unclear, and the g-ratio seemed to be slightly increased in the postoperative hemisphere.

Comparison of the Regional Values between Patients and Controls

The regional MVF values in patients with MMD were significantly lower than those in healthy controls in all regions (Fig 2). The regional AVF values in bilateral MCA regions in the patients were significantly lower than those in the healthy controls. The g-ratio tended to be higher in patients than the controls in all regions, but the difference was not statistically significant.

Correlation between the Regional Values and Cognitive Assessments

Across the 6 regions evaluated, the right PCA area showed the highest number of significant correlations between the MR imaging metrics and cognitive performance. The AVF in the right PCA area was significantly correlated with the Processing Speed Index and TMT-A and -B (Fig 3). The g-ratio in the right PCA area and the left ACA area was positively correlated with the Processing Speed Index (Fig 2 and On-line Table 3; $r = 0.49$, $P = .04$ in left ACA area). In the right MCA area, the MVF and AVF were negatively correlated with the TMT-B scores (On-line Table 2; $r = -0.49$, $P = .04$ and $r = -0.55$, $P = .02$, respectively). No significant correlations were observed between other combinations of the MR imaging metrics and cognitive performance (On-line Table 2).

The details of the methods and results are provided in the On-line Appendix, and the full dataset is available from the corresponding author on reasonable request.

DISCUSSION

Consistent with our hypothesis, we found statistically significant decreases in the MVF and AVF in the patients with MMD compared with healthy controls. Meanwhile, the g-ratio in the patients tended to be higher than that in the controls but was not statistically significant in any region. The significant decrease in the AVF and MVF suggests that concomitant axonal and myelin damage might have buffered the difference in the g-ratio between the patients and controls. This finding is consistent with a previous animal study suggesting that myelin damage precedes axonal damage,[25] and a diffusion MR imaging study showing that myelin damage is more widespread than axonal damage in patients with MMD without an operation.[7] The decrease in the MVF in our patients seems to be more widespread and prominent than the decrease in the AVF; therefore, it is possible that myelin breakdown precedes axonal destruction under chronic ischemic conditions in patients with MMD.

Unexpectedly, we found significant correlations between the MVF or g-ratio values and cognitive performance in only a few areas. A previous study showed that myelin damage in patients with stroke is correlated with motor impairment and function;[26]

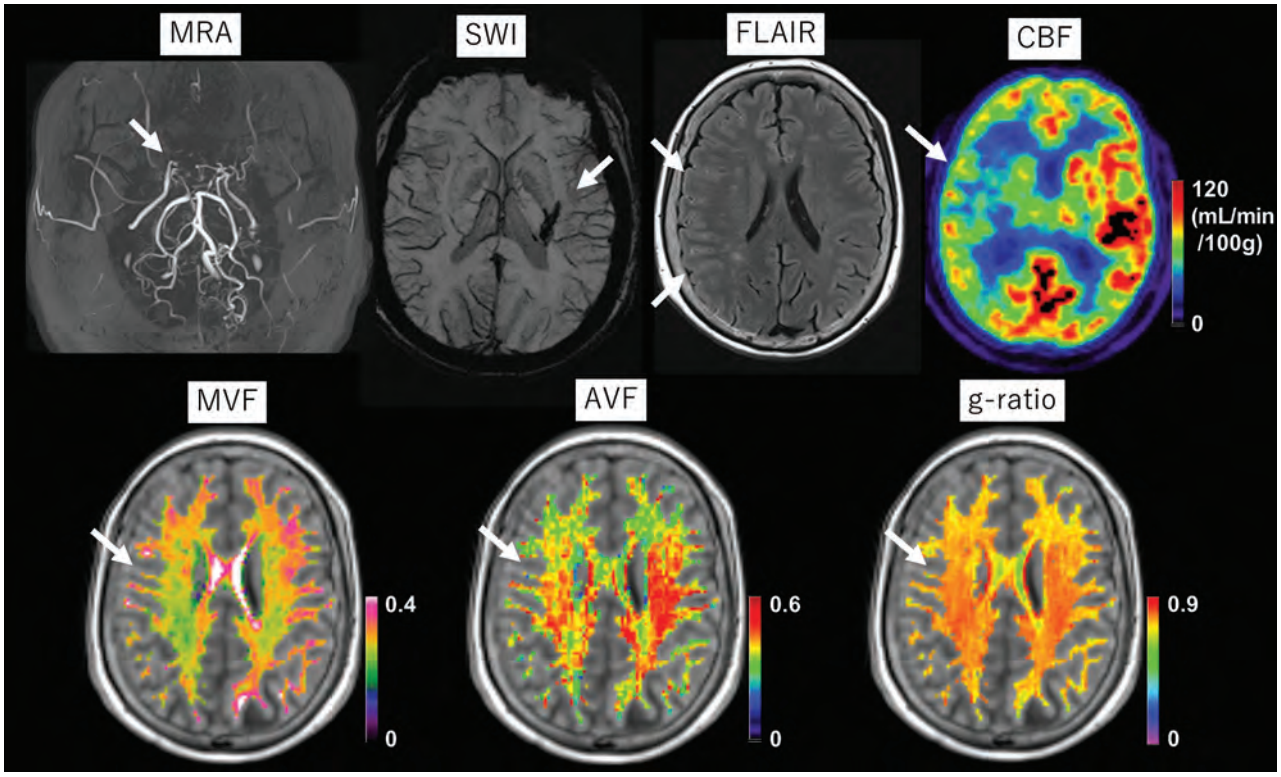

FIG 1. A 55-year-old female patient with MMD who had a history of thalamic hemorrhage >20 years ago (*arrow* on SWI). During the annual follow-up, though she remained asymptomatic, the arterial stenosis on the right side gradually progressed (*arrow* in MRA), and an ivy sign emerged on the right hemisphere (*arrows* on FLAIR). [^{15}O]-gas PET reveals decreased CBF on the right side (*arrow*). The myelin volume fraction and axon volume fraction are visually decreased in the right hemisphere (*arrows*). The right-left difference in the g-ratio (*arrow*) is not as evident as the differences in the MVF and AVF.

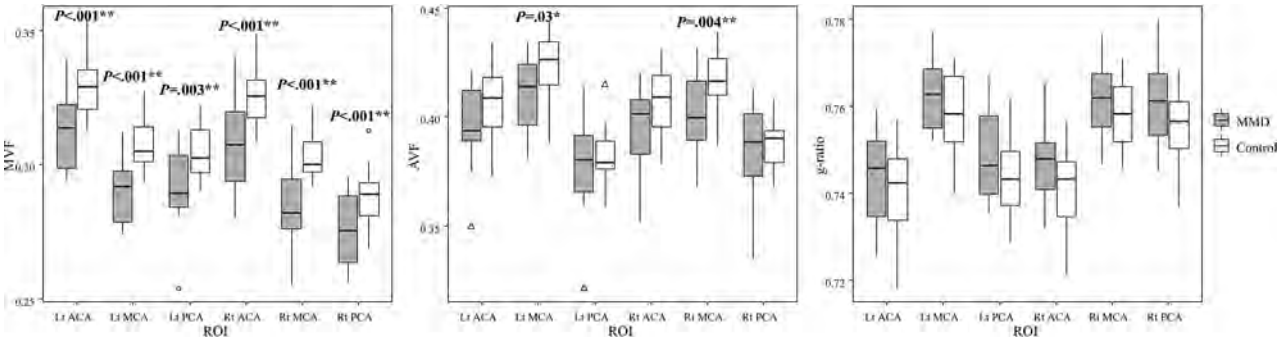

FIG 2. Comparison of the myelin volume fraction, axon volume fraction, and g-ratio between the patients and healthy controls. The *asterisk* indicates $P < .05$; *double asterisks*, $P < .05$ (Bonferroni correction for comparing 3 parameters). Lt indicates left; Rt, right.

therefore, we presumed that myelin damage (decreased MVF and increased g-ratio) in patients with MMD is related to cognitive tasks measuring processing speed that must reflect nerve-conduction velocity.[14] The difference between patients with stroke without MMD and patients with MMD might be partially explained by the fact that ischemic damage in patients with stroke without MMD is sudden and focal, while ischemic damage in patients with MMD is chronic and diffuse.[6,7] Perhaps because of the uniform and widespread decrease in the myelin content, the MVF values showed relatively small variation in patients compared with the AVF values and, thus, did not correlate with various degrees of cognitive performance.

In addition to the few correlations among the MVF, g-ratio, and cognitive performances, the observed correlation between the Processing Speed Index and the g-ratio was positive, a finding inconsistent with our hypothesis. As discussed above, the decrease in the MVF and the increase in the g-ratio might precede the decrease in the AVF and the decrease in the g-ratio.[7,25] Moreover, in patients with MMD, both the cortex and white matter are affected by chronic ischemia,[5–7,27,28] and while direct ischemic damage to white matter might result in more myelin damage than axonal damage, cortical damage must cause both myelin and axonal damage due to the decrease in axonal fibers radiating from the affected cortex. Thus, the presence of axonal

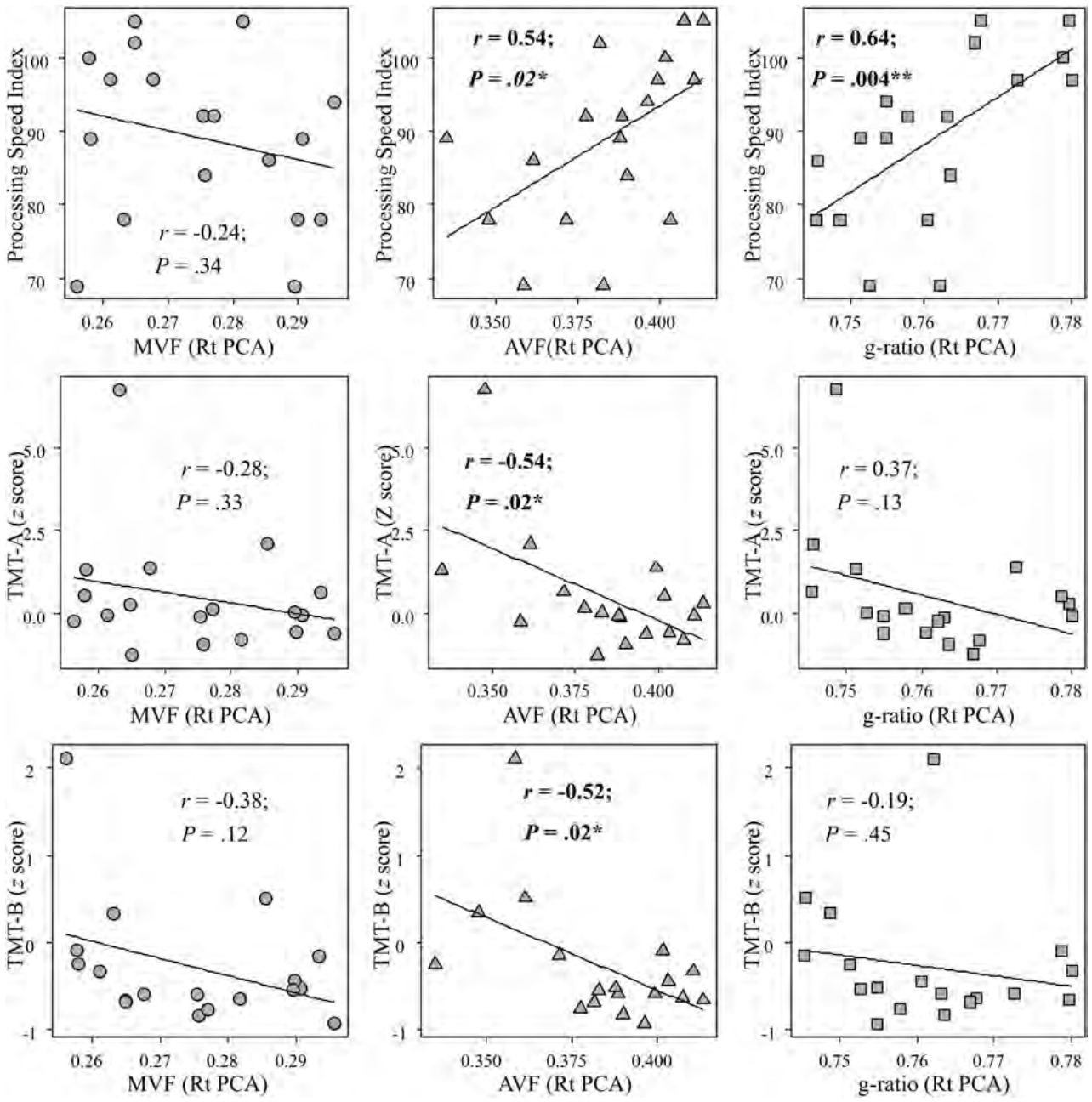

FIG 3. Correlations between cognitive performance and the myelin volume fraction, axon volume fraction, and g-ratio in the right PCA area of patients with Moyamoya disease. *The asterisk* indicates $P < .05$; *double asterisks*, $P < .05$ (Bonferroni correction for comparing 3 parameters).

damage might reflect more global damage than myelin damage in this disease population. This assumption is consistent with the finding that the decrease in the AVF is not as widespread as the decrease in the MVF in our patients. The lack of a correlation with the MVF and the positive correlation with the AVF might lead to the positive correlation between the g-ratio and the Processing Speed Index. The decrease in the AVF causing the increase in the g-ratio might be more critical for cognitive function in patients than the decrease in the MVF causing the increase in the g-ratio, thus resulting in a stronger correlation with the g-ratio and the Processing Speed Index than the AVF.

The strongest correlation between the MR imaging metrics and cognitive performance in the patients with MMD was found in the right PCA area. This finding was unexpected because generally, ischemic damage to the frontal lobe is regarded as the cause of cognitive decline in patients with MMD, and all our patients were right-handed and the dominant hemisphere is supposedly the left side. Regarding laterality, some studies reported that the right side of the brain is related to the cognitive performance of patients with MMD,[29,30] though the reason for laterality is unclear. The laterality of the result might have been affected by our finding that PCA lesions more frequently occurred on the right side than on the left side, though the difference was not statistically significant (On-line Table 1: 9/18 versus 6/18, $P = .28$ by a paired *t* test). Regarding the posterior part of the brain and cognition, some studies have reported a relationship between the

posterior part of the brain and cognitive function in patients with MMD.[6,30] We speculated that the significant correlation only in the PCA area is due to the variation in the ischemic condition and the parametric values in this area, while the ACA and MCA areas were uniformly affected in many patients and had a relatively smaller variation in the parametric values. The nonsignificant correlation among the cognitive tasks measuring working memory, which is regarded as a frontal lobe function, is also consistent with this assumption[27] (On-line Tables 2 and 3).

Although approximately half of the patients in this study were in a postoperative status and clinically stable without symptoms at the time of the study (eg, the patient in Fig 3), the differences in the MVF and AVF between the patients and healthy controls were statistically significant in many regions. These results suggest that ischemic damage to myelin and axons in patients with MMD might be, at least partially, irreversible.[6,27] Postoperative improvements in microstructural integrity evaluated by diffusion MR imaging are reported in patients with MMD[28] and carotid artery stenosis,[31] but whether these observed changes are due to an increase in axon integrity, such as remyelination, or a decrease in interstitial fluid[32] remains unclear. Compared with diffusion MR imaging, which indirectly assesses the presence of myelin damage by evaluating increased water diffusion in the brain parenchyma, the MTsat method has the strength of being directly sensitive to myelin. To clarify whether microstructural damage to myelin and axons is reversible, we are currently conducting a prospective study to re-evaluate preoperative patients 1 year after bypass surgery using the same MR imaging protocol. If microstructural damage is irreversible, surgical revascularization to restore hemodynamic impairments might be required to protect patients from future cognitive dysfunction, even among those without any symptoms.

Limitations of this study include the small sample size and heterogeneous patient backgrounds, and we did not evaluate the cognitive performance of the healthy controls; thus, the results, especially those related to cognitive function, should be considered preliminary. Most of our patients were previously surgically treated; thus, the relationships between the cerebral hemodynamics and microstructural parameters were difficult to assess because many patients showed improved hemodynamic conditions, such as the patient in On-line Fig 2. However, our study revealed that postoperative patients who have improved hemodynamic conditions might still have myelin damage. Because many myelin-specific imaging techniques are available, it is possible that different types of myelin-sensitive imaging might show different results.[33-36] Given the complicated postprocessing, myelin imaging may not be practical for routine application in clinical settings compared with conventional diffusion parameters (On-line Table 2). Despite these limitations, this study is the first to directly investigate myelin damage using a myelin-sensitive MR imaging technique in adult patients with MMD and its relationship with cognitive function. Future studies may further elucidate the consequences and clinical significance of myelin damage in this disease population.

CONCLUSIONS

Using a myelin-sensitive MR imaging technique, we found that myelin damage may exist in patients with MMD. Although preliminary in many aspects, the results suggest that axonal damage might be more critical for cognitive performance than myelin damage in this disease population.

ACKNOWLEDGMENTS

We thank Maki Mukawa and Yaeko Furuhashi for performing the gene analysis and the Department of Radiology of Tokyo Medical Clinic for acquiring MR images.

Disclosures: Shoko Hara—*RELATED*: *Grant*: Grants-in Aid for Scientific Research "KAKENHI" (grant 19K18406), research grant from the Japanese Society for Neuroradiology. Shigeki Aoki—*UNRELATED*: *Board Membership*: Canon, *Comments*: Canon MR Advisory Board; *Grants/Grants Pending*: Medi-Physics, Daiichi Sankyo, Eisai, FUJIFILM Toyama Chemical Co, Guerbet, *Comments*: grant for diagnostic radiology from Medi-Physics, Daiichi Sankyo, Eisai, FUJIFILM Toyama Chemical Co, Guerbet*; *Payment for Lectures Including Service on Speakers Bureaus*: Bayer Yakuhin, Canon, FUJIFILM Toyama Chemical Co, Eisai, Guerbet, GE Healthcare, Medi-Physics, Siemens, Daiichi Sankyo, *Comments*: payment for lectures/Chair from Bayer Yakuhin, Canon, FUJIFILM Toyama Chemical Co, Eisai, Guerbet, GE Healthcare, Medi-Physics, Siemens, Daiichi Sankyo; *Payment for Manuscript Preparation*: MIWA-SHOTEN, Gakken Medical Shujunsha, *Comments*: payment as Journal Editorial Board member of MIWA-SHOTEN, Gakken Medical Shujunsha. *Money paid to the institution.

REFERENCES

1. Farkas E, Luiten PG, Bari F. **Permanent, bilateral common carotid artery occlusion in the rat: a model for chronic cerebral hypoperfusion-related neurodegenerative diseases.** *Brain Res Rev* 2007;54:162–80 CrossRef Medline
2. Kuroda S, Houkin K. **Moyamoya disease: current concepts and future perspectives.** *Lancet Neurol* 2008;7:1056–66 CrossRef Medline
3. Hara S, Tanaka Y, Ueda Y, et al. **Noninvasive evaluation of CBF and perfusion delay of Moyamoya disease using arterial spin-labeling MRI with multiple postlabeling delays: comparison with ^{15}O-gas PET and DSC-MRI.** *AJNR Am J Neuroradiol* 2017;38:696–702 CrossRef Medline
4. Hirai S, Inaji M, Tanaka Y, et al. **Correlation between clinical presentations and hemodynamic parameters measured by dynamic susceptibility contrast magnetic resonance imaging in adult patients with Moyamoya disease.** *J Stroke Cerebrovasc Dis* 2017;26:2814–20 CrossRef Medline
5. Kazumata K, Tha KK, Narita H, et al. **Chronic ischemia alters brain microstructural integrity and cognitive performance in adult Moyamoya disease.** *Stroke* 2015;46:354–60 CrossRef Medline
6. Hara S, Hori M, Murata S, et al. **Microstructural damage in normal-appearing brain parenchyma and neurocognitive dysfunction in adult Moyamoya disease.** *Stroke* 2018;49:2504–07 CrossRef Medline
7. Kazumata K, Tha KK, Narita H, et al. **Characteristics of diffusional kurtosis in chronic ischemia of adult Moyamoya disease: comparing diffusional kurtosis and diffusion tensor imaging.** *AJNR Am J Neuroradiol* 2016;37:1432–39 CrossRef Medline
8. Stikov N, Campbell JS, Stroh T, et al. **In vivo histology of the myelin g-ratio with magnetic resonance imaging.** *Neuroimage* 2015;118:397–405 CrossRef Medline
9. Helms G, Dathe H, Kallenberg K, et al. **High-resolution maps of magnetization transfer with inherent correction for RF inhomogeneity and T1 relaxation obtained from 3D FLASH MRI.** *Magn Reson Med* 2008;60:1396–1407 CrossRef Medline
10. Hori M, Hagiwara A, Fukunaga I, et al. **Application of quantitative microstructural MR imaging with atlas-based analysis for the**

spinal cord in cervical spondylotic myelopathy. *Sci Rep* 2018;8:5213 CrossRef Medline

11. Kamagata K, Zalesky A, Yokoyama K, et al. **MR g-ratio-weighted connectome analysis in patients with multiple sclerosis.** *Sci Rep* 2019;9:13522 CrossRef Medline
12. Hagiwara A, Hori M, Yokoyama K, et al. **Analysis of white matter damage in patients with multiple sclerosis via a novel in vivo MR method for measuring myelin, axons, and g-ratio.** *AJNR Am J Neuroradiol* 2017;38:1934–40 CrossRef Medline
13. Zhang H, Schneider T, Wheeler-Kingshott CA, et al. **NODDI: practical in vivo neurite orientation dispersion and density imaging of the human brain.** *Neuroimage* 2012;61:1000–16 CrossRef Medline
14. Rushton W. **A theory of the effects of fibre size in medullated nerve.** *J Physiol (Lond)* 1951;115:101–22 CrossRef Medline
15. Research Committee on the Pathology and Treatment of Spontaneous Occlusion of the Circle of Willis; Health Labour Sciences Research Grant for Research on Measures for Infractable Diseases. **Guidelines for diagnosis and treatment of Moyamoya disease (spontaneous occlusion of the circle of Willis).** *Neurol Med Chir (Tokyo)* 2012;52:245–66 CrossRef Medline
16. Morrell GR, Schabel MC. **An analysis of the accuracy of magnetic resonance flip angle measurement methods.** *Phys Med Biol* 2010; 55:6157–74 CrossRef Medline
17. Mohammadi S, Carey D, Dick F, et al. **Whole-brain in-vivo measurements of the axonal g-ratio in a group of 37 healthy volunteers.** *Front Neurosci* 2015;9:441 CrossRef Medline
18. Campbell JS, Leppert IR, Narayanan S, et al. **Promise and pitfalls of g-ratio estimation with MRI.** *NeuroImage* 2018;182:80–96 CrossRef Medline
19. Smith SM, Jenkinson M, Woolrich MW, et al. **Advances in functional and structural MR image analysis and implementation as FSL.** *Neuroimage* 2004;23(Suppl 1):S208–19 CrossRef Medline
20. Andersson JL, Skare S, Ashburner J. **How to correct susceptibility distortions in spin-echo echo-planar images: application to diffusion tensor imaging.** *Neuroimage* 2003;20:870–88 CrossRef Medline
21. Jenkinson M, Beckmann CF, Behrens TE, et al. **FSL.** *Neuroimage* 2012;62:782–90 CrossRef Medline
22. Hagiwara A, Kamagata K, Shimoji K, et al. **White matter abnormalities in multiple sclerosis evaluated by quantitative synthetic MRI, diffusion tensor imaging, and neurite orientation dispersion and density imaging.** *AJNR Am J Neuroradiol* 2019;40:1642–48 CrossRef Medline
23. Desikan RS, Segonne F, Fischl B, et al. **An automated labeling system for subdividing the human cerebral cortex on MRI scans into gyral based regions of interest.** *Neuroimage* 2006;31:968–80 CrossRef Medline
24. Mutsaerts H, van Dalen JW, Heijtel DF, et al. **Cerebral perfusion measurements in elderly with hypertension using arterial spin labeling.** *PLoS One* 2015;10:e0133717 CrossRef Medline
25. Kurumatani T, Kudo T, Ikura Y, et al. **White matter changes in the gerbil brain under chronic cerebral hypoperfusion.** *Stroke* 1998;29: 1058–62 CrossRef Medline
26. Lakhani B, Hayward KS, Boyd LA. **Hemispheric asymmetry in myelin after stroke is related to motor impairment and function.** *Neuroimage Clin* 2017;14:344–53 CrossRef Medline
27. Hara S, Hori M, Ueda R, et al. **Unraveling specific brain microstructural damage in Moyamoya disease using diffusion magnetic resonance imaging and positron emission tomography.** *J Stroke Cerebrovasc Dis* 2019;28:1113–25 CrossRef Medline
28. Kazumata K, Tha KK, Tokairin K, et al. **Brain structure, connectivity, and cognitive changes following revascularization surgery in adult Moyamoya disease.** *Neurosurgery* 2019;85:E943–52 CrossRef Medline
29. Roder C, Haas P, Fudali M, et al. **Neuropsychological impairment in adults with moyamoya angiopathy: preoperative assessment and correlation to MRI and H215O PET.** *Neurosurgical Review* 2019 Nov 14. [Epub ahead of print] CrossRef Medline
30. Hosoda C, Nariai T, Ishiwata K, et al. **Correlation between focal brain metabolism and higher brain function in patients with Moyamoya disease.** *Int J Stroke* 2010;5:367–73 CrossRef Medline
31. Sato Y, Ito K, Ogasawara K, et al. **Postoperative increase in cerebral white matter fractional anisotropy on diffusion tensor magnetic resonance imaging is associated with cognitive improvement after uncomplicated carotid endarterectomy: tract-based spatial statistics analysis.** *Neurosurgery* 2013;73:592–98; discussion 598–99 CrossRef Medline
32. Hara S, Hori M, Inaji M, et al. **Regression of white matter hyperintensity after indirect bypass surgery in a patient with Moyamoya disease.** *Magn Reson Med Sci* 2019;18:247–48 CrossRef Medline
33. Duhamel G, Prevost VH, Cayre M, et al. **Validating the sensitivity of inhomogeneous magnetization transfer (ihMT) MRI to myelin with fluorescence microscopy.** *Neuroimage* 2019;199:289–303 CrossRef Medline
34. Maekawa T, Hagiwara A, Hori M, et al. **Effect of gadolinium on the estimation of myelin and brain tissue volumes based on quantitative synthetic MRI.** *AJNR Am J Neuroradiol* 2019;40:231–37 CrossRef Medline
35. Saccenti L, Hagiwara A, Andica C, et al. **Myelin measurement using quantitative magnetic resonance imaging: a correlation study comparing various imaging techniques in patients with multiple sclerosis.** *Cells* 2020;9:393 CrossRef Medline
36. Hagiwara A, Hori M, Kamagata K, et al. **Myelin measurement: comparison between simultaneous tissue relaxometry, magnetization transfer saturation index, and T1w/T2w ratio methods.** *Sci Rep* 2018;8:10554 CrossRef

COVID-19 and Involvement of the Corpus Callosum: Potential Effect of the Cytokine Storm?

C. Rasmussen, I. Niculescu, S. Patel, and A. Krishnan

ABSTRACT

SUMMARY: Neurologic findings are being increasingly recognized in coronavirus disease 2019. We present a patient with a unique involvement of the corpus callosum that we relate to the cytokine storm seen in patients with Severe Acute Respiratory Syndrome coronavirus 2 infection. As the infection is increasingly seen around the world, recognition of these unique patterns may facilitate early identification of the progression of this disease and potentially facilitate appropriate management.

ABBREVIATIONS: COVID-19 = coronavirus disease 2019; SARS-Cov-2 = Severe Acute Respiratory Syndrome coronavirus 2

Since December 2019, coronavirus disease 2019 (COVID-19) caused by Severe Acute Respiratory Syndrome coronavirus 2 (SARS-CoV-2) has spread across the globe, infecting hundreds of thousands of patients. This virus, while known for causing severe respiratory illness, has been reported to affect multiple organ systems, including the central nervous system. Approximately 36% of patients with COVID-19 develop neurologic symptoms such as headache, altered mental status, and paresthesia.[1] Also of note, these neurologic symptoms may be the first signs of illness and appear to affect more severely infected patients.[2] We discuss an adult patient managed in the intensive care unit with unusual imaging findings centered in the corpus callosum and discuss the potential pathophysiology, including the relation to the cytokine storm.

Case Description

A 66-year-old woman with a medical history of pulmonary sarcoidosis, coronary artery disease, type 2 diabetes, hypertension, and hyperlipidemia presented to the emergency department with a 2-day history of fevers, chills, and severe headache with associated blurry vision, which progressed to severe shortness of breath and chest pain. On admission, the patient's labs were remarkable for hyperglycemia, mild normocytic anemia, acute kidney injury, lymphopenia (0.4 bil/L), and elevated C-reactive protein (130 mg/L) and ferritin (630 mg/mL) levels. The patient subsequently tested positive for SARS-CoV-2 from a nasopharyngeal swab and was started on azithromycin and hydroxychloroquine. Eight days after symptom onset, the patient had a rapid decline with increasing respiratory distress requiring intubation and transfer to the intensive care unit. At transfer, D-dimer (1782 ng/mL) and fibrinogen (606 mg/dL) levels were elevated. These markers peaked several days later: D-dimer > 10,000 ng/mL and fibrinogen > 1000 mg/dL. She was also placed on intravenous heparin (therapeutic dosing), given the elevated levels of D-dimer. During the patient's intensive care unit stay, she required hemodialysis for her acute kidney injury, which was thought secondary to the COVID-19 infection. After reduction in sedation on hospital day 19, right-sided weakness was noted and a noncontrast head CT was obtained. This scan demonstrated hypodensities within the left parietotemporal region, as well as a more unusual hypodensity within the corpus callosum (Fig 1).

Despite an overall improvement in the patient's respiratory status, extubation was delayed secondary to decreased mentation. On hospital day 27, an electroencephalography was performed, which demonstrated a triphasic morphology, most consistent with toxic encephalopathy with no evidence of epileptiform discharges. At that time, the patient was lethargic and aphasic with a poor prognosis for functional neurologic recovery. Subsequent noncontrast head CTs demonstrated areas of hemorrhage within the regions of hypodensity seen on the initial scan (Fig 2). The IV heparin was discontinued. The patient's mental status slowly improved with spontaneous eye opening/tracking and movement of the left extremities, though she remained aphasic. Secondary to improved mental status, the patient was eventually extubated.

Received May 29, 2020; accepted after revision June 3.

From the Departments of Diagnostic Radiology and Molecular Imaging (C.R., S.P., A.K.), and Internal Medicine (IN), Beaumont Health, Royal Oak, Michigan; and Oakland University William Beaumont School of Medicine (A.K.), Rochester, Michigan.

Please address correspondence to Anant Krishnan, MD, Department of Diagnostic Radiology and Molecular Imaging, Beaumont Health-Royal Oak, 3601 W. 13 Mile Road, Royal Oak, MI, 48073; e-mail: anant.krishnan@beaumont.edu

Indicates open access to non-subscribers at www.ajnr.org

http://dx.doi.org/10.3174/ajnr.A6680

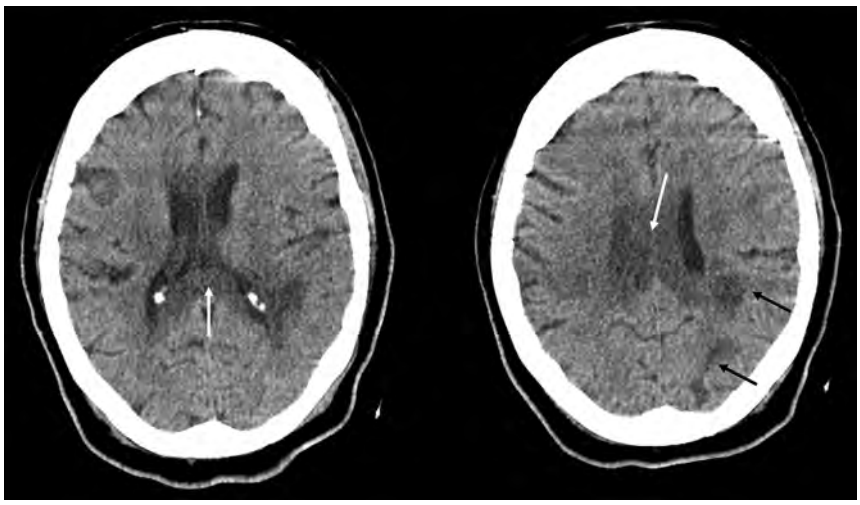

FIG 1. Initial noncontrast head CT images demonstrate hypodensities in the left posterior parietal (*black arrows*) and peritrigonal regions as well as the corpus collosum (*white arrows*). No evidence of hemorrhage, mass effect, or midline shift is seen at this time.

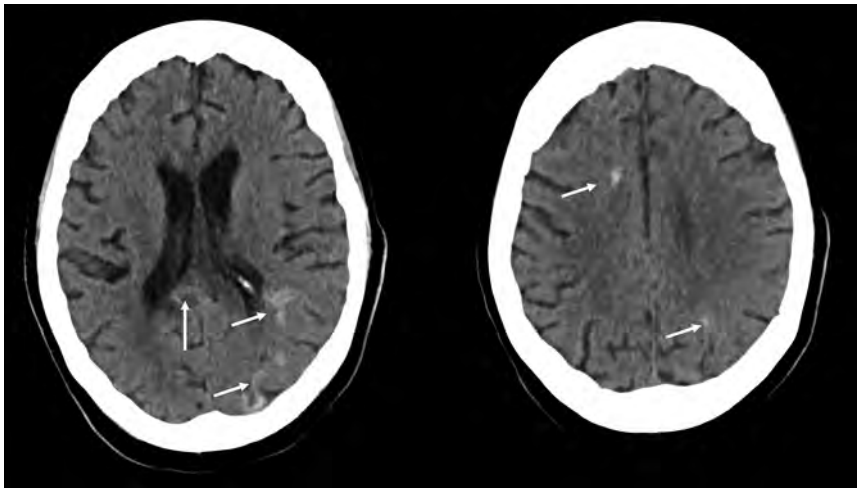

FIG 2. Subsequent head CT demonstrates hemorrhage (*white arrows*) within the previously seen hypodensities. The posterior corpus collosum is involved.

Brain MR imaging obtained on hospital day 36 demonstrated multiple areas of diffusion restriction within the corpus callosum, corona radiata, and centrum semiovale, with associated T2-FLAIR hyperintensities. Multiple areas of microhemorrhage were also detected (Figs 3 and 4). The thalami, brain stem, and cerebellum were spared. At the time of this writing, the patient is receiving continued inpatient treatment.

DISCUSSION

There appear to be multiple mechanisms for SARS-CoV-2 to cause neurologic damage, including direct neuronal injury, hypoxic damage from unresolved respiratory distress, autoimmune injury from the induced cytokine storm with resultant blood-brain barrier breakdown, vasculitis, and acute ischemic injury from a hypercoagulable state.[1-5] A recent case report described acute necrotizing encephalopathy,[4] a condition well-described in children from a multitude of causes.[4,5] In these cases, the predominant findings are located in the thalami, with additional less common locations being the brain stem, cerebral white matter, and cerebellum.[4] In contrast, our patient demonstrated extensive diffusion restriction within the corpus callosum (most severe in the splenium) without involvement of the thalami, brain stem, or cerebellum.

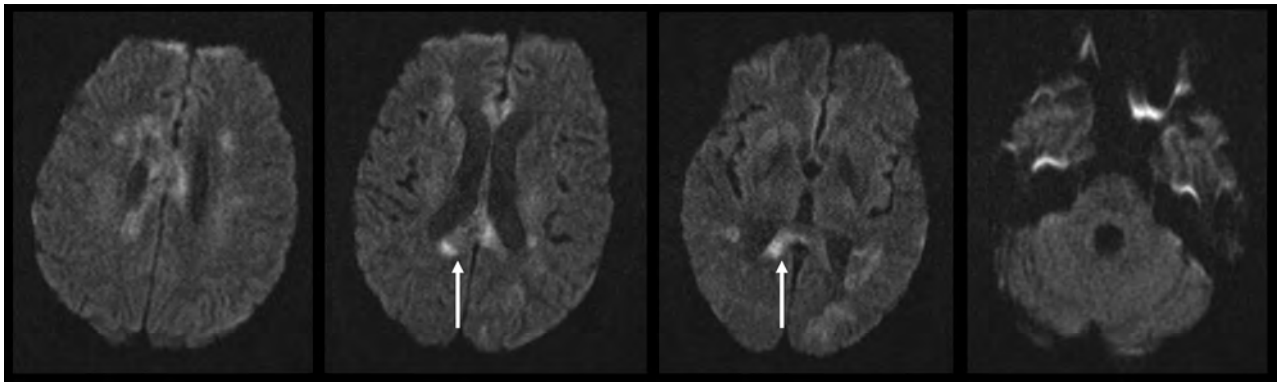

FIG 3. Multiple diffusion-weighted images demonstrate restriction centered in the corpus collosum (*white arrows*), with some additional areas in the adjacent deep white matter including the centrum semiovale. In addition, there is faint diffusion restriction in the left occipital and temporal lobes, possibly representing subacute strokes. The thalami, brain stem, and cerebellum are spared.

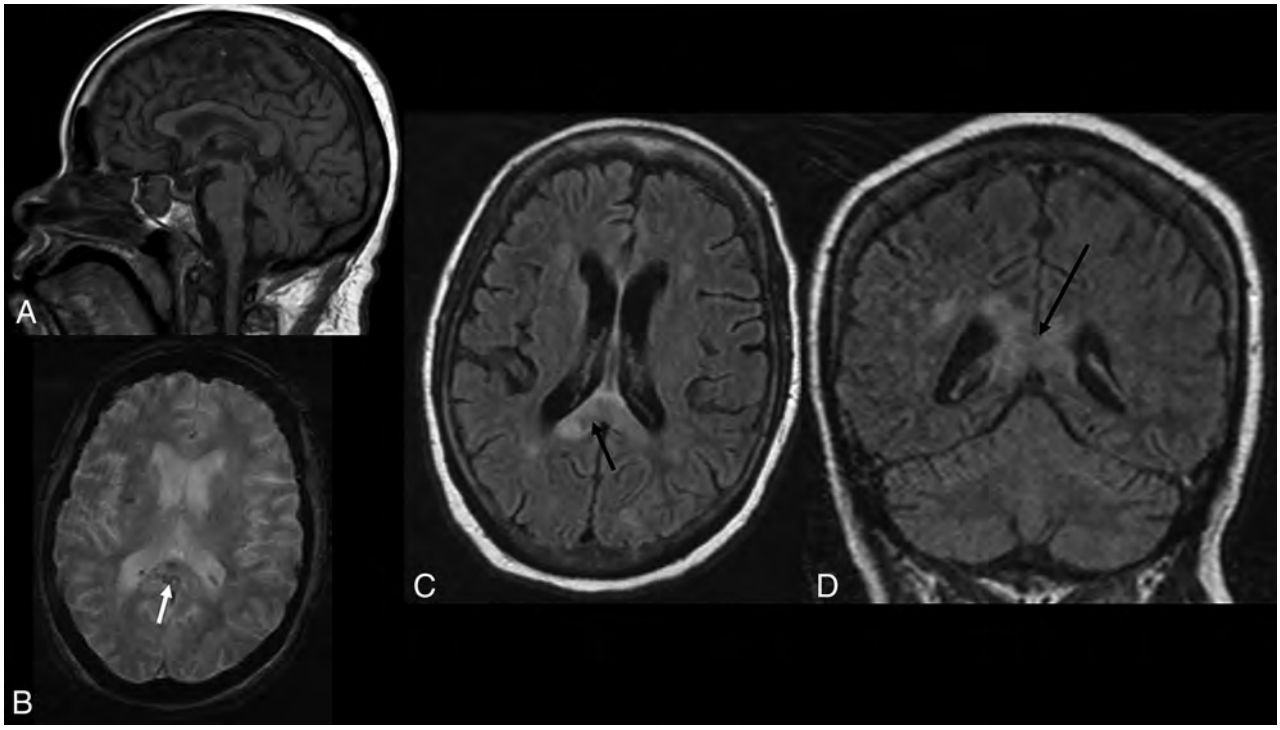

FIG 4. *A*, Sagittal T1. Hypointense signal within the corpus collosum, most prominent in the splenium. *B*, Axial T2* sequence. Multiple punctate hypointensities compatible with hemorrhages are present within the corpus collosum (*white arrow*) and optic radiations, which are not shown. Axial (*C*) and coronal (*D*) T2 FLAIR. Increased T2 signal is seen with the corpus callosum (*black arrows*).

One entity that has a similar appearance is a condition called cytotoxic lesions of the corpus callosum (CLOCC).[6] These have been described with several pathologies, including drug-associated conditions, trauma, malignancy, metabolic disorders, and, most importantly, infection, including several viruses such as adenovirus, H1N1 influenza, Epstein-Barr, and rotavirus.[6] When cytokine release and inflammation are present in sufficient levels within the brain, astrocytes are stimulated to release glutamate as well as block the reuptake of this neurotransmitter.[6-8] The greatly increased amount of glutamate within the extracellular space leads to excitotoxic action on multiple glutamate receptors, sodium-potassium pumps, and aquaporins, resulting in an influx of water trapped within the cells.[6,9-11] These effects manifest on imaging as diffusion restriction, as seen in our patient.[6]

It is believed that the corpus callosum is vulnerable to cytokine-induced injury due to the high density of cytokine, glutamate, and other receptors present within this region of the brain, particularly the splenium.[6,12-17] These previously described mechanisms combined with our patient's extremely elevated markers for acute-phase reactants, suggest initial autoimmune injury from a cytokine storm. With other infectious diseases, the involvement of the corpus callosum is typically transitory; however, in the setting of COVID-19, this has yet to be determined.[6,16] The patient also had ischemic changes in other parts of the brain, and an alternative consideration is a stroke of the corpus callosum. However, the redundant blood supply to the corpus callosum, including the anterior communicating artery, the pericallosal artery, and the posterior pericallosal artery, makes strokes of the corpus callosum rare.[18] The subsequent hemorrhage in these areas is likely multifactorial, with evolution of necrosis from a cytokine storm being a possible contributing factor. While the use of therapeutic-dose heparin was initially shown to improve patient mortality,[19] this medication could also have played a role.

CONCLUSIONS

There is currently limited literature on the neuroimaging findings in COVID-19. To our knowledge, involvement of the corpus callosum related to the cytokine storm has not yet been described with this infection. While as of yet, the transitory nature of this complication is unknown, the authors believe that with continued surveillance, this question is likely to be answered. As management is directed to the cytokine storm, knowledge of this imaging pattern could be invaluable.

Disclosures: Anant Krishnan—*UNRELATED: Expert Testimony: Various.*

REFERENCES

1. Wu Y, Xu X, Chen Z, et. al. **Nervous system involvement after infection with COVID-19 and other coronaviruses.** *Brain Behav Immun.*2020;87:18–22 CrossRef Medline
2. Li YC, Bai WZ, Hashikawa T. **The neuroinvasive potential of SARS-COV-2 may play a role in the respiratory failure of COVID-19 patients.** *J Med Virol.* 2020;92;552–55 CrossRef Medline
3. Chen T, Wu D, Chen H, et al. **Clinical characteristics of 113 deceased patients with coronavirus disease 2019: retrospective study.** *BMJ* 2020;368:m1091 CrossRef Medline

4. Poyiadji N, Shahin G, Noujaim D, et al. **COVID-19-associated acute hemorrhagic necrotizing encephalopathy: CT and MRI features.** *Radiology* 2020 Mar 31. [Epub ahead of print] CrossRef Medline
5. Rossi A. **Imaging of acute disseminated encephalomyelitis.** *Neuroimaging Clin N Am* 2008;18:149–61 CrossRef Medline
6. Starkey J, Kobayashi N, Numaguchi Y, et al. **Cytotoxic lesions of the corpus callosum that show restricted diffusion: mechanisms, causes, and manifestations.** *Radiographics* 2017;37:562–76 CrossRef Medline
7. Miller AH, Haroon E, Raison CL, et al. **Cytokine targets in the brain: impact on neurotransmitter and neurocircuits.** *Depress Anxiety* 2013;30:297–306 CrossRef Medline
8. Phelps C, Korneva E, et al. Neuroimmune biology. *Cytokines and the Brain*. Vol 6. Elsevier; 2008:295–98
9. Leonoudakis D, Braithwaite SP, Beattie MS, et al. **TNFa-induced AMPA-receptor trafficking in CNS neurons: relevance to excitotoxicity?** *Neuron Glia Biol* 2004;1:263–73 CrossRef Medline
10. Prow NA, Irani DN. **The inflammatory cytokine, interleukin-1 beta, mediates loss of astroglial glutamate transport and drives excitotoxic motor neuron injury in the spinal cord during acute viral encephalomyelitis.** *J Neurochem* 2008;105:1276–86 CrossRef Medline
11. Matute C, Alberdi E, Domercq M, et al. **Excitotoxic damage to white matter.** *J Anat* 2007;210:693–702 CrossRef Medline
12. Hassel B, Boldingh KA, Narvesen C, et al. **Glutamate transport, glutamate synthetase and phosphate-activated glutaminase in rat CNS white matter: a quantitative study.** *J Neurochem* 2003;87:230–37 CrossRef Medline
13. Domercq M, Matute C. **Expression of glutamate transporters in adult bovine corpus callosum.** *Brain Res Mol Brain Res* 1999;67:296–302 CrossRef Medline
14. Goursaud S, Kozlova EN, Maloteaux J-M, et al. **Cultured astrocytes derived from corpus callosum or cortical grey matter show distinct glutamate handling properties.** *J Neurochem* 2009;108:1442–52 CrossRef Medline
15. Moritani T, Smoker WR, Sato Y, et al. **Diffusion-weighted imaging of acute excitotoxic brain injury.** *AJNR Am J Neuroradiology* 2005;26:216–28 Medline
16. Takayama H, Kobayashi M, Sugishita M, et al. **Diffusion-weighted imaging demonstrates transient cytotoxic edema involving the corpus callosum in a patient with diffuse brain injury.** *Clin Neurol Neurosurg* 2000;102:135–39 CrossRef Medline
17. Kimura EN, Okamoto S, Uchida Y, et al. **A reversible lesion of the corpus callosum splenium with adult influenza-associated encephalitis/encephalopathy: a case report.** *J Med Case Rep* 2008;2:220 CrossRef Medline
18. Yang LI, Huang YN, Cui ZT. **Clinical features of acute corpus callosum infarction patients.** *Int J Clin Exp Pathol* 2014;7:5160–64 Medline
19. Tang N, Bai H, Chen X, et al. **Anticoagulant treatment is associated with decreased mortality in severe coronavirus disease 2019 patients with coagulopathy.** *J Thromb Haemost* 2020;18:1094–99 CrossRef Medline

MR Susceptibility Imaging with a Short TE (MR-SISET): A Clinically Feasible Technique to Resolve Thalamic Nuclei

S. Chung, P. Storey, T.M. Shepherd, and Y.W. Lui

ABSTRACT

SUMMARY: The thalamus consists of several functionally distinct nuclei, some of which serve as targets for functional neurosurgery. Visualization of such nuclei is a major challenge due to their low signal contrast on conventional imaging. We introduce MR susceptibility imaging with a short TE, leveraging susceptibility differences among thalamic nuclei, to automatically delineate 15 thalamic subregions. The technique has the potential to enable direct targeting of thalamic nuclei for functional neurosurgical guidance.

ABBREVIATIONS: MR-SISET = MR susceptibility imaging with a short TE; STh = subthalmic; CM = centromedian

The thalamus plays a critical role as a central relay hub and comprises functionally specific nuclei. However, it appears relatively homogeneous in structure on conventional imaging (Fig 1*A*). This appearance limits the ability of physicians to accurately target specific nuclei in functional neurosurgical therapies, such as the ventral intermediate/lateral and subthalamic (STh) nuclei for the treatment of essential tremor and tremor-dominant Parkinson disease[1] and the centromedian (CM) nucleus for the treatment of refractory epilepsy[2] and Tourette syndrome.[3] Neurosurgical outcome is critically dependent on accurate targeting; however, current clinical practice relies on indirect localization based on standard coordinates because there is no reliable, noninvasive means currently available to resolve individual nuclei. Indirect targeting is suboptimal due to anatomic variation across individuals, which may lead to inaccurate targeting with potential implications for clinical outcome. Histology-based atlases may improve accuracy[4] but are subject to limitations such as the typically small number of subjects on which they are based and registration errors when mapping from atlas to patient. DTI tractography techniques aimed at delineating thalamic nuclei are problematic when white matter tracts are difficult to track.[5]

The thalamus is a deep gray matter structure that contains a considerable amount of WM. In the thalamus, iron content, degree of WM myelination,[6] and WM fiber orientation[7] may all contribute to susceptibility differences within the structure. There are recent reports showing the potential of susceptibility imaging for delineating thalamic nuclei at 7T;[8,9] however, clinically practical protocols at 3T are lacking. Here, we introduce a novel method, leveraging short TEs, termed MR susceptibility imaging with a short TE (MR-SISET), to bring out differences in contrast among thalamic nuclei and provide an automated method to delineate the intrathalamic subregions using K-means clustering.

Technique

The study was approved by the local institutional review board, and all subjects provided informed consent. Ten healthy controls were included in the study spanning a broad age range (23–65 years of age; 3 men) to assess intersubject variation due to age-related myelination changes. MR-SISET was performed on 3T MR imaging scanners (Magnetom Skyra/Prisma [6/4 subjects]; Siemens) using a 3D multiecho gradient-echo sequence: FOV = 220 × 170 × 75 mm^3, matrix = 176 × 136 × 60, 1.25-mm isotropic resolution, flip angle = 22°, TR = 92 ms, 20 multiple TE = 1.90–45.98 ms with echo spacing of 2.32 ms, bandwidth = 840 Hz/pixel. MR-SISET maps were generated using the MEDI toolbox[10] with a relatively high regularization parameter ($\lambda = 2000$) related to data fidelity and sharpness to optimize image contrast. Automatic delineation was performed using a K-means algorithm

Received November 13, 2019; accepted after revision May 11, 2020.

From the Center for Advanced Imaging Innovation and Research (CAI2R), and Bernard and Irene Schwartz Center for Biomedical Imaging, Department of Radiology, New York University Grossman School of Medicine, New York, New York.

This work was supported by the National Institutes of Health R01 NS039135-11, R21 NS090349, P41 EB017183; and the Leon Lowenstein Foundation.

Please address correspondence to Sohae Chung, PhD, 660 1st Ave, 4th floor, NY, NY10016; e-mail: sohae.chung@nyulangone.org

Indicates open access to non-subscribers at www.ajnr.org
Indicates article with supplemental on-line table.
Indicates article with supplemental on-line photo.
http://dx.doi.org/10.3174/ajnr.A6683

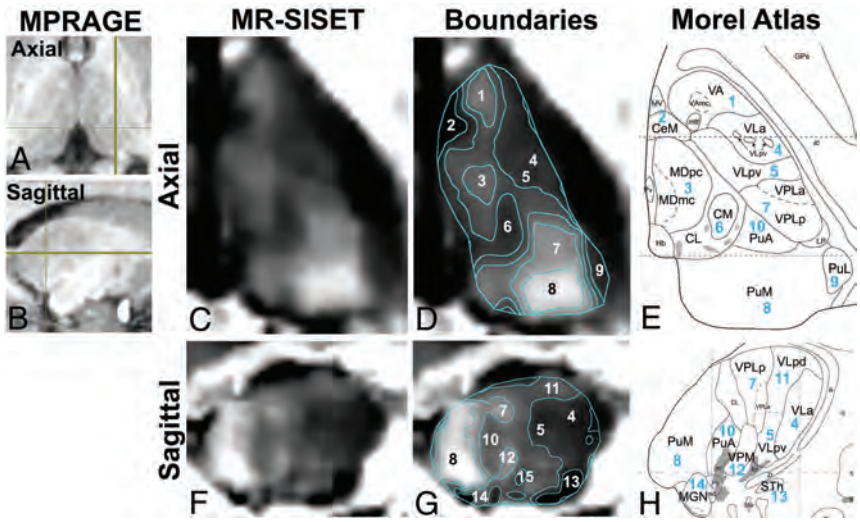

FIG 1. MPRAGE images are shown in the axial (*A*) and sagittal planes (*B*), indicating section location. Axial images: *C*, MR-SISET map. *D*, Boundaries of 15 thalamic nuclei derived from K-means clustering. *E*, Corresponding Morel atlas labels are shown. *F–H*, Sagittal images (1-VA, 2-CeM, 3-MD, 4-VLa, 5-VLpv, 6-CM, 7-VPL, 8-PuM, 9-PuL, 10-PuA, 11-VLpd, 12-VPM, 13-STh, 14-MGN, 15-VM (not shown in *H*). Reprinted with permission from Morel, 2007.[6]

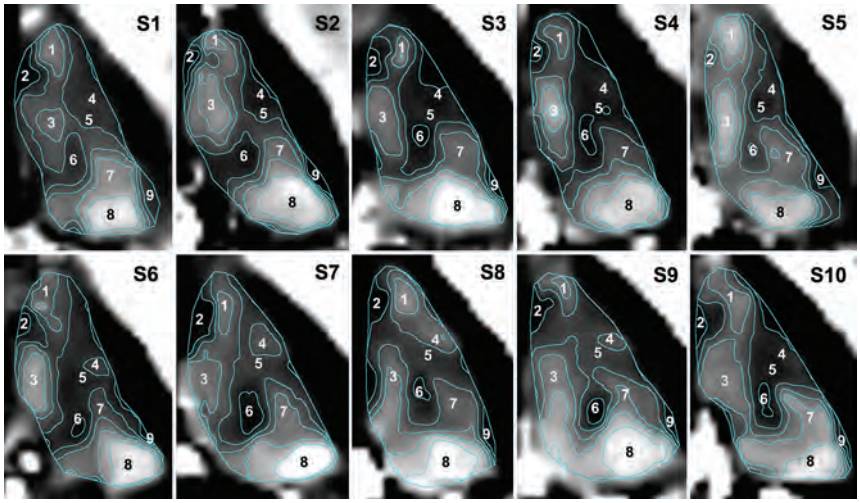

FIG 2. MR-SISET maps with corresponding boundaries for all 10 subjects, showing clear similarities between subjects with several subregions that were consistently segmented. S indicates subject.

with 6 different intensity clusters (Matlab R2019b; MathWorks). Subregions were visually inspected and compared against known thalamic nuclei as delineated in the Morel atlas.[4] Susceptibility contrast relative to that of the CM nucleus was calculated for each subregion.

RESULTS

MR-SISET maps showed clear internal heterogeneity with 15 distinct nuclei showing a high degree of signal contrast with neighboring nuclei (Fig 1). There were clear similarities between subjects with several subregions that were consistently segmented and appeared to correspond to the following thalamic nuclei on the Morel atlas (Fig 2 and On-line Figure): CM (1), central medial (CeM, 0.92 ± 0.08), lateral pulvinar (PuL, 0.87 ± 0.09), STh (0.62 ± 0.17), and ventral medial (VM 0.95 ± 0.08) regions were consistently darker than their neighbors, while ventral anterior (VA, 1.32 ± 0.09), mediodorsal (MD, 1.41 ± 0.2), ventral posterior lateral (VPL, 1.29 ± 0.11), ventral posterior medial (VPM, 1.29 ± 0.13), and medial pulvinar (PuM, 1.79 ± 0.31) regions were brighter than their surroundings (contrast ratios are shown in parentheses). The ventral lateral anterior (VLa, 1.10 ± 0.1) and ventral lateral posterior, ventral division (VLpv, 1.04 ± 0.06) regions were not easily separable. The anterior pulvinar (PuA, 1.17 ± 0.13), ventral lateral posterior, dorsal division (VLpd, 1.17 ± 0.15), and medial geniculate (MGN, 1.18 ± 0.19) regions had similar contrast. The terms are defined and contrast ratios are summarized in the On-line Table.

DISCUSSION

MR-SISET delineates 15 distinct thalamic subregions at 3T, as a result of a greater sensitivity to myelin content and WM packing geometry, supported by previous works.[11] A limitation of this study is the lack of ground truth. Instead, indirect comparisons have been performed against the Morel atlas, which is based on histology, though from a small number of subjects. The regions segmented using MR-SISET do appear to correspond well to nuclei delineated in the Morel atlas. Further work is warranted in patients with relevant pathology to assess the potential utility in patients undergoing functional neurosurgery.

CONCLUSIONS

MR-SISET enables subject-specific delineation of intrathalamic structures. Thus far, magnetic susceptibility–based techniques have not been widely exploited for resolving intrathalamic structures, particularly at 3T. Our preliminary results suggest that MR-SISET has the potential to aid in more personalized, direct visualization of thalamic nuclei for functional neurosurgery.

Disclosures: Sohae Chung—*RELATED*: *Grant*: National Institutes of Health R01 NS039135-11, R21 NS090349, P41 EB017183.* Pippa Storey—*RELATED*: *Grant*: National

Institutes of Health.* Timothy M. Shepherd—*UNRELATED*: *Stock/Stock Options*: Microstructure Imaging, *Comments*: founder and equity for startup, no money has been paid to me or my institution. Yvonne W. Lui—*RELATED*: *Grant*: National Institutes of Health*; *UNRELATED*: *Grants/Grants Pending*: Leon Lowenstein Foundation, Department of Defense.* *Money paid to the institution.

REFERENCES

1. Benabid AL, Pollak P, Gervason C, et al. **Long-term suppression of tremor by chronic stimulation of the ventral intermediate thalamic nucleus.** *Lancet* 1991;337:403–06 CrossRef Medline
2. Son BC, Shon YM, Choi JG, et al. **Clinical outcome of patients with deep brain stimulation of the centromedian thalamic nucleus for refractory epilepsy and location of the active contacts.** *Stereotact Funct Neurosurg* 2016;94:187–97 CrossRef Medline
3. Vandewalle V, van der Linden C, Groenewegen HJ, et al. **Stereotactic treatment of Gilles de la Tourette syndrome by high frequency stimulation of thalamus.** *Lancet* 1999;353:724 CrossRef Medline
4. Morel A, Magnin M, Jeanmonod D. **Multiarchitectonic and stereotactic atlas of the human thalamus.** *J Comp Neurol* 1997;387:588–630 CrossRef Medline
5. Sammartino F, Krishna V, King NK, et al. **Tractography-based ventral intermediate nucleus targeting: novel methodology and intraoperative validation.** *Mov Disord* 2016;31:1217–25 CrossRef
6. Morel A. *Stereotactic Atlas of the Human Thalamus and Basal Ganglia*. Informa Healthcare; 2007:13–53
7. Lancione M, Tosetti M, Donatelli G, et al. **The impact of white matter fiber orientation in single-acquisition quantitative susceptibility mapping.** *NMR Biomed* 2017;30:10.1002/nbm.3798 CrossRef Medline
8. Abosch A, Yacoub E, Ugurbil K, et al. **An assessment of current brain targets for deep brain stimulation surgery with susceptibility-weighted imaging at 7 Tesla.** *Neurosurgery* 2010;67:1745–56; discussion 1756 CrossRef Medline
9. Deistung A, Schafer A, Schweser F, et al. **Toward in vivo histology: a comparison of quantitative susceptibility mapping (QSM) with magnitude-, phase-, and R2*-imaging at ultra-high magnetic field strength.** *Neuroimage* 2013;65:299–314 CrossRef Medline
10. Liu T, Xu W, Spincemaille P, et al. **Accuracy of the morphology enabled dipole inversion (MEDI) algorithm for quantitative susceptibility mapping in MRI.** *IEEE Trans Med Imaging* 2012;31:816–24 CrossRef Medline
11. Sood S, Urriola J, Reutens D, et al. **Echo time-dependent quantitative susceptibility mapping contains information on tissue properties.** *Magn Reson Med* 2017;77:1946–58 CrossRef Medline

Neurovascular Complications in COVID-19 Infection: Case Series

A.M. Franceschi, R. Arora, R. Wilson, L. Giliberto, R.B. Libman, and M. Castillo

ABSTRACT

SUMMARY: We present a series of 10 hospitalized patients with confirmed coronavirus 2019 infections who developed severe neurovascular complications and discuss the possible reasons for these findings and their relationship to the novel Severe Acute Respiratory Syndrome coronavirus 2 infection.

ABBREVIATIONS: ACE2 = angiotensin-converting enzyme 2; COVID-19 = coronavirus 2019; CRP = C-reactive protein; CSS = cytokine storm syndrome; ICU = intensive care unit; LDH = lactate dehydrogenase; PCR = polymerase chain reaction; SARS-CoV-2 = Severe Acute Respiratory Syndrome coronavirus 2

Coronavirus disease 2019 (COVID-19) is a predominantly acute respiratory disease caused by the novel Severe Acute Respiratory Syndrome coronavirus 2 (SARS-CoV-2).[1] In addition to progressive atypical respiratory system distress, other organ systems including the CNS may be affected in part due to the marked affinity of the virus for the angiotensin-converting enzyme 2 (ACE2) receptors.[2,3] Furthermore, a subgroup of patients with severe COVID-19 develop cytokine storm syndrome (CSS), characterized by hyperinflammation due to rapid accumulation of T-cells and macrophages, resulting in the release of massive levels of cytokines into the bloodstream to eliminate the offending pathogen, causing numerous clinical manifestations including atypical respiratory system distress and fever, progressing to widespread multiorgan dysfunction.[4-7]

An increasingly recognized feature of COVID-19 infection is a thromboembolic diathesis, often resulting in brain ischemia, even in young patients despite anticoagulation/antiplatelet treatment. The comorbidity of pneumonia and thromboembolic complications in patients with COVID-19 may be explained, in part, by a causal relationship of severe inflammation and infection as precipitating factors.[6-8]

Here, we present the neurovascular complications in 10 hospitalized patients with COVID-19 infection at our institutions. Available neuroimaging studies including head CT, head and neck CTA, and brain MR imaging were reviewed.

Case Reports

Patient 1. A 59-year-old woman with a medical history of hypertension and morbid obesity was admitted with hypoxic respiratory failure requiring mechanical ventilation.

Initially, she experienced cough but no fever and went to an emergency department and was advised to get a head CT but left against medical advice. She drove to a different state and developed weakness and difficulty moving her legs, increased thirst, and dyspnea. She presented to our emergency department with acute hypoxic respiratory failure, fever, acute renal failure, and bilateral lung opacities on chest x-ray. She tested positive for COVID-19 by polymerase chain reaction (PCR) and was subsequently intubated and transferred to the intensive care unit (ICU), where she developed septic shock and labile blood pressures. Laboratory values included elevated D-dimer, lactate dehydrogenase (LDH), C-reactive protein (CRP), and ferritin levels, suggesting CSS. Chest CT demonstrated diffusely scattered ground-glass opacities in the nondependent lung with consolidation in the dependent lung parenchyma compatible with atypical respiratory system distress in the setting of COVID-19 infection. She developed a sudden right hemineglect, and head CT demonstrated focal low attenuation in the left posterior frontal/anterior parietal lobes consistent with an infarction (Fig 1). The patient did not improve and died 21 days following admission.

Patient 2. A 37-year-old man with a history of hypertension and morbid obesity presented to an outside hospital with fever and difficulty breathing, initially attributed to influenza. PCR testing

Received May 4, 2020; accepted after revision May 22.

From the Neuroradiology Section (A.M.F.), Departments of Radiology and Neurology (R.A., L.G., R.B.L.), Donald and Barbara Zucker School of Medicine at Hofstra/Northwell Health, Manhasset, New York; and Neuroradiology Section (R.W., M.C.), Department of Radiology, The University of North Carolina School of Medicine, Chapel Hill, North Carolina.

Please address correspondence to Ana M. Franceschi, MD, Department of Radiology, 300 Community Dr, Manhasset, NY, 11030-3816; e-mail: afranceschi@northwell.edu

Indicates open access to non-subscribers at www.ajnr.org

http://dx.doi.org/10.3174/ajnr.A6655

was performed and was positive for COVID-19, and he was admitted for medical care.

He developed acute renal failure and required mechanical ventilation with increasingly difficult oxygenation. Laboratory findings were supportive of CSS with elevated D-dimer, LDH, CRP, and ferritin levels. Chest CT revealed diffusely scattered consolidative and ground-glass opacities in the nondependent lung and consolidations in the dependent lung consistent with atypical infection and atypical respiratory system distress. After weaning from sedatives and paralytics, he was unresponsive for several hours and again was transferred to the ICU where he was noted to have no movement of the extremities and dilated, fixed pupils. Noncontrast CT of the head showed intra-axial hemorrhages in the cerebellar hemispheres and diffuse cerebral edema (Fig 2). A neurologist confirmed brain death.

FIG 1. Axial noncontrast head CT demonstrates focal low attenuation in the left posterior frontal/anterior parietal lobes in the region consistent with an acute infarction.

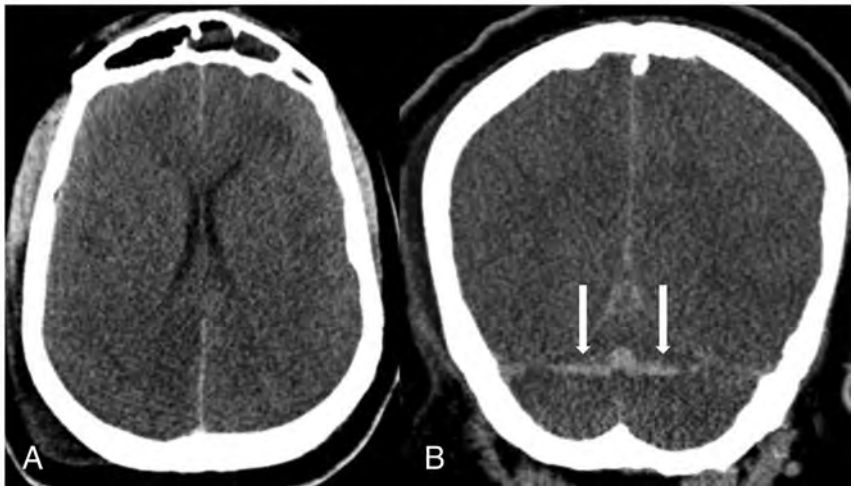

FIG 2. Axial (*A*) and coronal (*B*) noncontrast CT demonstrates diffuse cerebral edema. There are horizontally oriented intra-axial hemorrhages (*arrows*) in the cerebellar hemispheres on the coronal view.

Patient 3. A 33-year-old man with no relevant medical history presented following 12 days of self-treatment with acetaminophen for respiratory symptoms. On the day of admission, he developed sudden-onset left-sided weakness and numbness. PCR testing was positive for COVID-19, and he was admitted.

Chest CT revealed diffuse consolidative and ground-glass opacities bilaterally. Laboratory values were concerning for sepsis (lactate, 9.9 mm/L; CRP, 312 mg/L) and coagulopathy (D-dimer, >50,000 ng/mL; ferritin, 1636 ng/mL). He developed septic shock requiring vasopressor support. He was found to be in severe acute hypoxic respiratory failure (O_2 saturation, 11%), was intubated, and was noted to have a right forced-gaze deviation and left hemiparesis. He was treated with IV tPA for suspected acute right MCA infarction and placed on extracorporeal membrane oxygenation. Head CT demonstrated subacute infarctions in the right frontal, right parietal, and right parieto-occipital regions with edema and mass effect resulting in subfalcine herniation and an associated small hemorrhage in the right parietal region (Fig 3). CTA of the head and neck demonstrated no major vessel narrowing or occlusion. The patient remains in the neurologic ICU while on argatroban (direct thrombin inhibitor) drip and a 3% hypertonic saline drip for cerebral edema.

Patient 4. A 71-year-old man with diabetes mellitus type 2, hyperlipidemia, and hypertension presented with altered mental status and 2 days of fever and cough. Due to exposure to COVID-19 from a family member, he was tested and was positive for the disease.

Laboratory results showed hypoglycemia and acute renal failure. Noncontrast head CT and CTA findings were unremarkable. MR imaging of the brain showed no acute findings. He remained stable the first week and underwent a course of hydroxychloroquine and an interleukin-2 receptor antagonist with improvement in his respiratory status. On hospital day 8, he developed acute encephalopathy and respiratory failure and was intubated. His D–dimer level spiked to 31,000 ng/mL, and chest x-ray showed bilateral multifocal pneumonia and pulmonary edema. Noncontrast head CT was performed and demonstrated a large left MCA infarction with evolving low attenuation in the left frontal, parietal, and temporal lobes extending to the left basal ganglia (Fig 4). He subsequently developed multiorgan failure and died.

Patient 5. A 40-year-old man with recently diagnosed diabetes mellitus, hypertension, and hyperlipidemia with a PCR positive for COVID-19 was discharged on supportive treatment after a brief hospital stay for a cough.

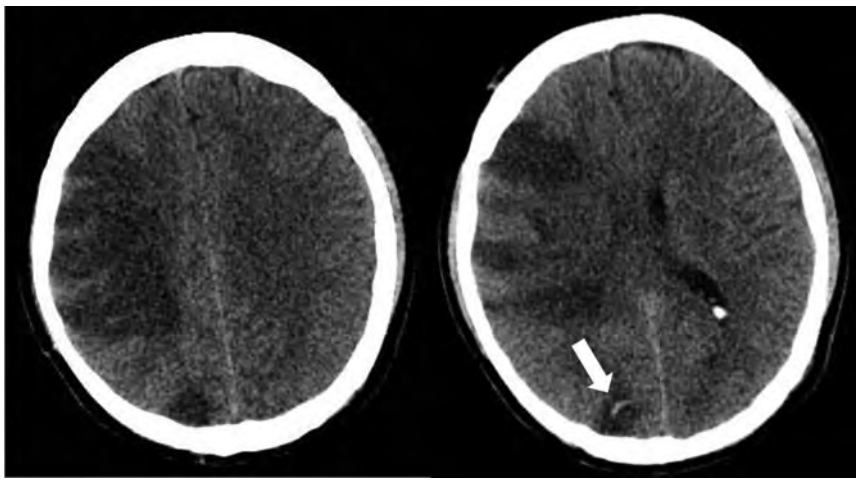

FIG 3. Axial noncontrast CT demonstrates acute infarctions in the right frontal and parietal regions. There is a subcentimeter hemorrhage (*arrow*) in the right parietal region.

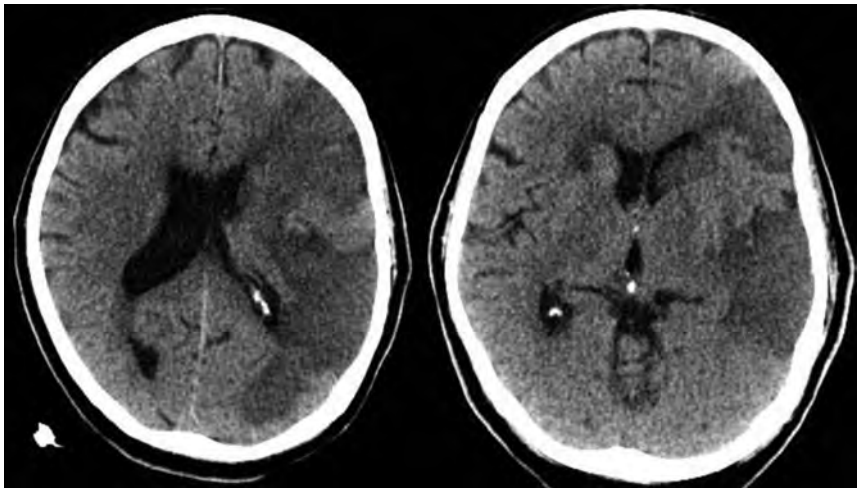

FIG 4. Axial noncontrast CT demonstrates acute infarctions in the left frontal, parietal, and temporal lobes extending to the left basal ganglia and insular cortex, with additional small infarcts in the right anterior limb of the internal capsule and right frontal subcortical white matter.

Thereafter, he developed altered mental status, bilateral loss of vision, and headache. Laboratory results were notable for lymphocytosis and 1% bands, hemoglobin and platelets elevated at 17.6 g/dL and 762,000 respectively, international normalized ratio elevated at 1.39, and fibrinogen level elevated at 902. His D-dimer level was elevated at 3115 ng/mL, with the following values: lactate, 7.5 mm/L; blood urea nitrogen/creatinine, 13 mg/dL/1.37 mg/dL (baseline creatinine, 0.8 mg/dL); aspartate transaminase, slightly elevated at 56 u/L; alanine aminotransferase, normal at 67u/L; and LDH, elevated at 577u/L. He developed a presumed CSS and was intubated and moved to the ICU. Noncontrast head CT showed low attenuation in the parietal and temporal lobes compatible with acute infarcts (Fig 5*A*). A head CT venogram showed occlusion of the right internal carotid artery extending to the supraclinoid segment where there was reconstitution of flow through collaterals (Fig 5*B*). CTA of the neck demonstrated filling defects in the distal common carotid arteries extending to the bulbs and external carotid arteries (Fig 5*C*). There was occlusion of the right internal carotid artery at the C2 level. CT venogram findings were normal.

The patient remains in critical condition in the ICU on full-dose anticoagulation without improvement in his neurologic status.

FIG 5. Noncontrast CT (*A*) demonstrates low attenuation in the parietal and temporal lobes compatible with acute infarctions. Head CTV (*B*) demonstrates occlusion of the cavernous segment of the right internal carotid artery (*arrow*). Neck CTA (*C* and *D*) shows extensive intraluminal thrombi (*arrows*) in the distal common carotid arteries, extending to the carotid bulbs and external carotid arteries.

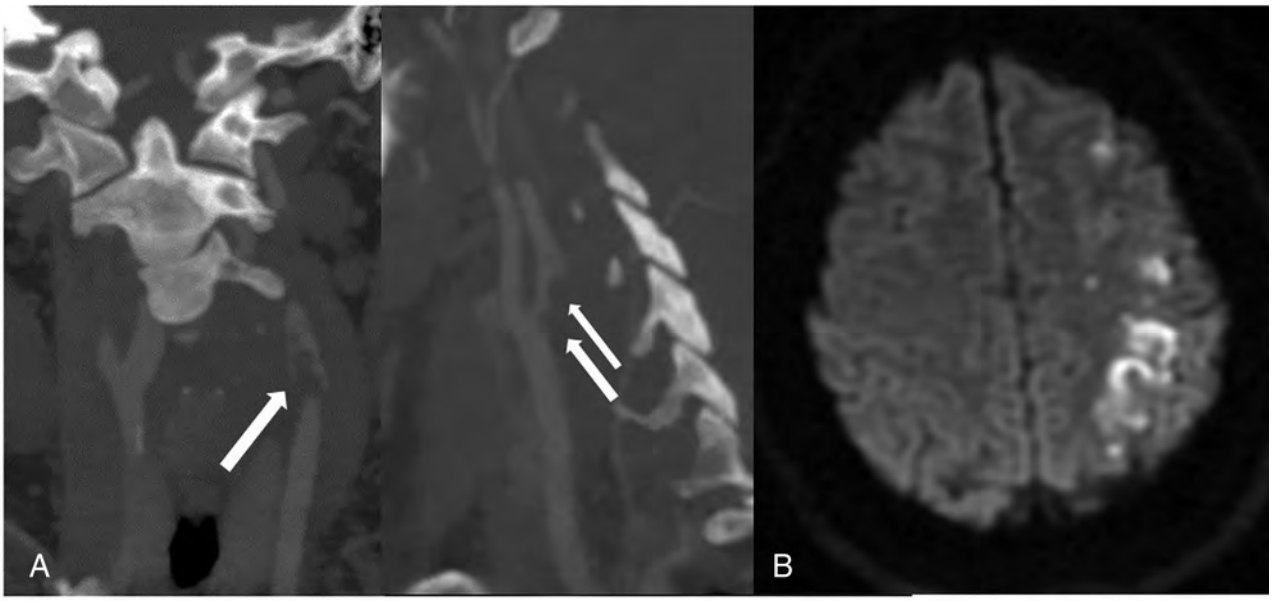

FIG 6. Coronal and sagittal neck CTA (*A*) demonstrates nonocclusive intraluminal thrombus (*arrows*) extending from the left common carotid artery to the proximal internal carotid artery. Axial DWI (*B*) demonstrates acute infarcts in the left frontal and parietal regions.

Patient 6. A 37-year-old woman with a medical history of morbid obesity presented with right upper extremity weakness, slurred speech, and headaches. She reported chest congestion for 1 week prior, and a subsequently obtained PCR was positive for COVID-19. She was admitted for hypoxic respiratory failure, but mechanical ventilation was not required. Laboratory values including D-dimer levels were within normal limits. Hypercoagulable work-up revealed a weakly positive immunoglobulin M anticardiolipin antibody with negative findings on a dilute Russell viper venom time screen.

Noncontrast head CT and neck CTA showed intraluminal thrombus extending from the left common carotid artery into the proximal internal carotid artery (Fig 6*A*). Brain MR imaging revealed areas of restricted diffusion in the left frontal and parieto-occipital regions consistent with acute infarctions (Fig 6*B*). She remained hemodynamically stable throughout her hospital stay and was discharged on full-dose anticoagulation.

Patient 7. A 71-year-old man with a medical history of asthma, hypertension, and atrial fibrillation presented with fever, shortness of breath, and dry cough for 10 days, followed by a syncopal episode. PCR for COVID-19 was positive.

Chest CT revealed bilateral linear and ground-glass opacities with a peripheral predominance. Abnormal laboratory values included CRP, 25 mg/L; LDH, 474 mm/L; and serum ferritin, 602 ng/mL. He developed acute respiratory failure with hypoxia despite O_2 supplementation and was intubated. He was enrolled in an anti-interleukin 6 antibody treatment study and also received hydroxychloroquine and a course of methylprednisolone, resulting in improvement in his respiratory status. He was extubated, after which he was noted to be encephalopathic. Head CT revealed focal low attenuation in the right centrum semiovale and right frontal subcortical region, suggestive of infarctions (Fig 7*A*, -*B*). Brain MR imaging demonstrated acute and subacute infarcts in the frontal lobes (right greater than left), bilateral centrum semiovale, right corona radiata, occipital lobes, and left cerebellar hemisphere (Fig 7*C*-7*E*). Concurrently performed MRA of the head and neck demonstrated no major vessel narrowing or occlusion. He remains in the ICU and is able to follow simple commands.

Patient 8. A 62-year-old woman with morbid obesity, diabetes mellitus type 2, hypertension, and hyperlipidemia presented with cough and fever and an outside chest CT with bilateral ground-glass opacities in a posterior and peripheral distribution.

PCR for COVID-19 was twice negative. Laboratory values were significant for elevated CRP, ferritin, and LDH, suggestive of CSS. Her D-dimer level was 12,000 ng/mL. The patient's oxygenation deteriorated, and she was intubated.

Ten days later, she developed altered mental status, and a head CT demonstrated low attenuation in the left occipital lobe (Fig 8*A*). Neck and head CTA findings were unremarkable. MR imaging showed restricted diffusion in the left occipital and parietal lobes. Pial enhancement was noted overlying the left occipital infarct as well as diffuse dural enhancement. SWI showed numerous microhemorrhages in the cerebral hemispheres, left cerebellum, and left occipital lobe (Fig 8*B*-8*E*). She ultimately tested PCR-positive for COVID-19. Her respiratory status improved, and she was extubated. She was maintained on full-dose anticoagulation with enoxaparin and was discharged to a rehabilitation facility.

Patient 9. A 73-year-old man with no significant medical history presented with fever and nonproductive cough for 1 week. Given the local high-prevalence region, a PCR for COVID-19 was performed and was positive. Admission chest x-ray demonstrated bilateral lung opacities. Abnormal laboratory results

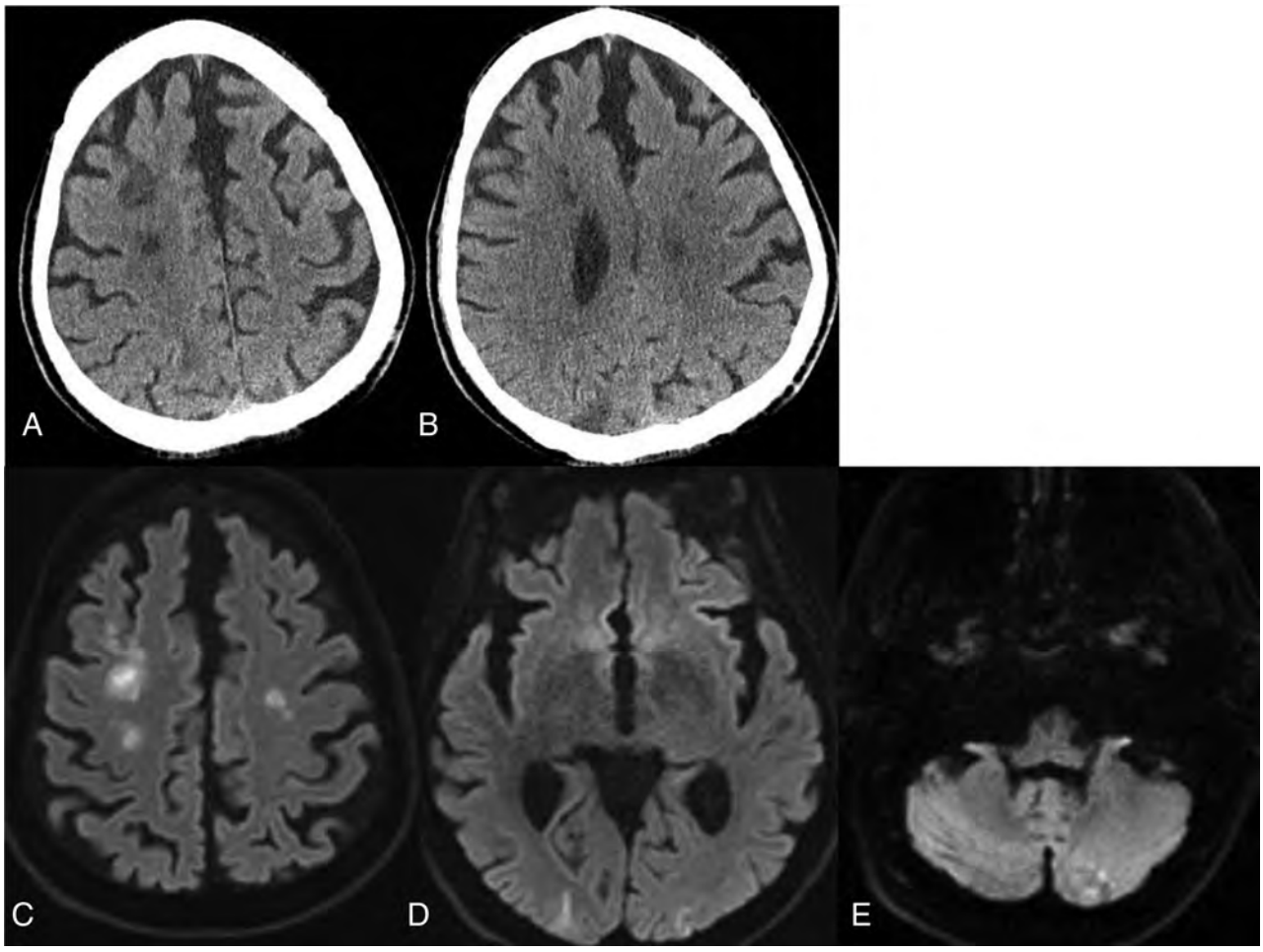

FIG 7. Noncontrast CT demonstrates focal low attenuation in the right frontal centrum semiovale and right frontal subcortical region (*A*) and a wedge-shaped area of low attenuation in the right parietal region (*B*). DWI demonstrate small infarcts in the frontal lobes (*C*), both occipital lobes (*D*), and the left cerebellum (*E*).

included the following values: elevated D-dimer, 27,000ng/mL; CRP, 25 mg/L; lactate, 3.1 mm/; and pro-B-type natriuretic peptide, 9550. He was intubated due to acute hypoxic respiratory failure and treated with an interleukin-2 receptor antagonist, steroids, and hydroxychloroquine.

Chest CT showed worsening pneumonia with diffuse, consolidative, and ground-glass opacities throughout both lungs. He then developed altered mental status and seizures, and a head CT showed focal low attenuation in the occipital and right frontal lobes, compatible with infarctions (Fig 9). CTA of the head and neck was not performed due to the patient's poor overall condition. During the next 2 days, his respiratory status deteriorated and he died.

Patient 10. A 62-year-old woman with a medical history of emphysema and lung cancer presented with acute encephalopathy and hypoxic respiratory failure requiring intubation and ventilator support. A PCR for COVID-19 was positive.

Abnormal laboratory results included mild leukocytosis (white blood cell count, 12 $\times$ 10^3/mm^3); elevated D-dimer level, 5628 ng/dL; elevated inflammatory markers (CRP and ferritin); elevated troponins; and marked respiratory acidosis. A chest x-ray showed bilateral opacities. Head CT demonstrated extensive low attenuation in the right frontal, temporal, and parietal regions consistent with infarction (Fig 10*A*). There was also subtle high attenuation in the right MCA (Fig 10*B*).

Head and neck CTA showed thrombus leading to occlusion of the right internal carotid artery. Intracranially, there was occlusion of the right internal carotid and middle cerebral arteries (Fig 10*C*, -*D*). Follow-up head CT on the same day revealed a right middle cerebral artery territory acute infarction and areas of low attenuation in the left temporal region and cerebellar hemispheres (Fig 10*E*-10*G*).

Several days later, she developed profound refractory hypotension and severe hypoxia despite high-dose vasopressors and maximum ventilator support, and she died.

DISCUSSION

According to the World Health Organization, the ongoing COVID-19 global pandemic has infected >3 million people worldwide, resulting in nearly 218,000 deaths as of late April 2020, with cases reported in 213 countries, areas, and territories.[1] Various risk factors have been reported as predictors of

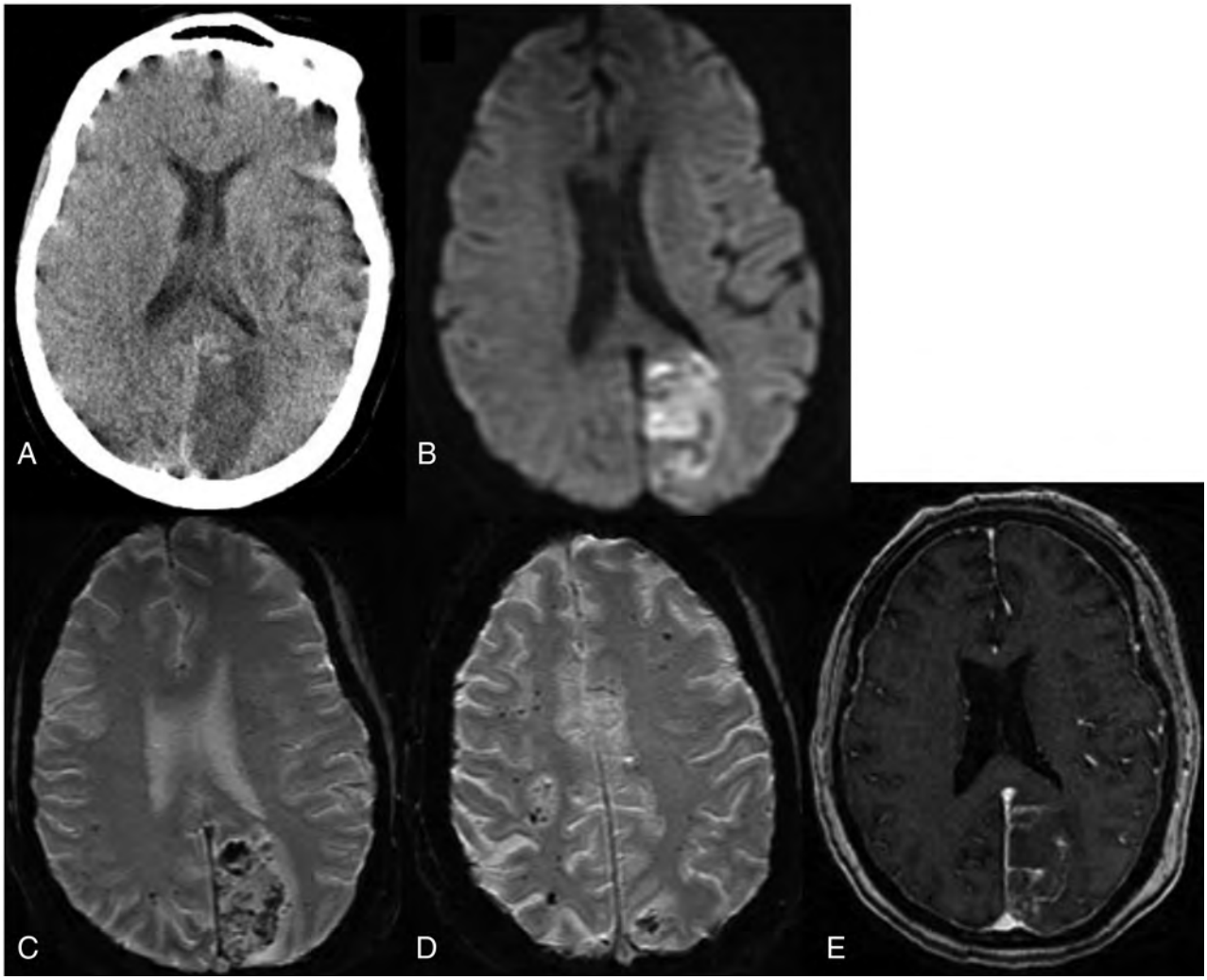

FIG 8. Noncontrast CT (*A*) demonstrates low attenuation in the left occipital lobe. DWI (*B*) confirms a left occipital infarction. Corresponding SWI (*C*) shows confluent hemorrhages in the region of the acute infarction. SWI through the centrum semiovale (*D*) shows numerous bilateral microhemorrhages. Postcontrast TI-weighted image (*E*) shows leptomeningeal enhancement overlying the left occipital infarction and diffuse dural enhancement.

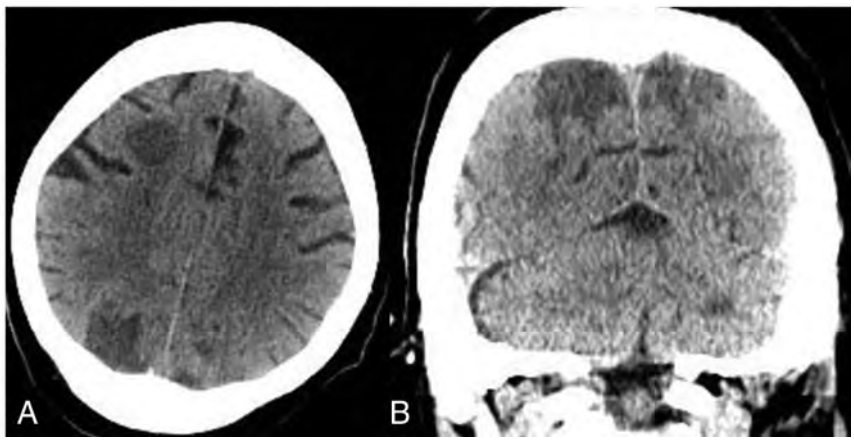

FIG 9. Non-contrast CT axial (*A*) and coronal (*B*) views demonstrate focal low attenuation in the parietal and right frontal lobes compatible with acute infarctions.

mortality and poor outcome, including advanced age, obesity, pre-existing cardiovascular or cerebrovascular diseases, and underlying immunosuppression.[9,10]

Given the propensity of COVID-19 infection to involve the respiratory system, initial scientific effort in diagnosis and therapeutics focused on the respiratory aspects of the disease.[11] There is increasing evidence that thrombi are a major cause of multisystem organ dysfunction, including respiratory failure in severe cases of infection. According to several publications, clotting plays a major role in disease severity and mortality.[12,13] In addition to arterial clots, others have observed high rates of venous thromboembolism in critically ill patients who otherwise lack the classic risk factors for venous thromboembolism.[10] A postmortem examination of 1 patient with severe COVID-19 disease revealed numerous pulmonary microthrombi. One feature of these diffuse capillary thrombi was the presence of

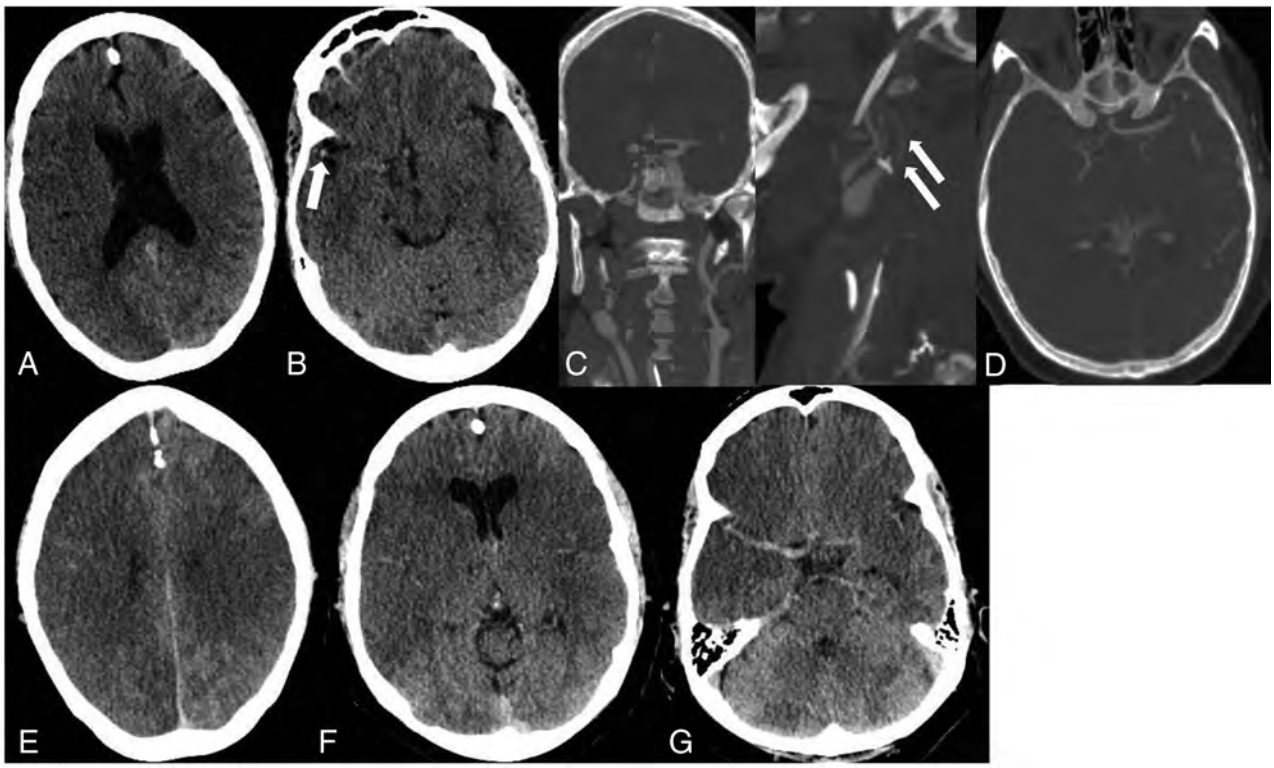

FIG 10. Non-contrast CT demonstrates low attenuation suggestive of an acute right MCA territory infarction (*A*). There is subtle high attenuation (arrow) in the right Sylvian fissure suggesting thrombus (*B*). Coronal and sagittal CTA views demonstrate long-segment thrombus resulting in occlusion (arrow) of the right internal carotid artery (*C*). Head view (*D*) demonstrates occlusion of the right middle cerebral artery. Follow-up head CT obtained on the same day as CTA reveals a right middle cerebral artery territory acute infarction and possible infarctions in the left parietal lobe and left temporal region (*E* and *F*). Cerebellar infarctions were also present (*G*).

megakaryocytes, platelets, fibrin, and inflammatory cells, eg, neurophils.[14] Similarly, postmortem examinations from the SARS outbreak of the early 2000s demonstrated pulmonary thrombi, pulmonary infarcts, and microthrombi in other organs.[6,7]

Patients infected with COVID-19 may have a massive inflammatory reaction, presumably due to rapid accumulation of T-cells and macrophages releasing cytokines into the bloodstream, which aim to destroy the virus, resulting in CSS.[4,5] Laboratory findings of CSS include decreased T-cells and natural killer cells and an increase in interleukin 6. Hypoxia is a trigger of inflammation and contributes to an intense proinflammatory state.[15,16] In addition, the COVID-19 virus has an affinity for ACE2 receptors, which are found in the capillary endothelium.[2,3] Data suggest that engagement of the endothelium by the virus damages it, increasing the permeability of the blood-brain barrier, resulting in encephalopathy, encephalitis, and thrombosis and hemorrhage.[17-19] Hemorrhages may be related to a coagulopathy due to endothelial dysfunction as sequelae of CSS and/or liver dysfunction and consumption of clotting factors leading to disseminated intravascular coagulation.

Neurologic manifestations are now recognized and, in 1 series, were present in 36.4% of patients.[20,21] These findings may be, at least in part, due to the affinity of COVID-19 for the ACE2 receptors, which are relatively common in the respiratory and nervous systems.[2,3] Occasionally, CNS symptoms precede other manifestations and may be the only indicators of the disease.[21] Postmortem examinations have shown brain hyperemia and edema as well as neuronal degeneration in patients with COVID-19.[22]

As in other series, most of our patients (8 of 10) had significant comorbidities, more commonly hypertension ($n = 6$), morbid obesity ($n = 4$), diabetes ($n = 3$), and cancer ($n = 1$). Obesity is associated with a risk of stroke, not only due to the propensity for comorbid diabetes, hypertension, and hyperlipemia, all independent risk factors for cardiovascular disease, but also because fatty tissues are inherently proinflammatory and hypofibrinolytic.[23] Being overweight is also a documented risk for poor outcome in COVID-19 infection,[24] and its link to an enhanced inflammatory state and inherent prothrombotic state may also explain the high prevalence of cerebral infarctions in these patients. The number of cases herein described is too small to determine whether specific comorbidities lead to specific CNS manifestations. The high number of comorbidities in our patients may explain why only 3 were older than 65 years when advancing age has been a predisposing factor in other series.

We cannot speculate on the frequency of cerebral infarctions in our patients with COVID-19 because the cases shown here were specifically chosen to review these complications. In 1 large series, slightly >36% of patients had CNS complications.[21] In that same series, 88 of 214 patients had severe infections, and they were the ones with CNS complications. Of these patients, 4 had ischemic strokes and 1 a cerebral hemorrhage. Most them also had severe hypertension, which was present in most of our patients. In a small series from France, 13 patients underwent

brain MR imaging and 3 showed cerebrovascular abnormalities, which, by description, were small compared with the ones in our series, and 8 showed leptomeningeal enhancement, which we saw in only 1 patient.[25] One of our patients showed diffuse cerebral edema, and it is unclear whether this was the result of anoxia induced by lung disease or a different reason. It is notable that 6 of our patients had symptoms and laboratory values suggesting CSS but their brain imaging findings varied widely, and none corresponded to findings described previously for this syndrome.[20]

Thus, it seems that the neurovascular complications of COVID-19, as illustrated by our cases and those of others,[26-30] are common and varied, including multifocal infarctions, multiple arterial occlusions, and/or intraluminal thrombi with or without hemorrhages, which may be the result of a combination of diffuse endothelial dysfunction, systemic hypercoagulability, and hypoxic-ischemic damage from cardiopulmonary dysfunction.[21] Previously, we reported posterior reversible encephalopathy syndrome–like findings in 2 patients, whom we decided not to include in these series.[31]

CONCLUSIONS

We presented 10 hospitalized patients with COVID-19 who had severe intracranial ischemic complications, and most had comorbidities, including hypertension, morbid obesity, and diabetes. Although probably multifactorial, in many patients, neurovascular ischemic diathesis in the setting of COVID-19 infection may be explained by a combination of cytokine release syndrome resulting in severe inflammation, leading to endothelial dysfunction; a hypercoagulable state; and cardiopulmonary dysfunction with hypoxia and hemodynamic insufficiency accentuated by direct viral-mediated breakdown of the blood-brain barrier. Although our study is a small observational series, it demonstrates the wide range of ischemic brain lesions in patients with COVID-19, and these should be kept in mind when imaging such patients.

REFERENCES

1. Geneva: World Health Organization. **Coronavirus disease (COVID-19) pandemic.** https://www.who.int/emergencies/diseases/novel-coronavirus-2019. Accessed April 30, 2020
2. Hamming I, Timens W, Bulthuis MLC, et al. **Tissue distribution of ACE2 protein, the functional receptor for SARS coronavirus: a first step in understanding SARS pathogenesis.** *J Pathol* 2004;203:631–37 CrossRef Medline
3. Li WH, Moore MJ, Vasilieva NY, et al. **Angiotensin-converting enzyme 2 is a functional receptor for the SARS coronavirus.** *Nature* 2003;426:450–54 CrossRef Medline
4. Mehta P, McAuley DF, Brown M, et al; HLH Across Speciality Collaboration, UK. **COVID-19: consider cytokine storm syndromes and immunosuppression.** *Lancet* 2020;395:1033–34 CrossRef Medline
5. Wang W, He J, Lie P, et al. **The definition and risks of cytokine release syndrome-like in 11 COVID-19-infected pneumonia critically ill patients: disease characteristics and retrospective analysis.** *medRxiv* February 27, 2020. https://doi.org/10.1101/2020.02.26.20026989. Accessed April 30, 2020
6. Ding Y, He L, Zhang Q, et al. **Organ distribution of severe acute respiratory syndrome (SARS) associated coronavirus (SARS-CoV) in SARS patients: implications for pathogenesis and virus transmission pathways.** *J Pathol* 2004;203:622–30 CrossRef Medline
7. Ding Y, Wang H, Shen H, et al. **The clinical pathology of severe acute respiratory syndrome (SARS): a report from** *J Pathol* 2003;200:282–89 CrossRef Medline
8. Klok FA, Kruip M, van der Meer NJ, et al. **Incidence of thrombotic complications in critically ill ICU patients with COVID-19.** *Thromb Res* 2020;191:145-7 CrossRef Medline
9. Xie J, Tong Z, Guan X, et al. **Clinical characteristics of patients who died of coronavirus disease 2019 in China.** *JAMA Netw Open* 2020;3:e205619 CrossRef Medline
10. Ruan Q, Yang K, Wang W, et al. **Clinical predictors of mortality due to COVID-19 based on an analysis of data of 150 patients from Wuhan, China.** *Intensive Care Med* 2020;46:846–48 CrossRef Medline
11. Jin Y, Cai L, Cheng Z, et al; for the Zhongnan Hospital of Wuhan University Novel Coronavirus Management and Research Team, Evidence-Based Medicine Chapter of China International Exchange and Promotive Association for Medical and Health Care (CPAM). **A rapid advice guideline for the diagnosis and treatment of 2019 novel coronavirus (2019-nCoV) infected pneumonia (standard version).** *Mil Med Res* 2020;7:4 CrossRef Medline
12. Wadman M. **How does coronavirus kill? Clinicians trace a ferocious rampage through the body, from brain to toes.** *Science* 2020 April 17 CrossRef
13. Poor HD, Ventetuolo CE, Tolbert T, et al. **COVID-19 critical illness pathophysiology driven by diffuse pulmonary thrombi and pulmonary endothelial dysfunction responsive to thrombolysis.** *Clinical and Translational Medicine* May 13, 2020. https://onlinelibrary.wiley.com/doi/abs/10.1002/ctm2.44. Accessed May 15, 2020
14. Fox SE, Akmatbekov A, Harbert JL, et al. **Pulmonary and cardiac pathology in Covid-19: the first autopsy series from New Orleans.** *Research Gate* April 2020. https://www.researchgate.net/publication/340563942_Pulmonary_and_Cardiac_Pathology_in_Covid-19_The_First_Autopsy_Series_from_New_Orleans. Accessed April 30, 2020
15. Eltzschig HK, Carmeliet P. **Hypoxia and inflammation.** *N Engl J Med* 2011;364:656–65 CrossRef Medline
16. Bartels K, Grenz A, Eltzschig HK. **Hypoxia and inflammation are two sides of the same coin.** *Proc Natl Acad Sci U S A* 2013;110:18351–52 CrossRef Medline
17. Baig AM, Khaleeq A, Ali U, et al. **Evidence of the COVID-19 virus targeting the CNS: tissue distribution, host-virus interaction, and proposed neurotropic mechanisms.** *ACS Chem Neurosci* 2020;11:995–98 CrossRef Medline
18. Netland J, Meyerholz DK, Moore S, et al. **Severe acute respiratory syndrome coronavirus infection causes neuronal death in the absence of encephalitis in mice transgenic for human ACE2.** *J Virol* 2008;82:7264–75 CrossRef Medline
19. Li YC, Bai WZ, Hashikawa T. **The neuroinvasive potential of SARS-CoV2 may play a role in the respiratory failure of COVID-19.** *J Med Virol* 2020 Feb 27. [Epub ahead of print] CrossRef Medline
20. Filatov A, Sharma P, Hindi F, et al. **Neurological complications of coronavirus (COVID-19): encephalopathy.** *Cureus* 2020;12:e7352 CrossRef Medline
21. Mao L, Jin H, Wang M, et al. **Neurologic manifestations of hospitalized patients with coronavirus disease 2019 in Wuhan, China.** *JAMA Neurol* 2020 Apr 10. [Epub ahead of print] CrossRef Medline
22. National Health Commission of the People's Republic of China. **Diagnosis and treatment of the novel coronavirus pneumonia.** 2020 http://www.nhc.gov.cn/. Accessed April 15, 2020
23. Blokhin IO, Lentz SR. **Mechanisms of thrombosis in obesity.** *Curr Opin Hematol* 2013;20:437–44 CrossRef Medline
24. Petrilli CM, Jones SA, Yang J, et al. **Factors associated with hospital admission and critical illness among 5279 people with coronavirus**

disease 2019 in New York City: prospective cohort study. *BMJ* 2020;369:m1966 CrossRef Medline

25. Helms J, Kremer S, Merdji H, et al. **Neurologic features in severe SARS-CoV-2 infection.** *N Engl J Med* 2020 Apr 15. [Epub ahead of print] CrossRef Medline
26. Avula A, Nalleballe K, Narula N, et al. **COVID-19 presenting as stroke.** *Brain Behav Immun* 2020 Apr 28. [Epub ahead of print] CrossRef Medline
27. Beyrouti R, Adams ME, Benjamin L, et al. **Characteristics of ischaemic stroke associated with COVID-19.** *J Neurol Neurosurg Psychiatry* 2020 Apr 30. [Epub ahead of print] CrossRef Medline
28. Aggarwal G, Lippi G, Henry M. **B. Cerebrovascular disease is associated with an increased disease severity in patients with coronavirus disease 2019 (COVID-19): a pooled analysis of published literature.** *Int J Stroke* 2020 Apr 20. [Epub ahead of print] CrossRef Medline
29. Oxley TJ, Mocco J, Majidi S, et al. **Large-vessel stroke as a presenting feature of Covid-19 in the young.** *N Engl J Med* 2020;382:e60 CrossRef Medline
30. Radmanesh A, Raz E, Zan E, et al. **Brain imaging utilization and findings in COVID-19: A single academic center experience in the epicenter of disease in the United States.** *AJNR Am J Neuroradiol* 2020 May 28. [Epub ahead of print] CrossRef Medline
31. Franceschi AM, Ahmed O, Giliberto L, et al. **Hemorrhagic Posterior Reversible Encephalopathy Syndrome as a Manifestation of COVID-19 Infection.** *AJNR Am J Neuroradiol* 2020 May 21. [Epub ahead of print] CrossRef Medline

Leukoencephalopathy Associated with Severe COVID-19 Infection: Sequela of Hypoxemia?

M. Lang, K. Buch, M.D. Li, W.A. Mehan, Jr, A.L. Lang, T.M. Leslie-Mazwi, and S.P. Rincon

ABSTRACT

SUMMARY: There is increasing evidence to suggest that complications of coronavirus disease 2019 (COVID-19) infection are not only limited to the pulmonary system but can also involve the central nervous system. Here, we report 6 critically ill patients with COVID-19 infection and neuroimaging findings of leukoencephalopathy. While these findings are nonspecific, we postulate that they may be a delayed response to the profound hypoxemia the patients experienced due to the infection. No abnormal enhancement, hemorrhage, or perfusion abnormalities were noted on MR imaging. In addition, Severe Acute Respiratory Syndrome coronavirus 2 was not detected in the CSF collected from the 2 patients who underwent lumbar puncture. Recognition of COVID-19-related leukoencephalopathy is important for appropriate clinical management, disposition, and prognosis.

ABBREVIATIONS: COVID-19 = coronavirus disease 2019; PaO_2 = partial pressure of oxygen; SARS-CoV-2 = Severe Acute Respiratory Syndrome coronavirus 2; MR = magnetic resonance; CT = computed tomography; CSF = cerebrospinal fluid

There is mounting evidence that Severe Acute Respiratory Syndrome coronavirus 2 (SARS-CoV-2) can affect the central nervous system, with hematogenous spread or direct neural propagation via the olfactory pathway proposed as possible mechanisms of SARS-CoV-2 neurotropism.[1] The angiotensin converting enzyme 2 receptor plays a role in the mechanism by which the SARS-CoV-2 gains cellular entry and is expressed in the brain.[2,3] Furthermore, the SARS-CoV-2 virus has been detected in the CSF of a patient with coronavirus disease 2019 (COVID-19).[4] Neurologic symptoms are commonly reported in patients with COVID-19 infection; a study from France reported that 91% of patients with COVID-19 infection demonstrated neurologic symptoms, while a study from China reported a lower prevalence of 36%.[5,6] Moreover, there are case reports of encephalitis, including a case of hemorrhagic necrotizing encephalopathy, associated with COVID-19 infection.[7-10] Recently, there is emerging evidence of white matter injury associated with COVID-19 infection in the form of demyelinating lesions and leukoencephalopathy without a clear etiology.[11,12] Here, we report a case series of suspected white matter injury in patients with COVID-19 infection.

Received May 18, 2020; accepted after revision May 30.

From the Departments of Radiology (M.L., K.B., M.D.L., W.A.M., Jr, S.P.R.), Anesthesia, Critical Care, and Pain Medicine (A.L.L.), and Neurosurgery and Neurology (T.M.L.-M.), Massachusetts General Hospital, Harvard Medical School, Boston, Massachusetts.

Please address correspondence to Min Lang, MD, MSc, Department of Radiology, MA General Hospital, 55 Fruit St, Boston, MA 02114; e-mail: mlang@mgh.harvard.edu

Indicates open access to non-subscribers at www.ajnr.org

Indicates article with supplemental on-line table.

http://dx.doi.org/10.3174/ajnr.A6671

CASE SERIES

Our study was performed retrospectively, at a large, urban, academic medical center and was approved by the institutional review board with a waiver of informed consent. A total of 42 patients who tested positive for COVID-19 via real-time reverse transcription polymerase chain reaction underwent brain MR imaging, and the imaging was reviewed. Six patients were found to have imaging findings of leukoencephalopathy and were included in this study.

All 6 patients presented to our hospital for increased difficulty in breathing, and all without neurologic impairment at the time of presentation. The average age of the patients was 64 years (range, 60–76 years; 4 men and 2 women). No patients had a history of neurologic disease or were immunocompromised. One patient had brain MR imaging 1 year prior, which demonstrated minimal nonspecific white matter changes without other abnormalities. All 6 patients required intubation in the emergency department for hypoxic respiratory failure. The lowest recorded arterial oxygen level (partial pressure of oxygen [PaO_2]) was between 46 and 66 mm Hg during their hospital course, with an average of 55 mm Hg (On-line Table). All 6 patients were weaned off sedation between admission days 9 and 24 when their respiratory status improved, with 2 patients successfully extubated. All patients exhibited altered mental status and neurologic symptoms between admission days 15 and 30.

Five of the 6 patients underwent noncontrast-enhanced CT imaging first, with a mean time to CT of 23 days (range, 14–30 days) from date of admission. Four of the 5 CT

studies were unremarkable, with only patient 2 exhibiting multiple bilateral hypodense lesions in the deep cerebral white matter (Fig 1).

All 6 patients eventually underwent MR imaging of the brain with a mean time to MR imaging of 26 days (range, 14–34 days) from date of admission. The mean duration between the PaO_2 nadir and MR imaging was 22 days (range, 13–29 days). All MR imaging examinations performed at our institution included axial diffusion-weighted imaging ($b = 1000$), susceptibility-weighted imaging, axial T2 FLAIR, and axial T2-weighted imaging. Three patients had contrast-enhanced T1-weighted imaging, 2 patients had MRA, and 3 patients had arterial spin-labeling.

On MR images, all 6 patients exhibited symmetric T2 FLAIR hyperintense signal and restricted diffusion involving the deep white matter of both cerebral hemispheres, with relative sparing of the subcortical U-fibers (Figs 2 and 3). Additional sites of white matter involvement were also observed in the 6 patients: corpus callosum in patient 2 (Fig 2); middle cerebellar peduncles in patients 1, 2, 4, 5, and 6 (Fig 4); and corticospinal tracts in patients 2, 3 and 4. On the fractional anisotropy map, focal areas of white matter tract disruption were observed only in patient 2 (Fig 2). No evidence of brain stem or basal ganglia involvement, mass effect, hemorrhage, or other acute findings was observed. Of the patients who also underwent contrast-enhanced MR imaging, MRA, or arterial spin-labeling, no abnormal gadolinium enhancement, vascular pathology, or perfusion abnormality was observed (Figs 4 and 5). The imaging findings of restricted diffusion with corresponding T2 FLAIR hyperintensity in the white matter are consistent with leukoencephalopathy.

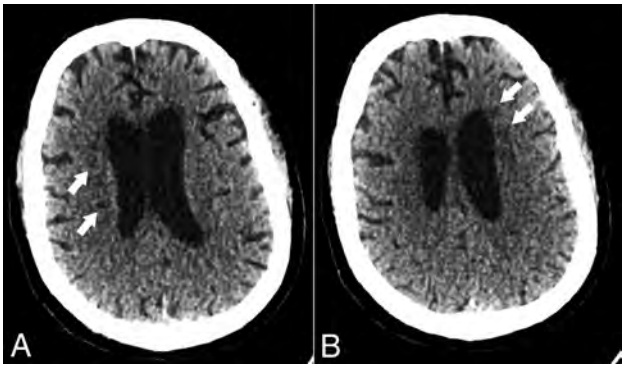

FIG 1. Head CT of a critically ill patient (patient 2) with COVID-19 infection. Axial CT images demonstrate multiple hypodense foci within the bilateral periventricular white matter (*white arrows*) without evidence of hemorrhage.

DISCUSSION

Neurologic complications related to COVID-19 infection are not uncommon, but associated neuroimaging manifestations have

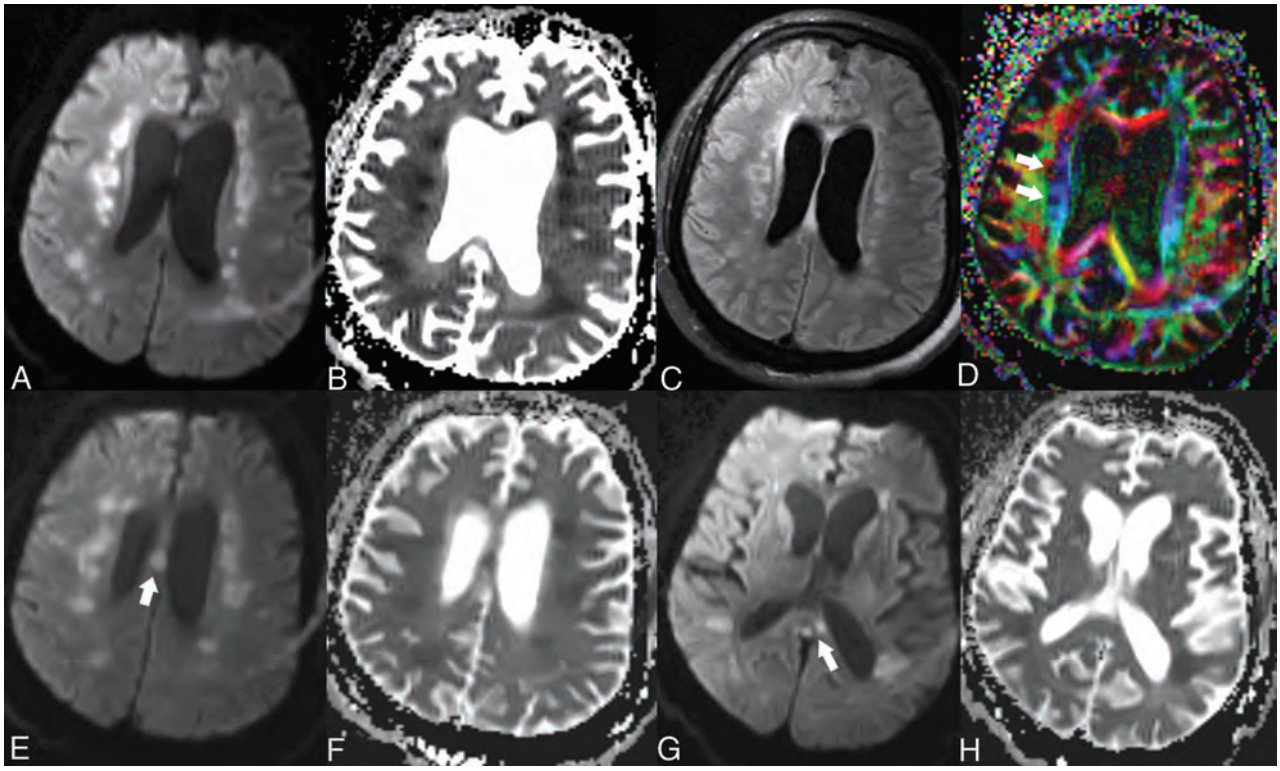

FIG 2. Brain MR images of a critically ill patient (Patient 2) with COVID-19 infection exhibiting impaired arousal, aphasia, and lethargy. *A* and *B*, Paired axial DWI and ADC map show symmetric foci of restricted diffusion involving the deep white matter of both cerebral hemispheres. *C*, Axial T2/FLAIR image through the same level shows associated increased T2/FLAIR hyperintensity corresponding to the regions of restricted diffusion. *D*, Axial fractional anisotropy map shows focal disruption of white matter tracts in the regions of diffusion restriction (*white arrows*). *E* and *F*, Paired axial DWI and ADC map show restricted diffusion of the body of the corpus callosum (*arrow*). *G* and *H*, Paired axial DWI and ADC map show restricted diffusion of the splenium of the corpus callosum (*arrow*).

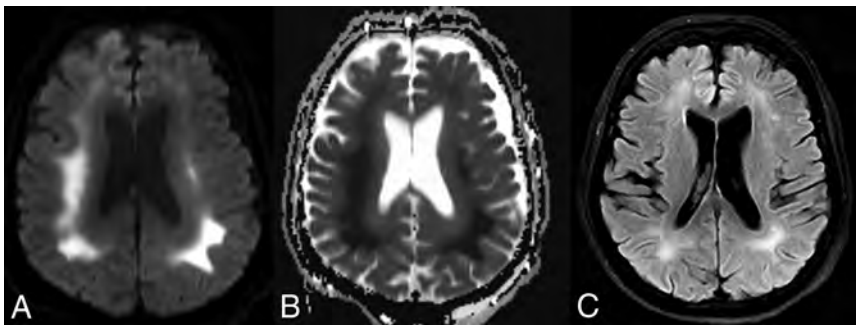

FIG 3. Brain MR images of a critically ill patient (patient 1) with COVID-19 infection exhibiting altered mental status. *A* and *B*, Paired axial DWI and ADC map show symmetric restricted diffusion of the deep white matter of both cerebral hemispheres. *C*, Axial T2 FLAIR image through the same level shows associated increased T2 FLAIR hyperintensity corresponding to the regions of restricted diffusion.

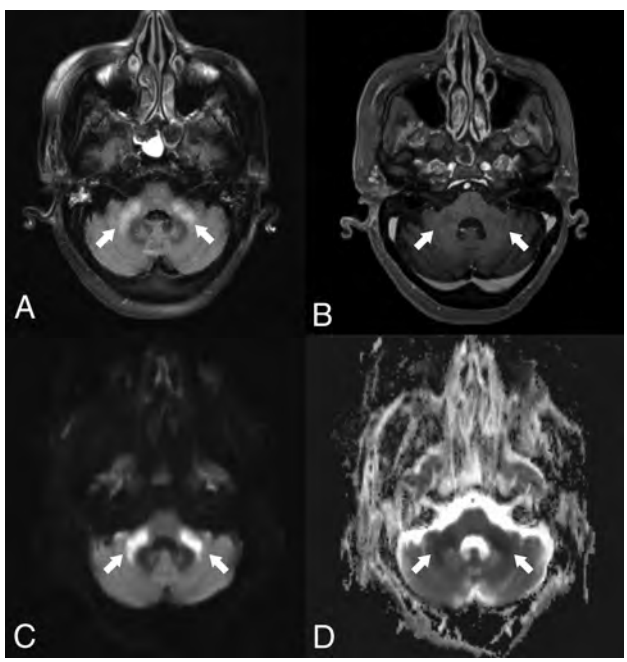

FIG 4. Brain MR images of a critically ill patient (patient 5) with COVID-19 infection exhibiting impaired arousal and diffuse hypertonicity. *A*, Axial FLAIR image shows increased T2 FLAIR signal in the bilateral middle cerebellar peduncles (*arrows*). *B*, Contrast-enhanced T1-weighted image shows absence of abnormal enhancement of the bilateral middle cerebellar peduncles (*arrows*). *C* and *D*, Paired axial DWI and ADC map show corresponding restricted diffusion of bilateral middle cerebellar peduncles (*arrows*).

not been extensively investigated.[5,7,10,13] Initial reported neuroimaging findings related to COVID-19 infection included infarction, hemorrhage, and encephalopathy.[5,7,13-15] Recently, leukoencephalopathy with intracranial microhemorrhages was reported.[11] Specifically, the authors observed posterior predominant white matter FLAIR hyperintensity, posterior circulation hyperperfusion, and susceptibility signal in the corpus callosum. The mechanism underlying leukoencephalopathy in the setting of COVID-19 infection, however, remains unclear. While neurotropism has been proposed as an underlying cause for neurologic symptoms related to COVID-19 infection, there may be additional mechanisms at play.[1] Specifically, the brain is sensitive to oxygen deprivation, and severe COVID-19 infection is known to be associated with hypoxemia.[16] In our case series, we present evidence of white matter–specific injury, which may be the sequela of COVID-19-related hypoxemia.

On MR imaging, all patients in our case series exhibited sparing of the subcortical U-fibers and brain stem, with relatively symmetric involvement of the deep cerebral white matter, which is reminiscent of delayed posthypoxic leukoencephalopathy.[17] Severe cases of COVID-19 infection are associated with profound hypoxemia, and all 6 patients in our series required intubation and experienced marked hypoxemia. It has been postulated that prolonged or severe hypoxemia can lead to myelin sheath damage through dysfunction of the adenosine triphosphate–dependent enzymes responsible for myelin secretion and maintenance—a cycle of approximately every 23 days.[18] Neurologic symptoms in all 6 patients were first detected between 14 and 23 days after the date of the lowest recorded PaO_2. Furthermore, the mean duration between MR imaging and the PaO_2 nadir was 22 days, which could be consistent with a posthypoxemic etiology.

Infection-related leukoencephalopathy due to neurotropism is also possible, and similar features have been reported with other infectious agents, including human immunodeficiency virus, human polyomavirus JC, and *Borrelia burgdorferi* (Lyme disease).[17] SARS-CoV-2, however, was not detected in the CSF samples of 2 patients in our series who underwent lumbar puncture, and no other abnormalities were noted in the CSF samples (On-line Table).[17] There is the possibility of false-negative CSF findings as the sensitivity and specificity of SARS-CoV-2 detection in the CSF has not been established. Confirmation of tropism to the cerebral white matter by SARS-CoV-2 requires further pathology and postmortem investigation. Vascular and toxic/metabolic causes of leukoencephalopathy are also possible; however, the absence of perfusion abnormalities, infarction, hemorrhage, and the lack of clear toxin or medication-related culprits in these patients make these etiologies less likely.[17] Finally, neural injury related to the cytokine storm syndrome has been proposed, with Poyiadji et al[7] reporting neuroimaging findings of acute necrotizing encephalopathy in a case of COVID-19 infection.[19] These imaging features, however, were absent in our case series but this may be related to differences in disease severity, imaging at different stages of the disease, or different underlying processes. Further investigation into the inflammatory response associated with neurologic injury in patients with COVID-19 infection is warranted.

There are several limitations of our case series, the first of which is the small number of patients. Second, only 1 patient had brain MR imaging 1 year prior, which showed minimal nonspecific white matter changes. The remaining 5 patients had no baseline imaging studies. However, given the normal neurologic status of the 6

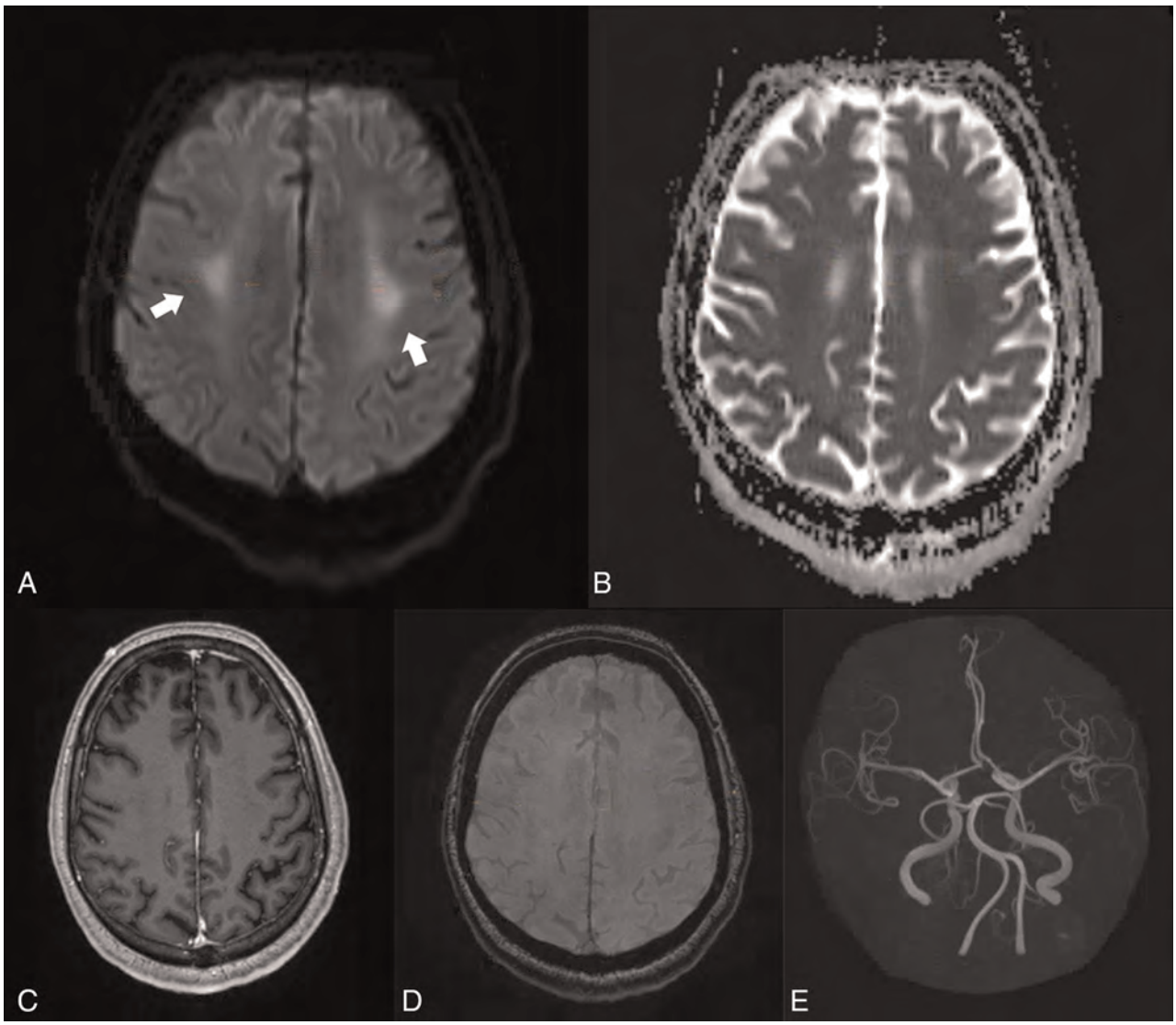

FIG 5. Brain MR images of a critically ill patient (patient 4) with COVID-19 infection exhibiting impaired arousal and left distal lower extremity paresis. *A* and *B*, Paired axial DWI and ADC map show symmetric restricted diffusion of the bilateral perirolandic white matter (*arrows*). *C*, Axial contrast-enhanced T1-weighted image at the same level demonstrates no corresponding abnormal enhancement. *D*, Susceptibility-weighted image at the same level demonstrates no susceptibility effect to suggest hemorrhage. *E*, 3D reconstruction of the circle of Willis from time-of-flight imaging demonstrates no vascular abnormality.

patients before admission, the white matter abnormalities seen in our case series were unlikely to be chronic in nature. Third, given the critical condition of these patients, serial imaging was not performed to assess the ongoing evolution of these neuroimaging findings. Larger cohort studies with standardized imaging sequences are required to better evaluate the spectrum of neuroimaging findings related to COVID-19 infection.

Recognition of a clinical syndrome is an initial step in deciphering disease mechanisms, introducing and testing therapeutic modalities, and ultimately modifying the course for improved patient outcomes. Health care providers should be aware of the potential for a COVID-19-related delayed leukoencephalopathy syndrome in patients infected with SARS-CoV-2 and displaying subacute neurologic deficits, despite improvement in respiratory status. The consequences of delayed post-hypoxic leukoencephalopathy can be severe, including both morbidity from chronic neurologic deficits and mortality. Further research is necessary to better understand this entity.

Disclosures: Karen Buch—*UNRELATED*: *Employment*: Massachusetts General Hospital. William A. Mehan, Jr—*UNRELATED*: *Consultancy*: Independent Review Committee member Kura Oncology, *Comments*: radiology reviewer for head and neck cancer clinical trial; *Expert Testimony*: medicolegal expert consulting work. Thabele M. Leslie-Mazwi—*UNRELATED*: *Employment*: Massachusetts General Hospital.

REFERENCES

1. Conde Cardona G, Quintana Pajaro LD, Quintero Marzola ID, et al. **Neurotropism of SARS-CoV 2: mechanisms and manifestations.** *J Neurol Sci* 2020;412:116824 CrossRef Medline
2. Hoffmann M, Kleine-Weber H, Schroeder S, et al. **SARS-CoV-2 cell entry depends on ACE2 and TMPRSS2 and is blocked by a clinically proven protease inhibitor.** *Cell* 2020;181:271–80.e278 CrossRef Medline

3. Xia H, Lazartigues E. **Angiotensin-converting enzyme 2 in the brain: properties and future directions.** *J Neurochem* 2008;107: 1482–94 CrossRef Medline
4. Hung EC, Chim SS, Chan PK, et al. **Detection of SARS coronavirus RNA in the cerebrospinal fluid of a patient with severe acute respiratory syndrome.** *Clin Chem* 2003;49:2108–09 CrossRef Medline
5. Mao L, Jin H, Wang M, et al. **Neurologic manifestations of hospitalized patients with coronavirus disease 2019 in Wuhan, China.** *JAMA Neurol* 2020 Apr 10. [Epub ahead of Print] CrossRef Medline
6. De Felice FG, Tovar-Moll F, Moll J, et al. **Severe acute respiratory syndrome coronavirus 2 (SARS-CoV-2) and the central nervous system.** *Trends Neurosci* 2020;43:355–57 CrossRef Medline
7. Poyiadji N, Shahin G, Noujaim D, et al. **COVID-19-associated acute hemorrhagic necrotizing encephalopathy: CT and MRI features.** *Radiology* 2020 Mar 31. [Epub ahead of Print] CrossRef Medline
8. Ye M, Ren Y, Lv T. **Encephalitis as a clinical manifestation of COVID-19.** *Brain Behav Immun* 2020 Apr 10. [Epub ahead of Print] CrossRef Medline
9. Zanin L, Saraceno G, Panciani PP, et al. **SARS-CoV-2 can induce brain and spine demyelinating lesions.** *Acta Neurochir (Wien)* 2020 May 4. [Epub ahead of Print] CrossRef Medline
10. Moriguchi T, Harii N, Goto J, et al. **A first case of meningitis/encephalitis associated with SARS-Coronavirus-2.** *Int J Infect Dis* 2020;94:55–58 CrossRef Medline
11. Sachs JR, Gibbs KW, Swor DE, et al. **COVID-19-associated leukoencephalopathy.** *Radiology* 2020 May 14. [Epub ahead of Print] CrossRef Medline
12. Kandemirli SG, Dogan L, Sarikaya ZT, et al. **Brain MRI findings in patients in the intensive care unit with COVID-19 infection.** *Radiology* 2020 May 8. [Epub ahead of Print] CrossRef Medline
13. Helms J, Kremer S, Merdji H, et al. **Neurologic features in severe SARS-CoV-2 infection.** *N Engl J Med* 2020;382:2268–70 CrossRef Medline
14. Oxley TJ, Mocco J, Majidi S, et al. **Large-vessel stroke as a presenting feature of Covid-19 in the young.** *N Engl J Med* 2020;382:e60 CrossRef Medline
15. Jain R, Young M, Dogra S, et al. **COVID-19 related neuroimaging findings: a signal of thromboembolic complications and a strong prognostic marker of poor patient outcome.** *J Neurol Sci* 2020; 414:116923 CrossRef Medline
16. Marini JJ, Gattinoni L. **Management of COVID-19 respiratory distress.** *JAMA* 2020 April 24. [Epub ahead of Print] CrossRef Medline
17. Sarbu N, Shih RY, Jones RV, et al. **White matter diseases with radiologic-pathologic correlation.** *Radiographics* 2016;36:1426–47 CrossRef Medline
18. Beeskow AB, Oberstadt M, Saur D, et al. **Delayed post-hypoxic leukoencephalopathy (DPHL): an uncommon variant of hypoxic brain damage in adults.** *Front Neurol* 2018;9:708 CrossRef Medline
19. Mehta P, McAuley DF, Brown M, et al; HLH Across Speciality Collaboration, UK. **COVID-19: consider cytokine storm syndromes and immunosuppression.** *Lancet* 2020;395:1033–34 CrossRef Medline

Level of Evidence during the COVID-19 Pandemic: Making the Case for Case Series and Case Reports

I recently peer-reviewed case report and case series manuscripts of Severe Acute Respiratory Syndrome coronavirus 2 (SARS-CoV-2) and coronavirus disease 2019 (COVID-19). Case reports and case series can lack the power to distinguish a statistically significant difference, which could hide a potential risk or benefit to diagnostic testing or treatment. The hierarchy of research evidence has worked its way into medical education and clinical practice. The research applied to clinical practice is often considered more trustworthy when using higher levels of research evidence (such as high-powered, prospective, randomized controlled trials or a meta-analysis of high-quality studies). Several national organizations, scientific panels, and clinical academies give case reports and case series some of their lowest rankings with regard to level of research evidence.[1] Some journals have gone a step further and discontinued case reports, accepting only higher-level research study designs for publication. Academic promotions also consider the rigor of research, giving little credit for case reports and case series.

However, we still need case reports and case series. They provide us with data for rare diseases, as well as early news and potential clinical insights for evolving illnesses. Initial cases may provide the impetus for more organized, higher-level research. Higher-powered, prospective, randomized controlled trials provide a high quality of research evidence but may require funding, organization, and time to collect and analyze data, and a delay in information publication during a rapidly evolving global pandemic may not be optimal. A meta-analysis requires other research to be completed and published before one can even consider taking the time to do the meta-analysis. Applying higher levels of research evidence is absolutely vital to the practice of medicine, but lower levels of research evidence should not be dismissed.

During this COVID-19 pandemic, I have seen neuroimaging findings differ between separate case series. The astute radiologists and ordering clinicians may assimilate case series into their practice, realizing that the limitations will necessitate adaptation when additional information and better research become available. For example, the article "Leukoencephalopathy Associated with Severe COVID-19 Infection: Sequela of Hypoxemia?"[2] found a lack of hemorrhage in their entire case series, but we have seen case reports and case series with petechial hemorrhage in patients with COVID-19.[3,4] There were also no changes in enhancement or cerebral perfusion for this case series, but we have observed these changes in other reported cases.[5] Publication of this case series[2] without any hemorrhages, enhancement, or cerebral perfusion abnormality is not necessarily to contradict the literature, but instead adds data to the scientific community when we have a new illness in evolution. Combined with other publication findings, this case series[2] will perhaps, in the future, help distinguish patient variables protective from hemorrhage (or clarify risk factors for hemorrhage) in COVID-19. Hopefully, these data motivate the clinical and scientific communities to do further research for better information so that one day we might have good knowledge for evidence-based medical practice and eventual medical wisdom.

In a busy clinical practice, it can be difficult to piece together the vast array of case series with inconsistent variables being reported. Maybe an ambitious researcher will tie it all together, perhaps with a meta-analysis. I remain hopeful that good evidence-based medical knowledge will eventually be available from high-level research evidence, but until then, careful incorporation of case reports and case series may have to suffice.

REFERENCES

1. Committee on Standards for Developing Trust and Institute of Medicine. *Clinical Practice Guidelines We Can Trust.* The National Academies Press; 2011
2. Lang M, Buch K, Li MD, et al. **Leukoencephalopathy Associated with Severe COVID-19 Infection: Sequela of Hypoxemia?** *AJNR Am J Neuroradiol* 2020
3. Sachs JR, Gibbs KW, Swor DE, et al. **COVID-19-associated leukoencephalopathy.** *Radiology* 2020. May 14. [Epub ahead of print] CrossRef Medline
4. Radmanesh A, Derman A, Lui YW, et al. **COVID-19-associated diffuse leukoencephalopathy and microhemorrhages.** *Radiology* 2020 May 21. [Epub ahead of print] CrossRef Medline
5. Helms J, Kremer S, Merdji H, et al. **Neurologic features in severe SARS-CoV-2 infection.** *N Engl J Med* 2020;382:2268–70 CrossRef Medline

I. Ikuta
Department of Radiology & Biomedical Imaging
Yale University School of Medicine
New Haven, Connecticut

http://dx.doi.org/10.3174/ajnr.A6676

Emergent Premedication for Contrast Allergy Prior to Endovascular Treatment of Acute Ischemic Stroke

D.A. Tonetti, S.M. Desai, A. Morrison, B.A. Gross, T.G. Jovin, B.T. Jankowitz, and A.P. Jadhav

ABSTRACT

BACKGROUND AND PURPOSE: Management of contrast media allergies may lead to treatment delays in patients with acute ischemic stroke undergoing endovascular therapy. The optimal premedication strategy remains unclear. The aim of this report was to analyze our experience with emergent administration of premedication regimens before endovascular therapy.

MATERIALS AND METHODS: We retrospectively reviewed prospective data for all patients undergoing endovascular therapy from 2012 to 2019 at an academic comprehensive stroke center. Records of patients with documented contrast allergy were reviewed and analyzed. Data collected included stroke risk factors and characteristics, historical contrast reaction details, premedication regimens administered, and signs or symptoms of allergic reaction developing post-endovascular therapy. Hospital arrival time to endovascular therapy was compared with that in those who did not have a history of contrast allergy.

RESULTS: We analyzed 1521 patients undergoing endovascular therapy; 60 (4%) had documented contrast allergies and constituted the study cohort. The median age was 73 years (interquartile range, 66–81 years), and 65% were women. The median time from premedication to contrast was 24 minutes (interquartile range, 0–36 minutes). Forty-three patients (72%) proceeded directly to endovascular therapy; in 17 patients, the first contrast exposure was CTA. Time from hospital arrival to endovascular therapy was not slower for patients with documented allergies (96 versus 134 minutes, $P = .32$). No patients experienced a contrast media reaction.

CONCLUSIONS: In a single-institution cohort study of 60 consecutive patients with documented contrast allergies undergoing endovascular therapy with emergent premedication en route to (or in) the neuroangiography suite, no patients experienced allergic symptoms. This pragmatic approach may be safe for patients who have documented contrast media allergies.

ABBREVIATIONS: EVT = endovascular therapy; ICM = iodinated contrast media; IQR = interquartile range; LVO = large-vessel occlusion

Allergic reactions occur in 0.1%–0.6% of patients after exposure to modern nonionic iodinated contrast media (ICM), of which 1%–5% are severe.[1-4] Similarly, documentation of contrast dye allergies is not uncommon in electronic health records.[3] Documentation of a contrast media reaction may lead to delays in care for patients with acute ischemic stroke who require the administration of contrast for cerebrovascular imaging in the form of CTA and/or endovascular therapy (EVT) in an emergent manner.

There are no guidelines regarding antireaction medication paradigms for patients with a documented contrast dye allergy undergoing emergent EVT for large-vessel occlusion (LVO), and practices vary widely. Furthermore, contrast allergy is typically considered a contraindication for enrollment in EVT clinical trials, so high-quality data regarding best practices in this population are lacking. A documented contrast allergy may result in delay and/or avoidance of performing contrast-based cerebrovascular imaging (eg, CTA) per local institutional practices. At our center, a protocol was introduced in which patients presenting with emergent LVO bypass CTA and proceed directly to the neurointerventional suite. These patients were then administered prophylactic premedication as soon as possible for their contrast allergy, with the aim of avoiding delays to revascularization.

The objective of this report was to analyze our institutional experience administering emergent premedication regimens to consecutive patients with a documented history of ICM allergy at the time of emergent EVT.

Received May 6, 2020; accepted after revision June 15.

From the Department of Neurological Surgery (D.A.T., B.A.G.) and Stroke Institute (D.A.T., S.M.D., B.A.G., A.P.J.), University of Pittsburgh Medical Center, Pittsburgh, Pennsylvania; University of Pittsburgh School of Medicine (A.M.), Pittsburgh, Pennsylvania; and Cooper University Hospitals (T.G.J., B.T.J.), Camden, New Jersey.

Please address correspondence to Ashutosh P. Jadhav, MD, Stroke Institute, University of Pittsburgh, Suite C-400, UPMC Presbyterian, 200 Lothrop St, Pittsburgh, PA 15213; e-mail: jadhav.library@gmail.com; @DanTonettiMD; @AshuPJadhav

http://dx.doi.org/10.3174/ajnr.A6720

MATERIALS AND METHODS

We performed a retrospective review of prospectively collected patient records at a single academic comprehensive stroke center (University of Pittsburgh Medical Center) from 2012 to 2019. All patients who were referred for EVT for emergent LVO during this time were included if they had a documented history of a reaction to contrast media. Patients were referred for EVT by a fellowship-trained vascular neurologist, and EVT was performed by 1 of 4 neurointerventionalists. This study was approved by our local institutional review board.

The study protocol began when a patient with a documented history of ICM allergy was referred for EVT; patients in the protocol who presented directly to the comprehensive stroke center would bypass noninvasive cerebrovascular imaging (eg, CTA) and proceed directly to the neurointerventional angiography suite. For patients who were transferred from outside facilities, CTA may have been performed per local institutional protocols, and these patients were included in the analysis. Contrast premedication was administered at the discretion of the treating physicians before EVT in all cases. Premedication regimens and dosages were tabulated and recorded, along with the time from premedication administration to contrast administration.

EVT was performed with the patient under monitored anesthesia care or general anesthesia using Isovue-300 (Bracco) and conventional thrombectomy methods. Contrast dosages used for EVT were recorded. The dose of contrast used for the DSA was calculated by subtracting the contrast remaining at the end of the case from the amount of contrast in bottles opened. All patients were monitored by both an anesthesiology team and a trained neurointerventional nurse before, during, and after the procedure. Patients were then observed in a dedicated neurointensive care unit and monitored for symptoms of allergic reaction for 24 hours postprocedure.

Additional data collected and recorded included stroke risk factors and characteristics, historical contrast reaction details (which contrast agent and what type of reaction, when available), the necessity for further treatment of contrast reactions (additional medication, intubation for airway protection), and symptoms of allergic reactions during or after the procedure for up to 24 hours.

Outcome Measures

The primary outcome was any indication of allergic reaction to contrast media at any point up to 24 hours postprocedure. Symptoms including nausea, emesis, rash, shortness of breath, anaphylaxis, or unexplained hypotension were reviewed and recorded. The need for additional antiallergy medication or intubation was recorded. Time metrics were then compared with those of patients undergoing EVT without documented contrast allergy during the same study period to assess differences or delays in care.

RESULTS

Between 2012 and 2019, in the setting of an LVO, 1521 patients with acute ischemic stroke underwent EVT. Of those, 60 patients (4%) had a documented contrast allergy (Figure). Forty-three patients (43/60, 72%) bypassed noninvasive vascular imaging and proceeded directly to the angiography suite; another 17 patients (28%) underwent CTA before EVT and were premedicated before CTA. In patients who bypassed CTA, the presence of an LVO was suspected on the basis of CT of the head without contrast findings (ie, hyperdense thrombus sign) or by clinical examination (NIHSS score > 12). Occlusion location was the middle cerebral artery (segment 1, M1) in 45% or the ICA terminus in 27% (Table 1). The median time from last-known-well to hospital arrival was 4.3 hours (interquartile range [IQR] = 2.4–8.1 hours), the median NIHSS score was 18 (IQR = 13–23), and the median ASPECTS was 9 (IQR = 8–10). Intravenous tPA was administered in 16 patients (16/60, 27%).

Previously documented allergic reactions were tabulated and recorded when available at the time of EVT. Reaction types were as follows: rash (20/60, 33%), anaphylaxis (10/60, 17%), shortness of breath (5/60, 8%), and nausea/emesis (9/60, 15%) with previous ICM administration. Twenty-one patients (35%) with documented ICM allergy lacked specific details regarding a prior allergic response. At the time of admission, 1 patient (1.7%) was taking 3 mg of prednisone daily for polymyalgia rheumatica; no other patients were on pre-existing chronic oral steroid regimens.

Premedication Regimen

Fifty-six patients (93%) received a combination of corticosteroid and diphenhydramine as premedication immediately before EVT (Table 2). All medications were administered as intravenous pushes. The remaining 4 patients received corticosteroid only. Hydrocortisone was the most commonly used corticosteroid, and the most common dose was 200 mg. When methylprednisolone was used (n = 11, 18%), doses between 100 and 200 mg were used. The average dose of diphenhydramine was 50 mg. Ten milligrams of dexamethasone was used in conjunction with diphenhydramine in 1 patient (1.7%). No patients had adverse effects attributable to corticosteroid or antihistamine administration.

EVT was performed with 88% of patients achieving modified TICI 2b or higher reperfusion using an average contrast dose of 151 ± 32 mL of Isovue 300. The median time from premedication administration to contrast exposure was 24 minutes (IQR = 5–54 minutes) and was not significantly different between those who underwent CTA first versus those who underwent DSA only (P = .53).

Primary Outcome

No patients experienced intraprocedural or immediate post-EVT reactions manifesting as nausea/emesis, shortness of breath or wheezing, new rash, or anaphylaxis in response to ICM administration. One patient with a known drug reaction with eosinophilia and systemic symptoms syndrome who had an LVO while undergoing an inpatient work-up for a severe cutaneous rash over her flank and back had a persistent rash that did not worsen with EVT. No patients experienced delayed hypersensitivity reactions manifesting as delayed urticaria or shortness of breath within 24 hours post-EVT.

Impact of Premedication Administration on Time

For patients with documented contrast allergies, the median time from hospital arrival to EVT was 45 minutes (IQR = 23–

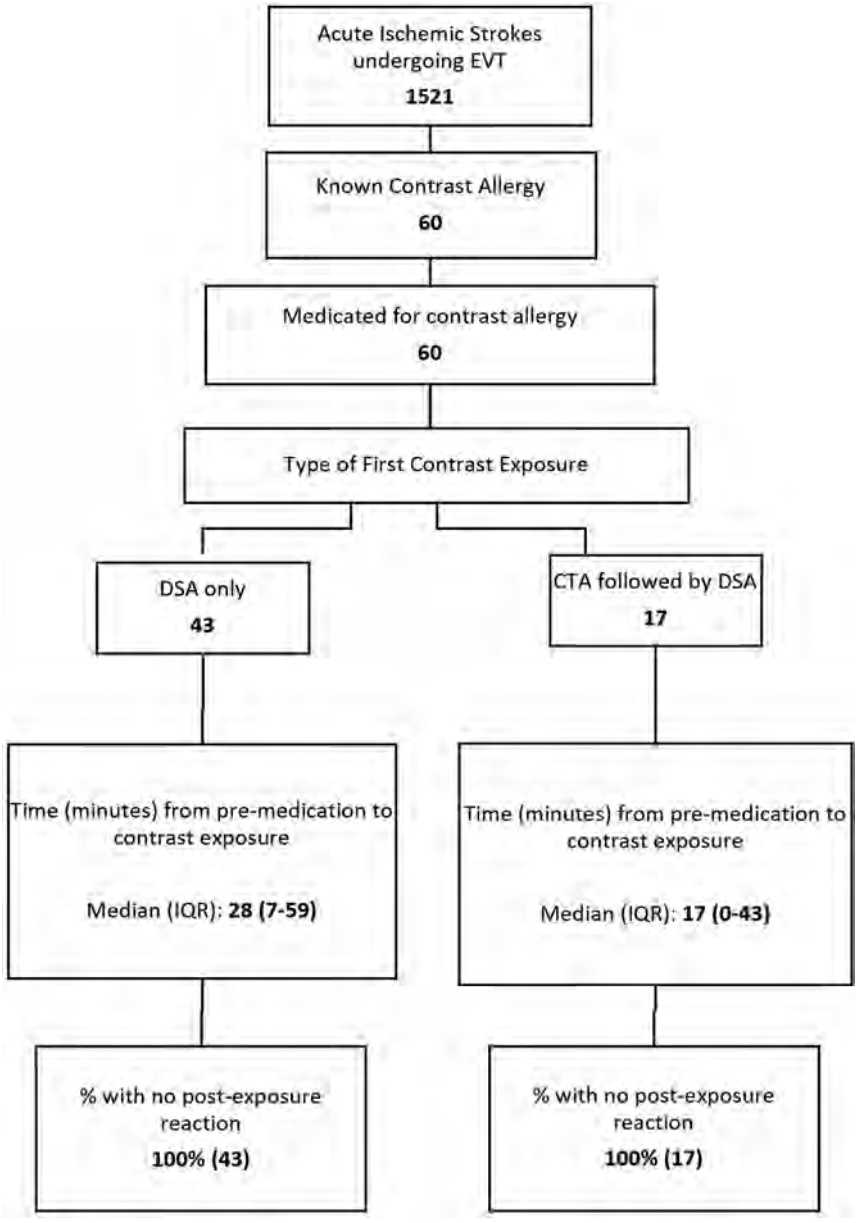

FIGURE. Patient flow diagram.

85 minutes) (Table 3). For all other patients undergoing EVT during the study period, the median time from hospital arrival to puncture was 60 minutes (IQR = 20–105 minutes), a difference that was not statistically significant ($P = .31$).

DISCUSSION

The most important finding of this study is that patients with contrast allergy with LVO who receive emergency pretreatment can safely undergo EVT without delay. Here, we describe a single-institution consecutive series of patients with documented allergies to ICM who were referred for emergent EVT with premedication administered either en route to or in the angiography suite. Among 1521 patients undergoing thrombectomy during the study period, 60 (4%) had documented contrast allergies. We found that in the cohort of 60 patients referred for EVT with documented ICM allergies during 8 years, undergoing EVT after receiving premedication resulted in no observable reactions.

Contrast dye allergy documentation in the electronic health records is not uncommon; in a cross-sectional analysis of 2.7 million patients in a large health care system in the United States, 1.3% had documented contrast allergies.[3] A prior allergic-like reaction to ICM is the most substantial risk factor for a recurrent allergic-like adverse event,[5-7] and the risk of anaphylactoid reactions is higher in women.[8] In the setting of premedication, repeat reactions to contrast agents occur uncommonly.[9,10] When they do occur, reactions are usually of similar severity to the index event and are rarely severe.[7,9,10] Unfortunately, it is exceptionally common for electronic health records to be ambiguous and lack details regarding imaging-technique-specific allergies or allergies to specific contrast agents.[3] Regardless of accuracy or reliability, a documented allergy can result in delays in obtaining necessary

Table 1: Baseline characteristics

Characteristics	No. (%)
Age (median) (IQR) (yr)	73 (66–81)
Male sex	21 (35%)
NIHSS score (median) (IQR)	18 (13–23)
Comorbidities	
Hypertension	50 (83%)
Hyperlipidemia	39 (65%)
Atrial fibrillation	35 (58%)
Diabetes mellitus	19 (32%)
ASPECTS (median) (IQR)	9 (8–10)
TLKW to arrival (median) (IQR) (hr)	4.3 (2.4–8.1)
IV tPA	16 (27%)
Occlusion location	
ICA	16 (27%)
MCA-M1	27 (45%)
MCA-M2	10 (17%)
Basilar artery	7 (12%)
mTICI ≥ 2b	53 (88%)
Prior allergic reactions	
Type of allergic reactions	
Nausea, vomiting	9 (15%)
Rash	20 (33%)
SOB, wheezing	5 (8%)
Anaphylaxis	10 (17%)
Other	5 (8%)
Not recorded	21 (35%)

Note:—TLKW indicates time last known well; SOB, shortness of breath; mTICI, modified TICI.

Table 2: Precontrast exposure medication regimen and resultant reactions

Pre-Exposure Regimen	No. (%)
Diphenhydramine and corticosteroid	56 (93%)
Corticosteroid only	4 (7%)
Medication specifics	*n* (%)
Diphenhydramine (median dose)	56 (93%), 50 mg
Corticosteroids (median dose)	
Hydrocortisone	48 (80%), 200 mg
Methylprednisolone	11 (18%), 100 mg
Dexamethasone	1 (1.7%), 10 mg
Postexposure reaction	
Nausea, vomiting	0 (0)
Rash	0 (0)
SOB, wheezing	0 (0)
Anaphylaxis	0 (0)
Other	0 (0)

Note:—SOB indicates shortness of breath.

Table 3: Impact of contrast allergy on time from hospital arrival to puncture

Arrival to Puncture	Mean (SD)	Median (IQR)
Patients with prior documented contrast allergy (min) ($n = 60$)	96 (167)	45 (23–85)
All other patients (min) ($n = 1403$)[a]	134 (291)	60 (20–105)

[a] Excluding patients with incomplete data.

imaging and thereby pose a challenge to the neurointerventionalist advocating for workflow efficiency in obtaining care for the patient with a suspected LVO. For example, some radiology departments may require pretreatment medication before noninvasive vascular imaging (ie, CTA), resulting in delays to revascularization. At our institution, these delays ultimately resulted in the development of a protocol in which patients with contrast allergies bypass noninvasive vessel imaging and proceed directly to the neuroangiography suite.

In this report, we included those patients who underwent contrast exposure in the form of CTA at other institutions before transfer to our center for completion. However, in 43 patients older than 8 years of age who presented directly to our center and bypassed noninvasive imaging, proceeding with EVT as emergently as possible with premedication given en route resulted in no observable allergic reactions and numerically reduced the average time from hospital arrival to puncture (though this did not achieve significance).

Prior retrospective reports of patients undergoing percutaneous coronary interventions using ICM have demonstrated low rates of adverse reactions among patients with or without prior ICM allergy, leading some to advocate for reconsideration of the necessity of premedication with low-ionic ICM.[11] Regardless, current recommendations from the *American College of Radiology Manual on Contrast Media* in 2020 are premedication regimens consisting of an antihistamine (eg, diphenhydramine) and a steroid (eg, hydrocortisone), with a minimum of 4 hours until contrast exposure for patients with documented ICM allergy.[7] These guidelines were not designed for, nor are they tailored to, address the emergent nature of EVT. Our study may have relevance in other scenarios in which emergent contrast administration may be indicated in a time-sensitive manner (eg, percutaneous coronary intervention, trauma, pulmonary embolism). The modified emergent premedication protocol used in our study could be considered in these other situations.

In 1986, Greenberger et al[12] proposed a regimen of 200 mg of intravenous hydrocortisone immediately, then every 4 hours until the procedure is completed, and 50 mg of intravenous diphenhydramine 1 hour before emergency procedures. We have altered that protocol by delivering both classes of medications as soon as possible before needle puncture and by lowering exposure via bypassing noninvasive cerebrovascular imaging. Biologic effects of an intravenous hydrocortisone peak at 1–2 hours (half-life: 1.7 hours)[13] and almost immediately after administration for intravenous diphenhydramine (half-life: 8.4 hours);[14] despite these effects, there remains no definite proof that steroids or antihistamines given at the time of first contrast exposure, compared with several hours before a procedure, offer protection from an allergic reaction.[7,15,16] However, because delaying EVT for LVO confers significant harm, the risk-to-benefit ratio favors intervention despite a potential allergic reaction. Thus, we believe that administering premedications en route to the neuroangiography suite, followed by close patient monitoring by trained staff for signs of allergy or reaction, is safe and practical. The data presented in this report represent a real-world, pragmatic, standardized approach to the care of a patient with an LVO and a known and/or documented contrast media allergy. While under ideal circumstances, patients with suspected LVO would be triaged with a noninvasive imaging technique, the unique challenge of balancing time to reperfusion with patient safety may justify a direct-to-

angiography suite paradigm in this patient population with consideration of recommendations. If MR angiography without contrast can be performed without delay, this approach may be a reasonable alternative.

Limitations

This report has several limitations and must be interpreted with caution. First, this is a single-institution study of moderate size with no control cohort. Thus, this is not a valid comparison of one pretreatment paradigm versus any other. There were no patients with documented ICM allergies who did not receive premedication, and it is possible that the patients presented here would have the same outcomes had they not been administered premedication. Second, the cohort described here had documented allergies of varying severities and symptomatology and may not adequately sample patients with severe reactions. This analysis, predicated on documentation of allergic reactions to contrast media, may have excluded patients with an undocumented allergy. As with any procedure, the potential benefits of the procedure must be balanced against the risks for any individual patient. Third, delayed adverse reactions (most commonly urticaria[17]) are rare but may develop from 30 to 60 minutes up to 1 week following exposure, with most occurring in the first 48 hours.[7,18] It is possible that minor delayed reactions beyond 24 hours would not be captured in this analysis. Fourth, determination of allergic reactions involving the airway is more difficult for the minority of patients who require intubation before undergoing EVT and may limit this analysis.

The strengths of this report are that the paradigm here consists of a standard regimen of widely available medications that are immediately accessible at most centers caring for these patients and results in minimal delays of patient care. The cohort reported here also includes patients with a variety of reactions and severities, therefore the results presented here are likely to have some degree of external validity.

CONCLUSIONS

In a single-institution cohort study of 60 consecutive patients with documented contrast allergies undergoing EVT for LVO with premedications administered en route to the neuroangiography suite, no patients experienced allergic symptoms. This pragmatic approach may be safe for patients who have documented contrast media allergies.

Disclosures: Shashvat M. Desai—*RELATED*: *Comments*: Award Number U10NS086489 (National Institutes of Health Stroke Trials Network, Regional Coordinating Center University of Pittsburgh).* Bradley A. Gross—*UNRELATED*: *Consultancy*: Medtronic and MicroVention. Brian T. Jankowitz—*UNRELATED*: *Consultancy*: Stryker, Medtronic. *Money paid to the institution.

REFERENCES

1. Sodagari F, Mozaffary A, Wood CG, 3rd, et al. **Reactions to both nonionic iodinated and gadolinium-based contrast media: incidence and clinical characteristics.** *AJR Am J Roentgenol* 2018;210:715–19 CrossRef Medline
2. Hunt CH, Hartman RP, Hesley GK. **Frequency and severity of adverse effects of iodinated and gadolinium contrast materials: retrospective review of 456,930 doses.** *AJR Am J Roentgenol* 2009; 193:1124–27 CrossRef Medline
3. Deng F, Li MD, Wong A, et al. **Quality of documentation of contrast agent allergies in electronic health records.** *J Am Coll Radiol* 2019;16:1027–35 CrossRef Medline
4. Lasser EC, Lyon SG, Berry CC. **Reports on contrast media reactions: analysis of data from reports to the U.S. Food and Drug Administration.** *Radiology* 1997;203:605–10 CrossRef Medline
5. Brockow K. **Contrast media hypersensitivity: scope of the problem.** *Toxicology* 2005;209:189–92 CrossRef Medline
6. Kopp AF, Mortele KJ, Cho YD, et al. **Prevalence of acute reactions to iopromide: postmarketing surveillance study of 74,717 patients.** *Acta Radiol* 2008;49:902–11
7. American College of Radiology Committee on Drugs and Contrast Media. *American College of Radiology Manual on Contrast Media.* ACR;2020:22–26
8. Lang DM, Alpern MB, Visintainer PF, et al. **Gender risk for anaphylactoid reaction to radiographic contrast media.** *J Allergy Clin Immunol* 1995;95:813–17 CrossRef Medline
9. Davenport MS, Cohan RH, Caoili EM, et al. **Repeat contrast medium reactions in premedicated patients: frequency and severity.** *Radiology* 2009;253:372–79 CrossRef Medline
10. Mervak BM, Davenport MS, Ellis JH, et al. **Rates of breakthrough reactions in inpatients at high risk receiving premedication before contrast-enhanced CT.** *AJR Am J Roentgenol* 2015;205:77–84 CrossRef
11. Topaz G, Karas A, Kassem N, et al. **Iodinated contrast media allergy in patients hospitalized for investigation of chest pain.** *J Allergy Clin Immunol Pract* 2018;6:2059–64 CrossRef Medline
12. Greenberger PA, Halwig JM, Patterson R, et al. **Emergency administration of radiocontrast media in high-risk patients.** *J Allergy Clin Immunol* 1986;77:630–34 CrossRef Medline
13. Derendorf H, Mollmann H, Barth J, et al. **Pharmacokinetics and oral bioavailability of hydrocortisone.** *J Clin Pharmacol* 1991;31: 473–76 CrossRef Medline
14. Blyden GT, Greenblatt DJ, Scavone JM, et al. **Pharmacokinetics of diphenhydramine and a demethylated metabolite following intravenous and oral administration.** *J Clin Pharmacol* 1986;26:529–33 CrossRef Medline
15. Lasser EC, Berry CC, Talner LB, et al. **Pretreatment with corticosteroids to alleviate reactions to intravenous contrast material.** *N Engl J Med* 1987;317:845–49 CrossRef Medline
16. Ring J, Rothenberger KH, Clauss W. **Prevention of anaphylactoid reactions after radiographic contrast media infusion by combined histamine H1- and H2-receptor antagonists: results of a prospective controlled trial.** *Int Arch Allergy Appl Immunol* 1985;78:9–14 CrossRef Medline
17. Christiansen C, Pichler WJ, Skotland T. **Delayed allergy-like reactions to x-ray contrast media: mechanistic considerations.** *Eur Radiol* 2000;10:1965–75 CrossRef Medline
18. Meth MJ, Maibach HI. **Current understanding of contrast media reactions and implications for clinical management.** *Drug Saf* 2006;29:133–41 CrossRef Medline

Shape Modification is Common in Woven EndoBridge–Treated Intracranial Aneurysms: A Longitudinal Quantitative Analysis Study

J. Rosskopf, M. Braun, J. Dreyhaupt, M. Beer, B.L. Schmitz, and Y. Ozpeynirci

ABSTRACT

BACKGROUND AND PURPOSE: After endovascular treatment of intracranial aneurysms with the Woven EndoBridge (WEB) device, worsening of aneurysm occlusion or re-opening was reported to be possibly associated with WEB shape modification. This study analyzed quantitatively the WEB shape modification with time in association with anatomic results.

MATERIALS AND METHODS: Thirty patients with 32 WEB-treated intracranial aneurysms fulfilled the inclusion criteria of cranial CT at baseline (day of intervention) and a follow-up CT at least >1 months' later (median follow-up time, 11.4 months; interquartile range, 6.5–21.5 months). Adequate occlusion was observed in 84.4%, and aneurysm remnant, in 15.6%. WEB shape modification was quantified by a semiautomated approach on CT scans. Time courses were evaluated graphically and analytically; association analyses were performed by linear mixed-effects regression models.

RESULTS: In 29/32 WEB devices (90.6%), the reduction in height was found to be at least 5%. The decrease in height with time was significantly associated with the time interval in days since the intervention ($P < .0001$): A stronger decrease in WEB height was associated with a longer time since the intervention (median reduction in 1 year, 19.2%; range, 8.6%–52.3%). No significant association was found with the quality of aneurysm occlusion, device size, rupture status of the aneurysm, aneurysm location, and reintervention rate.

CONCLUSIONS: Shape modification was common in WEB-treated intracranial aneurysms with a median height reduction of 19.2% in 1 year. The quality of aneurysm occlusion was not associated with WEB modification.

ABBREVIATIONS: ASA = acetylsalicylic acid; SL = single-layer; SLS = single-layer sphere; WEB = Woven EndoBridge

As a novel endovascular aneurysm occlusion device, the Woven EndoBridge (WEB) (Sequent Medical) was designed to divert the intrasaccular flow, promoting intra-aneurysmal clot formation.[1] Although the safety and efficacy of the WEB have been confirmed in several clinical trials,[2-9] some uncertainty still remains about the WEB shape-modification phenomenon reported to be possibly associated with worsening of aneurysm occlusion during follow-up.[10-12] The underlying mechanisms of WEB shape modification are rarely investigated, and corresponding theories range from clot retraction to high arterial inflow.[13-16] Therefore, quantitative measurement of WEB shape modification might be valuable for association analysis of anatomic results across time. Of note, only 1 previous DSA-based study reported descriptive results from a quantitative WEB shape-modification assessment without performing association analysis.[16]

The present study aimed to quantify the reduction in height of the WEB device in mid- and long-term follow-up. On the basis of findings of DSA studies,[16,17] we hypothesized that the decrease in height assessed on successive CT scans by the use of a semiautomated approach would be common in WEB-treated aneurysms and would correlate across time. Furthermore, no association of the quality of aneurysm occlusion with WEB shape modification was expected. Finally, association analyses were performed with anatomic and clinical parameters like device size, rupture status of the aneurysm, aneurysm location, and re-intervention rates.

MATERIALS AND METHODS

Study Population

The study was approved by the ethics committee of the University of Ulm, Ulm, Germany (reference #16/20), and the

Received March 26, 2020; accepted after revision May 27.

From the Department of Radiology (J.R., M. Beer, B.L.S.), Institute of Epidemiology and Medical Biometry (J.D.), University of Ulm, Ulm, Germany; Department of Neuroradiology (M. Braun, B.L.S.), Bezirkskrankenhaus Günzburg, Günzburg, Germany; and Institute of Neuroradiology (Y.O.), Ludwig Maximilian University, Munich, Germany.

Please address correspondence to Johannes Rosskopf, MD, Department of Radiology, University of Ulm, Albert-Einstein-Allee 23, 89081 Ulm, Germany; e-mail: johannes.rosskopf@uni-ulm.de

Indicates article with supplemental on-line photos.

http://dx.doi.org/10.3174/ajnr.A6669

requirement for patient consent was waived because of its retrospective nature.

All patients who underwent endovascular treatment with a WEB device between April 2013 and April 2020 were collected from our institutional data base. Single-layer (SL) and single-layer sphere (SLS) WEB devices were used for treatment of the aneurysms. Inclusion criteria were cranial CT at baseline (the day of the intervention) and a follow-up CT at least >1 months' later. Aneurysms treated with additional devices like coils and stents were excluded.

In our institution, the decision-making process between surgery or endovascular treatment of aneurysms was performed on a case-by-case basis by a multidisciplinary team of neurologists, neurosurgeons, and interventional neuroradiologists.

Treatment Technique

Our institutional standard procedure has been previously described in detail.[18] In brief, endovascular aneurysm treatment with the WEB was performed with the patient under general anesthesia on a biplane angiographic system (Axiom Artis zee; Siemens, Erlangen, Germany) by 4 interventional neuroradiologists. Unilateral femoral puncture was accompanied by a single intravenous heparin bolus of 5000 IU without further systemic heparinization during or after the procedure. After navigating the guiding catheter into the relevant supraaortic artery, the aneurysm was catheterized with a dedicated VIA microcatheter (Sequent Medical). Aneurysm measurements were performed on 3D rotational angiography images and 2D working projections on 2 planes. According to the manufacturer's instructions, the WEB device was slightly oversized to exceed the average width of the aneurysm sac by at least 1 mm to secure the maximum stable position inside the aneurysm. A control angiogram, including a 3D rotational angiography in complex cases, verified the optimal opening and location of the WEB. A routine postoperative nonenhanced cranial CT (Brilliance 40; Philips Healthcare) was performed to exclude an immediate procedure-related complication. Scan parameters were as follows: 40–detector row multidetector CT, 80 kV, 556 mA, volume CT dose index = 23.5 mGy, 0.75-second gantry rotation time, pitch = 0.675, section width = 0.54 mm.

Antiplatelet Regimen

Pre- and postoperative antiplatelet regimens were the following: Unruptured cases received 100 mg of acetylsalicylic acid (ASA) and 75 mg of clopidogrel 5 days before treatment if possible. Otherwise, they were loaded with 500 mg of ASA and 375 mg of clopidogrel the day before treatment. Depending on the extent of WEB protrusion into the parent vessel or neck size of the aneurysm, either a double-antiplatelet regimen for a further 4–6 weeks or a single-antiplatelet regimen (100 mg of ASA daily) for up to 3 months was continued. In ruptured aneurysms, a single antiplatelet, usually ASA, 100 mg daily, was given for 4–6 weeks.

In case of periprocedural thromboembolic complications irrespective of rupture status, intravenous tirofiban (Aggrastat) was administered during the procedure and usually continued for 4–6 hours, followed by a loading dose of ASA (500 mg) and clopidogrel (375 mg). Maintenance double-antiplatelet therapy was continued as described above.

Follow-Up and Reevaluation of Images

Follow-up angiographic controls with DSA or CTA were scheduled, depending on the preceding results. Imaging data were independently re-evaluated on the 3-grade scale derived from the WEB Occlusion Scale[19] by 3 interventional neuroradiologists (J.R., Y.O., and M. Braun) in a random order. In case of disagreement, consensus was found between 2 interpreters with the help of the most experienced senior neuroradiologist (B.L.S.). Adequate occlusion was defined as complete occlusion or neck remnant.[20] Taken together, the quality of aneurysm occlusion was determined by the classification on the 3-grade scale as well as the differentiation between adequate and inadequate occlusion.

Image Analysis

The decrease in height of the WEB device was used as a surrogate for shape modification. On thin-section cranial CT scans with a section width of 0.54 mm, reduction in height was quantified in a semiautomatic multistage process by the use of the software package ImageJ 1.52a (National Institutes of Health).[21] The detailed step-by-step method is illustrated in On-line Fig 1. Briefly, this included the following: 1) image reconstruction of the WEB device, overturning the principal axis to the maximum distance between the proximal marker (near the aneurysm neck) and the distal marker (near the aneurysm apex), 2) bridging the distance between the 2 markers on the image by placing a line specifically chosen to be slightly less dense than the markers, and 3) determining the full width at half maximum between the 2 by line-bridged markers of the WEB.

Statistical Analysis and Time Course Analysis

All statistical analyses were performed using SAS (version 9.4; https://www.sas.com/en_us/software/sas9.html) and R statistical and computing software (Version 3.5.1; http://www.r-project.org/). For statistical analysis, measured values for the height of the WEB device in millimeters were converted to percentage values in each case by defining baseline as 100% and the follow-up scan as the corresponding decrease in height in percentage from baseline. Linear mixed-effects regression models were used to examine the influence of time, aneurysm occlusion rate, device size, rupture status, aneurysm location, and reintervention rate on the quantified deepening of the proximal and distal concave recesses of the WEB device across time. A 2-sided P value of .05 was considered statistically significant. Due to the exploratory nature of this study, all results from statistical tests have to be interpreted as hypothesis-generating. An adjustment for multiple testing was not performed. The measurement error was determined on 11 randomly selected patients (10% of the total number of measurements, $n = 111$). WEB height varied between −3.1% and +3.4%. Therefore, a decrease of >5% was considered relevant.

Time course analysis of WEB shape modification was performed graphically and analytically. In each case of an

investigated WEB-treated aneurysm, the decrease of WEB height across time in days was visualized as line graphs, yielding a total of 32 graphs. For analytic analysis, the slopes from a univariate linear regression model separate for each WEB device were calculated (individual changes in percentage/month). Derived from this, the median annual reduction was determined. All available data were used in each WEB device for this calculation.

Table 1: Follow-up aneurysm occlusion rates on a 3-grade scale

Anatomic Results at Follow-Up	Total (%)
Complete occlusion (grade 1)	13/32 (40.6)
Neck remnant (grade 2)	8/32 (25.0)
Aneurysm remnant (grade 3)	11/32 (34.4)
Retreatment	5/32 (15.6)
Complication rate	2/32 (6.3)

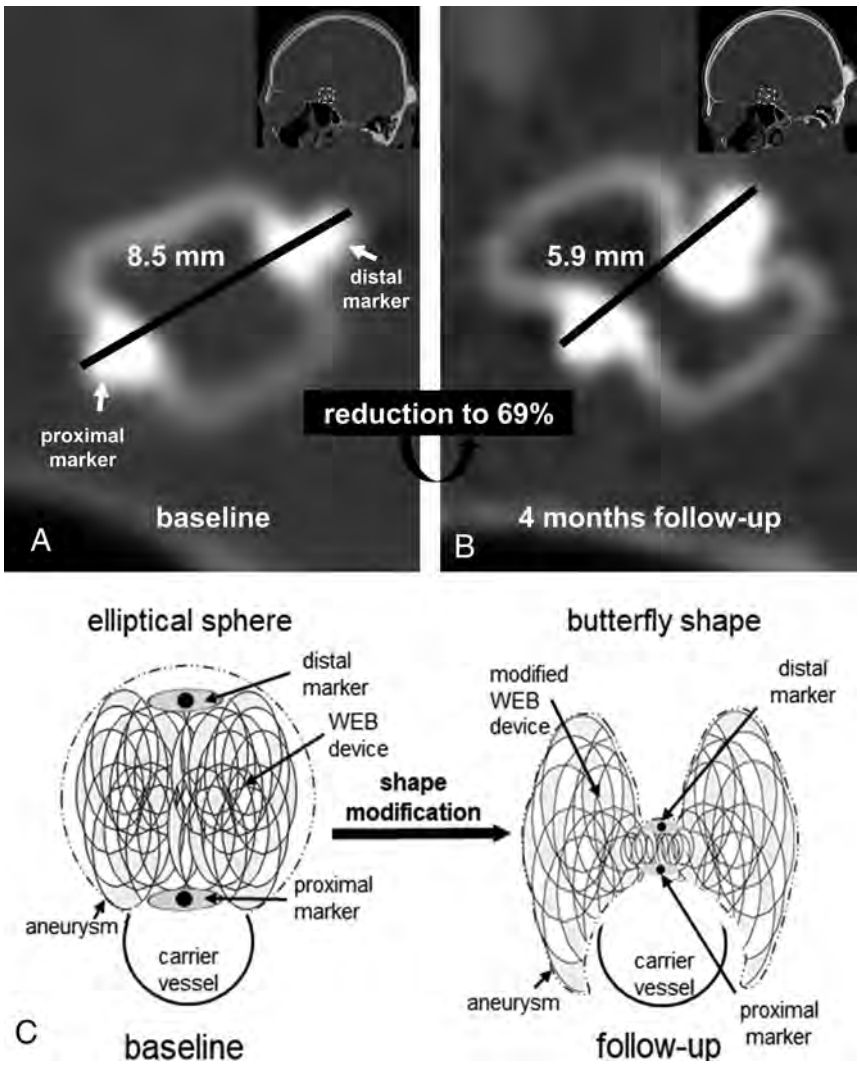

FIG 1. Aneurysm at the anterior communicating artery treated with a 7 × 4 WEB device (SL) on CT at the day of the intervention (baseline) (*A*) and 4 months later (*B*). The distance (*black line*) between the proximal marker (near the aneurysm neck) and the distal marker (near the aneurysm apex) decreases from 8.5 to 5.9 mm, yielding a reduction to 69%. Schematic illustration (*C*) of WEB shape modification from an elliptical sphere at baseline to a figure that might be comparable with a "butterfly shape" on follow-up. With deepening of the proximal and distal marked concave recesses, the WEB device appears to be shaped in the middle like the trunk of a butterfly and its wings are a semicircle that encompasses the carrier vessel due to elements of the WEB device being pushed aside.

RESULTS

Study Population

Sixty-seven patients with aneurysms were treated with the WEB device between April 2013 and April 2020 in our institution. Thirty patients with 32 WEB-treated aneurysms (2 patients with 2 aneurysms) fulfilled the inclusion criteria of baseline CT and follow-up CT at least >1 months' later. Thirty-seven patients treated with the WEB device were excluded because aneurysms were occluded with additional devices (coils and stents) or the patient's CT image timeline did not fulfill the inclusion criteria, respectively. The mean patient age of 6 men and 24 women was 56.5 ±10.4 years (range, 39.0–79.0 years). Thirty WEB-SL devices (93.8%) and 2 WEB-SLS devices (6.3%) with a minimum of 3.5 × 2 mm to a maximum of 11 × 9 mm were used. Thirteen ruptured (40.6%) and 19 unruptured (59.4%) WEB-treated aneurysms were located at the intradural internal carotid artery or middle cerebral artery in 8/32 (25.0%), at the anterior communicating artery in 13/32 (40.6%), and at the posterior inferior cerebellar artery or superior cerebellar artery or basilar artery in 11/32 (34.4%). The median of the latest CT follow-up was 11.4 months, with an interquartile range of 6.5–21.5 months comprising 9/32 (28.1%) cases with 1-time follow-up, 10/32 (31.3%) cases with 2-time, 4/32 (12.5%) cases with 3-time, 7/32 (21.9%) cases with 4-time, and 2/32 (6.3%) cases with 5-time follow-up measurements. In 10/32 cases (31.3%), long-term data with the follow-up time exceeding the 18-month interval were available.

Anatomic Results and Complications

Anatomic results were evaluated on CTA follow-up scans and DSA. Adequate occlusion was observed in 27/32 (84.4%), and aneurysm remnant, in 5/32 (15.6%) cases. Results of the detailed 3-grade scale are summarized in Table 1. In 5 cases, reintervention due to inadequate occlusion was necessary, with additional coiling in 3 cases (within a delay of 4, 5, and 8 months, respectively) as well as stent placement in 2 cases (delay of 5 and 8 months, respectively). One thromboembolic event occurred, and another patient had a dissection of the internal carotid artery. In both situations, the patients remained asymptomatic.

Table 2: Results of association analysis of WEB shape modification and anatomic results performed by mixed-effects regression models

Parameters	Regression Coefficient (95% Confidence Interval)	*P* Value[a]
Time course (days)	−0.00017 (−0.00023 to −0.00011)	<.001
Aneurysm occlusion rate	0.02722 (−0.05656−0.1110)	.52
Device size (mm)	0.002948 (−0.01371−0.01961)	.73
Rupture status of aneurysm (ruptured vs unruptured)	−0.01868 (−0.08609− 0.04873)	.58
Aneurysm location	0.04867 (−0.02391−0.1213)	.40
	0.01904 (−0.06410−0.1022)	
Reintervention (yes vs no)	−0.07277 (−0.1588−0.01329)	.10

[a] A 2-sided *P* value of .05 is considered statistically significant.

Association Analysis

In 29/32 WEB devices (90.6%), the reduction in height was found to be at least 5% (Fig 1). The decrease in height across time was significantly associated with the time interval in days since the intervention ($P < .0001$); a stronger decrease in WEB height was associated with a longer time since the intervention, with an average 0.017% decrease (95% confidence interval, 0.011%–0.023%) per day. Adequately occluded aneurysms by the WEB had a 2.7% (95% confidence interval, −5.7%−11.1%) greater decrease in the height of the WEB than the aneurysm remnant, which was not significant ($P = .52$) and in line with results of the association analysis with the aneurysm occlusion rate on the detailed 3-grade scale ($P = .78$). Rupture status of the aneurysm, aneurysm location, and re-intervention rate were not significantly related to the degree of shape modification ($P = .58$, $P = .40$, and $P = .10$) (Table 2).

Time Course Analysis of WEB Shape Modification

The graphic analysis (On-line Fig 2) of the depicted line graphs of each WEB-treated aneurysm case separately revealed mixed patterns of shape modification, with a continuous strong as well as weak decrease in the WEB height during the time course. However, cases with an initial strong decrease and a subsequent plateau phase were also observed. The analytic analysis of the depicted line graphs via univariate linear regression model analysis separate for each WEB device revealed a median slope reduction in percentages per month of −1.599% (interquartile range, −0.143 to −0.024%), yielding an annual median reduction of 19.2% (interquartile range, 8.6%–52.3%).

DISCUSSION

In the current study, we quantitatively analyzed shape modification of the WEB device during follow-up of 32 WEB-treated aneurysms and evaluated its association with anatomic results. By means of a semiautomated approach on CT scans, shape modification was common in WEB-treated aneurysms (90.6%). The decrease in height was statistically significant across time. No significant association was found between shape change and the quality of aneurysm occlusion, device size, rupture status of the aneurysm, aneurysm location, or re-intervention rate. The graphic and analytic evaluation of time courses revealed mixed patterns of shape modification, with a median slope reduction of 19.2% per year.

As a novelty aspect of the present study, the shortening of the distance between the proximal and distal markers of the WEB device as a surrogate for shape modification was assessed quantitatively on CT scans by a semiautomated method and revealed a higher rate of WEB modification of 90.6% compared with previously reported rates of 25%–73%,[10,11,13,14] most likely due to different study designs with solely qualitative methods.

WEB shape modification was not associated with the quality of aneurysm occlusion as already previously reported by Janot et al.[16] The exact mechanism of shape modification of the WEB device is not clear yet. Cognard and Januel[10] assessed this issue as a hemodynamic phenomenon and suggested a water-hammer effect due to high arterial inflow. Caroff et al[13] were able to show a clear association with aneurysm flow exposure using computational fluid dynamics simulations in a series of 19 aneurysms. They detected shape change in 57.9% (11/19) of aneurysms. It might be deductive because of the tendency of higher aneurysmal inflow in bifurcation aneurysms for which the WEB device was initially used. However, they also reported 3 cases (3/11, 27.2%) with low inflow, which also showed shape modification during follow-up. Additionally, Pierot[15] interpreted WEB shape modification rather as a part of a healing process initiated with thrombus formation, continuing with clot retraction, and eventually ending with fibrosis or formation of scar tissue.

Results of the present study confirmed that shape modification might be a healing process because no association with worsening of occlusion was found. During this process, we found that the WEB device underwent a change of form from an elliptical sphere into a figure that might be comparable with a "butterfly shape" (Fig 1*C*); with shortening of the distance between 2 markers, the markers in the middle represented the trunk and the bilateral wires pushed aside represented the wings. Moreover, in the present series, device size, rupture status, and the re-intervention rate appeared to play a minor role in shape modification of the WEB because no significant association with a decrease in WEB height was observed. Most interesting, Caroff et al[13] also found no statistically significant association of device modification with aneurysm volume, aspect ratio, or neck size in a cohort of 22 patients with WEB-treated unruptured middle cerebral artery or basilar tip aneurysms.

In the current study, time course evaluation revealed a mixed pattern of continuous decline in device height with different slopes. Janot et al[16] previously investigated WEB shape modification quantitatively on DSA at the end of the procedure and on control angiograms at 6 and 18 months. They reported that most of the shape modifications were already noticed at short-term follow-up (6-month DSA) and increased across time until the 18-month control. In our series, it was not possible to distinguish between distinct follow-up points in time due to extremely

different CT follow-up timelines among the patients. However, our results indicated a statistically significant continuous decrease of WEB height also beyond the 18-month interval because our analysis included quantitative data up to a 5.9-year interval.

Limitations of the study included its retrospective design and the relatively small sample size. Furthermore, no subgroup analysis was performed between SL and SLS types of devices due to the unbalanced ratio (30 SLs versus 2 SLSs). Moreover, the artifacts produced by coils and stents did not allow determining the distance between the 2 WEB markers by the developed semiautomated approach. Thus, for methodologic reasons, aneurysms treated with additional devices had to be excluded.

CONCLUSIONS

Ninety-one percent of patients treated with a WEB showed shape modification of the device during follow-up with a median annual reduction rate of 19% in height. WEB shape modification was not associated with the quality of aneurysm occlusion.

REFERENCES

1. Asnafi S, Rouchaud A, Pierot L, et al. **Efficacy and safety of the Woven EndoBridge (WEB) device for the treatment of intracranial aneurysms: a systematic review and meta-analysis.** *AJNR Am J Neuroradiol* 2016;37:2287–92 CrossRef Medline
2. Arthur AS, Molyneux A, Coon AL, et al; WEB-IT Study investigators. **The safety and effectiveness of the Woven EndoBridge (WEB) system for the treatment of wide-necked bifurcation aneurysms: final 12-month results of the pivotal WEB intrasaccular therapy (WEB-IT) study.** *J Neurointerv Surg* 2019;11:924–30 CrossRef Medline
3. Pierot L, Moret J, Turjman F, et al. **WEB treatment of intracranial aneurysms: clinical and anatomic results in the French Observatory.** *AJNR Am J Neuroradiol* 2016;37:655–59 CrossRef Medline
4. Pierot L, Gubucz I, Buhk JH, et al. **Safety and efficacy of aneurysm treatment with the WEB: results of the WEBCAST 2 study.** *AJNR Am J Neuroradiol* 2017;38:1151–55 CrossRef Medline
5. Pierot L, Moret J, Barreau X, et al. **Safety and efficacy of aneurysm treatment with WEB in the cumulative population of three prospective, multicenter series.** *J Neurointerv Surg* 2018;10:556–62 CrossRef Medline
6. Pierot L, Klisch J, Liebig T, et al. **WEB-DL endovascular treatment of wide-neck bifurcation aneurysms: long-term results in a European series.** *AJNR Am J Neuroradiol* 2015;36:2314–19 CrossRef Medline
7. Gawlitza M, Soize S, Januel AC, et al. **Treatment of recurrent aneurysms using the Woven EndoBridge (WEB): anatomical and clinical results.** *J Neurointerv Surg* 2018;10:629–33 CrossRef Medline
8. Mine B, Goutte A, Brisbois D, et al. **Endovascular treatment of intracranial aneurysms with the Woven EndoBridge device: mid term and long term results.** *J Neurointerv Surg* 2018;10:127–32 CrossRef Medline
9. Van Rooij S, Peluso JP, Sluzewski M, et al. **The new low-profile WEB 17 system for treatment of intracranial aneurysms: first clinical experiences.** *AJNR Am J Neuroradiol* 2018;39:859–63 CrossRef Medline
10. Cognard C, Januel AC. **Remnants and recurrences after the use of the WEB intrasaccular device in large-neck bifurcation aneurysms.** *Neurosurgery* 2015;76:522–30 CrossRef Medline
11. Sivan-Hoffmann R, Gory B, Riva R, et al. **One-year angiographic follow-up after WEB-SL endovascular treatment of wide-neck bifurcation intracranial aneurysms.** *AJNR Am J Neuroradiol* 2015;36:2320–24 CrossRef Medline
12. Armoiry X, Turjman F, Hartmann DJ, et al. **Endovascular treatment of intracranial aneurysms with the WEB device: a systematic review of clinical outcomes.** *AJNR Am J Neuroradiol* 2016;37:868–72 CrossRef Medline
13. Caroff J, Mihalea C, Da Ros V, et al. **A computational fluid dynamics (CFD) study of WEB-treated aneurysms: can CFD predict WEB "compression" during follow-up?** *J Neuroradiol* 2017;44:262–68 CrossRef Medline
14. Herbreteau D, Bibi R, Narata AP, et al. **Are anatomic results influenced by WEB shape modification? Analysis in a prospective, single-center series of 39 patients with aneurysms treated with the WEB.** *AJNR Am J Neuroradiol* 2016;37:2280–86 CrossRef Medline
15. Pierot L. **Letter: WEB aneurysm treatment—occlusion stability and "compression."** *Neurosurgery* 2015;77:E666–67 CrossRef Medline
16. Janot K, Herbreteau D, Amelot A, et al. **Quantitative evaluation of WEB shape modification: a five-year follow-up study.** *J Neuroradiol* 2020;47:193–96 CrossRef Medline
17. Cagnazzo F, Ahmed R, Zannoni R, et al. **Predicting factors of angiographic aneurysm occlusion after treatment with the Woven EndoBridge device: a single-center experience with midterm follow-up.** *AJNR Am J Neuroradiol* 2019;40:1773–78 CrossRef Medline
18. Ozpeynirci Y, Braun M, Pala A, et al. **WEB-only treatment of ruptured and unruptured intracranial aneurysms: a retrospective analysis of 47 aneurysms.** *Acta Neurochir (Wien)* 2019;161:1507–13 CrossRef Medline
19. Fiorella D, Arthur A, Byrne J, et al. **Interobserver variability in the assessment of aneurysm occlusion with the WEB aneurysm embolization system.** *J Neurointerv Surg* 2015;7:591–95 CrossRef Medline
20. Rouchaud A, Brinjikji W, Ding YH, et al. **Evaluation of the angiographic grading scale in aneurysms treated with the WEB device in 80 rabbits: correlation with histologic evaluation.** *AJNR Am J Neuroradiol* 2016;37:324–29 CrossRef Medline
21. Schneider CA, Rasband WS, Eliceiri KW. **NIH Image to ImageJ: 25 years of image analysis.** *Nat Methods* 2012;9:671–75 CrossRef Medline

The Distribution and Role of M1 and M2 Macrophages in Aneurysm Healing after Platinum Coil Embolization

Z. Khashim, D. Daying, D.Y. Hong, J.A. Ringler, S. Herting, D. Jakaitis, D. Maitland, D.F. Kallmes, and R. Kadirvel

ABSTRACT

BACKGROUND AND PURPOSE: Impairment of macrophage polarization from a proinflammatory macrophage type 1 (M1) population to an anti-inflammatory macrophage type 2 (M2) population is a hallmark of poor wound healing. In this study, we aimed to evaluate the distribution of M1 and M2 macrophages and to analyze their association with healing in aneurysms embolized by endovascular coiling.

MATERIALS AND METHODS: Elastase-induced aneurysms were created in female rabbits and subsequently embolized with platinum coils. Aneurysm occlusions were evaluated with angiographic imaging at 1 ($n = 6$), 3 ($n = 5$), or 6 ($n = 6$) months. Aneurysm tissues were harvested for histologic analysis, quantification of M1 and M2 macrophages by immunofluorescence, and collagen deposition determined by Masson trichrome staining. Histologic grading of aneurysm healing was also performed. Untreated aneurysms were used as controls ($n = 6$).

RESULTS: The M1 macrophage population was highest at 1 month posttreatment, progressively decreasing at 3 and 6 months. The M2 macrophage population progressively increased at 3 and 6 months posttreatment. The highest collagen deposition was at 6 months posttreatment. We found a moderate-to-weak direct correlation between the percentage of M2 macrophages and collagen deposition, as well as total histologic scores overall, and a strongly positive direct correlation between the percentage of M2 macrophages and total histologic scores at 6 months posttreatment.

CONCLUSIONS: Our data support the direct correlation between M2 macrophage polarization and healing in aneurysm tissues. Our results show a positive relationship between M2 macrophage populations and total histologic scores at later stages of healing after endovascular coiling. We conclude that interventions aimed at stimulating M2 macrophage expression locally may improve aneurysm healing after coil embolization.

ABBREVIATIONS: CD80 = cluster of differentiation 80; CD206 = cluster of differentiation 206; M1 = macrophage type 1; M2 = macrophage type 2

Endovascular coiling is a safe and effective treatment to achieve occlusion of saccular intracranial aneurysms. With time, however, incomplete occlusion and recurrence remain challenging obstacles to successful endovascular treatment.[1,2] Several previous studies have demonstrated associations between poor occlusion or recurrence of aneurysms and factors such as aneurysm size and volume, coil packing density, coil compaction,[3,4] unorganized thrombus, blood pressure, lack of neointima formation, and regulation of cells.[5,6] Few studies have evaluated the infiltration of inflammatory cells into the aneurysm dome during the healing process after endovascular coiling.[7,8]

Inflammatory cells are emerging as a topic of clinical interest in this area. Macrophages may be particularly valuable, due to the unique process of macrophage polarization and its potential impact on wound healing and tissue remodeling. The remarkable plasticity of macrophages enables these cells to change their form and functional phenotype from classically activated macrophage type 1 (M1) to alternatively activated macrophage type 2 (M2) in response to signals in their local environment.[9,10]

Received March 27, 2020; accepted after revision June 4.

From the Department of Radiology (Z.K., D.D., D.Y.H., J.A.R., D.J., D.F.K., R.K.), Mayo Clinic, Rochester, Minnesota; and Biomedical Engineering (S.H., D.M.), Texas A&M University, College Station, Texas.

This study was supported by a grant from the National Institutes of Health (R01NS076491 and U01-NS089692) and, in part, by a fellowship award through the National Defense Science and Engineering Graduate Fellowship Program, sponsored by the Air Force Research Laboratory, the Office of Naval Research, and the Army Research Office.

Please address correspondence to Ramanathan Kadirvel, PhD, Department of Radiology, Mayo Clinic, 200 First St Southwest, Rochester, MN, 55905; e-mail: kadir@mayo.edu

Indicates open access to non-subscribers at www.ajnr.org

http://dx.doi.org/10.3174/ajnr.A6719

The regulation of macrophage subtype M1 (cluster of differentiation 80 [CD80]) and M2 (cluster of differentiation 206 [CD206]) markers has been studied in several disease models.[11-14] Previous studies have demonstrated the persistence of a proinflammatory M1 macrophage population without a subsequent transition to an anti-inflammatory M2 phenotype in poorly healing wounds. Enhancement of T1 M2 macrophage polarization could be a potential therapeutic option in wound healing.[15,16]

In this study, we aimed to evaluate the distribution of M1 and M2 macrophages and to analyze their association with healing in aneurysms embolized by endovascular coiling.

MATERIALS AND METHODS

Aneurysm Creation and Tissue Harvest

Elastase-induced saccular aneurysms were created in 23 New Zealand white female rabbits, weighing between 2.5 and 4 kg. The procedures for aneurysm creation were performed as described previously.[17] Aneurysms were permitted to mature for at least 3 weeks after creation. All treated aneurysms were embolized with the standard bare platinum coils as previously described.[18] The animals were euthanized by lethal injection of pentobarbital at 1 month ($n = 6$), 3 months ($n = 5$), or 6 months ($n = 6$) after endovascular treatment. Untreated control animals were sacrificed at 1 month ($n = 3$) and 3 months ($n = 3$). The harvested aneurysm tissue samples were fixed in 10% neutral buffered formalin, embedded in paraffin, and sectioned as previously described.[19] Some of the rabbits used in this study were originally part of another investigation, in which bare platinum coils were used to treat the aneurysms. The original investigation was entirely unrelated to this project,[20] and did not interfere with the goals of this study.

Angiography

DSA images were obtained immediately after coil implantation and just before sacrifice. The follow-up, presacrifice images were assessed by comparing them with the images after coil implantation using a 3-category grading system (stable occlusion, progressive occlusion, recanalization [coil compaction]).

Immunofluorescence

The paraffin-embedded tissue sections were mounted on microscope slides (Superfrost; Cardinal Health) and incubated for 2 hours at 56°C. The slides were de-paraffinized with xylene and alcohol and washed with water. Antigen retrieval was performed by boiling at 95°C for 15 minutes in a 0.1- mol/L citric acid buffer. The slides were then blocked with appropriate blocking buffer for 30 minutes at room temperature. Slide sections were incubated overnight at 4°C in primary antibodies for M1 (CD80, 1:100 dilution, catalog number 8679; ProSci) or M2 (CD206, 1:50 dilution, catalog number AF2535; R&D Systems). The slides were washed and incubated in secondary antibodies (Cy3; Jackson ImmunoResearch Laboratories) for 2 hours. The slides then were counterstained with nucleic acid stain (Hoechst 33258; Thermo Fisher Scientific) for 5 minutes, then washed, dehydrated, and mounted with mounting medium (Shandon Consul-Mount; Thermo Fisher Scientific). Five randomly assigned fields were chosen and captured on a FluoView FV1200 confocal microscope (Olympus Life Science). Human tonsil was used as a positive control and for a negative control when the primary antibody was omitted. The number of positively staining cells in each image was counted manually by 3 separate individuals.

Aneurysm geometry results of all the study groups[a]

Groups	Untreated Control	1 Month Postcoiling	3 Months Postcoiling	6 Months Postcoiling
Neck width	3.73 ± 0.48	3.0 ± 0.71	3.7 ± 0.94	3.6 ± 1.79
Width	4.18 ± 0.84	2.8 ± 0.37[b]	4.3 ± 0.47	3 ± 0.51[c]
Height	9.73 ± 0.75	9.3 ± 1.06	8.0 ± 1.58	7.7 ± 2.11

[a] All data are reported as mean (mm) ± SD.
[b] $P < .05$.
[c] $P < .01$.

Collagen Deposition

Collagen deposition was analyzed quantitatively through Masson trichrome staining as previously described.[21] The images were captured using microscopy imaging (RTV 5.0; Qimaging MicroPublisher). The images were analyzed using a recently described and experimentally verified image analysis technique,[22] using Photoshop software (Adobe).

Histologic Grading

Histologic grading of aneurysm tissues was performed by an experienced reviewer (>15 years of experience in aneurysm-specific pathology), and grading was followed according to the previously described protocol.[21,23] Neck healing was based on both gross and microscopic inspection. The scores of the gross (0–3) and microscopic inspection (0–4) were averaged to yield a single neck score. If different areas of the aneurysm neck showed different levels of healing, intermediate scores (0.5) were used. Microcompaction assessment (0–3) was based on the shape of the coil mass across the neck, from concave to convex. Healing characteristics in the dome (0–5) were categorized on the basis of the density of cellular infiltration and the area of organized tissue. Accordingly, each score was added together to obtain a total histologic score, as described in Equation 1.

Equation 1: Calculation of total histologic score

$$\frac{\text{Gross Neck Score} + \text{Microneck Score}}{2} + \text{Neck Compaction} + \text{Dome Score} = \text{Total Histologic Score}.$$

Statistical Analysis

All statistical analyses were performed using GraphPad Prism software (GraphPad Software). The differences between the treatment-to-sacrifice time groups were evaluated using the Student t test. The strength of the linear relationships between M2 macrophages and both collagen deposition and histologic grading was evaluated using the Pearson correlation coefficient. Descriptive data were presented as means ± standard error of mean. A P value of $< .05$ was considered statistically significant.

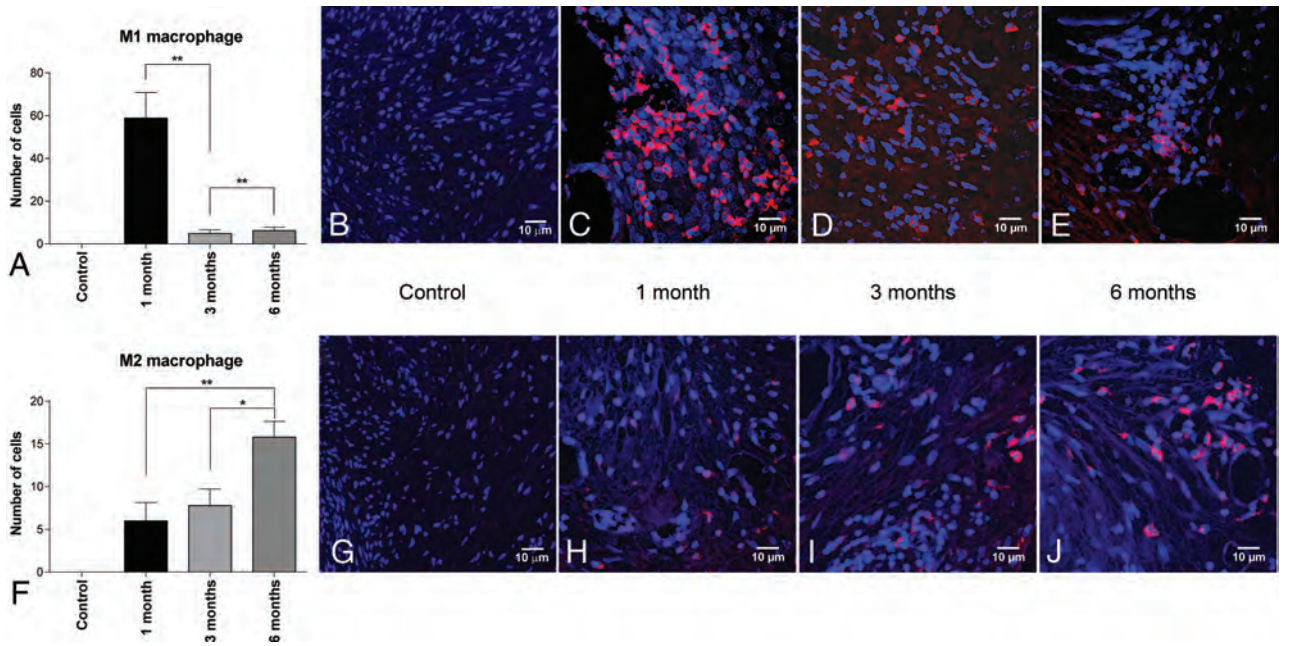

FIG 1. M1 and M2 macrophage populations in aneurysm tissues after endovascular coiling for control and treatment groups. *A*, Mean number of M1 macrophages ± standard error of the mean. Representative confocal microscopy images of cells staining positive for CD80 (60× oil magnification) at 1 month (*C*), 3 months (*D*), and 6 months (*E*). *F*, Mean number of M2 macrophages ± standard error of the mean. Representative confocal microscopy images of cells staining positive for CD206 (60× oil magnification) at 1 month (*H*), 3 months (*I*), and 6 months (*J*). *B* and *G*, Representative confocal images of control aneurysm tissues stained for CD80 and CD206, respectively, at 1 month (20× oil magnification). *Asterisk* indicates $P < .05$; *double asterisks*, $P < .01$.

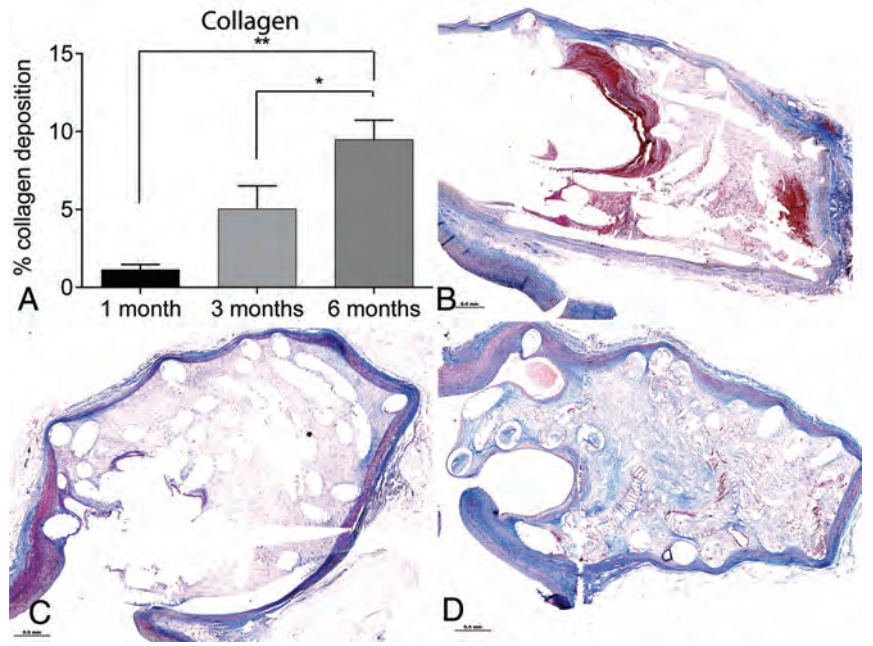

FIG 2. Collagen deposition in aneurysm tissues after endovascular coiling for 3 treatment-to-sacrifice time groups. *A*, Mean percentage of collagen deposition ± standard error of the mean. Photomicrographs of collagen deposition using Masson trichrome stain are shown for 1 month (*B*), 3 months (*C*), and 6 months (*D*) (2.5× magnification; scale bar = 0.4 mm). *Asterisk* indicates $P < .05$; *double asterisks*, $P < .01$.

RESULTS

Angiography

Angiographic imaging of aneurysms before coiling indicated that the mean measurements did not differ significantly among the 3 treatment-to-sacrifice time groups (Table). Follow-up images obtained 1 month posttreatment demonstrated stable occlusion in 4/6 (66.7%) aneurysms, progressive occlusion in 1/6 (16.7%) aneurysms, and coil compaction in 1/6 (16.7%) aneurysms. In the group sacrificed 3 months posttreatment, 5/5 (100%) aneurysms showed stable occlusion. In the group sacrificed 6 months posttreatment, 5/6 (83.3%) aneurysms showed stable occlusion and 1/6 aneurysms (16.7%) showed progressive occlusion. All control, untreated aneurysms remained patent before sacrifice.

M1 and M2 Macrophage Populations

The mean number of proinflammatory M1 macrophages (CD80) found

in the 1-month posttreatment group (58.86 ± 29.52) was significantly higher compared with both the 3-month posttreatment group (4.96 ± 3.79, $P = .003$) and the 6-month posttreatment group (6.2 ± 3.67, $P < .01$) (Fig 1). The number of M1 macrophages did not differ significantly between the 3- and 6-month groups ($P = .587$). In contrast, the mean number of anti-inflammatory M2 macrophages (CD206) was significantly higher in the 6-month posttreatment group (15.8 ± 4.50) compared with both the 1-month group (6 ± 5.23, $P < .01$) and the 3-month group (7.8 ± 4.32, $P = .015$). No significant differences were observed between 1 and 3 months ($P = .555$). There were no positively staining cells observed in the untreated aneurysm control group for either M1 or M2 markers (Fig 1*B*).

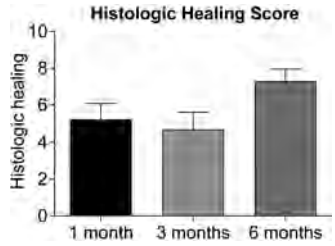

FIG 3. Total histologic healing scores for aneurysm tissues after endovascular coiling for 3 treatment-to-sacrifice time groups.

Collagen Deposition

The mean percentage of collagen deposition was significantly higher in the 6-month posttreatment group (9.48 ± 3.07%) compared with both the 1-month (1.14 ± 0.81%, $P < .001$) and 3-month (7.43 ± 3.29%, $P < .05$) posttreatment groups (Fig 2). No significant difference was observed between 1 and 3 months posttreatment ($P > .05$).

Histologic Grading

The mean total histologic scores at 1 month posttreatment (5.21 ± 2.12) did not differ significantly compared with the 3-month (4.7 ± 2.03, $P > .05$) or 6-month (7.3 ± 1.59, $P > .05$) posttreatment groups (Fig 3). There was also no significant difference between the 3- and 6-month posttreatment groups ($P > .05$).

M2 Macrophages and Correlations with Collagen Deposition and Histologic Grading

The prevalence of M2 macrophages had a moderately positive correlation with collagen deposition in both the 1-month ($r = 0.450$) and the 3-month ($r = 0.446$) posttreatment groups (Fig 4). A weak positive correlation between M2 macrophages and collagen deposition was observed in the 6-month posttreatment group ($r = 0.206$). M2 macrophages were strongly positively correlated with the total histologic grading score in the 6-month posttreatment group ($r = 0.806$); this relationship was weakly positive in the 3-month ($r = 0.166$) and 1-month ($r = 0.323$) posttreatment groups.

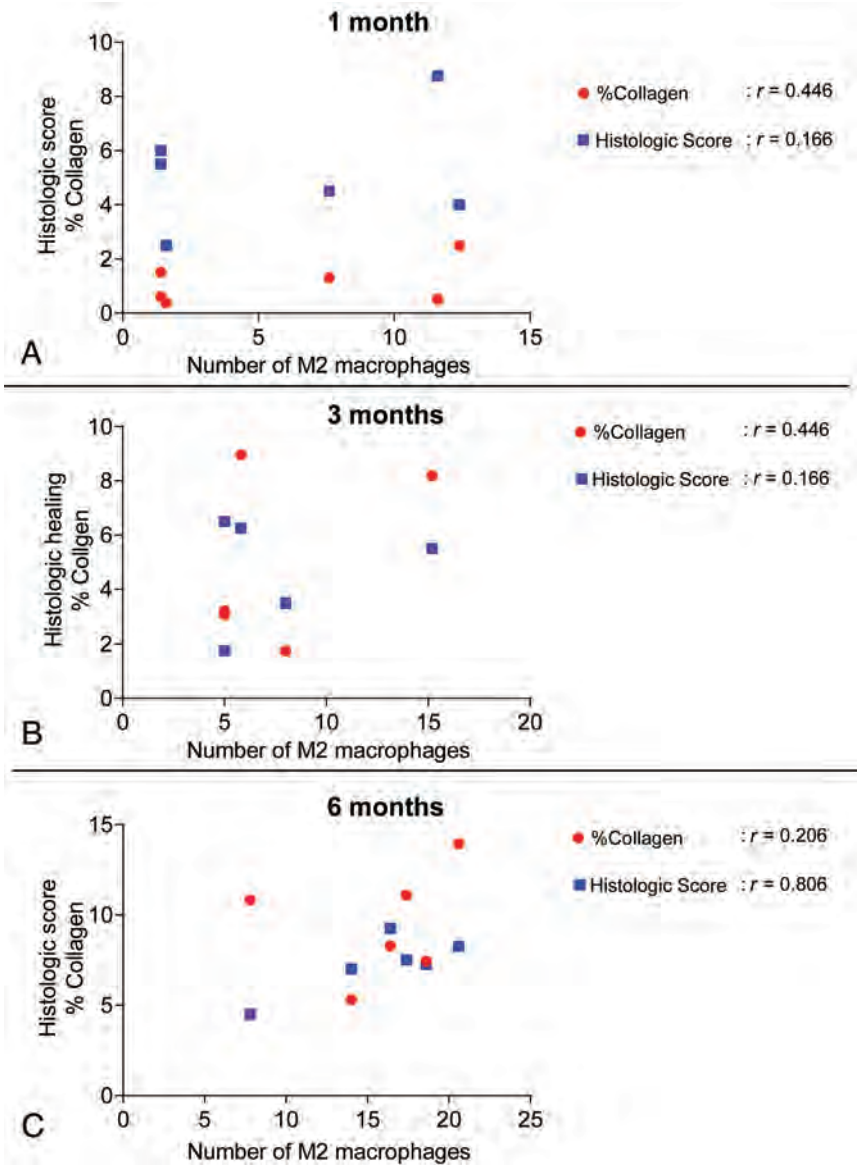

FIG 4. Correlational relationships of M2 macrophages to collagen deposition and histologic grading in aneurysm tissues after endovascular coiling for 3 treatment-to-sacrifice time groups. *A*, One month posttreatment. *B*, Three months posttreatment. *C*, Six months posttreatment.

DISCUSSION

In this study, we found that the presence of proinflammatory M1 macrophages in aneurysm tissues was significantly higher at 1 month after endovascular coiling compared with 3 or 6 months posttreatment. In contrast, the prevalence of anti-inflammatory

M2 macrophages was highest at 6 months after endovascular coiling. These findings demonstrate that macrophage polarity is skewed toward the M1 phenotype in aneurysms on initial tissue damage, whereas M2 macrophages predominate in the later healing phases of tissue formation and remodelling.[9,24] The M2 macrophage phenotype has been found to be important for promoting wound healing and tissue repair and for resolving inflammation.[9] Studies have suggested that increasing the ratio of M2-to-M1 macrophages in wounds can accelerate the healing process. This has been demonstrated experimentally by reducing the effects of endogenous M1 macrophages using neutralizing antibodies or by delivering exogenous polarized M2 macrophages to stimulate wound healing in animal models.[25,26] Previous approaches using proinflammatory coatings on inert platinum coils showed promise in some preclinical models,[27,28] succeeding in stimulating inflammation in clinical trials but failing to reduce recurrence rates,[29,30] possibly due to an unfavorable balance between M1 and M2 macrophages. Coil-mediated delivery of the proinflammatory cytokine, monocyte chemotactic protein-1, has been shown to accelerate aneurysm healing through macrophage inflammatory protein-1α and macrophage inflammatory protein-2-dependent pathways in a mouse model.[27] Our findings suggest that similar interventions aimed at stimulating M2 polarization may improve aneurysm healing after treatment. However, a robust study is needed to delineate the role of M2 macrophage activation in a coil-implanted aneurysm.

We also found that the percentage of collagen deposition progressively increased with time, with statistically significant differences at both 3 and 6 months after treatment. These data are consistent with the findings of a previous study in which we reported that the aneurysm dome became acellular and vascularized with visualized connective tissue and observed increased collagen deposition 3 months after endovascular coiling.[31] Additionally, we have previously demonstrated that collagen synthesis and increased histologic scores are associated with improved healing of aneurysms.[19,31] One way in which M2 macrophages could be involved in this healing process is through secretion of transforming growth factor β1. Factors like transforming growth factor β1 induce the proliferation of fibroblasts, which differentiate into myofibroblasts. These cells are responsible for collagen production and closure of skin wounds.[10] Thus, in this study, we evaluated any potential correlation between M2 macrophage polarity and collagen deposition. Our data demonstrate a moderate-to-weak positive correlation between M2 macrophages and collagen deposition in each of the 3 treatment-to-sacrifice time groups and a strongly positive correlation between M2 macrophages and the total histologic score at 6 months posttreatment. These findings suggest that the activity of M2 macrophages in aneurysm wound healing is not limited to collagen deposition but may also be aided by other mechanisms, such as promoting secretion of platelet-derived growth factor, chemoattractant stabilizing pericytes, extracellular matrix deposition and augmentation, and sprouting endothelial cells.[24,32] In the control group, as expected, we did not find any M1 or M2 macrophages because inflammation is absent in the rabbit "untreated" aneurysm wall beyond 2 weeks following the model creation.[33] Coil treatment itself increases the inflammatory response in the rabbit model.[34] Our findings indicate that M1 and M2 macrophage levels are due to tissue responses to coil implants.

This study has several limitations. It focused exclusively on M1 and M2 macrophage numbers in relation to collagen deposition and total histologic scoring in coil-embolized aneurysms. We did not study the correlation between M1/M2 polarization and the recurrence rate, due to the small sample size. Furthermore, high-throughput microarray or gene profiling will facilitate a better understanding of the underlying mechanisms of the M2 phenotype switch. However, in the current preliminary work, we have only analyzed the distribution of the macrophage subtype (M1 and M2) population in the coil-treated aneurysm environment. A more in-depth study of macrophage subtypes and other immune cells involved in aneurysm healing will give us a deeper understanding of aneurysm healing after coil implantation. All of our current observations are based on animal aneurysm tissues; studying the distribution of macrophage subtypes in human aneurysm tissues will be more directly applicable for future therapeutic approaches.

CONCLUSIONS

We found that the number of M2 macrophages had a strong positive correlation with total histologic scores at a later stage of healing (6 months) after embolization treatment in a rabbit aneurysm model. This finding provides an important impetus for further studies aimed at understanding possible associations between M2 macrophages and other vascular components involved in the healing of coil-embolized aneurysms.

ACKNOWLEDGMENTS

The authors acknowledge Superior Medical Experts for editing assistance.

Disclosures: Scott Herting—*RELATED*: *Grant*: Department of Defense, National Defense Science and Engineering Graduate Fellowship, *Comments*: The National Defense Science and Engineering Graduate fellowship supported me by providing tuition and stipends during graduate school. Duncan Maitland—*RELATED*: *Grant*: National Institutes of Health, *Comments*: National Institute of Neurological Disorders and Stroke, *Grant/Award No.*: U01-NS089692*; *UNRELATED*: *Board Membership*: Shape Memory Medical Inc, *Comments*: Shape Memory Medical Inc (shapemem.com) is commercializing neuorvascular and other vascular occlusion devices. These devices and Shape Memory Medical Inc were not involved in the work in this article. I am a cofounder and board member at Shape Memory Medical Inc; *Patents (Planned, Pending or Issued)*: Texas A&M University and Lawrence Livermore National Laboratory, *Comments*: I have 40 issued patents and many pending related to vascular occlusion technology. None of the technology that I developed was part of this work; *Royalties*: Texas A&M University and Lawrence Livermore National Laboratory, *Comments*: I receive licensing royalty payments from the license of vascular occlusion technology by Shape Memory Medical Inc, paid to my former (Lawrence Livermore) and current (Texas A&M) employers. None of my licensed principal investigator was involved in this work; *Stock/Stock Options*: Shape Memory Medical Inc, *Comments*: I own stock and stock options in Shape Memory Medical Inc. Shape Memory Medical Inc was not involved in this article. David F. Kallmes—*UNRELATED*: *Grants/Grants Pending*: Medtronic, MicroVention, NeuroSigma, Neurogami, *Comments*: preclinical aneurysm research support.* Ram Kadirvel—*RELATED*: *Grant*: National Institutes of Health.* *Money paid to the Institution.

REFERENCES

1. Crobeddu E, Lanzino G, Kallmes DF, et al. **Review of 2 decades of aneurysm-recurrence literature, part 1: reducing recurrence after endovascular coiling.** *AJNR Am J Neuroradiol* 2013;34:266–70 CrossRef Medline

2. Crobeddu E, Lanzino G, Kallmes DF, et al. **Review of 2 decades of aneurysm-recurrence literature, Part 2: managing recurrence after endovascular coiling.** *AJNR Am J Neuroradiol* 2013;34:481–85 CrossRef Medline
3. Knap D, Gruszczyńska K, Partyka R, et al. **Results of endovascular treatment of aneurysms depending on their size, volume and coil packing density.** *Neurol Neurochir Pol* 2013;47:467–75 CrossRef Medline
4. Leng B, Zheng Y, Ren J, et al. **Endovascular treatment of intracranial aneurysms with detachable coils: correlation between aneurysm volume, packing, and angiographic recurrence.** *J NeuroIntervent Surg* 2014;6:595–99 CrossRef Medline
5. Ozawa T, Tamatani S, Koike T, et al. **Histological evaluation of endothelial reactions after endovascular coil embolization for intracranial aneurysm: clinical and experimental studies and review of the literature.** *Interv Neuroradiol* 2003;9:69–82 CrossRef Medline
6. Boecher-Schwarz HG, Ringel K, Kopacz L, et al. **Ex vivo study of the physical effect of coils on pressure and flow dynamics in experimental aneurysms.** *AJNR Am J Neuroradiol* 2000;21:1532–36 Medline
7. Ishihara S, Mawad ME, Ogata K, et al. **Histopathologic findings in human cerebral aneurysms embolized with platinum coils: report of two cases and review of the literature.** *AJNR Am J Neuroradiol* 2002;23:970–74 Medline
8. Shimizu S, Kurata A, Takano M, et al. **Tissue response of a small saccular aneurysm after incomplete occlusion with a Guglielmi detachable coil.** *AJNR Am J Neuroradiol* 1999;20:546–48 Medline
9. Ferrante CJ, Leibovich SJ. **Regulation of macrophage polarization and wound healing.** *Adv Wound Care (New Rochelle)* 2012;1:10–16 CrossRef Medline
10. Hesketh M, Sahin KB, West ZE, et al. **Macrophage phenotypes regulate scar formation and chronic wound healing.** *Int J Mol Sci* 2017;18:1545 CrossRef Medline
11. Zhou Y, Yoshida S, Kubo Y, et al. **Different distributions of M1 and M2 macrophages in a mouse model of laser-induced choroidal neovascularization.** *Mol Med Rep* 2017;15:3949–56 CrossRef Medline
12. Nawaz A, Aminuddin A, Kado T, et al. **CD206(+) M2-like macrophages regulate systemic glucose metabolism by inhibiting proliferation of adipocyte progenitors**. *Nat Commun* 2017;8:286 CrossRef Medline
13. Trombetta AC, Soldano S, Contini P, et al. **A circulating cell population showing both M1 and M2 monocyte/macrophage surface markers characterizes systemic sclerosis patients with lung involvement.** *Respir Res* 2018;19:186 CrossRef Medline
14. Raggi F, Pelassa S, Pierobon D, et al. **Regulation of human macrophage M1-M2 polarization balance by hypoxia and the triggering receptor expressed on myeloid cells-1.** *Front Immunol* 2017;8:1097 CrossRef Medline
15. Khanna S, Biswas S, Shang Y, et al. **Macrophage dysfunction impairs resolution of inflammation in the wounds of diabetic mice.** *PLoS One* 2010;5:e9539 CrossRef Medline
16. Mirza R, Koh TJ. **Dysregulation of monocyte/macrophage phenotype in wounds of diabetic mice.** *Cytokine* 2011;56:256–64 CrossRef Medline
17. Altes TA, Cloft HJ, Short JG, et al. **1999 ARRS Executive Council Award: creation of saccular aneurysms in the rabbit—a model suitable for testing endovascular devices. American Roentgen Ray Society.** *AJR Am J Roentgenol* 2000;174:349–54 CrossRef Medline
18. Kallmes DF, Helm GA, Hudson SB, et al. **Histologic evaluation of platinum coil embolization in an aneurysm model in rabbits.** *Radiology* 1999;213:217–22 CrossRef Medline
19. Dai D, Ding YH, Kadirvel R, et al. **Relationship between aneurysm volume and histologic healing after coil embolization in elastase-induced aneurysms: a retrospective study.** *AJNR Am J Neuroradiol* 2008;29:98–101 CrossRef Medline
20. Herting SD, Boyle AJ, Dai D, et al. **In vivo comparison of shape memory polymer foam-coated and bare metal coils for aneurysm occlusion in the rabbit elastase model.** *J Biomed Mater Res B Appl Biomater*2019;107:2466–75 CrossRef Medline
21. Dai D, Yong-Hong D, Rezek I, et al. **Healing of saccular aneurysms following platinum coil embolization: lack of improved efficacy with vitamin C supplementation.** *J Neurointerv Surg* 2013;5:591–96 CrossRef Medline
22. Dai D, Ding YH, Danielson MA, et al. **Endovascular treatment of experimental aneurysms with use of fibroblast transfected with replication-deficient adenovirus containing bone morphogenetic protein-13 gene.** *AJNR Am J Neuroradiol* 2008;29:739–44 CrossRef Medline
23. Dai D, Ding YH, Lewis DA, et al. **A proposed ordinal scale for grading histology in elastase-induced, saccular aneurysms.** *AJNR Am J Neuroradiol* 2010;31:132–38 CrossRef Medline
24. Murray PJ, Wynn TA. **Protective and pathogenic functions of macrophage subsets.** *Nat Rev Immunol* 2011;11:723–37 CrossRef Medline
25. Goren I, Muller E, Schiefelbein D, et al. **Systemic anti-TNFalpha treatment restores diabetes-impaired skin repair in ob/ob mice by inactivation of macrophages.** *J Invest Dermatol* 2007;127:2259–67 CrossRef Medline
26. Jetten N, Roumans N, Gijbels MJ, et al. **Wound administration of M2-polarized macrophages does not improve murine cutaneous healing responses.** *PLoS one* 2014;9:e102994 CrossRef Medline
27. Hoh BL, Hosaka K, Downes DP, et al. **Monocyte chemotactic protein-1 promotes inflammatory vascular repair of murine carotid aneurysms via a macrophage inflammatory protein-1alpha and macrophage inflammatory protein-2-dependent pathway.** *Circulation* 2011;124:2243–52 CrossRef Medline
28. Murayama Y, Tateshima S, Gonzalez NR, et al. **Matrix and bioabsorbable polymeric coils accelerate healing of intracranial aneurysms: long-term experimental study.** *Stroke* 2003;34:2031–37 CrossRef Medline
29. McDougall CG, Johnston SC, Gholkar A, et al; MAPS Investigators. **Bioactive versus bare platinum coils in the treatment of intracranial aneurysms: the MAPS (Matrix and Platinum Science) trial.** *AJNR Am J Neuroradiol* 2014;35:935–42 CrossRef Medline
30. Pierot L, Cognard C, Ricolfi F, et al. CLARITY investigators. **Mid-term anatomic results after endovascular treatment of ruptured intracranial aneurysms with Guglielmi detachable coils and Matrix coils: analysis of the CLARITY series.** *AJNR Am J Neuroradiol* 2012;33:469–73 CrossRef Medline
31. Brinjikji W, Kallmes DF, Kadirvel R. **Mechanisms of healing in coiled intracranial aneurysms: a review of the literature.** *AJNR Am J Neuroradiol* 2015;36:1216–22 CrossRef Medline
32. Spiller KL, Anfang RR, Spiller KJ, et al. **The role of macrophage phenotype in vascularization of tissue engineering scaffolds.** *Biomaterials* 2014;35:4477–88 CrossRef Medline
33. Kadirvel R, Ding YH, Dai D, et al. **The influence of hemodynamic forces on biomarkers in the walls of elastase-induced aneurysms in rabbits.** *Neuroradiology* 2007;49:1041–53 CrossRef Medline
34. Herting SM, Ding Y, Boyle AJ, et al. **In vivo comparison of shape memory polymer foam-coated and bare metal coils for aneurysm occlusion in the rabbit elastase model.** *J Biomed Mater Res Part B Appl Biomater* 2019;107:2466–75 CrossRef Medline

Fusion Image Guidance for Supra-Aortic Vessel Catheterization in Neurointerventions: A Feasibility Study

A. Feddal, S. Escalard, F. Delvoye, R. Fahed, J.P. Desilles, K. Zuber, H. Redjem, J.S. Savatovsky, G. Ciccio, S. Smajda, M. Ben Maacha, M. Mazighi, M. Piotin, and R. Blanc

ABSTRACT

BACKGROUND AND PURPOSE: Endovascular navigation through tortuous vessels can be complex. Tools that can optimise this access phase need to be developed. Our aim was to evaluate the feasibility of supra-aortic vessel catheterization guidance by means of live fluoroscopy fusion with MR angiography or CT angiography.

MATERIALS AND METHODS: Twenty-five patients underwent preinterventional diagnostic MRA, and 8 patients underwent CTA. Fusion guidance was evaluated in 35 sessions of catheterization, targeting a total of 151 supra-aortic vessels. The time for MRA/CTA segmentation and fluoroscopy with MRA/CTA coregistration was recorded. The feasibility of fusion guidance was evaluated by recording the catheterizations executed by interventional neuroradiologists according to a standard technique under fluoroscopy and conventional road-mapping independent of the fusion guidance. Precision of the fusion roadmap was evaluated by measuring (on a semiquantitative 3-point scale) the maximum offset between the position of the guidewires/catheters and the vasculature on the virtual CTA/MRA images. The targeted vessels were divided in 2 groups according to their position from the level of the aortic arch.

RESULTS: The average time needed for segmentation and image coregistration was 7 ± 2 minutes. The MRA/CTA virtual roadmap overlaid on live fluoroscopy was considered accurate in 84.8% (128/151) of the assessed landmarks, with a higher accuracy for the group of vessels closer to the aortic arch (92.4%; OR, 4.88; 95% CI, 1.83–11.66; $P = .003$).

CONCLUSIONS: Fluoroscopy with MRA/CTA fusion guidance for supra-aortic vessel interventions is feasible. Further improvements of the technique to increase accuracy at the cervical level and further studies are needed for assessing the procedural time savings and decreasing the x-ray radiation exposure.

With the increasing use of endovascular treatments for cerebrovascular diseases, in an aging population, physicians are more frequently facing complex endovascular navigation. Limitations to the navigation of endovascular devices from the aortic arch to the intracranial vessels still remain,[1,2] and the speed and safety of access through the vascular tortuosity need to be enhanced.[3] Access through tortuous vessels can make the treatment complex and leads to increased procedural time, x-ray exposure, and rate of adverse events or failure.[2,4-6]

Routine supra-aortic vessel catheterization in neurovascular procedures uses conventional road-mapping (superimposition of contrast-filled vessels on fluoroscopy using digital subtraction). It provides good spatial and contrast resolution and enhances direct catheterization, which can cause vasospasm, dissection, and thromboembolic events due to wire and guide traumatic manipulation and atheromatous plaque dislodgement.

However, its main limitation is inherent in its static projection. Because tortuous anatomy is more frequently encountered in clinical practice, physicians require different working projections, varying the C-arm detector angle to clear an ostium or delineate loops. This requirement leads to extra contrast administration each time a new roadmap is generated.

Live 3D road-mapping techniques allow dynamic vessel road-mapping, with live adaptation to the C-arm movements. This technique combines real-time fluoroscopy with a previously performed CTA or MRA and has gained wide acceptance for aortic or peripheral endovascular procedures. It is claimed and now widely recognized that it could enhance catheterization abilities and reduce extra contrast administration and procedural time, especially in complex vascular catheterizations.[7-10]

The use of such fusion imaging techniques is also gaining acceptance in the interventional neuroradiology field for intracranial use,[11-13] especially for primary access (navigation of the

Received March 13, 2020; accepted after revision June 3.

From the Interventional Neuroradiology Unit (A.F., S.E., F.D., R.F., J.P.D., K.Z., H.R., G.C., S.S., M.B.M., M.M., M.P., R.B.) and Diagnostic Neuroradiology Unit (J.S.S.), Fondation Ophtalmologique Adolphe de Rothschild, Paris, France; Université Paris Denis Diderot (J.P.D., M.M., M.P., R.B.), Sorbonne Paris Cite, Paris, France; Laboratory of Vascular Translational Science (J.P.D., M.M., M.P., R.B.), U1148 Institut National de la Santé et de la Recherche Médicale, Paris, France.

Please address correspondence to Raphaël Blanc, MD, MSc, Department of Interventional Neuroradiology, Fondation Ophtamologique A de Rothschild, 29 Rue Manin, 75019 Paris, France; e-mail: rblanc@for.paris
http://dx.doi.org/10.3174/ajnr.A6707

guiding catheter or long introducer sheath) either through venous[14] or arterial approaches.[15]

The goal of our study was to assess the feasibility and evaluate the spatial accuracy of aortic arch and supra-aortic cervical vessel catheterization by means of fusion guidance using VesselNavigator software (Philips Healthcare).

MATERIALS AND METHODS

This study is a single-center (Fondation Ophtalmologique Adolphe de Rothschild, Paris, France) prospective study designed to evaluate the feasibility of aortic arch and supra-aortic cervical vessel catheterization under fusion guidance in neurointerventional diagnostic or therapeutic angiograms. VesselNavigator software has a CE Mark but was used off-label for this study.

The patients were offered participation in the study if they had a confirmed indication for either a diagnostic or therapeutic angiography for any cerebrovascular condition and had undergone noninvasive encephalic and aortic arch vessel MRA or CTA as a part of their diagnostic management. No additional encephalic or aortic arch vessel imaging was based for the specific purpose of the study. No selection was based on age, atherosclerosis status, or any MRA or CTA features predicting a difficult catheterization (vascular tortuosity, anatomic variants).

Oral and written information about fusion guidance was delivered during a medical consultation before the procedure. The study was approved by the institutional ethics committee, and written consent was waived. This study is registered under clinicaltrial.org identifier NCT03269734.

Preprocedural Noninvasive Vascular Imaging

MRA. Patients were scanned before the procedure on a 3T MR imaging system (Ingenia 3T; Philips Healthcare) using a 16-channel head coil. All examinations included a contrast-enhanced MR angiography of the aortic arch, supra-aortic trunks, and intracranial vessels using the following parameters: coronal plane covering 250 slices, active TR/TE = 5.5/2.2 ms, flip angle = 27°, number of excitations = 1, acquisition bandwidth = 476.7 Hz, FOV = 380 × 321, voxel size = 0.5 × 0.5 × 1 mm (interpolation = 0.495 × 0.495 × 0.5 mm). The imaging time was 1 minute 9 seconds. A bolus-tracking injection technique was used to time the start of data acquisition.

CTA. Patients were scanned (Brilliance CT 64, Philips Healthcare) in a caudocranial fashion from the aortic arch to the circle of Willis (vertex). A bolus injection of contrast was given according to the patient's weight (usually 60–80 mL) through an intravenous access (18- or 20-ga catheter, antecubital fossa) at a rate of 3–5 mL per second with a 30-mL saline chaser bolus after contrast injection. An automatic bolus-tracking technique was used with an ROI in the ascending thoracic aorta. Data were acquired when the threshold of 110 HU was reached with a minimum delay of 4 seconds. The technical parameters of our acquisition protocol were the following: collimation = 64 × 0.6 mm, gantry rotation = 330 ms, tube voltage = 120 kV(peak). The overall acquisition time (250 mm) was around 4 seconds. The 0.6-mm thickness images were reconstructed at 0.4 mm in the axial plane and sent to the PACS and used for dedicated MPRs, MIPs, and 3D rendering in the postprocessing workstation.

Anesthesia Protocol. At our institution, all procedures are performed with the patient under the supervision of an anesthesiologist; scheduled patients (excluding emergencies) have dedicated consultation with an anesthesiologist before the intervention. Diagnostic or follow-up angiograms are obtained with the patient under conscious sedation using remifentanil, in addition to local anesthesia for vascular puncture. Embolization procedures (intracranial aneurysms, arteriovenous fistulas, and arteriovenous malformations) are performed with the patient under general anesthesia. Mechanical thrombectomies are usually performed with the patient under conscious sedation.

Procedural Image Fusion and Dynamic 3D Roadmap

Step 1: Preprocedural Vessel Segmentation. MRA/CTA tridimensional DICOM datasets were imported into the Xtravision workstation and loaded in the VesselNavigator application before the patient was admitted to the suite.

Using a semiautomatic segmentation algorithm incorporated in the software, either the first or the second operator extracted the aortic arch and supra-aortic vessels from the soft tissues.

We defined 9 relevant ROIs to assess the accuracy of the fusion, located 1 cm above the ostia of the brachiocephalic artery trunk, the right and left common carotid arteries, the right and left internal carotid arteries, the right and left subclavian arteries, and the right and left vertebral arteries. Landmarks were placed on those 9 ROIs, using dedicated circular labels in the VesselNavigator application (Fig 1).

The time needed to complete segmentation and landmark labeling was monitored.

During this step, the operator could define optimal working projections to be used by rotating the segmented vessels. Specific projection angles were stored and were recalled during catheterization. The operator could identify the catheter most adapted to the arterial tree anatomy.

Step 2: 2D–3D Coregistration. The patient was admitted in the operating room and positioned supine on the angiography table. His or her head was set in a neutral position, using head-and-shoulder supports. Additional restraining straps were added in case of general anesthesia to immobilize the head in a specific position when necessary.

Image fusion was performed using a 2D–3D alignment: The patient's thorax was positioned at the isocenter of the image (FOV = 48 cm). The first operator acquired 2 short fluoroscopy runs with the anterior-posterior C-arm, first in right anterior oblique view, then a second short run orthogonal to the previous view.

The segmented 3D volume dataset was merged with fluoroscopy images, matching anatomic features (heart shadow, aortic knob, pulmonary arteries, bones structures) either on the Xtravision workstation outside the operating suite or at tableside using the digital screen with a sterile plastic cover. 3D roadmap opacity and contrast were adjusted to the first operator's convenience.

Step 3: Perioperative Image Fusion: 3D Dynamic Roadmap. Once the coregistration was set, the VesselNavigator application allowed augmented navigation under 3D dynamic roadmap guidance with

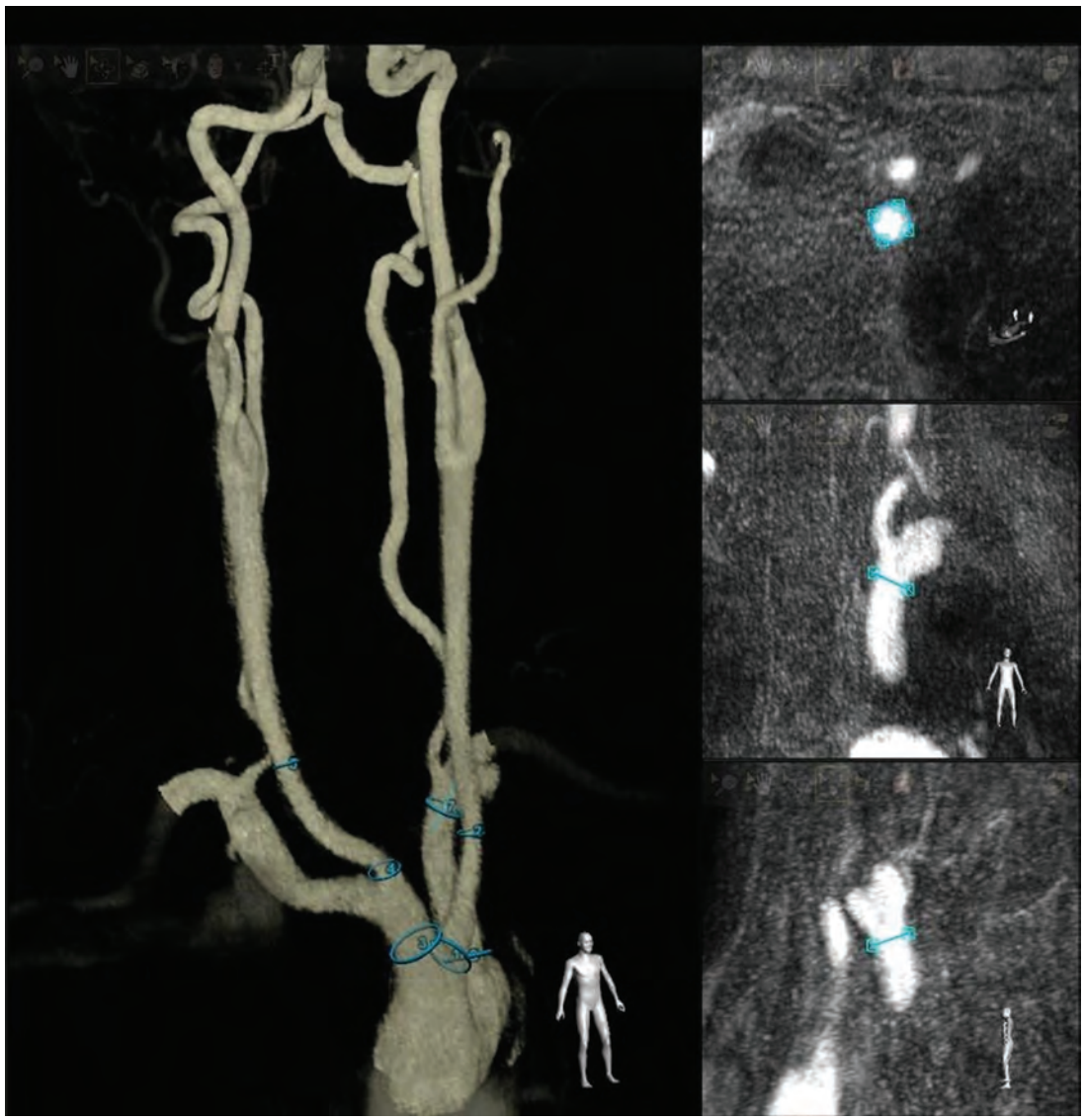

FIG 1. Example of a virtual roadmap of supra-aortic vessels. The vasculature is segmented from the MRA dataset with VesselNavigator software, with landmarks added on the brachiocephalic artery trunk, the right and left common carotid arteries, and the left subclavian artery. During this step, the operator saves projection angles, which can be recalled during catheterization.

the frontal C-arm. The image fusion was real-time, regardless of the C-arm position, magnification, or table manipulation. The first operator performed primary access by navigation of the catheter (diagnostic 5F or 6F guiding catheter or long introducer sheath) and guidewire from a femoral or radial access to cervical target positions. The operator was able to use, at his or her convenience, classic roadmap or augmented visualization to clear ostia and delineate vascular loops.

During catheterization, the second operator took screenshots of the merged images when the wire reached the labeled ROI. These screenshots were used to assess the accuracy of the fusion.

The 3 steps of the workflow are summarized in Fig 2.

Fusion Imaging Assessment

Spatial accuracy of the MRA/CTA–fluoroscopy fusion roadmap was visually scored using perioperative recorded screenshots and videos.

The operator used a 3-category semiquantitative scale to score the offset: accurate, if the catheter projected within the landmark on the virtual roadmap; mismatch, if the catheter projected out of the virtual landmark but within a distance inferior to the diameter of the vessel; and inaccurate, if the catheter projected out of the landmark with a distance superior to the diameter of the vessel (Fig 3).

Statistical Analysis

We first calculated the proportion of accurate, mismatch, and inaccurate virtual roadmaps for the 9 ROIs. In a second part, we reunited these ROIs in 2 groups according to their distance from the aortic arch. We defined as close to the arch (group 1) the landmarks labeled on the brachiocephalic artery trunk, the right SCA and vertebral artery, the left common carotid artery, and the left SCA and vertebral artery. We defined as distant from the arch (group 2) the landmarks labeled on the right common carotid artery and ICA, and the left ICA.

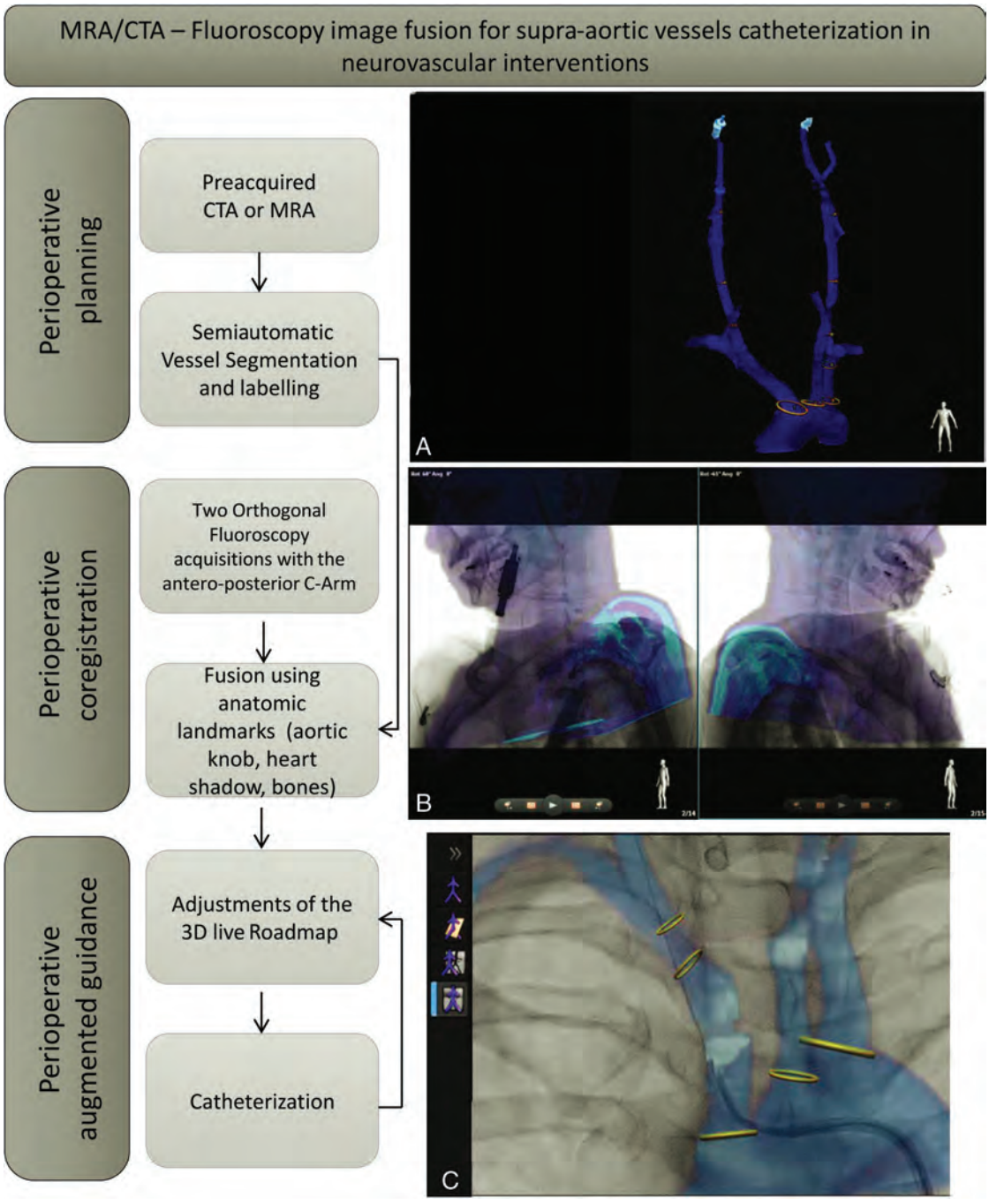

FIG 2. Detailed workflow of the MRA-fluoroscopy or CTA-fluoroscopy image fusion process for supra-aortic vessel catheterization in neurovascular interventions. Preoperative planning starts with uploading the MRA/CTA dataset on VesselNavigator. *A*, 3D semiautomatic segmentation of the aortic arch and the supra-aortic vessels and ostium labeling. *B*, Perioperative 2D–3D coregistration with 2 orthogonal positions of the anterior-posterior C-arm using anatomic landmarks. *C*, Perioperative augmented guidance.

We compared spatial accuracy between groups 1 and 2 using a mixed-effects logistic regression. A patient random effect was included to take into account the multiple supra-aortic vessels analyzed in the same patients. We used the lme4 package (https://cran.r-project.org/web/packages/lme4/lme4.pdf) for the mixed-effects model. All statistical analyses were performed using R statistical and computing software, Version 3.6.1 (http://www.r-project.org/). A P value $< .05$ was considered statistically significant.

RESULTS

Between May 2019 and October 2019, thirty-three patients (Table 1) underwent a total of 35 sessions of catheterization under MRA/CTA fusion guidance using the VesselNavigator software. Among them, 23 had preprocedual MRA and 12 had preprocedual CTA. A total of 151 supra-aortic vessels were targeted using fusion guidance, from radial access in 4 cases and femoral access in 31 cases. The mean time needed for dataset segmentation and coregistration was 7 ± 2 minutes.

FIG 3. Spatial accuracy assessment of MRA/CTA–fluoroscopy fusion. A 3-category semiquantitative scale was used to measure the maximum offset. *A*, Example of an accurate fusion at the ostium of the brachiocephalic artery trunk: The catheter projects within the lumen of the vessel in the ROI. *B*, Example of a mismatch at the ostium of the right common carotid artery: The catheter projects out of the lumen but within a distance inferior to the diameter of the vessel. *C*, Example of an inaccurate fusion at the ostium of the left common carotid artery: The catheter projects out of the vessel at a distance superior to the diameter.

Table 1: Patient characteristics (demographics, cardiovascular risk, procedure features, and aortic arch type)

Patient Characteristics	
Age (yr)	
Median (Interquartile range)	55 (50–68)
Sex	
Female (No.) (%)	20 (61%)
Male (No.) (%)	13 (39%)
Cardiovascular risk factors[a] (No.) (%)	
0	12 (34%)
1	6 (16%)
≥2	17 (50%)
Procedure type (No.) (%)	
Diagnostic/follow-up angiography	23 (66%)
Intracranial embolization	9 (16%)
Mechanical thrombectomy	3 (8%)
Anesthesia (No.) (%)	
Conscious sedation	26 (74%)
General anesthesia	9 (26%)
Noninvasive imaging for navigation (No.) (%)	
CTA	12 (34%)
MRA	23 (66%)
Aortic arch type (No.) (%)	
I	20 (57%)
II	8 (23%)
III	7 (20%)
Bovine variant	9 (26%)

[a] We considered smoking, high blood pressure, high low-density lipoprotein and low high-density lipoprotein cholesterol levels, age, and obesity.

Semiquantitative assessment showed that 84.8% (128/151) of the virtual landmarks from MRA/CTA overlaid on fluoroscopy were completely accurate, with no need for adjustment or conventional roadmap; 9.9% (15/151) of the virtual landmarks were overlaid with a mismatch, resulting from vessel deformation caused by endovascular devices; and 5.3% (8/151) of virtual landmarks were inaccurate, requiring an adjustment or an additional conventional roadmap (Table 2).

Spatial accuracy of the virtual roadmap was higher at the aortic arch level and proximal cervical level (group 1, 92.4%, 85/92) than at the distal cervical level (group 2, 72.9%, 43/59). A mixed-effects logistic regression showed a statistically significant difference (P value = .003). The odds ratio was estimated at 4.88 (95% confidence interval, 1.83–11.66), meaning that the odds of an accurate roadmap were almost 5 times higher in vessels at the aortic arch and proximal cervical level than at the distal cervical level (Table 3: comparison of spatial accuracy between the arch level and proximal cervical level (group 1) and distal cervical level (group 2)).

DISCUSSION

MRA/CTA fusion guidance for supra-aortic vessel catheterization is feasible in routine clinical practice. The virtual 3D roadmap offers high spatial accuracy during catheterization, compatible with the safety of neurovascular interventions. Dedicated software such as VesselNavigator allows a fluid workflow, with a duration of <10 minutes from MRA/CTA data uploading to 2D–3D coregistration.

The benefits of augmented navigation provided by image fusion are now recognized for endovascular procedures, in cardiology or aortic endografts. It has been found to reduce procedural time, x-ray exposure, and contrast media.[8,10,16-21]

Planning primary access is a requisite step prior to MRA/CTA–fluoroscopy fusion. The main benefits are the ability to plan the C-arm position for image acquisition and identify vessel origins and tortuosities on the navigation path. The working angles that accurately identify the targeted vessel ostium might aid catheterization, and they can be stored and recalled during catheterization if needed. The operator could also, at this point, identify the most adapted guidewire or catheter. It is likely that fusion guidance would apply to complex aortic arch catheterizations, especially among the elderly and patients with cardiovascular risk factors. In our study, 25% of patients were older than 68 years of age, and 50% had at least 2 cardiovascular risk factors. However, we reported no adverse events related to difficult catheterization (thromboembolic event, dissection, or failure in catheterization).

We used 2D–3D registration, which is faster and easier, especially at the thoracic level. We used 2 orthogonal projections to coregister the segmented 3D-MRA or CTA with live fluoroscopy. A recent work[22] reported that an accurate localization is possible with 2 projections acquired even at a small (~10°) angular separation. Moreover, 2D registration by fluoroscopic orthogonal shots is a fast, easy technique. The effective x-ray dose is significantly reduced compared with 3D–3D coregistration using cone-beam CT with the C-arm.[23] Few attempts have been made to use MRA/CTA image fusion for neurovascular applications: 3D roadmap navigation is routinely used, and this technique uses

Table 2: Spatial accuracy assessment of the virtual 3D roadmap for the 9 ROIs

ROIs of the Virtual Roadmap/Spatial Accuracy	No. (%)
Brachiocephalic artery trunk	
Accurate	27 (96.4)
Mismatch	1 (3.6)
Inaccurate	
All	28 (100)
Right subclavian artery	
Accurate	8 (100)
Mismatch	
Inaccurate	
All	8 (100)
Right vertebral artery	
Accurate	5 (100)
Mismatch	
Inaccurate	
All	5 (100)
Right common carotid artery	
Accurate	16 (69.6)
Mismatch	3 (13.0)
Inaccurate	4 (17.4)
All	23 (100)
Right internal carotid artery	
Accurate	10 (66.7)
Mismatch	3 (20.0)
Inaccurate	2 (13.3)
All	15 (100)
Left common carotid artery	
Accurate	24 (85.7)
Mismatch	3 (10.7)
Inaccurate	1 (3.6)
All	28 (100)
Left internal carotid artery	
Accurate	17 (81.0)
Mismatch	3 (14.3)
Inaccurate	1 (4.8)
All	21 (100)
Left subclavian artery	
Accurate	13 (92.9)
Mismatch	1 (7.1)
Inaccurate	
All	14 (100)
Left vertebral artery	
Accurate	8 (88.9)
Mismatch	1 (11.1)
Inaccurate	
All	9 (100)
Overall	
Accurate	128 (84.8)
Mismatch	15 (9.9)
Inaccurate	8 (5.3)
All	

Table 3: Comparison of spatial accuracy between aortic arch and cervical level (group 1) and the distal cervical level (group 2)

Spatial Accuracy	Group 1 No. (%)	Group 2 No. (%)	Overall No. (%)
Accurate	85 (92.4)	43 (72.9)	128 (84.8)
Mismatch/inaccurate	7 (7.6)	16 (27.1)	23 (15.2)

image fusion from the same technique. It results in a highly accurate registration[11,24-26] but is complex to implement at the aortic arch level. Multimodal imaging fusion at the intracranial level is gaining wider acceptance even though reports remain scarce.[12,27-29] At the aortic arch level, no other reports, to our knowledge, have been published since the pioneering work of Lin et al.[15]

The VesselNavigator image fusion technique was evaluated in 151 supra-aortic vessels, showing a high spatial accuracy for catheterization at the aortic arch and proximal cervical level. However, we observed that the mismatch increased when reaching distal cervical vessels. This limitation has already been reported for abdominal endovascular procedures even with 3D–3D fusion.[7]

We observed that the patient's head positioning significantly differed on the angiography table from the preoperative MRA/CTA, which resulted in distal cervical vessel distortion. Furthermore, the introduction of stiff guidewires and catheters increased deformation of cervical vessels. As a result, the perioperative vasculature was likely to have a different tridimensional conformation from the MRA/CTA segmented version, leading to fusion mismatch.

Despite the improvement that MRA/CTA fusion brings to catheterization, multiple limitations still prevent its widespread use. Optimizing the workflow with more automated and accurate segmentation and registration processes is necessary. Indeed, these processes are time- and effort-consuming and are considered to interfere with clinical practice, preventing their adoption by physicians. Serious effort in training and dedicated environments might be helpful in the future.[30,31]

The first step that delivers a segmented dataset of the aorta and supra-aortic vessels could be enhanced to provide more accurate datasets for planning the procedure (such as the vessel centerlines, angular information on the vascular path to the target zone, vessel tortuosity index, ostium plane, and so forth).

The benefits of 3D-MRA/CTA fusion guidance might differ according to the type of procedures. For emergency procedures such as patients with stroke, for whom head positioning and agitation will limit distal accuracy of the fusion guidance, great help can be provided to catheterize the proximal supra-aortic trunks in case of complex aortic arch anatomy, which can be challenging in this population. Patients with stroke for whom a diagnostic MRA or CTA has been performed could benefit from fusion guidance with a very moderate increase of procedural time because preprocedural segmentation can be performed before the patient arrives in the angiography suite. Nevertheless, for elective procedures, such as angiograms and aneurysm or AVM treatments, more benefits are expected in terms of reduction of procedural times, x-ray exposure, and contrast medium use. For these patients, adding a preprocedural CTA or MRA only for fusion guidance is questionable and must be further studied but might be beneficial in a selected population for whom more difficult catheterization is expected (especially among the elderly and patients with cardiovascular risk factors).

The registration of the high-resolution 3D model segmented from MRA or CTA should be subdivided according to anatomic landmarks (thoracic, cervical low, cervical high, or intracranial level) to take into account the vasculature distortion related to head position.

Further validations of MRA/CTA fusion techniques in neurovascular interventions will require comparing 2D–3D versus 3D–3D registration in larger studies, at multicentric levels, and using quantitative assessment of the alignment accuracy.

CONCLUSIONS

Fluoroscopy with MRA/CTA fusion guidance for supra-aortic vessel interventions is feasible and accurate. Further improvements of the technique to increase accuracy at the distal cervical level and further studies for assessing the procedural time savings and decreasing x-ray radiation exposure for the patient and staff are needed. The potential benefits would apply to complex aortic arch catheterizations, especially among the elderly and patients with cardiovascular risk factors.

Disclosures: Julien S. Savatovsky—*UNRELATED*: *Payment for Lectures Including Service on Speakers Bureaus*: Sanofi, Biogen, Philips Healthcare; *Travel/Accommodations/Meeting Expenses Unrelated to Activities Listed*: Bayer Healthcare SAS.

REFERENCES

1. Faggioli GL, Ferri M, Freyrie A, et al. **Aortic arch anomalies are associated with increased risk of neurological events in carotid stent procedures.** *Eur J Vasc Endovasc Surg* 2007;33:436–41 CrossRef Medline
2. Werner M, Bausback Y, Bräunlich S, et al. **Anatomic variables contributing to a higher periprocedural incidence of stroke and TIA in carotid artery stenting: single center experience of 833 consecutive cases.** *Catheter Cardiovasc Interv* 2012;80:321–28 CrossRef Medline
3. Riga CV, Bicknell CD, Hamady MS, et al. **Evaluation of robotic endovascular catheters for arch vessel cannulation.** *J Vasc Surg* 2011;54:799–809 CrossRef Medline
4. Demertzis S, Hurni S, Stalder M, et al. **Aortic arch morphometry in living humans.** *J Anat* 2010;217:588–96 CrossRef Medline
5. Yu SC, Leung TW, Hung EH, et al. **Angioplasty and stenting for intracranial atherosclerotic stenosis with nitinol stent.** *Operative Neurosurg* 2012;70(1 Suppl Operative):104–13 CrossRef Medline
6. Madhwal S, Rajagopal V, Bhatt DL, et al. **Predictors of difficult carotid stenting as determined by aortic arch angiography.** *J Invasive Cardiol* 2008;20:200–04 Medline
7. Goudeketting SR, Heinen SG, van den Heuvel DA, et al. **The use of 3D image fusion for percutaneous transluminal angioplasty and stenting of iliac artery obstructions: validation of the technique and systematic review of literature.** *J Cardiovasc Surg (Torino)* 2018;59:26–36 CrossRef Medline
8. Kaladji A, Daoudal A, Clochard E, et al. **Interest of fusion imaging and modern navigation tools with hybrid rooms in endovascular aortic procedures.** *J Cardiovasc Surg (Torino)* 2017;58:458–66 CrossRef Medline
9. Kaladji A, Duménil A, Mahé G, et al. **Safety and accuracy of endovascular aneurysm repair without pre-operative and intra-operative contrast agent.** *Eur J Vasc Endovasc Surg* 2015;49:255–61 CrossRef Medline
10. Sailer AM, de Haan MW, Peppelenbosch AG, et al. **CTA with fluoroscopy image fusion guidance in endovascular complex aortic aneurysm repair.** *Eur J Vasc Endovasc Surg* 2014;47:349–56 CrossRef Medline
11. Blanc R, Seiler A, Robert T, et al. **Multimodal angiographic assessment of cerebral arteriovenous malformations: a pilot study.** *J Neurointerv Surg* 2015;7:841–47 CrossRef Medline
12. Kocer N, Kizilkilic O, Babic D, et al. **Fused magnetic resonance angiography and 2D fluoroscopic visualization for endovascular intracranial neuronavigation.** *J Neurosurg* 2013;118:1000–02 CrossRef Medline
13. Perhac J, Spaltenstein J, Pereira VM, et al. **Improving workflows of neuro-interventional procedures with autostereoscopic 3D visualization of multi-modality imaging in hybrid interventional suites.** *Int J Comput Assist Radiol Surg* 2016;11:189–96 CrossRef Medline
14. Blanc R, Fahed R, Roux P, et al. **Augmented 3D venous navigation for neuroendovascular procedures.** *J Neurointerv Surg* 2018;10:649–52 CrossRef Medline
15. Lin CJ, Blanc R, Clarençon F, et al. **Overlying fluoroscopy and preacquired CT angiography for road-mapping in cerebral angiography.** *AJNR Am J Neuroradiol* 2010;31:494–95 CrossRef Medline
16. McNally MM, Scali ST, Feezor RJ, et al. **Three-dimensional fusion computed tomography decreases radiation exposure, procedure time, and contrast use during fenestrated endovascular aortic repair.** *J Vasc Surg* 2015;61:309–16 CrossRef Medline
17. Tacher V, Lin M, Desgranges P, et al. **Image guidance for endovascular repair of complex aortic aneurysms: comparison of two-dimensional and three-dimensional angiography and image fusion.** *J Vasc Interv Radiol* 2013;24:1698–1706 CrossRef Medline
18. Kaladji A, Giovannetti M, Pascot R, et al. **Preoperative CT-scan-based sizing and in-stent restenosis in peripheral endovascular revascularizations.** *Vascular* 2017;25:504–13 CrossRef Medline
19. Klein AJ, Tomkowiak MT, Vigen KK, et al. **Multimodality image fusion to guide peripheral artery chronic total arterial occlusion recanalization in a swine carotid artery occlusion model: unblinding the interventionalist.** *Cathet Cardiovasc Interv* 2012;80:1090–98 CrossRef Medline
20. Kobeiter H, Nahum J, Becquemin JP. **Zero-contrast thoracic endovascular aortic repair using image fusion.** *Circulation* 2011;124:e280–82 CrossRef Medline
21. Schulz CJ, Schmitt M, Böckler D, et al. **Feasibility and accuracy of fusion imaging during thoracic endovascular aortic repair.** *J Vasc Surg* 2016;63:314–22 CrossRef Medline
22. Uneri A, Otake Y, Wang AS, et al. **3D–2D registration for surgical guidance: Effect of projection view angles on registration accuracy.** *Phys Med Biol* 2013;59:271–87 CrossRef Medline
23. van den Berg JC. **Update on new tools for three-dimensional navigation in endovascular procedures.** *Aorta (Stamford)* 2014;2:279–85 CrossRef Medline
24. Ruijters D, Homan R, Mielekamp P, et al. **Validation of 3D multimodality roadmapping in interventional neuroradiology.** *Phys Med Biol* 2011;56:5335–54 CrossRef Medline
25. Soderman M, Babic D, Homan R, et al. **3D roadmap in neuroangiography: technique and clinical interest.** *Neuroradiology* 2005;47:735–34 CrossRef Medline
26. Xu R, Leng LZ, Rubin DG, et al. **Fusion of intraoperative three-dimensional rotational angiography and flat-panel detector computed tomography for cerebrovascular neuronavigation.** *World Neurosurg* 2013;79:504–09 CrossRef Medline
27. Zhang Q, Sun Q, Zhang Y, et al. **Three-dimensional image fusion of CTA and angiography for real-time guidance during neurointerventional procedures.** *J Neurointerv Surg* 2017;9:302–06 CrossRef Medline
28. Tritt S, Ommer B, Gehrisch S, et al. **Optimization of the surgical approach in AVMs using MRI and 4D DSA fusion technique: a technical note.** *Clin Neuroradiol* 2017;27:443–50 CrossRef Medline
29. Ide S, Hirai T, Morioka M, et al. **Usefulness of 3D DSA-MR fusion imaging in the pretreatment evaluation of brain arteriovenous malformations.** *Acad Radiol* 2012;19:1345–52 CrossRef Medline
30. Crossley R, Liebig T, Holtmannspoetter M, et al. **Validation studies of virtual reality simulation performance metrics for mechanical thrombectomy in ischemic stroke.** *J Neurointerv Surg* 2019;11:775–80 CrossRef Medline
31. Rudarakanchana N, Van Herzeele I, Bicknell CD, et al. **Endovascular repair of ruptured abdominal aortic aneurysm: technical and team training in an immersive virtual reality environment.** *Cardiovasc Intervent Radiol* 2014;37:920–27 CrossRef Medline

Predictors of Favorable Outcome after Endovascular Thrombectomy in MRI: Selected Patients with Acute Basilar Artery Occlusion

M. Mahmoudi, C. Dargazanli, F. Cagnazzo, I. Derraz, C. Arquizan, A. Wacogne, J. Labreuche, A. Bonafe, D. Sablot, P.H. Lefevre, G. Gascou, N. Gaillard, C. Scott, V. Costalat, and I. Mourand

ABSTRACT

BACKGROUND AND PURPOSE: Clinical outcomes after endovascular treatment for acute basilar artery occlusions need further investigation. Our aim was to analyze predictors of a 90-day good functional outcome defined as mRS 0–2 after endovascular treatment in MR imaging–selected patients with acute basilar artery occlusions.

MATERIALS AND METHODS: We analyzed consecutive MR imaging–selected patients with acute basilar artery occlusions endovascularly treated within the first 24 hours after symptom onset. Successful and complete reperfusion was defined as modified TICI scores 2b–3 and 3, respectively. Outcome at 90 days was analyzed in univariate and multivariate analysis regarding baseline patient treatment characteristics and periprocedural outcomes.

RESULTS: One hundred ten patients were included. In 10 patients, endovascular treatment was aborted for failed proximal/distal access. Overall, successful reperfusion was achieved in 81.8% of cases ($n = 90$; 95% CI, 73.3%–88.6%). At 90 days, favorable outcome was 31.8%, with a mortality rate of 40.9%; the prevalence of symptomatic intracranial hemorrhage within 24 hours was 2.7%. The median time from symptom onset to groin puncture was 410 minutes (interquartile range, 280–540 minutes). In multivariable analysis, complete reperfusion (OR = 6.59; 95% CI, 2.17–20.03), lower pretreatment NIHSS (OR = 0.77; 95% CI, 0.64–0.94), the presence of posterior communicating artery collateral flow (OR = 2.87; 95% CI, 1.05–7.84), the absence of atrial fibrillation (OR = 0.18; 95% CI, 0.03–0.99), and intravenous thrombolysis administration (OR = 2.75; 95% CI, 1.04–7.04) were associated with 90-day favorable outcome.

CONCLUSIONS: In our series of MR imaging–selected patients with acute basilar artery occlusions, complete reperfusion was the strongest predictor of a good outcome. Lower pretreatment NIHSS, the presence of posterior communicating artery collateral flow, the absence of atrial fibrillation, and intravenous thrombolysis administration were associated with favorable outcome.

ABBREVIATIONS: ABAO = acute basilar artery occlusion; BSS = brain stem score; EVT = endovascular treatment; GCS = Glasgow Coma Scale; IQR = interquartile range; IVT = intravenous thrombolysis; mTICI = modified TICI; PC-ASPECTS = posterior circulation ASPECTS; PcomA = posterior communicating artery; sICH = =symptomatic intracranial hemorrhage

Acute basilar artery occlusion (ABAO) is a devastating type of stroke, with a natural history showing a mortality rate of up to 90% and a severe residual deficit in 65% of patients without treatment.[1]

Although endovascular treatment (EVT) is the criterion standard therapy for patients with acute ischemic stroke in the anterior circulation and proximal arterial occlusion, results from randomized clinical trials regarding the effectiveness of EVT for ABAO are still lacking.[2] Nevertheless, EVT is considered useful and routinely performed in real-world practice. Expert opinions have encouraged this practice[3] to maximize the chance of reperfusion and good clinical outcome.

However, there are contradictory results on predictors of functional outcome as well as on the best reperfusion strategies (IV thrombolysis [IVT] alone, EVT, bridging therapy) in patients with ABAO. The Acute Basilar Artery Occlusion: Endovascular Interventions versus Standard Medical Treatment (BEST) randomized trial was stopped ahead of time because of the higher rate of crossover between treatment groups.[4]

Received February 3, 2020; accepted after revision June 7.

From the Departments of Neuroradiology (M.M., C.D., F.C., I.D., A.B., P.H.L., G.G., V.C.), Neurology (C.A., N.G., I.M.), and Reanimation (C.S.), Centre Hospitalier Universitaire Gui De Chauliac, Montpellier, France; Neurology Department (A.W.), Centre Hospitalier Universitaire Caremeau, Nimes, France; Biostatistics Department (J.L.), Centre Hospitalier Universitaire Lille, Lille, France; and Neurology Department (D.S.), Centre Hospitalier de Perpignan, Perpignan, France.

Please address correspondence to Mehdi Mahmoudi, MD, MSc, Department of Neuroradiology, University Hospital Center of Montpellier, Gui de Chauliac Hospital, 80 avenue Augustin Fliche 34090 Montpellier, France; e-mail: m-mahmoudi@chu-montpellier.fr

Indicates article with supplemental on-line tables.

Indicates article with supplemental on-line photos.

http://dx.doi.org/10.3174/ajnr.A6741

Using data from our prospective registry, we aimed to investigate predictive factors of 90-day good functional outcome in a large cohort of patients with ABAO. Because of the high sensitivity in detecting posterior fossa ischemic lesions and infarct volume, MR imaging is the main selection technique for patients with acute ischemic stroke at our department, and all included subjects were MR imaging–selected.

MATERIALS AND METHODS

Inclusion Criteria and Patient Characteristics

We reviewed all patients referred to our hospital with ABAO confirmed by MR imaging and subsequently treated with EVT from January 2011 to October 2018. The inclusion criteria for EVT were the following: 1) patients with ABAO and acute stroke detected on cerebral MR imaging admitted within 24 hours from symptom onset; 2) patients with pertinent clinical deficits undergoing an evaluation by a physician (without NIHSS limits); and 3) confirmation of ABAO on angiography. Patients were considered not eligible for EVT (and received medical management) on the basis of the following exclusion criteria: 1) prestroke mRS score of more than two; 2) life expectancy of <6 months; 3) imaging evidence of cerebellar mass effect or acute hydrocephalus; and 4) bilateral extended brain stem ischemia.

Baseline characteristics, NIHSS, Glasgow Coma Scale (GCS), mothership or drip and ship strategy, and use and time of IVT were assessed by a stroke neurologist on admission. An NIHSS score of 40 was assigned to comatose patients with a GCS of 3. The local ethics committee approved the use of the patients' data for this study.

Neuroimaging Assessment

We recorded 2 scores to measure early ischemic changes on DWI in the posterior circulation: 1) the posterior circulation ASPECTS (PC-ASPECTS),[5] and 2) the DWI brain stem score (BSS).[6]

The DWI BSS separately analyzes the medulla, pons, and midbrain, considering the right and left sides separately. One point was given for each unilateral DWI lesion at the brain stem level (medulla, pons, and midbrain) that occupied less than half of the area; and 2 points were given if the lesion occupied more than half of the area. The brain stem DWI lesion score ranged from 0 to 12. There were no limits on the PC-ASPECTS and DWI BSS scales for inclusion of patients.

The level of ABAO was determined as follows: proximal segment of the basilar artery (from the vertebral artery junction to the anterior inferior cerebellar artery), middle segment (from the anterior inferior cerebellar artery to the superior cerebellar artery), and distal segment (above the superior cerebellar artery).[7] The pretreatment collateral score for the posterior circulation was collected and defined as follows: 0, no posterior communicating artery (PcomA); 1, unilateral PcomA; and 2, bilateral PcomA.[8]

Pretreatment imaging findings were retrospectively assessed by an experienced interventional neuroradiologist (M.M.) blinded to the clinical outcome. For each patient, imaging was retrospectively assessed by a second interventional neuroradiologist (C.D.), blinded to both the first reader's scoring and the clinical outcome. In case of discrepancy, a consensus was reached with an additional reader (I.D.).

Reperfusion Therapy

Patients received either bridging therapy (EVT combined with IVT) or EVT alone. IVT was administered within a maximum of 4.5 hours from symptom onset, according to the current guidelines.[9] Conventional clinical and laboratory inclusion and exclusion criteria for IVT thrombolysis were applied. Because it has been reported that larger cerebellar infarct volume (>75%) is potentially associated with hemorrhagic transformation, IVT was not administrated in case of extensive cerebellar ischemia on DWI sequences.[10]

All patients were treated in a neuroangiography suite under general anesthesia or conscious sedation, after evaluation by a dedicated anesthesiologist team. An 8F (Neuron Max; Penumbra) guiding catheter was advanced into the V2 segment of the vertebral artery, usually the largest one. For stent retriever thrombectomy, a 0.021-inch microcatheter was navigated through the basilar occlusion using a 0.014-inch microwire under fluoroscopic guidance. A Solitaire FR (Medtronic) or Trevo (Stryker) device was used for EVT.

Stent retriever[11] or a Direct Aspiration First-Pass Technique[12] (with a SOFIA 5F or 6F [MicroVention] intermediate catheter) was used.

Successful and complete reperfusion was defined as a modified TICI (mTICI) 2b–3 and 3, respectively. In the absence of a specific definition in the posterior circulation of TICI 2b and according to our experience, we considered TICI 2b a partial perfusion with distal occlusion of a posterior cerebral artery, AICA, PICA, or superior cerebellar artery.[13]

We recorded periprocedural complications: embolization in an unaffected territory, arterial dissection/perforation, vasospasm, and subarachnoid hemorrhage.

Delays from stroke-onset to MR imaging, stroke-onset to IVT, stroke-onset to groin puncture, MR imaging to groin-puncture, stroke-onset to reperfusion, and groin puncture to reperfusion were recorded for all patients.

Follow-Up and Outcome

All patients underwent cerebral CT or MR imaging within the 24 hours after the procedure. Growth of the infarct core, basilar artery early re-occlusion, and hemorrhagic complications were recorded. Symptomatic intracranial hemorrhage (sICH) was defined as imaging demonstrating hemorrhage associated with an increase of ≥4 points in the NIHSS score.[9]

The 90-day mRS was assessed by a stroke neurologist or by a phone call with the patient, his or her relatives, or his or her general practitioner. Favorable outcome was defined by mRS ≤ 2, and poor outcome, mRS 3–6. Mortality at 90 days was also recorded.

Statistical Analysis

Continuous variables are expressed as means ± SD or medians (interquartile range, [IQR]), and categoric variables are expressed as numbers (percentage). Normality of distributions was assessed using histograms and the Shapiro-Wilk test. Rates of angiographic

Table 1: Angiographic and clinical outcomes[a]

Outcomes	No.	Values
Successful reperfusion (mTICI 2b–3)	110	90 (81.8)
Complete reperfusion (mTICI 3)	110	67 (60.9)
Onset to successful reperfusion (median) (IQR) (min)[b]	90	455 (340–570)
Groin puncture to successful reperfusion (median) (IQR) (min)	90	45 (22–70)
No. of passes (median) (IQR)	110	1 (1–2)
Re-occlusion	110	6 (5.5)
Procedural complications	110	20 (18.2)
Dissection[c]		13 (11.8)
Embolization		8 (7.3)
Vasospasm		2 (1.8)
Growth of infarct core	110	35 (31.8)
Any ICH	110	13 (11.8)
sICH	110	3 (2.7)
Favorable outcome (90-day mRS 0–2)	110	35 (31.8)
Poor outcome (90-day mRS 3–6)	110	75 (68.1)
90-Day all-cause mortality	110	45 (40.9)

Note:—ICH indicates intracranial hemorrhage.
[a] Values are No. (%) unless otherwise as indicated.
[b] Data among patients with successful reperfusion.
[c] Involved V1 segment ($n = 1$), V3 segment ($n = 3$), V4 segment ($n = 3$), and basilar artery ($n = 6$).

and clinical outcomes were estimated by calculating the exact binomial 95% confidence intervals. Baseline characteristics (patient and treatment characteristics) and periprocedural outcomes (recanalization and adverse events) were compared between patients with and without favorable outcomes at 90 days using the Student t test for Gaussian continuous variables, the Mann-Whitney U test for non-Gaussian continuous variables, and the χ^2 test (or Fisher exact test when the expected cell frequency was <5) for categoric variables, as appropriate. To assess the independent predictors of favorable outcomes, we performed a first-multivariable Firth penalized-likelihood logistic regression to account for the small sample size[14]), including all patient and treatment characteristics with a $P < .10$ in univariate analyses, using a backward selection procedure with $P < .10$ as a selection criterion. Before developing the multivariable model, we examined the log-linearity assumption for continuous characteristics (irrespective of previous univariate analyses) using restricted cubic spline functions by comparing the models using only a linear term with models containing both the linear and cubic spline terms using a likelihood ratio test (all log-linearity assumptions were established and all continuous variables were analyzed without transformation). We also examined the absence of colinearity between the candidate predictors by calculating the variance inflation factors.[15,16]

To prevent collinearity between pretreatment NIHSS and pretreatment GCS (variance inflation factor >8; for all other predictors, variance inflation factors values were <2), we performed separate multivariate analyses, including either pretreatment NIHSS or pretreatment GCS. Two multivariable models were performed by including and excluding complete recanalization as a covariate. This performance was to determine the impact of the other investigated pretreatment variables, independent of the angiographic result. We examined the performance of the selected models in terms of calibration using the Hosmer-Lemeshow goodness-of-fit test and discrimination by calculating the C-statistics.[14] We also derived the McFadden Pseudo R-Squared from the likelihood for the selected models and the null model (including intercept only). The results of multivariate analyses are expressed as odds ratios with 95% confidence intervals of favorable outcome. Statistical testing was performed at the 2-tailed α level of .05. Data were analyzed using the SAS software package, release 9.4 (SAS Institute).

RESULTS

Overall, 226 consecutive patients with ABAO were admitted to our hospital. One hundred seven patients treated by conservative management alone (antiplatelet/anticoagulant/IVT) and 9 patients without MR imaging performed before EVT were excluded, resulting in a total of 110 included MR imaging–selected patients who underwent EVT (On-line Fig 1). Patient and treatment characteristics are reported in On-line Table 1. The mean age was 67 ± 12 years, 60% ($n = 66$) were men, and the median pretreatment NIHSS score was 22 (IQR, 14–40). Thirty-four (31%) patients had proximal ABAO, 23 (21%) had middle ABAO, and 53 (48%) presented with a distal ABAO. The median door-to-puncture time was 67 minutes (IQR, 34–530 minutes). Seventy-nine patients (72%) were intubated for low GCS scores ($n = 23$) and for EVT ($n = 56$).

IVT before thrombectomy was administered in 37% ($n = 41$) of patients. The median time from symptom onset to groin puncture was 410 minutes (IQR, 280–540 minutes). In 10 patients, EVT was unsuccessful because of the impossibility of crossing the occlusion ($n = 4$) or impossible access/tortuosity ($n = 4$) and perforation ($n = 2$).

Of the 100 patients receiving at least 1 device pass, the first-line treatment strategy was stent retriever in 30%, contact aspiration in 23.6%, and a combined stent retriever and contact aspiration strategy in the remaining 37.3%.

Angiographic and Clinical Outcomes

Main outcomes are summarized in Table 1. Successful reperfusion (mTICI 2b–3) was achieved in 81.8% ($n = 90$; 95% CI, 73.3%–88.6%) with a median number of passes of 1 (IQR, 1–2), and a median time of 45 minutes (IQR, 22–70 minutes) from groin puncture. Reperfusion was complete (mTICI 3) in 60.9% of patients ($n = 67$; 95% CI, 51.1%–70.1%). Overall, procedural complications occurred in 18.2% ($n = 20$; 95% CI, 11.4%–26.7%) of patients. These included 13 (11.8%) vertebral dissections, 5 distals embolisations (4, 6%) angiographic distal embolizations, and 2 (1.8%) vasospasms. Intracranial hemorrhagic complications within 24 hours occurred in 11.8% ($n = 13$; 95% CI, 6.4%–19.4%) of patients, with 3 (2.7%) symptomatic events. At 90 days, 35 patients (31.8%; 95% CI, 23.2%–41.4%) achieved good outcome (mRS 0–2), 75 (68.1%; 95% CI, 59%–76%) had a poor outcome (mRS 3–6), and among those, 45 subjects (40.9%; 95% CI, 31.6%–50.7%) died. Overall, 64 patients had post-EVT MR imaging. Of these, 51 (79.7%) had successful recanalization (TICI 2b-3), while 13 (20.3%) were TICI 0–2a. Among those having a successful recanalization, 28 (55%) presented with an infarct growth. Functional independence at 3 months was lower (30% versus

Table 2: Independent predictors of favorable outcome[a]

	Model 1		Model 2	
	OR (95% CI)	*P*	OR (95% CI)	*P*
Pretreatment NIHSS	0.77 (0.64–0.94)	.007	0.82 (0.68–0.98)	.030
PcomA collateral flow	2.87 (1.05–7.84)	.039	3.38 (1.20–8.96)	.021
IV thrombolysis	2.71 (1.04–7.04)	.040	Not selected	
Atrial fibrillation	0.18 (0.03–0.99)	.049	Not selected	
Onset to groin puncture	0.95 (0.89–1.01)	.062	Not selected	
Pretreatment DWI BSS	0.76 (0.54–1.06)	.096	0.74 (0.52–1.02)	.069
Complete recanalization	Not included	–	6.59 (2.17–20.03)	.001
C-statistics (95% CI)	0.803 (0.710–0.897)		0.816 (0.732–0.901)	
Pseudo-R^2	0.248		0.232	
Goodness-of-fit test	$P = .85$		$P = .74$	

Note:—– indicates not available.

[a] ORs were calculated using a backward-stepwise multivariable penalized-likelihood logistic model. Candidate predictors in model 1 were mothership, admission to intensive care, atrial fibrillation, pretreatment NIHSS, pretreatment ASPECTS, pretreatment DWI BSS, IV thrombolysis, PcomA collateral flow, thalamus involvement, and onset-to-groin puncture time. Candidate predictors in model 2 were mothership, admission to intensive care, atrial fibrillation, pretreatment NIHSS, pretreatment PC-ASPECTS, pretreatment DWI BSS, IV thrombolysis, PcomA collateral flow, thalamus involvement, onset-to-groin puncture time, and complete recanalization (mTICI 3).

70%) in the group with infarct growth compared with the group without infarct growth (details in the On-line Fig 2).

Predictors of Favorable Outcome at 90 Days

In univariate analyses, lower pretreatment NIHSS and GCS scores, lower DWI BSS values and PC-ASPECTS, the presence of PcomA collateral flow, the absence of thalamus involvement, IVT before EVT, the absence of atrial fibrillation, onset-to-groin puncture time, no admission to the intensive care unit, and mothership–treated strategy were associated with a good outcome (P value $< .10$, On-line Table 2) and were included in the multivariable analyses. Due to the strong collinearity between 2 variables, 2 separate multivariate analyses were performed, including either pretreatment NIHSS (Table 2) or GCS (On-line Table 3).

Multivariable Model Including NIHSS

We tested 2 models: 1) excluding complete recanalization (mTICI 3), and 2) including complete recanalization as an independent candidate predictor. In the first model, lower pretreatment NIHSS ($P = .007$), the presence of PcomA collateral flow ($P = .039$), IVT administration ($P = .04$), and absence of atrial fibrillation ($P = .049$) were significantly associated with the likelihood of good outcome (Table 2). Association with onset-to-groin puncture and pretreatment DWI BSS was on the borderline of significance.

In model 2, including mTICI 3 recanalization, lower pretreatment NIHSS ($P = .03$), the presence of PcomA collateral flow ($P = .02$), and complete reperfusion ($P < .001$) were significantly associated the good outcome.

Both multivariate models had good discrimination (C = 0.803 for the first and C = 0.816 for the second model) with no deviation in calibration as indicated by the Hosmer-Lemeshow goodness-of-fit test ($P = .85$ for the first and $P = .74$ for the second model).

Multivariable Model Including GCS

Similar results were found when the pretreatment GCS was considered as a candidate variable rather than the pretreatment NIHSS (On-line Table 3).

DISCUSSION

Our study, analyzing 110 MR imaging–selected patients with ABAO, highlighted complete reperfusion after EVT as the strongest predictor of 90-day good functional outcome. Moreover, a lower pretreatment NIHSS score, the absence of atrial fibrillation, PcomA collateral flow, and IVT (bridging therapy) were predictors of functional independence. Although GCS was also strongly associated with a good neurologic outcome, the NIHSS score was considered more accurate in the evaluation of the pretreatment clinical status.

Influence of Complete Reperfusion on Favorable Outcomes

Our rate of successful reperfusion (mTICI 2b–3, 81.8%) was in the range of those reported in other series showing a rate between 79% and 96%.[17–21] Patients with mTICI 3 reperfusion had a better mRS at 90 days than patients with mTICI 2b (44.8% among mTICI 3 versus 8.7% among patients with mTICI 2b). On-line Figure 3 shows as complete recanalization (mTICI 3) increased the rate of good functional outcome compared with mTICI 0-2b. In addition, there was a shift to higher rates of independence in the group with successful reperfusion compared with unsuccessful recanalization. Furthermore, in a multivariate analysis, complete reperfusion (obtained in 60.9% of patients) was the strongest predictor of a 90-day favorable outcome. This result is in accordance with what was reported in previous published series of mechanical thrombectomy for posterior circulation acute ischemic stroke.[20,22-24] This point probably underlines the importance of achieving complete reperfusion in the posterior circulation, likely due to the extremely functional anatomic region involved.

Not surprisingly, failure to achieve reperfusion has been reported as a strong predictor of mortality.[17] These results are important because they outline the efficacy of EVT in ABAO and the impact on the clinical outcome.

Clinical Predictors of Outcome

In our series, the rate of favorable outcome was slightly lower (31.8%) compared with other reports (42%–54%),[4,17,19,25-28] with higher rates of mortality (40.9% versus 12%–35%)[4,19,25-29] and poor outcome (mRS 3–5, 27%). These results suggest that among

patients with posterior circulation ischemic stroke, if reperfusion appears to be an important factor in functional independence, other variables potentially influence the final neurologic status. It has been suggested that occlusion of small perforating arteries in thromboembolic ABAO may persist even after clot removal and recanalization of the basilar artery, leading to irreversible brain stem ischemic lesions.[20]

In addition, compared with the literature, our patient group was older (mean age, 66.9 versus 58–64 years),[26,29,30] with higher initial stroke severity (mean baseline NIHSS score of 22 versus 13–17).[11,21,25,29] Furthermore, >70% of patients (80 comatose patients) required admission to the intensive care unit for mechanical ventilation.

Younger age has been demonstrated to be associated with favorable outcomes.[25] On the other hand, 60 years of age and older was an independent predictor of mortality.[17] A higher GCS score and a lower baseline NIHSS are known to be predictors of good outcome in patients with ABAO.[25,26,28,31] Most interesting, it has been shown that despite recanalization, patients with ABAO with a baseline NIHSS of ≥13 have poorer outcomes compared with those with a mild-to-moderate deficit.[17] In our series, the median NIHSS score among patients achieving a poor outcome was 40, and the median GCS was 3. Accordingly, we can reasonably state that patients with very severe disease at admission have a quite low probability of achieving a good neurologic outcome even if treated with the best medical management and with the most advanced interventional techniques.

Delay of Reperfusion Therapy

Our regional network organization [31] may explain our longer median time from onset to groin puncture and imaging to puncture time (410 minutes versus 242–405 minutes and 99 minutes versus 50–60 minutes) compared with previous findings.[17,25,26,32]

Hospitals in our region (>2,700,000 habitants with an area of 27,376 km^2) are not geographically close together, so most of those with the drip and ship paradigm (representing 71.6% of subjects) underwent a re-evaluation MR imaging on arrival at our comprehensive stroke center, which might increase the onset-to-groin puncture time and imaging-to-puncture time.

In addition, 72% of patients (79 subjects) needed to be intubated for their low GCS ($n = 23$) and for EVT ($n = 56$). All these factors contributed to an increase in the median time from onset to groin puncture and imaging to groin puncture.

The Basilar Artery International Cooperation Study (BASICS) demonstrated that the probability of poor outcome was significantly increased when recanalization therapy was started after 6 hours.[33] However, data in the literature are contradictory, with series showing a not significant correlation between patients treated before and after 6 hours.[26] In our study, onset-to-groin puncture was not independently associated with 90-day mRS 0–2 at multivariable analysis. These data support the hypothesis that functional prognosis might be governed by other factors such as baseline neurologic presentation, collateral flow, and initial ischemia.[27]

Influence of Atrial Fibrillation

Different from what was reported before, in our cohort, the absence of atrial fibrillation was associated with a favorable outcome. Atrial fibrillation, associated with fresh thrombus and less atherosclerotic vessel damage, was an independent predictor of successful reperfusion in previous series.[34] In addition, it has been reported that cardiac embolism is more frequently related to distal basilar artery occlusion, which is generally associated with higher rates of successful recanalization after EVT.[35,36]

PcomA Collateral Flow

The positive impact of collateral blood flow on clinical outcomes has been previously demonstrated.[19,21,28,37] Scores used to determine collateral flow are heterogeneous, and there is not a consensus for the posterior circulation. Here, the presence of collateral flow in the PcomA was defined using an easy-to-use, validated scale assessed on baseline MR imaging[8] and was associated with a 90-day favorable outcome. Moreover, other authors reported that better collateral supply significantly increases recanalization rates,[19] providing blood flow to the penumbral tissue and decreasing the final infarct core.[38] It is conceivable that the presence of a PcomA artery should be checked during the pretreatment imaging and patient selection, considering that subjects with PcomA collateral flows are more likely to benefit from mechanical thrombectomy and have a higher chance of recovery. In addition, the presence of a PcomA artery impacted the outcome independent of complete reperfusion, indicating the importance of the collateral blood flow in patients with ABAO.

Impact of Bridging Therapy

In our cohort, the use of IVT (37.3% of patients) increased the 90-day favorable outcome, without higher hemorrhagic risk. Similarly, Gory et al[17] reported higher mortality rates among patients with ABAO not receiving IVT. These findings may support the use of IVT in ABAO, underlining its role in reperfusion strategy. In our study, the sICH rate was quite low (2.7%) compared with that reported in other series (0 to 11.8%).[17-19,25-28] In agreement with recent series,[39] it is likely that the low rate of sICH is partly explained by the MR imaging–based patient selection, with no administration of IVT for patients with large stroke volumes.

Limitations

Our study has limitations. First, it is a monocentric retrospective, nonrandomized observational registry study. Our sample size remains limited to assess the predictors of favorable outcome, despite being the largest EVT study of MR imaging–selected patients with ABAO. First, we could not exclude several predictors not being identified due to lack of adequate statistical power. Although there is no single sample calculation, we performed an a posteriori power calculation by calculating the smallest effect size (expressed as an odds ratio) that our sample size (35 patients with favorable outcome and 75 patients without it) allows to detect a 5% significance level (2-sided) with a 80% power. On the basis of our study sample, we could detect odds ratios of 4.24 and 3.38, assuming an exposure prevalence of 10% and 50% in patients without favorable outcome. In addition, we could not exclude a risk of overfitting in multivariate analysis. For these reasons, the present findings should be confirmed in further larger studies or in the ongoing randomized controlled trials.[40]

CONCLUSIONS

This study emphasizes the impact of complete successful reperfusion in patients with ABAO, which appeared the strongest predictor of a 90-day favorable outcome. The presence of PcomA collateral flow, lower pretreatment NIHSS scores, the absence of atrial fibrillation, and IV thrombolysis administration was also associated with favorable outcomes. Nevertheless, further randomized controlled trials are warranted to assess the patient-related factors determining clinical outcome.

Disclosures: Julien Labreuche—*RELATED*: Fees for participation in review activities such as data monitoring boards, statistical analysis, endpoint committees, and the like. Alain Bonafe—*UNRELATED*: *Consultancy*: Medtronic, Stryker, MicroVention. Pierre Henri Lefevre—*UNRELATED*: Payment for development of educational presentations: Medtronic, Stryker.

REFERENCES

1. Mattle HP, Arnold M, Lindsberg PJ, et al. **Basilar artery occlusion.** *Lancet Neurol* 2011;10:1002–14 CrossRef Medline
2. Goyal M, Menon BK, van Zwam WH, et al; HERMES collaborators. **Endovascular thrombectomy after large-vessel ischaemic stroke: a meta-analysis of individual patient data from five randomised trials.** *Lancet* 2016;387:1723–31 CrossRef Medline
3. Kayan Y, Meyers PM, Prestigiacomo CJ, Society of NeuroInterventional Surgery, et al. **Current endovascular strategies for posterior circulation large vessel occlusion stroke: report of the Society of NeuroInterventional Surgery Standards and Guidelines Committee.** *J Neurointerv Surg* 2019;11:1055–62 CrossRef Medline
4. Liu X, Dai Q, Ye R, et al; BEST Trial Investigators. **Endovascular treatment versus standard medical treatment for vertebrobasilar artery occlusion (BEST): an open-label, randomised controlled trial.** *Lancet Neurol* 2020;19:115–22 CrossRef Medline
5. Tei H, Uchiyama S, Usui T, et al. **Posterior circulation ASPECTS on diffusion-weighted MRI can be a powerful marker for predicting functional outcome.** *J Neurol* 2010;257:767–73 CrossRef Medline
6. Mourand I, Machi P, Nogué E, et al. **Diffusion-weighted imaging score of the brain stem: a predictor of outcome in acute basilar artery occlusion treated with the Solitaire FR device.** *AJNR Am J Neuroradiol* 2014;35:1117–23 CrossRef Medline
7. Archer CR, Horenstein S. **Basilar artery occlusion: clinical and radiological correlation.** *Stroke* 1977;8:383–90 CrossRef Medline
8. Goyal N, Tsivgoulis G, Nickele C, et al. **Posterior circulation CT angiography collaterals predict outcome of endovascular acute ischemic stroke therapy for basilar artery occlusion.** *J Neurointerv Surg* 2016;8:783–86 CrossRef Medline
9. Hacke W, Kaste M, Bluhmki E, et al; ECASS Investigators. **Thrombolysis with alteplase 3 to 4.5 hours after acute ischemic stroke.** *N Engl J Med* 2008;359:1317–29 CrossRef Medline
10. Sakamoto Y, Kimura K, Iguchi Y, et al. **Hemorrhagic transformation in acute cerebellar infarction.** *Cerebrovasc Dis* 2011;32:327–33 CrossRef Medline
11. Maus V, Styczen H, Liman J, et al. **Intracranial mechanical thrombectomy of large vessel occlusions in the posterior circulation using SAVE.** *BMC Neurol* 2019;19:197 CrossRef Medline
12. Ducroux C, Piotin M, Gory B, et al; ASTER Trial investigators. **First pass effect with contact aspiration and stent retrievers in the Aspiration versus Stent Retriever (ASTER) trial.** *J Neurointerv Surg* 2020;12:386–91 CrossRef Medline
13. Zaidat OO, Yoo AJ, Khatri P, et al; Cerebral Angiographic Revascularization Grading (CARG) Collaborators; STIR Re-vascularization working group; STIR Thrombolysis in Cerebral Infarction (TICI) Task Force. **Recommendations on angiographic revascularization grading standards for acute ischemic stroke.** *Stroke* 2013;44:2650–63 CrossRef Medline
14. Heinze G. **A comparative investigation of methods for logistic regression with separated or nearly separated data.** *Stat Med* 2006;25:4216–26 CrossRef Medline
15. Harrell FE, Lee KL, Mark DB. **Multivariable prognostic models: issues in developing models, evaluating assumptions and adequacy, and measuring and reducing errors.** *Statist Med* 1996;15:361–87 CrossRef
16. Allison PD. *Multiple Regression: A Primer*. Pine Forge Press; 1999
17. Gory B, Mazighi M, Labreuche J, et al, ETIS (Endovascular Treatment in Ischemic Stroke) Investigators. **Predictors for mortality after mechanical thrombectomy of acute basilar artery occlusion.** *Cerebrovasc Dis* 2018;45:61–67 CrossRef Medline
18. Gory B, Eldesouky I, Sivan-Hoffmann R, et al. **Outcomes of stent retriever thrombectomy in basilar artery occlusion: an observational study and systematic review.** *J Neurol Neurosurg Psychiatry* 2016;87:520–25 CrossRef Medline
19. Singer OC, Berkefeld J, Nolte CH, et al; ENDOSTROKE Study Group. **Mechanical recanalization in basilar artery occlusion: the ENDOSTROKE study—Recanalization in BA Occlusion.** *Ann Neurol* 2015;77:415–24 CrossRef Medline
20. Deb-Chatterji M, Flottmann F, Leischner H, et al. **Recanalization is the key for better outcome of thrombectomy in basilar artery occlusion.** *Clin Neuroradiol* 2019 Dec 23. [Epub ahead of print] CrossRef Medline
21. Ravindren J, A, Pérez M, Hellstern V, et al. **Predictors of outcome after endovascular thrombectomy in acute basilar artery occlusion and the 6 hr time window to recanalization.** *Front Neurol* 2019;10:923 CrossRef Medline
22. Gory B, Mazighi M, Blanc R, et al. **Mechanical thrombectomy in basilar artery occlusion: influence of reperfusion on clinical outcome and impact of the first-line strategy (ADAPT vs stent retriever).** *J Neurosurg* 2018;129:1482–91 CrossRef Medline
23. Mokin M, Sonig A, Sivakanthan S, et al. **Clinical and procedural predictors of outcomes from the endovascular treatment of posterior circulation strokes.** *Stroke* 2016;47:782–88 CrossRef Medline
24. Dargazanli C, Consoli A, Barral M, et al. **Impact of modified TICI 3 versus modified TICI 2b reperfusion score to predict good outcome following endovascular therapy.** *AJNR Am J Neuroradiol* 2017;38:90–96 CrossRef Medline
25. Kang D, Jung C, Yoon W, et al. **Endovascular thrombectomy for acute basilar artery occlusion: a multicenter retrospective observational study.** *J Am Heart Assoc* 2018;7:e009419 CrossRef Medline
26. Li C, Zhao W, Wu C, et al. **Outcome of endovascular treatment for acute basilar artery occlusion in the modern era: a single institution experience.** *Neuroradiology* 2018;60:651–59 CrossRef
27. Phan K, Phan S, Huo YR, et al. **Outcomes of endovascular treatment of basilar artery occlusion in the stent retriever era: a systematic review and meta-analysis.** *J Neuronterv Surg* 2016;8:1107–15 CrossRef Medline
28. Yoon W, Kim SK, Heo TW, et al. **Predictors of good outcome after stent-retriever thrombectomy in acute basilar artery occlusion.** *Stroke* 2015;46:2972–75 CrossRef Medline
29. Tran AT, Nguyen HA, Vu DL, et al. **Basilar artery thrombectomy: assessment of outcome and identification of prognostic factors.** *Acta Neurol Belg* 2020;120:99–105 CrossRef Medline
30. Bouslama M, Haussen DC, Aghaebrahim A, et al. **Predictors of good outcome after endovascular therapy for vertebrobasilar occlusion stroke.** *Stroke* 2017;48:3252–57 CrossRef Medline
31. Mourand I, Machi P, Milhaud D, et al. **Mechanical thrombectomy with the Solitaire device in acute basilar artery occlusion.** *J Neurointerv Surg* 2014;6:200–04 CrossRef Medline
32. Guillaume M, Lapergue B, Gory B, et al. **Rapid successful reperfusion of basilar artery occlusion strokes with pretreatment diffusion-weighted imaging posterior-circulation ASPECTS <8 is associated with good outcome.** *J Am Heart Assoc* 2019;8:e010962 CrossRef Medline
33. Schonewille WJ, Wijman CA, Michel P, et al; BASICS study group. **Treatment and outcomes of acute basilar artery occlusion in the Basilar Artery International Cooperation Study (BASICS): a**

prospective registry study. *Lancet Neurol* 2009;8:724–30 CrossRef Medline
34. Nagel S, Schellinger PD, Hartmann M, et al. **Therapy of acute basilar artery occlusion: intraarterial thrombolysis alone vs bridging therapy.** *Stroke* 2009;40:140–46 CrossRef Medline
35. Caplan LR. **Vertebrobasilar embolism.** *Clin Exp Neurol* 1991;28:1–22 Medline
36. Cross DT, Moran CJ, Akins PT, et al. **Relationship between clot location and outcome after basilar artery thrombolysis.** *AJNR Am J Neuroradiol* 1997;18:1221–28 Medline
37. van der Hoeven EJ, McVerry F, Vos JA, et al; BASICS registry investigators. **Collateral flow predicts outcome after basilar artery occlusion: the posterior circulation collateral score.** *Int J Stroke* 2016;11:768–75 CrossRef Medline
38. Bang OY, Saver JL, Kim SJ, et al. **Collateral flow predicts response to endovascular therapy for acute ischemic stroke.** *Stroke* 2011;42:693–99 CrossRef Medline
39. Kim JT, Cho BH, Cho KH, et al. **Magnetic resonance imaging versus computed tomography angiography based selection for endovascular therapy in patients with acute ischemic stroke.** *Stroke* 2019;50:365–72 CrossRef Medline
40. van der Hoeven EJ, Schonewille WJ, Vos J, et al; BASICS Study Group, **The Basilar Artery International Cooperation Study (BASICS): study protocol for a randomised controlled trial.** *Trials* 2013;14:200 CrossRef Medline

Intraluminal Carotid Artery Thrombus in COVID-19: Another Danger of Cytokine Storm?

A.Y. Mohamud, B. Griffith, M. Rehman, D. Miller, A. Chebl, S.C. Patel, B. Howell, M. Kole, and H. Marin

ABSTRACT

SUMMARY: Coronavirus disease 2019 (COVID-19) is associated with a severe inflammatory response. Inflammation affects atherosclerotic plaque vulnerability and promotes a thrombogenic environment. We report a series of 6 patients with COVID-19 with acute ischemic stroke due to intraluminal carotid artery thrombus presenting during an 8-day period. Six patients were included (5 men) with a mean age of 65.8 years (range, 55–78 years). COVID-19 was diagnosed by detection of Severe Acute Respiratory Syndrome coronavirus 2 in 5 patients and was presumed due to typical clinical and imaging findings in 1 patient. All patients had vascular risk factors including diabetes (83%), hyperlipidemia (100%), and smoking (17%). Four patients presented with large infarcts with initial NIHSS scores of 24–30. During their hospitalization, all patients had elevated D-dimer and C-reactive protein levels, 5 patients had elevated lactate dehydrogenase and ferritin levels, 3 had elevated interleukin-6 levels, and 2 had elevated troponin levels. Inflammation related to COVID-19 may result in rupture of vulnerable atherosclerotic plaques, resulting in thrombosis and acute ischemic stroke.

ABBREVIATIONS: COVID-19 = coronavirus disease 2019; ICT = intraluminal carotid artery thrombus; IL-6 = interleukin-6; LVO = large-vessel occlusion; SARS-CoV-2 = Severe Acute Respiratory Syndrome coronavirus 2

Since emerging in late 2019, the Severe Acute Respiratory Syndrome coronavirus 2 (SARS-CoV-2) and associated coronavirus disease 2019 (COVID-19) have rapidly progressed to a global pandemic. Current understanding suggests that COVID-19 causes an excessive immune response, resulting in inflammation and extensive tissue damage.[1] Those patients who develop severe disease have been found to have significantly elevated levels of interleukin-6 (IL-6) and other inflammatory cytokines in what is termed a "cytokine storm."[2] This pattern of severe inflammation is of concern in the realm of vascular neurology because previous coronavirus and influenza epidemics have demonstrated an increased risk of cardiovascular complications.[3] These findings were attributed primarily to the substantial inflammatory response along with localized vascular inflammation.[3,4] More recent studies have also found that flulike illnesses increase the odds of cerebral infarction by nearly 3-fold during the initial 15 days, with inflammation again identified as a potential culprit.[5]

A specific subtype of acute ischemic stroke, large-vessel occlusion (LVO), is characterized by occlusion of a major extracranial (carotid or vertebral artery) or intracranial vessel and represents 24%–38% of all acute ischemic strokes when defined as blockage of the intracranial ICA, M1, M2, A1, vertebral artery, P1, or basilar artery.[6] One important cause of LVO is artery-to-artery embolism, usually due to the presence of an atherothrombotic plaque or thrombosis at the site of a plaque rupture. Of particular concern are atherosclerotic plaques that are considered vulnerable, meaning those that have a high probability of undergoing rupture and causing local thrombosis and embolism. Plaque vulnerability is determined, in part, by plaque morphology, which is influenced by pathophysiologic mechanisms occurring at the cellular and molecular levels.[7] One factor that has been reported to have a key role in promoting plaque vulnerability is inflammation, which can lead to thinning of the fibrous caps, enhanced influx of lipids and expansion of the lipid core, as well as increased neoangiogenesis.[8]

Cerebral infarction related to supracardiac atherosclerosis and subsequent thromboembolism is an increasingly recognized cause of embolic stroke.[9] A 2019 meta-analysis found atherosclerotic plaques with high-risk features to be 5 times more prevalent in the ipsilateral compared with the contralateral carotid artery in

Received May 9, 2020; accepted after revision June 1.

From the Departments of Neurology (A.Y.M., M.R., D.M., A.C., B.H.), Radiology (B.G., S.C.P., H.M.), and Neurosurgery (M.K.), Henry Ford Health System, Detroit, Michigan.

Ali Y. Mohamud and Brent Griffith contributed equally to this work.

Please address correspondence to Brent Griffith, MD, Department of Radiology, K3, Henry Ford Hospital, 2799 West Grand Blvd, Detroit, MI 48202; e-mail: brentg@rad.hfh.edu; @BrentDGriffithl

Indicates open access to non-subscribers at www.ajnr.org

Indicates article with supplemental on-line appendix and table.

http://dx.doi.org/10.3174/ajnr.A6674

Patient demographics and stroke clinical details

Pt. No.	Age (yr)	Sex	Days from COVID-19 Sx Onset	Initial NIHSS	Cervical Occlusion or Near-Occlusion Location	Cranial Occlusion Location	Atherosclerotic Plaque Location	TICI Score	mRS	LOS (days)
1	55	M	0	24	Left ICA bifurcation	Left ICA petrous segment	L petrous ICA	2a	4	8
2	78	F	12	25	Left ICA bifurcation	None	Carotid bulb	NA	5	18
3	62	M	0	25	Right ICA bifurcation	Right M1	Carotid bulb	NA	5	18
4	74	M	14	5	Right ICA bifurcation	None	Carotid bulb	NA	2	8
5	59	M	4	1	Right ICA bifurcation	Right M2	None	NA	1	2
6	67	M	7	30	Left ICA bifurcation	Left M1	Carotid bulb	2b	4	12

Note:—Pt. indicates patient; Sx, symptom; LOS, length of stay; NA, not applicable.

embolic stroke of underdetermined source.[10] Nevertheless, identification of intraluminal carotid artery thrombus (ICT) is less common. In the North American Symptomatic Carotid Endarterectomy Trial (NASCET),[11] the frequency of ICT was only 1.1% in symptomatic patients with <70% stenosis versus 4.3% and 5.5% in patients with ≥70% and >85% stenosis, respectively.[12] While ICT can occur in patients with and without significant atherosclerotic disease, in patients without underlying carotid stenosis, ICT is often associated with a hypercoagulable state.[12]

In the context of the current pandemic, initial reports have indicated that fewer patients are seeking emergency care for stroke symptoms, possibly to avoid exposure to the coronavirus. Despite an overall reduction in our total institutional stroke volumes, we noted an unusually high number of patients with COVID-19 who presented during 8 days with strokes due to ICT within the proximal internal carotid artery lumen. We present the clinical presentation, laboratory studies, and imaging findings of 6 such patients.

Case Series

Institutional review board approval with waived consent was obtained for this Health Insurance Portability and Accountability Act–compliant retrospective Clinical Report. The case series consists of patients with COVID-19 presenting with acute cerebral infarction with varying degrees of intraluminal clot within the internal carotid artery. Patients were selected from those admitted to a large comprehensive stroke center. COVID-19 was diagnosed via detection of SARS-CoV-2 with real-time reverse transcriptase polymerase chain reaction assay performed on specimens obtained via nasopharyngeal or nasal swabs. One patient with real-time reverse transcriptase polymerase chain reaction negative for SARS-CoV-2 but with high suspicion for COVID-19 was also included. That patient had a clinical presentation and laboratory findings typical of COVID-19, as well as chest CT findings of bilateral subpleural consolidative opacities and a large region of ground-glass opacity, which fit the typical appearance of COVID-19 pneumonia according to the Radiological Society of North America Expert Consensus Statement.[13] Laboratory values reported include peak levels during the hospitalization course, as well as peak levels within the 24 hours before or after initial identification of ICT on imaging. This is a descriptive study reporting the imaging and clinical characteristics of this series of patients.

Six patients were included (5 men, 1 woman) with a mean age of 65.8 years (range, 55–78 years) (Table). All patients had a history of vascular risk factors, including diabetes (83%), hyperlipidemia (100%), and smoking (17%). Four patients presented with large infarcts with initial NIHSS scores ranging from 24 to 30. Four patients (67%) presented with tandem occlusions identified on CTA. One patient received IV alteplase, and 2 patients underwent mechanical thrombectomy with TICI reperfusion scores ranging from TICI 2a to TICI 2b. With regard to COVID-19 status, 4 patients (67%) had previous symptoms consistent with COVID-19 ranging from 4 to 14 days before the onset of infarction. Two patients (33%) presented with cerebral infarction and later developed respiratory symptoms. One patient tested negative for COVID-19 via nasal swab but was treated as positive for COVID-19 on the basis of clinical, radiographic, and laboratory findings.

During their hospitalization course (On-line Table), all patients (100%) had elevated D-dimer and C-reactive protein levels, 5 (83%) had elevated lactate dehydrogenase and ferritin levels and reduced absolute lymphocyte counts, and 2 (33%) had elevated troponin levels. In addition, of the 4 patients with IL-6 levels tested during their hospitalization, 3 (75%) had elevated levels. Within the 24 hours before or after ICT detection on imaging, of those tested, levels of D-dimer, C-reactive protein, and lactate dehydrogenase were elevated in 100% (5/5 patients tested), absolute lymphocyte counts were reduced in 67% (4/6), ferritin was elevated in 60% (3/5), fibrinogen was elevated in 50% (2/4), and troponin was elevated in 40% (2/5). In addition, of the 3 patients who underwent IL-6 testing during that timeframe, 100% (3/3) had elevated levels. Four patients were significantly debilitated on discharge with mRS scores of 4–5, and 2 patients were discharged with mild deficits (mRS, 1–2).

Patient 1. A 55-year-old man with a history of prior acute ischemic stroke and stenosis of the paraclinoid left ICA presented 24 hours after last known well with altered mental status, right hemiplegia, and global aphasia with an initial NIHSS score of 24. Noncontrast CT demonstrated early ischemic changes involving the left thalamus and putamen. CTA showed near-occlusion of the left ICA at the bifurcation due to a large intraluminal clot with complete occlusion more distally and reconstitution at the supraclinoid segment (Fig 1). CT perfusion demonstrated ischemic penumbra and core infarct volumes of 189 and 46 mL, respectively. The patient

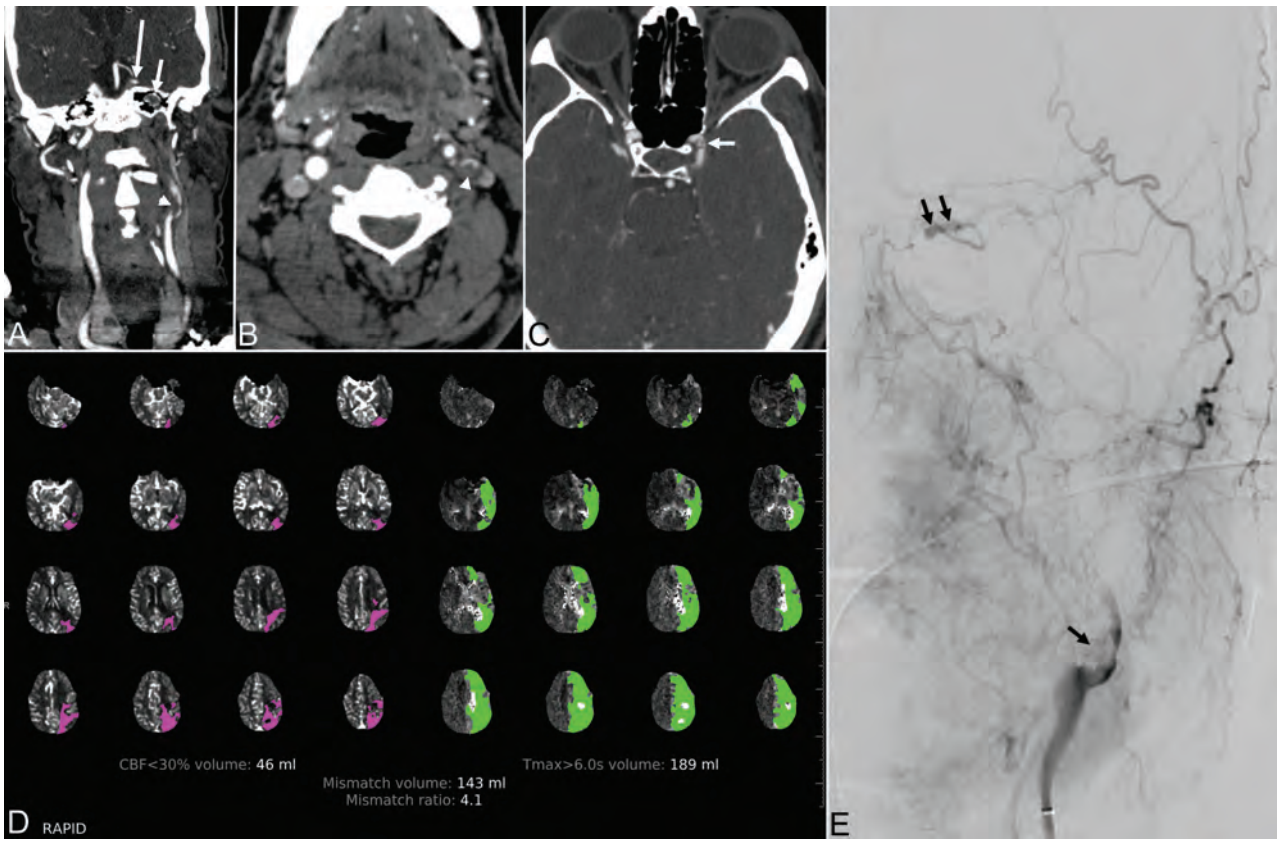

FIG 1. Patient 1. A 55-year-old man with COVID-19 and an NIHSS score of 24. *A* and *B*, Coronal reformatted and axial images from CT angiography of the head and neck demonstrate an irregular plaque at the left internal carotid artery bifurcation (*arrowhead*) and nonopacification of the high cervical and petrous (*short arrow*) left internal carotid artery from tandem occlusion, with reconstitution of the supraclinoid segment (*long arrow*). *C*, CT angiography 3 years prior shows moderate focal stenosis of the left paraclinoid ICA (*white arrow*). *D*, CT perfusion map shows a large volume of hypoperfusion (time-to-maximum >6 seconds) involving the left anterior and middle cerebral artery territory and a considerably smaller volume of presumed core infarct (CBF of $<30\%$) in the left parietal region. *E*, Digital subtraction angiography of the left internal carotid artery demonstrates an eccentric filling defect of the left carotid bifurcation (*black arrow*) and left ICA occlusion, with recanalization at the level of the left ophthalmic artery from external-to-internal carotid collaterals (*double black arrow*).

underwent mechanical thrombectomy of the carotid bifurcation and supraclinoid ICA with removal of a large clot and a final TICI 2a reperfusion grade.

Patient 2. A 78-year-old woman presented with a 1-week history of fatigue, anorexia, headache, and respiratory distress. Following admission with bilateral air space opacities suggestive of multifocal pneumonia, the patient's condition stabilized and she was weaned off supplemental oxygen. The next morning the patient was found to be mute and hemiplegic on the right with an initial NIHSS score of 25. Noncontrast CT demonstrated evolving ischemic changes in the left caudate nucleus, putamen, and left frontal and parietal cortices (Fig 2). CTA demonstrated an irregular plaque at the left ICA bifurcation and intraluminal clot extending superiorly. The patient did not receive thrombolytic therapy because she was outside the treatment window of 4.5 hours. She did not undergo mechanical thrombectomy because no LVO was present on CTA.

Patient 3. A 62-year-old man with a history of diabetes and hypertension presented with sudden-onset left-sided weakness. On arrival, the patient was noted to be hypoxic requiring oxygen supplementation, and his physical examination was notable for left hemiplegia and dysarthria with an initial NIHSS score of 25. Noncontrast CT demonstrated an acute infarct involving the right frontal and temporal lobes. CTA demonstrated complete occlusion of the right ICA from its origin with reconstitution at the paraclinoid segment. Distally, there was occlusion of the mid-to-distal M1 segment of the right MCA. The patient did not receive thrombolytic therapy because he was discovered 18 hours after symptom onset, and mechanical thrombectomy was not performed due to a large established infarct on noncontrast CT.

Patient 4. A 74-year-old man with a medical history of hypertension, chronic kidney disease, and type 2 diabetes presented with altered mental status and hypoxia. On examination, the patient had a mild right facial droop and hemiparesis, with an initial NIHSS score of 5. Noncontrast CT demonstrated no acute abnormality. CT angiography showed thrombus in the right carotid bulb extending into the proximal right internal carotid artery. The patient underwent emergent carotid endarterectomy.

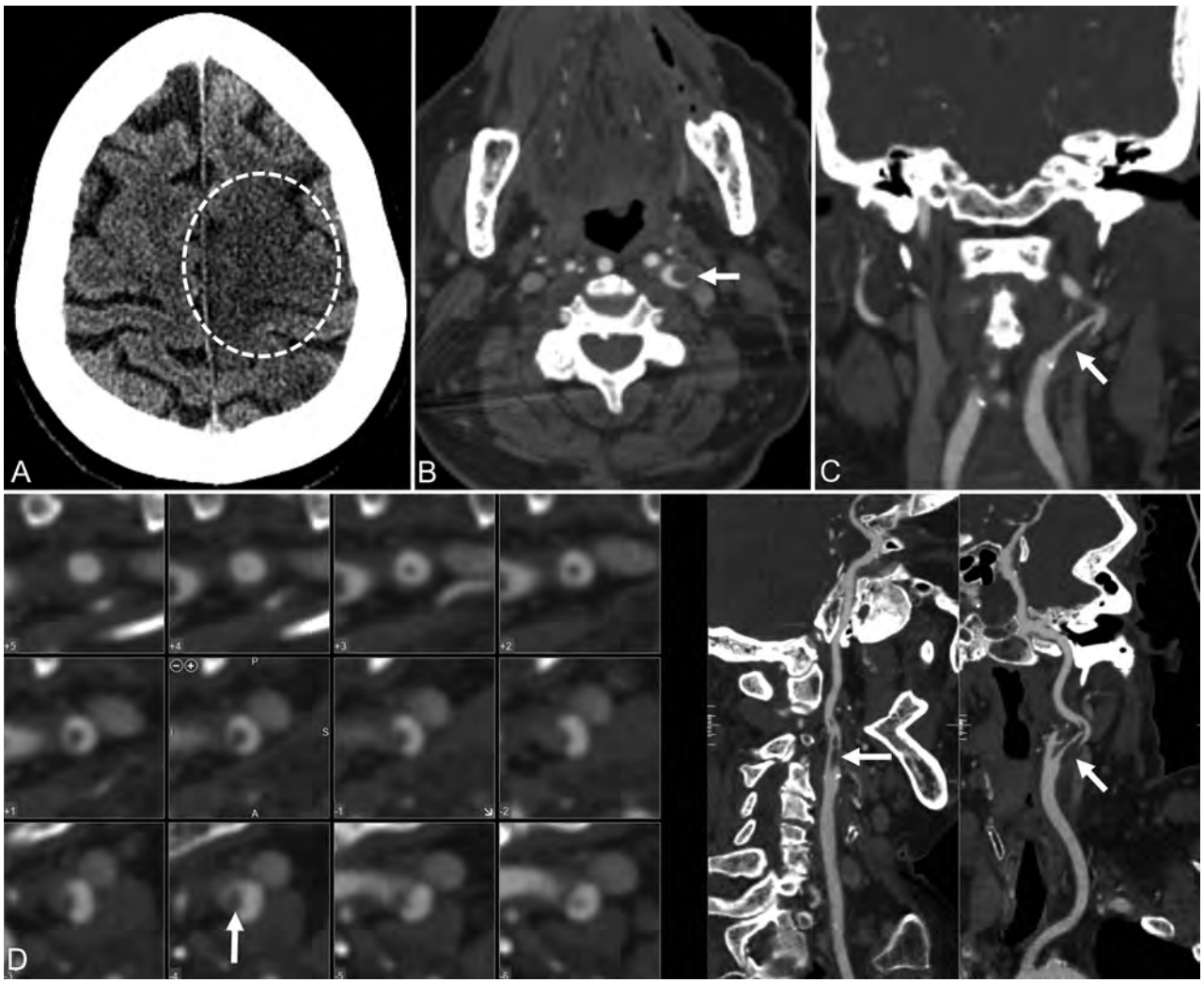

FIG 2. Patient 2. A 78-year-old woman with COVID-19 and an NIHSS score of 25. *A*, CT of the head without contrast demonstrates an evolving ischemic infarct in the left frontoparietal paracentral cortex (*dotted circle*) with a smaller infarct posteriorly in the left parietal cortex. *B–D*, Axial, coronal, and curved reformatted images from CT angiography of the head and neck demonstrate an irregular plaque at the left internal carotid artery bifurcation and an intraluminal filling defect (*arrow*) extending superiorly in the left internal carotid artery, corresponding to ruptured plaque with clot formation.

Patient 5. A 59-year-old man presented with sudden-onset speech changes. The physical examination was notable for slurred speech and an initial NIHSS of 1. Noncontrast CT demonstrated hyperdensity involving the M2 segment of the right MCA. CTA confirmed occlusion of an M2 segment branch of the right MCA in addition to a noncalcified low-density filling defect along the wall of the right ICA immediately distal to the bifurcation, consistent with a ruptured atherosclerotic plaque with adherent thrombus. The patient was treated with IV alteplase, resulting in improvement of the neurologic deficits. MR imaging demonstrated an acute infarct involving the right frontal, temporal, and parietal lobes.

Patient 6. A 67-year-old man with a medical history of hyperlipidemia presented with fever and sudden loss of consciousness. On examination, the patient had left-gaze deviation, dense left hemiplegia, and aphasia with an initial NIHSS of 30. Noncontrast CT revealed a hyperdense left MCA, but otherwise no acute process (Fig 3). CTA showed near-occlusive ruptured plaque and thrombus in the left ICA origin, along with complete occlusion of the M1 segment of the left MCA. CT perfusion demonstrated ischemic penumbra and core infarct volumes of 159 and 36 mL, respectively. The patient underwent mechanical thrombectomy of the carotid bifurcation and supraclinoid ICA with a final TICI 2b reperfusion grade after removal of 2 separate clots. The patient's physical examination findings following intervention were notable for improvement in language but continued right hemiplegia and dysphagia.

DISCUSSION

These cases demonstrate 6 patients with COVID-19 (5 confirmed, 1 presumed) presenting with acute ischemic infarction. Each patient had evidence of ICT within the proximal internal carotid artery, most likely secondary to plaque rupture followed by thrombus formation and subsequent artery-to-artery

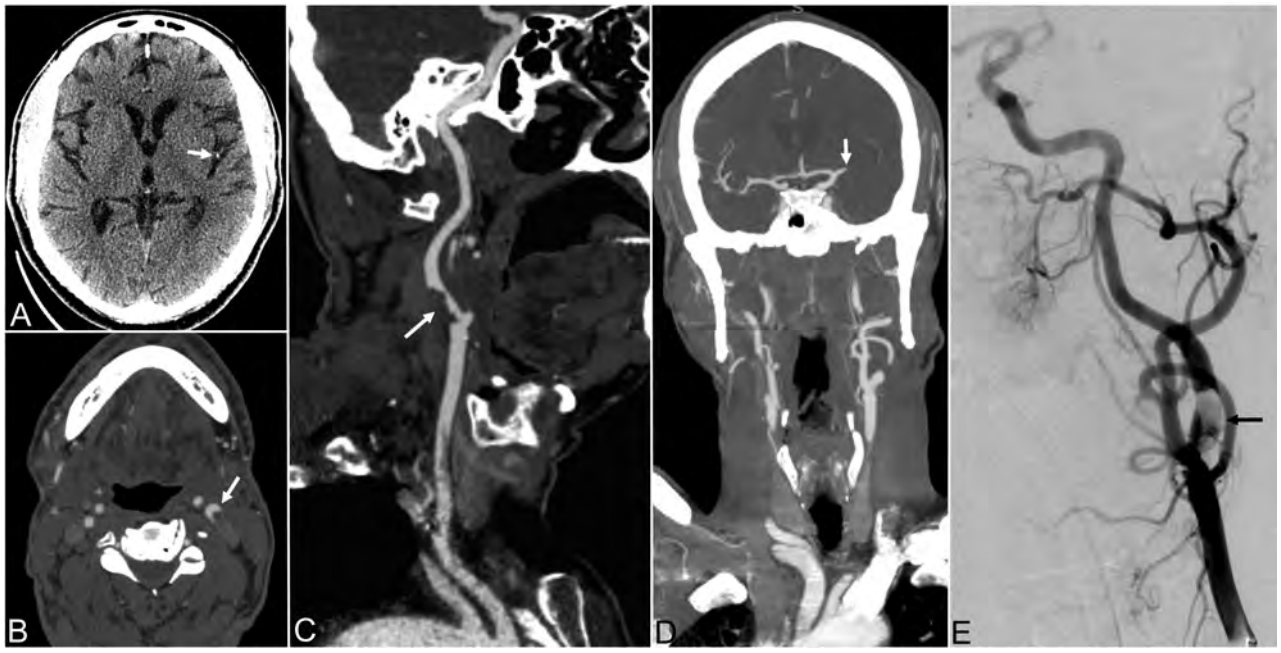

FIG 3. Patient 6. A 67-year-old man presenting with fever and sudden loss of consciousness. *A*, Axial noncontrast CT of the head demonstrates a hyperdense left MCA branch (*arrow*) without evidence of acute infarct. *B* and *C*, Axial and curved reformatted images from CT angiography of the head and neck demonstrate an intraluminal clot projecting into the left internal carotid artery at the bifurcation (*arrows*). *D*, Coronal MIP from CT angiography of the head and neck demonstrates occlusion of the M1 segment of the left MCA. *E*, Digital subtraction angiography of the left internal carotid artery demonstrates an eccentric filling defect of the left carotid bifurcation (*black arrow*).

embolism. There is evidence that inflammation promotes the development of atherosclerosis and is also associated with plaque rupture.[14] The Canakinumab Anti-Inflammatory Thrombosis Outcome Study noted that patients who received an IL-1 inhibitor had significantly decreased levels of IL-6 and reduced rates of myocardial and cerebral infarction.[15]

We suspect that in our cases, the proinflammatory state caused by COVID-19 infection contributed to plaque instability and rupture, with subsequent thrombosis promoted by the thrombogenic environment also caused by the ongoing COVID-19 infection. There is evidence suggesting that cytokine storms play a role in cases of severe COVID-19; and for some patients, this inflammatory state, coupled with the thrombogenic environment, may play an important role in clot formation and subsequent infarction. All patients in this series had a history of vascular risk factors, including diabetes, hyperlipidemia, and smoking, which may have increased their susceptibility to plaque rupture and thrombosis.

Notably, all 6 patients presented with no-or-mild COVID-19 symptoms, and 5 of the 6 patients (83%) presented with stroke symptoms as the chief symptoms. This suggests that even mild cases of COVID-19 can result in thrombogenicity, inflammation, and ultimately plaque rupture and thrombosis. In previous studies examining complications related to coronavirus-related diseases, most complications were seen in critically ill patients.[16,17] However, the fact that most of our patients had milder COVID-19 symptoms suggests that a contributing factor may be a direct effect of the SARS-CoV-2 infection rather than systemic inflammation alone or a post-infectious prothrombotic state.

Viral infections are known to have the potential for causing vascular disease, including through atherogenesis, endothelial activation leading to altered coagulation and fibrinolytic systems, as well as direct endothelial cell invasion.[18] In addition, recent studies have found evidence of direct infection of the endothelium by SARS-CoV-2 with diffuse endothelial inflammation, further supporting the role of the virus in these cases.[19] The fact that all patients presented with involvement at the carotid bifurcation may be due to its pre-existing propensity for atherosclerosis and turbulent flow; the latter can damage the endothelium and lead to platelet aggregation.

The limitations of this study include the inability to prove causality between COVID-19 infection and ICT due to the retrospective nature of the study and the small number of patients. Additionally, there was neither consistent assessment of the same systemic inflammatory markers in all patients nor pathologic confirmation of the embolic material or carotid plaque. Finally, baseline and follow-up arterial wall imaging beyond CTA was not performed.

Our findings suggest that there is an increased risk of LVO due to ICT in patients with COVID-19 infection who have typical vascular risk factors. Additionally, our patients most often presented with symptoms of cerebral ischemia rather than typical COVID-19 symptoms. Furthermore, cerebral ischemia due to ICT was not limited to patients with severe COVID-19 symptoms. The possible coincidence of cerebral ischemia due to ICT and COVID-19 infection is an essential consideration, particularly in the evaluation of encephalopathy, which is common with viral illnesses. This recognition is important to ensure that an appropriate diagnostic work-up is performed, including

carotid imaging, as well as the timely treatment of acute cerebral ischemia and initiation of antithrombotic therapy for stroke prevention.

Disclosures: Ali Y. Mohamud—*UNRELATED*: *Employment*: Henry Ford Health System, *Comments*: current postgraduate year 2 neurology resident. Mohammed Rehman—*UNRELATED*: *Payment for Lectures Including Service on Speakers Bureaus*: Portola Pharmaceuticals, American Academy of Neurology. Daniel Miller—*UNRELATED*: *Payment for Lectures Including Service on Speakers Bureaus*: Boston Scientific, BioTelemetry Inc, *Comments*: 1 engagement each; both unrelated to this topic. Alex Chebl—*UNRELATED: Payment for Lectures Including Service on Speakers Bureaus*: Medtronic, *Comments*: speaker 23 months ago.

REFERENCES

1. Huang C, Wang Y, Li X, et al. **Clinical features of patients infected with 2019 novel coronavirus in Wuhan, China.** *Lancet* 2020;395:497–506 CrossRef Medline
2. Zhou F, Yu T, Du R, et al. **Clinical course and risk factors for mortality of adult inpatients with COVID-19 in Wuhan, China: a retrospective cohort study.** *Lancet* 2020;395:1054–62 CrossRef Medline
3. Madjid M, Safavi-Naeini P, Solomon SD, et al. **Potential effects of coronaviruses on the cardiovascular system: a review.** *JAMA Cardiol* 2020 Mar 27. [Epub ahead of print] CrossRef Medline
4. Boehme AK, Luna J, Kulick ER, et al. **Influenza-like illness as a trigger for ischemic stroke.** *Ann Clin Transl Neurol* 2018;5:456–63 CrossRef Medline
5. American Heart Association. **Flu, flu-like illnesses linked to increased risk of stroke, neck artery tears.** January 30, 2019. https://www.sciencedaily.com/releases/2019/01/190130075757.htm. Accessed April 6, 2020
6. Rennert RC, Wali AR, Steinberg JA, et al. **Epidemiology, natural history, and clinical presentation of large vessel ischemic stroke.** *Neurosurgery* 2019;85:S4–S8 CrossRef Medline
7. Nighoghossian N, Derex L, Douek P. **The vulnerable carotid artery plaque: current imaging methods and new perspectives.** *Stroke* 2005;36:2764–72 CrossRef Medline
8. Kataoka Y, Puri R, Nicholls SJ. **Inflammation, plaque progression and vulnerability: evidence from intravascular ultrasound imaging.** *Cardiovasc Diagn Ther* 2015;5:280–89 CrossRef Medline
9. Ntaios G, Wintermark M, Michel P. **Supracardiac atherosclerosis in embolic stroke of undetermined source: the underestimated source.** *Eur Heart J* 2020 Apr 16. [Epub ahead of print] CrossRef Medline
10. Kamtchum-Tatuene J, Wilman A, Saqqur M, et al. **Carotid plaque with high-risk features in embolic stroke of undetermined source: systematic review and meta-analysis.** *Stroke* 2020;51:311–14 CrossRef Medline
11. Villarreal J, Silva T, Eliasziw M, et al. **For the North American Symptomatic Carotid Endarterectomy Trial (NASCET) Group. Prognosis of patients with an intraluminal thrombus in the internal carotid artery.** *Stroke* 1998;29:276
12. Vellimana AK, Kadkhodayan Y, Rich KM, et al. **Symptomatic patients with intraluminal carotid artery thrombus: outcome with a strategy of initial anticoagulation.** *J Neurosurg* 2013;118:34–41 CrossRef Medline
13. Simpson S, Kay FU, Abbara S, et al. **Radiological Society of North America Expert Consensus Statement on Reporting Chest CT Findings Related to COVID-19: endorsed by the Society of Thoracic Radiology, the American College of Radiology, and RSNA.** *J Thorac Imaging* 2020 Apr 28. [Epub ahead of print] CrossRef Medline
14. Paoletti R, Gotto AM Jr, Hajjar DP. **Inflammation in atherosclerosis and implications for therapy.** *Circulation* 2004;109:III20–26 CrossRef Medline
15. Ridker PM, Everett BM, Thuren T, et al; CANTOS Trial Group. **Antiinflammatory therapy with canakinumab for atherosclerotic disease.** *N Engl J Med* 2017;377:1119–31 CrossRef Medline
16. Umapathi T, Kor AC, Venketasubramanian N, et al. **Large artery ischaemic stroke in severe acute respiratory syndrome (SARS).** *J Neurol* 2004;251:1227–31 CrossRef Medline
17. Arabi YM, Harthi A, Hussein J, et al. **Severe neurologic syndrome associated with Middle East respiratory syndrome corona virus (MERS-CoV).** *Infection* 2015;43:495–501 CrossRef Medline
18. Keller TT, Mairuhu AT, de Kruif MD, et al. **Infections and endothelial cells.** *Cardiovasc Res* 2003;60:40–48 CrossRef Medline
19. Varga Z, Flammer AJ, Steiger P, et al. **Endothelial cell infection and endotheliitis in COVID-19.** *Lancet* 2020;395:1417–18 CrossRef Medline

MRI Findings of Immune Checkpoint Inhibitor–Induced Hypophysitis: Possible Association with Fibrosis

R. Kurokawa, Y. Ota, W. Gonoi, A. Hagiwara, M. Kurokawa, H. Mori, E. Maeda, S. Amemiya, Y. Usui, N. Sato, Y. Nakata, T. Moritani, and O. Abe

ABSTRACT

BACKGROUND AND PURPOSE: Hypophysitis is one of the well-known adverse effects of immune checkpoint inhibitors. Immune checkpoint inhibitor–induced hypophysitis frequently causes irreversible hypopituitarism, which requires long-term hormone replacement. Despite the high frequency and clinical significance, characteristic MR imaging findings of immune checkpoint inhibitor–induced hypophysitis have not been established. In the present study, we aimed to review and extract the MR imaging features of immune checkpoint inhibitor–induced hypophysitis.

MATERIALS AND METHODS: This retrospective international multicenter study comprised 20 patients with melanoma who were being treated with immune checkpoint inhibitors and clinically diagnosed with immune checkpoint inhibitor–induced hypophysitis. Three radiologists evaluated the following MR imaging findings: enlargement of the pituitary gland and stalk; homogeneity of enhancement of the pituitary gland; presence/absence of a well-defined poorly enhanced area and, if present, its location, shape, and signal intensity in T2WI; and enhancement pattern in contrast-enhanced dynamic MR imaging. Clinical symptoms and hormone levels were also recorded.

RESULTS: Enlargement of the pituitary gland and stalk was observed in 12 and 20 patients, respectively. Nineteen patients showed poorly enhanced lesions (geographic hypoenhancing lesions) in the anterior lobe, and 11 of these lesions showed hypointensity on T2WI. Thyrotropin deficiency and corticotropin deficiency were observed in 19/20 and 12/17 patients, respectively, which persisted in 12/19 and 10/12 patients, respectively, throughout the study period.

CONCLUSIONS: Pituitary geographic hypoenhancing lesions in the anterior lobe of the pituitary gland are characteristic and frequent MR imaging findings of immune checkpoint inhibitor–induced hypophysitis. They reflect fibrosis and are useful in distinguishing immune checkpoint inhibitor–induced hypophysitis from other types of hypophysitis/tumors.

ABBREVIATIONS: CTCAE = Common Terminology Criteria for Adverse Events; CTLA-4 = cytotoxic T-lymphocyte-associated antigen-4; ICI = immune checkpoint inhibitor; ICI-H = immune checkpoint inhibitor–induced hypophysitis; PD-1 = programmed death-1; PD-L1 = programmed death-ligand-1

Recent advances in the understanding of tumor immunology have led to the development of immune checkpoint inhibitors (ICIs), such as cytotoxic T-lymphocyte-associated antigen-4 (CTLA-4) inhibitors, programmed death-1 (PD-1) inhibitors, and programmed death-ligand-1 (PD-L1) inhibitors, which are widely used as breakthrough treatments for a wide variety of malignancies, such as melanoma, pancreatic cancer, and non-small-cell lung cancer. ICIs exert their antitumor effects by promoting the attack on activated T-cells in tumors; however, a risk of adverse effects prevails due to the infiltration of activated T-cells into systemic organs, where they may cause an excessive immune response.[1] Such adverse effects are called immune-related adverse effects because they present symptoms similar to those of autoimmune diseases, such as skin rash, hypothyroidism, and adrenal insufficiency. Immune-related adverse effects can be expressed in all organs of the body, including the skin, endocrine system, respiratory system, gastrointestinal system, and central nervous system.

Received April 11, 2020; accepted after revision June 2.

From the Department of Radiology (R.K., W.G., E.M., S.A., Y.U., O.A.), Graduate School of Medicine, The University of Tokyo, Tokyo, Japan; Division of Neuroradiology (Y.O., T.M.), Department of Radiology, Michigan Medicine, Ann Arbor, Michigan; Department of Radiology (A.H.), Juntendo University School of Medicine, Tokyo, Japan; Department of Radiology (M.K.), Tokyo Metropolitan Cancer and Infectious Diseases Center Komagome Hospital, Tokyo, Japan; Department of Radiology (H.M.), Jichi Medical University, Tochigi-ken, Japan; Department of Radiology (N.S.), Tokyo Metropolitan Neurological Hospital, Tokyo, Japan; and Department of Radiology (Y.N.), National Center of Neurology and Psychiatry, Tokyo, Japan.

Please address correspondence to Wataru Gonoi, MD, Department of Radiology, Graduate School of Medicine, The University of Tokyo, 7-3-1 Hongo, Bunkyo-ku, Tokyo 113-8655, Japan; e-mail: watapi-tky@umin.net

Indicates open access to non-subscribers at www.ajnr.org

http://dx.doi.org/10.3174/ajnr.A6692

Hypophysitis is an inflammation of the pituitary gland and is one of the typical symptoms of immune-related adverse effects; it results in headache and secondary endocrinopathy, depending on the site and extent of injury due to the pituitary infiltration of activated T-cells.[1] Hypophysitis caused by the anti-CTLA-4 antibody, ipilimumab (Yervoy; Bristol-Myers Squibb), was first reported in 2003 by Phan et al.[2] According to a systematic review by Barroso-Sousa et al,[3] ICI-induced hypophysitis (ICI-H) occurs in association with ICI therapy in the following order of frequency: combination therapy (ipilimumab plus PD-1 inhibitors, 6.4%), ipilimumab alone (3.2%), PD-1 inhibitors alone (0.4%), and PD-L1 inhibitors alone (<0.1%). The fatality rate with ICI-H has been reported to be 2%, and the associated endocrine toxicity is very high (>91%).[4,5] Endocrinopathy due to ICI-H is often irreversible and requires hormone replacement in >89% of patients.[4-7] Despite its high incidence, knowledge of the histopathologic findings of ICI-H is scarce. The first postmortem case was reported in 2016 by Caturegli et al,[5] who reported a case of tremelimumab-(an immunoglobulin-2 monoclonal antibody against CTLA-4 produced by AstraZeneca) induced hypophysitis. A postmortem examination revealed near-complete destruction of the anterior lobe of the pituitary gland caused by extensive necrosis and fibrosis and pathologically exhibited lymphocytic and necrotizing hypophysitis.[5] Contrast MR imaging in the same patient showed a poorly enhanced area in the anterior lobe of the pituitary gland, which was thought to reflect necrosis.[5] However, there are no comprehensive reports of MR imaging findings specific to ICI-H that summarize the enhancement and enlargement of the pituitary gland and/or stalk, as in other types of hypophysitis.[6,8-15] Therefore, in the present study, we aimed to review and extract the MR imaging findings specific to ICI-H.

MATERIALS AND METHODS

This international multicenter retrospective study was approved by the local ethics committees (The University of Tokyo Hospital and Michigan Medicine; IRB 2019310NI), and the requirement for informed consent from study participants was waived due to the retrospective design of the study.

Patients

Between January 2013 and March 2020, twenty patients with malignant melanoma who received ICIs and were clinically diagnosed with ICI-H in 2 hospitals in Japan and the United States were included. We collected the following clinical and laboratory data of the patients: the symptoms of the patients; the stage of malignant melanoma; ICIs used for treatment; and the levels of corticotropin, cortisol, thyroid-stimulating hormone, free thyroxine, prolactin, luteinizing hormone, follicle-stimulating hormone, testosterone (if male), growth hormone, and insulin-like growth factor 1. The Common Terminology Criteria for Adverse Events (CTCAE), Version 4.03, were used to assess the severity of adverse effects. The diagnosis of ICI-H was made clinically when ≥1 pituitary hormonal dysfunction, such as hyposecretion of corticotropin or thyroid-stimulating hormone, was identified in patients during or just after the treatment with ICIs with or without physical symptoms, such as headache and nausea. Pituitary dysfunction was diagnosed on the basis of the laboratory reference ranges.

MR Imaging Scanning Protocol

The MR imaging of the pituitary glands was performed using a 1T, 1.5T, or 3T scanner. The following scans were required for all patients: axial and/or coronal T2-weighted (TR range: 2222–4851 ms; TE range: 80–120 ms; in-plane resolution: 0.41×0.41–0.90×0.90 mm^2; section thickness: 2–5 mm), axial and/or coronal T1-weighted (TR range: 450–2000 ms; TE range: 9–20 ms; in-plane resolution: 0.41×0.41–0.90×0.90 mm^2; section thickness: 2–5 mm), contrast-enhanced 3D-T1-weighted (axial, sagittal, or coronal; TR range: 7.2–600 ms; TE range: 2.3–28.3 ms; voxel size: $0.31 \times 0.31 \times 0.8$–$1 \times 1 \times 1$ mm^3), and/or contrast-enhanced 2D T1-weighted (axial, sagittal, and coronal; dynamic or nondynamic; TR range: 450–1800 ms; TE range: 9–15 ms; in-plane resolution: 0.41×0.41–0.90×0.90 mm^2; section thickness: 2–5 mm). Contrast-enhanced 3D-T1-weighted images were reconstructed in the axial, coronal, and sagittal planes. Contrast-enhanced MR imaging was performed 90 seconds after the administration of intravenous contrast medium. Contrast-enhanced dynamic MR imaging was performed 15, 30, 45, 60, 75, and 90 seconds after the administration of intravenous contrast medium. MR imaging parameters varied among institutions because of the difference in examination protocols used by the institutions.

Image Analysis

In total, 3 diagnostic radiologists participated in the process. Two of the 3 diagnostic radiologists (with 6 and 8 years of experience in neuroradiology, and the latter being board-certified) separately interpreted all MR images and determined the numeric and nominal values mentioned below. Final numeric values were obtained by averaging the values of the 2 diagnostic radiologists. In case nominal values were interpreted differently by the 2 radiologists, the final decision was made by the third board-certified diagnostic radiologist with 15 years of experience in neuroradiology. The numeric imaging factor evaluated was thickness of the pituitary stalk. Nominal imaging factors evaluated were as follows: the presence or absence of enlargement of the pituitary gland and stalk; homogeneity of enhancement of the pituitary gland (homogeneous or heterogeneous); the presence or absence of a well-defined, poorly enhanced area and, if present, the location (anterior, middle, or posterior; right, center, left, or bilateral), shape (nodular, linear, ring-shaped, or irregular), and signal intensity in T2WI (hyperintensity, isointensity, or hypointensity). For cases with contrast-enhanced MR imaging, the enhancement pattern was categorized into no enhancement, washout, plateau, or gradually enhancing.

Enlargement of the pituitary gland was diagnosed when its height was ≥2 SDs of its reported average in healthy individuals of the same age group—age range, 21–30 years: 6.6 ± 1.5 mm for men, 7.0 ± 1.9 mm for women; age range, 31–40 years: 6.3 ± 1.4 mm and 6.5 ± 1.7 mm; age range, 41–50 years: 6.1 ± 1.5 mm and 6.4 ± 1.3 mm; older than 50 years of age: 6.0 ± 1.6 mm and 6.7 ± 1.9 mm.[16] During pregnancy or postpartum, independent standards for women were set from 6.0 ± 0.99 mm to 8.8 ± 0.67 mm.[17] Enlargement of the pituitary stalk was diagnosed when the anterolateral diameter of the pituitary insertion of the stalk was ≥2 SDs longer than its reported average in healthy individuals:

2.32 ± 0.39 mm.[18] All MR images were evaluated in 3D in each case.

Statistical Analysis

Interreader agreement was assessed using κ statistics and was interpreted as poor ($\kappa < 0.20$), fair ($\kappa = 0.21$–0.40), moderate ($\kappa = 0.41$–0.60), good ($\kappa = 0.61$–0.80), or very good ($\kappa \geq 0.81$). Statistical analyses were performed using JMP software (Version 14.2.0; SAS Institute).

RESULTS

Patient characteristics and clinical data are summarized in Tables 1 and 2, respectively. The mean age of the participants was 55.7 years (range, 30–86 years), and half of the patients were men. No female patient was pregnant or in the postpartum state. All patients were treated for stage III or IV melanoma, and the CTCAE grade was 3 in all cases. ICIs used for treatment were as follows: nivolumab (anti-PD-1 monoclonal antibody, Opdivo; Bristol Myers Squibb) + ipilimumab, 11/20 patients (55.0%); and ipilimumab alone, 9/20 patients (45.0%). Blood tests revealed endocrinologic abnormalities such as thyrotropin deficiency (19/20 [95.0%]), corticotropin deficiency 12/17 (70.6%), and gonadotropin deficiency (9/16 [56.3%]). After the mean follow-up period of 21.4 months (range, 2–62 months), thyrotropin deficiency in 12/19 (63.2%) and corticotropin deficiency in 10/12 (83.3%) patients persisted. Hormonal replacement was administered to all patients, and it was continued throughout the course in 17/20 (85.0%) patients.

Table 1: Patient characteristics

Characteristic	
Age (mean) (range) (yr)	55.7 (30–86)
Sex	M/F = 10:10
Follow-up period (mean) (range) (mo)	20.4 (1–62)
Clinical stage (No.)	
≤II	0
III	3
IV	17
CTCAE grade (No.)	
0–2	0
3	20
4, 5	0
ICIs (No.)	
Ipilimumab + nivolumab	11
Ipilimumab	9
Main physical symptoms (No.)	
Headache	13
Fatigue/malaise	3
Nausea/vomiting	2
Edema	1
Numbness	1
Loss of vision/visual field disorder	0
Diabetes insipidus	0
No symptom	0

The characteristics of MR imaging findings are summarized in Table 3. Enlargement of the pituitary gland and stalk was observed in 12 (60.0%) and 20 patients (100%), respectively. Nineteen patients (95.0%) demonstrated geographic hypoenhancing lesions. All these geographic hypoenhancing lesions were located in the anterior lobes; and 11/19 patients (57.9%) showed hypointensity, 7 patients (36.8%) showed iso-intensity, and 1 patient (5.3%) showed high intensity on T2WI. Contrast dynamic MR imaging was performed in 2 patients, and pituitary geographic hypoenhancing lesions were enhanced gradually, showing a low intensity in T2WI. Representative cases are shown in Figs 1–3. Four patients showed nonenhanced nodules between the anterior and intermediate middle lobes of the pituitary gland, indicating a Rathke cleft cyst, and all these patients had pituitary geographic hypoenhancing lesions in the anterior lobes separate from the cysts. T2*-weighted images were available for 12 patients with pituitary geographic hypoenhancing lesions, and the blooming effect indicating hemosiderin deposition was not observed in these patients. Interreader agreement was good or very good for each factor ($\kappa = 0.64$–1, Table 4). All patients showed an improvement in physical symptoms with immunotherapy, including high-dose prednisone or interleukin-2, and/or brief withdrawal of the ICIs. Previous MR imaging and follow-up MR imaging were performed in 13 and 12 patients, respectively (previous MR imaging: mean, 136 days [range, 53–375 days] before; follow-up MR imaging: mean, 262 days [range, 20–949 days] after the MR imaging when ICI-H was diagnosed). All previous MR imaging in 13 patients and follow-up MR imaging in 8 patients were performed with contrast material, and the remaining follow-up MR imaging in 4 patients was performed without contrast material. Previous MR imaging showed no abnormal findings, and follow-up MR imaging in all the patients who underwent it confirmed the resolutions of the abnormal findings.

DISCUSSION

In the present study, we found that the MR imaging of ICI-H demonstrated not only the nonspecific enlargement of pituitary glands and stalks but also the characteristic geographic hypoenhancing lesions in the anterior lobe, and all but 1 patient showed hypo- or isosignal intensities, respectively, in T2WI. These characteristic and frequent MR imaging findings, along with the

Table 2: Hormone abnormalities

	Laboratory Reference Range	Pituitary Hormone Abnormalities (%)	Last Follow-Up, Hormone Abnormalities (%)	Hormonal Recovery (%)
Corticotropin deficiency	ACTH, 5–63.3 pg/mL	12/17 (70.6)	10/12 (83.3)	2/12 (16.7)
Thyrotropin deficiency	TSH, 0.30–5.50 μIU/mL	19/20 (95.0)	12/19 (63.2)	7/19 (36.8)
Gonadotropin deficiency	FSH, 1.5–10.0 mIU/mL (male); 2.0–131 mIU/mL (female)[a]	9/16 (56.3)	1/5 (20.0)	–
Diabetes insipidus	Based on symptom	0/20 (0)	–	–

Note:—ACTH indicates adrenocorticotropic hormone; TSH, thyroid stimulating hormone; FSH, follicle stimulating hormone; mIU, milli-international units.
[a] Depending on age.

patient being under treatment with ICIs, are useful for the diagnosis of ICI-H.

MR imaging is a recommended technique for diagnosing hypophysitis; particularly, gadolinium-enhanced pituitary MR imaging has been reported to be useful for the diagnosis.[7,14] However, previous studies have summarized MR imaging findings of ICI-H as moderate to intense, with homogeneous enhancement and enlargement of the pituitary gland with or without enlargement of the pituitary stalk,[6,7,14] which are nonspecific and common in hypophysitis due to other causes.[8-13] Pathologic variants of hypophysitis include lymphocytic, granulomatous, immunoglobulin-4-related, xanthomatous, and necrotizing.

Table 3: MR imaging findings

Finding	No. (%)
Enlargement of pituitary gland	12 (60.0)
Gadolinium-enhanced MR imaging ($n = 20$)	
Enlargement of pituitary stalk	20 (100)
Hypoenhancing lesions in the pituitary gland	19 (95.0)
High intensity on T2WI	1/19 (5.3)
Isointensity on T2WI	7/19 (36.8)
Low intensity on T2WI	11/19 (57.9)
Shape of hypoenhancing lesion ($n = 19$)	
Linear	8 (42.1)
Nodular	4 (21.1)
Ring-shaped	1 (5.3)
Irregular	6 (31.6)

Characteristic MR imaging findings are not established for ICI-H.[7,9] Of note, we found pituitary geographic hypoenhancing lesions in all but 1 patient. More than half of these lesions showed a low intensity on T2WI (57.9%) without blooming effect in all patients with T2*-weighted imaging, which is suggestive of fibrosis rather than necrosis, cystic degeneration, or hemorrhage as seen in a few patients with lymphocytic hypophysitis, xanthomatous hypophysitis, and necrotizing hypophysitis.[19-21] Two patients showed a gradual enhancement consistent with the low signal intensity on T2WI, which is also supportive of fibrosis. On the contrary, 1 patient with a pituitary geographic hypoenhancing lesion (5.0%) showed a high intensity on T2WI, suggesting a cystic change, but taking into consideration the postmortem report of tremelimumab (anti-CTLA4)-induced hypophysitis by Caturegli et al,[5] it seems to be a necrosis rather than a cystic change. On the basis of the MR imaging findings mentioned above, we speculate that ICI-H has a unique tendency to cause fibrosis and rarely becomes necrotic.

Furthermore, we discuss the distribution and morphology of pituitary geographic hypoenhancing lesions. It is well-established that in patients with ICI-H, the anterior lobe of the pituitary gland is mainly involved, whereas the involvement of the posterior lobe is less frequent.[22-24] Therefore, in the present study, all pituitary geographic hypoenhancing lesions were localized in the anterior lobe. Although the existence of pituitary geographic hypoenhancing lesions was previously unknown, this MR imaging finding could be retrospectively found in some case reports;

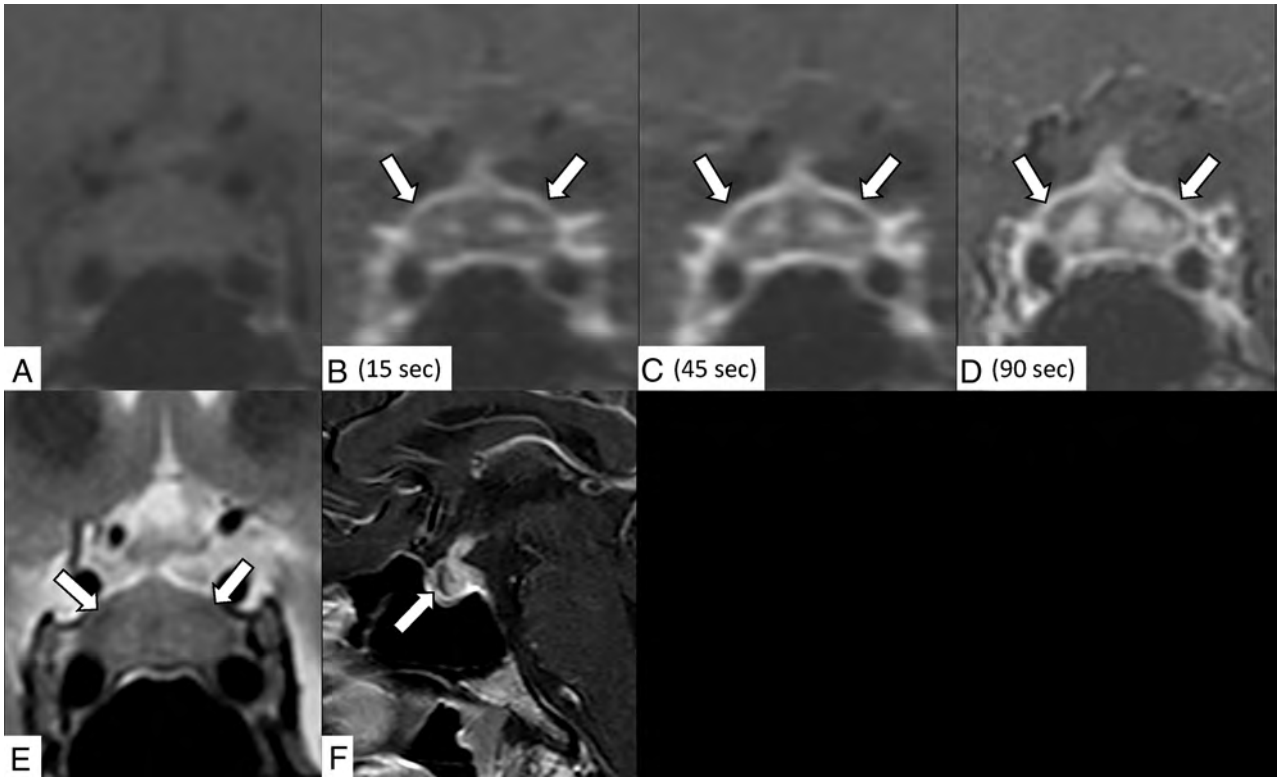

FIG 1. A 31-year-old man receiving ipilimumab for stage IV melanoma with hypothyroidism and headache for a week. Contrast-enhanced coronal dynamic MR imaging demonstrates an enlarged pituitary gland and stalk and a gradually enhanced bilateral ring-shaped hypoenhancing lesion (precontrast [*A*]; 15, 45, and 90 seconds after contrast medium injection [*B–D*]; *arrows* indicate lesions). The lesion shows mild hypointensity on the T2-weighted coronal image (*E*, *arrows*). Contrast-enhanced sagittal MR imaging shows the hypoenhancing lesion in the anterior lobe (*F*, *arrow*).

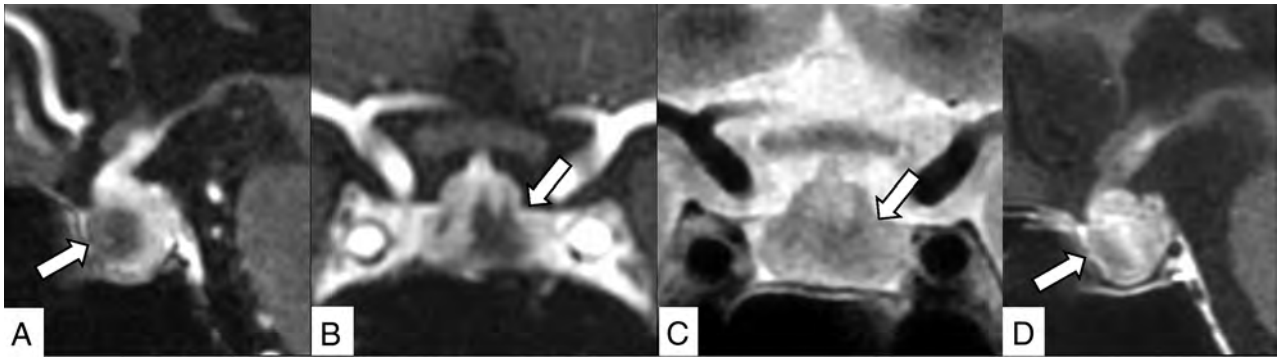

FIG 2. An 82-year-old woman receiving nivolumab plus ipilimumab for stage IV melanoma with corticotropin deficiency, hypothyroidism, and headache for 9 days. Contrast-enhanced 3D-MR imaging (90 seconds after contrast medium injection) demonstrates an enlarged pituitary gland and stalk and an irregularly shaped hypoenhancing lesion in the anterior lobe (*A*, sagittal reconstruction; *B*, coronal reconstruction, *arrows*). The lesion shows mild hypointensity on T2WI (*C*, *arrow*). The lesion is gradually enhanced in contrast-enhanced 2D sagittal MR imaging performed 90 more seconds after the 3D MR imaging (*D*, *arrow*).

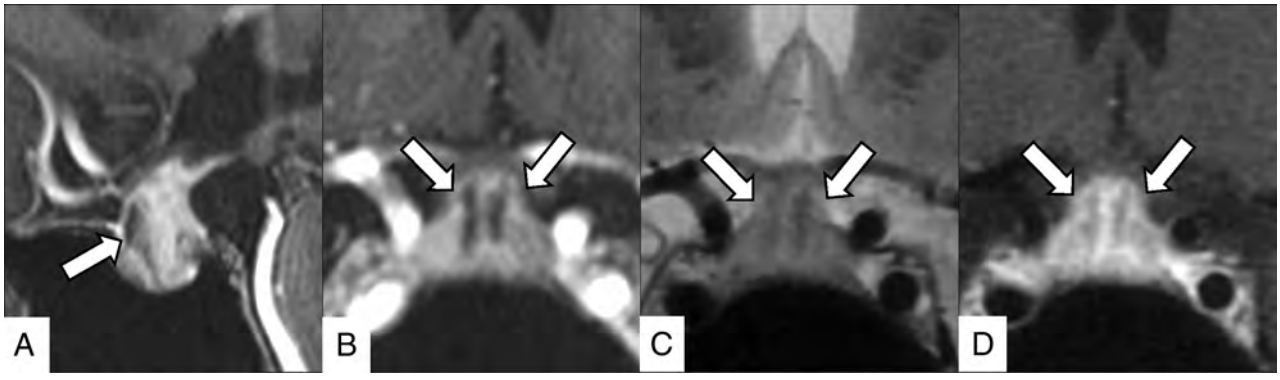

FIG 3. A 40-year-old woman receiving nivolumab plus ipilimumab for stage IV melanoma with corticotropin deficiency, hypothyroidism, and hand edema for 10 days. Contrast-enhanced 3D-MR imaging (90 seconds after contrast medium injection) demonstrates an enlarged pituitary gland and stalk and bilateral linear hypoenhancing lesions (*A*, sagittal reconstruction; *B*, coronal reconstruction, *arrows*). These lesions show hypointensity on the T2-weighted coronal image (*C*, *arrows*), and gradual enhancement is demonstrated in contrast-enhanced 2D coronal MR imaging performed 90 more seconds after the 3D MR imaging (*D*, *arrows*).

Table 4: Interrater reliability between 2 raters

MR Imaging Finding	κ
Pituitary height	0.8326
Stalk thickness	0.9136
Homogeneity of enhancement	1
Hypoenhancing lesion	0.6429[a]
Shape	0.8535
Signal intensity in T2WI	0.8077
Location (AP)	1
Location (RL)	0.8462
Pattern of enhancement	1

Note:—AP indicates anterior-posterior; RL, right-left.

[a] The difference in judgment between the 2 raters was observed only in 1 case (rater 1, 19/20 versus rater 2, 18/20); this was subsequently arbitrated by a third radiologist as positive for a hypoenhancing lesion.

for example, 1 of the 3 patients in the report of Carpenter et al,[15] 1 patient in the study of Albarel et al,[14] and 1 patient in the study of Caturegli et al[5] demonstrated pituitary geographic hypoenhancing lesions in the anterior lobe of the pituitary gland. The pituitary geographic hypoenhancing lesions showed a variety of shapes, probably due to differences in the distribution of fibrosis and necrosis in each patient. In terms of endocrinologic prognosis, prolonged hormonal replacement is required for patients with ICI-H in general, especially for corticotropin deficiency, and multidisciplinary follow-up should be performed.[14] According to the review by Albarel et al,[14] in 2019, corticotropin deficiency and thyrotropin deficiency persisted in 63/72 (84.9%) and 34/75 (45.3%) patients, respectively, during the last follow-up; and long-term hormone replacement was needed in patients with ICI-H. These findings are consistent with the findings of this study, in which corticotropin deficiency and thyrotropin deficiency persisted in 10/12 (83.3%) and 12/19 (63.2%) patients, respectively, throughout the study period. The high frequency of anterior hypopituitarism and the rarity of diabetes insipidus seem to correlate with the high frequency of anterior lobe involvement in ICI-H.

In the present study, ipilimumab was used in all patients, and it was given as a combination therapy with nivolumab in 10/19 patients (52.6%). Immune-related adverse effects are caused by injury to the target organ by a combination of autoreactive T-cells, autoantibodies, and/or proinflammatory cytokines, but the frequency and extent of adverse reactions varied between drugs.[1] ICI-H is observed more frequently (3.2%) with CTLA-4 inhibitors than other ICIs, and the expression of CTLA-4 on normal pituitary

cells is expected to be the underlying cause.[3,25] The frequency of PD-1 inhibitor-induced hypophysitis is low at 0.4%, whereas the frequency of hypophysitis caused by combination therapy (ipilimumab plus PD-1 inhibitors) is higher at 6.4%.[3] Furthermore, hypophysitis associated with combination therapy or ipilimumab alone is more frequently high-grade (≥3) in CTCAE than with PD-1/PD-L1 inhibitors.[26,27] Consistently, the CTCAE grade was 3 for all patients in the present study.

According to the review by Larkin et al,[27] the frequency of high-grade-versus-low-grade ICI-H was 1.0% (3/313) versus 6.1% (19/313) for combination therapy (nivolumab plus ipilimumab) and 1.9% (6/311) versus 1.9% (6/311) for ipilimumab alone. Thus, it is likely that more than an equal number of patients with potential low-grade (CTCAE grade ≤2) hypophysitis existed during the current patient enrollment period but were not diagnosed because their conditions were clinically and endocrinologically mild. Further studies on the MR imaging findings of ICI-H in patients with low-grade hypophysitis are needed in the future.

This study had the following limitations: First, histologic confirmation of the pituitary gland was not performed. However, the possibility of other types of hypophysitis or tumors is low, because all patients developed physical symptoms during or immediately after the immunotherapy with ICIs, and the symptoms improved with additional immunotherapy or withdrawal of ICIs. In addition, none of the patients with previous MR imaging showed abnormal findings in the pituitary gland, and all patients with follow-up MR imaging showed the resolution of the abnormal findings. Second, the frequency of pituitary geographic hypoenhancing lesions in hypophysitis due to other causes was not examined. To the best of our knowledge, there are no reports in the literature of a high incidence of poorly enhanced areas and fibrosis in hypophysitis due to other causes. Third, patients with low-grade ICI-H with a CTCAE grade of ≤2 were not included in the present study. Therefore, the frequency of MR imaging findings, such as pituitary geographic hypoenhancing lesions, might be different in patients with low-grade ICI-H. Finally, all patients included in the present study were administrated ipilimumab-containing therapies, but one case series including 4 patients have reported that patients with PD-1/PD-L1 blockade–induced hypophysitis did not show any abnormalities in MR imaging.[28] To clarify whether "pituitary geographic hypoenhancing lesions" are unique to ipilimumab, further studies investigating ICI-H associated with other ICI therapies are needed.

CONCLUSIONS

Contrast MR imaging of ICI-H frequently demonstrates T2-weighted low-intensity pituitary geographic hypoenhancing lesions in the anterior lobe of the pituitary gland. These characteristic and frequent MR imaging findings may reflect fibrosis and are useful in distinguishing ICI-H from other types of hypophysitis and tumors.

ACKNOWLEDGMENTS

We thank Dr Naohiro Makise, Department of Pathology, The University of Tokyo Hospital, for his advice on histopathology.

Disclosures: Osamu Abe—*UNRELATED: Grants/Grants Pending*: Bayer Yakuhin, Ltd, Canon Medical Systems, Eisai Co Ltd, FUJIFILM Toyama Chemical Co Ltd, GE Healthcare, Guerbet Japan, Philips Healthcare, Siemens Healthcare Diagnostics KK, Daiichi Sankyo Company Ltd, Fuji Pharma Co Ltd, and Nihon Medi-Physics Co Ltd*; *Payment for Lectures Including Service on Speakers Bureaus*: Bayer Yakuhin Ltd, Canon Medical Systems, Eisai Co Ltd, FUJIFILM Toyama Chemical Co Ltd, GE Healthcare, Guerbet Japan, Philips Healthcare, and Siemens Healthcare Diagnostics KK. *Money paid to the institution.

REFERENCES

1. Thompson JA, Schneider BJ, Brahmer J, et al. **Management of immunotherapy-related toxicities, version 1. 2019.** *J Natl Compr Canc Netw* 2019;17:255–89 CrossRef Medline
2. Phan GQ, Yang JC, Sherry RM, et al. **Cancer regression and autoimmunity induced by cytotoxic T lymphocyte-associated antigen 4 blockade in patients with metastatic melanoma.** *Proc Natl Acad Sci USA* 2003;100:8372–77 CrossRef Medline
3. Barroso-Sousa R, Barry WT, Garrido-Castro AC, et al. **Incidence of endocrine dysfunction following the use of different immune checkpoint inhibitor regimens: a systematic review and meta-analysis.** *JAMA Oncol* 2018;4:173–82 CrossRef Medline
4. Wang DY, Salem JE, Cohen JV, et al. **Fatal toxic effects associated with immune checkpoint inhibitors: a systematic review and meta-analysis.** *JAMA Oncol* 2018;4:1721–88 CrossRef Medline
5. Caturegli P, Di Dalmazi G, Lombardi M, et al. **Hypophysitis secondary to cytotoxic T-lymphocyte-associated protein 4 blockade: insights into pathogenesis from an autopsy series.** *Am J Pathol* 2016;186:3225–35 CrossRef Medline
6. Tan MH, Iyengar R, Mizokami-Stout K, et al. **Spectrum of immune checkpoint inhibitors-induced endocrinopathies in cancer patients: a scoping review of case reports.** *Clin Diabetes Endocrinol* 2019;5:1 CrossRef Medline
7. Joshi MN, Whitelaw BC, Carroll PV. **Mechanisms in endocrinology: hypophysitis: diagnosis and treatment.** *Eur J Endocrinol* 2018;179:R151–63 CrossRef Medline
8. Nakata Y, Sato N, Masumoto T, et al. **Parasellar T2 dark sign on MR imaging in patients with lymphocytic hypophysitis.** *AJNR Am J Neuroradiol* 2010;31:1944–50 CrossRef Medline
9. Bando H, Iguchi G, Fukuoka H, et al. **The prevalence of IgG4-related hypophysitis in 170 consecutive patients with hypopituitarism and/or central diabetes insipidus and review of the literature.** *Eur J Endocrinol* 2014;170:161–72 CrossRef Medline
10. Iseda I, Hida K, Tone A, et al. **Prednisolone markedly reduced serum IgG4 levels along with the improvement of pituitary mass and anterior pituitary function in a patient with IgG4-related infundibulo-hypophysitis.** *Endocr J* 2014;61:195–203 CrossRef Medline
11. Kong X, Wang R, Yang Y, et al. **Idiopathic granulomatous hypophysitis mimicking pituitary abscess.** *Medicine (Baltimore)* 2015;94:e1099 CrossRef Medline
12. Unlu E, Puyan FO, Bilgi S, et al. **Granulomatous hypophysitis: presentation and MRI appearance.** *J Clin Neurosci* 2006;13:1062–66 CrossRef Medline
13. Gutenberg A, Caturegli P, Metz I, et al. **Necrotizing infundibulohypophysitis: an entity too rare to be true?** *Pituitary* 2012;15:202–08 CrossRef Medline
14. Albarel F, Castinetti F, Brue T. **Management of endocrine disease: immune check point inhibitors-induced hypophysitis.** *Eur J Endocrinol* 2019;181:R107–18 CrossRef Medline
15. Carpenter KJ, Murtagh RD, Lilienfeld H, et al. **Ipilimumab-induced hypophysitis: MR imaging findings.** *AJNR Am J Neuroradiol* 2009;30:1751–53 CrossRef Medline
16. Yadav P, Singhal S, Chauhan S, et al. **MRI evaluation of size and shape of normal pituitary gland: age and sex related changes.** *J Clin Diagn Res* 2017;11:TC01–04 CrossRef
17. Dinç, H, Esen F, Demirci A, et al. **Pituitary dimensions and volume measurements in pregnancy and postpartum MR assessment.** *Acta Radiol* 1998;39:64–69 CrossRef Medline
18. Satogami N, Miki Y, Koyama T, et al. **Normal pituitary stalk: high-resolution MR imaging at 3T.** *AJNR Am J Neuroradiol* 2010;31:355–59 CrossRef Medline

19. Lee SJ, Yoo HJ, Park SW, et al. **A case of cystic lymphocytic hypophysitis with cacosmia and hypopituitarism.** *Endocr J* 2004;51:375–80 CrossRef Medline
20. Hanna B, Li YM, Beutler T, et al. **Xanthomatous hypophysitis.** *J Clin Neurosci* 2015;22:1091–97 CrossRef Medline
21. Ćaćić M, Marinković J, Kruljac I, et al. **Ischemic pituitary apoplexy, hypopituitarism and diabetes insipidus: a triad unique to necrotizing hypophysitis.** *Acta Clin Croat* 2018;57:768–71 CrossRef Medline
22. Dillard T, Yedinak CG, Alumkal J, et al. **Anti-CTLA-4 antibody therapy associated autoimmune hypophysitis: serious immune related adverse events across a spectrum of cancer subtypes.** *Pituitary* 2010;13:29–38 CrossRef Medline
23. Nallapaneni NN, Mourya R, Bhatt VR, et al. **Ipilimumab-induced hypophysitis and uveitis in a patient with metastatic melanoma and a history of ipilimumab-induced skin rash.** *J Natl Compr Canc Netw* 2014;12:1077–81 CrossRef Medline
24. Zhao C, Tella SH, Del Rivero J, et al. **Anti-PD-L1 treatment induced central diabetes insipidus.** *J Clin Endocrinol Metab* 2018;103:365–69 CrossRef Medline
25. Postow MA, Sidlow R, Hellmann MD. **Immune-related adverse events associated with immune checkpoint blockade.** *N Engl J Med* 2018;378:158–68 CrossRef Medline
26. Robert C, Schachter J, Long GV, et al. **Pembrolizumab versus ipilimumab in advanced melanoma.** *N Engl J Med* 2015;372:2521–32 CrossRef
27. Larkin J, Chiarion-Sileni V, Gonzalez R, et al. **Combined nivolumab and ipilimumab or monotherapy in untreated melanoma.** *N Engl J Med* 2015;373:23–34 CrossRef Medline
28. Lupi I, Brancatella A, Cosottini M, et al. **Clinical heterogeneity of hypophysitis secondary to PD-1/PD-L1 blockade: insights from four cases.** *Endocrinol Diabetes Metab Case Rep* 2019;2019:19–102 CrossRef Medline

A Simple Formula to Estimate Parathyroid Weight on 4D-CT, Predict Pathologic Weight, and Diagnose Parathyroid Adenoma in Patients with Primary Hyperparathyroidism

R. Yeh, Y.-K.D. Tay, L. Dercle, L. Bandeira, M.R. Parekh, and J.P. Bilezikian

ABSTRACT

BACKGROUND AND PURPOSE: Parathyroid gland weight is a clinically relevant parameter used to diagnose parathyroid adenomas intraoperatively. We evaluated the accuracy of a formula to estimate parathyroid weight on preoperative 4D-CT.

MATERIALS AND METHODS: A single-institution retrospective study was performed in patients with primary hyperparathyroidism who underwent 4D-CT between January 2013 and December 2014 with subsequent parathyroidectomy and surgical cure. All patients had correct localization of a solitary parathyroid adenoma. The longest 3 dimensions of all identified parathyroid glands were measured on CT, and weight was estimated using the formula: $\text{weight}_{\text{4D-CT}}$ (mg) = 1 mg/mm^3 × Length (mm) × Width (mm) × Height (mm) × $\pi/6$. We correlated $\text{weight}_{\text{4D-CT}}$ with pathology specimen weight ($\text{weight}_{\text{pathology}}$). Using receiver operating characteristic analysis, we estimated the performance of $\text{weight}_{\text{4D-CT}}$ to discriminate a parathyroid adenoma from normal glands on 4D-CT and determined the optimal threshold based on the Youden index.

RESULTS: One hundred sixteen patients (85 women, 31 men) were evaluated. $\text{Weight}_{\text{4D-CT}}$ was shown to be strongly correlated with $\text{weight}_{\text{pathology}}$ as demonstrated by Spearman $\rho = 0.73$ ($P < .01$), concordance correlation coefficient = 0.92 (95% CI, 0.89–0.94), and Cronbach $\alpha = 0.96$. The performance of $\text{weight}_{\text{4D-CT}}$ for the diagnosis of parathyroid adenoma was excellent, with an area under the curve of 0.955 (95% CI, 0.925–0.985; $P < .001$). Based on the Youden index, the optimal threshold was >50 mg, with a sensitivity of 96.7% and a specificity of 95.7%.

CONCLUSIONS: Radiologists can accurately estimate parathyroid adenoma weight on 4D-CT. This metric is highly correlated with pathologic weight, and a threshold cutoff of >50 mg can be used to distinguish parathyroid adenoma from normal glands.

ABBREVIATIONS: AUC = area under the curve; IQR = interquartile range; ROC = receiver operating characteristic

Parathyroid 4D-CT is a relatively new imaging technique for preoperative localization of parathyroid adenomas in patients with primary hyperparathyroidism. First reported by Rodgers et al,[1] in 2006, 4D-CT has increasingly gained acceptance, most commonly as a second-line approach to the traditional methods of nuclear scintigraphy and sonography. It has also demonstrated the potential to be used as a first-line parathyroid imaging technique.[2] Studies have demonstrated a relatively high sensitivity of 4D-CT for localization of parathyroid adenomas and hyperplasia, with reported sensitivities ranging from 76% to 88%[1,3,4] and superior localization compared with sestamibi and sonography.[4-6] Accurate preoperative imaging allows surgeons to appropriately select patients for minimally invasive parathyroidectomy by localizing a single parathyroid adenoma and excluding multigland disease.[2]

While identification of parathyroid adenomas by 4D-CT relies on their characteristic differential enhancement across time, the classic enhancement pattern is observed in only a minority of adenomas (20%).[7] In the setting of variable enhancement patterns, gland size may serve as an additional 4D-CT parameter for identifying adenomas preoperatively, particularly in distinguishing normal from abnormal glands. This is in line with the intraoperative approach of the parathyroid surgeon, because weight and size are the most frequently used criteria for

Received February 17, 2020; accepted after revision June 2.

From the Department of Radiology (R.Y.), Molecular Imaging and Therapy Service, Memorial Sloan Kettering Cancer Center, New York, New York; Department of Endocrinology (Y.-K.D.T.), Sengkang General Hospital, Singhealth, Singapore; Department of Radiology (R.Y., L.D., M.R.P.), New York-Presbyterian Hospital/Columbia University Medical Center, New York, New York; Department of Endocrinology (L.B.), Federal University of Sao Paulo, Sao Paulo, Brazil; Fleury Group (L.B.), Sao Paulo, Brazil; Department of Radiology (M.R.P.), Thomas Jefferson University Hospital, Philadelphia, Pennsylvania; and Department of Medicine (J.P.B.), Division of Endocrinology, College of Physicians & Surgeons, Columbia University, New York, New York.

Please address correspondence to Randy Yeh, MD, Department of Radiology, Molecular Imaging and Therapy Service, Memorial Sloan Kettering Cancer Center, 1275 York Ave, New York, NY 10065; e-mail: yehr@mskcc.org

Indicates article with supplemental on-line photo.

http://dx.doi.org/10.3174/ajnr.A6687

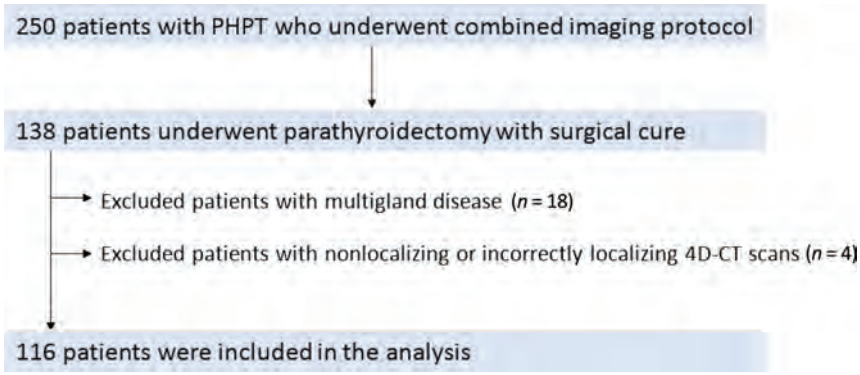

FIG 1. Study flowchart with inclusion and exclusion criteria. PHPT indicates primary hyperparathyroidism.

identifying abnormal glands, with additional intraoperative features including shape, consistency, and histologic features.[8] The weight of the pathologic specimen is considered to be the best measure of gland size, as opposed to gland length, due to the variable shape of parathyroid glands.[9] Normal parathyroid glands generally weigh 20–40 mg, with glands of >60 mg usually considered abnormal by pathologists and surgeons.[8,10]

The high spatial resolution of 4D-CT allows delineation of adenomas from adjacent structures, which in theory, would allow an accurate estimate of adenoma size. While a pathologic size threshold may be inferred to 4D-CT, several factors may influence such estimates, such as adenoma shape, location, and relationship to and mass effect from adjacent structures, such as an enlarged multinodular thyroid gland or esophagus. These potential confounders do not affect the actual weight of the pathologic specimen following surgical resection. Studies in lung cancer and renal cell carcinoma correlating tumor sizes as measured on CT scans with pathologic specimens have shown poor correlation, with statistically significant differences in measured size on CT compared with pathologic size.[11,12]

Differential contrast enhancement remains the dominant factor in the detection of parathyroid adenomas, but a potential role for estimated adenoma weight by preoperative 4D-CT has not been evaluated. The size cutoff on 4D-CT to distinguish a normal gland from an adenomatous gland remains unknown. The aims of our study were to correlate the estimated gland weight of parathyroid adenoma on 4D-CT with the weight of the pathologically resected adenoma in patients with primary hyperparathyroidism and single-gland disease and to determine whether 4D-CT can define a threshold weight that distinguishes a normal gland from an adenomatous gland. We hypothesized that estimating weight on 4D-CT using a predefined formula will have a strong correlation with pathologic weight, and a threshold CT weight cutoff can differentiate adenomas from normal glands.

MATERIALS AND METHODS

Patients

A retrospective review was conducted of 250 consecutive patients with biochemical evidence of primary hyperparathyroidism referred to our institution for preoperative imaging using a combined imaging protocol of 4D-CT and sestamibi SPECT/CT between January 2013 and December 2014. Of note, an analysis of the diagnostic performance of this combined imaging protocol has been previously published by our group,[6] and there is some overlap of patients from that study with patients in this cohort. Figure 1 summarizes the study patient flow. Of 250 patients, 138 patients underwent parathyroidectomy with surgical cure, defined by a 50% drop in intraoperative parathyroid hormone levels into the normal range. Intraoperative parathyroid hormone monitoring has been shown to have excellent accuracy in predicting surgical cure and is recommended by the Endocrine Society Guidelines.[13,14] Most patients (n = 90 patients) had intraoperative parathyroid hormone normalization within 10 minutes of adenoma resection. Twenty-two patients were excluded for the following reasons: Eighteen patients had multigland disease, and 4 patients had nonlocalization or incorrect localization on 4D-CT. The remaining 116 patients with solitary adenoma correctly localized on 4D-CT were used for this analysis.

The study did not include patients in whom 4D-CT did not correctly localize the culprit solitary adenoma (3.3%, n = 4/120) with a mean adenoma pathologic weight of 136 mg. The reason for not including these individuals is that this was a correlation analysis of weight estimated on 4D-CT and pathologic specimen weight. The intention of the study was also to discriminate between the weights of normal and abnormal glands on 4D-CT, thus requiring inclusion only of those individuals with correct localization. This study was Health Insurance Portability and Accountability Act–compliant and approved by the institutional review board at Columbia University Medical Center.

4D-CT Imaging Protocol

The imaging protocol consisted of a combined sestamibi SPECT and 4D-CT consecutively acquired in a single setting previously published by our group.[6] In brief, the protocol consists of a dual-phase technetium Tc99m sestamibi SPECT, followed by a 4D-CT performed immediately after acquisition of the delayed phase sestamibi SPECT/CT. For the purposes of this study, only the 4D-CT protocol will be discussed. All imaging was performed with a Symbia T 16-slice SPECT/CT scanner (Siemens).

The 4D-CT protocol consisted of helical scans acquired in noncontrast, arterial, and delayed (venous) phases at predetermined times. For all phases, scanning parameters were the following: 130 kV(peak), 120–300 mA by automatic exposure control, 0.6-second rotation time, 0.8 pitch, and 1.0-mm detector configuration with a beam width of 10 mm. Coronal and sagittal reformats were reconstructed with 1-mm section thickness. The FOV extended from the level of the mandibular angle to the carina. Following the noncontrast CT acquisition, iodinated contrast (iohexol, Omnipaque 350; GE Healthcare) was injected at 4 mL per second with a total dose of 75 mL. The arterial phase

Table 1: Patient demographics, baseline characteristics, and parathyroid gland weights[a]

Parameter Value	Data	IQR
Age (yr)	63 ± 14 (19–89)	
Sex (No. of patients)		
Women	85 (73.3%)	
Men	31 (26.7%)	
Weight (kg)	76.4 ± 19.9 (38.1–146)	
BMI	28.0 ± 7.0 (16.6–53.7)	
Biochemical profile[b]		
PTH (median) (IQR) (pg/mL)[c]	101 (67.0–135)	
Calcium (median) (IQR) (mg/dL)	10.8 (10.4–11.4)	
Parathyroid gland weights (median) (range) (IQR)		
CT weight, adenoma (mg) ($n = 116$)	310 (30–11,218)	145–536
Pathology weight, adenoma (mg) ($n = 116$)	500 (22–9400)	238–800
CT weight, normal gland (mg) ($n = 291$)	18 (4–144)	12–24

Note:—PTH indicates parathyroid hormone; BMI, body mass index.
[a] Data are presented as mean ± SD with ranges or percentages in parentheses.
[b] Data are presented as median (interquartile range).
[c] Normal ranges for parathyroid hormone and serum calcium are 10–65 pg/mL and 8.4–10.2 mg/dL, respectively.

CT was acquired 30 seconds after the beginning of contrast infusion, and the delayed phase CT was acquired 30 seconds after the arterial phase acquisition.

Parathyroid Adenoma Localization and CT Estimated Weight

4D-CT images were interpreted for preoperative localization by 2 radiologists with dual board certification in radiology and nuclear medicine. 4D-CT images were reviewed on a PACS workstation. Parathyroid adenomas and normal parathyroid glands were identified using location and temporal contrast enhancement on serial phases. Following identification, adenoma volume was estimated in cubic millimeters using the formula for ellipsoid volume (V):

$$V_{4D\text{-}CT}\ (mm^3) = L\ (mm) \times W\ (mm) \times H\ (mm) \times \pi/6.$$

Using the arterial phase CT, dimensions for length (L) and width (W) were measured on the axial plane in the longest perpendicular dimension, while height (H) was measured on either the coronal or sagittal plane, depending on the plane on which the adenomas were best visualized. Then, adenoma weight was estimated in milligrams by converting volume to weight. To this end, we assumed that all adenomas had the density of water (1 mg/mm^3) and used the formula, weight (W) = density × volume (V).

$$W_{4D\text{-}CT}\ (mg) = 1 mg/mm^3 \times V_{adenoma}\ (mm^3).$$

Therefore, the formula used for parathyroid weight on 4D-CT ($weight_{4D\text{-}CT}$) was

$$Weight_{4D\text{-}CT}\ (mg) = 1\ mg/mm^3 \times L\ (mm) \times W\ (mm) \times H\ (mm) \times \pi/6.$$

Estimated weights of suspected parathyroid adenomas and any additional visualized normal parathyroid glands were measured and described in the original radiology report, per standard clinical practice at our institution. Both interpreting radiologists were trained on this method for estimating weight on CT. Of the 116 patients, 75 patients had 4D-CT scans that identified and estimated CT weights of 3 normal parathyroid glands in addition to the abnormal parathyroid adenoma, 30 patients had 2 normal parathyroid glands identified, 6 patients had 1 normal parathyroid gland identified, and 5 patients had no normal parathyroid glands identified. In total, 407 parathyroid glands (normal, $n = 291$, and adenomas, $n = 116$) were identified in 116 patients.

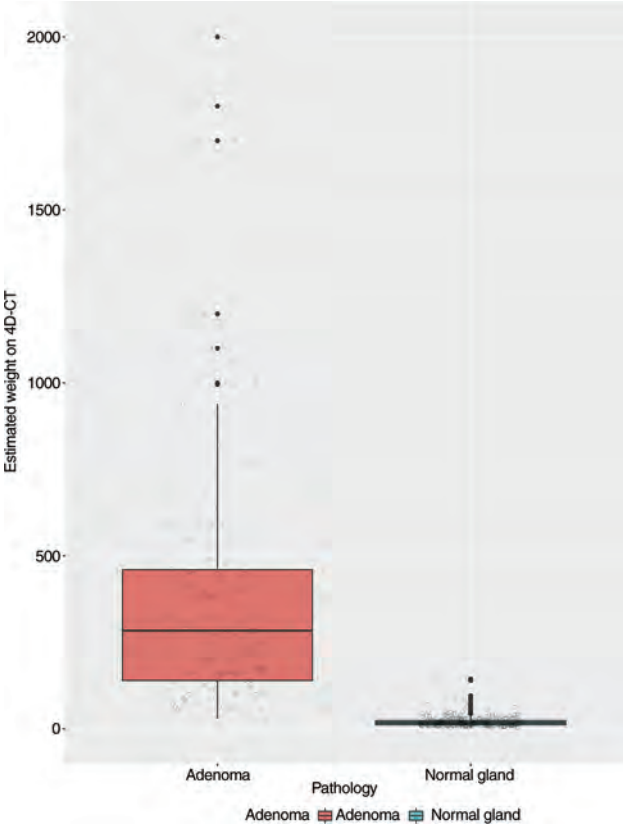

FIG 2. Boxplot of $weight_{4D\text{-}CT}$ in milligrams of parathyroid adenomas compared with normal parathyroid glands.

Pathology

Surgically resected parathyroid glands were placed in formalin for fixation. Extracapsular fat was dissected off the surgical specimen, when appropriate. The weight (milligrams) of the surgical specimen was recorded. Pathologic examination of the specimen was performed to confirm parathyroid adenoma.

Statistical Analysis

The radiology, operative, and pathology reports were retrieved from the Electronic Medical Record. CT-estimated weight and

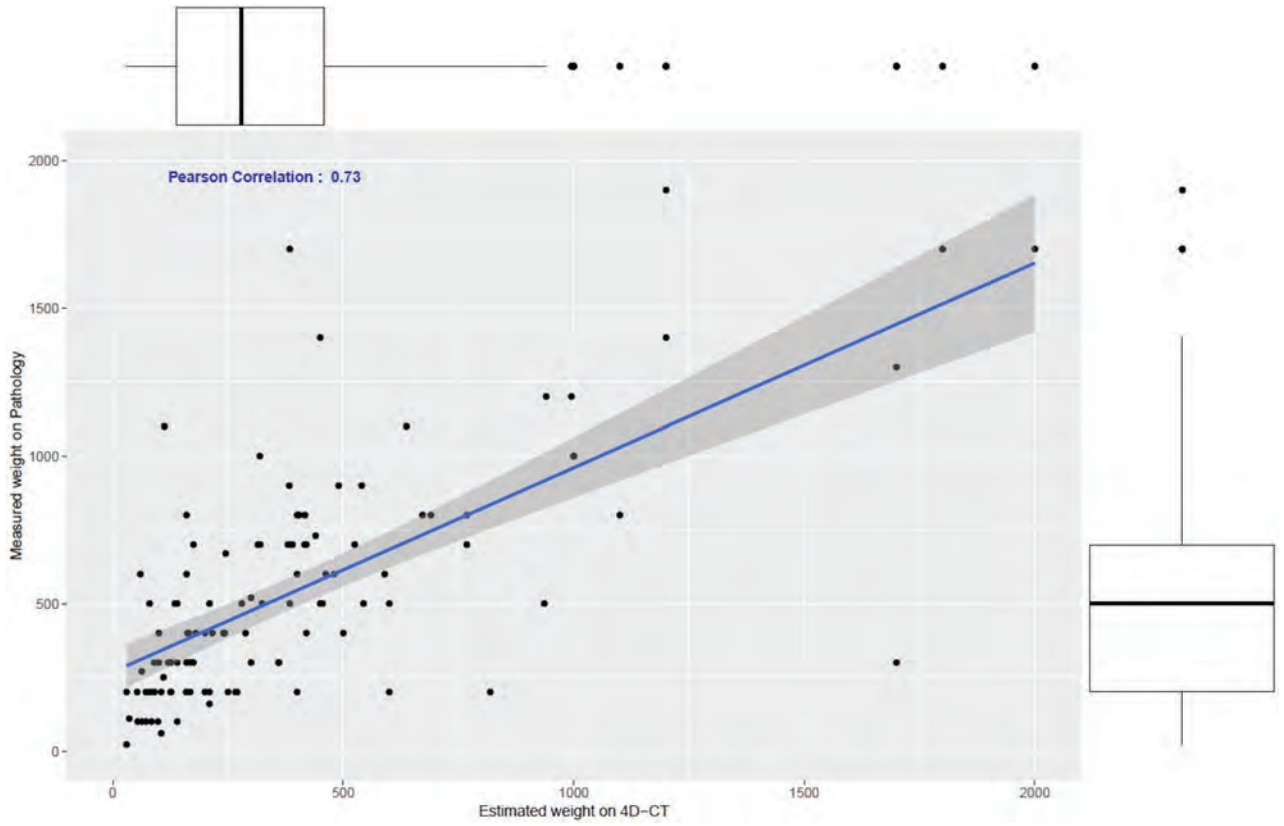

FIG 3. Scatterplot showing the relationship between $weight_{4D\text{-}CT}$ in milligrams of the parathyroid adenoma (x-axis) and the measured pathologic weight of the resected parathyroid adenoma, $weight_{pathology}$ (y-axis). The *blue line* indicates the Pearson correlation ($r = 0.73$, $P < .01$).

pathologic weight were recorded on the basis of original radiology and pathology reports, respectively, and no re-interpretation or repeat measurements were performed.

Data were assessed for normality by visual inspection of the histograms. Normally distributed data are presented as mean ± SD, while nonparametric data are presented as median and interquartile range (Q25–Q75). We used 3 metrics to compare CT-estimated weight and pathologic weight measurements: the Spearman correlation coefficient, the concordance correlation coefficient, and the Cronbach α.[15]

To determine the weight cutoff for parathyroid adenomas on 4D-CT, we constructed a receiver operating characteristic (ROC) curve with the normal parathyroid gland or parathyroid adenoma as the state variable and CT-estimated weight as the test variable, and the area under the ROC curve (AUC) and 95% confidence interval were estimated. Because multiple gland weights were included per patient, ROC analysis incorporating clustering of observations within a patient was performed. The Youden index (sensitivity + specificity − 1) was calculated to determine the optimal threshold for CT-estimated weight to discriminate a parathyroid adenoma from a normal gland. Using cross-validation analysis, we randomly selected 80% of the sample for the training set and applied ROC curve analysis to obtain the optimal threshold. We then tested the threshold against the remaining 20% of the sample for its performance. As an ancillary study, we also evaluated the performance of parathyroid length (millimeters) using the longest single dimension. All statistical tests were 2-tailed, and $P < .05$ was considered significant. All analyses were performed with SPSS 23.0 for Windows (IBM).

RESULTS

Patient Characteristics

Table 1 summarizes the study patient characteristics and parathyroid gland weights. The study population ($n = 116$) was predominantly female ($n = 85$, 73.3%), with a mean age of 63 ± 14 years. Median serum parathyroid hormone and calcium levels were 101 pg/mL (interquartile range [IQR] = 67.0–135 pg/mL) and 10.8 mg/dL (IQR = 10.4–11.4 mg/dL), respectively. Parathyroid adenomas ($n = 116$) had a median CT weight of 310 mg (IQR = 145–536 mg) and pathologic weight of 500 mg (IQR = 238–800 mg), with a mean difference of 130 mg between CT and pathologic weights. Normal parathyroid glands ($n = 291$) had a median CT weight of 18 mg (IQR = 12–24 mg). Figure 2 demonstrates a boxplot of CT weights of parathyroid adenomas compared with normal glands.

Correlation between $Weight_{4D\text{-}CT}$ and $Weight_{pathology}$

CT-estimated weight had a strong positive correlation with the pathologic adenoma weight ($r = 0.73$, $P < .01$) (Fig 3). The concordance correlation coefficient between the 2 measurements was 0.92 (95% CI, 0.89–0.94), showing moderate agreement, and the Cronbach α was measured as 0.96, demonstrating excellent reliability. A Bland-Altman plot showed good agreement between the estimated weight by CT and the measured pathologic weight

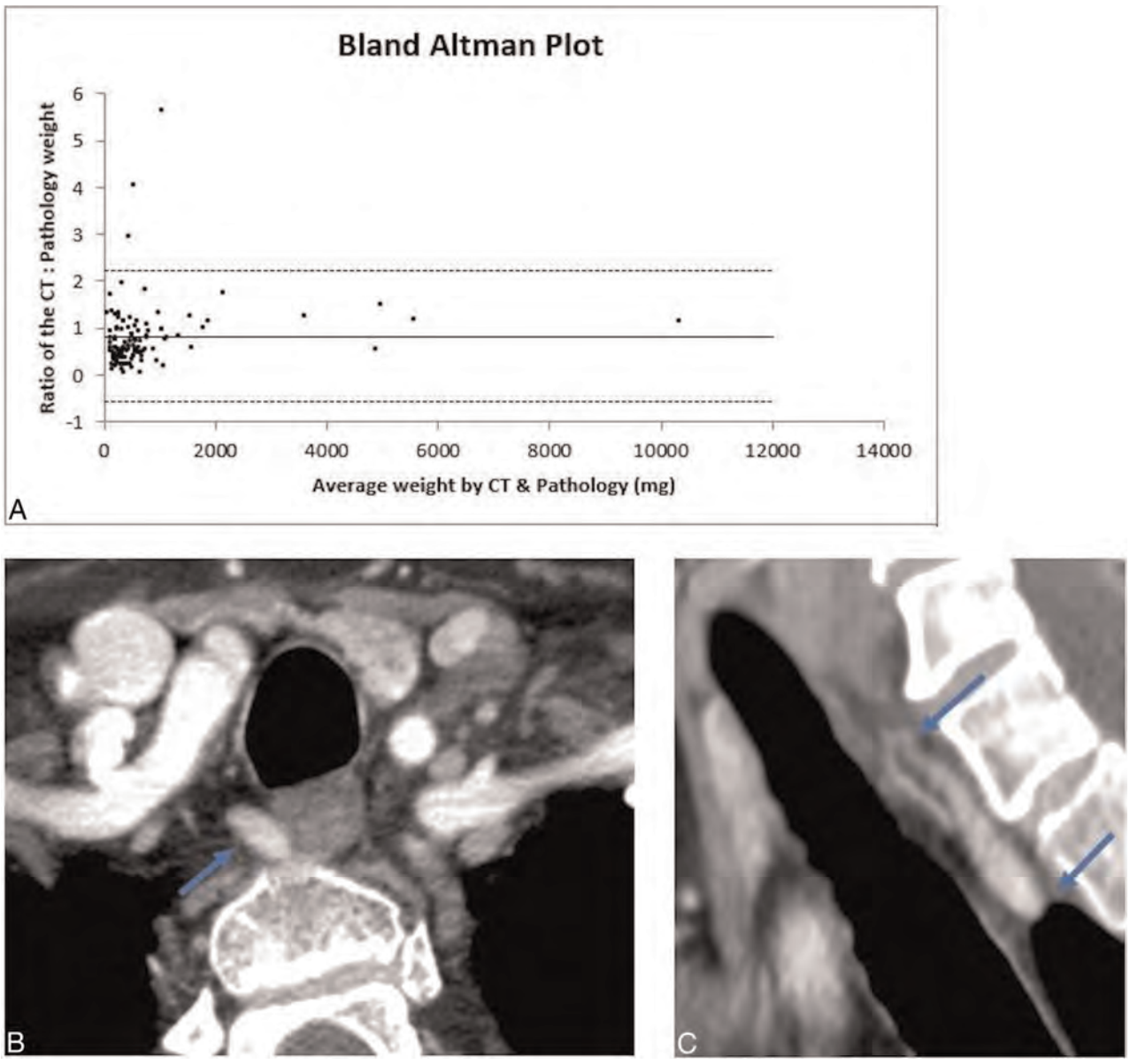

FIG 4. Correlation between $Weight_{4D\text{-}CT}$ and $Weight_{pathology}$. *A*, Bland-Altman plot. The *solid line* represents the mean ratio (0.83), and the *dashed lines* represent the lower and upper 95% limits of agreement at 0.56 and −2.22, respectively. Representative imaging case of 63-year-old woman with right upper parathyroid adenoma. Axial (*B*) and Sagittal (*C*) arterial phase images from preoperative 4D-CT demonstrate a teardrop-shaped right upper parathyroid adenoma in the right tracheoesophageal groove measuring 10 × 5 × 19 mm (transverse × anterior-posterior × cranio-caudal), with $weight_{4D\text{-}CT}$ of 475 mg. $Weight_{pathology}$ was 530 mg with CT: pathologic weight ratio of 0.90.

(Fig 4). There was a negative systemic bias, with the CT-estimated weight underestimating the pathologic weight, with a mean ratio of $weight_{4D\text{-}CT}$ to $weight_{pathology}$ of 0.83. Thus, the pathologic weight can be predicted by the formula:

$$\begin{aligned} \text{weight}_{\text{pathalogy}}(\text{mg}) &= \text{weight}_{4\text{D}-\text{CT}}(\text{mg})/0.83 \\ &= 1.2 \times \text{weight}_{4\text{D}-\text{CT}}(\text{mg}) \end{aligned}$$

Diagnostic Accuracy of $Weight_{4D\text{-}CT}$ for the Diagnosis of Parathyroid Adenoma

CT-estimated weight (Fig 5) reached an AUC of 0.955 (95% CI, 0.92–0.985; $P < .001$) for the prediction of parathyroid adenoma. On the basis of the Youden index, a threshold weight >50 mg was the most optimal in discriminating between a parathyroid adenoma and normal parathyroid gland, with a sensitivity of 96.7% and a specificity of 95.7%. We tested the threshold cutoff of 50 mg in the validation set, with a similar sensitivity of 100% and a specificity of 96.6%. Of note, the performance characteristics were similar across a range of thresholds from 40 to 80 mg (Table 2). For example, a threshold of >40 mg had a sensitivity of 96.4% and a specificity of 92.3%, a threshold of >60 mg had a sensitivity of 94.4% and a specificity of 96.2%, and a threshold of >80 mg had a sensitivity of 90.0% and a specificity of 97.4%. Figure 6 demonstrates a case of a patient with a small adenoma and additional identified normal glands.

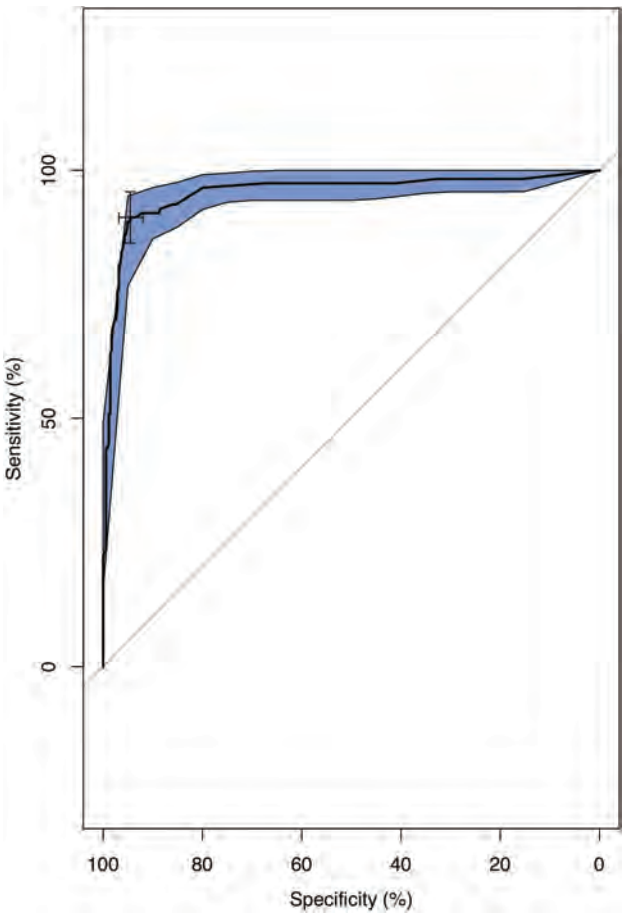

FIG 5. ROC curve showing the diagnostic performance of CT-estimated parathyroid weight in discriminating parathyroid adenoma from the normal parathyroid gland, with confidence intervals (blue) (AUC = 0.955; 95 CI, 0.925–0.985; $P < .001$).

Table 2: Performance characteristics for various CT-estimated weight thresholds

$Weight_{4D\text{-}CT}$ (mg)	Sensitivity (%)	Specificity (%)	Youden Index
40	96.4	92.3	0.890
50	96.7	95.7	0.924
60	94.4	96.2	0.906
70	91.1	97.0	0.881
80	90.0	97.4	0.874

Using longest dimension of a parathyroid gland on CT, the AUC was 0.981 (95% CI, 0.969–0.993) for prediction of parathyroid adenoma (On-line Figure), with an optimal threshold length of >6.5 mm based on the Youden index, yielding a sensitivity of 94.8% and a specificity of 95.9%.

DISCUSSION

We evaluated the use of preoperative 4D-CT in estimating parathyroid adenoma weight with a predefined formula of CT-derived measurements compared with the pathologic weight in patients with primary hyperparathyroidism and solitary parathyroid adenomas. Our results showed that CT-estimated weight and pathologic weight had a strong positive correlation, moderate agreement, and excellent reliability. These findings demonstrate that 4D-CT can closely predict the parathyroid adenoma weight at resection using a simple formula. Because CT underestimates the pathologic weight by a mean ratio of 0.83, we propose using a refined formula to predict pathologic weight: $weight_{pathology} = 1.2\ mg/mm^3 \times L\ (mm) \times W\ (mm) \times H\ (mm) \times \pi/6$, which can be simplified further to $weight_{pathology} = 0.63\ mg/mm^3 \times L\ (mm) \times W\ (mm) \times H\ (mm)$. In clinical practice, this formula could be easily implemented using an automated calculator or Excel (Microsoft) spreadsheet and the estimated parathyroid weight reported in the radiology report. Adenoma weight is a critical factor in the surgeon's intraoperative approach and decision-making, and providing an accurate preoperative weight estimate allows the surgeon to more effectively plan the operation.

Our study also determined an optimal CT size cutoff of >50 mg to distinguish a parathyroid adenoma from a normal gland, with high diagnostic performance. This suggests that CT-estimated weight can be used to distinguish solitary parathyroid adenomas from normal parathyroid glands and is particularly important in localizing smaller adenomas or when differential CT contrast enhancement is equivocal or unreliable, occurring not infrequently due to poor contrast bolus timing or streak artifacts from contrast injection or the patient's shoulders. Because accurate localization of the abnormal parathyroid adenoma is critical for a minimally invasive parathyroidectomy, a low false-negative rate and thus a higher sensitivity may be more favorable to surgeons. For our refined formula, we propose a corrected CT size cutoff of >60 mg (1.2 × 50 mg). This finding is concordant with the pathologic weight cutoff of >60 mg used by pathologists and surgeons[8,10] and demonstrates that similar thresholds were still obtained despite using differing methodologies of preoperative CT scans and autopsy studies. In addition, the CT-estimated weights of normal glands in our study are similar to those reported in prior autopsy studies.[16,17]

There are several potential reasons for the slight underestimation of adenoma weight on 4D-CT. Given the location of the parathyroid glands, parathyroid adenomas are in close proximity to other anatomic structures, including the thyroid, thymus, carotid artery, jugular vein, and neck muscles, which can result in mass effect and compression of parathyroid adenomas. For example, compression of a parathyroid adenoma can be seen in cases of concomitant enlarged multinodular thyroid goiter or when parathyroid adenomas are very large and confined by adjacent structures. Second, surgical specimens may include adjacent fat and thymic gland, which may lead to a higher measured pathologic weight. Third, our method of estimating weight on CT is based on assumptions that parathyroid adenomas are ellipsoid and have a density equal to that of water. Differences in adenoma shape (teardrop, cylindric, and so forth) would, therefore, affect the CT-estimated weight. Also, the true density of parathyroid tissue is slightly greater than that of water, with density in the range of 1.049–1.069 mg/mm.[3,18] The amount of stromal fat in

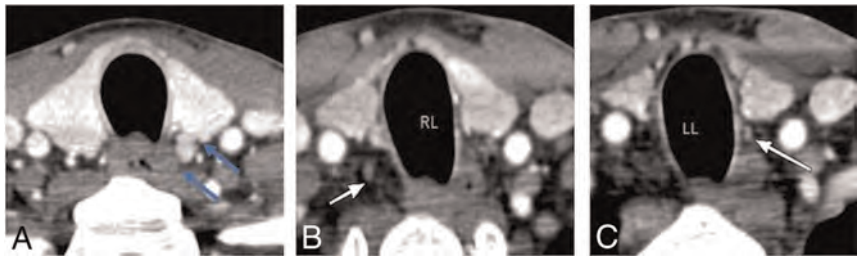

FIG 6. A 61-year-old woman with left upper parathyroid adenoma. *A*, Axial arterial phase CT image demonstrates a left upper parathyroid (*blue arrows*) with CT-estimated weight of 70 mg. Additional normal right lower (24 mg) (*B*) and left lower (18 mg) (*C*) parathyroid glands are identified (*white arrows*). RL indicates right lower; and LL, left lower.

the parathyroid gland may also affect the density of the gland.[19] It is plausible that adenomatous changes in the parathyroid gland decrease the fat content and render the parathyroid adenoma denser, another factor for underestimation of the pathologic weight by CT-based weight estimates. Only 1 prior study has evaluated the correlation of CT-estimated weight and pathologic weight and showed a positive correlation with a Pearson correlation coefficient of 0.96.[20] We also found a positive correlation with a Spearman correlation coefficient of 0.73. The Spearman correlation was used in our study because of the skewed distribution in our dataset.

Prior studies have shown that parathyroid adenoma size can affect the localization accuracy of sestamibi,[21,22] with lower accuracy in smaller glands. However, the effect of parathyroid adenoma size on the diagnostic accuracy of 4D-CT is not as well-established, with few studies in the literature. Day et al[23] evaluated 4D-CT in patients with negative findings on sonography or sestamibi scans and found that the mean pathologic weight of glands successfully localized by 4D-CT was 404 mg compared with 259 mg for those not localized by 4D-CT. Similarly, Galvin et al[3] showed that the mean weight of glands missed on 4D-CT was 0.3 g compared with 0.6 g in detected glands, but there was no statistical difference ($P = .15$). In our cohort, the mean pathologic weight of adenomas not successfully localized on 4D-CT was 136 mg; however, this estimate is based on only 4 patients. While prior studies were based on postoperative pathologic weight, our study allows extrapolation of these findings to preoperative CT-estimated weight by demonstrating a strong positive correlation between CT-estimated weight and pathologic weight. A preoperative 4D-CT size evaluation by Sho et al[24] demonstrated that abnormal parathyroid glands missed on 4D-CT were smaller, with mean of 8.6 mm versus 12.4 mm ($P < .001$), and parathyroid glands of ≥10 mm had higher chances of nonlocalization on 4D-CT (odds ratio = 4.37; 95% CI, 2.24–8.54). We found that a parathyroid gland length cutoff of >6.5 mm for the longest dimension could potentially be used to differentiate adenomas from normal glands; however, the longest dimension may not be the most accurate measurement of parathyroid size, given the differences in parathyroid gland shape and morphology.

There are several limitations in our study. First, our CT-estimated weights were calculated assuming an ellipsoid volume and density of water. More accurate volume assessments can be obtained through manual CT segmentation of the adenoma; however, this method would not be ideal in standard clinical workflow. Second, we included only patients with parathyroid adenomas correctly localized by 4D-CT with subsequent surgical cure, which may influence our results. Only 4 patients had unsuccessful localization on 4D-CT, and this is probably due to the high diagnostic accuracy of 4D-CT. Last, we also limited the study to include only patients with solitary parathyroid adenomas; thus, whether these results can be applied to patients with multigland disease remains to be studied.

CONCLUSIONS

This study demonstrates that using a formula to estimate parathyroid adenoma weight on 4D-CT is valid and reproducible, and a CT weight cutoff of >50 mg can be used to distinguish a parathyroid adenoma from normal glands. Our findings can be applied in routine clinical practice to help radiologists improve interpretation and reporting of 4D-CT scans and guide surgeons in preoperative planning. Future directions include evaluating this formula in patients with multigland disease.

REFERENCES

1. Rodgers SE, Hunter GJ, Hamberg LM, et al. **Improved preoperative planning for directed parathyroidectomy with 4-dimensional computed tomography.** *Surgery* 2006;140:932–41 CrossRef Medline
2. Hoang JK, Sung WK, Bahl M, et al. **How to perform parathyroid 4D CT: tips and traps for technique and interpretation.** *Radiology* 2014;270:15–24 CrossRef Medline
3. Galvin L, Oldan JD, Bahl M, et al. **Parathyroid 4D CT and scintigraphy: what factors contribute to missed parathyroid lesions?** *Otolaryngol Head Neck Surg* 2016;154:847–53 CrossRef Medline
4. Starker LF, Mahajan A, Björklund P, et al. **4D parathyroid CT as the initial localization study for patients with de novo primary hyperparathyroidism.** *Ann Surg Oncol* 2011;18:1723–28 CrossRef Medline
5. Suh YJ, Choi JY, Kim SJ, et al. **Comparison of 4D CT, ultrasonography, and 99mTc sestamibi SPECT/CT in localizing single-gland primary hyperparathyroidism.** *Otolaryngol Head Neck Surg* 2015;152:438–43 CrossRef Medline
6. Yeh R, Tay YK, Tabacco G, et al. **Diagnostic performance of 4D CT and sestamibi SPECT/CT in localizing parathyroid adenomas in primary hyperparathyroidism.** *Radiology* 2019;291:469–76 CrossRef Medline
7. Bahl M, Sepahdari AR, Sosa JA, et al. **Parathyroid adenomas and hyperplasia on four-dimensional CT scans: three patterns of enhancement relative to the thyroid gland justify a three-phase protocol.** *Radiology* 2015;277:454–62 CrossRef Medline
8. Yao K, Singer FR, Roth SI, et al. **Weight of normal parathyroid glands in patients with parathyroid adenomas.** *J Clin Endocrinol Metab* 2004;89:3208–13 CrossRef Medline
9. Grimelius L, Bondeson L. **Histopathological diagnosis of parathyroid diseases.** *Pathol Res Pract* 1995;191:353–65 CrossRef Medline
10. Kunstman JW, Kirsch JD, Mahajan A, et al. **Parathyroid localization and implications for clinical management.** *J Clin Endocrinol Metab* 2013;98:902–12 CrossRef Medline

11. Lampen-Sachar K, Zhao B, Zheng J, et al. **Correlation between tumor measurement on computed tomography and resected specimen size in lung adenocarcinomas.** *Lung Cancer* 2012;75:332–35 CrossRef Medline
12. Tann M, Sopov V, Croitoru S, et al. **How accurate is helical CT volumetric assessment in renal tumors?** *Eur Radiol* 2001;11:1435–38 CrossRef Medline
13. Bilezikian JP, Khan AA, Potts JT Jr; Third International Workshop on the Management of Asymptomatic Primary Hyperthyroidism. **Guidelines for the management of asymptomatic primary hyperparathyroidism: summary statement from the third international workshop.** *J Clin Endocrinol Metab* 2009;94:335–39 CrossRef Medline
14. Richards ML, Thompson GB, Farley DR, et al. **An optimal algorithm for intraoperative parathyroid hormone monitoring.** *Arch Surg* 2011;146:280–85 CrossRef Medline
15. Lin LI. **A concordance correlation coefficient to evaluate reproducibility.** *Biometrics* 1989;45:255–68 Medline
16. Akerström G, Grimelius L, Johansson H, et al. **The parenchymal cell mass in normal human parathyroid glands.** *Acta Pathol Microbiol Scand A* 1981;89:367–75 CrossRef Medline
17. Gilmour JR, Martin WJ. **The weight of the parathyroid glands.** *J Pathol Bacteriol* 1937;44:431–62 CrossRef
18. Wang CA, Rieder SV. **A density test for the intraoperative differentiation of parathyroid hyperplasia from neoplasia.** *Ann Surg* 1978;187:63–67 CrossRef Medline
19. Roth SI, Gallagher MJ. **The rapid identification of "normal" parathyroid glands by the presence of intracellular fat.** *Am J Pathol* 1976;84:521–28 Medline
20. Stucken EZ, Kutler DI, Moquete R, et al. **Localization of small parathyroid adenomas using modified 4-dimensional computed tomography/ultrasound.** *Otolaryngol Head Neck Surg* 2012;146:33–39 CrossRef Medline
21. Nichols KJ, Tronco GG, Palestro CJ. **Influence of multigland parathyroid disease on 99mTc-sestamibi SPECT/CT.** *Clinl Nucl Med* 2016;41:282–88 CrossRef Medline
22. Tay YD, Yeh R, Kuo JH, et al. **Pre-operative localization of abnormal parathyroid tissue by (99m)Tc-sestamibi in primary hyperparathyroidism using four-quadrant site analysis: an evaluation of the predictive value of vitamin D deficiency.** *Endocrine* 2018;60:36–45 CrossRef Medline
23. Day KM, Elsayed M, Beland MD, et al. **The utility of 4-dimensional computed tomography for preoperative localization of primary hyperparathyroidism in patients not localized by sestamibi or ultrasonography.** *Surgery* 2015;157:534–39 CrossRef Medline
24. Sho S, Yuen AD, Yeh MW, et al. **Factors associated with discordance between preoperative parathyroid 4-dimensional computed tomographic scans and intraoperative findings during parathyroidectomy.** *JAMA Surg* 2017;152:1141–47 CrossRef Medline

Diagnostic Accuracy of MRI-Based Morphometric Parameters for Detecting Olfactory Nerve Dysfunction

M.K. Lee, J.H. Lee, J.H. Kim, H. Kim, L. Joo, M. Kim, S.J. Cho, C.H. Suh, S.R. Chung, Y.J. Choi, and J.H. Baek

ABSTRACT

BACKGROUND AND PURPOSE: Although olfactory dysfunction is a common cranial nerve disorder, there are no simple objective morphometric criteria to assess olfactory dysfunction. The aim of this study was to evaluate the diagnostic performance of MR imaging morphometric parameters for detecting olfactory dysfunction.

MATERIALS AND METHODS: This prospective study enrolled patients from those presenting with olfactory symptoms who underwent both an olfactory function test and MR imaging. Controls without olfactory dysfunction were recruited during the preoperative work-up for pituitary adenoma. Two independent neuroradiologists measured the olfactory bulb in 3D and assessed olfactory bulb concavity on MR imaging while blinded to the clinical data. Diagnostic performance was assessed using receiver operating characteristic curve analysis.

RESULTS: Sixty-four patients and 34 controls were enrolled. The patients were significantly older than the controls (mean age, 57.8 ± 11.9 years versus 47.1 ± 12.1 years; $P < .001$). Before age adjustment, the olfactory bulb height was the only olfactory bulb parameter showing a significant difference between patients and controls (1.6 ± 0.3 mm versus 2.0 ± 0.3 mm, $P < .001$). After age adjustment, all parameters and olfactory bulb concavity showed significant intergroup differences, with the olfactory bulb height having the highest area under the curve (0.85). Olfactory bulb height was confirmed to be the only significant parameter showing a difference in the detection of olfactory dysfunction in 22 pairs after matching for age and sex (area under the curve = 0.87, $P < .001$). Intraclass correlation coefficients revealed moderate-to-excellent degrees of inter- and intrareader agreement.

CONCLUSIONS: MR imaging morphometric analysis can differentiate patients with olfactory dysfunction, with the olfactory bulb height having the highest diagnostic performance for detecting olfactory dysfunction irrespective of age.

ABBREVIATIONS: APD = anterior-posterior diameter; AUC = area under the curve

Olfactory dysfunction is a common cranial nerve disorder. In population-based studies, the prevalence of olfactory dysfunction is about 19%–24%, with this rate being higher in older men.[1-3] The etiologies of olfactory loss include postviral upper respiratory infection, sinonasal disease, head trauma, aging, congenital causes, toxins/drugs, idiopathic loss, and neurologic disorders such as Parkinson disease and Alzheimer disease.[4] Olfaction serves as a warning for hazards such as poisonous fumes and microbial harm and helps with food intake.[5] Loss of olfaction can result in severe problems, including loss of personal hygiene and social communication and reduction in the quality of life.[6]

Precise assessment of a patient's olfactory status should be made ahead of starting treatment, to predict the prognosis and provide proper counseling. Olfactory function is generally assessed by using olfactory function tests such as the Sniffin' Sticks test (Burghardt),[7] the University of Pennsylvania Smell Identification Test,[8] and the Connecticut Chemosensory Clinical Research Center Threshold test.[9] MR imaging can provide anatomic information on the olfactory pathway, and the evaluation of olfactory dysfunction using imaging parameters has been attempted previously.[4,10,11] The volume of the olfactory bulb is one such imaging parameter, with changes in volume being known to correlate with olfactory loss or odor-threshold

Received April 29, 2020; accepted after revision June 9.

From the Department of Radiology and Research Institute of Radiology (M.K.L., J.H.L., H.K., L.J., M.K., S.J.C., C.H.S., S.R.C., Y.J.C., J.H.B.), and Department of Otorhinolaryngology (J.H.K.), University of Ulsan College of Medicine, Asan Medical Center, Seoul, Republic of Korea; and Department of Radiology (M.K.L.), Yeouido St. Mary's Hospital, College of Medicine, The Catholic University of Korea, Seoul, Korea.

Please address correspondence to Jeong Hyun Lee, MD, PhD, Department of Radiology and Research Institute of Radiology, University of Ulsan College of Medicine, Asan Medical Center, 86 Asanbyeongwon-Gil, Songpa-Gu, Seoul 05505, Republic of Korea; e-mail: jeonghlee@amc.seoul.kr

Indicates article with supplemental on-line table.

http://dx.doi.org/10.3174/ajnr.A6697

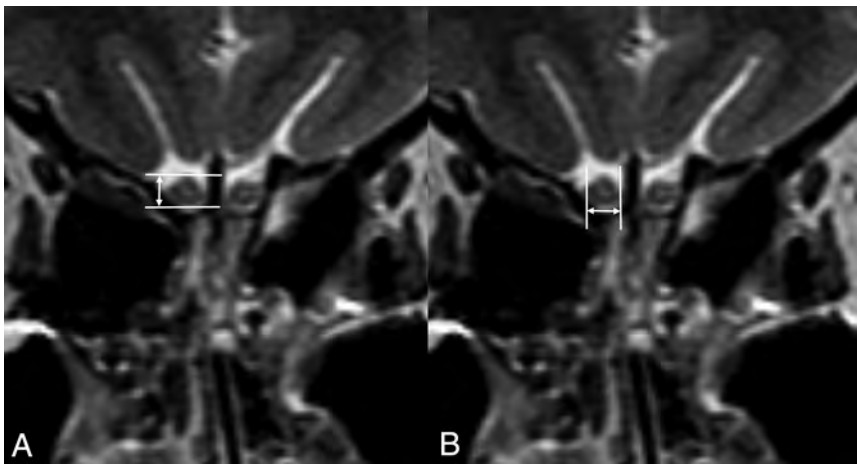

FIG 1. A 41-year-old male control subject. Coronal T2WI is used to show how to measure the height (*A*) and width (*B*) of the olfactory bulb, 2.8 and 3.5 mm, respectively.

changes.[12-14] However, measurement of olfactory bulb volume is not commonly used to evaluate the olfactory pathway in routine practice because volumetric analysis using planimetric manual contouring of multiple sections is difficult and complicated compared with visual analysis.[11,13-15] Recently, Chung et al[4] suggested that olfactory bulb atrophy seen on MR imaging can be used to objectively detect olfactory dysfunction in patients with subjective olfactory loss. Despite the suppleness of their method, their report was limited by the use of a subjective definition of olfactory bulb atrophy, and corrections were not made for patient age.

To make MR imaging diagnosis more robust, repeatable, and reproducible, we are still in need of simple objective morphometric criteria to assess olfactory dysfunction. Furthermore, although olfactory function is known to be affected by aging,[2] no published study has evaluated the effects of aging on olfactory bulb size. Therefore, the purpose of our study was to evaluate simple morphometric parameters of the olfactory bulb measured on MR imaging and to determine their diagnostic accuracy in patients with subjective olfactory dysfunction, making comparisons with healthy controls after age adjustment and matching.

MATERIALS AND METHODS

Study Population

Our institutional review boards Asan Medical Center approved this prospective study, and written informed consent was obtained from all participants. The study enrolled patients from those who presented with subjective olfactory nerve symptoms at a single tertiary referral center between March 2017 and November 2018. The enrollment criterion was olfactory nerve dysfunction revealed by the threshold-discrimination-identification score.[16] According to previous studies using the Korean version of the Sniffin' Sticks test II kit,[4,16,17] those patients with a threshold-discrimination-identification score of <28 were diagnosed as having objective olfactory nerve dysfunction. The enrolled patients agreed to undergo MR imaging with protocols dedicated to imaging the olfactory nerve.

The control participants were recruited during preoperative work-up for functioning pituitary adenoma. The subjects were routinely screened by a questionnaire for olfactory dysfunction, which was ruled out using the threshold-discrimination-identification score for subjective olfactory dysfunction. MR imaging of the olfactory nerve was added to the preoperative imaging of the pituitary mass after obtaining informed consent. The exclusion criteria were an age younger than 18 years, history of a previous endoscopic transnasal or endonasal operation, history of skull base fracture, radiation treatment to the head and neck area, active sinonasal disease, and psychiatric or neurologic conditions.

The presumptive causes of olfactory dysfunction were classified into 4 categories: post-upper respiratory infection,[4,14] chronic rhinosinusitis,[18] posttraumatic or postsurgical causes,[4,14] and idiopathic causes. Idiopathic olfactory dysfunction was defined when patients did not have a definite cause for the subjective olfactory nerve dysfunction after an extensive evaluation.[19] The patients' medical histories were evaluated, especially for the presence of Parkinson disease because olfactory dysfunction is a common symptom in Parkinson disease, having a similar frequency to resting tremor.[20-22]

MR Imaging Acquisition

MR images were acquired on a 3T unit (Ingenia 3T CX; Philips Healthcare) with a 64-channel head and neck coil. The imaging sequences used to evaluate the olfactory nerve included coronal 2D-T2WI. The imaging parameters for the 2D-T2WI included the following: matrix, 512×512; TR/TE, 300/80 ms; FOV, 90×190 mm; section thickness, 1.5 mm without interval; voxel size, $0.43 \times 0.43 \times 1.5$ mm; bandwidth, 209 Hz/pixel; TSE factor, 15; scan time, 3 minutes.

MR Imaging Analysis

Two independent board-certified neuroradiologists with 22 and 6 years of experience assessed the MR images and measured the following morphometric parameters on 2D T2WI: olfactory bulb height and width and anterior-posterior diameter (APD) of the olfactory bulb (Fig 1). The olfactory bulb height and width were measured directly on the largest cross-sectional image of the olfactory bulb using coronal T2WI. The APD was measured by summation of the slices containing a visible olfactory bulb. The neuroradiologists also assessed the presence of olfactory bulb concavity, defined as the line connecting both edges of the bulb being equal to or higher than the center of the bulb on coronal sections (Fig 2). The measurements were performed blinded to the patients' clinical information. To assess intrareader agreement, 1 radiologist repeated the analysis within a 2-week interval.

Statistical Analyses

The means of the olfactory bulb height, width, and APD measurements made on both sides of a patient were used for

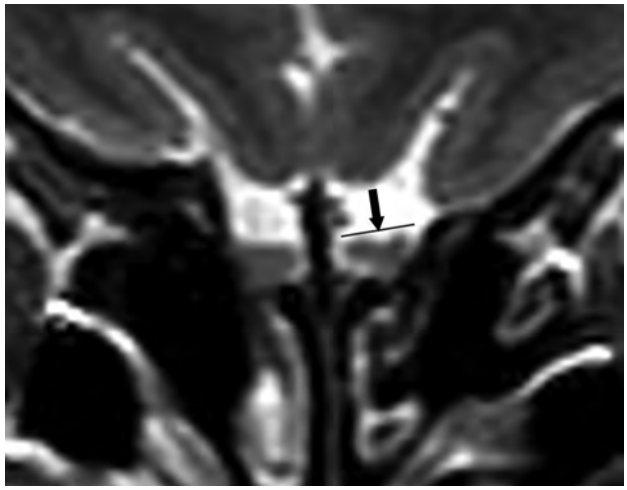

FIG 2. A 59-year-old female patient with idiopathic olfactory dysfunction with a threshold-discrimination-identification score of 14. Coronal T2WI shows olfactory bulb concavity (*arrow*) on the left side compared with the normal oval shape on the right side. The olfactory bulb heights and lateral diameters were 2.1 and 3.5 mm, respectively, on the right side and 1.3 and 3.5 mm on the left side.

Table 1: Summary of the demographic data of the patient and control groups

	Patients ($n = 64$)	Controls ($n = 34$)	*P* Value
Age (yr)[a]	57.8 ± 11.9	47.1 ± 12.2	<.001
Male sex[b]	29 (45)	14 (41)	.910
Duration of symptoms (yr)	6.3 ± 12.7	NA	
Threshold-discrimination-identification score	15.7 ± 6.7	NA	
Presumptive cause of olfactory dysfunction[b]			
Chronic rhinosinusitis	23 (36)	NA	
Post-upper respiratory infection	16 (25)	NA	
Posttraumatic or postsurgical	7 (11)	NA	
Idiopathic	18 (28)	NA	

Note:—NA indicates not applicable.
[a] Numbers are presented as mean ± SD.
[b] Number of patients. Numbers in parentheses are percentages.

Table 2: Morphometric parameters in the patient and control groups

MR Imaging Parameters	Patients ($n = 64$)	Controls ($n = 34$)	*P* Value
APD (mm)[a]	11.9 ± 1.9	12.5 ± 1.8	.107
Width (mm)[a]	4.1 ± 0.5	4.1 ± 0.4	.881
Height (mm)[a]	1.6 ± 0.3	2.0 ± 0.3	<.001
Olfactory bulb concavity[b]	26 (41)	9 (24)	.126

[a] Numbers are presented as mean ± SD.
[b] Number of patients. Numbers in parentheses are percentages.

the statistical analysis. The primary outcomes were the differences in the measured olfactory bulb height, width, APD, and olfactory bulb concavity between patients and controls. Demographic data are presented using descriptive statistics. Continuous variables were assessed for normal distribution using the Shapiro-Wilk test. Continuous data were analyzed with the Student *t* test or Mann-Whitney test according to the results of the Shapiro-Wilk test. Nominal data were analyzed with the χ^2 test.

Because there was a significant difference in age distribution between the patients and controls, a logistic regression model including age and each morphometric parameter as a covariate was developed to detect olfactory nerve dysfunction. The discriminative ability of this model was evaluated using receiver operating characteristic curve analysis and the area under the curve (AUC). The discriminative ability of the morphometric parameters was also evaluated in 22 pairs of patients and controls matched for age and sex to control for selection bias. The balance of the matches was checked using the standardized mean difference. Interreader and intrareader agreement were assessed using intraclass correlation coefficients. A P value $< .05$ was considered statistically significant. Statistical analysis was performed using R statistical and computing software (R version 3.6.1; http://www.r-project.org/) and MedCalc (MedCalc Software).

RESULTS

Among the 103 patients who visited with subjective olfactory nerve symptoms during the study period, 64 patients (male/female ratio = 29:35; mean age, 57.8 years; range, 22–84 years) were finally enrolled and underwent olfactory nerve MR imaging after exclusion of 39 patients with normal results on the threshold-discrimination-identification test. The presumptive causes for olfactory nerve dysfunction were chronic rhinosinusitis in 23 patients, post-upper respiratory infection in 16, and posttraumatic or postsurgical causes in 7, while 18 cases were idiopathic. Two patients had a history of Parkinson disease. The average duration of olfactory dysfunction was 6.3 ± 12.7 years.

Thirty-four subjects (male/female ratio = 14:20; mean age, 47.1 years; range, 26–69 years) were enrolled as controls. The patients were significantly older than the controls (mean age, 57.8 ± 11.9 versus 47.1 ± 12.2 years; $P < .001$), but there was no significant difference in sex distribution (Table 1).

Table 2 shows the differences in morphometric parameters between patients and controls. The patients had significantly smaller olfactory bulb heights (1.6 ± 0.3 mm versus 2.0 ± 0.3 mm, $P < .001$) than the controls (Fig 3). Olfactory bulb concavity was seen more frequently in patients than in controls, but the difference was not statistically significant (41% versus 24%, $P = .13$). All the parameters demonstrated moderate-to-excellent interreader and intrareader agreement (intraclass correlation coefficient = 0.69–0.85; On-line Table 1).

On-line Table 2 shows the diagnostic performance of the morphometric parameters for differentiating patients from controls before and after age adjustment in all cases and in 22 pairs

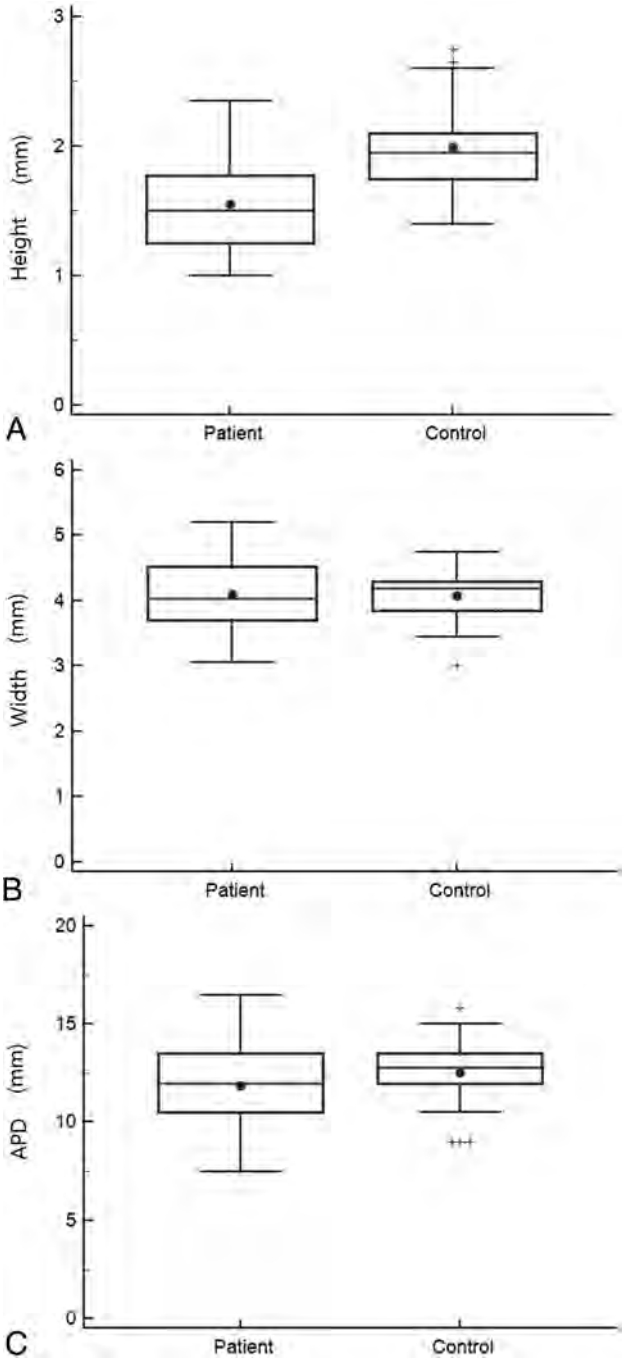

FIG 3. Box-and-whisker plots of the olfactory bulb height (*A*), width (*B*) and anterior-posterior diameters (*C*), showing comparisons between patients and controls. The *solid circles* represent the mean values of the parameters, and the *horizontal lines* represent the median values (median patient olfactory bulb height = 1.5 mm, median control olfactory bulb height = 2.0 mm; median patient olfactory bulb width = 4.0 mm, median control olfactory bulb width = 4.2 mm; median patient APD = 12.0 mm, median control APD = 12.8 mm). The *tops and bottoms* of the boxes represent the upper and lower quartiles, the *tops* and *bottoms* of the *whiskers* represent the highest and lowest observations, and the *crosses* represent outliers.

after matching for age and sex. Before age adjustment, olfactory bulb height was the only parameter showing significant differences between patients and controls in the detection of olfactory dysfunction (AUC = 0.83; 95% CI, 0.75–0.91; $P < .001$). After age adjustment, all the morphometric parameters showed a significant difference between patients and controls (all, $P < .001$), with olfactory bulb height having the highest AUC value (AUC = 0.85; 95% CI, 0.77–0.93; $P < .001$). After matching for age and sex, olfactory bulb height remained the only parameter showing a significant difference in detecting olfactory dysfunction (AUC = 0.87; 95% CI, 0.74–0.95; $P < .001$).

DISCUSSION

Our study revealed that a simple morphometric parameter of the olfactory bulb could be useful for detecting patients with olfactory nerve dysfunction. Given that age is a significant factor affecting the morphometry of the olfactory bulb and olfactory bulb height was the only parameter significantly different between patients and controls before and after matching, we suggest that olfactory bulb height is potentially the best single parameter to assess olfactory dysfunction on MR imaging.

There have been previous studies evaluating imaging features of olfactory nerve dysfunction, with volume measurement of the olfactory bulb by planimetric manual contouring on each section of an MR image sequence being one of the reported methods.[10,11,13,15,23] The authors reported positive correlations between olfactory performance and olfactory bulb volume in patients with different presumptive causes, including post-upper respiratory infection, head trauma, idiopathic loss, and Parkinson disease. Some researchers also evaluated the depth of the olfactory sulcus but found no significant correlation with olfactory function in patients with idiopathic olfactory loss.[13,15] Although the olfactory bulb volume typically shows a significant correlation with olfactory function, the method is difficult to apply in routine clinical practice.

Recently, Chung et al[4] proposed relatively simple imaging criteria to diagnose olfactory dysfunction. They used visual assessment of the olfactory bulb on coronal T2WI, 3D-T2-FLAIR, and 3D-T2 volume isotropic TSE acquisition images and reported that MR imaging evaluation of olfactory bulb atrophy can be used to diagnose olfactory dysfunction in patients with subjective olfactory loss. They defined olfactory bulb atrophy as flattening and thinning of the olfactory bulb, with loss of the normal oval or J-shape[24] and an asymmetric decrease in the size of the olfactory bulb compared with that on the contralateral side.[25] However, despite the suppleness of the method, we still need quantitative and repeatable morphometric parameters to objectively detect olfactory dysfunction.

Our prospective study is important because of the following features: First, we propose a simple morphometric analytic tool to detect olfactory dysfunction with excellent interreader and intrareader agreement, which is easily and readily applicable in routine clinical practice using thin-section T2WI. Thin-section TSE T2WI has advantages over the steady-state sequences such as CISS or FIESTA, which are commonly used to evaluate the cranial nerves in the cisternal spaces. TSE T2WI is free from the banding artifacts of the steady-state sequences occurring in the areas of air/bone and soft-tissue interfaces such as the olfactory sulcus. Moreover, the intrinsic contrast resolution of a nerve is better in spin-echo images compared with the CISS sequence.[26] Second, we found that age was not only a significant factor influencing olfactory performance but that it also showed a relationship with the size of the olfactory bulb on clinical MR imaging. In previous cross-sectional

studies,[2,27-29] olfactory function and pathophysiologic change showed significant relationships with the aging process, but no study has previously shown age-related change in the size of the olfactory bulb on MR imaging. This is the first study to demonstrate such a relationship. Finally, we provide a clearer definition of olfactory bulb concavity, one that is similar to the concept of olfactory atrophy described by Chung et al.[4]

Despite these merits, there are also several limitations to our study. First, although we demonstrated that our simple morphometric analysis could be useful for detecting olfactory dysfunction, we could not suggest the size criteria for defining olfactory dysfunction for any of the parameters except olfactory bulb concavity, partly due to the relatively small sample size. Further investigation to determine the optimal olfactory morphometry size criteria for diagnosing olfactory dysfunction should be performed on larger cohorts using subject groups with even age distributions. Second, we could not compare the morphometric parameters among patients with different presumptive causes of olfactory dysfunction. Third, the APD was calculated by summing up the section numbers showing the olfactory bulb, not by directly measuring the olfactory bulb on sagittal or axial images. Direct measurement of APD might be more helpful for diagnosing olfactory dysfunction; however, our method has the advantage of being quite simple and able to be performed on a single MR imaging sequence.

CONCLUSIONS

Our study demonstrated that morphometric parameters that can be simply measured on coronal T2WI are helpful for objectively assessing olfactory dysfunction in patients with subjective olfactory dysfunction, and it also showed that age is a significant factor affecting olfactory bulb size. Among the measured parameters, olfactory bulb height shows the best potential for detecting olfactory dysfunction irrespective of age. However, a further larger-scale study with an even age distribution between groups is necessary to suggest diagnostic cutoff values for the parameters.

Disclosures: Jung Hwan Baek—*UNRELATED*: *Consultancy*: radiofrequency, *Comments*: consultant of STARmed Healthcare and radiofrequency medical companies from 2017.

REFERENCES

1. Brämerson A, Johansson L, Ek L, et al. **Prevalence of olfactory dysfunction: the Skövde population-based study.** *Laryngoscope* 2004;114:733–37 CrossRef Medline
2. Murphy C, Schubert CR, Cruickshanks KJ, et al. **Prevalence of olfactory impairment in older adults.** *JAMA* 2002;288:2307–12 CrossRef Medline
3. Vennemann MM, Hummel T, Berger K. **The association between smoking and smell and taste impairment in the general population.** *J Neurol* 2008;255:1121–26 CrossRef Medline
4. Chung MS, Choi WR, Jeong HY, et al. **MR imaging-based evaluations of olfactory bulb atrophy in patients with olfactory dysfunction.** *AJNR Am J Neuroradiol* 2018;39:532–37 CrossRef Medline
5. Stevenson RJ. **An initial evaluation of the functions of human olfaction.** *Chem Senses* 2010;35:3–20 CrossRef Medline
6. Croy I, Nordin S, Hummel T. **Olfactory disorders and quality of life: an updated review.** *Chem Senses* 2014;39:185–94 CrossRef Medline
7. Hummel T, Sekinger B, Wolf SR, et al. **'Sniffin' sticks': olfactory performance assessed by the combined testing of odor identification, odor discrimination and olfactory threshold.** *Chem Senses* 1997;22:39–52 CrossRef Medline
8. Doty RL, Shaman P, Kimmelman CP, et al. **University of Pennsylvania Smell Identification Test: a rapid quantitative olfactory function test for the clinic.** *Laryngoscope* 1984;94:176–78 CrossRef Medline
9. Cain WS, Gent JF, Goodspeed RB, et al. **Evaluation of olfactory dysfunction in the Connecticut Chemosensory Clinical Research Center.** *Laryngoscope* 1988;98:83–88 CrossRef Medline
10. Buschhuter D, Smitka M, Puschmann S, et al. **Correlation between olfactory bulb volume and olfactory function.** *Neuroimage* 2008;42:498–502 CrossRef Medline
11. Haehner A, Rodewald A, Gerber JC, et al. **Correlation of olfactory function with changes in the volume of the human olfactory bulb.** *Arch Otolaryngol Head Neck Surg* 2008;134:621–24 CrossRef Medline
12. Mueller A, Rodewald A, Reden J, et al. **Reduced olfactory bulb volume in post-traumatic and post-infectious olfactory dysfunction.** *Neuroreport* 2005;16:475–78 CrossRef Medline
13. Rombaux P, Potier H, Markessis E, et al. **Olfactory bulb volume and depth of olfactory sulcus in patients with idiopathic olfactory loss.** *Eur Arch Otorhinolaryngol*. 2010;267:1551–56 CrossRef Medline
14. Rombaux P, Huart C, Deggouj N, et al. **Prognostic value of olfactory bulb volume measurement for recovery in postinfectious and post-traumatic olfactory loss.** *Otolaryngol Head Neck Surg* 2012;147:1136–41 CrossRef Medline
15. Wang J, You H, Liu JF, et al. **Association of olfactory bulb volume and olfactory sulcus depth with olfactory function in patients with Parkinson disease.** *AJNR Am J Neuroradiol* 2011;32:677–81 CrossRef Medline
16. Hong SC, Yoo YS, Kim ES, et al. **Development of KVSS Test (Korean Version of Sniffin' Sticks Test).** *Korean J Otorhinolaryngol-Head Neck Surg* 1999;42:855–60
17. Cho JH, Jeong YS, Lee YJ, et al. **The Korean version of the Sniffin' stick (KVSS) test and its validity in comparison with the cross-cultural smell identification test (CC-SIT).** *Auris Nasus Larynx* 2009;36:280–86 CrossRef Medline
18. Fokkens WJ, Lund VJ, Mullol J, et al. **EPOS 2012: European position paper on rhinosinusitis and nasal polyps 2012: a summary for otorhinolaryngologists.** *Rhinology* 2012;50:1–12 CrossRef Medline
19. Hoekman PK, Houlton JJ, Seiden AM. **The utility of magnetic resonance imaging in the diagnostic evaluation of idiopathic olfactory loss.** *Laryngoscope* 2014;124:365–68 CrossRef Medline
20. Ansari K, Johnson A. **Olfactory function in patients with Parkinson's disease.** *J Chronic Dis* 1975;28:493–97 CrossRef Medline
21. Doty RL, Deems DA, Stellar S. **Olfactory dysfunction in parkinsonism: a general deficit unrelated to neurologic signs, disease stage, or disease duration.** *Neurology* 1988;38:1237–37 CrossRef Medline
22. Mesholam RI, Moberg PJ, Mahr RN, et al. **Olfaction in neurodegenerative disease: a meta-analysis of olfactory functioning in Alzheimer's and Parkinson's diseases.** *Arch Neurol* 1998;55:84–90 CrossRef Medline
23. Rombaux P, Mouraux A, Bertrand B, et al. **Olfactory function and olfactory bulb volume in patients with postinfectious olfactory loss.** *Laryngoscope* 2006;116:436–39 CrossRef Medline
24. Schneider JF, Floemer F. **Maturation of the olfactory bulbs: MR imaging findings.** *AJNR Am J Neuroradiol* 2009;30:1149–52 CrossRef Medline
25. Booth TN, Rollins NK. **Spectrum of clinical and associated MR imaging findings in children with olfactory anomalies.** *AJNR Am J Neuroradiol* 2016;37:1541–48 CrossRef Medline
26. Li Z, Chen YA, Chow D, et al. **Practical applications of CISS MRI in spine imaging.** *Eur J Radiol Open* 2019;6:231–42 CrossRef Medline
27. Doty RL, Shaman P, Applebaum SL, et al. **Smell identification ability: changes with age.** *Science* 1984;226:1441–43 CrossRef Medline
28. Doty RL, Kamath V. **The influences of age on olfaction: a review.** *Front Psychol* 2014;5:20 CrossRef Medline
29. Duffy VB, Backstrand JR, Ferris AM. **Olfactory dysfunction and related nutritional risk in free-living, elderly women.** *J Am Diet Assoc* 1995;95:879–84 CrossRef Medline

Anosmia in COVID-19 Associated with Injury to the Olfactory Bulbs Evident on MRI

M.F.V.V. Aragão, M.C. Leal, O.Q. Cartaxo Filho, T.M. Fonseca, and M.M. Valença

ABSTRACT

SUMMARY: Patients with coronavirus disease 2019 (COVID-19) may have symptoms of anosmia or partial loss of the sense of smell, often accompanied by changes in taste. We report 5 cases (3 with anosmia) of adult patients with COVID-19 in whom injury to the olfactory bulbs was interpreted as microbleeding or abnormal enhancement on MR imaging. The patients had persistent headache ($n = 4$) or motor deficits ($n = 1$). This olfactory bulb injury may be the mechanism by which the Severe Acute Respiratory Syndrome coronavirus 2 causes olfactory dysfunction.

ABBREVIATIONS: COVID-19 = coronavirus disease 2019; SARS-CoV-2 = Severe Acute Respiratory Syndrome coronavirus 2

Coronavirus has the human respiratory system as its main target but also has neuroinvasive capabilities and can spread from the respiratory tract to the CNS.[1-3] Therefore, patients with coronavirus disease 19 (COVID-19) may present with neurologic symptomatology with repercussions on imaging examinations,[4-18] and these have been described in association with ischemic infarct,[8,9] hemorrhage,[11] acute hemorrhagic necrotizing encephalopathy,[10] cerebral venous thrombosis,[13] and diffuse leukoencephalopathy with microhemorrhage.[15]

Transmission from person to person occurs mainly by direct contact or droplets spread by coughing or sneezing by an infected individual with Severe Acute Respiratory Syndrome coronavirus 2 (SARS-CoV-2).[5,19] Symptoms of COVID-19 usually appear after an incubation period of about 5 days. The most common symptoms are fever, cough, fatigue, headache, and dyspnea.[5,19,20] In the most severe cases, patients may develop pneumonia, acute respiratory failure, distress syndrome, and acute heart problems.[5,19,20]

Anosmia or partial loss of the sense of smell, usually accompanied by changes in taste, is a frequent symptom that helps in the diagnosis of COVID-19.[21-28] It is often a transitory phenomenon, lasting just a few weeks.[21] However, the mechanism by which anosmia occurs has not yet been established.[29]

The hypothesis is that the virus enters the central nervous system through the first neurons of the olfactory pathway, also called olfactory sensory neurons, located in the olfactory mucosa. The olfactory mucosa is a specialized neuroepithelium located in the highest portion of the nasal cavity in direct contact with the external environment below to the cribriform plate.[1] Therefore, the virus crosses the cribriform plate to reach the olfactory bulbs, which contain the second olfactory neurons.[1,30]

There are currently only 2 reports evaluating olfactory bulb imaging, and they are discordant.[18,31] The first report showed bilateral inflammatory obstruction of the olfactory clefts that was confirmed on MR imaging of the nasal cavity, but no anomalies of the olfactory bulbs and tracts.[31] The second study reported a case with anosmia evaluated with 3D-CISS T2WI, which demonstrated severe enlargement and an abnormal high signal intensity on T2, being interpreted as bilateral olfactory bulb edema and also olfactory cleft mild edema.[18] The control MR imaging (D24) showed a reduction in the volume of the bulbs.[18]

To our knowledge, no other report has evaluated the characteristics of the olfactory bulb, especially using fat-suppressed T1WI. Also, no report evaluates and shows the presence of bleeding or a break in the blood-brain barrier in the olfactory bulbs and tracts as the possible pathophysiology of olfactory neuropathy associated with COVID-19.

Thus, in this study, the authors demonstrate by MR imaging that a possible mechanism by which the SARS-CoV-2 causes olfactory dysfunction is by affecting, intracranially, the olfactory bulbs by a likely microvascular phenomenon.

Received May 20, 2020; accepted after revision June 1.

From the Universidade Federal de Pernambuco (M.F.V.V.A., M.C.L., M.M.V.), Recife, Brazil; Centro Diagnostico Multimagem (M.F.V.V.A.), Recife, Brazil; and Real Hospital de Beneficencia Portuguesa (M.C.L., O.Q.C.F., T.M.F.), Recife, Brazil.

Please address correspondence to Maria Fatima Viana Vasco Aragão, MD, Rua Frei Matias Teves, 194, Ilha do Leite, Recife, PE, Brazil, 50070-450; e-mail: fatima.vascoaragao@gmail.com

Indicates open access to non-subscribers at www.ajnr.org
Indicates article with supplemental on-line table.

http://dx.doi.org/10.3174/ajnr.A6675

MATERIALS AND METHODS

This retrospective study was approved by the institutional review board of the ethics committee of Universidade Federal de Pernambuco, Brazil. Informed consent was waived.

All scans were initially analyzed by the institution's own neuroradiologists. Subsequently, all images were reviewed independently by 2 neuroradiologists (M.F.V.V.A. and O.Q.C.F, who were certified by the Ministry of Education and Culture of Brazil and the Brazilian College of Radiology) with 30 and 18 years, respectively, of neuroradiology experience, with no discordant results. MR imaging was indicated mainly because of a persistent incapacitating headache.

The intensity of the olfactory bulbs is defined as normal when the bulbs have the same cortical intensity, as typically seen in healthy controls. Abnormal olfactory bulb intensity is defined when the bulb is more hyperintense than the cortex on T1WI and STIR.

After gadolinium injection on T1WI, enhancement of the olfactory bulbs is defined when they become more hyperintense in comparison with their intensity on pregadolinium T1WI. However, when there is only the postgadolinium T1WI and the bulb is more hyperintense than the normal cortex, these features represent olfactory bulb intensity abnormality and may be an enhancement or microbleeding (methemoglobin), as interpreted in the present study. Microbleeding (methemoglobin) in the olfactory bulb is considered when there is a hyperintense olfactory bulb, compared with the normal cortex or the normal contralateral bulb, on pregadolinium fat-suppressed T1WI.

Brain MR imaging of patients with COVID-19 was evaluated from April 1, 2020, to May 18, 2020. Five patients were included in this study because their brain MRIs assessed their olfactory bulbs appropriately, with at least 2 sequences with thin slices examining the anterior cranial fossa. All 5 patients were evaluated with 2 coronal sequences with thin slices: postcontrast fat-suppressed T1WI and STIR. Only 1 patient also had thin-slice pregadolinium fat-suppressed T1WI.

The brain MRIs of the patients were performed on two 1.5T machines with the main technical parameters of the sequences described as follows. The coronal fat-suppressed T1WI (spectral presaturation with inversion recovery) parameters were, respectively, on both MR imaging machines the following: TR/TE = 561–605/15–9 ms, matrix = 256–88, FOV = 190–150 mm, thickness = 3 mm, 3.5-mm section, coronal orientation, bandwidth = 181–96.6 Hz, time = 3.39–4.49 minutes, NEX = 1–3.

The coronal STIR sequence had the following parameters in each MR imaging machine, respectively: TR/TE = 4000–2650/51–90 ms, TI = 180 ms, matrix = 256–224, FOV = 190–150 mm, thickness = 3–3.45 mm, section orientation = coronal, bandwidth = 190–232.4 Hz, time = 2.46–3.42 minutes, and NEX = 1–2.

RESULTS

All 5 patients with COVID-19 (On-line Table) had fever, headache, and cough. The medical indications for the performance of MR imaging were persistent headache ($n = 4$) or motor deficit ($n = 1$). All 5 patients had injury to the olfactory bulbs demonstrated by MR imaging with the following sequences: coronal pre-contrast (Fig 1*A*) and post-contrast fat suppression T1WI (Figs 1*B* and 2*A*, -*D*) and coronal STIR (Fig 1*C*).

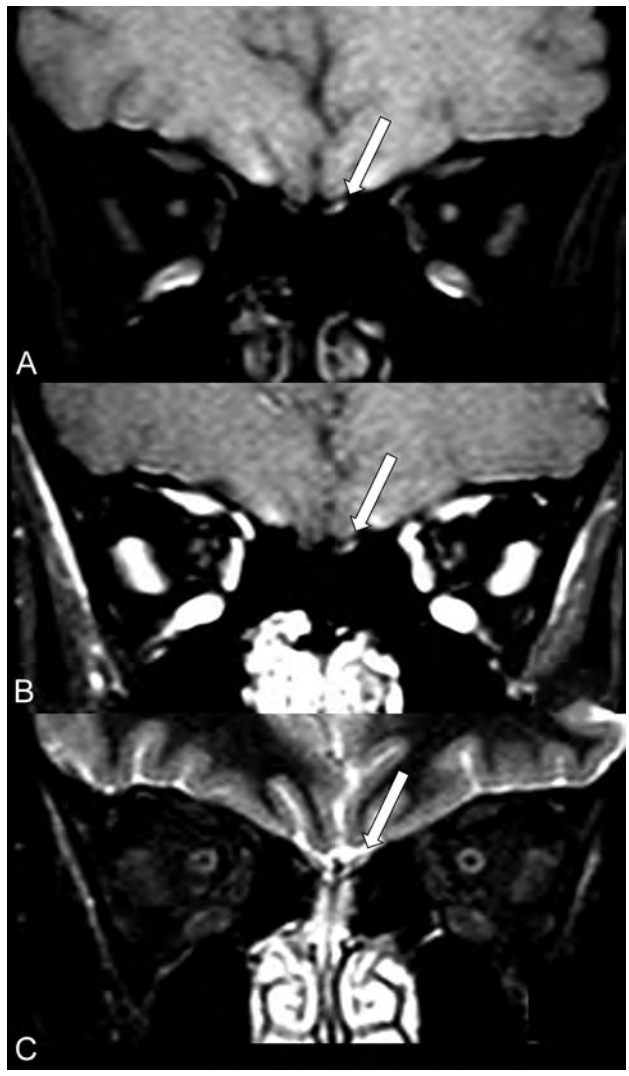

FIG 1. MR imaging shows probably microbleeding (methemoglobin) in the left olfactory bulb of a patient (case 1) with COVID-19 and anosmia. The left olfactory bulb (*long arrows*) has partial hyperintensity on precontrast fat-suppressed TIWI (*A*) and also on postcontrast fat-suppressed TIWI (*B*) and STIR (*C*).

The only patient who had pregadolinium fat-suppressed T1WI (case 1) showed a small hyperintensity in the left olfactory bulb (Fig 1*A*), which remained hyperintense on the postgadolinium sequence (Fig 1*B*) and also on STIR (Fig 1*C*). This finding was suggestive of a small area of methemoglobin in the left olfactory bulb in this patient with anosmia.

In the 4 patients who did not have a pregadolinium sequence, we did not have information about anosmia in 1 patient (Fig 2*A*; case 2), and 2 of them with anosmia (Fig 2*B*, -*C*; Cases 3 and 4) showed hyperintensity suggestive of enhancement of both olfactory bulbs following gadolinium injection. However, only in the patient with COVID-19 without clinical anosmia (case 5) was there a suggestive enhancement in the left olfactory bulb (Fig 2*D*). The case 5 had a negative result of the CSF real-time RT-PCR for SARS-CoV-2. The differential diagnosis in these cases is

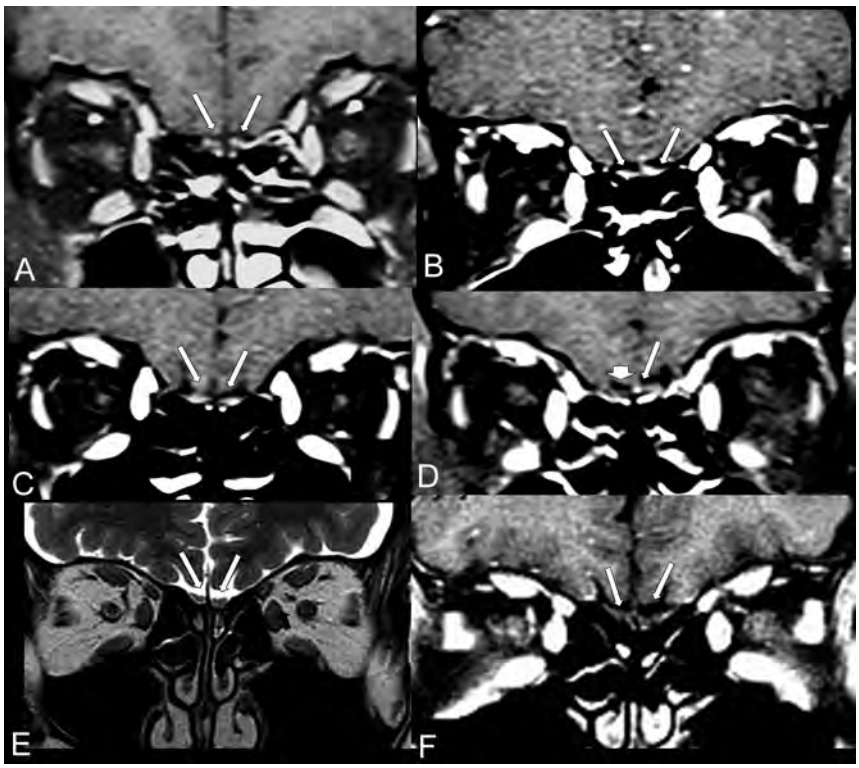

FIG 2. The coronal postcontrast fat-suppressed T1WI shows hyperintensity suggestive of enhancement or methemoglobin in the olfactory bulbs of 4 patients with COVID-19 (*A–D*; cases 2–5) compared with a healthy patient with normal olfactory bulbs (*E* and *F*). The coronal postcontrast fat-suppressed T1WI in 3 patients with COVID-19 (*A–C*; cases 2–4) shows that both olfactory bulbs (*long arrows*) are small oval images that are hyperintense with contrast, having signal intensity higher than the intensity of the cortex. *D*, A patient (case 5) with COVID-19 shows hyperintensity only on the left bulb (*long arrow*), the right olfactory bulb being normal (*short arrow*). In a healthy 60-year-old man, the coronal T2WI (*E*) and the postcontrast fat-suppressed T1WI (*F*) demonstrate normal olfactory bulbs (*long arrows*), which are isointense to the cortex and normally hypointense on postgadolinium sequence (*F*).

mainly microbleeding (methemoglobin) because the pregadolinium sequence was not performed. Coronal STIR of the anterior cranial fossa did not show any abnormality in the olfactory bulbs in these 4 patients.

MR imaging of a healthy individual was used as a comparative control (Fig 2*E*, -*F*) to demonstrate that the normal olfactory bulbs do not enhance and are isointense to the cerebral cortex.

DISCUSSION

This case series demonstrates abnormal intensity of the olfactory bulbs in 5 adult patients with COVID-19, three of whom had anosmia. In 1 patient (case 1), the abnormal intensity could represent microbleeding (methemoglobin). However, in the other 4 patients, it could represent abnormal enhancement or microbleeding (methemoglobin) because they only underwent the sequence after injection of gadolinium in fat-suppressed T1WI.

Previously, it was demonstrated, using an experimental mouse model, that the SARS-CoV could travel from the nose to the olfactory bulb.[32] Regarding the SAR-CoV infection, there was a time delay of about 60 hours from the time of nasal infection until the detection of the virus in the olfactory bulb.[1,32]

The literature has already reported that some other viruses can use the olfactory nerve as a shortcut into the CNS, such as influenza A virus, herpesviruses, poliovirus, paramyxoviruses, vesicular stomatitis virus, rabies virus, parainfluenza virus, adenoviruses, Japanese encephalitis virus, West Nile virus, chikungunya virus, La Crosse virus, mouse hepatitis virus, and bunya viruses.[30] van Riel et al[30] have reported that "Viral infection of the CNS can lead to damage from infection of nerve cells per se, from the immune response, or from a combination of both. Clinical consequences range from nervous dysfunction in the absence of histopathological changes to severe meningoencephalitis and neurodegenerative disease." However, to our knowledge, no study evaluated and documented, by brain MR imaging, the abnormalities such as microbleeding and/or enhancement in the olfactory bulbs occurring in these other kinds of viruses.

Probably, the impairment of olfactory function is much more frequent in COVID-19 because, strictly speaking, unilateral anosmia can only be detected through a detailed physical examination. The patient hardly perceives unilateral anosmia.

Recognizing this hypersignal in the olfactory bulbs on the thin slices of pre- and/or postgadolinium fat-suppressed T1WI, identified in this study, may help to suggest or support the etiologic diagnosis of COVID-19 during and after this new pandemic.

Thus, we suggest, henceforth, including in the routine brain MR imaging protocol at least a sequence with coronal thin-slice pre- and/or postgadolinium fat-suppressed T1WI in the anterior fossa of the cranium. This feature will be more important in cases of refractory headache associated or not with other symptoms and signs such as fever and anosmia.

The weakness of this work is that it is a retrospective study with only a few cases in which it was possible to evaluate the olfactory bulbs. Brain MR imaging of patients with COVID-19 has not been routinely scheduled to adequately evaluate the olfactory bulbs because other neurologic complications were being investigated. The distortion at the air-tissue interface in fat-suppressed T1WI makes the findings somewhat difficult to interpret, but it seems that the images are true abnormal lesions along the olfactory bulbs. Future prospective studies geared to evaluating the olfactory bulbs with a larger sample size will be needed to confirm our findings.

In conclusion, the authors demonstrated by MR imaging that a possible mechanism by which the SARS-CoV-2 causes olfactory

dysfunction is by affecting, intracranially, the olfactory bulbs, with development of a microvascular phenomenon and injury such as microbleeding and/or a blood-brain barrier break. This seems to be the first time that a neuroimaging study has documented this type of olfactory bulb injury in patients with COVID-19.

REFERENCES

1. Fodoulian L, Tuberosa J, Rossier D, et al. **SARS-CoV-2 receptor and entry genes are expressed by sustentacular cells in the human olfactory neuroepithelium.** *bioRxiv* 2020. https://www.biorxiv.org/content/10.1101/2020.03.31.013268v1. Accessed May 12, 2020
2. Desforges M, Le Coupanec A, Dubeau P, et al. **Human coronaviruses and other respiratory viruses: underestimated opportunistic pathogens of the central nervous system?** *Viruses* 2019;12:14 CrossRef Medline
3. Morris M, Zohrabian VM. **Neuroradiologists, be mindful of the neuroinvasive potential of COVID-19.** *AJNR Am J Neuroradiol* 2020 Apr 30. [Epub ahead of print] CrossRef Medline
4. Montalvan V, Lee J, Bueso T, et al. **Neurological manifestations of COVID-19 and other coronavirus infections: a systematic review.** *Clin Neurol Neurosurg* 2020;194:10592 CrossRef Medline
5. Whittaker A, Anson M, Harky A. **Neurological Manifestations of COVID-19: A review.** *Acta Neurol Scand* 2020;142:14–22 CrossRef Medline
6. Ahmad I, Rathore FA. **Neurological manifestations and complications of COVID-19: a literature review.** *J Clin Neurosci* 2020 May 6. [Epub ahead of print] CrossRef Medline
7. Asadi-Pooya AA, Simani L. **Central nervous system manifestations of COVID-19: a systematic review.** *J Neurol Sci* 2020;413:116832 CrossRef Medline
8. Goldberg MF, Cerejo R, Tayal AH. **Cerebrovascular disease in COVID-19.** *AJNR Am J Neuroradiol* 2020 May 14. [Epub ahead of print] CrossRef Medline
9. Aggarwal G, Lippi G, Michael Henry B. **Cerebrovascular disease is associated with an increased disease severity in patients with coronavirus disease 2019 (COVID-19): a pooled analysis of published literature.** *Int J Stroke* 2020;15:385–89 CrossRef Medline
10. Poyiadji N, Shahin G, Noujaim D, et al. **COVID-19-associated acute hemorrhagic necrotizing encephalopathy: CT and MRI features.** *Radiology* 2020 March 31. [Epub ahead of print] CrossRef Medline
11. Franceschi AM, Ahmed O, Giliberto L, et al. **Hemorrhagic posterior reversible encephalopathy syndrome as a manifestation of COVID-19 infection.** *AJNR Am J Neuroradiol* 2020 May 21. [Epub ahead of print] CrossRef Medline
12. Poillon G, Obadia M, Perrin M, et al. **Cerebral venous thrombosis associated with COVID-19 infection: causality or coincidence?** *J Neuroradiol* 2020 May 10. [Epub ahead of print] CrossRef Medline
13. Garaci F, Di Giuliano F, Picchi E, et al. **Venous cerebral thrombosis in COVID-19 patient.** *J Neurol Sci* 2020;414:116871 CrossRef Medline
14. Hughes C, Nichols T, Pike M, et al. **Cerebral venous sinus thrombosis as a presentation of COVID-19.** *Eur J Case Rep Intern Med* 2020;7:001691 CrossRef Medline
15. Radmanesh A, Derman A, Lui YW, et al. **COVID-19-associated diffuse leukoencephalopathy and microhemorrhages.** *Radiology* 2020 May 21. [Epub ahead of print] CrossRef Medline
16. Mahammedi A, Saba L, Vagal A, et al. **Imaging in neurological disease of hospitalized COVID-19 patients: an Italian multicenter retrospective observational study.** *Radiology* 2020 May 21. [Epub ahead of print] CrossRef Medline
17. Karimi-Galougahi M, Yousefi-Koma A, Bakhshayeshkaram M, et al. **^{18}FDG PET/CT scan reveals hypoactive orbitofrontal cortex in anosmia of COVID-19.** *Acad Radiol* 2020 May 3. [Epub ahead of print] CrossRef Medline
18. Laurendon T, Radulesco T, Mugnier J, et al. **Bilateral transient olfactory bulbs edema during COVID-19-related anosmia.** *Neurology* 2020 May 22. [Epub ahead of print] CrossRef Medline
19. Weiss P, Murdoch DR. **Clinical course and mortality risk of severe COVID-19.** *Lancet* 2020;395:1014–15 CrossRef Medline
20. Zhou F, Yu T, Du R, et al. **Clinical course and risk factors for mortality of adult inpatients with COVID-19 in Wuhan, China: a retrospective cohort study.** *Lancet* 2020;395:1054–62 CrossRef Medline
21. Hopkins C, Surda P, Whitehead E, et al. **Early recovery following new onset anosmia during the COVID-19 pandemic: an observational cohort study.** *J Otolaryngol Head Neck Surg* 2020;49:26 CrossRef Medline
22. Kaye R, Chang CW, Kazahaya K, et al. **Anosmia reporting tool: initial findings.** *Otolaryngol Head Neck Surg* 2020 Apr 28. [Epub ahead of print] CrossRef Medline
23. Gane SB, Kelly C, Hopkins C. **Isolated sudden onset anosmia in COVID-19 infection: a novel syndrome?** *Rhinology* 2020;58:299–301 CrossRef Medline
24. Ghiasvand F, SeyedAlinaghi S. **Isolated anosmia as a presentation of COVID-19: an experience in a referral hospital.** *Infect Disord Drug Targets* 2020 May 20. [Epub ahead of print] CrossRef Medline
25. Heidari F, Karimi E, Firouzifar M, et al. **Anosmia as a prominent symptom of COVID-19 infection.** *Rhinology* 2020;58:302–03 CrossRef Medline
26. Lechien JR, Barillari MR, Jouffe L, et al. **Anosmia Is a key symptom of COVID-19 infection and should be used as a diagnostic tool.** *Ear Nose Throat J* 2020 May 21. [Epub ahead of print] CrossRef Medline
27. Villalba NL, Maouche Y, Ortiz MB, et al. **Anosmia and dysgeusia in the absence of other respiratory diseases: should COVID-19 infection be considered?** *Eur J Case Rep Intern Med* 2020;7:001641 CrossRef Medline
28. Marinosci A, Landis BN, Calmy A. **Possible link between anosmia and COVID-19: sniffing out the truth.** *Eur Arch Otorhinolaryngol* 2020 Apr 17. [Epub ahead of print] CrossRef Medline
29. Vaira LA, Salzano G, Fois AG, et al. **Potential pathogenesis of ageusia and anosmia in COVID-19 patients.** *Int Forum Allergy Rhinol* 2020 Apr 27. [Epub ahead of print] CrossRef Medline
30. van Riel D, Verdijk R, Kuiken T. **The olfactory nerve: a shortcut for influenza and other viral diseases into the central nervous system.** *J Pathol* 2015;235:277–87 CrossRef Medline
31. Eliezer M, Hautefort C, Hamel AL, et al. **Sudden and complete olfactory loss function as a possible symptom of COVID-19.** *JAMA Otolaryngol Head Neck Surg* 2020 Apr 8. [Epub ahead of print] CrossRef Medline
32. Netland J, Meyerholz DK, Moore S, et al. **Severe acute respiratory syndrome coronavirus infection causes neuronal death in the absence of encephalitis in mice transgenic for human ACE2.** *J Virol* 2008;82:7264–75 CrossRef Medline

COVID-19–Associated Bifacial Weakness with Paresthesia Subtype of Guillain-Barré Syndrome

K.L. Hutchins, J.H. Jansen, A.D. Comer, R.V. Scheer, G.S. Zahn, A.E. Capps, L.M. Weaver, and N.A. Koontz

ABSTRACT

SUMMARY: We report a case of bifacial weakness with paresthesia, a recognized Guillain-Barré syndrome subtype characterized by rapidly progressive facial weakness and paresthesia without ataxia or other cranial neuropathies, which was temporally associated with antecedent coronavirus 2019 (COVID-19). This case highlights a potentially novel but critically important neurologic association of the COVID-19 disease process. Herein, we detail the clinicoradiologic work-up and diagnosis, clinical course, and multidisciplinary medical management of this patient with COVID-19. This case is illustrative of the increasingly recognized but potentially underreported neurologic manifestations of COVID-19, which must be considered and further investigated in this pandemic disease.

ABBREVIATIONS: BFP = bifacial weakness with paresthesia; CN = cranial nerve; COVID-19 = coronavirus 2019; GBS = Guillain-Barré syndrome; HSV = herpes simplex virus; Ig = immunoglobulin; PCR = polymerase chain reaction; SARS-CoV-2 = Severe Acute Respiratory Syndrome coronavirus 2

Severe Acute Respiratory Syndrome coronavirus 2 (SARS-CoV-2) is the novel coronavirus responsible for the pandemic coronavirus disease 2019 (COVID-19). First identified in Wuhan, China, in late December 2019,[1] global transmission increased rapidly, with the first case of COVID-19 reported in the United States on January 19, 2020[2] and >1.34 million cases and nearly 81,000 deaths reported in the United States as of May 12, 2020.[3] While the typical presentation is respiratory symptoms (dry cough and dyspnea), a number of other associated symptoms have been described, including fever, diarrhea, abdominal pain, fatigue, and altered mental status. Potential neurologic manifestations are increasingly recognized but may be underreported.[4-8] A potential association between COVID-19 and Guillain-Barré syndrome (GBS) has been suggested in 2 recent editorial correspondences;[7,8] however, the temporal relationship of GBS antecedent to COVID-19 symptomatology raised a question of causality in 1 report.[7] In this brief report, we detail a case of bifacial weakness with paresthesia subtype GBS that demonstrated a postinfectious temporal association with COVID-19, developing approximately 2 weeks after the onset of COVID-19 symptomatology. This Health Insurance Portability and Accountability Act–compliant investigation was reviewed by the institutional review board at our medical school and was (BFP) exempt from further review and monitoring.

Case Report

A 21-year-old man presented to the emergency department with progressive 4-day history of fever, cough, dyspnea, diarrhea, nausea, headache, and sinonasal congestion. Aside from a medical history of hypertension, prediabetes, and class I obesity, the patient was otherwise healthy and denied tobacco, alcohol, substance abuse, or recent travel. Vital signs were remarkable for a body temperature of 37.5°C, blood pressure of 116/57 mm Hg, pulse of 76 beats per minute, and oxygen saturation of 95% on room air. Physical examination documented nonlabored respirations and clear lungs. Neurologic examination was intact. Chest radiographs (Fig 1) demonstrated patchy bilateral air space opacities without lobar consolidation.

A nasopharyngeal swab was performed, and a respiratory pathogen panel was negative for all tested pathogens. Additionally, nasopharyngeal and oropharyngeal swab specimens were sent to an outside private laboratory for SARS-CoV-2 real-time reverse transcriptase polymerase chain reaction (PCR) assay. He was discharged home with pulse oximetry monitoring, self-isolation instructions, and strict return precautions.

Received April 19, 2020; accepted after revision May 22.

From the Departments of Neurology (K.L.H., A.D.C., R.V.S.), Emergency Medicine (J.H.J., G.S.Z., L.M.W.), Radiology and Imaging Sciences (A.E.C., N.A.K.), and Otolaryngology-Head & Neck Surgery (N.A.K.), Indiana University School of Medicine, Indianapolis, Indiana.

Katherine L. Hutchins and Jaclyn H. Jansen are co-first authors.

Please address correspondence to Nicholas A. Koontz, MD, 550 N University Blvd, Room 0063, Indianapolis, IN 46202; e-mail: nakoontz@iupui.edu; @nakoontz

Indicates open access to non-subscribers at www.ajnr.org

Indicates article with supplemental on-line tables.

http://dx.doi.org/10.3174/ajnr.A6654

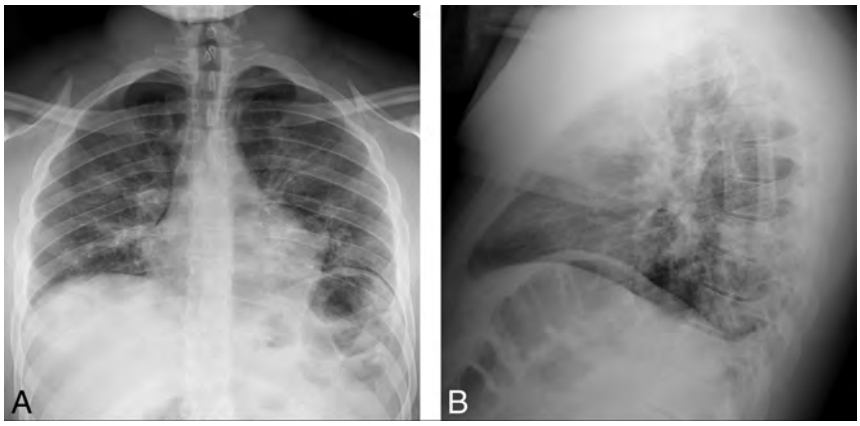

FIG 1. Initial chest radiographs in a patient with COVID-19 and subsequent bifacial weakness and paresthesia subtype Guillain-Barré syndrome. Posterior-anterior (*A*) and lateral (*B*) upright chest radiographs demonstrate low lung volumes with patchy bilateral air space opacities, but no lobar consolidation.

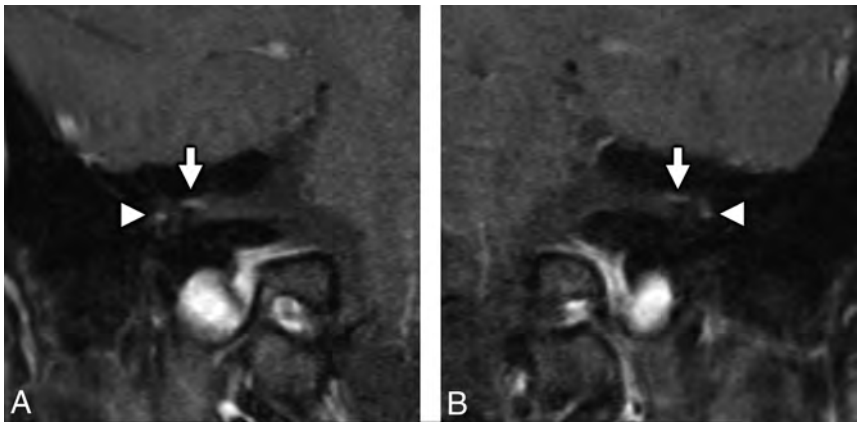

FIG 2. MR imaging of the temporal bones in a patient with antecedent COVID-19 and new-onset bifacial weakness and paresthesia subtype Guillain-Barré syndrome. Coronal postcontrast Tl-weighted fat-saturated MR imaging of the right (*A*) and left (*B*) temporal bones demonstrates abnormal "tuft-like" enhancement at the anterior-superior fundus of the internal auditory canal bilaterally (*white arrows*), corresponding to the distal canalicular segments of the facial nerves (CNVII). Note additional contrast enhancement along the tympanic segments of the facial nerve bilaterally (*white arrowheads*), which is greater in degree than typically encountered. Enhancement along the canalicular segments of the facial nerves (*white arrows*) is always considered abnormal on MR imaging, though mild tympanic segment enhancement is considered within normal limits.

During the next 24 hours, the patient experienced increased dizziness with oxygen saturation falling into the mid-80s documented by pulse oximetry. He returned to the emergency department febrile (body temperature of 39.1°C), mildly tachycardic (102 beats per minute), tachypneic (28 breaths per minute), and hypoxic (89% on room air). Chest radiographs demonstrated increased bilateral air space opacities, and a complete blood count revealed lymphopenia (absolute lymphocyte count of 0.7 K/mm^3). He was admitted for oxygen support and monitoring, and blood oxygenation was weaned from 2 L by nasal canula to room air. He was discharged home on hospital day 4, and his sent-out testing confirmed COVID-19 positivity the day after discharge.

He initially did well with convalescence at home, but on day 16 of illness, he began to experience right-sided facial numbness and weakness. During 24 hours, his symptoms became bilateral and resulted in severe dysarthria, necessitating a return to the emergency department. He also reported associated hypogeusia. Neurologic examination demonstrated a bilateral lower motor neuron pattern of facial weakness with otherwise normal cranial nerve (CN) examination findings, preserved strength and sensation in all extremities, and intact muscle stretch reflexes. He was admitted for observation and underwent MR imaging of the brain and temporal bones, as well as fluoroscopically guided lumbar puncture for CSF sampling. The CSF was negative for bacterial culture and stain and demonstrated normal glucose levels (65 mg/dL), no leukocytes, and mildly elevated protein levels (49 mg/dL). MR imaging demonstrated abnormal enhancement of the facial (CNVII) and abducens (CNVI) nerves bilaterally, as well as the right oculomotor nerve (CNIII) (Figs 2–4).

The patient was discharged with stable facial weakness, no progression of symptoms, and oxygen saturation of 99% on room air. Neurology outpatient follow-up was arranged with multiple CSF and serum lab results pending. On day 19 of illness, he reported new subjective bilateral lower extremity weakness, bilateral upper extremity paresthesia, and continued facial weakness, prompting readmission for further work-up and treatment. Repeat neurologic examination demonstrated unchanged bifacial weakness, but new grade 4/5 weakness in the deltoids and hip flexors bilaterally, as well as diffuse areflexia. MR imaging of the total spine was performed, which did not reveal any suspicious spinal cord signal abnormality or abnormal enhancement of the cord or cauda equina. Electromyography and nerve conduction studies demonstrated findings consistent with an acute sensorimotor polyneuropathy with both demyelinating and axonal features (On-line Tables 1–4).

For religious reasons, he declined treatment with intravenous immunoglobulin (Ig) and alternatively underwent treatment with 5 cycles of plasma exchange, which he tolerated well with slight improvement in facial weakness and paresthesia. Findings of CSF labs and serologies remained negative except for serum herpes simplex virus (HSV), immunoglobulin G (IgG), and immunoglobulin M (IgM), and the patient was discharged to inpatient rehabilitation. He declined a repeat lumbar puncture that was offered before discharge.

MATERIALS AND METHODS

Diagnostic Testing for COVID-19

At the initial emergency department visit, chest radiography (Fig 1) was performed, and nasopharyngeal swab specimens were sent for multiplex reverse transcription polymerase chain reaction via a NxTAG Respiratory Pathogen Panel (Luminex) to assess adenovirus, influenza A, influenza B, parainfluenza 1, parainfluenza 2, parainfluenza 3, parainfluenza 4, *Chlamydia pneumoniae*, *Mycoplasma pneumoniae*, bocavirus, coronavirus, respiratory syncytial virus A, respiratory syncytial virus B, metapneumovirus, rhinovirus, and enterovirus infection (On-line Table 5). Additional nasopharyngeal and oropharyngeal swab specimens were sent to an outside private laboratory (Viracor Eurofins Clinical Diagnostics) for SARS-CoV-2 real-time reverse-transcriptase polymerase chain reaction testing. During subsequent hospital readmissions and before final discharge, COVID-19 status was tested with nasopharyngeal/oropharyngeal swabs and SARS-CoV-2 PCR assays performed at our hospital laboratory.

Diagnostic Testing for GBS

MR imaging of the brain, temporal bones, and total spine was performed (Figs 2–4). Respective serologic, stool, and urine antibody tests, including antiganglioside (GM1, GD1b, and GQ1b IgG and IgM), aquaporin-4 receptor (IgG), HIV 1/2, HSV 1/2 (IgG and IgM), cytomegalovirus (IgM), *Mycoplasma pneumoniae* (IgG and IgM), *Borrelia burgdorferi* (IgG and IgM), *Bartonella* species (IgG and IgM), and syphilis (Venereal Disease Research Laboratory test), were obtained (On-line Tables 6–9). A serum angiotensin-converting enzyme level was also obtained to screen for sarcoidosis. CSF was tested for cell count, protein and glucose levels, red blood cell count, and infectious etiologies, including bacterial and fungal culture and stain, meningoencephalitis panel (varicella zoster virus, cytomegalovirus, enterovirus, HSV 1, HSV 2, human herpesvirus 6, human parechovirus, Epstein-Barr virus, *Cryptococcus neoformans/gattii*, *Escherichia coli*, *Haemophilus influenzae*, *Listeria monocytogenes*, *Neisseria meningitidis*, *Streptococcus agalactiae*, and *Streptococcus pneumoniae*), *Bartonella* species, syphilis, and Lyme disease (On-line Table 10).

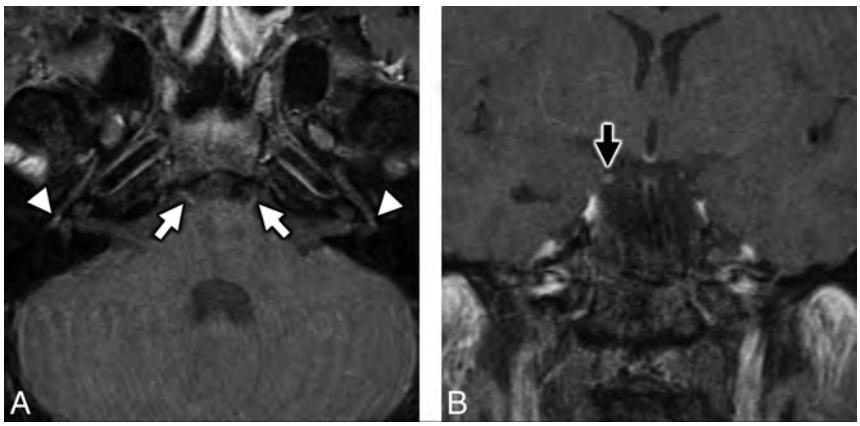

FIG 3. MR imaging of the temporal bones in a patient with antecedent COVID-19 and new-onset bifacial weakness and paresthesia subtype Guillain-Barré syndrome. Axial postcontrast T1-weighted fat-saturated MR imaging of the temporal bones (*A*) shows subtle-but-abnormal enhancement along the cisternal segments of the abducens nerves (CNVI) bilaterally (*white arrows*), as well as subtle enhancement along the tympanic segments of the intratemporal facial nerves (CNVII) bilaterally (*white arrowheads*). Coronal postcontrast T1-weighted fat-saturated MR imaging (*B*) shows subtle asymmetric enhancement along the cisternal segment of the right oculomotor nerve (CNIII, *black arrow*).

RESULTS

Specimen Testing for COVID-19

Positive SARS-CoV-2 viral status was confirmed via initial sent-out nasopharyngeal/oropharyngeal swabs. On subsequent hospital readmission, internal PCR reconfirmed SARS-CoV-2 viral status. Repeat PCR before discharge was negative for SARS-CoV-2 detection.

FIG 4. MRI of the brain in a patient with antecedent COVID-19 and new onset bifacial weakness and paresthesias subtype Guillain-Barré syndrome. Axial post-contrast T1-weighted SPoiled Gradient-Recalled (SPGR) MRI shows abnormal enhancement of the right oculomotor nerve (CNIII, *white arrow, A*), the cisternal segments of the abducens nerves (CNVI) bilaterally (*white arrowheads, B*), the distal canalicular segments of the facial nerves (CNVII) bilaterally (*black arrows, C*), and the proximal tympanic segments of the intratemporal facial nerves (CNVII) bilaterally (*black arrowheads, C*).

Specimen Testing for GBS

Serologic testing for infectious and inflammatory mimics was unremarkable apart from elevated HSV-1 IgG of >8.0 and initial HSV-1/2 IgM of 1.07 index values (On-line Tables 6–9). Repeat HSV-1/2 IgM at 10 days postpresentation was further elevated at 2.39 index values. CSF protein was mildly elevated (49 mg/dL, which corrected to 46 mg/dL when accounting for 2425 red blood cells) with no white blood cells. CSF stains were negative for bacterial or fungal organisms, and cultures demonstrated no growth. The CSF meningoencephalitis panel and *Bartonella* species, syphilis, and Lyme disease tests were also negative (On-line Table 10).

DISCUSSION

Our report details a case of bifacial weakness and paresthesia subtype Guillain-Barré syndrome that was temporally associated with COVID-19. In our case, a patient with antecedent community-acquired COVID-19 pneumonia developed rapidly progressive bilateral facial weakness, extremity paresthesia, and mild proximal extremity weakness without ataxia or other cranial neuropathies 16 days after the onset of COVID-19 symptomatology. He exhibited clinicoradiologic features most consistent with GBS, affecting CNVII bilaterally and lacking antiganglioside antibodies, concordant with prior reports of BFP subtype GBS.[8-10] Our patient demonstrated imaging findings that align with prior reports of GBS following antecedent viral infections.[11,12] Enhancement of the cranial nerves is a known MR imaging finding in GBS,[8,13,14] and most interesting, our patient demonstrated abnormal enhancement of CNVI bilaterally and the right CNIII, which were clinically asymptomatic. On the basis of clinical grounds, we suspect that this indicates subclinical disease in the BFP variant of GBS, rather than the Miller Fisher variant of GBS,[15] given lack of ophthalmoparesis and ataxia. Our patient did not demonstrate any typical spinal imaging manifestations of GBS, which may include thickening of the cauda equina nerve roots with enhancement, often with a ventral nerve root predilection.[16,17]

To date, a recent editorial correspondence reports a small observational series of 5 cases of suspected COVID-19–associated GBS,[8] but no prior detailed clinical reports have been published. In a previously reported case of possible COVID-19–associated GBS in a patient with recent travel to Wuhan, the patient manifested an atypical temporal profile with acute bilateral lower extremity weakness as an initial presenting symptom and subsequent development of COVID-19 pneumonia on hospital day 8, raising concern for coincidental disease processes and possible nosocomial infection.[7]

Our case demonstrates a postinfectious temporal relationship between antecedent SARS-CoV-2 infection and GBS symptomatology, but positive HSV serologies remain a confounder. Although ubiquitous, HSV infection has been reported as an extremely rare antecedent to GBS.[18-22] Whether in our case the GBS was directly caused by COVID-19, the COVID-19–associated systemic inflammatory response unmasked or exacerbated an HSV-mediated GBS, or the patient simply manifested unfortunately timed coexisting disease processes remains unknowable. However, we note prior immunologic research by Ziganshin et al[19] that demonstrated an increased risk of GBS triggering in simultaneous polyviral infection, including HSV, which might have important implications for the pathoetiology of GBS in our patient. Most important, the temporal association of antecedent COVID-19 and subsequent development of GBS symptomatology in our patient necessitates physicians being made aware of this possible linkage consideration.

GBS is a diverse disorder of the peripheral nervous system characterized by acute immune-mediated neuropathy, which may be broadly categorized into acute motor axonal neuropathy, acute inflammatory demyelinating polyradiculoneuropathy, and acute motor-sensory axonal neuropathy,[23-25] as well as subdivided into clinically distinct variants, such as Miller Fisher variant and BFP.[9,10,15] GBS is commonly associated with immune stimulation from antecedent bacterial or viral infection, including gastrointestinal infection and upper respiratory tract infections.[23-26] GBS is thought to be due, in great part, to molecular mimicry,[23] whereby antibodies created in response to infectious antigens cross-react with neurons and the myelin sheath, causing demyelination and/or axonal damage. GBS is typically multiphasic, with rapid progression, a prolonged plateau, and variable recovery with approximately 15%–20% permanent disability at 1 year.[23,27] GBS-related mortality is approximately 5%, often due to neuromuscular respiratory failure and autonomic dysfunction.[23,27] Early intravenous immunoglobulin or plasma exchange, along with supportive care, is the mainstay of therapy.

There are limited data regarding neurologic manifestations of COVID-19 infection. A recently published retrospective, observational case series from Mao et al[4] suggested that neurologic manifestations of COVID-19 may be underrecognized. They report neurologic manifestations in up to 36% of hospitalized patients with COVID-19, including dizziness (16.8%), headache (13.1%), and altered level of consciousness (7.5%), as well as impaired taste (5.6%), smell (5.1%), and vision (1.4%), but no cases of GBS. COVID-19 has recently been implicated as a presumptive cause of acute hemorrhagic necrotizing encephalopathy, which may represent an intracranial manifestation of a COVID-19–related cytokine storm.[5] There is also suspicion that the prothrombotic and proinflammatory states associated with COVID-19 may increase the incidence of cerebrovascular disease,[4,6] though there is a paucity of evidence in the currently published literature. Neurotropic animal and human coronaviruses have been identified,[28] and coronavirus-associated GBS has been previously reported, including Middle East Respiratory Syndrome.[29,30] Given genetic similarities among the coronaviruses, it is conceivable that similar neuropathology might be seen with SARS-CoV-2.

CONCLUSIONS

This report details a case of postinfectious acute peripheral polyneuropathy in a patient recently diagnosed with and convalescing from community-acquired COVID-19, highlighting the multidisciplinary collaboration required to diagnose and manage this complex patient. The clinicoradiologic features and temporal profile are most consistent with a BFP subtype of GBS. Given the paucity of data regarding neurologic manifestations of COVID-

19, this case highlights the need for continued close attention to and reporting of its potential neurologic sequelae.

Disclosures: Richard V. Scheer—*UNRELATED: Expert Testimony*: Hume Smith Geddes Green & Simmons. Lindsay Weaver—*UNRELATED: Employment*: Indiana State Department of Health, *Comments:* Chief Medical Officer.

REFERENCES

1. Zhu N, Zhang D, Wang W, et al; China Novel Coronavirus Investigating and Research Team. **A novel coronavirus from patients with pneumonia in China, 2019.** *N Engl J Med* 2020;382:727–33 CrossRef Medline
2. Holshue ML, DeBolt C, Lindquist S, et al; Washington State 2019-nCoV Case Investigation Team. **First case of 2019 novel coronavirus in the United States.** *N Engl J Med* 2020;382:929–36 CrossRef Medline
3. Centers for Disease Control and Prevention. **Coronavirus disease 2019 (COVID-19): cases in U.S. 2020.** https://www.cdc.gov/coronavirus/2019-ncov/cases-updates/cases-in-us.html#2019coronavirus-summary. Accessed May 13, 2020
4. Mao L, Jin H, Wang M, et al. **Neurologic manifestations of hospitalized patients with coronavirus disease 2019 in Wuhan, China.** *JAMA Neurol* 2020 Apr 10. [Epub ahead of print] CrossRef Medline
5. Poyiadji N, Shahin G, Noujaim D, et al. **COVID-19-associated acute hemorrhagic necrotizing encephalopathy: CT and MRI features.** *Radiology* 2020 Mar 31. [Epub ahead of print] CrossRef Medline
6. Zhang Y, Xiao M, Zhang S, et al. **Coagulopathy and antiphospholipid antibodies in patients with Covid-19.** *N Engl J Med* 2020;382:e38 CrossRef Medline
7. Zhao H, Shen D, Zhou H, et al. **Guillain-Barre syndrome associated with SARS-CoV-2 infection: causality or coincidence?** *Lancet Neurol* 2020;19:383–84 CrossRef Medline
8. Toscano G, Palmerini F, Ravaglia S, et al. **Guillain-Barre Syndrome associated with SARS-CoV-2.** *N Engl J Med* 2020;19:383–84 CrossRef Medline
9. Wakerley BR, Yuki N. **Isolated facial diplegia in Guillain-Barre syndrome: bifacial weakness with paresthesias.** *Muscle Nerve* 2015;52:927–32 CrossRef Medline
10. Kim JK, Oh SY, Sohn EH, et al. **When is facial diplegia regarded as a variant of Guillain-Barre syndrome?** *J Peripher Nerv Syst* 2015;20:32–36 CrossRef Medline
11. Hygino da Cruz LC Jr, Nascimento OJ, Lopes F, et al. **Neuroimaging findings of Zika virus-associated neurologic complications in adults.** *AJNR Am J Neuroradiol* 2018;39:1967–74 CrossRef Medline
12. Wu S, Zeng Y, Lerner A, et al. **Nervous system injury and neuroimaging of Zika virus infection.** *Front Neurol* 2018;9:227 CrossRef Medline
13. Zuccoli G, Panigrahy A, Bailey A, et al. **Redefining the Guillain-Barre spectrum in children: neuroimaging findings of cranial nerve involvement.** *AJNR Am J Neuroradiol* 2011;32:639–42 CrossRef Medline
14. Fulbright RK, Erdum E, Sze G, et al. **Cranial nerve enhancement in the Guillain-Barre syndrome.** *AJNR Am J Neuroradiol* 1995;16:923–25 Medline
15. Al Othman B, Raabe J, Kini A, et al. **Update: the Miller Fisher variants of Guillain-Barre syndrome.** *Curr Opin Ophthalmol* 2019;30:462–66 CrossRef Medline
16. Byun WM, Park WK, Park BH, et al. **Guillain-Barre syndrome: MR imaging findings of the spine in eight patients.** *Radiology* 1998;208:137–41 CrossRef Medline
17. Dodson SC, Koontz NA. **Spinal manifestations of systemic disease.** *Radiol Clin North Am* 2019;57:281–306 CrossRef Medline
18. Hao Y, Wang W, Jacobs BC, et al. **Antecedent infections in Guillain-Barre syndrome: a single-center, prospective study.** *Ann Clin Transl Neurol* 2019;6:2510–17 CrossRef Medline
19. Ziganshin RH, Ivanova OM, Lomakin YA, et al. **The pathogenesis of the demyelinating form of Guillain-Barre sndrome (GBS): proteopeptidomic and immunological profiling of physiological fluids.** *Mol Cell Proteomics* 2016;15:2366–78 CrossRef Medline
20. De Fine Olivarius B, Buhl M. **Herpes simplex virus and Guillain-Barre polyradiculitis.** *BMJ* 1975;1:192–93 CrossRef Medline
21. Yuki N, Susuki K, Odaka M, et al. **Overlapping Guillain-Barre syndrome and Bickerstaff's brainstem encephalitis associated with anti-GQ1b IgG antibody after herpes simplex virus infection.** *Acta Neurol Scand* 2001;104:57–60 CrossRef Medline
22. Hunt DP, Muse VV, Pitman MB. **Case records of the Massachusetts General Hospital: case 12-2013—an 18-year-old woman with pulmonary infiltrates and respiratory failure.** *N Engl J Med* 2013;368:1537–45 CrossRef Medline
23. Willison HJ, Jacobs BC, van Doorn PA. **Guillain-Barre syndrome.** *Lancet* 2016;388:717–27 CrossRef
24. Grimaldi-Bensouda L, Alperovitch A, Besson G, et al; Lucien Abenhaim for the GBS-PGRx Study Group. **Guillain-Barre syndrome, influenza-like illnesses, and influenza vaccination during seasons with and without circulating A/H1N1 viruses.** *Am J Epidemiol* 2011;174:326–35 CrossRef Medline
25. Dardiotis E, Sokratous M, Tsouris Z, et al. **Association between Helicobacter pylori infection and Guillain-Barre syndrome: a meta-analysis.** *Eur J Clin Invest* 2020;50:e13218 CrossRef Medline
26. Petras M, Lesna IK, Danova J, et al. **Is an increased risk of developing Guillain-Barre syndrome associated with seasonal influenza vaccination? A systematic review and meta-analysis.** *Vaccines (Basel)* 2020;8:E150 CrossRef Medline
27. Rajabally YA, Uncini A. **Outcome and its predictors in Guillain-Barre syndrome.** *J Neurol Neurosurg Psychiatry* 2012;83:711–18 CrossRef Medline
28. Desforges M, Le Coupanec A, Brison E, et al. **Neuroinvasive and neurotropic human respiratory coronaviruses: potential neurovirulent agents in humans.** *Adv Exp Med Biol* 2014;807:75–96 CrossRef Medline
29. Kim JE, Heo JH, Kim HO, et al. **Neurological complications during treatment of Middle East respiratory syndrome.** *J Clin Neurol* 2017;13:227–33 CrossRef Medline
30. Sharma K, Tengsupakul S, Sanchez O, et al. **Guillain-Barre syndrome with unilateral peripheral facial and bulbar palsy in a child: a case report.** *SAGE Open Med Case Rep* 2019;7:2050313X19838750 CrossRef Medline

Internal Auditory Canal Diverticula among Pediatric Patients: Prevalence and Assessment for Hearing Loss and Anatomic Associations

P.M. Bunch, M.E. Zapadka, C.M. Lack, E.P. Kiell, D.J. Kirse, and J.R. Sachs

ABSTRACT

BACKGROUND AND PURPOSE: Internal auditory canal diverticula are focal lucencies along the anterior-inferior aspect of the internal auditory canal fundus. Studies in adults report conflicting data on the etiology and clinical relevance of this finding. We would expect a pediatric study to help elucidate the significance of internal auditory canal diverticula. The primary goals of this study were to determine the temporal bone CT prevalence of diverticula among pediatric patients and to assess possible hearing loss and anatomic associations.

MATERIALS AND METHODS: For this retrospective study including 283 pediatric temporal bone CTs, 4 neuroradiologists independently assessed for diverticula. Discrepancies were resolved by consensus. One neuroradiologist assessed for an enlarged vestibular aqueduct, labyrinthine dysplasia, cochlear cleft, and otospongiosis. Patient demographics, audiologic data, and pertinent clinical history were recorded. One-way analysis of variance and the Fisher exact test were used to assess possible associations between diverticula and specific patient characteristics.

RESULTS: Diverticula were observed in 42/283 patients (14.8%) and were more commonly bilateral. There was no significant association with age, sex, hearing loss, enlarged vestibular aqueduct, labyrinthine dysplasia, or cochlear cleft. A statistically significant association was observed with otospongiosis ($P = .013$), though only 1 study patient had this disease.

CONCLUSIONS: Internal auditory canal diverticula are a common finding on pediatric temporal bone CT. In the absence of clinical or imaging evidence for otospongiosis, diverticula likely fall within the range of a normal anatomic variation. Familiarity with these findings may prevent neuroradiologists from recommending unnecessary additional testing in pediatric patients with isolated internal auditory canal diverticula.

ABBREVIATION: IAC = internal auditory canal

Internal auditory canal (IAC) diverticula are focal, well-demarcated osseous lucencies along the anterior-inferior aspect of the IAC fundus.[1,2] This finding has also been referred to as "cavitary otospongiosis"[3-5] and IAC "cupping."[6,7]

Previous radiologic studies of IAC diverticula report conflicting data on the underlying etiology and clinical relevance of this finding. More specifically, one study of temporal bone CT examinations obtained in a cohort of 47 patients with otospongiosis identified IAC diverticula in >30% of otospongiotic temporal bones and characterized the finding as representing cavitary otospongiosis.[5] However, temporal bone CT studies performed in larger cohorts report IAC diverticula in the absence of otospongiosis (ie, isolated IAC diverticula), with a prevalence of ~5%.[1,8] One of these studies reported an independent association between isolated IAC diverticula and sensorineural hearing loss,[8] and the other concluded that isolated IAC diverticula represent a normal anatomic variant not associated with hearing loss.[1]

These previous radiologic studies of IAC diverticula have been performed predominantly[1] or exclusively[5,8,9] in adults with no peer-reviewed published literature currently available on the prevalence of IAC diverticula among children. Given the rarity of otospongiosis among children and adolescents,[10] we expect that a study of IAC diverticula among pediatric patients would help elucidate whether isolated IAC diverticula represent normal anatomic variants or acquired pathology. We hypothesize that if

Received April 3, 2020; accepted after revision May 22.

From the Departments of Radiology (P.M.B., M.E.Z., C.M.L., J.R.S.), Otolaryngology, Head and Neck Surgery (E.P.K., D.J.K.), and Pediatrics (D.J.K.), Wake Forest School of Medicine, Winston Salem, North Carolina.

Previously presented as an electronic scientific poster at: Annual Meeting of the American Society of Head and Neck Radiology, October 2–6, 2019; Scottsdale, Arizona.

Please address correspondence to P.M. Bunch, MD, Department of Radiology, Wake Forest School of Medicine, Medical Center Blvd, Winston Salem, NC 27157; e-mail: paul.m.bunch@gmail.com; @pbunchmd

http://dx.doi.org/10.3174/ajnr.A6691

isolated IAC diverticula represent a normal variant, the pediatric prevalence should be comparable with the adult prevalence. Conversely, if isolated IAC diverticula are a manifestation of acquired pathology (eg, otospongiosis or other), we would expect the prevalence among children to be less than that in adults. The primary goals of this study were the following: 1) to determine the prevalence of IAC diverticula among pediatric patients on temporal bone CT, 2) to assess possible associations between IAC diverticula and hearing loss, and 3) to assess possible associations between IAC diverticula and other temporal bone CT findings of interest.

Most previous radiologic studies of IAC diverticula were performed with a single neuroradiologist reader.[1,8,9] Moreover, there is variability among these studies with respect to what is defined as constituting an IAC diverticulum. One previous study included 2 neuroradiologist readers, though interrater reliability was not reported in this study.[5] In our clinical practice, we have encountered uncertainty as to whether a mild contour irregularity of the IAC is sufficient to be classified as an IAC diverticulum. If IAC diverticula represent a clinically relevant finding, uncertainty and variability in radiologic diagnosis would be problematic. Thus, a secondary goal of this study was to assess interobserver variability with respect to what practicing neuroradiologists identify as IAC diverticula based on descriptions in the existing literature.

MATERIALS AND METHODS

Subjects

For this retrospective, Health Insurance Portability and Accountability Act–compliant, institutional review board–approved study, a local institutional radiology data base (mPower; Nuance Healthcare) was queried for patients satisfying the following inclusion criteria: 1) age younger than 18 years, and 2) temporal bone CT examination performed between December 2015 and February 2019. Examinations were excluded if a temporal bone CT had already been included in the study cohort for the same patient. Additionally, unilateral temporal bones were excluded if the diagnostic assessment of the IAC was precluded by severe artifacts or if no IAC was present.

Medical Record Review

Patient age, patient sex, and the presence or absence of a clinical diagnosis of otospongiosis were recorded. When available, audiogram data were also reviewed and used to classify hearing as normal, sensorineural hearing loss, conductive hearing loss, or mixed hearing loss.

Image Acquisition

All temporal bone CT examinations were performed within the health system of our institution on multidetector row CT systems. Given the retrospective nature of this study, there was variability with respect to CT scanners used to acquire images as well as specific CT acquisition parameters. However, most temporal bone CT examinations were acquired on a Discovery 750 HD (GE Healthcare) with the following acquisition parameters: 120 kV(peak), 250–330 mAs, 0.531 pitch, 1.0-second rotation time. Multiplanar reconstructions were generated, including 0.625-mm axial (9.6-cm FOV; bone plus kernel) and 0.6-mm coronal (9.6-cm FOV; bone plus kernel) images.

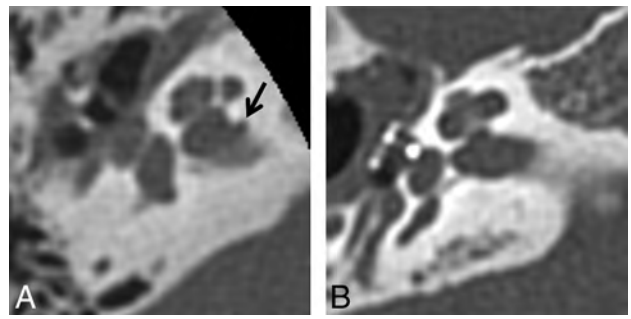

FIG 1. Axial temporal bone CT image (*A*) at the level of the inferior aspect of the right internal auditory canal demonstrates the typical appearance of an internal auditory canal diverticulum (*arrow*). An image obtained at the same level in a different patient without an internal auditory canal diverticulum is provided for comparison (*B*).

Reader Assessment

Four fellowship-trained neuroradiologists (3 years', 12 years', 4 years', and 6 years' subspecialty experience) served as readers for this retrospective study. Each reader participated in an initial image review as well as a subsequent image review. For both image reviews, the neuroradiologists were instructed to first assess the axial 0.625 mm bone algorithm images to determine the presence or absence of an IAC diverticulum (Fig 1). If necessary or desired, the coronal bone algorithm images could also be used to aid in making this determination. A subjective determination of the presence or absence of an IAC diverticulum was used rather than a minimum size threshold to be consistent with the described methods of Mihal et al,[1] Puac et al,[5] and Pippin et al.[8] In addition to the initial and subsequent image reviews in which the 4 neuroradiologists participated, 1 of the neuroradiologists (3 years' subspecialty experience) reviewed the temporal bone CT images to determine the presence or absence of an enlarged vestibular aqueduct, labyrinthine dysplasia, cochlear cleft, and otospongiosis.

Initial Review. For the initial image review, the readers were instructed to assess the temporal bone CT images for the presence or absence of IAC diverticula based on their current understanding of this entity as described in the literature. This nonstandardized initial review was intended to facilitate assessment of interobserver variability in the identification of IAC diverticula among practicing neuroradiologists. For the initial review, 100 temporal bone CT examinations were evaluated by all 4 neuroradiologists, and interrater reliability was calculated on the basis of the recorded assessments of these 100 examinations. All remaining temporal bone CT examinations were assessed by 2 neuroradiologist readers.

Subsequent Review. After the 4 neuroradiologists had completed their initial reviews, the group discussed the observed variability of the results and reviewed together a total of 10 representative discrepant cases selected from the 100-case cohort reviewed by all 4 neuroradiologists. On the basis of this discussion and

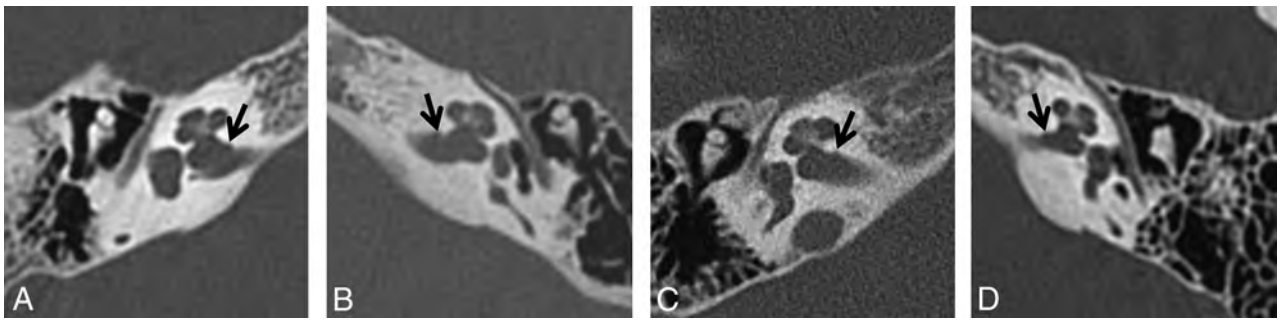

FIG 2. Visual threshold developed after the initial review and applied during the subsequent review by the 4 neuroradiologist readers. The visual threshold consists of axial temporal bone CT images obtained in 4 different patients and is intended to depict the minimum contour irregularity necessary to be considered an internal auditory canal diverticulum (*arrows*) for the second review performed in this study.

Table 1: Characteristics of the study group

Sex	
Male	157 (55%)
Female	126 (45%)
Age	
Mean (SD) (yr)	7.8 (4.8)
Minimum	6 weeks
Maximum	17 years
Audiogram (temporal bone sides)	
Normal	152 (27%)
Sensorineural loss	158 (28%)
Mixed loss	39 (7%)
Conductive loss	112 (20%)
Unavailable	100 (18%)

Table 2: Temporal bone CT findings within the study group

Individual Temporal Bones (Sides)	
Internal auditory canal diverticulum	
Yes	64 (11%)
No	497 (89%)
Enlarged vestibular aqueduct	
Yes	43 (8%)
No	518 (92%)
Labyrinthine dysplasia	
Yes	66 (12%)
No	495 (88%)
Cochlear cleft	
Yes	205 (37%)
No	356 (63%)
Otospongiosis	
Yes	2[a] (0.4%)
No	559 (99.6%)

[a] Single patient who also had clinical diagnosis of bilateral otospongiosis.

discrepant case review, a consensus visual threshold for what should be called an IAC diverticulum (Fig 2) was proposed and developed for use in the second review, with the understanding that a candidate diverticulum should be at least as conspicuous as the examples in the agreed-upon threshold to be considered present.

All temporal bone CT examinations identified by at least 1 neuroradiologist as showing an IAC diverticulum (unilateral or bilateral) in the initial review were included in the second review to be reassessed. The examinations for which no neuroradiologist identified an IAC diverticulum on the initial review were considered not to contain an IAC diverticulum and were, therefore, excluded from the second review. The time interval between the initial and subsequent reviews was 2 months.

For the subsequent image review, all 4 neuroradiologists reviewed the CT images of the included temporal bone CT examinations (both sides) to assess the presence of an IAC diverticulum using the agreed-upon visual threshold. The recorded results were reviewed, and discrepancies were resolved by consensus.

Statistical Analysis

Mean, SD, and range are reported for continuous variables. Absolute and relative frequencies are reported for categoric variables. The Fisher exact test was used to compare proportions. One-way analysis of variance was used to compare continuous variables. The Light κ coefficient was calculated to assess interrater reliability. All analyses were performed with JMP, Version 14 (SAS Institute), and a P value $< .05$ indicated a statistically significant difference.

RESULTS

Subjects

A total of 284 temporal bone CT examinations (568 sides) were reviewed. Among these, 6 sides were excluded for artifacts precluding diagnostic assessment of the IAC, and 1 side was excluded for congenital absence of the IAC, which yielded a study cohort of 283 patients and 561 temporal bones. Audiologic data were available in 234 patients (82.6%). One patient (0.4%) had a clinical diagnosis of otospongiosis. Patient age, sex, and audiogram data are summarized in Table 1. Temporal bone CT findings are summarized in Table 2.

Reader Assessment

Initial Review. On the initial review of 283 patients (561 individual temporal bones), neuroradiologist 1 identified IAC diverticula in 19.1% of individual temporal bones (24.7% of patients), neuroradiologist 2 identified IAC diverticula in 13.1% of temporal bones (8.5% of patients), neuroradiologist 3 identified IAC diverticula in 9.0% of temporal bones (9.2% of patients), and neuroradiologist 4 identified IAC diverticula in 5.1% of temporal bones (3.5% of patients). For the 100 examinations reviewed by all 4

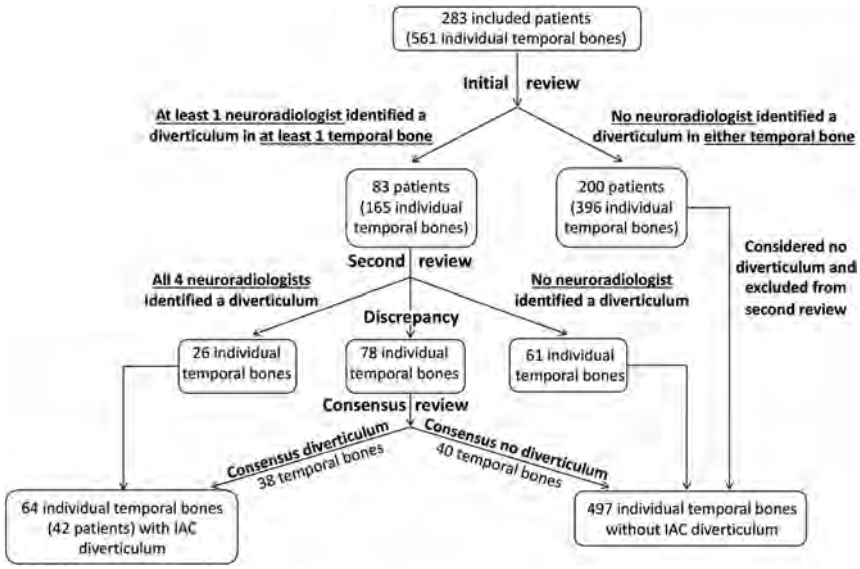

FIG 3. Flow chart depicting the initial and subsequent image reviews.

Table 3: Internal auditory canal diverticula association assessment

	Internal Auditory Canal Diverticulum		
	Yes	No	*P*
Sex[a]			
Male	28	129	.13
Female	14	112	
Age (mean) (SD) (yr)	7.7 (5.0)	7.8 (4.8)	.91
Audiogram[b]			
Normal hearing	20	132	.65
Hearing loss	36	273	
Conductive	16	96	.86
Sensorineural	16	142	.48
Mixed	4	35	.79
Enlarged vestibular aqueduct[b]			
Yes	2	41	.21
No	62	456	
Labyrinthine dysplasia[b]			
Yes	7	59	1.00
No	57	438	
Cochlear cleft[b]			
Yes	30	175	.07
No	34	322	
Otospongiosis[b]			
Yes	2	0	.013
No	62	497	

[a] Denotes number of patients.
[b] Denotes number of individual temporal bones (sides).

neuroradiologists, the Light κ coefficient was 0.44, indicating moderate agreement.

Subsequent Review. A total of 83 temporal bone CT examinations were included in the subsequent review (Fig 3), having been identified by at least 1 neuroradiologist as having an IAC diverticulum on at least 1 side. Following consensus review, IAC diverticula were present in 42 patients (14.8% of the 283 subject cohort) (mean age, 7.7 ± 5.0 years; range, 2 months to 17 years) and 64 IACs (11.4% of the 561 included individual temporal bones). IAC diverticula were bilateral in 22 patients (52.4%) and unilateral in 20 patients (47.6%). For these 83 temporal bone CT examinations included in the subsequent review, the Light κ coefficient was 0.48, indicating moderate agreement.

Association Assessment

There was no statistically significant association between IAC diverticula (Table 3) and age ($P = .91$). IAC diverticula were more common among males (17.8%) than females (11.0%); however, this observed difference was not statistically significant ($P = .13$). No statistically significant association was observed between IAC diverticula and conductive ($P = .86$), sensorineural ($P = .48$), or mixed hearing loss ($P = .79$). Additionally, there were no statistically significant associations between IAC diverticula and an enlarged vestibular aqueduct ($P = .21$), labyrinthine dysplasia ($P = .1.00$), or cochlear cleft ($P = .07$). The 1 child in the study cohort with otospongiosis also had bilateral IAC diverticula; thus, a statistically significant association between IAC diverticula and otospongiosis ($P = .013$) was observed.

DISCUSSION

IAC diverticula have been a topic of interest in the recent radiologic[1,5,8] and otolaryngologic[2,9,11,12] literature, and there is uncertainty with respect to the underlying etiology and clinical relevance of this finding. IAC diverticula have been described in otospongiotic temporal bone specimens,[13,14] have been identified in >30% of patients with otospongiosis,[5,12] and may be associated with poorer postoperative audiologic outcomes following stapedotomy for otospongiosis.[11] However, IAC diverticula have also been identified histologically[2,6,7] and radiologically[1,8,9] in the absence of clinical, histopathologic, or imaging evidence of otospongiosis. Although there are some data suggesting an association between isolated IAC diverticula and sensorineural hearing loss,[8] the preponderance of evidence indicates that isolated IAC diverticula are more likely a normal anatomic variant.[1,2,9]

The current study documents that isolated IAC diverticula, occurring in the absence of otospongiosis, are a relatively common finding on pediatric temporal bone CT, occurring in nearly 15% of patients and comprising 97% of IAC diverticula in this

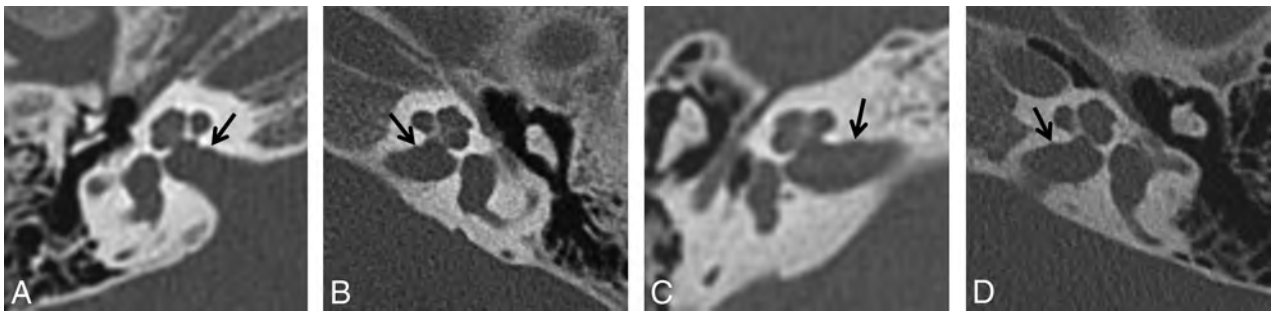

FIG 4. Axial temporal bone CT images from 4 different patients depict representative examples of subtle IAC contour irregularities (*arrows*) determined during consensus review of discrepant cases to not reach the visual threshold necessary to be considered an IAC diverticulum.

cohort. Furthermore, this study supports the hypothesis that isolated IAC diverticula fall within the range of normal anatomic variation because no statistically significant associations were observed between IAC diverticula and hearing loss, enlarged vestibular aqueduct, or labyrinthine dysplasia.

Only 1 patient in this pediatric cohort had clinical or imaging evidence of otospongiosis; however, this 1 patient also had bilateral IAC diverticula. Although firm conclusions should not be drawn on the basis of findings in a single patient, this association is in keeping with previous work indicating that IAC diverticula are more frequently observed in the presence of otospongiosis[5,12] and hypothesizing a predilection for otospongiosis to involve the anterior-inferior aspect of the IAC fundus in addition to the region of the fissula ante fenestram.[5,8]

The observed prevalence of IAC diverticula in this pediatric cohort (11.4% of IACs, 14.8% of patients) is higher than the 5%–6% prevalence reported in previous large radiologic studies[1,8,9] but less than the 25% prevalence reported in a small histologic study.[2] The reasons for the higher observed prevalence in this study compared with previous radiologic studies are unclear and warrant further investigation.

One possibility is that the consensus visual threshold used in this study represents a lower threshold for classifying an IAC diverticulum as present relative to previous published work on the topic. However, this is difficult to determine with confidence because a similar visual threshold was not provided with other studies of IAC diverticula.[1,5,8] Of note, Mihal et al[1] reported that 25% of isolated IAC diverticula observed in their study were < 0.9 mm, and Pippin et al[8] described the appearance of some IAC diverticula as "a small notch."

Another possible explanation for the higher prevalence of IAC diverticula observed in this pediatric study compared with previous radiologic studies performed predominantly or exclusively in adults is that IAC diverticula represent an embryologic remnant of the formation of the otic capsule from 14 ossification centers analogous to the fissula ante fenestram, the fossula post fenestram, and the hypoattenuated focus in the anterior otic capsule.[2,15-17] In such a scenario, the higher prevalence of IAC diverticula in this pediatric cohort relative to larger adult cohorts could be explained if in most children, the incompletely mineralized bone or cartilage corresponding to IAC diverticula became replaced or filled in by fully mineralized bone over the course of development, as is believed to occur with the cochlear cleft[18] and the hypoattenuated focus in the anterior otic capsule.[17] An association between IAC diverticula and the cochlear cleft as well as younger age might be expected if this hypothesis were true; however, none was observed in this study. These possibilities could be further investigated by a longitudinal study.

A secondary goal of this study was to assess interobserver variability in the identification of IAC diverticula, which has not been a focus of previous reports. In both our initial and subsequent reviews, there was substantial interobserver variability among the 4 experienced neuroradiologist readers in determining whether an IAC diverticulum was present despite the implementation of an agreed-upon visual threshold. During consensus review, discussions often centered on whether a subtle contour irregularity simply represented mild generalized undulation of the IAC versus a focal IAC diverticulum (Fig 4). These findings suggest that other neuroradiologists may also face uncertainty as to what exactly does and does not constitute an IAC diverticulum on temporal bone CT for purposes of both clinical practice and future research. Although our findings suggest isolated IAC diverticula to be a normal anatomic variant without clinical significance, a clear, easily applicable IAC diverticulum definition or threshold with relatively low interobserver variability would be useful for future research studies and particularly important in the event that isolated IAC diverticula are someday shown to be clinically relevant.

CONCLUSIONS

Internal auditory canal diverticula are a common finding on pediatric temporal bone CT, seen in approximately 15% of patients and 11% of IACs. There is no statistically significant association with hearing loss or congenital inner ear anomaly. In the absence of clinical or imaging evidence of otospongiosis, internal auditory canal diverticula likely fall within the range of normal anatomic variation. Familiarity with these findings may prevent neuroradiologists from recommending unnecessary additional testing in pediatric patients with isolated internal auditory canal diverticula.

REFERENCES

1. Mihal DC, Feng Y, Kodet ML, et al. **Isolated internal auditory canal diverticula: a normal anatomic variant not associated with sensorineural hearing loss.** *AJNR Am J Neuroradiol* 2018;39:2340–44 CrossRef Medline
2. Muelleman T, Maxwell AK, Lopez I, et al. **Histopathologic characteristics of internal auditory canal diverticula.** *Otol Neurotol* 2019;40:e653–56 CrossRef Medline

3. Makarem AO, Hoang TA, Lo WW, et al. **Cavitating otosclerosis: clinical, radiologic, and histopathologic correlations.** *Otol Neurotol* 2010;31:381–84 CrossRef Medline
4. Bou-Assaly W, Mukherji S, Srinivasan A. **Bilateral cavitary otosclerosis: a rare presentation of otosclerosis and cause of hearing loss.** *Clin Imaging* 2013;37:1116–18 CrossRef Medline
5. Puac P, Rodríguez A, Lin HC, et al. **Cavitary plaques in otospongiosis: CT findings and clinical implications.** *AJNR Am J Neuroradiol* 2018;39:1135–39 CrossRef Medline
6. Kollias S. Imaging of the congenitally malformed temporal bone. In: Lemmerling M, Kollias S, eds. *Radiology of the Petrous Bone*. Springer-Verlag; 2004:121
7. Gulya A, Schuknecht H. The inner ear. In: Gulya A, ed. *Gulya and Schuknecht's Anatomy of the Temporal Bone with Surgical Implications*. 3rd ed. Informa Healthcare; 2007:168–69
8. Pippin KJ, Muelleman TJ, Hill J, et al. **Prevalence of internal auditory canal diverticulum and its association with hearing loss and otosclerosis.** *AJNR Am J Neuroradiol* 2017;38:2167–71 CrossRef Medline
9. Muelleman TJ, Pippin K, Shew M, et al. **The size of internal auditory canal diverticula is unrelated to degree of hearing loss.** *Laryngoscope* 2020;130:1011–15 CrossRef Medline
10. Lescanne E, Bakhos D, Metais JP, et al. **Otosclerosis in children and adolescents: a clinical and CT-scan survey with review of the literature.** *Int J Pediatr Otorhinolaryngol* 2008;72:147–52 CrossRef Medline
11. Shim YJ, Bae YJ, An GS, et al. **Involvement of the internal auditory canal in subjects with cochlear otosclerosis: a less acknowledged third window that affects surgical outcome.** *Otol Neurotol* 2019;40:e186–90 CrossRef Medline
12. Wang F, Yoshida T, Shimono M, et al. **Significance of internal auditory canal diverticula in ears with otosclerosis.** *Acta Otolaryngol* 2018;138:1066–69 CrossRef Medline
13. Schuknecht HF, Barber W. **Histologic variants in otosclerosis.** *Laryngoscope* 1985;95:1307–17 CrossRef Medline
14. Hueb MM, Goycoolea MV, Paparella MM, et al. **Otosclerosis: the University of Minnesota temporal bone collection.** *Otolaryngol Head Neck Surg* 1991;105:396–405 CrossRef Medline
15. Anson BJ, Cauldwell EW, Bast TH. **The fissula ante fenestram of the human otic capsule; developmental and normal adult structure.** *Ann Otol Rhinol Laryngol* 1947;56:957–85 CrossRef Medline
16. Bast T, Anson B. *The Temporal Bone and the Ear*. CC Thomas; 1949
17. Moser T, Veillon F, Sick H, et al. **The hypodense focus in the petrous apex: a potential pitfall on multidetector CT imaging of the temporal bone.** *AJNR Am J Neuroradiol* 2008;29:35–39 CrossRef Medline
18. Chadwell JB, Halsted MJ, Choo DI, et al. **The cochlear cleft.** *AJNR Am J Neuroradiol* 2004;25:21–24 Medline

Deep Learning for Pediatric Posterior Fossa Tumor Detection and Classification: A Multi-Institutional Study

J.L. Quon, W. Bala, L.C. Chen, J. Wright, L.H. Kim, M. Han, K. Shpanskaya, E.H. Lee, E. Tong, M. Iv, J. Seekins, M.P. Lungren, K.R.M. Braun, T.Y. Poussaint, S. Laughlin, M.D. Taylor, R.M. Lober, H. Vogel, P.G. Fisher, G.A. Grant, V. Ramaswamy, N.A. Vitanza, C.Y. Ho, M.S.B. Edwards, S.H. Cheshier, and K.W. Yeom

ABSTRACT

BACKGROUND AND PURPOSE: Posterior fossa tumors are the most common pediatric brain tumors. MR imaging is key to tumor detection, diagnosis, and therapy guidance. We sought to develop an MR imaging–based deep learning model for posterior fossa tumor detection and tumor pathology classification.

MATERIALS AND METHODS: The study cohort comprised 617 children (median age, 92 months; 56% males) from 5 pediatric institutions with posterior fossa tumors: diffuse midline glioma of the pons ($n = 122$), medulloblastoma ($n = 272$), pilocytic astrocytoma ($n = 135$), and ependymoma ($n = 88$). There were 199 controls. Tumor histology served as ground truth except for diffuse midline glioma of the pons, which was primarily diagnosed by MR imaging. A modified ResNeXt-50-32x4d architecture served as the backbone for a multitask classifier model, using T2-weighted MRIs as input to detect the presence of tumor and predict tumor class. Deep learning model performance was compared against that of 4 radiologists.

RESULTS: Model tumor detection accuracy exceeded an AUROC of 0.99 and was similar to that of 4 radiologists. Model tumor classification accuracy was 92% with an F_1 score of 0.80. The model was most accurate at predicting diffuse midline glioma of the pons, followed by pilocytic astrocytoma and medulloblastoma. Ependymoma prediction was the least accurate. Tumor type classification accuracy and F_1 score were higher than those of 2 of the 4 radiologists.

CONCLUSIONS: We present a multi-institutional deep learning model for pediatric posterior fossa tumor detection and classification with the potential to augment and improve the accuracy of radiologic diagnosis.

ABBREVIATIONS: PF = posterior fossa; EVD = external ventricular drain; CAMs = class activation maps; DMG = diffuse midline glioma of the pons; EP = ependymoma; MB = medulloblastoma; PA = pilocytic astrocytoma; PF = posterior fossa; ROC = receiver operating characteristic; t-SNE = t-distributed stochastic neighbor embedding

Pediatric brain tumors are the most common solid cancer and the leading cause of cancer-related deaths in children, with approximately 4600 new diagnoses per year in the United States alone.[1,2] MR imaging plays a key role in tumor detection, and preliminary imaging diagnosis[3] helps guide initial management.

While the final diagnosis and treatment depend on surgical specimens, accurate classification before surgery can help optimize the surgical approach and the extent of tumor resection. MR imaging contributes to presurgical planning by defining the spatial relationship of the tumor within the brain. In addition, it allows high-dimensional image-feature analysis[4] that

Received January 12, 2020; accepted after revision May 27.

From the Departments of Neurosurgery (J.L.Q., G.A.G., M.S.B.E.), Electrical Engineering (E.H.L.), Radiology (E.T., M.I.), and Pathology (H.V.), Stanford University, Stanford, California; Department of Radiology (W.B., J.S., M.P.L., K.W.Y.), and Division of Child Neurology (P.G.F.), Lucile Packard Children's Hospital, Stanford University, Palo Alto, California; Department of Urology (L.C.C.), Stanford University School of Medicine (L.H.K., M.H., K.S.), Stanford, California; Department of Radiology (J.W.), Seattle Children's Hospital, University of Washington School of Medicine, Seattle, Washington; Departments of Clinical Radiology & Imaging Sciences (K.R.M.B., C.Y.H.), Riley Children's Hospital, Indiana University, Indianapolis, Indiana; Departments of Radiology (T.Y.P.), Boston Children's Hospital, Boston, Massachusetts; Departments of diagnostic Imaging (S.L.), and Neurosurgery (M.D.T.), and Haematology/Oncology (V.R.), The Hospital for Sick Children, University of Toronto, Toronto, Ontario, Canada; Department of Neurosurgery (R.M.L.), Dayton Children's Hospital, Wright State University Boonshoft School of Medicine, Dayton, Ohio; Division of Pediatric Hematology/Oncology (N.A.V.), Department of Pediatrics, University of Washington, Seattle Children's Hospital, Seattle Washington; Fred Hutchinson Cancer Research Center (N.A.V.), Seattle, Washington; and Departments of Neurosurgery (S.H.C.), University of Utah School of Medicine, Salt Lake City, Utah.

Paper previously presented, in part, at: Annual Meeting of the American Academy of Neurological Surgery/Congress of Neurological Surgery, Section on Pediatric Neurological Surgery.

J.L. Quon and W. Bala contributed equally to this work.

Please address correspondence to Kristen W. Yeom, Department of Radiology, Lucile Packard Children's Hospital, Stanford University School of Medicine, 725 Welch Rd, MC 5654, Palo Alto, CA 94304; e-mail: kyeom@stanford.edu

Indicates article with supplemental on-line tables.

Indicates article with supplemental on-line photos.

http://dx.doi.org/10.3174/ajnr.A6704

can potentially be correlated to the molecular profiling[5-8] included in recent updates to the World Health Organization brain tumor classification system.[9]

Modern advances in computing power and machine learning tools such as deep learning can augment real-time clinical diagnosis.[10,11] Deep learning is an improvement over radiomics and other traditional machine learning approaches that use labor- and time-intensive handcrafted feature extraction.[3,4,11] In this study, we aimed to develop an MR imaging–based deep learning model for predicting pediatric posterior fossa (PF) tumor pathology and to compare its performance against that of board-certified radiologists. We targeted PF tumors, given their high incidence in the pediatric population and leveraged a large, multi-institutional image dataset for deep learning.

MATERIALS AND METHODS

Study Cohort

Data-use agreements were developed between the host institution (Stanford Lucile Packard Children's Hospital) and 4 academic pediatric hospitals across North America (The Hospital for Sick Children, Seattle Children's, Indiana Riley Children's, Boston Children's) for this retrospective, multicenter study, after institutional review board approval at each institution. The following served as the inclusion criteria for 803 patients with tumors: brain MR imaging of treatment-naïve PF brain tumors: medulloblastoma (MB), ependymoma (EP), pilocytic astrocytoma (PA), and diffuse midline glioma of the pons (DMG, formerly DIPG); and tissue specimens that served as ground truth pathology except for DMG. A subset of patients were included who required emergent ventricular drain placement before tumor resection or other therapies. Brain MR imaging from 199 children without brain tumors were randomly sampled from the normal database of the host institution to serve as controls. A board-certified pediatric neuroradiologist (K.W.Y. with >10 years' experience), with a Certificate of Added Qualification, visually inspected all scans for quality control to confirm that they met the inclusion criteria.

The study cohort was subdivided into development (training and validation) and held-out test sets using stratified random sampling by tumor subtype. For tumor MRIs, the breakdown was 70% and 10% for the training/validation sets and 20% for the test set. For patients with >1 preintervention scan, all scans of that patient were included in either the development or test set, with no crossover. For control MRIs without tumor, data distribution was 10% and 90% for the validation and held-out test sets, respectively, as normal MRIs were not used to train the model.

MR Imaging Protocols

MR imaging scans were obtained at 1.5 or 3T at multiple centers with equipment from the following vendors: GE Healthcare, Siemens, Philips, and Toshiba Medical Systems (Canon Medical Systems). The T2 scans were the following: T2 TSE clear/sense, T2 FSE, T2 PROPELLER, T2 BLADE (Siemens), T2 drive sense (TR/TE = 2475.6–9622.24/80–146.048; slice thickness = 1–5 mm with 0.5-or 1-mm skip; matrix ranges = 224–1024 × 256–1024. T1 postgadolinium scans included T1 MPRAGE, T1 BRAVO (GE Healthcare), T1 fast-spoiled gradient recalled, T1 spoiled gradient-echo, and T1 spin-echo. ADC maps were created using a mono exponential algorithm with b-values from 0 to 1000 s/mm^2, varying by institution.

Image Processing and Data Augmentation

Axial DICOM images were processed using the Python language with the pydicom (https://pypi.org/project/pydicom/) and SimpleITK (https://anaconda.org/SimpleITK/simpleitk) packages. Images were resampled to 256 × 256 pixels in the axial dimension. Slice thickness was not modified. Data augmentation was performed by incorporating random flips, rotations, translations, and crops to 224 × 224 pixels to improve model generalizability. Gray-scale images were fed as RGB color images into an adapted ResNeXt model (https://github.com/titu1994/Keras-ResNeXt).

Ground Truth Labels

Pathology from surgical specimens served as ground truth (MB, EP, PA) except for most patients with DMG who were diagnosed primarily by MR imaging. An attending pediatric neuroradiologist (K.W.Y.) manually classified each axial slice as having tumor versus no tumor: A slice was considered positive if any tumor was visible.

Deep Learning Model Architecture

We chose a 2D ResNeXt-50-32x4d deep learning architecture (https://github.com/titu1994/Keras-ResNeXt) rather than a 3D architecture, given the wide variation in slice thickness across scans. Transfer learning was implemented using weights from a model pretrained on ImageNet (http://image-net.org/),[12] a consortium of >1.2 million images with 1000 categories (On-line Fig 1*A*), for all layers except the final fully connected layer, which was modified to predict 1 of 5 categories: no tumor, DMG, EP, MB, or PA. The model was trained to minimize cross-entropy loss, or error, between the predicted and actual tumor type. The architecture was modified to predict the relative slice position of tumor tissue within the entire scan, calculated by interpolating the most inferior axial slice as zero and the most superior as 1 (On-line Fig 1*B*). Relative slice position was included to account for differences in slice thickness in the z-plane across different scans. Thus, position was normalized to each individual patient. With normalization, the zero position referred to the foramen magnum; the 1 position, to the vertex; and 0.5 varied slightly between the upper midbrain and the midbrain-thalamic junction, depending on head size and image acquisition. This component was trained to minimize mean-squared loss between the predicted-versus-actual slice location. Setting the slice position contribution to 10% of the total loss had the most improvement (On-line Table 1). A final ensemble of 5 individual models was used to generate a confidence-weighted vote for the predicted class for each slice (On-line Fig 1*C*). To generate the model prediction for the entire scan, we aggregated all slice-level predictions. Scans with a proportion of tumor slices that exceeded a certain threshold were considered to have tumor (On-line Fig 1*D*). Based on the results from our training and validation sets, the minimal detection threshold was set to 0.05. For scans predicted to have tumor, the model then predicted the tumor subtype using a confidence-weighted voting system (On-line Fig 1*E*).

Table 1: Complete dataset of 803 patients from 5 institutions with 4 tumor types[a]

	Institution 1	Institution 2	Institution 3	Institution 4	Institution 5
MB	90	117	20	30	41
DMG	85	0	0	45	21
EP	42	41	41	22	8
PA	129	0	0	45	26

[a] One hundred eighty-six patients with no T2 sequences or only postintervention imaging were excluded.

Table 2: A total of 739 scans were distributed into a training set, a validation set, and a held-out test set

	Training	Validation	Test	Total
MB	242	34	55	331
DMG	88	10	24	122
EP	83	13	15	111
PA	114	20	41	175
Total	527	77	135	739

Model Training

An Ubuntu computer (https://ubuntu.com/download) with 4 TitanXp Graphic Processing Units (NVIDA) with 12 GB of memory was used for model development. Batch size was 160 slices per iteration. Training was performed using Adam optimization with an initial learning rate of 0.003 for 50 epochs and a cosine annealing learning rate decay to zero. Drop-out was set to 10% in the final fully connected layer to reduce overfitting. All model layers were fined-tuned throughout training. Models were saved if they improved validation set performance following a 10-epoch patience period. The top 5 models with the best validation results were selected for the final slice-level ensemble model.

Model Evaluation

Tumor-detection accuracy was evaluated based on whether the model correctly predicted the presence or absence of a tumor for the entire scan. Receiver operating characteristic (ROC) curves were generated by varying the set threshold for the proportion of tumors slices. For tumor classification, the F_1 score was calculated as the harmonic mean of precision (positive predictive value) and recall (sensitivity). Sensitivity and specificity for each tumor type were calculated by grouping all of the nontarget tumors together as negative examples.

Radiologist Interpretation

Board-certified attending radiologists with Certificates of Added Qualification in either Pediatric Radiology (J.S. with >10 years' experience; M.P.L. with >5 years' experience) or Neuroradiology (M.I. with >5 years' experience; E.T. with >2 years' experience) were given all T2 scans from the held-out test set and asked to detect tumors and select pathology among the 4 subtypes (MB, EP, PA, DMG). Radiologists were blinded to the ground truth labels and other clinical information and allowed to interpret at their own pace. They were permitted to window the scans and view in all orientations (axial, sagittal, or coronal).

Comparative Performance and Statistical Analysis

Subgroup analysis of model classification accuracy was performed using a Fisher's exact test. Radiologists' tumor detection sensitivity and specificity were plotted against the tumor-detection ROC curve of the model. Model and radiologists' tumor-detection and classification accuracy were compared using McNemar's test, with a P value threshold of .05.

RESULTS

PF Tumor Dataset

Of 803 patients with the 4 tumor types from 5 pediatric hospitals (Table 1), we excluded 186 patients due to lack of T2 scans, resulting in a total of 617 patients with tumors. Ages ranged from 2.5 months to 34-years old (median, 81 months); 56% were boys. Some patients had multiple preintervention scans from different dates, resulting in a total of 739 T2 scans. The training, validation, and test sets included 527, 77, and 135 scans, respectively (Table 2).

Deep Learning Model

Given that radiologists benefit from using multiple image sequences, we isolated a subset of the tumor cohort ($n = 260$ scans) with all 3 MR imaging sequences (T2-weighted, T1-weighted post-gadolinium, and ADC). To identify the MR imaging sequences most likely to allow successful model development, we compared the use of these 3 sequences versus a single T2-weighted scan (T2-scan) as model input. Surprisingly, we found superior initial model performance with T2-scans alone (On-line Table 2) and thus focused on T2-scans. Given that T2-based MRIs are also commonplace among clinical protocols for the initial evaluation of clinical symptoms, a deep learning model using T2 alone would also be more broadly applicable.

Several convolutional deep learning approaches, including the ResNet, ResNeXt, and DenseNet (https://towardsdatascience.com/densenet-2810936aeebb) architectures with varying numbers of layers as well as the InceptionV3 architecture (https://blog.paperspace.com/popular-deep-learning-architectures-resnet-inceptionv3-squeezenet/), were evaluated on a subset of the training data. Preliminary experiments demonstrated that the ResNeXt-50-32x4d architecture best balanced accuracy with computational cost. Our final model architecture consisted of modified 2D ResNeXt-50-32x4d residual neural networks to generate a prediction for each axial slice in the scan (On-line Fig 1*A*). The baseline ResNeXt-50-32x4d, which classified each T2 axial slice as no tumor, MB, EP, PA, or DMG, achieved an F_1 score of 0.60 per axial slice. Given that radiologists and clinical experts often use tumor location to assess brain tumors, we modified the architecture for multitask learning to also predict the relative position of each slice, which improved performance by 4% (On-line Fig 1*A*-, *B*). Because prior studies have shown that combining multiple individual models improves overall performance by reducing variance between predictions,[13] we created an ensemble model comprising the 5 best-performing individual models (On-line Fig 1*C*), as this further improved accuracy while maintaining reasonable computational requirements (On-line Table 3).

To generate scan-level predictions, we then tallied all individual slice predictions (tumor versus no tumor) using a confidence-based voting algorithm (On-line Fig 1*D*). This schema resulted in accurate scan-level prediction of tumor versus no tumor with an area under the ROC curve of 0.99. Setting the

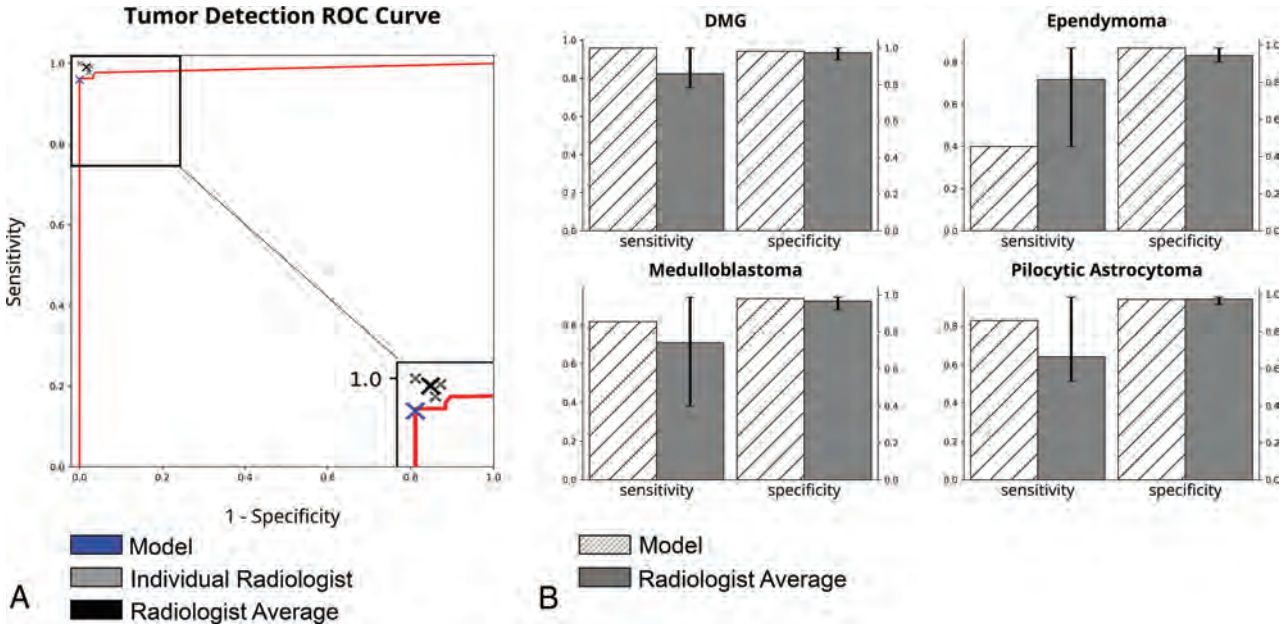

FIG 1. Comparison of model-with-radiologist performance. *A*, ROC curve for scan-level tumor detection. Model, individual radiologist, and average radiologist performance are indicated with *crosshairs*. *B*, Model and average radiologist performance for tumor subtype classification results. *Error bars* represent standard error among radiologists.

threshold at 5% (at least 1 tumor slice per every 20 slices) allowed maximal specificity and a sensitivity of at least 95% in the validation set. A 5% threshold achieved a sensitivity of 96% and a specificity of 100% on the held-out test set (Fig 1). Final scan-level tumor-type classification accuracy was 92% with an F_1 score of 0.80. Subgroup analysis demonstrated no difference in classification accuracy between patients younger and older than 2 years of age ($P = .22$) and no difference between patients with tumor with and without external ventricular drains (EVDs) ($P = .50$).

Class Activation Maps for Discriminative Localization of Tumor Type

Internal operations of deep learning algorithms often appear opaque and have been referred to as a "black box." Post hoc approaches for interpreting results have been described, such as using class activation maps (CAMs) to improve transparency and understanding of the model.[14] CAMs can serve as a quality assurance tool such that they highlight image regions relevant to the model's prediction and denote the model's confidence in the prediction but are not intended to precisely segment tumor voxels.[15] We implemented CAMs to visualize which regions of the image were most contributory to model prediction (Fig 2).[16] Qualitatively, pixels in close vicinity to the tumor appeared to strongly influence correct predictions, whereas incorrect predictions showed scattered CAMs that prioritized pixels in non-tumor regions. Because CAMs are not intended to provide perfect segmentations of tumor boundaries, we performed additional analyses to evaluate whether CAM mismatch correlated with the softmax score. The CAM for each slice was thresholded so that only intensities beyond a certain intensity threshold were considered positive tumor regions.[16] Next, for each image slice, we calculated the Dice similarity coefficient [(2x true positives)/(2x true positives + false positives + false negatives)][17] between positive CAM regions and manual tumor segmentation by a board-certified pediatric neuroradiologist (K.W.Y.). Finally, we correlated the Dice score with model confidence (softmax score) for each slice-level prediction. We found that at a threshold of 0.25, model confidence, in fact, correlated with the Dice score ($r = 0.42$, $P < .001$).

Visualization of Learned Features Using Principal Component Analysis and t-SNE

DMG occupied the most distinct feature space, followed by PA and MB, whereas the EP feature space overlapped with MB. The feature vectors were also analyzed using t-distributed stochastic neighbor embedding (t-SNE), which can show nonlinear relationships and potentially more distinct clustering,[18] and a similar clustering pattern was found for the 4 tumor pathologies (Fig 3*B*).

Comparison of Deep Learning Model versus Radiologist Performance

Four board-certified radiologists read the scans in the held-out test set and generated predictions for each scan. The radiologists detected the presence of tumor with an average sensitivity and specificity of 0.99 and 0.98, respectively (Fig 1 and Table 3), which was not statistically different from the detection accuracy of the model. For tumor subtype classification, the model showed higher sensitivity and specificity for PA, MB, and DMG, but lower sensitivity in predicting EP compared with the radiologists' average (Fig 1). Model classification accuracy and the F_1 score were higher than those of 2 of the 4 radiologists (C and D) and not statistically different from those of the other 2 radiologists (A and B) (Table 3 and On-line Fig 2).

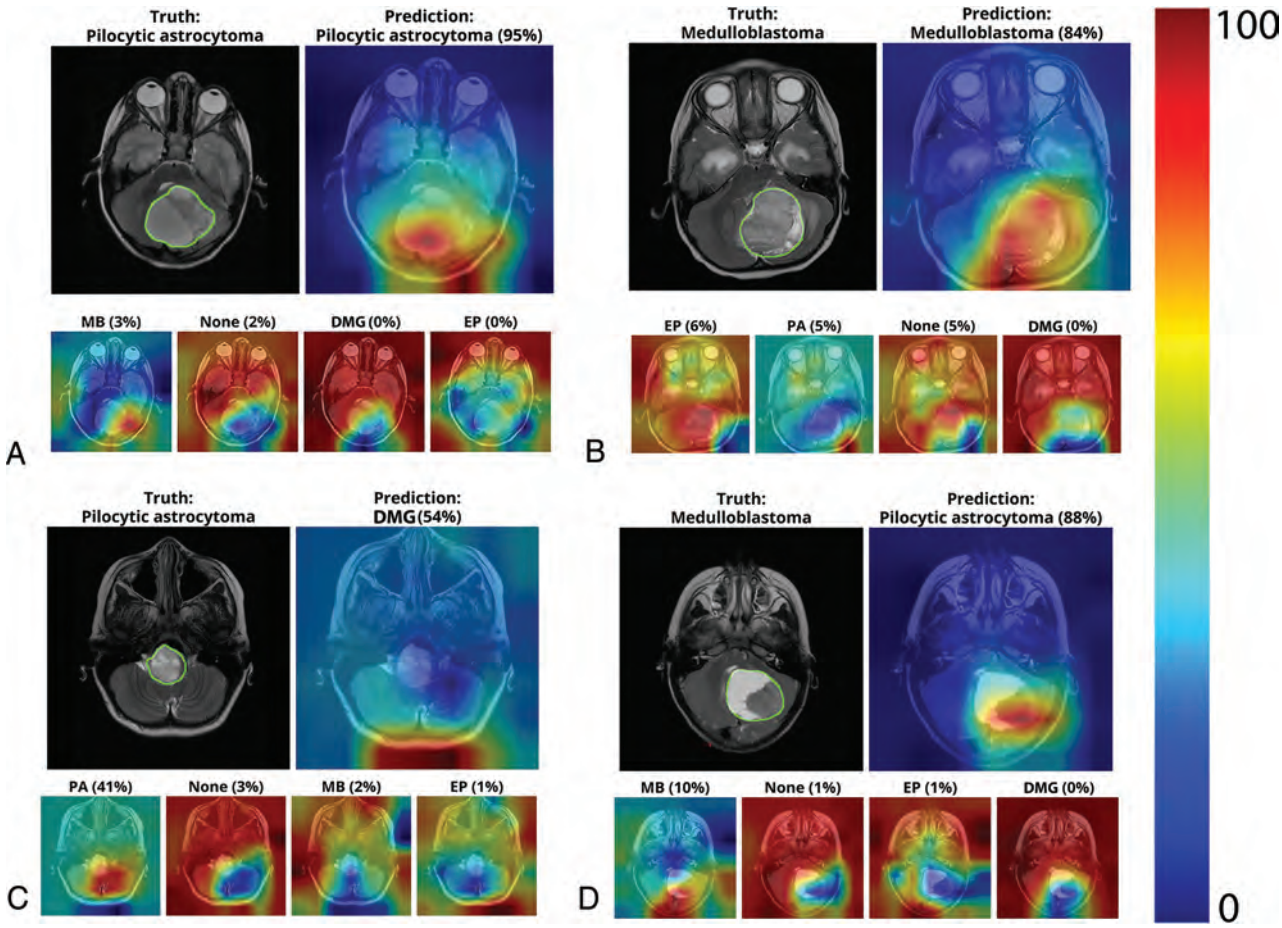

FIG 2. CAMs depicting the areas of the input slice that the model preferentially emphasizes when predicting tumor subtype on individual scan slices. The *upper row* of each subpanel shows the T2 slice with tumor areas manually denoted (*upper left*) and CAM overlay of the most confident prediction of the model (*upper right*). The *lower row* of each panel shows less confident predictions. Examples of correct predictions of PA (*A*) and MB (*B*) and incorrect predictions of PA (*C*) and MB (*D*) are shown.

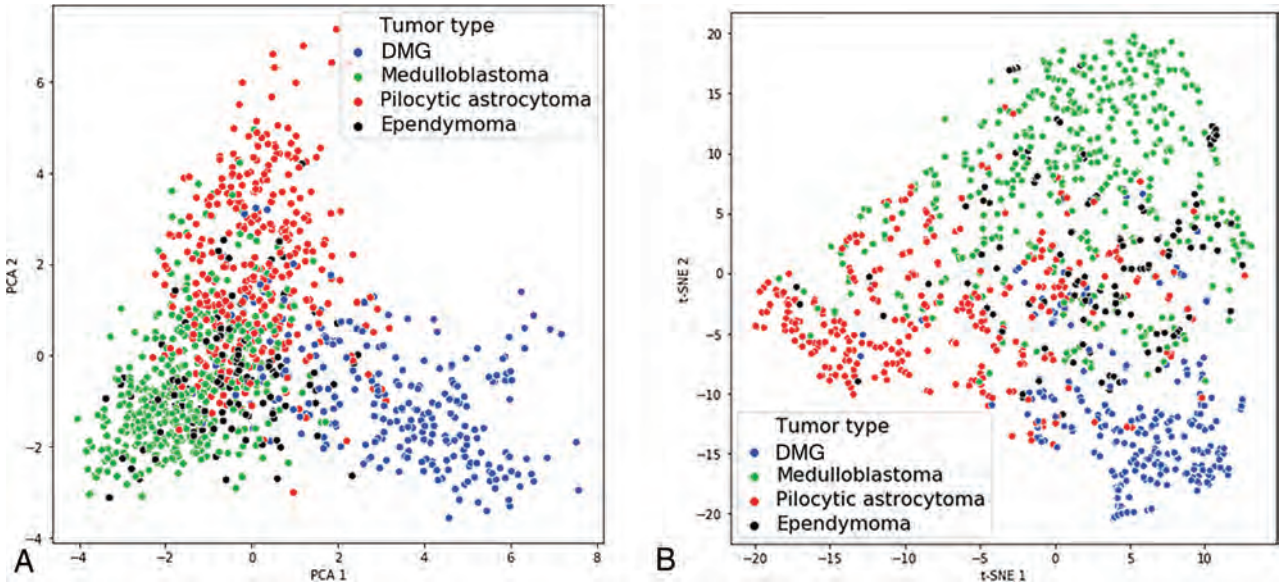

FIG 3. Learned feature vectors were reduced to 2D and visualized using principal component analysis (PCA) (*A*) and t-SNE (*B*). DMG has the most distinctive feature space, followed by PA and MB. EP has the least distinctive feature space and overlaps with MB.

Table 3: Comparison of tumor detection and classification results between the deep learning model and radiologists[a]

	Tumor Detection			Tumor Classification		
	Sensitivity	Specificity	*P*	Accuracy	F_1 Score	*P*
Model	0.96	1.00	–	0.92	0.80	–
Radiologist average	0.99	0.98	–	0.87	0.75	–
Radiologist A	1.00	1.00	.06	0.95	0.89	.09
Radiologist B	0.99	0.97	1.00	0.89	0.79	.24
Radiologist C	0.99	0.98	1.00	0.79	0.61	<.01
Radiologist D	0.98	0.98	.73	0.84	0.70	<.01

Note:— –indicates n/a.
[a] *P* value calculated using the McNemar test comparing the model with individual radiologists.

DISCUSSION

In this study, we present a deep learning model to detect and classify the 4 most common pediatric PF tumor pathologies using T2-weighted MRIs. We modified a state-of-the-art deep learning architecture and trained our model using MRIs from >600 patients with PF tumors at 5 independent pediatric institutions, representing the largest pediatric PF tumor imaging study to date. The model achieved an overall tumor-detection and classification accuracy that was comparable with the performance of 4 board-certified radiologists.

While prior machine learning approaches for PF tumor classification have applied feature engineering or a priori hand-crafted feature extraction, no prior study has used deep learning. Deep learning offers the advantages of automated high-dimensional feature learning through billions of parameters that pass through nonlinear functions within the deep layers of neural networks to tackle complex pattern-recognition tasks.[19,20] Unlike feature-engineering methods such as radiomics that require manual tumor segmentation and hand-crafted computational feature extraction for statistical modeling, data labeling for our deep-learning model was relatively simple: The model required only axial slices from T2-scans with labels of "no tumor"" or the specific tumor subtype present on the slice. Notably, the present detection and classification model is not dependent on the precise segmentation of the tumor region of the model. Rather, the model uses the entire slice to make a prediction. Because deep learning models are task-oriented and tailored to the task at hand, the model is essentially free to extract any relevant imaging features to assist with the task. Therefore, we implemented several techniques to better understand the performance of the model. While CAMs do not provide precise tumor segmentations, they can help identify areas of focus. Our finding that the CAM Dice score correlated with the softmax score suggests that when the focus areas of the model had higher overlap with the precise tumor boundary, the model was more confident in the tumor-type prediction.

Additionally, our large, heterogeneous dataset from geographically distinct institutions consisted of scans from multiple vendors and magnet strengths, thus allowing increased generalizability of our model as previous simulation studies have suggested.[21] By evaluating our model on a previously unseen held-out test, our model accuracy is likely to be reflective of real-world accuracy, unlike prior studies with much smaller datasets that used leave-one-out or k-fold cross-validation approaches, which are more prone to overfitting.[22-24]

Prior studies have shown variation in radiologists' interpretations.[25] In this study, we also observed differences among the performance of individual radiologists (Table 3). As the discussion on artificial intelligence in medicine continues to evolve, the radiology community has suggested a potential role for artificial intelligence in augmenting care by bridging knowledge gaps among clinical experts.[26] In this context, we propose that our model could serve to augment the radiologist's performance, particularly among those less experienced in pediatric neuro-oncology.

While our deep learning model exhibited an overall high accuracy for tumor classification, its performance varied with tumor pathology, with the highest accuracy for DMG, followed by PA and MB. Compared with the average performance of human experts, the model more accurately predicted all tumor types except for EP. This outcome might be attributed to the smaller proportion of EP in the training set. It is also possible that learned features for EP overlapped with those of MB, as shown by the principal component analysis and t-SNE plots (Fig 3), which contributed to a more difficult decision boundary for EP and, to a lesser degree, MB. Future studies with even more EP scans could help address these possibilities.

There are several limitations of this study. We restricted model input to T2 scans because our initial experiments showed that training on T2 scans alone outperformed training on a combination of T2, T1-postcontrast, and ADC sequences. We attribute these findings to model overfitting when using all 3 sequences. With the T1-postcontrast/ADC/T2 model, there was a greater difference in performance accuracy between the training and validation sets, indicating that there was more model overfitting. This is likely due to the increased number of input parameters when using all 3 sequences compared to only 1 sequence. In addition, the T2 parameters had greater consistency compared to the T1 parameters (such as image-contrast dynamic range) between institutions: Most used fast spin-echo or turbo spin-echo. T1-postcontrast images, on the other hand, were acquired at a wide variety of parameters and included spin-echo, spoiled gradient recalled echo (SPGR)/Magnetization Prepared - Rapid Gradient Echo (MPRAGE) /Bravo and fluid attenuated inversion recovery (FLAIR). Although we compared the performance using different sequences for the exact same subset of patients, the parameter variation between scans essentially limited the number of T1-postcontrast images within each parameter subtype.

Finally, there was lower scan resolution and greater noise with ADC sequences compared to the anatomic scans (T1- and T2-

sequences). The combination of these three factors likely contributed to our finding that a T2-only model outperformed a T1-postcontrast/ADC/T2 model within our subset of 260 scans. It is possible that with more training data, performance of the T1-postcontrast/ADC/T2 model could improve. Given our dataset and preliminary findings as well as our clinical motivations, we decided to focus our study on optimizing a T2 only model. Thus, our radiologists' performances may have been limited by the restriction to T2-only and may have been improved if they had access to T1-postcontrast and ADC sequences. However, T2 scans are the most universally acquired MR imaging sequences because they are relatively fast, easy to implement, and ubiquitous across the vendors. Our decision to use T2-scans also allowed maximal use of our dataset without incurring the computational cost of sequence coregistration, additional image preprocessing, and potentially larger neural networks that would be required for incorporation of other MR imaging sequences. Nevertheless, our model showed high predictive performance with wide generalizability. Its flexibility in accepting T2-derivative scans across multiple vendors and magnet strengths, with variable slice thicknesses, could also facilitate direct clinical translation.

We also did not evaluate model performance for classifying other pediatric or PF tumors. Because our model was trained on only the 4 most common tumor pathologies, it is not generalizable to other PF tumors, such as choroid plexus tumors or atypical teratoid/rhabdoid tumors. Furthermore, our model was not trained to distinguish between molecular subtypes for each tumor type. Given the growing importance of molecular subtyping for understanding tumor behavior, treatment response, and patient outcomes, we hope to incorporate such information in future iterations of our model.

Finally, our model was not trained to segment precise tumor regions but rather make slice- and scan-level predictions of tumor presence and type. However, tumor segmentation plays a valuable role in monitoring tumor growth and treatment response and is the focus of future work.

CONCLUSIONS

We present a multi-institutional deep learning model for pediatric PF tumor detection and classification with the potential to augment clinical diagnosis. Our work represents applied artificial intelligence in medicine and encourages future research in this domain.

Disclosures: Jennifer Quon—*RELATED: Support for Travel to Meetings for the Study or Other Purposes*: Stanford University, *Comments*: I received institutional reimbursement from the Stanford Neurosurgery Department for travel to the 2019 Pediatric Section Meeting of American Association of Neurological Surgeons to present the preliminary findings of this work. Jayne Seekins—*UNRELATED*: *Consultancy*: Genentech, *Comments*: This is consultancy related to adult malignancies. Matthew P. Lungren—*UNRELATED*: *Consultancy*: Nine-AI, Segmed; *Stock/Stock Options*: Nine-AI, Segmed, Bunker Hill. Tina Y. Poussaint—*UNRELATED*: *Grants/Grants Pending*: Pediatric Brain Tumor Consortium Neuroimaging Center, National Institutes of Health*; *Royalties:* Springer Verlag, book royalties. Hannes Vogel—*UNRELATED*: *Employment:* Stanford University; *Expert Testimony*: miscellaneous; *Grants/Grants Pending*: miscellaneous.* *Money paid to the institution.

REFERENCES

1. Pollack IF, Agnihotri S, Broniscer A. **Childhood brain tumors: current management, biological insights, and future directions.** *J Neurosurg Pediatr* 2019;23:261–73 CrossRef Medline
2. Segal D, Karajannis MA. **Pediatric brain tumors: an update.** *Curr Probl Pediatr Adolesc Health Care* 2016;46:242–50 CrossRef Medline
3. Medina LS, Kuntz KM, Pomeroy S. **Children with headache suspected of having a brain tumor: a cost-effectiveness analysis of diagnostic strategies.** *Pediatrics* 2001;108:255–63 CrossRef Medline
4. Zhou M, Scott J, Chaudhury B, et al. **Radiomics in brain tumor: image assessment, quantitative feature descriptors, and machine-learning approaches.** *AJNR Am J Neuroradiol* 2018;39:208–16 CrossRef Medline
5. Northcott PA, Korshunov A, Witt H, et al. **Medulloblastoma comprises four distinct molecular variants.** *J Clin Oncol* 2011;29:1408–14 CrossRef Medline
6. Ramaswamy V, Remke M, Bouffet E, et al. **Risk stratification of childhood medulloblastoma in the molecular era: the current consensus.** *Acta Neuropathol* 2016;131:821–31 CrossRef
7. Nejat F, El Khashab M, Rutka JT. **Initial management of childhood brain tumors: neurosurgical considerations.** *J Child Neurol* 2008;23:1136–48 CrossRef Medline
8. Capper D, Jones DTW, Sill M, et al. **DNA methylation-based classification of central nervous system tumours.** *Nature* 2018;555:469–74 CrossRef Medline
9. Louis DN. *WHO Classification of Tumours of the Central Nervous System*. International Agency for Research on Cancer; 2016
10. Park A, Chute C, Rajpurkar P, et al. **Deep learning-assisted diagnosis of cerebral aneurysms using the HeadXNet model.** *JAMA Netw Open* 2019;2:e195600 CrossRef Medline
11. El-Dahshan ES, Mohsen HM, Revett K, et al. **Computer-aided diagnosis of human brain tumor through MRI: a survey and a new algorithm.** *Expert Systems with Applications* 2014;41:5526–45 CrossRef
12. Deng J, Dong W, Socher R, et al. **ImageNet: a large-scale hierarchical image database.** In: *Proceedings of the 2009 IEEE Conference on Computer Vision and Pattern Recognition*, Miami, Florida. June 20–25, 2009:248–55
13. Krizhevsky A, Sutskever I, Hinton GE. **Imagenet classification with deep convolutional neural networks.** In: *Proccedings of the Advances in Neural Information Processing Systems Conference*, Lake Tahoe, California. December 3–8, 2012;1097–1105
14. Arrieta AB, Díaz-Rodríguez N, Del Ser J, et al. **Explainable Artificial Intelligence (XAI): concepts, taxonomies, opportunities and challenges toward responsible AI**. *Information Fusion* 2019;58:82–115 CrossRef
15. Simonyan K, Vedaldi A, Zisserman A. **Deep inside convolutional networks: visualising image classification models and saliency maps.** *arXiv* December 2013. https://arxiv.org/pdf/1312.6034.pdf. Accessed April 5, 2020
16. Zhou B, Khosla A, Lapedriza A, et al. **Learning deep features for discriminative localization.** *In: Proceedings of the 2016 IEEE Conference on Computer Vision and Pattern Recognition*, Las Vegas, Nevada. June 27–30, 2016:2921–29
17. Dice LR. **Measures of the amount of ecologic association between species.** *Ecology* 1945;26:297–302 CrossRef
18. van der Maaten L, Hinton G. **Visualizing data using t-SNE.** *Journal of Machine Learning Research* 2008;9:2579–2605
19. Hosny A, Parmar C, Quackenbush J, et al. **Artificial intelligence in radiology.** *Nat Rev Cancer* 2018;18:500–10 CrossRef Medline
20. Savadjiev P, Chong J, Dohan A, et al. **Demystification of AI-driven medical image interpretation: past, present and future.** *Eur Radiol* 2019;29:1616–24 CrossRef Medline
21. Chang K, Balachandar N, Lam C, et al. **Distributed deep learning networks among institutions for medical imaging.** *J Am Med Inform Assoc* 2018;25:945–54 CrossRef Medline
22. Rodriguez Gutierrez D, Awwad A, Meijer L, et al. **Metrics and textural features of MRI diffusion to improve classification of pediatric posterior fossa tumors.** *AJNR Am J Neuroradiol* 2014;35:1009–15 CrossRef Medline
23. Arle JE, Morriss C, Wang ZJ, et al. **Prediction of posterior fossa tumor type in children by means of magnetic resonance image**

properties, spectroscopy, and neural networks. *J Neurosurg* 1997;86:755–61 CrossRef Medline

24. Bidiwala S, Pittman T. **Neural network classification of pediatric posterior fossa tumors using clinical and imaging data.** *Pediatr Neurosurg* 2004;40:8–15 CrossRef Medline
25. Abujudeh HH, Boland GW, Kaewlai R, et al. **Abdominal and pelvic computed tomography (CT) interpretation: discrepancy rates among experienced radiologists.** *Eur Radiol* 2010;20:1952–57 CrossRef Medline
26. Allen B, Jr., Seltzer SE, Langlotz CP, et al. **A Road Map for Translational Research on Artificial Intelligence in Medical Imaging: From the 2018 National Institutes of Health/RSNA/ACR/The Academy Workshop.** *J Am Coll Radiology* 2019;16:1179–89 CrossRef Medline

Assessment of Maturational Changes in White Matter Anisotropy and Volume in Children: A DTI Study

G. Coll, E. de Schlichting, L. Sakka, J.-M. Garcier, H. Peyre, and J.-J. Lemaire

ABSTRACT

BACKGROUND AND PURPOSE: Anisotropy is a good indicator of white matter fascicle macrostructure and organization but the interpretation of its changes with age remains difficult. The increase of WM fascicle fractional anisotropy with time and its relationship with WM fascicle volume have never been examined during childhood. We studied the maturation of associative WM fascicles during childhood using MR imaging–based DTI. We explored whether the fractional anisotropy increase of the main WM fascicles persists beyond the period of brain growth and is related to WM fascicle volume increase.

MATERIALS AND METHODS: In a series of 25 healthy children, the fractional anisotropy and volume of 15 associative WM fascicles were calculated. Several regression linear mixed models were used to study maturation parameters (fractional anisotropy, volume, and total telencephalon volume) considered as dependent variables, while age and sex were independent variables (the variable identifying the different WM fascicles was considered as a repeated measure).

RESULTS: In children older than 8 years of age, WM fascicle fractional anisotropy increased with age (P value = .045) but not its volume (P value = .7) or the telencephalon volume (P value = .16). The time course of WM fascicle fractional anisotropy and volume suggested that each WM fascicle might follow a specific pattern of maturation.

CONCLUSIONS: The fractional anisotropy increase of several WM fascicles after 8 years of age may not result from an increase in WM fascicle volume. It might be the consequence of other developmental processes such as myelination.

ABBREVIATION: FA = fractional anisotropy

The maturation of human WM is a complex process that takes place from the fetal period to adulthood.[1] WM is made of fascicles, ie, bundles of neurons' axon of gray matter, which interconnect functional regions of the central nervous system. One can distinguish 3 types of bundles: 1) commissural fascicles that connect right and left cortices (eg, the forceps major), right and left nuclei (eg, the Forel commissure), or both (eg, the anterior commissure); 2) projection fascicles that connect the cortex with the deep brain (eg, the thalamic radiations that do not cross the midline) or the spinal cord (eg, the pyramidal fascicle crossing the midline); 3) associative fascicles that interconnect cortical areas or nuclei unilaterally (eg, the arcuate fascicle). The development of WM fascicles across time depends on 3 processes: fasciculation or organization in bundles, growth in volume, and myelination.[2] Axons are the main constituents of WM. The fasciculation is driven by pioneering axons growing under the control of their distally located cones and environmental signals, such as chemical agents, neurotransmitters, electrical signals, and growth factor.[2,3] WM bundle growth, myelination, and functional maturation are asynchronous processes. Cortical sensory regions and related WM fascicles are known to mature earlier than associative regions, eg, frontal regions, which develop later and slowly until the end of adolescence.[2,4]

Nevertheless, the relationship between myelination and brain function is complex because fiber myelination and functional maturation could be uncorrelated in different cerebral pathways. Indeed, the myelination of auditory pathways reaches maturity at 3 years of age, whereas the hearing function is effective since birth;[2] conversely the myelination of the corticospinal fascicle

Received April 6, 2020; accepted after revision June 7.

From the Service de Neurochirurgie (G.C., E.d.S., L.S., J.-J.L.) and Service de Radiologie Pédiatrique (J.-M.G.), Centre Hospitalier Universitaire Clermont-Ferrand, Clermont-Ferrand, France; Centre National de la Recherche Scientifique (G.C., J.-J.L.), SIGMA Clermont, Institut Pascal, Université Clermont Auvergne, Clermont-Ferrand, France; Laboratoire d'Anatomie et d'Organogenèse, Laboratoire de Biophysique Sensorielle (L.S., J.-M.G.) NeuroDol, Faculté de Médecine, Université Clermont Auvergne, Clermont-Ferrand, France; Service de Psychiatrie de l'Enfant et de l'Adolescent, Hôpital Robert Debré (H.P.), Assistance Publique–Hôpitaux de Paris, Paris, France.

Please address correspondence to Guillaume Coll, MD, Service de Neurochirurgie, Hôpital Gabriel-Montpied, 58 rue Montalembert, 63000 Clermont-Ferrand, France; e-mail: gcoll@chu-clermontferrand.fr

Indicates article with supplemental on-line table.

http://dx.doi.org/10.3174/ajnr.A6709

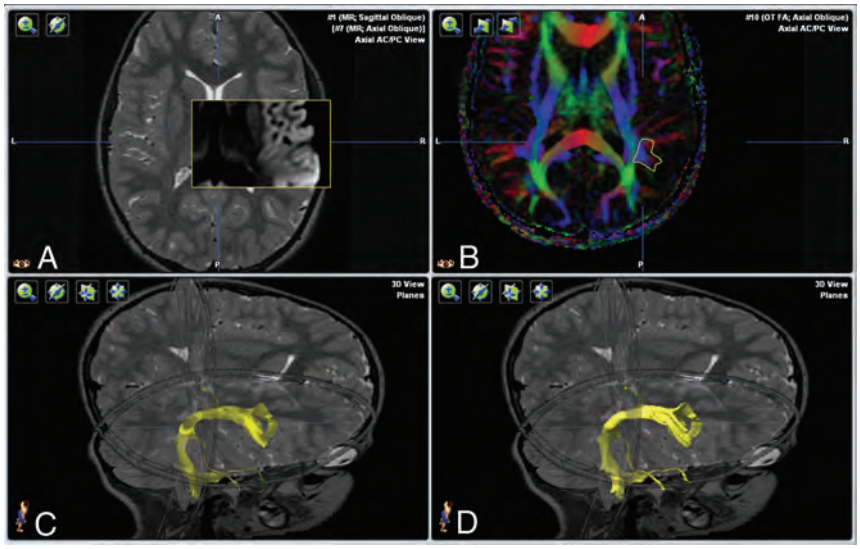

FIG 1. Image processing in a 7-year-old girl. Image datasets. *A*, Coregistration (mutual information algorithm) after anterior/posterior commissure alignment using iPlan Stereotaxy 3.0. T2-3D-weighted sequence. FA color-coded fiber-direction maps. *B*, Positioning of the ROI on the FA color-coded map to track the right arcuate fasciculus. *C*, Generating the right arcuate fasciculus. *D*, Generating the volume corresponding to the tractogram on a T2-weighted 3D dataset.

starts before birth, yet neonate motor capacities are limited.[2] Moreover, myelination is associated with the development of cognitive functions because it induces a dramatic increase in the conduction velocity of the action potential,[2,5] improving the functional efficiency of neural networks.[2,6] Myelination has been explored in vivo by MR imaging since the early 2000s, using T1- and T2-weighted MR imaging sequences[2,4] and DTI.[7] DTI provides insight into WM architecture, notably the fascicles, probing water diffusion within each voxel.

A parameter derived from DTI computing, fractional anisotropy (FA), ranging from 0, isotropic diffusion, to 1, anisotropic diffusion, features fasciculation and myelination characteristics of WM fibers.[2,8,9] FA value increases with age as myelination and bundling take place.[2,8,9] Most interesting, bundling increases anisotropy even in the absence of myelin,[2,10,11] and myelination increases anisotropy, ensheathing axons with oligodendroglial processes, further decreasing both membrane permeability and extracellular distance.[2] In childhood, the whole volume of WM of the brain increases with age.[12,13] Indeed, the growth of brain volume is rapid because 80% of brain volume is reached during the first 1.5 years of life.[12] The growth of WM and the GM follow different patterns because 80% of the volume of GM is reached at the end of the first year of life, while the volume of WM grows initially rapidly and thereafter at a lower rate.[12] The total GM volume peaks during childhood/adolescence and decreases thereafter, whereas total WM volume increases up to young adulthood.[12]

In summary, WM volume increases at a higher rate than GM volume throughout childhood.[13] Few studies, to our knowledge, have specifically studied the growth of fascicles.[14-16] The increase in the volume of fascicles slows down from 6 to 12 years of age,[14-16] and the increase of fiber density and the volume of fascicles could explain the increase in FA with age,[17] yet the chronologic sequence of simultaneous modifications of FA and the volume of fascicles has not been specifically examined. Thus, we aimed to analyze WM fascicle features (volume and mean FA value) by age, in a sample of 25 subjects from 1 to 17 years of age, hypothesizing that the increase in FA of the main WM fascicles could surpass the period of increase in total brain volume. Fifteen main fascicles were studied by DTI tractography, enabling 3D reconstruction and measurements of volume and mean FA value.

MATERIALS AND METHODS

Subjects

We retrospectively included MR imaging datasets of 25 children scanned in our institution following a medical request between November 2015 and November 2016. This retrospective study was approved by our institutional review board (Comité de protection des personnes VI CHU G. MONTPIED) and did not raise ethical issue and falled outside the scope of the rules governing biomedical research (articles L.1121-1-1 and R1121-3 of the Code of Public Health). The indication of all MR imaging was headache. MR imaging was included if no cerebral pathology was suspected on MR imaging and clinical records and if informed consent was signed by the patient's legal representative.

MR Imaging Datasets

MR imaging was performed following rectal injection of pentobarbital, 3–5 mg/kg (maximum dose of 100 mg), and oral intake of alimemazine (4% drop, 1 drop/kg, ie, 1.25 mg/kg) if required for children younger than 4 years of age, enabling movement-free imaging.

Examinations were performed on a 1.5T machine (Optima MR450w; GE Healthcare).

T2-weighted sequences were used for anatomic reference: TR = 2400 ms, TE = 88.32 ms, flip angle = 90°, B_0 = 600 s/mm^2, 272 joined axial slices, matrix = 512 × 512, voxel size = 0.47 × 0.47 × 0.6 mm^3, total acquisition time = 6 minutes.

DTI acquisition used a single-shot echo-planar dual spin-echo sequence: TR = 7719 ms, TE = 81.7 ms, flip angle = 90°, 20 diffusion gradients, B_0 = 600 s/mm^2, 34 joined axial slices, matrix = 256 × 256, voxel size = 0.98 × 0.98 × 4 mm^3, total acquisition time = 6 minutes.

Image Processing

DTI and related computed maps (FA and color-coded direction of diffusion tensors) were coregistered (mutual information algorithm) with T2 images after anterior/posterior commissure alignment and correction of eddy currents (iPlan Stereotaxy 3.0; Brainlab) (Fig 1*A*).[18] Accuracy of automatic registration was

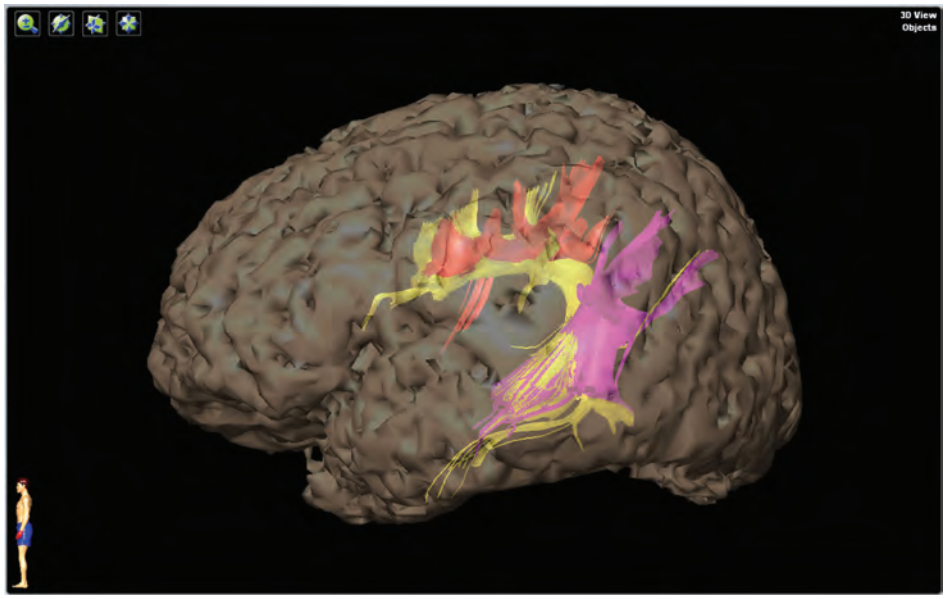

FIG 2. 3D surface renderings of the telencephalon in a 7-year-old girl from T2-weighted MR images used to map the left superior longitudinal fasciculus (anterior part in red, arcuate part in yellow, and posterior part in pink).

carefully reviewed (visual analysis of merged images; test–retests) according to anatomic landmarks: putamen, pallidum, corpus callosum (body, major and minor forceps), anterior and posterior limbs of the internal capsule, cerebellum, cerebellar tentorium, Sylvian region, upper brain stem, ventricles (frontal horns and trigone), interhemispheric fissure, and main cerebral gyrations.

WM fascicle fiber tracking within the right and left hemispheres was performed by 2 trained clinical neuroanatomists (G.C. and E.d.S.) with the clinical software (iPlan Stereotaxy 3.0), relying on 2 methods of fiber assignment, continuous tracking[19] and tensor deflection.[20] The FA threshold was set to 0.20, meaning that only FA values superior to 0.20 were considered by voxel. This minimal FA threshold was selected because it allowed eliminating the values of the fraction of anisotropy corresponding to the free water or the cerebral cortex while keeping as much fiber as possible.[19,21] In a previous study, the FA threshold was 0.13 for performing the tracking of an area containing both gray and white matter.[22] The threshold of 0.15 was used in another study for brain stem fiber tracking,[23] and the 0.10 threshold, for gray matter.[24] Our interest in highly myelinated fibers caused us to increase this threshold to 0.20 to perform the tractography of white matter fibers exclusively. The minimum fiber length for tracking was set fascicle by fascicle: 35 mm for the superior longitudinal fasciculus (parietofrontal or anterior part, frontotemporal or arcuate part, parietotemporal or posterior part); the inferior fronto-occipital fasciculus; 16 mm for the uncinate fasciculus and the corpus callosum; and 5 mm for the cingulum. Seed ROIs were placed in WM regions of "obligatory passages" along the path of each WM fascicle, tracing streamlines of each WM fascicle irrespective of cortical terminations, which can vary from hemisphere to hemisphere and from subject to subject (Fig 1*B*) (intra- and interindividual variability).[18]

Each fascicle was generated as follows:[18] 1) guided by color-coded direction maps, positioning of 2 seed ROIs on FA maps within WM voxels where the fascicle fibers were easily identifiable (Fig 1*B*); 2) iterative test-retests, changing the size and shape of the ROIs, checking that no fibers belonging to the fascicle were missed; 3) use of a "fiber exclusion" tool (iPlan Stereotaxy 3.0) when the on-line reconstruction produced aberrant fibers (eg, the presence of a frontoparietal fiber when tracking the arcuate fasciculus (AF)); and 4) generation of the tractogram (Fig 1*C*). Each tractogram of a WM fascicle was reviewed (G.C.) before generating its envelope by automatic wrapping (iPlan Stereotaxy 3.0) (Fig 1*D*). Fifty WM fascicles were analyzed.[25-27] Seven were associative and intrahemispheric: the superior longitudinal fasciculus (parietofrontal or anterior part, frontotemporal or arcuate part, parietotemporal or posterior part), the inferior longitudinal fasciculus, the fronto-occipital fasciculus, the uncinate fasciculus, and the cingulum; and 1 was commissural, the corpus callosum. For each child, the 3D surface of the supratentorial brain (telencephalon) was automatically generated from T2-weighted MR images, an atlas-based automatic segmentation (iPlan Stereotaxy 3.0), enabling retrieving its volume (telencephalon volume in cubic millimeters) for further analysis (Fig 2). The telencephalon volume included supratentorial white and gray matter and excluded the CSF signal (on the T2 sequences that corresponded to the subarachnoidal and the ventricular spaces). We retrieved the volume and the mean FA value of voxels within the envelope for each fascicle of both hemispheres. The fascicle volume and mean FA of voxels within the envelope were standardized (z score) as follows:

$$\frac{(\text{Mean Value of WM-Fascicle Parameters of the Sample} - \text{Mean Value of WM-Fascicle Parameters of the Sample})}{\text{The SD of WM-Fascicle Parameters of the Sample}}.$$

The telencephalon volume was standardized as well.

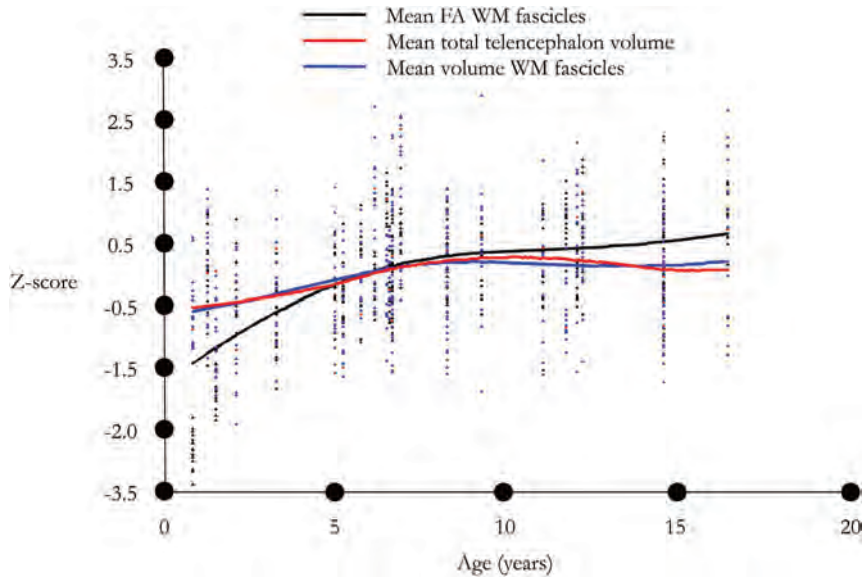

FIG 3. Lowess smoothing curve with a bandwidth of 0.8. Standardized. Black indicates mean WM fascicle FA; red, mean total telencephalon volume; blue, mean WM fascicle volume.

Data Analyses

We graphically examined the distribution of standardized WM fascicle parameters by age using locally weighted scatterplot smoothing (ie, Lowess smoothing curve; bandwidth = 0.8). A first graph (Fig 3) was performed using all the WM fascicles. On the basis of the graphic inspection of Fig 3, we identified an age threshold at 8 years of age corresponding to a slowdown of the increase of the total telencephalon volume. This age threshold was thought to mark the end of the period of increase in total telencephalon volume. We subsequently used this age threshold in regression analyses to test the changes with age in FA, volume of the WM fascicles, and total telencephalon volume in the subsamples of participants with ages below and above this threshold separately. Linear regression mixed models were used with standardized WM fascicle FA and volume and total telencephalon volume as dependent variables and age and sex as independent variables. The variable identifying the different WM fascicles was considered as a repeated measure (except for the model of total telencephalon volume). In the subsamples of participants with ages younger than 8 years, we also examined more closely each WM fascicle to determine the effects of age on WM fascicle FA and volume and to test the difference in slope between the effect of age on WM fascicle FA and the effect of age on WM fascicle volume. These models were also adjusted for sex. Statistical analysis (SAS 9.4 software; SAS Institute) was conducted on the basis of a 2-sided type I error of 5%. This study is exploratory in nature; hence no adjustment for multiple testing was performed.

RESULTS

In our sample of 25 participants (10 males, 15 females), the mean age was 8.81 ± 4.47 years (On-line Table). Non-normalized mean values of WM fascicle FA, WM fascicle volume, and total telencephalon volume are shown in the On-line Table. The total telencephalon volume reached a plateau from 8 years of age (Fig 3). This was also true for WM fascicle volume.

In the subsample of participants younger than 8 years of age ($n = 14$), our regression linear mixed models indicated an increase with age of FA (β standardized = 0.29 ± 0.03, P value < .001) and volume of the WM fascicles (β standardized = 0.15 ± 0.03, P value < .001), as well as volume of the telencephalon (β standardized = 0.17 ± .03, P value < .001). However, in the subsample of participants older than 8 years of age ($n = 11$), our linear regression mixed models indicated an increase of FA with age (β standardized = 0.05 ± 0.02, P value = .045) and no increase of the volume of the WM fascicles (β standardized = −0.01 ± 0.03, P value = .7) or the volume of the telencephalon (β standardized = −0.03 ± 0.02, P value = .16).

We then further examined each fascicle separately in the subsample of participants older than 8 years of age. The FA of the right (β standardized = 0.13 ± 0.05, P value = .043) and left (β standardized = 0.14 ± 0.07, P value = .083) inferior fronto-occipital fascicles tended to increase with age (Table), whereas the volume of these fascicles did not (right: β standardized = −0.10 ± 0.09, P value = .3; left: β standardized = −0.16 ± 0.07, P value = .062). Thus, we found a significant interaction between the effects of age and the parameter considered (FA versus volume) for the left (P value = .017) and a marginally significant one for the right (P value = .072) inferior fronto-occipital fascicles.

The FA of the arcuate part of the right superior longitudinal fasciculus (β standardized = 0.15 ± 0.06, P value = .042) increases with age as well as the volume of this fascicle (β standardized = 0.17 ± 0.10, P value = .11); thus, no interaction (P = .5) between the effect of age on FA and fascicles volume was found. An inspection of the evolution of the FA and volume of each WM fascicle also suggested different patterns of maturation processes according to the fasciculus (Fig 4).

DISCUSSION

After 8 years of age, the age at which the total telencephalon volume reaches a plateau, we found a global increase of FA of the WM fascicles with age without an associated increase in the volume of the WM fascicles. The evolution of the FA and volume of each WM fascicle revealed differences in the pattern of maturation processes of fascicles. For the right and left inferior fronto-occipital fascicles, the FA increased in correlation to age, and no correlation was found between age and fascicle volume. However, both the FA and volume of the arcuate part of the superior right longitudinal fasciculus were found to increase with age. Altogether, one could speculate that the increase in FA after

Effect of age on WM fascicle FA and volume, and test for difference in slope between the effect of age on WM fascicle FA and the effect of age on WM fascicle volume, in the subsamples of participants older than 8 years of age

	Effect of Age on WM Fascicle FA			Effect of Age on WM Fascicle Volume			Interaction between the Effect of Age on WM Fascicle FA and WM Fascicle Volume
	β	SD	*P* Value	*β*	SD	*P* Value	*P* Value
F1, corpus callosum	0.05	0.06	.447	−0.01	0.09	.901	.770
F2, right cingulum	0.02	0.08	.822	0.02	0.12	.847	.734
F3, left cingulum	0.03	0.09	.736	−0.10	0.11	.396	.459
F4, superior longitudinal fasciculus, right anterior part	0.03	0.08	.718	0.19	0.09	.060	.175
F5, superior longitudinal fasciculus, left anterior part	0.07	0.11	.514	0.01	0.13	.925	.852
F6, superior longitudinal fasciculus, right arcuate part	0.15[a]	0.06[a]	.042[a]	0.17	0.10	.111	.506
F7, superior longitudinal fasciculus, left arcuate part	0.10	0.06	.142	0.01	0.07	.860	.308
F8, superior longitudinal fasciculus, right posterior part	0.01	0.07	.868	−0.13	0.14	.360	.434
F9, superior longitudinal fasciculus, left posterior part	0.02[a]	0.09[a]	.842[a]	−0.22	0.12	.109	.547
F10, right inferior fronto-occipital fasciculus	0.13	0.05	.043	−0.10	0.09	.296	.072
F11, left inferior fronto-occipital fasciculus	0.14	0.07	.083	−0.16	0.07	.062	.017
F12, right inferior longitudinal fasciculus	0.06	0.08	.480	0.09	0.12	.471	.802
F13, left inferior longitudinal fasciculus	0.01	0.10	.951	0.01	0.10	.900	.983
F14, right uncinate fasciculus	0.00	0.07	.963	0.06	0.09	.533	.521
F15, left uncinate fasciculus	−0.03	0.09	.731	−0.06	0.07	.431	.641

[a] *P* value < .05, without correction for multiple testing.

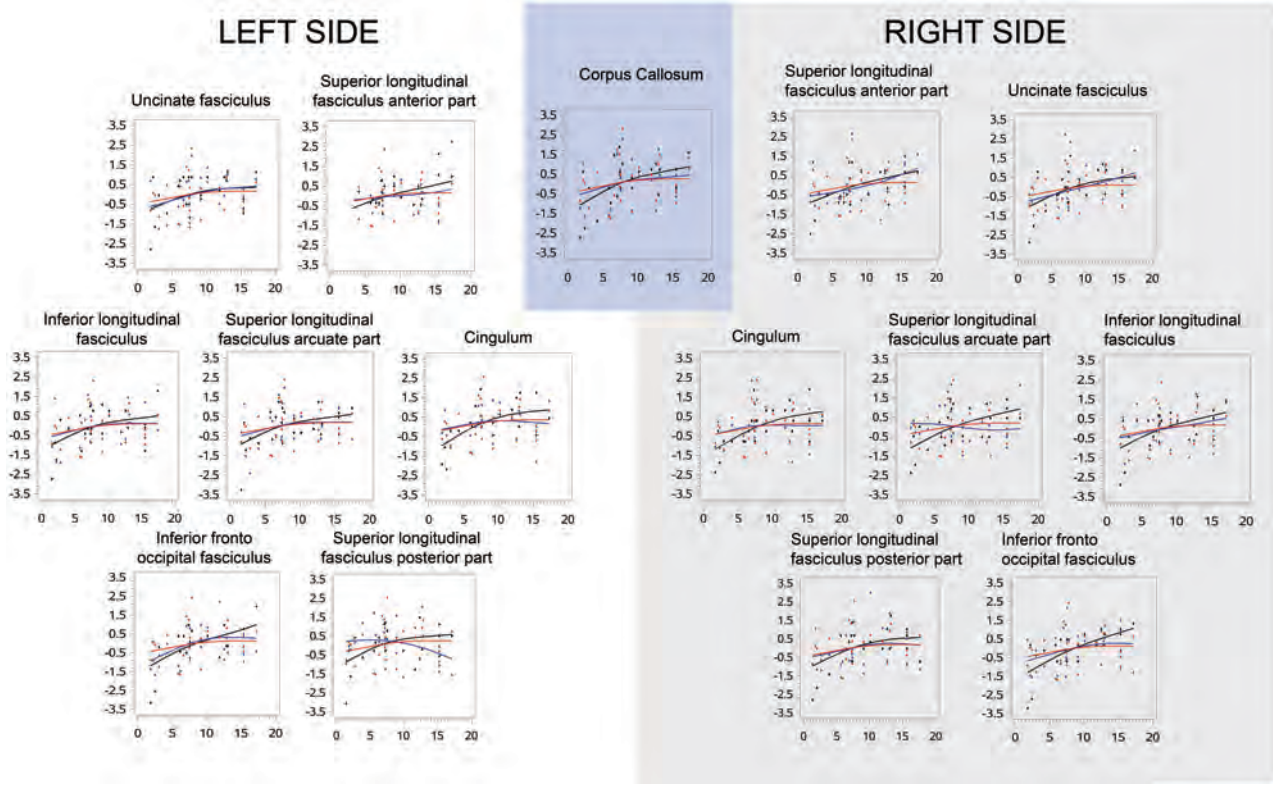

FIG 4. Lowess smoothing curve for each WM bundle with a bandwidth of 0.8. Standardized. Black indicates mean WM bundle FA; red, mean telencephalon volume; blue, mean WM bundle volume.

8 years of age may not be the consequence of an increase in the volume of the fascicles but rather the consequence of other processes, such as myelination. Our methodologic approach allowed us to better understand the development of the WM fascicles from infancy to adulthood, even though our analyses were based on a small sample ($n = 25$).

Methodologic Implications

FA is described as the most sensitive marker for evaluating changes in the organization of different fascicles.[17,28] To assess the evolution of FA with age, we used the already published original quantification approach, which quantifies the 3D-tracked fascicles, rather than the conventional ROI approach.[17] Although

few references concerning the evolution of the anisotropy fraction for the whole WM bundle are available, some publications consider that the average value of the FA of the whole bundle should be preferred. Indeed FA SDs in the fascicles across infants were smaller with the tract approach than with the ROI approach.[17] It should be kept in mind that maturation differs along the same bundle since the myelination progresses in the direction of the conduction of the action potential.[17,29] The approach of using the average value of the FA in whole fascicles is therefore questionable.[17] We preferred to use a manual method for generating the tractograms of the fascicles of each patient. Although automatic methods using atlases are more commonly used because they save time, they can induce a bias in the measurement of FA with values 20 (per cent) lower than the average values calculated by the manual method.[30]

Increases in FA Values Are Not Only Due to the Bundle Growth

Once the white matter is organized into a network of fibers, the connections become progressively functionally mature due to the myelination, which improves the conduction of the action potential.[2,5,29] Myelination (deposit of myelin around the axons) constitutes the last stage of the development of the WM, which covers the period from the second part of pregnancy to the end of adolescence.[2,31-38] It occurs earlier and faster under the following conditions: 1) in proximal pathways rather than in distal ones, 2) in sensory pathways (somatosensory, vision, auditory) rather than in motor ones, 3) in projection fibers rather than in associative ones, 4) in central regions rather than in polar ones, and 5) in the occipital pole rather than in the posterior parietal WM and the temporal and frontal poles.[2] This asynchrony in the maturation sequence is supposed to depend on the hierarchy of connections between cortical areas: The early maturation of receptive sensory areas (responsible for low-level processing) would enable a stabilization of the information used by integrative areas (involved in high-level processing), which develops later on.[2,36]

Regarding the evolution of the FA and the volume of all the fascicles as well as the evolution of the volume of the telencephalon (gray and white matter) in our study, we found an increase in FA and volume with age. However, there is a slowdown in the volume growth of the fascicles at 8 years of age, which corresponds to a slowdown in volume growth of the telencephalon. It can then be assumed that the increase in FA of some fascicles after 8 years of age is not the consequence of an increase in the volume of the fascicles but probably the consequence of the myelination. Such discrepancy may be explained by the necessity to maintain similar latencies between brain regions since myelination compensate the delay of latencies caused by brain growth.[2,37] In the visual system, for example, the latency of the first positive wave of response to a stimulus reaches the adult latency (100 ms) at around 4 postnatal months, whereas the distance between the retina and the calcarine fissures still increases by around 6 cm until adulthood.[2,37]

DTI studies and a postmortem series have shown that myelination increases, respectively, earlier in projection fibers than in associative fibers during childhood,[2,38] and earlier in commissural and projection fibers than in the associative fibers, just as it begins earlier in the occipital and temporal regions than in the frontal regions,[33] in agreement with our results on associative fascicles and a single commissural bundle.

The results of the present study must be interpreted with caution given the small sample. In particular, analyses aiming to determine the effect of age on each WM fascicle FA and volume and those testing the difference in slope between the effect of age on WM fascicle FA and the effect of age on WM fascicle volume were largely underpowered. Further studies conducted on larger samples are warranted to examine more closely the different patterns of maturation processes according to the fasciculus.

CONCLUSIONS

After 8 years, the age at which the total volume of the telencephalon does not increase any longer, we observed an overall increase in the FA of the WM fascicles but not of their volume. The evolution of the FA and the volume of each fascicle follows a maturation process specific to each fascicle. For right and left inferior fronto-occipital fascicles, our analyses indicated an increase in FA with age but not an increase in volume with age. However, the FA and volume of the arcuate part of the superior right longitudinal fasciculus increased with age. Together, these results show that in some fascicles, the augmentation of the FA after 8 years of age may not be the consequence of an increase in the volume of the fascicles but rather the consequence of other processes, such as myelination. Our methodologic approach allows us to shed new light on the development of the WM fascicles between infancy and adulthood, even if our analyses concerned small samples.

REFERENCES

1. Geng X, Gouttard S, Sharma A, et al. **Quantitative tract-based white matter development from birth to age 2 years.** *Neuroimage* 2012; 61:542–57 CrossRef Medline
2. Dubois J, Dehaene-Lambertz G, Kulikova S, et al. **The early development of brain white matter: a review of imaging studies in fetuses, newborns and infants.** *Neuroscience* 2014;276:48–71 CrossRef Medline
3. Huttenlocher PR, Bonnier C. **Effects of changes in the periphery on development of the corticospinal motor system in the rat.** *Brain Res Dev Brain Res* 1991;60:253–60 CrossRef Medline
4. Paus T, Collins DL, Evans AC, et al. **Maturation of white matter in the human brain: a review of magnetic resonance studies.** *Brain Res Bull* 2001;54:255–66 CrossRef Medline
5. Baumann N, Pham-Dinh D. **Biology of oligodendrocyte and myelin in the mammalian central nervous system.** *Physiol Rev* 2001;81: 871–927 CrossRef Medline
6. van der Knaap MS, Valk J, Bakker CJ, et al. **Myelination as an expression of the functional maturity of the brain.** *Dev Med Child Neurol* 1991;33:849–57 CrossRef Medline
7. Hermoye L, Saint-Martin C, Cosnard G, et al. **Pediatric diffusion tensor imaging: normal database and observation of the white matter maturation in early childhood.** *Neuroimage* 2006;29:493–504 CrossRef Medline
8. Neil JJ, Shiran SI, McKinstry RC, et al. **Normal brain in human newborns: apparent diffusion coefficient and diffusion anisotropy measured by using diffusion tensor MR imaging.** *Radiology* 1998; 209:57–66 CrossRef Medline

9. Hüppi PS, Warfield S, Kikinis R, et al. **Quantitative magnetic resonance imaging of brain development in premature and mature newborns.** *Ann Neurol* 1998;43:224–35 CrossRef Medline
10. Beaulieu C. **The basis of anisotropic water diffusion in the nervous system: a technical review.** *NMR Biomed* 2002;15:435–55 CrossRef Medline
11. Wimberger DM, Roberts TP, Barkovich AJ, et al. **Identification of "premyelination" by diffusion-weighted MRI.** *J Comput Assist Tomogr* 1995;19:28–33 CrossRef Medline
12. Groeschel S, Vollmer B, King MD, et al. **Developmental changes in cerebral grey and white matter volume from infancy to adulthood.** *Int J Dev Neurosci* 2010;28:481–89 CrossRef Medline
13. Matsuzawa J, Matsui M, Konishi T, et al. **Age-related volumetric changes of brain gray and white matter in healthy infants and children.** *Cereb Cortex* 2001;11:335–42 CrossRef Medline
14. Hasan KM, Iftikhar A, Kamali A, et al. **Development and aging of the healthy human brain uncinate fasciculus across the lifespan using diffusion tensor tractography.** *Brain Res* 2009;1276:67–76 CrossRef Medline
15. Wakana S, Caprihan A, Panzenboeck MM, et al. **Reproducibility of quantitative tractography methods applied to cerebral white matter.** *Neuroimage* 2007;36:630–44 CrossRef Medline
16. Malykhin N, Concha L, Seres P, et al. **Diffusion tensor imaging tractography and reliability analysis for limbic and paralimbic white matter tracts.** *Psychiatry Res* 2008;164:132–42 CrossRef Medline
17. Dubois J, Hertz-Pannier L, Dehaene-Lambertz G, et al. **Assessment of the early organization and maturation of infants' cerebral white matter fiber bundles: a feasibility study using quantitative diffusion tensor imaging and tractography.** *Neuroimage* 2006;30:1121–32 CrossRef Medline
18. Vassal F, Schneider F, Boutet C, et al. **Combined DTI tractography and functional MRI study of the language connectome in healthy volunteers: extensive mapping of white matter fascicles and cortical activations.** *PLoS One* 2016;11:e0152614 CrossRef Medline
19. Mori S, van Zijl P. **Fiber tracking: principles and strategies: a technical review.** *NMR Biomed* 2002;15:468–80 CrossRef Medline
20. Lazar M, Weinstein DM, Tsuruda JS, et al. **White matter tractography using diffusion tensor deflection.** *Hum Brain Mapp* 2003;18:306–21 CrossRef Medline
21. Oishi K, Zilles K, Amunts K, et al. **Human brain white matter atlas: identification and assignment of common anatomical structures in superficial white matter.** *Neuroimage* 2008;43:447–57 CrossRef Medline
22. Lemaire JJ, Frew AJ, McArthur D, et al. **White matter connectivity of human hypothalamus.** *Brain Res* 2011;1371:43–64 CrossRef Medline
23. Wakana S, Jiang H, Nagae-Poetscher LM, et al. **Fiber tract-based atlas of human white matter anatomy.** *Radiology* 2004;230:77–87 CrossRef Medline
24. Niogi SN, Mukherjee P, Ghajar J, et al. **Extent of microstructural white matter injury in postconcussive syndrome correlates with impaired cognitive reaction time: a 3T diffusion tensor imaging study of mild traumatic brain injury.** *AJNR Am J Neuroradiol* 2008;29:967–73 CrossRef Medline
25. Catani M, Thiebaut de Schotten M. **A diffusion tensor imaging tractography atlas for virtual in vivo dissections.** *Cortex* 2008;44:1105–32 CrossRef Medline
26. Catani M, Howard RJ, Pajevic S, et al. **Virtual in vivo interactive dissection of white matter fasciculi in the human brain.** *Neuroimage* 2002;17:77–94 CrossRef Medline
27. Thiebaut de Schotten M, Ffytche DH, Bizzi A, et al. **Atlasing location, asymmetry and inter-subject variability of white matter tracts in the human brain with MR diffusion tractography.** *Neuroimage* 2011;54:49–59 CrossRef Medline
28. Partridge SC, Mukherjee P, Berman JI, et al. **Tractography-based quantitation of diffusion tensor imaging parameters in white matter tracts of preterm newborns.** *J Magn Reson Imaging* 2005;22:467–74 CrossRef Medline
29. van der Knaap MS, Valk J. **MR imaging of the various stages of normal myelination during the first year of life.** *Neuroradiology* 1990;31:459–70 CrossRef Medline
30. Gouttard S, Goodlett CB, Kubicki M, et al. **Measures for validation of DTI tractography.** *Proc SPIE Int Soc Opt Eng* 2012;8314:8314 CrossRef Medline
31. Prayer D, Prayer L. **Diffusion-weighted magnetic resonance imaging of cerebral white matter development.** *Eur J Radiol* 2003;45:235–43 CrossRef Medline
32. Friede RL. **Control of myelin formation by axon caliber (with a model of the control mechanism).** *J Comp Neurol* 1972;144:233–52 CrossRef Medline
33. Brody BA, Kinney HC, Kloman AS, et al. **Sequence of central nervous system myelination in human infancy, I: an autopsy study of myelination.** *J Neuropathol Exp Neurol* 1987;46:283–301 CrossRef Medline
34. Kinney HC, Brody BA, Kloman AS, et al. **Sequence of central nervous system myelination in human infancy, II: patterns of myelination in autopsied infants.** *J Neuropathol Exp Neurol* 1988;47:217–34 CrossRef Medline
35. Yakovlev PI. **Morphological criteria of growth and maturation of the nervous system in man.** *Res Publ Assoc Res Nerv Ment Dis* 1962;39:3–46 Medline
36. Guillery RW. **Is postnatal neocortical maturation hierarchical?.** *Trends Neurosci* 2005;28:512–17 CrossRef Medline
37. Salami M, Itami C, Tsumoto T, et al. **Change of conduction velocity by regional myelination yields constant latency irrespective of distance between thalamus and cortex.** *Proc Natl Acad Sci U S A* 2003;100:6174–79 CrossRef Medline
38. Lancaster JL, Andrews T, Hardies LJ, et al. **Three-pool model of white matter.** *J Magn Reson Imaging* 2003;17:1–10 CrossRef Medline

Focal Areas of High Signal Intensity in Children with Neurofibromatosis Type 1: Expected Evolution on MRI

S. Calvez, R. Levy, R. Calvez, C.-J. Roux, D. Grévent, Y. Purcell, K. Beccaria, T. Blauwblomme, J. Grill, C. Dufour, F. Bourdeaut, F. Doz, M.P. Robert, N. Boddaert, and V. Dangouloff-Ros

ABSTRACT

BACKGROUND AND PURPOSE: Focal areas of high signal intensity are T2WI/T2-FLAIR hyperintensities frequently found on MR imaging of children diagnosed with neurofibromatosis type 1, often thought to regress spontaneously during adolescence or puberty. Due to the risk of tumor in this population, some focal areas of high signal intensity may pose diagnostic problems. The objective of this study was to assess the characteristics and temporal evolution of focal areas of high signal intensity in children with neurofibromatosis type 1 using long-term follow-up with MR imaging.

MATERIALS AND METHODS: We retrospectively examined the MRIs of children diagnosed with neurofibromatosis type 1 using the National Institutes of Health Consensus Criteria (1987), with imaging follow-up of at least 4 years. We recorded the number, size, and surface area of focal areas of high signal intensity according to their anatomic distribution on T2WI/T2-FLAIR sequences. A generalized mixed model was used to analyze the evolution of focal areas of high signal intensity according to age, and separate analyses were performed for girls and boys.

RESULTS: Thirty-nine patients (ie, 285 MR images) with a median follow-up of 7 years were analyzed. Focal areas of high signal intensity were found in 100% of patients, preferentially in the infratentorial white matter (35% cerebellum, 30% brain stem) and in the capsular lenticular region (22%). They measured 15 mm in 95% of cases. They appeared from the age of 1 year; increased in number, size, and surface area to a peak at the age of 7; and then spontaneously regressed by 17 years of age, similarly in girls and boys.

CONCLUSIONS: Focal areas of high signal intensity are mostly small (<15 mm) abnormalities in the posterior fossa or capsular lenticular region. Our results suggest that the evolution of focal areas of high signal intensity is not related to puberty with a peak at the age of 7 years. Knowledge of the predictive evolution of focal areas of high signal intensity is essential in the follow-up of children with neurofibromatosis type 1.

ABBREVIATIONS: FASI = focal areas of high signal intensity; HH = hippocampal hyperintensity; NF1 = neurofibromatosis type 1

Neurofibromatosis type 1 (NF1) is a relatively common neurocutaneous disorder, with an estimated prevalence of 1 in 3000–4000 individuals.[1] The most common brain lesions in patients with NF1 (60%–70% of children[2,3]) identified on MR imaging are T2WI hyperintensities, also termed focal areas of high signal intensity (FASI) or unidentified bright objects. FASI are usually considered a benign process caused by increased fluid accumulation in intramyelinic vacuoles.[4,5] Their clinical significance remains largely unknown; an association between clinical symptoms in NF1 and FASI has rarely been reported, notably cognitive dysfunction when FASI involved the thalamus and basal ganglia.[6-10]

To date, the literature suggests that these lesions can vary in size and number with time, though published articles have variable

Received January 21, 2020; accepted after revision June 7.

From the Pediatric Radiology Department (S.C., R.L., R.C., C.-J.R., D.G., N.B., V.D.-R.), Pediatric Neurosurgery Department (K.B., T.B.), and Ophthalmology Department (M.P.R.), Hôpital Universitaire Necker-Enfants Malades, Assistance Publique-Hôpitaux de Paris, Paris, France; Paris University (R.L., C.-J.R., D.G., K.B., T.B., F.B., F.D., M.P.R., N.B., V.D.-R.), PRES Sorbonne Paris Cité, Paris, France; Institut National de la Santé et de la Recherche Médicale UA10 (R.L., C.-J.R., D.G., N.B., V.D.-R.), Paris, France; Institut Imagine (R.L., C.-J.R., D.G., N.B., V.D.-R.), Unite Mixte de Recherche 1163, Paris, France; Radiology Department (Y.P.), Fondation Rothschild, Paris, France; Department of Pediatric and Adolescent Oncology (J.G., C.D.), Gustave Roussy Institute, Villejuif, France; Oncology Center SIREDO (Care Innovation and Research for Children, Adolescents and Young Adults with Cancer) (F.B., F.D.), Institute Curie, Paris, France.

Please address correspondence to Volodia Dangouloff-Ros, MD, MSc, Assistance-Publique Hôpitaux de Paris, Hôpital Universitaire Necker-Enfants Malades, Department of Pediatric Radiology, 149 rue de Sèvres, 75015 Paris, France; e-mail: Volodia.dangouloff-ros@aphp.fr

Indicates article with supplemental on-line photo.

http://dx.doi.org/10.3174/ajnr.A6740

follow-up duration (mean time interval generally <4 years[11-14]) or a relatively small number of patients and/or MR imaging examinations. Most studies suggested that FASI tend to decrease in size during adolescence.[8,11,13-17] However, these children may also develop confounding MR images because they are at risk of developing low-grade gliomas within but also outside the optic pathways. Therefore, knowing the expected growth and vanishing pattern of FASI is essential to correctly assess abnormalities on MR imaging in these children.

Moreover, previous studies reported signal change within the hippocampi, which led to some discordance among authors because some have described diffuse and bilateral hyperintensities as a distinct lesion,[16] while others have considered these hyperintensities to be FASI.[2,18,19] Knowing the characteristics and temporal evolution of these signal changes in comparison with other FASI could help to conclude whether they should be considered the same pathologic entity.

In the current study, we retrospectively reviewed serial MR imaging findings in a cohort of children with confirmed NF1 who had long-term MR imaging follow-up. We aimed to quantify the temporal evolution of FASI according to their regional distribution and sex, using a wide series of MR imaging examinations. In addition, we examined hippocampal intensity on T2WI and T2 FLAIR sequences.

MATERIALS AND METHODS

We followed the Strengthening the Reporting of Observational Studies in Epidemiology guidelines[20] for this retrospective observational study. Local institutional review board authorization was granted (EDRACT 2014-A-00541-46), and the requirement for written informed consent was waived.

Population and Procedures

We performed a retrospective review of the NF1 data base of Necker Enfants Malades Hospital, Paris, France, from January 2007 to December 2018. Inclusion criteria were the following: children younger than 18 years of age at the time of their first MR imaging, with a diagnosis of NF1, using the National Institutes of Health Consensus criteria[21] and having undergone ≥2 brain MR imaging examinations at least 4 years apart. To avoid bias in FASI evaluation, we excluded children with a history of radiation therapy or surgery involving the ROI due to the potential for major posttherapeutic sequelae.

MR Imaging Acquisition

MR imaging equipment and techniques varied in the cases with the longest follow-up, and some of the patients underwent brain MR imaging at outside institutions before referral to our unit. All MR imaging examinations at our institution (67% of the cohort) were performed using a Signa HDxt 1.5T system (GE Healthcare) and a 12-channel head-neck-spine coil.

Our older brain MR imaging protocol included 2D sequences acquired in the axial plane: T2WI spin-echo sequence (TR/TE = 7522/117 ms, section thickness = 4 mm, intersection gap = 0.4 mm, voxel size = 1.3 mm, 2 excitations) and a T2-FLAIR spin-echo sequence (TR/TE = 9000/2250/150 ms, section thickness = 4 mm, intersection gap = 0.4 mm, voxel size = 1.2 mm, 2 excitations). All measurements were preferentially made on the T2-FLAIR sequence unless it was of insufficient quality.

In recent years, 3D sequences became standard practice in our institution: 3D T2WI spin-echo sequences (TR/TE = 2500/102 ms, FOV = 512 × 512 mm^2, section thickness = 1 mm, intersection gap = 0.5 mm, flip angle = 90°) or 3D-T2-FLAIR-weighted spin-echo sequences (TR/TE = 8400/2234/166 ms, FOV = 512× 512 mm^2, section thickness = 1.2 mm, intersection gap = 0.6 mm, flip angle = 90°).

Image Analysis

We used a medical image viewer. Two radiologists, a junior radiologist (S.C. with 4 years of experience) and an experienced neuroradiologist (R.L. with 7 years of experience), analyzed each case in consensus.

FASI were defined by visual inspection as areas of T2WI or T2-FLAIR hyperintensity greater than normal gray matter, without mass effect, contrast enhancement, or restriction on DWI.

Counting and surface area measurements were performed manually by 1 observer (S.C.) by drawing irregular ROIs in the axial or coronal planes, with the resulting surface area computed by the image viewer. If FASI were present on >1 contiguous section, an individual lesion was measured once on the section where it appeared the largest. FASI were categorized by size, according to their maximal diameter (5 groups defined as <5 mm; 5–10 mm; 10–15 mm; 15–20 mm; >20 mm) in each anatomic region (7 clusters in infra- and supratentorial regions, both left and right sides: capsular lenticular, caudate nucleus, thalamus, corpus callosum, cerebral white matter, brain stem, and cerebellum), reflecting the pattern of FASI distribution in previous reports.

Each surface area (in square millimeters) represented the addition of all FASI surface areas within a given anatomic region. Total lesion number and surface area per region for each MR imaging of all patients were recorded.

For the analysis of the hippocampi, a hyperintensity was defined as an area of intensity higher than that of the cortex, as assessed by the 2 readers in consensus. The presence of a hyperintensity, its unilateral/bilateral location, diffuse/focal features, and the parameters of the corresponding sequence (2D, 3D, T2WI, T2-FLAIR) have been listed above.

Statistics

All analyses were performed using SAS software, Version 9.4 of the SAS System for Windows (SAS Institute).

Descriptive analyses were performed by sex and overall for the total number, total surface area, and number by size for each of the 10 considered anatomic regions (overall, 2 zones [infra- and supratentorial], 7 clusters). For each of the considered regions and each of the 5 size classes, the total number in the class was counted and descriptive qualitative analyses were performed by sex and for the overall cohort.

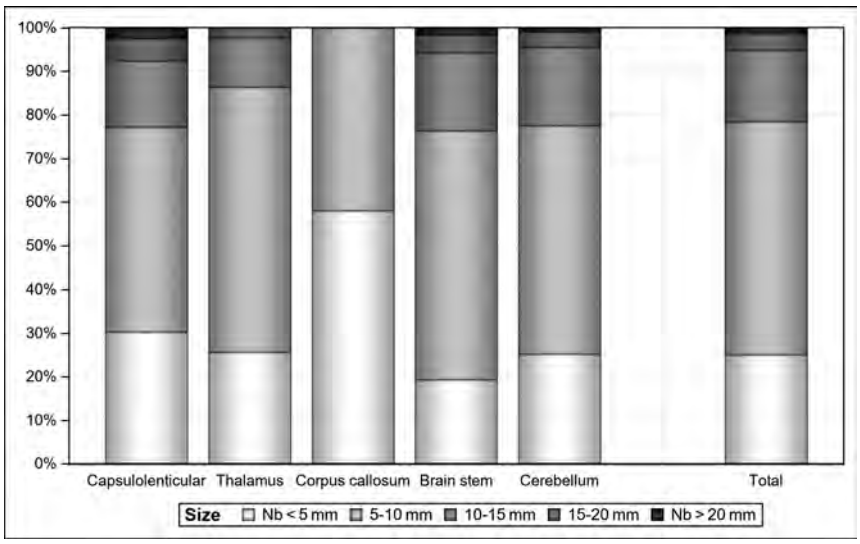

FIG 1. The distribution of FASI on all MR imaging examinations in size classes by clusters. Seventy-nine percent of FASI were <10 mm. FASI of >20 mm appeared only for females ($n = 7$ females, 2 of whom were outliers) and only in the capsular lenticular region, brain stem, and cerebellum clusters.

Due to the presence of outliers, some analyses were performed with and without them (3 patients whose total surface area was >750 mm^2). Some analyses were performed including a linear regression model between the number of lesions and surface area, using a cubic B-spline to fit a smooth curve through a scatterplot of age versus surface area, and some regressions, stepwise or not, between patient age and the total surface area.

A generalized linear mixed model ("proc mixed" in SAS) was used to take into account the repetition of MRIs in patients and the nonequally spaced time intervals between MR imaging examinations (repeated statement with spatial power) including effects for age, age^2, age^3, sex, and the 3 interactions, sex with age, age^2, age^3. Each analysis was performed interactively as a stepwise analysis: First, all effects were included in the model, and for each subsequent step, the effect with the higher P value was excluded and so on until all P values were <.05. The final model retained is the model with the effects for age, age^2, age^3 (sex and all interactions are not significant); and from the final regression model with outliers, 2 ages of interest were calculated, the apex and the nadir of the surface area.

RESULTS

Patients and MR Imaging

Of the 53 patients who met the inclusion criteria, 14 were excluded because of surgical sequelae. No patient had a prior history of radiation therapy. Among the included patients, 23 had an optic pathway glioma (optic nerve, $n = 18$; optic chiasm, $n = 5$). No patient had a tumor outside the optic pathways or any mass effect or contrast enhancement outside the optic chiasm.

This study included 39 pediatric patients (22 females and 17 males, 56% and 44%) with an age range from 11 months to 13.7 years at the first available brain MR imaging examination (mean, 4.7 years; 95% CI, 3.8–5.6 years) and 5.4–18.8 years at the last available MR imaging (mean, 12.1 years; 95% CI, 11.0–13.3 years). They had undergone between 2 and 22 MR imaging examinations (mean, 7.3; 95% CI, 5.8–8.8) during a time interval from 4 to 14.4 years (mean, 7.4 years; 95% CI, 6.6–8.2 years).

From these 39 patients, 285 MR imaging examinations were available for review (female = 186, 65.3%; male = 99, 34.7%). Of these, there were 181 2D-T2WI sequences (63.5%), 190 2D-T2-FLAIR sequences (67%), 77 3D-T2WI sequences (27%), and 47 3D-T2 FLAIR sequences (16,5%). Seventy-four percent (211/285) of MRIs contained both T2WI and T2 FLAIR sequences. All patients had at least 1 examination with contrast media injection, but details of gadolinium molecule and dose were not available due to the long retrospective follow-up.

Number and Size of FASI Overall in the Study

The frequency of patients with FASI was 100% in our cohort. Among them, 4 patients had no FASI seen on one of their MR imaging examinations (4 patients: 0.9 years, 1.5 years, 2.8 years, and 15.0 years of age; 4/285 [1.4%] of studied MR images).

Overall, 3268 FASI were counted, 65.2% in the infratentorial region, of which 35.0% were in the cerebellum; 30.3%, in the brain stem; 21.5%, in the capsular lenticular region; 11.7%, in the thalamus; 1.5%, in the corpus callosum; and none in the caudate or white matter supratentorial clusters. Overall, 53.4% were of 5–10 mm; 25.1%, <5 mm; 16.3%, 10–15 mm; 3.9%, 15–20 mm; and 1.3%, >20 mm (Fig 1).

Number, Size, and Surface Area of FASI across Time

A linear relationship between the number of FASI and the total surface area was observed with an R^2 of 0.83. The scatterplots of number and surface area of FASI (Fig 2 and On-line Figure) show an appearance of FASI starting at 1 year, followed by an increase until the apex at about 7 years of age, followed by a decrease until the nadir at about 17–18 years of age (Fig 3). The mean age of the patients at the individual peak of FASI surface area was 7.2 years (Fig 4).

Among the 9 children younger than 2 years of age at first MR imaging, 3 did not have FASI (mean age, 1.7 years). These appeared in the time interval before the second MR imaging, performed at a mean age of 3.5 years.

The interpretation of the results for the group 16–19 years of age must be made with caution because only 7 MRIs for 5 patients were available (female = 1, male = 4). Contrary to the impression given by the curve, these patients showed a further decrease in or stability of their number of FASI/FASI surface areas, with the

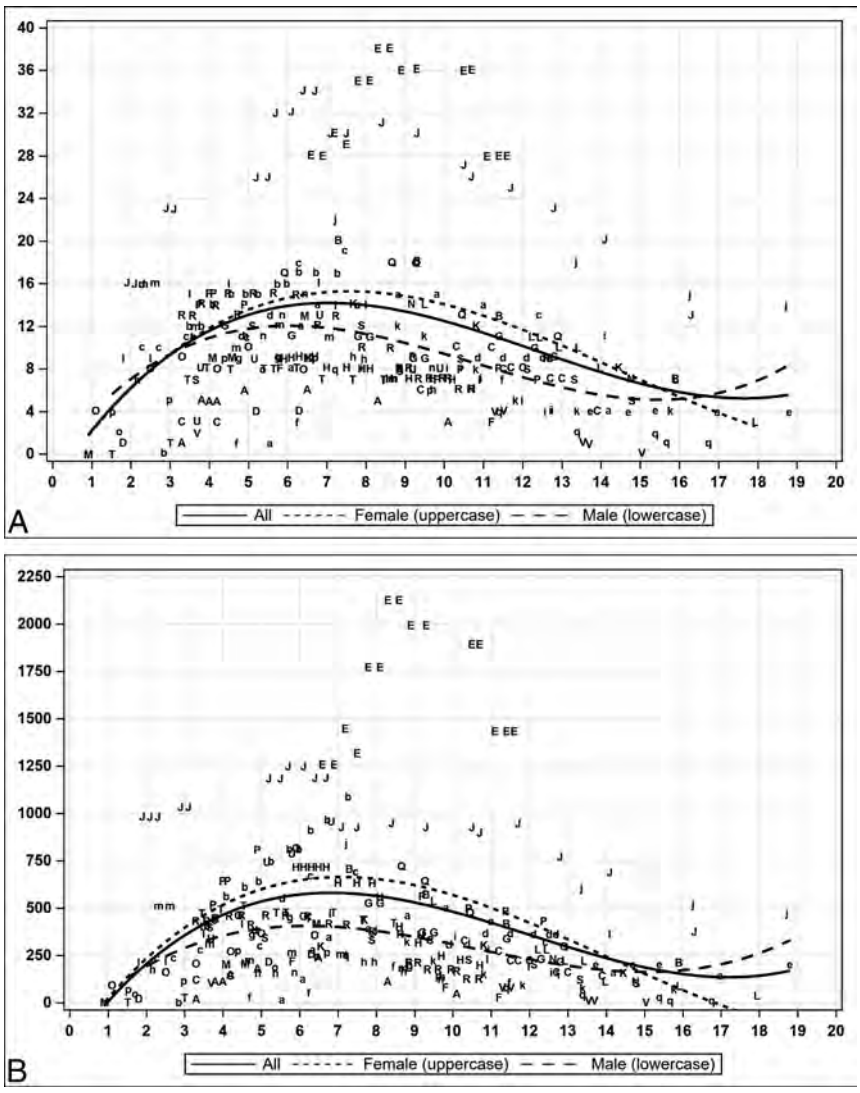

FIG 2. Temporal evolution of scatterplots of the total FASI number of all MRIs (*A*) and total FASI surface area of all MRIs (*B*). *Uppercase letters* are for females, and *lowercase letters* are for males. The regression curve is 3°. The x-axis represents age, the y-axis represents the number of FASI (*A*), and the surface area is in square millimeters (*B*). Female and male regression curves are descriptive.

apparent statistical increase being explained by the disappearance of patients with lower lesion load in the cohort.

The shapes of the regression curves were similar for the infratentorial region and flatter for the supratentorial region. From the complete regression model, no effect of sex was observed ($P = .76$). The same analysis without outliers (3 patients with total FASI surface area of $>750\ mm^2$) showed very similar results with an apex of 6.6 years and a nadir of 16.5 years. The same analysis performed on all MRIs for each anatomic region led to the same interpretation: The apex varied between 6.4 and 7.5 years, and the nadir, between 16.0 to 18.8 years.

Hippocampal Analysis

Of the 39 patients, 23 had a hippocampal hyperintensity (HH) on at least 1 MR imaging. The 23 patients included in this subgroup for analysis (59%, 12 female and 11 male) accounted for 163 MRIs (time interval = 7.6 years; 95% CI, 3.7–14.4 years; average MR imaging/patient = 7; 95% CI, 2–22; mean age = 8.7 years; 95% CI, 0.9–18.8 years). This subgroup included 55% of the total number of girls and 65% of the total number of boys without statistical difference ($P = .74$).

The HHs were diffuse, bilateral, and symmetric (100%) (Fig 5). The 23 patients with HH had a higher total surface area of FASI than the 16 patients without HH (mean, 394 mm^2; 95% CI, 0–1245 mm^2 versus mean, 507 mm^2; 95% CI, 0–2123 mm^2; $P = .03$).

Eighteen of 23 patients had HH on their first MR imaging (mean age, 6.2 years; 95% CI, 1.7–13.7 years), whereas 5 of 23 patients had normal hippocampi on their initial MR imaging. The HH appeared on follow-up MR imaging (mean age, 4.2 years; 95% CI, 2.6–6.7 years). No MR imaging performed before 3 years of age ($n = 9$) showed HH.

Eleven of 23 patients had at least 1 follow-up MR imaging with negative findings (mean age, 11.8 years; 95% CI, 6.5–17 years), and this consistently corresponded to a transition from 2D to 3D sequences. HH did not disappear on follow-up MR imaging with 2D sequences, including after 11 years of age.

Of the 163 MRIs, 112 MRIs included a 2D-T2-FLAIR sequence, of which 84 (75%) showed HH and 24 included a 3D-T2-FLAIR sequence, of which 2 (8%) showed HH. One hundred MRIs comprised both 2D-T2WI and 2D-T2-FLAIR sequences, of which 75 (75%) showed HH only on the 2D-T2-FLAIR sequences.

DISCUSSION

We report the neuroimaging findings in a large MR imaging study with long-term follow-up of children with NF1 and demonstrate the evolution pattern of FASI with time.

The frequency of patients with FASI was 100%, which is greater than all previously published results in the literature, probably because of the inclusion criterion of a 4-year follow-up period and also because our institution is a neurosurgical tertiary referral center with a probable selection bias toward symptomatic patients.

The spatial distribution of FASI in our series is in agreement with that of previously published data,[2,12,13,17,22-24] involving, in

order of decreasing frequency, the cerebellum, brain stem, capsulolenticular region, and thalamus. Some reports did not specifically identify involvement of the thalamus but combined it with other anatomic regions.[11,15] Because FASI were not frequently observed in the caudate nucleus, corpus callosum, or supratentorial white matter, the occurrence of T2 hyperintensities in these localizations could be a red flag for an atypical lesion, including a tumoral lesion, not a classic FASI.

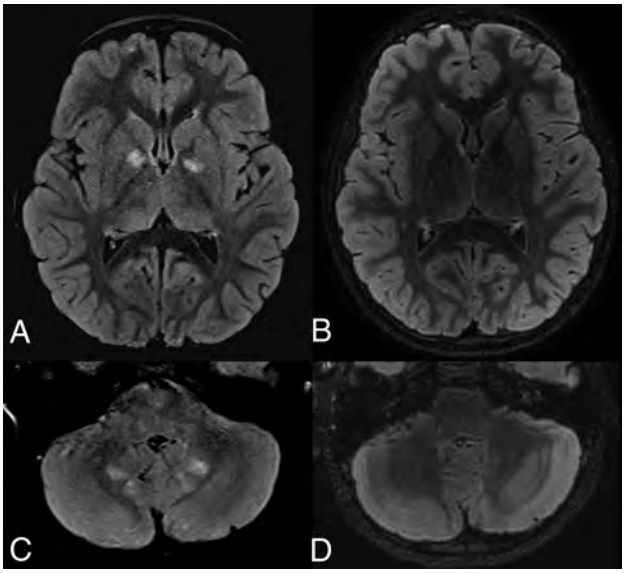

FIG 3. Temporal evolution of FASI on T2-FLAIR-weighted images. Axial T2-FLAIR sequences show capsular lenticular (*A*) and infratentorial white matter (*C*) FASI in a 6-year-old patient, then follow-up MR imaging in a 10-year-old patient with almost complete disappearance of these FASI (*B* and *D*).

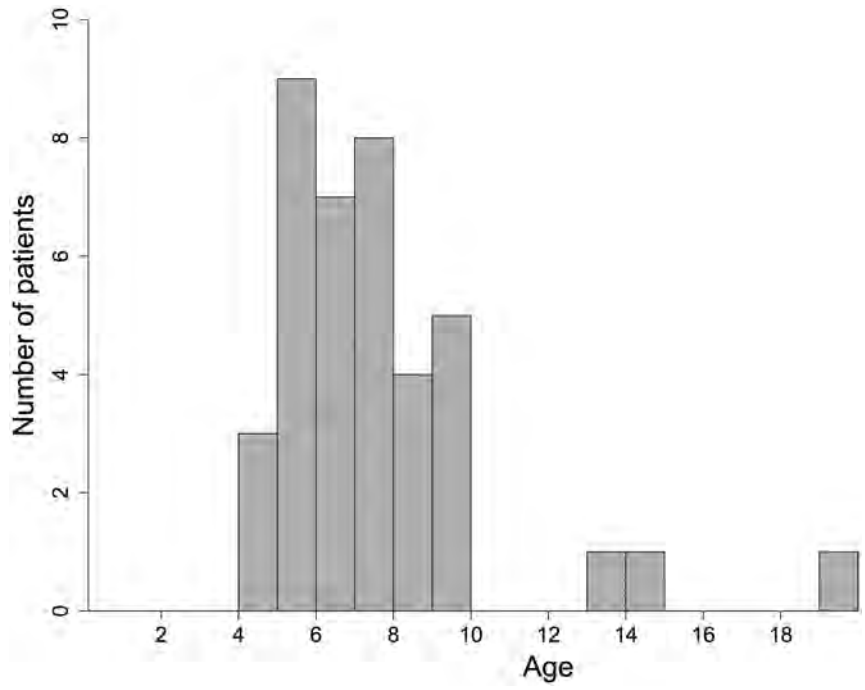

FIG 4. Age of the patients at the time of the peak of FASI surface. The mean age at the peak was 7.2 ± 2.8 years. The 3 patients with a peak age after 13 years had their first MR imaging after the age of 7 years (7.5, 13, and 13 years).

In agreement with a previous report,[14] FASI size was generally <10 mm. Other authors noted that FASI were 15 mm[25] or that the maximum lesion diameter was 25 mm.[24] Therefore, in the setting of larger FASI, while they may correspond to a confluence of many FASI, an underlying tumoral process cannot be excluded and should be followed up.

No FASI displayed a mass effect or contrast enhancement, and none eventually developed into a glioma. This finding may be explained by our exclusion criteria, which included surgery involving the ROI at any time during the study period. Radiologists should exercise caution when the presence of a mass effect, with or without contrast enhancement, is detected in relation to a FASI because these features can correspond to low-grade or even high-grade gliomas outside the optic pathways in patients with NF1.[26,27]

Our results confirm the findings from previous studies that FASI are transient and dynamic abnormalities. First, in our cohort, FASI appeared from 1 year of age. Among the studies that included children younger than 4 years,[2,15,24,25] none specified the age at the appearance of FASI.

Second, we found that an increase in size or de novo appearance of lesions is expected in young patients, with growth of characteristic FASI occurring until 7 years of age. The absence of such findings in other studies may reflect differences in methods because we did not have any predefined age group. In fact, most authors have studied patient groups consisting of age classifications with arbitrary thresholds, such as 10 years,[13,22,24] or 4 and 12 years,[17] or 15 years.[1,11] Other authors[18] analyzed brain MR imaging from children in age groups, particularly 4.0–6.9 and 7.0–9.9 years, and showed that most children accumulate FASI before 7 years of age, with a tendency toward FASI stabilization after that age (in the age range of 7.0–9.9 years). Furthermore, the larger size of our cohort and the longer follow-up of individual patients may better explain the age accuracy in our results.

Finally, after reaching the apex, FASI decrease until adulthood (nearly 17 years). Some authors concluded that FASI decrease from the beginning of adolescence[2,7,12,16] or that they increase in number and size until 12 years of age.[2] However, our results did not show such an association with puberty because we found that FASI tend to decrease earlier in childhood and are not correlated to sex. Some studies[12,16] included children older than 8 years of age, directly after the apex in our study, corresponding to the period when FASI have already started to decrease in number and size. Our data provide evidence of

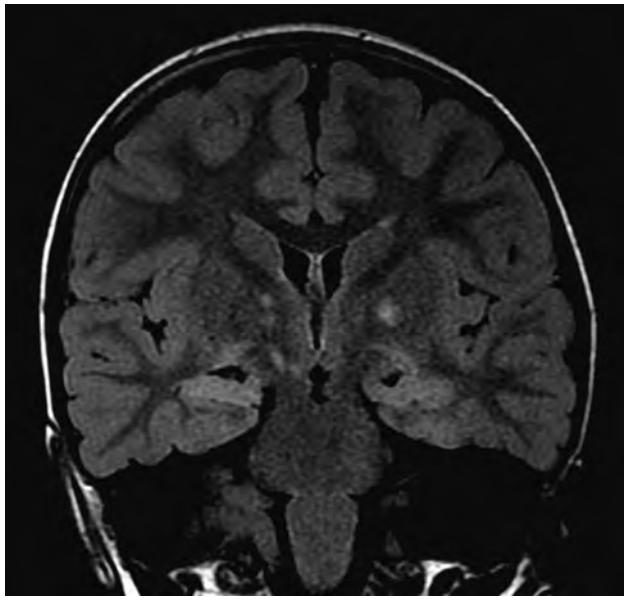

FIG 5. Hippocampal hyperintensity on T2 FLAIR image. Coronal T2 FLAIR sequence shows the diffuse homogeneous and symmetric hyperintensity of both hippocampi. FASI are also seen in the globus pallidus on both sides.

dissociation between the evolution of FASI and puberty. These findings indicate the necessity to evaluate the relationship between this evolution pattern and clinically determined pubertal status.

We did not find any difference between the evolution of anatomic regions and clusters, contrary to a previous report[11] that concluded that FASI in the cerebellum decreased earlier than those in the brain stem and basal ganglia. Likewise, 2 distinct patterns have been reported,[12] a linear decrease of FASI in the cerebellar hemisphere of adolescents and a nonlinear appearance/regression in the basal ganglia region, with an increase again in late adolescence.

Given the high frequency and specificity of the presence of FASI in NF1, some authors[2,23] recommended the inclusion of the presence of FASI as a diagnostic criterion for NF1 in children. It has been reported that the differential diagnosis for high-signal foci found in the cerebral white matter of 1.9% of healthy patients[28] versus those found in patients with NF1 should not be a problem because they have different characteristics and different anatomic predilections.[14] Because we demonstrate the temporal evolution of FASI, using them as a diagnostic criterion could be of interest for patients between 4 and 12 years of age but would not be very useful for early childhood or adolescence.

Hippocampal Analysis

There are few data on hippocampal abnormalities in NF1. Hippocampal hyperintensities have been described as bilateral and diffuse, present in 80% of 1 cohort[16] and easier to see on T2 FLAIR. Our study revealed diffuse, bilateral, and symmetric hippocampal hyperintensities in nearly 60% of patients.

Because we found no correlation between the temporal evolution and the number of FASI and that the total surface area of FASI was lower in patients with HH, our results would suggest that hippocampal hyperintensity is a separate entity from FASI, contrary to other studies[2,18,19] that considered the hippocampi as an anatomic region affected by FASI.

These signal abnormalities seem to depend on the technique used because the hyperintensity appears more frequently on the 2D-T2-FLAIR sequences compared with the 3D-T2-FLAIR and 2D-T2WI sequences. Moreover, the disappearance of these hyperintensities seems to be related to the change of technique and not to the age of the patients. 3D-T2-FLAIR seemed to be inferior to 2D-T2-FLAIR in terms of lesion contrast and conspicuity in the hippocampus, such as in patients with hippocampal sclerosis.[29] This feature could be explained by the higher signal of the normal hippocampus on 3D-T2-FLAIR; radiologists should be aware of this finding. FASI should not have this pitfall because 3D-T2-FLAIR has been shown to be equal or superior to 2D-T2-FLAIR for other gray or white matter lesions.[29] The subjectivity of these diffuse and symmetric signal changes and the dependence on the technique used may limit the clinical impact of this feature in patients with NF1. A potential link with clinical findings and the underlying pathophysiology remains to be demonstrated.

Limitations

Our study has some limitations, including selection bias. Our institution is a tertiary referral center that receives a high proportion of symptomatic or atypical patients. Furthermore, a minimum follow-up of 4 years increases the frequency of MR imaging findings. Patients with a history of surgery were excluded; therefore, our evolution criteria do not apply to them.

All of our data pertain to brain MR imaging at 1.5T, which limits the applicability of our results to MR imaging at 3T. It seems unlikely that this would have modified the longitudinal variations of FASI, but the analysis of hippocampal hyperintensity may be different at 3T.

Most patients underwent a combination of both 2D and 3D MR imaging sequences during the course of their follow-up, which could affect the variability of surface area measurements. However, we were unable to analyze this effect because the patients did not have 2D and 3D sequences at the same time. The surface area measurements of FASI were similar between T2WI and T2 FLAIR sequences. Because of the low number of 3D sequences, we were unable to use volumetric measurements for follow-up (instead of surface area), which could have been a more accurate way to measure FASI. 2D section thickness was high (4 mm), possibly hampering the accuracy of measurements of FASI using these sequences. Because our inclusion criteria mandated a long-term follow-up period and due to the larger size of our cohort, the inclusion of multiple different MR imaging techniques was unavoidable. As imaging becomes ever more sensitive, it will be increasingly important to define a standardized imaging protocol for brain MR imaging in the setting of NF1.

CONCLUSIONS

Our study, based on a large sample of MR imaging examinations with long-term follow-up of patients with NF1, provides a more complete view of FASI evolution.

Having demonstrated a predictable pattern of longitudinal variation of FASI in children with NF1, we suggest that FASI are

not related to puberty or adolescence because they decrease at an earlier age, from 7 years, and there is no significant difference according to sex. However, we did not assess pubertal status at the time of each MR imaging examination, precluding drawing any strong conclusions about this potential correlation. These results should be subject to future prospective studies with larger sample sizes and knowledge of pubertal status, which could lead to an improved understanding of FASI pathophysiology.

We also found that hippocampal hyperintensities frequently seen in patients with NF1 are not correlated with FASI evolution, supporting the hypothesis of a different process, which still needs to be elucidated.

We are convinced that a better understanding of FASI could have positive practical implications. A "watch and wait" approach could be implemented until the age of apex, provided no atypical imaging sign is present (mass effect, contrast enhancement). Knowledge of the predicted evolution allows more accurate prognostic advice to be conveyed to the referring physician and family during follow-up.

Disclosures: François Doz—*UNRELATED*: *Board Membership*: Bayer, Bristol Myers Squibb, Celgene, Loxo, Roche, Servier, Tesaro*; *Consultancy*: Servier*; *Grants/Grants Pending*: Synth Innove*; *Payment for Development of Educational Presentations*: Bristol Myers Squibb*; *Travel/Accommodations/Meeting Expenses Unrelated to Activities Listed*: Bayer, Bristol Myers Squibb, Roche. *Money paid to the institution.

REFERENCES

1. Nicita F, Di Biasi C, Sollaku S, et al. **Evaluation of the basal ganglia in neurofibromatosis type 1.** *Childs Nerv Syst ChNS Syst* 2014;30:319–25 CrossRef Medline
2. Lopes Ferraz Filho JR, Munis MP, Soares Souza A, et al. **Unidentified bright objects on brain MRI in children as a diagnostic criterion for neurofibromatosis type 1.** *Pediatr Radiol* 2008;38:305–10 CrossRef Medline
3. North KN, Riccardi V, Samango-Sprouse C, et al. **Cognitive function and academic performance in neurofibromatosis 1: consensus statement from the NF1 Cognitive Disorders Task Force.** *Neurology* 1997;48:1121–27 CrossRef Medline
4. DiPaolo DP, Zimmerman RA, Rorke LB, et al. **Neurofibromatosis type 1: pathologic substrate of high-signal-intensity foci in the brain.** *Radiology* 1995;195:721–24 CrossRef Medline
5. Billiet T, Mädler B, D'Arco F, et al. **Characterizing the microstructural basis of "unidentified bright objects" in neurofibromatosis type 1: a combined in vivo multicomponent T2 relaxation and multi-shell diffusion MRI analysis.** *Neuroimage Clin* 2014;4:649–58 CrossRef Medline
6. Ferner RE, Chaudhuri R, Bingham J, et al. **MRI in neurofibromatosis 1: the nature and evolution of increased intensity T2 weighted lesions and their relationship to intellectual impairment.** *J Neurol Neurosurg Psychiatry* 1993;56:492–95 CrossRef Medline
7. Hyman SL, Gill DS, Shores EA, et al. **T2 hyperintensities in children with neurofibromatosis type 1 and their relationship to cognitive functioning.** *J Neurol Neurosurg Psychiatry* 2007;78:1088–91 CrossRef Medline
8. Payne JM, Pickering T, Porter M, et al. **Longitudinal assessment of cognition and T2-hyperintensities in NF1: an 18-year study.** *Am J Med Genet A* 2014;164:661–65 CrossRef
9. Feldmann R, Schuierer G, Wessel A, et al. **Development of MRI T2 hyperintensities and cognitive functioning in patients with neurofibromatosis type 1.** *Acta Paediatr Oslo Paediatr* 2010;99:1657–60 CrossRef Medline
10. Ottenhoff MJ, Rietman AB, Mous SE, ENCORE-NF1 Team, et al. **Examination of the genetic factors underlying the cognitive variability associated with neurofibromatosis type 1.** *Genet Med* 2020; 22:889–97 CrossRef Medline
11. Itoh T, Magnaldi S, White RM, et al. **Neurofibromatosis type 1: the evolution of deep gray and white matter MR abnormalities.** *AJNR Am J Neuroradiol* 1994;15:1513–19 Medline
12. Kraut MA, Gerring JP, Cooper KL, et al. **Longitudinal evolution of unidentified bright objects in children with neurofibromatosis-1.** *Am J Med Genet A* 2004;129A:113–19 CrossRef Medline
13. Menor F, Marti-Bonmati L, Arana E, et al. **Neurofibromatosis type 1 in children: MR imaging and follow-up studies of central nervous system findings.** *Eur J Radiol* 1998;26:121–31 CrossRef Medline
14. Raininko R, Thelin L, Eeg-Olofsson O. **Non-neoplastic brain abnormalities on MRI in children and adolescents with neurofibromatosis type 1.** *Neuropediatrics* 2001;32:225–30 CrossRef Medline
15. DiMario FJ, Ramsby G. **Magnetic resonance imaging lesion analysis in neurofibromatosis type 1.** *Arch Neurol* 1998;55:500–05 CrossRef Medline
16. Gill DS, Hyman SL, Steinberg A, et al. **Age-related findings on MRI in neurofibromatosis type 1.** *Pediatr Radiol* 2006;36:1048–56 CrossRef Medline
17. Khan A, Beri S, Baheerathan A, et al. **Globus pallidus high-signal lesions: a predominant MRI finding in children with neurofibromatosis type 1.** *Ann Indian Acad Neurol* 2013;16:53–56 CrossRef Medline
18. Griffiths PD, Blaser S, Mukonoweshuro W, et al. **Neurofibromatosis bright objects in children with neurofibromatosis type 1: a proliferative potential?** *Pediatrics* 1999;104:e49 CrossRef Medline
19. Yamanouchi H, Kato T, Matsuda H, et al. **MRI in neurofibromatosis type I: using fluid-attenuated inversion recovery pulse sequences.** *Pediatr Neurol* 1995;12:286–90 CrossRef Medline
20. von Elm E, Altman DG, Egger M, et al. **The Strengthening the Reporting of Observational Studies in Epidemiology (STROBE) statement: guidelines for reporting observational studies.** *Lancet* 2007;370:1453–57 CrossRef
21. **Neurofibromatosis: Conference Statement—National Institutes of Health Consensus Development Conference.** *Arch Neurol* 1988;45:575–78 Medline
22. Ferraz-Filho JR, José da Rocha A, Muniz MP, et al. **Unidentified bright objects in neurofibromatosis type 1: conventional MRI in the follow-up and correlation of microstructural lesions on diffusion tensor images.** *Eur J Paediatr Neurol* 2012;16:42–47 CrossRef Medline
23. DeBella K, Poskitt K, Szudek J, et al. **Use of "unidentified bright objects" on MRI for diagnosis of neurofibromatosis 1 in children.** *Neurology* 2000;54:1646–51 CrossRef Medline
24. Sevick RJ, Barkovich AJ, Edwards MS, et al. **Evolution of white matter lesions in neurofibromatosis type 1: MR findings.** *AJR Am J Roentgenol* 1992;159:171–75 CrossRef Medline
25. Aoki S, Barkovich AJ, Nishimura K, et al. **Neurofibromatosis types 1 and 2: cranial MR findings.** *Radiology* 1989;172:527–34 CrossRef Medline
26. Campian J, Gutmann DH. **CNS tumors in neurofibromatosis.** *J Clin Oncol* 2017;35:2378–85 CrossRef Medline
27. Spyris CD, Castellino RC, Schniederjan MJ, et al. **High-grade gliomas in children with neurofibromatosis type 1: literature review and illustrative cases.** *AJNR Am J Neuroradiol* 2019;40:366–69 CrossRef Medline
28. Dangouloff-Ros V, Roux C-J, Boulouis G, et al. **Incidental brain MRI findings in children: a systematic review and meta-analysis.** *AJNR Am J Neuroradiol* 2019;40:1818–23 CrossRef Medline
29. Kakeda S, Korogi Y, Hiai Y, et al. **Pitfalls of 3D FLAIR brain imaging: a prospective comparison with 2D FLAIR.** *Acad Radiol* 2012; 19:1225–32 CrossRef Medline

Neuroimaging Appearance of Cerebral Malignant Epithelioid Glioneuronal Tumors in Children

G. Orman, S. Mohammed, H.D.B. Tran, F.Y. Lin, A. Meoded, N. Desai, T.A.G.M. Huisman, and S.F. Kralik

ABSTRACT

SUMMARY: Malignant epithelioid glioneuronal tumor is a rare high-grade, aggressive brain tumor that shows both glial and neuronal differentiation on histopathology but is not included in the current World Health Organization classification. The neuroimaging appearance is variable but may be secondary to the size of the mass and/or location of the tumor. In our series, all epithelioid glioneuronal tumors were encountered in the supratentorial space and included pineal, temporal, and extratemporal lobar cerebral hemisphere locations. When large, the tumors demonstrate cystic degeneration and necrosis, hemorrhage, contrast enhancement, and regions of low apparent diffusion coefficient scalars consistent with patterns seen with other high-grade pediatric brain tumors. The tumors also have a propensity to spread into the meninges at presentation and for distant CSF spread on follow-up imaging.

ABBREVIATION: MEGNT = malignant epithelioid glioneuronal tumor

Brain tumors are the second leading cause of cancer after leukemia in the pediatric population. Pediatric brain tumors are the most common among all causes of death from solid tumors in children.[1,2] Primary brain tumors are more common and are of various histologic types. Their prognosis and treatment depend on the histologic type, tumor grade, and, increasingly, the molecular features.[2]

Malignant epithelioid glioneuronal tumor (MEGNT) is a rare high-grade, aggressive brain tumor that shows both glial and neuronal differentiation on histopathology. MEGNT is not included in the current World Health Organization classification.[3] Patients usually present with signs and symptoms of increased intracranial pressure or symptoms related to the location of the lesion. Both pediatric and adult cases have been described in the neuropathology literature.[4-7] The first report described clinicopathologic features of 2 unusual MEGNTs in pediatric patients. The tumors shared histopathology and clinical aggressiveness with 3 cases previously described in adults.[5,7] The largest clinicopathologic study included 40 patients; 15% (6/40) of the patients were children. The authors evaluated all tumors diagnosed as MEGNTs in routine practice during a 2-year period during which neurofilament protein immunostaining was performed in any case of suspected malignant glioma with unusual clinical, radiographic, and/or histologic features.[6] Neuroimaging is essential for the initial diagnosis; however, a systematic review of the neuroimaging findings of pediatric MEGNT has not been described.[4] The purpose of this article was to describe the CT and MR imaging features of this rare and aggressive tumor in a pediatric case series.

Case Series

Following institutional review board approval, a retrospective review of CTs and MRIs from 10 pediatric patients (18 years of age or younger) with a pathology-proved MEGNT diagnosis was performed by 2 board-certified neuroradiologists (N.D., S.F.K.), each with 9 years of neuroradiology experience. Initial-presentation CTs were reviewed to determine the density of the solid portion of the tumor relative to the normal brain parenchyma (hyperdense, isodense, hypodense), the presence of calcification and/or hemorrhage, and bone changes (scalloping, bone erosion). Initial-presentation MRIs were reviewed to determine the following: tumor location; maximum diameter; T2WI appearance relative to the normal brain parenchyma (hyperintense, isointense, hypointense); presence of cysts/necrosis (yes/no); presence of flow voids (yes/no) and perilesional T2WI hyperintensity suggestive of vasogenic edema (none, mild, extensive); minimum ADC value of the solid portion of the tumor using a 5-mm^3 ROI; presence of hemorrhage or calcification on gradient-echo or specific

Received February 14, 2020; accepted after revision May 28.

From the Edward B. Singleton Department of Radiology (G.O., S.M., H.D.B.T., A.M., N.D., T.A.G.M.H., S.F.K.), and Department of Oncology (F.Y.L.), Texas Children's Hospital and Baylor College of Medicine, Houston, Texas.

Please address correspondence to Gunes Orman, MD, Texas Children's Hospital, Edward B. Singleton Department of Radiology, 6701 Fannin St, Suite 470, Houston, TX 77030; e-mail: gxorman@texaschildrens.org

http://dx.doi.org/10.3174/ajnr.A6668

calcification versus hemorrhage determined from phase-contrast images in susceptibility-weighted imaging; enhancement on postcontrast T1-weighted imaging (yes/no); and leptomeningeal/dural extension (yes/no) determined from postcontrast T1-weighted imaging. Initial presentation and follow-up MRIs of the brain and spine were reviewed for presence of CSF metastases in the brain and spine, defined as nodular or linear areas of abnormal enhancement along the meningeal surfaces.

The mean age of the children was 8.7 years (range, 3.8–18.4 years), and 50% were female. All tumors were supratentorial in the pineal ($n = 2$), temporal ($n = 2$), and extratemporal cerebral hemispheres including the frontal lobe ($n = 3$) and frontal and parietal lobes ($n = 3$). Of the 8 tumors involving the cerebral hemispheres, 7 tumors (88%) involved the cortical and subcortical regions, indicative of a peripheral predominance. One tumor involving the frontal and parietal lobes demonstrated 2 separate enhancing masses and was classified as multifocal, while the remainder demonstrated 1 single enhancing mass. Presenting signs and symptoms included headache, vomiting, abnormal gait, seizure, lethargy, hemiparesis, and confusion. All tumors underwent surgical resection followed by variable treatment, including chemotherapy and/or radiation therapy. Three patients died of the complications of their brain tumors.

The CT appearance of MEGNT was isodense (80%) and hyperdense (20%). Other CT findings included acute hemorrhage (10%), calcification (10%), bone scalloping (10%), and bone erosion (10%).

The MR imaging features of MEGNT were variable as seen in the Table. As a group, MEGNTs presented with a mean tumor diameter of 5.3 cm (range, 2.5–7.7 cm) and appeared T2WI isointense (50%) and hyperintense (40%), cystic-like and/or necrotic (80%) with T2WI flow voids (60%), perilesional vasogenic edema (none 20%, mild 30%, extensive 50%), calcification/hemorrhage (50%), enhancement (100%), leptomeningeal/dural extension (50%), and an average minimum ADC value of $737 \times 10^{-6}\,mm^2/s$ (range, $560–1158 \times 10^{-6}\,mm^2/s$).

When we considered MEGNT by location of pineal, temporal, or extemporal lobar tumors, a more noticeable pattern was evident as seen in the Table. Smaller means and ranges of maximum

MR imaging features of MEGNTs

	All	Temporal	Pineal	Extratemporal
Mean maximum diameter (cm)	5.3	3.2	2.7	6.8
Cyst/necrosis (+)	80%	0%	100%	100%
Flow voids (+)	60%	50%	0%	83%
Perilesional edema (+)	80%	50%	50%	100%
Calcification/hemorrhage (+)	50%	50%	50%	50%
T1WI+C enhancement	100%	0%	50%	100%
Leptomeningeal/dural extension (+)	50%	0%	0%	100%
CSF distant metastases	30%	50%	50%	17%
Mean ADC value (10–6 mm^2/s)	737	795	1008	658

Note:—T1WI+C indicates T1 weighted imaging with contrast.

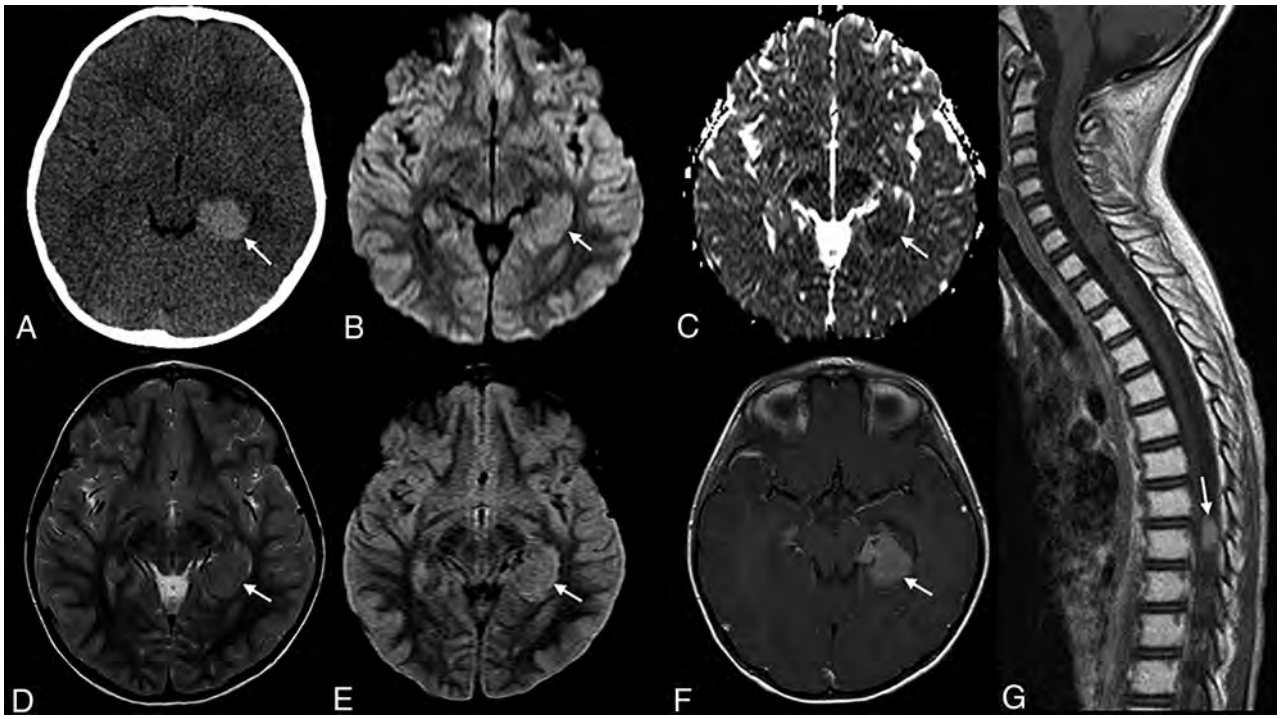

FIG 1. A 5-year-old girl with morning vomiting and headaches. *A*, Axial non-contrast-enhanced CT shows an oval homogeneous hyperdense mass lesion (*arrow*) located along the mesial left temporal lobe. *B* and *C*, Diffusion-weighted imaging and apparent diffusion coefficient map show no restricted diffusion (*arrow*) of the lesion. *D* and *E*, The lesion is nearly isointense (*arrow*) to gray matter on the T2-weighted and FLAIR imaging (*F*). The lesion shows avid homogeneous enhancement (*arrow*) on postcontrast T1-weighted imaging. The adjacent brain shows no edema. *G*, Follow-up sagittal postcontrast T1-weighted spine imaging after 6 months shows drop metastasis (*arrow*) with avid homogeneous enhancement.

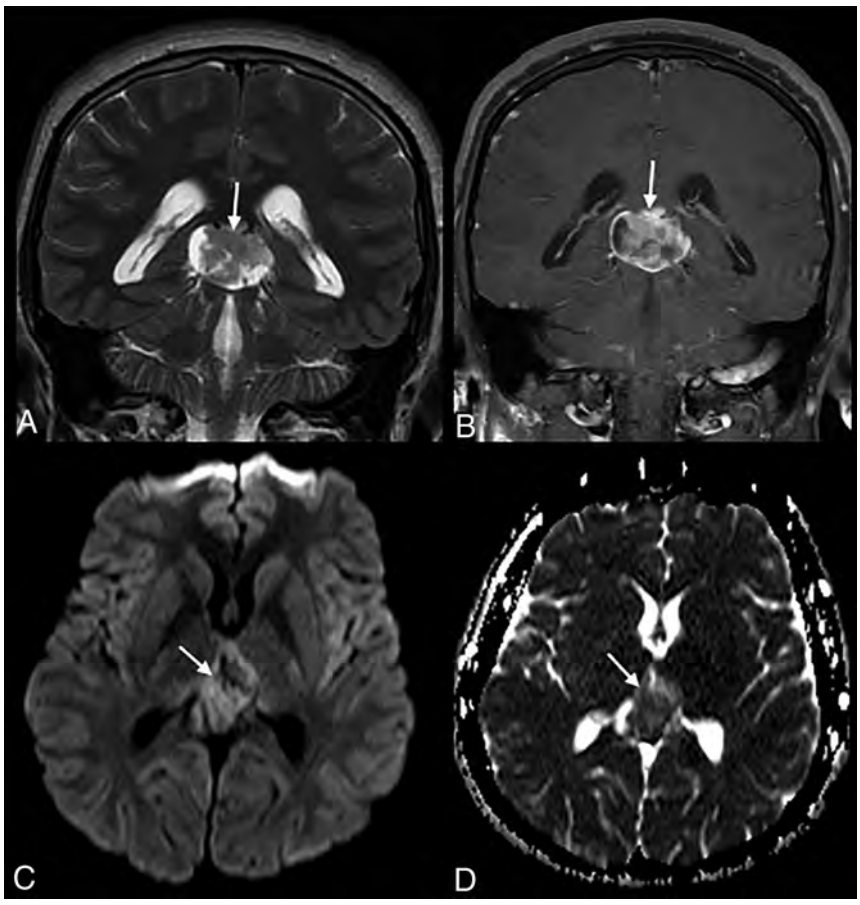

FIG 2. An 18-year-old man with a recent presentation of a 2-day history of headache and vomiting. *A*, Coronal T2-weighted imaging shows a large mass lesion (*arrow*) in the pineal gland region. *B*, The lesion shows heterogeneous contrast enhancement (*arrow*) on coronal T1-weighted imaging, with mild restricted diffusion (*arrow*, *C* and *D*) on diffusion-weighted imaging and the matching apparent diffusion coefficient map.

tumor diameters were seen with temporal tumors (3.2 cm; range, 2.9–3.4 cm) and pineal tumors (2.7 cm; range, 2.5–2.8 cm) compared with extratemporal tumors (6.8 cm; range, 5.4–7.8 cm). Cysts or necrosis or both were seen in all pineal (100%) and extratemporal tumors (100%) but in none of the temporal tumors (0%). Leptomeningeal/dural extension was more frequent with extratemporal tumors (100%) but was not seen with temporal (0%) or pineal (0%) tumors. Perilesional edema was present more frequently with extratemporal (100%) tumors than with temporal (50%) or pineal (50%) tumors. Flow voids were more frequent in extratemporal tumors (83%) compared with temporal (50%) and pineal tumors (0%). Calcification or blood products were similar for temporal (50%), pineal (50%), and extratemporal (50%) tumors. Mean and ranges of ADC values were overlapping for temporal (795×10^{-6} mm^2/s; range, 764–806 $\times$ 10^{-6} mm^2/s), pineal (1008×10^{-6} mm^2/s; range, 858–1158 $\times$ 10^{-6} mm^2/s), and extratemporal tumors (658×10^{-6} mm^2/; range, 560–899 $\times$ 10^{-6} mm^2/s).

Although no patient had remote CSF metastases at initial presentation, 3 patients (30%) developed distant leptomeningeal metastasis on follow-up imaging within both the brain and spine from 3 to 5 months from initial presentation. Representative examples of CT and MR imaging patterns of MEGNT are seen in Figs 1–5.

DISCUSSION

MEGNT is a rare aggressive brain tumor that can be encountered in both children and adults.[4,7] Neuroimaging features of MEGNT were described in only a few articles in the literature with various CT and MR imaging findings.[4,6] Varlet et al[6] reported a series of 40 cases, including both adults and children, of all tumors diagnosed as MEGNT in routine practice during a 2-year period, during which neurofilament protein immunostaining was performed in any case of suspected malignant glioma with unusual clinical, radiographic, and/or histologic features. Preoperative CT or MR imaging or both were reviewed in all except 1 case. Only 15% (6/40) of patients experienced initial symptoms during childhood (age range, 7–11 years).[6] To the best of our knowledge, our article is the largest case series focusing on neuroimaging features of pediatric MEGNT.

All tumors were supratentorial in our series, similar to the previously reported cases, being nearly always supratentorial, and most were in a temporal or frontal location.[4,6] Different from Varlet et al,[6] we encountered pineal region MEGNTs in 2 patients, which may indicate a more unique location in children compared with adults.

In our study, most cases (80%) were isodense on CT, with the uncommon presence of hemorrhage (10%) or calcification (10%). Similarly, calcifications on CT were reported in 17.6% of cases by Varlet et al.[6] An unusual finding on CT in one of our patients was an associated calvarial bone erosion and bone scalloping adjacent to the brain tumor, which have not been previously reported with MEGNT, likely because most of the nonpineal tumors involved the cortical and subcortical areas (88%) and leptomeningeal/dural extension was frequently identified on imaging and in pathology descriptions. This propensity for cortical involvement and leptomeningeal/dural extension is one feature that may distinguish this tumor type from other high-grade pediatric brain tumors and was not systematically reported in the literature.

Necrotic and/or cystic-like components were present in 80% of our patients, similarly reported in 85% of previous published series. We found contrast enhancement on MR imaging in 100% of patients, similar to the description of marked contrast enhancement on neuroimaging reported in 97.5% of patients in a prior study.[6] As demonstrated in our subgroup analysis of MEGNT by location and size, MEGNTs arising from the extratemporal cerebral hemispheres appear to be larger and more heterogeneous in appearance than the smaller MEGNTs in the

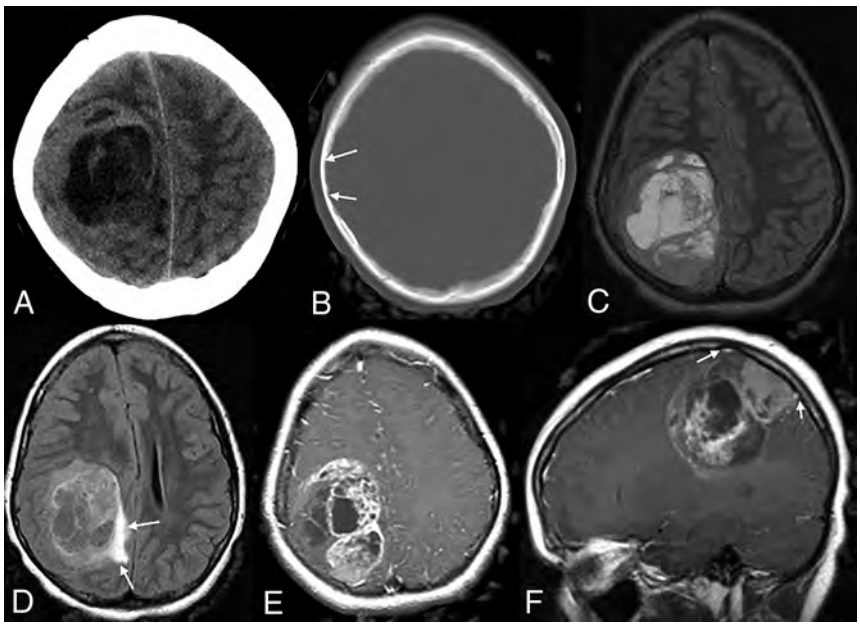

FIG 3. An 8-year-old girl with no medical history available in the patient records. *A* and *B*, Axial CT images demonstrate a solid and cystic mass with solid portions isodense to normal brain parenchyma and scalloping (*B*, *arrows*) of the adjacent inner table of the parietal bone. *C–F*, MR images demonstrate a large right frontoparietal mass with extensive cystic/necrotic areas (*C*), surrounding edema *(arrows*, *D*), enhancement (*E*), and dural extension (*arrows*, *F*). The lesion causes mass effect and mild right-to-left midline shift.

pineal region and temporal lobe. We suspect that as the tumors enlarge, they outgrow their blood supply and become more necrotic, thus accounting for the difference in imaging appearance. The patients with pineal tumors in our series presented with hydrocephalus, and the patient with one of the temporal tumors presented with a new onset of seizure, which may explain their smaller size at presentation. This subgroup analysis was chosen on the basis of prior reports of temporal lobe predilection of MEGNT and the notable differences encountered in this study.[6] The small sample size of our study limits the ability to correlate patient age and imaging features or tumor size.

Because prior studies have demonstrated that ADC values correlate with low-grade and high-grade tumors in pediatric patients with brain tumors, we found a similar pattern of low ADC values in MEGNT, consistent with a high-grade tumor.[8] Although ADC values for MEGNT have not

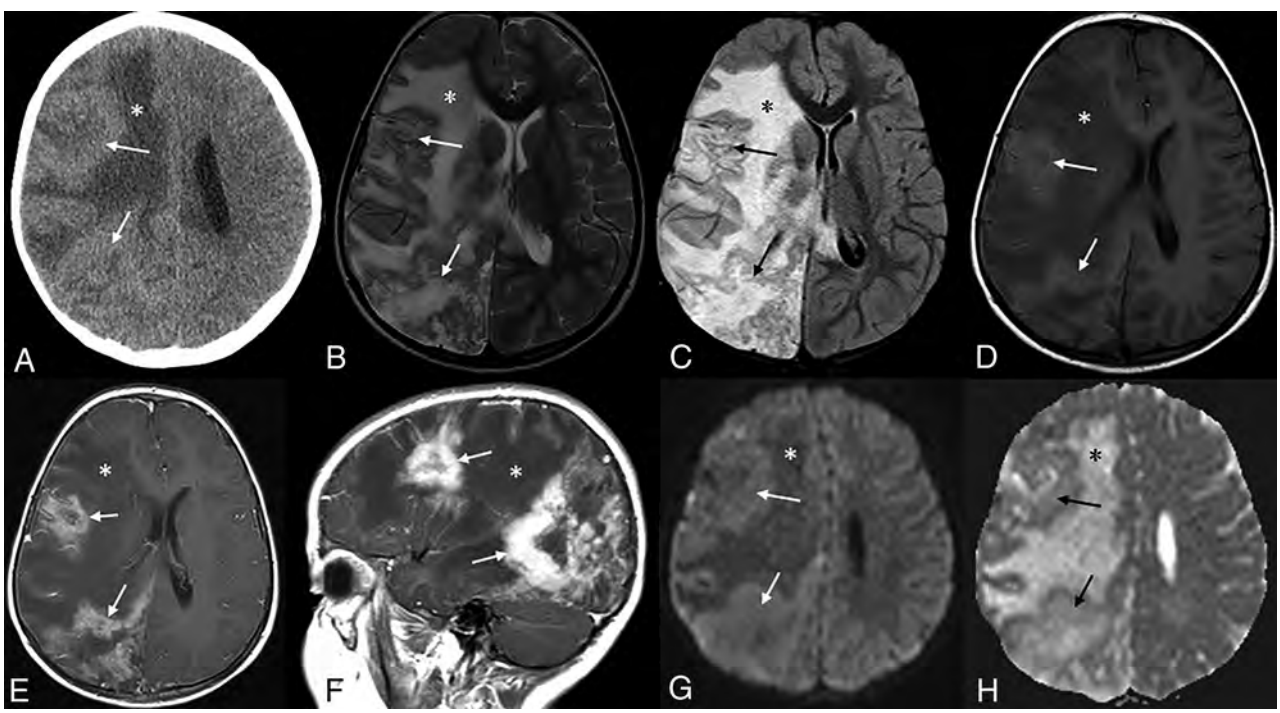

FIG 4. A 3-year-old girl who presented with left-sided hemiparesis. *A*, Axial noncontrast CT image demonstrates multifocal masses (*arrows*) in the right cerebral hemisphere that are isodense to normal brain and associated with a large region of edema (*asterisk*). *B–H*, MR images demonstrate an infiltrative right cerebral hemisphere tumor (*arrows*) extending into the basal ganglia and thalamus, with subsequent mass effect, diffuse right cerebral hemispheric edema (*asterisk*), and right-to-left midline shift. Multifocal areas of contrast enhancement (*arrows*) are seen on axial and sagittal T1 weighted imaging with contrast (*E* and *F*). DWI and ADC map images demonstrate that the solid portion of the mass (*arrows*) is isointense to normal brain parenchyma (*G* and *H*).

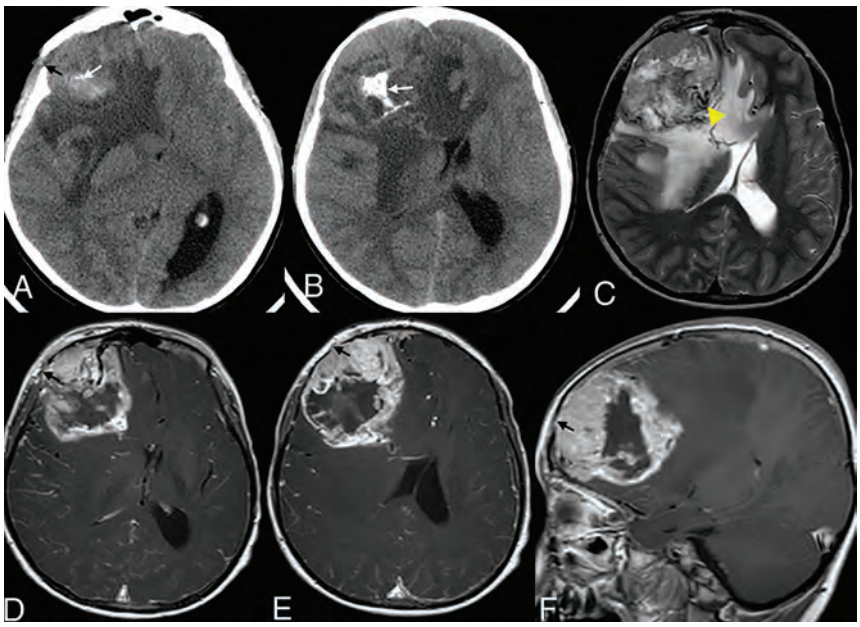

FIG 5. A 5-year-old boy who presented with vision loss. *A* and *B*. Axial noncontrast CT images demonstrate a solid and cystic mass with dystrophic calcification (*white arrow*) and adjacent bone erosion (*black arrow*). *C–F*, MR images demonstrate a right frontal lobe tumor with cystic/necrotic areas, flow voids (*C*, *arrowhead*), surrounding edema, contrast enhancement of the tumor, dural extension, and focal areas of bone erosion (*D–F*, *black arrow*). There is notable intracranial mass effect, including a right-to-left midline shift.

been previously reported, the mean ADC value of MEGNTs in this series is similar to that in a previous study that found a mean, minimum ADC value of 640 × 10^{-6} mm^2/s for supratentorial high-grade brain tumors in children in the first year of life.[9]

The imaging pattern of cystic degeneration/necrosis, hemorrhage, contrast enhancement, and regions of low ADC values of the tumors in our case series is not pathognomonic of MEGNT but is consistent with patterns seen with other high-grade pediatric brain tumors.[3] While no imaging feature is pathognomonic of MEGNT, the imaging features encountered with MEGNT support its designation as a high-grade tumor. The imaging patterns of pediatric MEGNT described herein may be clinically useful for radiologists encountering these rare tumors. The differential diagnosis should include glioblastoma multiforme, embryonal CNS tumor, anaplastic ependymoma, hemangiopericytoma, and atypical teratoid/rhabdoid tumor. In the pineal location, pineoblastoma would also be in the differential diagnosis. MEGNTs were found only in the supratentorial location and involved older children, which may indicate a less likely diagnosis of an atypical teratoid/rhabdoid tumor.[4] Last, MEGNTs demonstrated a propensity for distant CSF spread at a rate similar to that of medulloblastoma so that routine imaging surveillance of the spine is suggested.

CONCLUSIONS

MEGNT is a rare and aggressive tumor that can be seen in both the pediatric and adult populations. Neuroimaging features are not specific for a diagnosis, but the presence of cystic degeneration/necrosis, hemorrhage, contrast enhancement, and regions of low ADC signal of the tumors is consistent with patterns seen with other high-grade pineal and cerebral pediatric brain tumors.

REFERENCES

1. Poussaint TY, Panigrahy A, Huisman TA. **Pediatric brain tumors.** *Pediatr Radiol* 2015;45(Suppl 3):S443–53 CrossRef Medline
2. Koob M, Girard N. **Cerebral tumors: specific features in children.** *Diagn Interv Imaging* 2014;95:965–83 CrossRef Medline
3. Johnson DR, Guerin JB, Giannini C, et al. **2016 updates to the WHO Brain Tumor Classification System: what the radiologist needs to know.** *Radiographics* 2017;37:2164–80 CrossRef Medline
4. Rivera-Zengotita M, Rauch RA, Adesina AM, et al. Malignant epithelioid glioneuronal tumor. In: Adesina AM, Tihan T, Fuller CE, eds. *Atlas of Pediatric Brain Tumors*. Springer-Verlag; 2016:211–19
5. Rivera-Zengotita M, Whitehead W, Chintagumpala M, et al. **Malignant epithelioid glioneuronal tumor: unusual phenotype or new entity?** *Mod Pathol* 2008;21:324A
6. Varlet P, Soni D, Miquel C, et al. **New variants of malignant glioneuronal tumors: a clinicopathological study of 40 cases.** *Neurosurgery* 2004;55:1377–91 CrossRef Medline
7. Rodriguez FJ, Scheithauer BW, Port JD. **Unusual malignant glioneuronal tumors of the cerebrum of adults: a clinicopathologic study of three cases.** *Acta Neuropathol* 2006;112:727–37 CrossRef Medline
8. Porto L, Jurcoane A, Schwabe D, et al. **Differentiation between high and low grade tumours in paediatric patients by using apparent diffusion coefficients.** *Eur J Paediatr Neurol* 2013;17:302–07 CrossRef Medline
9. Kralik SF, Taha A, Kamer AP, et al. **Diffusion imaging for tumor grading of supratentorial brain tumors in the first year of life.** *AJNR Am J Neuroradiol* 2014;35:815–23 CrossRef Medline

The Evaluation and Prediction of Laminoplasty Surgery Outcome in Patients with Degenerative Cervical Myelopathy Using Diffusion Tensor MRI

X. Han, X. Ma, D. Li, J. Wang, W. Jiang, X. Cheng, G. Li, H. Guo, and W. Tian

ABSTRACT

BACKGROUND AND PURPOSE: DTI has been proved valuable for the diagnosis of degenerative cervical myelopathy, whereas its capacity for predicting the outcome of surgery is still under debate. Here we conduct a prospective cohort study to analyze the capacity of DTI for evaluating and predicting laminoplasty surgery outcome for degenerative cervical myelopathy.

MATERIALS AND METHODS: We recruited 55 patients with degenerative cervical myelopathy who underwent DTI before surgery and at 3- and 6-month follow-up stages, and 20 healthy subjects. For clinical assessment, the modified Japanese Orthopedic Association scale was recorded for each patient at different stages. DTI metrics were compared between patients before surgery and healthy subjects. Spearman correlation and receiver operating characteristic were used to analyze the evaluation and prediction capacity of DTI for the modified Japanese Orthopedic Association scale, respectively. We analyzed different vertebral levels: maximal compression level, average of all compression levels, and C2 level.

RESULTS: DTI metrics were significantly different between patients before surgery and healthy subjects. Before surgery, DTI for the maximal compression level or DTI for the average of all compression levels had no significant correlation with the modified Japanese Orthopedic Association scale. For all stages, DTI at the C2 level was correlated with the modified Japanese Orthopedic Association scale. DTI metrics at the C2 level before surgery were significantly correlated with the postoperative modified Japanese Orthopedic Association scale recovery rate. Receiver operating characteristic analysis demonstrated that fractional anisotropy at C2 was capable of predicting the postoperative modified Japanese Orthopedic Association scale recovery rate ($P = .04$).

CONCLUSIONS: The DTI metrics before laminoplasty surgery, especially fractional anisotropy at the C2 level, have the potential for evaluating and predicting the degenerative cervical myelopathy surgery outcome.

ABBREVIATIONS: AC = all compression; AD = axial diffusivity; DCM = degenerative cervical myelopathy; FA = fractional anisotropy; MC = maximal compression; MD = mean diffusivity; mJOA = modified Japanese Orthopedic Association scale; RD = radial diffusivity; ROC = receiver operating characteristic

Degenerative cervical myelopathy (DCM) is one of the most common causes of chronic spinal cord dysfunction.[1] Decompression surgery, including anterior and posterior surgery, is widely used in the treatment of DCM. However, the surgery outcome can vary among different patients. Therefore, a reliable tool is required to evaluate and predict the surgery outcome for patients with DCM.

Noninvasive MR imaging is routinely used for the diagnosis of DCM, especially T2-weighted MR imaging, which can provide high-resolution images of anatomic structures and superior contrast in the spinal cord. In recent years, diffusion MRI[2] has been used for the evaluation of spinal cord function. By measuring the Brownian motion of water molecules, diffusion MR imaging can depict microstructures in living tissue. On the basis of diffusion MR imaging, DTI acquires diffusion-weighted images along multiple directions; then, quantitative

Received February 2, 2020; accepted after revision June 9.

From the Departments of Spine Surgery (X.H., D.L., J.W., W.T.) and Radiology (W.J., X.C.), Beijing Jishuitan Hospital, Beijing, China; Beijing Institute of Traumatology and Orthopaedics (X.H.), Beijing, China; Center for Magnetic Resonance Research (X.M.), University of Minnesota, Minneapolis, Minnesota; National Center of Gerontology (D.L.), Beijing, China; Center for Biomedical Imaging Research (G.L., H.G.), Department of Biomedical Engineering, School of Medicine, Tsinghua University, Beijing, China.

Xiao Han and Xiaodong Ma are co-first authors.

This work was supported by Capital's Funds for Health Improvement and Research (code CFH2020-2-1121), Beijing JST Research Funding (code ZR-201912), National Natural Science Foundation of China (code 11871459), and Beijing Jishuitan Hospital "Nova Program" (code xkxx201614).

Please address correspondence to Wei Tian, MD, Department of Spine Surgery, Beijing Jishuitan Hospital, Beijing, China, 100035; e-mail: tianweispine@163.com

Indicates open access to non-subscribers at www.ajnr.org
Indicates article with supplemental on-line tables.
http://dx.doi.org/10.3174/ajnr.A6705

Table 1: Summary of previous studies about prediction of DCM surgery outcome using DTI

Publications	Correlation Method	Significance	DTI Metrics	Prediction Indexes	Vertebral Levels	Surgery Method
Jones et al, 2013[9]	Spearman	No	FA	mJOA	MC level, C2–C3	Not specified
Wen et al, 2014[15]	Spearman	Yes	FA	mJOA recovery rate	Average of C3 to C7	Not specified
Vedantam et al, 2017[5]	Pearson	Yes	FA	ΔmJOA	MC level	Not specified
Maki et al, 2017[16]	Spearman	Yes	FA	ΔmJOA, mJOA recovery rate	MC level	Posterior and anterior
Kitamura et al, 2020[17]	Spearman	Yes	FA	ΔmJOA, mJOA recovery rate	MC level	Posterior
Shabani et al, 2019[18]	Intraclass correlation coefficient	Yes (–)	FA	ΔmJOA	MC level	Not specified
Iwasaki et al, 2019[14]	Pearson	No	FA	mJOA	MC level	Posterior and anterior

Note:—(–) indicates negative correlation; ΔmJOA, difference between pre- and postoperative mJOA.

metrics can be calculated, including fractional anisotropy (FA), axial diffusivity (AD), radial diffusivity (RD), and mean diffusivity (MD).

Previous studies have shown that DTI has higher sensitivity in the diagnosis of DCM compared with T2-weighted MR imaging.[3,4] The ADC is higher and FA values are lower in patients with DCM than in healthy individuals,[5,6] and there are significant differences between preoperation and postoperation.[7,8] In addition, it has been shown that FA is significantly correlated with clinical assessment of the modified Japanese Orthopedic Association scale (mJOA),[9-13] the most frequently used clinical assessment for patients with DCM.

Although DTI has proved valuable for the diagnosis of DCM, its capability for predicting the outcome of surgery is still under debate. Here, we briefly summarize the results from previous publications (Table 1). We included 7 articles studying the correlation between preoperative DTI metrics (FA) and postoperative mJOA scale, reported from 2013 to 2019. Two articles[9,14] claimed a nonsignificant correlation, while the rest[5,15-18] claimed a significant correlation. Note, Shabani et al[18] showed a negative correlation between preoperative FA and the postoperative ΔmJOA (difference between post- and preoperative mJOA), while the other studies showed a positive correlation. Wen et al[15] claimed that the mean FA value of C3 through C7 vertebral levels before surgery is significantly correlated with the postoperative mJOA recovery rate, while the FA value at the maximal compression (MC) level is not. Different correlation methods, prediction indexes, and surgery methods were adopted in these studies, which are listed in Table 1.

The purpose of this study was to further investigate the evaluation and prediction ability of DTI for the surgery outcome of patients with DCM. Specifically, only patients with posterior laminoplasty surgery with nonmetal coral implants were included. Different from practices in previous studies, we acquired DTI data not only before surgery but also at 3 and 6 months after surgery. Using the acquired data, we analyzed the difference in preoperative DTI metrics at different vertebral levels between patients and healthy subjects, the correlation between DTI and mJOA at different stages before and after surgery, and the correlation between the preoperative DTI and the postoperative mJOA recovery rate.

MATERIALS AND METHODS

Subjects and Clinical Assessment

From January 2017 to December 2017, fifty-five patients diagnosed with DCM (21 women, 35–72 years of age; mean, 58.6 ± 6.8 years) and 20 healthy subjects (6 women, 50–65 years of age; mean, 57.29 ± 5.0 years) were recruited with written consent. This study was approved by the Review Board of Research Ethics in Jishuitan Hospital. The information for all patients is summarized in On-line Table 1. The inclusion criteria were patients with DCM with the following: 1) spinal cord compression of >3 vertebral levels caused by disk herniation, ossification of the posterior longitudinal ligament, ossification of the ligamentum flavum, cervical spondylosis, or spinal canal stenosis; 2) ages from 18 to 80 years; 3) regular conservative treatment that was ineffective, with posterior cervical laminoplasty planned; and 4) no clear contraindication for surgery. The exclusion criteria were those who were not able to undergo MR imaging, had a history of spine surgery, or had injury of spinal cord or nerve root due to an operation, from which the patient was not sufficiently recovered at the final-stage follow-up.

All patients underwent posterior cervical laminoplasty with nonmetal coral implants. Therefore, no metal artifacts were expected on the MR images. Each patient was clinically assessed using the mJOA before surgery and at 3 follow-up stages: 3 months (completed in 44 patients), 6 months (completed in 37), and 1–2 years (completed in 52) after the operation. The clinical assessment was scored by 2 board-certified spine surgeons. For each patient, he or she was scored by the same surgeon at different follow-up stages.

In addition, for each patient, we calculated the mJOA recovery rate to represent the surgery outcome, defined as the following: final-stage follow-up mJOA – preoperative mJOA) / (17 – preoperative mJOA) × 100%, where 17 refers to the full score of the mJOA.

MR Imaging Data Acquisition

MR imaging data were acquired on an Ingenia 3T scanner (Philips Healthcare) with a 16-channel head-neck coil. Three MR images were obtained for each patient, before surgery and at 3- and 6-month follow-up. DTI data were acquired using a single-shot EPI sequence on the axial view, with 17 slices in total

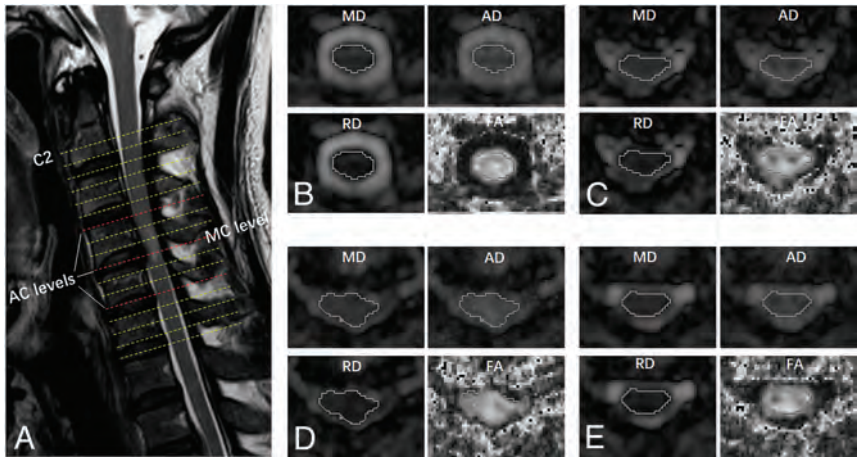

FIG 1. Example of DTI planes and ROI drawings from 1 patient. *A*, T2-weighted structural image with the locations of the C2 level and AC levels. *B*, ROI drawing at C2. *C–E*, ROI drawings at the AC levels. *D*, The MC level. Four DTI metrics were measured, including FA, AD, RD, and MD.

covering the vertebral levels from C2 to C7, shown in Fig 1. The imaging plane was parallel to the intervertebral disk at the maximal compression level. The reduced-FOV technique (FOV = 60×160 mm^2), outer volume suppression,[19,20] was used to reduce image distortion, with 2 saturation bands applied at both the anterior and posterior sides to suppress foldover artifacts. Three b-values were used, $b = 0$, 1000 s/mm^2, and 2000 s/mm^2. The parameters were the following: number of signal averages = 1; number of diffusion directions = 32; sensitivity-encoding factor = 2; partial Fourier factor = 0.75; TE/TR = 77/4500 ms; in-plane resolution = 1.5×1.5 mm^2; acquisition matrix size = 40×106; section thickness = 4 mm; section gap = 2 mm; total scan time = 5 minutes. In addition to DTI, the sagittal and axial T1-weighted and T2-weighted turbo spin-echo sequences were used for structural imaging. For each healthy subject, DTI, T1-weighted-, and T2-weighted-TSE images were acquired using the protocols identical to those of the patients. The reproducibility of DTI measurements was evaluated in our previous study,[13] in which the percentage coefficients of variation were below 10% for all DTI metrics (Table 1 in the original article), suggesting a reliable intrascan reproducibility for them.

Image Processing

The diffusion-weighted images from the DTI data were preprocessed using the motion-correction function in the Spinal Cord Toolbox (https://sourceforge.net/projects/spinalcordtoolbox/)[21] to register the images of different b-values and directions, which is a novel function that the Spinal Cord Toolbox offers with section-by-section translation estimation while ensuring regularization constraints along the section direction. Then, the DTI metrics FA, AD, RD, and MD were calculated from the registered images using the FMRIB Software Library (FSL; http://www.fmrib.ox.ac.uk/fsl).[22] The processing steps using the Spinal Cord Toolbox and FSL were performed in Linux by batch processing without manual intervention. Afterward, the DTI metrics were loaded into DTIStudio (Johns Hopkins University)[23] in Windows and measured with ROI analysis.

For each patient, ROIs were manually drawn along the contour of the whole spinal cord at all compressed levels as well as at the C2 level containing both the white and gray matter. An example of an ROI drawing is shown in Fig 1 Specifically, the ROIs were drawn on the MD map at first and then applied to all other metrics maps because the boundary between the spinal cord and CSF can be clearly identified on the MD map. Then, the average values of all voxels inside the ROI were recorded. Note that the edge of the spinal cord was excluded from the ROI to reduce the contamination of CSF. For healthy subjects, the DTI metrics at all vertebral levels from C2 to C7 were measured using the same ROI-analysis strategy.

Statistics

Statistical analysis was performed using SPSS Statistics, Version 20.0 (IBM).

The difference in DTI metrics between the patients before surgery and the healthy subjects (control group) was analyzed using an independent 2-sample *t* test (equal variance), *t'* test (unequal variance), or Mann-Whitney *U* test. If the means of the samples were normally distributed, a *t* test or *t'* test was used; otherwise, the Mann-Whitney *U* test was used. The MC level, the average of all compression (AC) levels, and the C2 level were analyzed independently. Specifically, for the MC level, the patients were first divided into 3 groups: the MC levels at C3–4; C4–5; and C5–6 or C6-7. Then DTI was compared between each patient group and the control group (Table 2). For the average of AC levels, DTI metrics for the patients were compared with the average of C3–4 to C5–6 levels for the healthy subjects.

The Spearman correlation was used to evaluate the relationship between mJOA and DTI at the same stage (before surgery and at 3- or 6-month follow-up stages) and to evaluate the relationship between the preoperative DTI and postoperative mJOA recovery rate.

We incorporated 3 T1-weighted and T2-weighted features into a linear regression model, including the axial spinal cord area, the spinal cord flattened rate (anterior-posterior diameter of the spinal cord divided by the transverse diameter of the spinal cord), and signal changes in the T1-weighted and T2-weighted images. When we considered the influence of multicollinearity in regression analysis, each DTI metric was incorporated into the regression model separately. In other words, for each analysis, 3 traditional MR imaging metrics and 1 DTI metric were incorporated into the regression model using a stepwise linear regression strategy. The correlation was examined between the incorporated metrics and the preoperative mJOA as well as the mJOA recovery rate. The MC, AC, and C2 levels were analyzed separately.

In addition, we divided patients into 3 subgroups based on the signal changes in the T1-weighted and T2-weighted images:

Table 2: Comparison of DTI metrics between patients before surgery and the control group for the MC level

Groups/Statistics	MD ($10^{-3}mm^2/s$)		AD ($10^{-3}mm^2/s$)		RD ($10^{-3}mm^2/s$)		FA	
	Patients	Controls	Patients	Controls	Patients	Controls	Patients	Controls
Group 1[a]	0.97 ± 0.16	0.72 ± 0.04	1.40 ± 0.11	1.35 ± 0.06	0.75 ± 0.21	0.40 ± 0.04	0.41 ± 0.14	0.66 ± 0.04
t/*t*' value	*t*' = −4.32		*t*' = −1.24		*t*' = −4.65		*t*' = 4.84	
P value	*P* = .003[d]		*P* = .25		*P* = .002[d]		*P* = .002[d]	
Group 2[b]	0.97 ± 0.17	0.73 ± 0.04	1.51 ± 0.16	1.32 ± 0.08	0.70 ± 0.21	0.44 ± 0.04	0.48 ± 0.14	0.61 ± 0.04
t/*t*' value	*t*' = −6.40		*t*' = −4.78		*t*' = −5.59		*t*' = 4.311	
P value	*P* < .001[d]		*P* < .001[d]		*P* < .001[d]		*P* < .001[d]	
Group 3[c]	0.99 ± 0.20	0.75 ± 0.05	1.47 ± 0.15	1.26 ± 0.10	0.76 ± 0.26	0.49 ± 0.04	0.43 ± 0.16	0.55 ± 0.05
t/*t*' value	*t*' = −5.89		*t* = −5.42		*t*' = −5.01		*t*' = 3.51	
P value	*P* < .001[d]		*P* < .001[d]		*P* < .001[d]		*P* = .001[d]	

[a] Group 1 of patients: MC level at C3–4 (*n* = 8).
[b] Group 2 of patients: MC level at C4–5 (*n* = 22).
[c] Group 3 of patients: MC level at C5–6 or C6–7 (*n* = 25).
[d] Significant correlation.

Table 3: Comparison of DTI metrics between patients before surgery and the control group for the average of AC levels

Groups/Statistics	MD ($10^{-3}mm^2/s$)	AD ($10^{-3}mm^2/s$)	RD ($10^{-3}mm^2/s$)	FA
Patients (*n* = 55)	0.87 ± 0.12	1.40 ± 0.12	0.61 ± 0.14	0.50 ± 0.10
Controls (*n* = 20)	0.73 ± 0.03	1.31 ± 0.07	0.44 ± 0.03	0.61 ± 0.03
t/*t*' value	*t*' = −8.19	*t* = −3.15	*t*' = −8.36	*t*' = 7.10
P value	*P* < .001[a]	*P* < .001[a]	*P* < .001[a]	*P* < .001[a]

[a] Significant correlation.

Table 4: Comparison of DTI metrics between the patients before surgery and the control group for the C2 level

Groups/Statistics	MD ($10^{-3}mm^2/s$)	AD ($10^{-3}mm^2/s$)	RD ($10^{-3}mm^2/s$)	FA
Patients (*n* = 52)	0.74 (0.71–0.77)[a]	1.35 (1.33–1.42)	0.42 (0.39–0.47)	0.64 (0.59–0.67)
Controls (*n* = 20)	0.75 (0.72–0.79)	1.43 (1.33–1.48)	0.41 (0.37–0.45)	0.68 (0.64–0.70)
Z value	*Z* = −0.33	*Z* = −1.62	*Z* = −1.04	*Z* = −2.44
P value	*P* = .74	*P* = .10	*P* = .30	*P* = .02[b]

[a] Mean (lower bound-upper bound).
[b] Significant correlation.

patients with no signal changes (group 1), with signal changes in only T2-weighted images (group 2), and in both T1-weighted and T2-weighted images (group 3). The correlation between the DTI metrics and the preoperative mJOA or mJOA recovery rate was analyzed in each subgroup.

Receiver operating characteristic (ROC) analysis was used to evaluate the predictive capability of preoperative DTI metrics for the mJOA recovery rate. The patients were considered to have a positive recovery if the rate was >50% and to be negative otherwise. According to the positive or negative recovery, the state variables in ROC analysis were set to 1 or 0. After the ROC analysis, the cutoff value was determined to be the value with the maximum Youden index (sensitivity + specificity –1), and the sensitivity and specificity of different DTI metrics were computed on the basis of the cutoff values.

In all statistical approaches above, the DTI metrics for the MC level, the average of AC levels, and the C2 level were analyzed independently. Due to scanning errors, the C2 level was missing on the preoperative DTI for 3 patients, so the subject size of preoperative DTI metrics at the C2 level was 52. The threshold for significance was set to .05.

RESULTS

Comparison of DTI metrics between patients before surgery with the healthy subjects is shown in Tables 2-4. For the MC level and average of AC levels, the patients had significantly lower FA and higher MD, AD, and RD than the healthy subjects, except AD at the MC level of group 1. At the C2 level, FA was significantly lower in the patients ($P = .02$), while MD, AD, or RD had no significant difference compared with the healthy subjects.

Before surgery, Spearman correlations showed that mJOA had no significant correlation with the DTI metrics for the MC level or with those for the average of AC levels. For the C2 level, mJOA was correlated with AD ($r = 0.36$, $P = .008$), RD ($r = -0.29$, $P = .04$), and FA ($r = 0.35$, $P = .01$) (Table 5).

At the 3-month follow-up, none of the DTI metrics for the MC level had significant correlations with mJOA. At 6-month follow-up, MD, RD, and FA for the MC level were correlated with mJOA. Specifically, MD and RD showed negative correlations ($r = -0.31$, $P = .04$ and $r = -0.32$, $P = .03$, respectively), and FA showed a positive correlation ($r = 0.33$, $P = .03$) (Table 6). For the C2 level, DTI metrics had significant correlations with mJOA at both 3- and 6-month follow-up, with the detailed values listed in Table 7.

The preoperative DTI metrics for MC or the average of AC levels had no correlations with the mJOA recovery rate, while at the C2 level, AD, RD, and FA had significant correlations with the mJOA recovery rate (Table 8). Notably, FA showed the strongest correlation among the 3 metrics, with $r = 0.51$ and $P < .001$.

Table 5: Spearman correlations between the DTI metrics at different levels and mJOA before surgery

Levels/DTI Metrics	Correlation Coefficient	*P* Value
MC level ($n = 55$)		
MD	−0.13	.34
AD	−0.13	.34
RD	−0.07	.62
FA	−0.004	.98
Average of AC levels ($n = 55$)		
MD	−0.15	.27
AD	−0.12	.39
RD	−0.12	.38
FA	0.07	.61
C2 level ($n = 52$)		
MD	−0.09	.55
AD	0.36	.008[a]
RD	−0.29	.04[a]
FA	0.35	.01[a]

[a] Significant correlation.

Table 6: Spearman correlations between the DTI metrics at the MC level and mJOA at 2 follow-up stages after surgery

Follow-Up Stages/DTI Metrics	Correlation Coefficient	*P* Value
3-Month follow-up ($n = 44$)		
MD	−0.12	.41
AD	−0.09	.54
RD	−0.10	.51
FA	0.10	.51
6-Month follow-up ($n = 37$)		
MD	−0.31	.04[a]
AD	−0.14	.36
RD	−0.32	.03[a]
FA	0.33	.03[a]

[a] Significant correlation.

Table 7: Spearman correlations between the DTI metrics for C2 level and mJOA at 2 follow-up stages after surgery

Follow-Up Stages/DTI Metrics	Correlation Coefficient	*P* Value
3-Month follow-up ($n = 44$)		
MD	−0.20	.21
AD	0.16	.33
RD	−0.35	.03[a]
FA	0.42	.005[a]
6-Month follow-up ($n = 37$)		
MD	−0.44	.01[a]
AD	0.15	.39
RD	−0.65	<.001[a]
FA	0.77	<.001[a]

[a] Significant correlation.

The results of linear regression analysis incorporating DTI, T1-weighted, and T2-weighted features are shown in Tables 9 and 10, where the features with significant results are listed. For the correlation with the preoperative mJOA (Table 9), only the axial spinal cord area showed significant correlation when the DTI metrics at the MC or AC levels were included, while all DTI metrics and the spinal cord flattened rate showed significant correlation when the DTI metrics at the C2 level were included. For the correlation with the mJOA recovery rate (Table 10), the DTI metrics and the spinal cord flattened rate showed significant correlation when every DTI metric at the C2 level or the FA at the AC levels was included, while only the axial spinal cord area showed significant correlation when the other DTI metrics (MD, AD, and RD at the AC levels and all DTI metrics at the MC level) were included.

Table 8: Spearman correlations between the preoperative DTI metrics of different levels and the postoperative mJOA recovery rate at the final follow-up (1 year)

Levels/DTI Metrics	Correlation Coefficient	*P* Value
MC level ($n = 55$)		
MD	−0.10	.34
AD	0.16	.34
RD	−0.12	.62
FA	0.19	.98
Average of AC levels ($n = 55$)		
MD	−0.19	.16
AD	0.08	.59
RD	-0.24	.08
FA	0.26	.06
C2 level ($n = 52$)		
MD	−0.15	.31
AD	0.40	.003[a]
RD	−0.42	.002[a]
FA	0.51	<.001[a]

[a] Significant correlation.

For the correlation analysis in each subgroup, in group 1 with no signal changes, the AD value at the C2 level was correlated with the preoperative mJOA ($r = 0.596$, $P = .041$), and the FA value at the C2 level was correlated with the mJOA recovery rate ($r = 0.634$, $P = .027$). In group 2 with T2-weighted signal changes only, the FA value of the C2 level was correlated with the mJOA recovery rate ($r = 0.484$, $P = .042$). In group 3 with both T1-weighted and T2-weighted signal changes, the AD values of AC levels and the AD, FA, and RD values of the C2 level were correlated with the mJOA recovery rate ($r = 0.462$, 0.469, 0.457, and −0.446; $P = .03$, .028, .033, and .037, respectively).

The ROC analysis suggests that for the MC or average of AC levels, no DTI metrics were predictive of the mJOA recovery rate. For the C2 level, FA showed predictive capability with an area under the curve = 0.68, $P = .04$, sensitivity = 0.56, specificity = 0.81 (Fig 2 and Table 11).

DISCUSSION

In this study, we investigated the evaluation and prediction capability of DTI for laminoplasty surgery outcome in patients with DCM. We found that DTI metrics were significantly different between patients before surgery and healthy subjects, findings consistent with those in previous studies.[4,7,10,15] Before surgery, DTI metrics including AD, RD, and FA for the C2 level were significantly correlated with the preoperative mJOA, while DTI metrics for the MC or the average of AC levels were not. AD, RD, and FA for C2 before the operation were significantly correlated with the postoperative mJOA recovery rate. The results of regression analysis incorporating T1-weighted and T2-weighted features supported the correlation analysis results when using the DTI metrics alone, suggesting that the DTI metrics at the C2 level have the predictive value for surgery outcome. Particularly, DTI metrics were found to be correlated with the mJOA recovery rate

for each subgroup of patients on the basis of T1-weighted and T2-weighted signal changes; this correlation indicates that it is possible to define a subgroup of patients that can only be categorized using DTI alone. In addition, ROC analysis demonstrated that FA for C2 was capable of predicting the mJOA recovery rate ($P = .04$).

We obtained DTI scans for the patients with DCM before surgery and at 3- and 6-month follow-up stages. To the best of our knowledge, this was the first time that DTI data were collected at 3 different stages in the same patients with DCM. The scans at different stages helped to reveal the relationships between DTI and mJOA in a long time range and to investigate the capability of DTI in evaluating and predicting surgery outcome.

We found that before surgery, the DTI metrics for the MC level were not significantly correlated with mJOA. This was surprising because most previous studies[5,6,9,11,15,17,18] reported significant correlation. After surgery, the DTI metrics for the MC level and mJOA were significantly correlated at 6-month follow-up, but not at 3-month follow-up. One possible explanation is that the MC level was affected by severe image artifacts. Partial volume and motion effects could be aggravated by compression before surgery, and image distortion could be intensified by residual inflammation from surgery at 3-month follow-up, whereas at 6-month follow-up, the artifacts would be reduced so that the MC level was less affected. Other factors such as different statistical methods or patient inclusion criteria may also account for our inconsistency with previous studies.

For the C2 level, the DTI metrics were significantly correlated with the mJOA at different stages: before surgery and at 3- and 6-month follow-up. This is not surprising because it has been proved that compression might affect the distal spinal cord, even in the noncompressed regions,[24-28] which may represent Wallerian degeneration that has spread from a more caudal area of stenosis.[29] Additionally, our results show that preoperative FA for the C2 level was correlated with the postoperative mJOA recovery rate. This correlation indicates that DTI has

Table 9: Results of linear regression to examine the correlation between DTI, T1-weighted, and T2-weighted features and preoperative mJOA

Level/Incorporated DTI Metrics	Significant Features	Slope (β)	*P* Value
MC level ($n = 55$)			
MD/AD/RD/FA	Axial spinal cord area	0.05	.01
Average of AC levels ($n = 55$)			
MD/AD/RD/FA	Axial spinal cord area	0.05	.01
C2 level ($n = 52$)			
MD	MD	–10.28	.03
	Spinal cord flattened rate	9.00	.005
AD	AD	5.58	.04
	Spinal cord flattened rate	6.38	.04
RD	RD	–8.93	.002
	Spinal cord flattened rate	8.32	.006
FA	FA	9.43	.002
	Spinal cord flattened rate	7.12	.02

Table 10: Results of linear regression to examine the correlation between DTI, T1-weighted, and T2-weighted features and the mJOA recovery rate

Level Incorporated DTI Metrics	Significant Features	Slope (β)	*P* Value
MC level ($n = 55$)			
MD/AD/RD/FA	Axial spinal cord area	0.70	.02
Average of AC levels ($n = 55$)			
MD/AD/RD	Axial spinal cord area	0.70	.02
FA	FA	108.67	.01
	Spinal cord flattened rate	105.64	.03
C2 level ($n = 52$)			
MD	MD	–157.98	.04
	Spinal cord flattened rate	141.57	.01
AD	AD	123.60	.01
RD	RD	–145.13	.004
	Spinal cord flattened rate	131.88	.01
FA	FA	170.92	.001
	Spinal cord flattened rate	111.82	.02

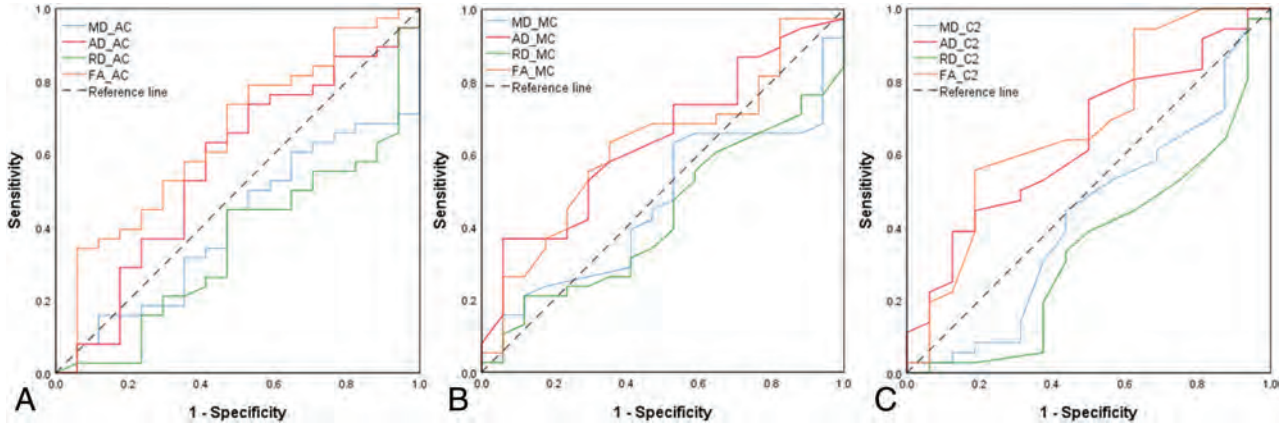

FIG 2. ROC analysis of the predictive value of DTI metrics for the postoperative mJOA recovery rate. Results for the average of all AC levels, MC level, and the C2 level, respectively. The area under the curve values for different metrics are shown in Table 11.

Table 11: Prediction capability of the preoperative DTI metrics at different levels for the postoperative mJOA recovery rate using ROC analysis

Level/DTI Metrics	AUC	*P* Value	Sensitivity	Specificity
MC level ($n = 55$)				
MD	0.46	.66	0.63	0.47
AD	0.64	.10	0.37	0.94
RD	0.43	.40	0.21	0.88
FA	0.62	.15	0.63	0.65
Average of AC levels ($n = 55$)				
MD	0.40	.26	0.16	0.88
AD	0.57	.43	0.63	0.59
RD	0.36	.09	0.95	0.06
FA	0.65	.07	0.34	0.94
C2 level ($n = 52$)				
MD	0.43	.39	0.97	0.06
AD	0.64	.12	0.39	0.88
RD	0.34	.07	0.97	0.06
FA	0.68	.04[a]	0.56[a]	0.81

Note:—AUC indicates area under the curve.
[a] Significant correlation.

the potential to predict DCM surgery outcome. For the MC or the average of the AC levels, however, the DTI metrics were not capable of predicting the mJOA recovery rate on the basis of the data in this study. This feature may also be due to the increased artifact level caused by compression. Another possible reason is that the DTI metrics at the compression levels are affected not only by altering of the intra- and extracellular environments but also by the aligned-fiber effect. In other words, FA might be elevated to some extent if the fibers are aligned due to compression so that FA reduction resulting from spinal cord dysfunction will be compensated.[14]

Although most previous results reported that preoperative FA for the MC level was significantly correlated with both the preoperative and postoperative mJOA, there were several studies that reported nonsignificant correlations. Jones et al[9] found that the preoperative FA for the MC and C2–C3 levels was correlated with the preoperative mJOA but was not correlated with the postoperative mJOA. They observed that FA at C2–C3 was more strongly correlated than at the MC level and speculated that it is due to the imaging artifacts (eg, EPI distortion) at the stenotic region, providing inconsistent DTI parameters. Wen et al[15] claimed that the mean FA of C3–C7, instead of the MC level or the C2 level alone, was able to predict the postoperative mJOA. While this finding is not fully consistent with the results in this study, it provides evidence that the spinal cord function is also associated with the DTI measurements at sites distant from the MC level. Iwasaki et al[14] also presented a nonsignificant correlation between the preoperative FA for the MC level and the postoperative mJOA. These studies (including the present study) have some differences in the methods, such as surgery strategy, statistics, prediction indexes, and so forth (Table 1).

To lower the image distortion, we used a reduced FOV technique, outer volume suppression, in the DTI data acquisition by applying saturation bands to suppress the signal outside the FOV along the phase-encoding direction. As shown in a previous study,[30] another reduced FOV technique, 2D radiofrequency excitation, is more effective in signal suppression, though it can lead to a smaller signal strength inside the FOV than outer volume suppression. Inner volume imaging–based reduced FOV has also been applied to DTI for patients with DCM,[31-34] which can achieve a shorter radiofrequency pulse duration compared with 2D radiofrequency excitation. However, the DTI sequence with 2D radiofrequency excitation or inner volume imaging–based reduced FOV was not available on the MR imaging system used in this study. Thus, we tried our best to optimize the outer volume suppression–based DTI on our system (3T Ingenia), including using B_1 shimming, subject-specific volume B_0 shimming, and the maximal gradient strength used for saturation. On the basis of our inspection, no obvious foldover artifacts were present on the diffusion-weighted images and calculated DTI metrics for all healthy volunteers and patients in this study. In the future, we will compare the performance difference in quantifying the spinal cord DTI metrics between outer volume suppression and 2D radiofrequency excitation when the latter is available.

As mentioned in the Materials and Methods section, the imaging plane of DTI was parallel to the intervertebral disk at the maximal compression level, which is a prescription commonly used in the previous studies. Due to the natural bending of the spinal cord, it is difficult to apply orthogonality to the nerve fibers along all cervical levels (eg, C2–C7), and the angles between the imaging plane and fiber directions may introduce bias for measuring DTI metrics. An ideal way to tackle this issue is to align the image plane of each section with the corresponding disk level through modifying the DTI pulse sequence. The viability for this modification requires investigation.

The methodology of this study had 2 major limitations. First, the diagnosis of patients included in the study was not uniform, eg, the surgical outcomes could be different between patients with ossification of the posterior longitudinal ligament and other patients with DCM, because usually the spinal cord of patients with ossification of the posterior longitudinal ligament has already been compressed for a long time; thus, their surgical outcome is relatively worse. Second, the DTI metrics of the white matter and gray matter were not analyzed separately. In this study, it is difficult to distinguish the WM and GM at the compressed levels, especially for the preoperative patients in whom the compressed spinal cord may present as only a few pixels. Even at noncompressed levels, measuring the GM and WM separately is not easy because of the limited resolution of DTI.

While we could not distinguish the WM and GM at the MC level for patients with severe compression, we were able to draw ROIs within the WM at the C2 level. For example, we drew an ROI on the dorsal column at the C2 level for all patients before surgery. The results shown in On-line Table 2 suggest that the AD of the dorsal column at the C2 level is significantly correlated with the mJOA recovery rate ($r = 0.341$, $P = .018$) and has a tendency to be correlated with the mJOA before surgery ($r = 0.264$, $P = .07$). When we used ROIs containing the whole spinal cord at the C2 level, as shown in the Results section, FA, AD, and RD were all correlated with the mJOA recovery rate. Although in theory, the spinal cord function is mainly related to WM, the ROI drawn in the dorsal column can also be contaminated by GM due to low image resolution. Additionally, the dorsal column

is a proprioceptive sensibility pathway in charge of proprioception/vibratory sense and discriminative touch, while the mJOA represents the overall sensation and motion function of the spinal cord. Furthermore, it is impractical to define the ROI of the entire WM freehand. One potential solution is to register diffusion-weighted images to the high-spatial-resolution structural images from which the GM and WM are better distinguished. We have tried to use the registration function provided by the Spinal Cord Toolbox, and it worked well for healthy subjects but failed for the preoperative patients; this outcome could be due to the influence of compression levels. Thus, a better registration algorithm is desirable for such special cases.

Overall, this study found that DTI showed the potential for predicting the mJOA recovery rate, which supports the conclusions in most previous studies. Both the Spearman correlation and ROC analysis yielded positive results for predicting the mJOA recovery rate after 1-year follow-up using the DTI metrics at the C2 level. In practice, DTI in the spinal cord inevitably faces technical limitations of spatial resolution, signal-to-noise ratio, and motion artifacts. Emerging advanced acquisition equipment such as ultra-high-field MR imaging systems[35] may alleviate these issues.

CONCLUSIONS

We provide a comprehensive analysis of the evaluation and prediction capability of DTI for laminoplasty surgery outcomes. Results showed that the DTI metrics at the C2 level before surgery have the potential for predicting the postoperative mJOA recovery rate.

REFERENCES

1. Tetreault L, Goldstein CL, Arnold P, et al. **Degenerative cervical myelopathy: a spectrum of related disorders affecting the aging spine.** *Neurosurgery* 2015;77:S51–67 CrossRef Medline
2. Basser PJ, Mattiello J, Lebihan D. **MR diffusion tensor spectroscopy and imaging.** *Biophys J* 1994;66:259–67 CrossRef Medline
3. Demir A, Ries M, Moonen CT, et al. **Diffusion-weighted MR imaging with apparent diffusion coefficient and apparent diffusion tensor maps in cervical spondylotic myelopathy.** *Radiology* 2003;229:37–43 CrossRef Medline
4. Kerkovsky M, Bednarik J, Dusek L, et al. **Magnetic resonance diffusion tensor imaging in patients with cervical spondylotic spinal cord compression: correlations between clinical and electrophysiological findings.** *Spine (Phila Pa 1976)* 2012;37:48–56 CrossRef Medline
5. Vedantam A, Rao A, Kurpad SN, et al. **Diffusion tensor imaging correlates with short-term myelopathy outcome in patients with cervical spondylotic myelopathy.** *World Neurosurg* 2017;97:489–94 CrossRef Medline
6. Ellingson BM, Salamon N, Grinstead JW, et al. **Diffusion tensor imaging predicts functional impairment in mild-to-moderate cervical spondylotic myelopathy.** *Spine J* 2014;14:2589–97 CrossRef Medline
7. Guan L, Chen X, Hai Y, et al. **High-resolution diffusion tensor imaging in cervical spondylotic myelopathy: a preliminary follow-up study.** *NMR Biomed* 2017;30 CrossRef Medline
8. Bhosale S, Ingale P, Srivastava S, et al. **Diffusion tensor imaging as an additional postoperative prognostic predictor factor in cervical myelopathy patients: an observational study.** *J Craniovertebr Junction Spine* 2019;10:10–13 CrossRef Medline
9. Jones JG, Cen SY, Lebel RM, et al. **Diffusion tensor imaging correlates with the clinical assessment of disease severity in cervical spondylotic myelopathy and predicts outcome following surgery.** *AJNR Am J Neuroradiol* 2013;34:471–78 CrossRef Medline
10. Yoo WK, Kim TH, Hai DM, et al. **Correlation of magnetic resonance diffusion tensor imaging and clinical findings of cervical myelopathy.** *Spine J* 2013;13:867–76 CrossRef Medline
11. Gao SJ, Yuan X, Jiang XY, et al. **Correlation study of 3T-MR-DTI measurements and clinical symptoms of cervical spondylotic myelopathy.** *Eur J Radiol* 2013;82:1940–45 CrossRef Medline
12. Furlan JC, Catharine Craven B. **Psychometric analysis and critical appraisal of the original, revised, and modified versions of the Japanese Orthopaedic Association score in the assessment of patients with cervical spondylotic myelopathy.** *Neurosurg Focus* 2016;40:E6 CrossRef Medline
13. Ma X, Han X, Jiang W, et al. **A follow-up study of postoperative DCM patients using diffusion MRI with DTI and NODDI.** *Spine (Phila Pa 1976)* 2018;43:E898–904 CrossRef Medline
14. Iwasaki M, Yokohama T, Oura D, et al. **Decreased value of highly accurate fractional anisotropy using 3-Tesla ZOOM diffusion tensor imaging after decompressive surgery in patients with cervical spondylotic myelopathy: aligned fibers effect.** *World Neurosurg X* 2019;4:100056 CrossRef Medline
15. Wen CY, Cui JL, Liu HS, et al. **Is diffusion anisotropy a biomarker for disease severity and surgical prognosis of cervical spondylotic myelopathy?** *Radiology* 2014;270:197–204 CrossRef
16. Maki S, Koda M, Kitamura M, et al. **Diffusion tensor imaging can predict surgical outcomes of patients with cervical compression myelopathy.** *Eur Spine J* 2017;26:2459–66 CrossRef Medline
17. Kitamura M, Maki S, Koda M, et al. **Longitudinal diffusion tensor imaging of patients with degenerative cervical myelopathy following decompression surgery.** *J Clin Neurosci* 2020;74:194–98 CrossRef Medline
18. Shabani S, Kaushal M, Budde M, et al. **Comparison between quantitative measurements of diffusion tensor imaging and T2 signal intensity in a large series of cervical spondylotic myelopathy patients for assessment of disease severity and prognostication of recovery.** *J Neurosurg Spine* 2019 Jun 7. [Epub ahead of Print] CrossRef Medline
19. Wilm BJ, Svensson J, Henning A, et al. **Reduced field-of-view MRI using outer volume suppression for spinal cord diffusion imaging.** *Magn Reson Med* 2007;57:625–30 CrossRef Medline
20. Wargo CJ, Gore JC. **Localized high-resolution DTI of the human midbrain using single-shot EPI, parallel imaging, and outer-volume suppression at 7T.** *Magn Reson Imaging* 2013;31:810–19 CrossRef Medline
21. De Leener B, Levy S, Dupont SM, et al. **SCT: Spinal Cord Toolbox, an open-source software for processing spinal cord MRI data.** *Neuroimage* 2017;145:24–43 CrossRef Medline
22. Jenkinson M, Beckmann CF, Behrens TE, et al. **FSL.** *Neuroimage* 2012;62:782–90 CrossRef Medline
23. Jiang H, van Zijl PC, Kim J, et al. **DtiStudio: resource program for diffusion tensor computation and fiber bundle tracking.** *Comput Methods Programs Biomed* 2006;81:106–16 CrossRef Medline
24. Bernabeu-Sanz A, Molla-Torro JV, Lopez-Celada S, et al. **MRI evidence of brain atrophy, white matter damage, and functional adaptive changes in patients with cervical spondylosis and prolonged spinal cord compression.** *Eur Radiol* 2020;30:357–69 CrossRef Medline
25. Cui L, Kong C, Chen X, et al. **Changes in diffusion tensor imaging indices of the lumbosacral enlargement correlate with cervical spinal cord changes and clinical assessment in patients with cervical spondylotic myelopathy.** *Clin Neurol Neurosurg* 2019;186:105282 CrossRef Medline
26. Budzik JF, Balbi V, Le Thuc V, et al. **Diffusion tensor imaging and fibre tracking in cervical spondylotic myelopathy.** *Eur Radiol* 2011;21:426–33 CrossRef Medline

27. Kang M, Anderer E, Elliott R, et al. **Diffusion tensor imaging of the spondylotic cervical spinal cord: a preliminary study of quantifiable markers in the evaluation for surgical decompression.** *Internet J Head Neck Surg* 2011;5. https://print.ispub.com/api/0/ispub-article/6765. Accessed January 15, 2019
28. Poplawski MM, Alizadeh M, Oleson CV, et al. **Application of diffusion tensor imaging in forecasting neurological injury and recovery after human cervical spinal cord injury.** *J Neurotrauma* 2019;36:3051–61 CrossRef Medline
29. Guleria S, Gupta RK, Saksena S, et al. **Retrograde Wallerian degeneration of cranial corticospinal tracts in cervical spinal cord injury patients using diffusion tensor imaging.** *J Neurosci Res* 2008;86:2271–80 CrossRef Medline
30. Wargo C, Jankiewicz M, Gore J. **Comparison of reduced FOV techniques for high resolution imaging at 7T.** *Proc Intl Soc Mag Reson Med* 2010;3012
31. Jeong EK, Kim SE, Guo J, et al. **High-resolution DTI with 2D interleaved multislice reduced FOV single-shot diffusion-weighted EPI (2D ss-rFOV-DWEPI).** *Magn Reson Med* 2005;54:1575–79 CrossRef Medline
32. Kim TH, Zollinger L, Shi XF, et al. **Quantification of diffusivities of the human cervical spinal cord using a 2D single-shot interleaved multisection inner volume diffusion-weighted echo-planar imaging technique.** *AJNR Am J Neuroradiol* 2010;31:682–87 CrossRef Medline
33. Park EH, Lee YH, Jeong EK, et al. **Diffusion tensor imaging focusing on lower cervical spinal cord using 2D reduced FOV interleaved multislice single-shot diffusion-weighted echo-planar imaging: comparison with conventional single-shot diffusion-weighted echo-planar imaging.** *Magn Reson Imaging* 2015;33:401–06 CrossRef Medline
34. Lee S, Lee YH, Chung TS, et al. **Accuracy of diffusion tensor imaging for diagnosing cervical spondylotic myelopathy in patients showing spinal cord compression.** *Korean J Radiol* 2015;16:1303–12 CrossRef Medline
35. Sigmund EE, Suero GA, Hu C, et al. **High-resolution human cervical spinal cord imaging at 7 T.** *NMR Biomed* 2012;25:891–99 CrossRef Medline

Respiratory Phase Affects the Conspicuity of CSF–Venous Fistulas in Spontaneous Intracranial Hypotension

T.J. Amrhein, L. Gray, M.D. Malinzak, and P.G. Kranz

ABSTRACT

SUMMARY: Spinal CSF–venous fistulas are a cause of spontaneous intracranial hypotension that can be difficult to detect on imaging. We describe how the respiratory phase affects the visibility of CSF–venous fistulas during myelography.

ABBREVIATIONS: CTM = CT myelography; CVF = CSF–venous fistula; SIH = spontaneous intracranial hypotension

Spontaneous intracranial hypotension (SIH) is a debilitating condition caused by spinal CSF leaks and CSF–venous fistulas (CVFs).[1] The localization of these spinal causes of SIH is critical for successful treatment.[2,3] CVFs are particularly difficult to identify on traditional myelographic imaging.[1,4] Technical modifications to the myelography technique such as decubitus imaging during dynamic myelography, digital subtraction myelography, and CT myelography (CTM) have been shown to improve the conspicuity of CVFs, which are often subtle.[5] However, additional methods for maximizing CVF identification remain desirable. We have observed that the ability to visualize CVFs varies with different phases of respiration, suggesting that attention to the respiratory phase of imaging may improve their detection in some patients.

MATERIALS AND METHODS

Subjects

This was a retrospective case series of 5 patients with SIH treated at a single major referral institution from January 2018 to February 2020. All patients met the International Classification of Headache Disorders-3 criteria for SIH and had preprocedural contrast-enhanced brain MR imaging that was positive for SIH.[6,7] Patients were included when the conspicuity of a spinal CVF was affected by the respiratory phase during image acquisition. In all cases, an initial prone CTM demonstrated findings suggestive of a spinal CVF, necessitating further myelography in the ipsilateral decubitus position. This study was Health Insurance Portability and Accountability Act–compliant and was approved by the institutional internal review board with a waiver of informed consent.

Myelogram Technique

Decubitus myelography was performed in all cases due to subtle findings suggestive of a spinal CVF on a prior prone CTM. Decubitus myelograms were obtained as previously described using 10 mL of iopamidol containing 300 mg/mL of iodine (Isovue-M 300; Bracco).[5] Dynamic myelograms were all obtained on the same C-arm fluoroscopy unit equipped with a tilting table (MultiDiagnost Eleva; Philips Healthcare). Digital subtraction was not used. CTMs were all performed on a single 64–detector row CT scanner (Discovery 750HD; GE Healthcare) with the following parameters: helical scan mode, rotation time = 0.8 seconds, pitch = 0.969, tube voltage = 120 kV (peak), automated exposure control, tube current = 300–800 mA, noise index = 19.5, section thickness = 2.5 mm, interval = 2.5 mm, reconstruction thickness = 0.625 mm. Imaging was focused over the nerve root associated with the suspected CVF to limit the radiation dose. In 4 of the 5 patients, both a dynamic myelogram and a CTM in the decubitus position were obtained. In the other patient, only a decubitus CTM was performed. Images were obtained during breath-hold for all cases at various phases of the respiratory cycle (eg, neutral, full inspiration, and full expiration).

RESULTS

Subjects

The mean patient age was 60 years (range, 44–68 years), and 40% were women. All patients in this series coincidentally had undergone 2 CTMs before images were acquired with attention to the phase of the respiratory cycle. In all patients, 1 of the 2 prior CTMs had negative findings, and the other demonstrated a subtle finding suspicious for a CVF, which formed the basis for the

Received March 28, 2020; accepted after revision May 5.

From the Department of Radiology, Duke University Medical Center, Durham, North Carolina.

Please address correspondence to Timothy J. Amrhein, MD, Department of Radiology, Box 3808, Duke University Medical Center, Durham, NC 27710; e-mail: timothy.amrhein@duke.edu; @TimAmrheinMD

http://dx.doi.org/10.3174/ajnr.A6663

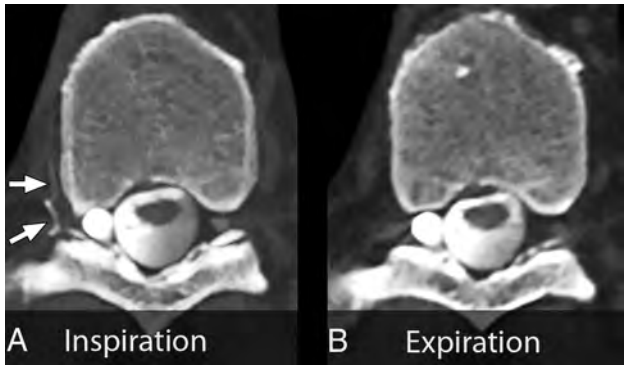

FIG 1. Maximum-intensity-projection CT myelograms of a right T9 nerve root sleeve CSF–venous fistula. *A*, Image acquisition during inspiration. Marked increased conspicuity of the CSF–venous fistula and hyperdense paraspinal vein (*arrows*). *B*, Image during expiration. The CSF–venous fistula is no longer visible.

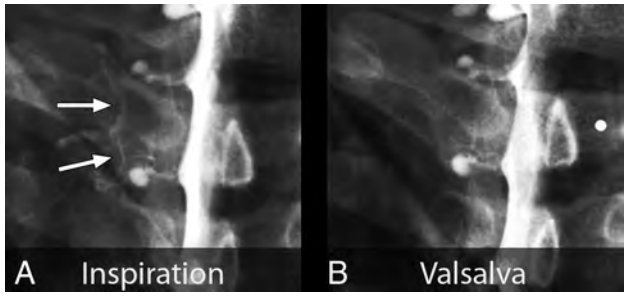

FIG 2. Spot-magnified radiographs of a left T2 nerve root sleeve CSF–venous fistula during an ipsilateral decubitus dynamic myelogram. *A*, Image acquired during inspiration demonstrates well the contrast-opacified CSF–venous fistula (*arrows*). *B*, Image during a Valsalva maneuver results in considerably reduced visualization of the CSF–venous fistula.

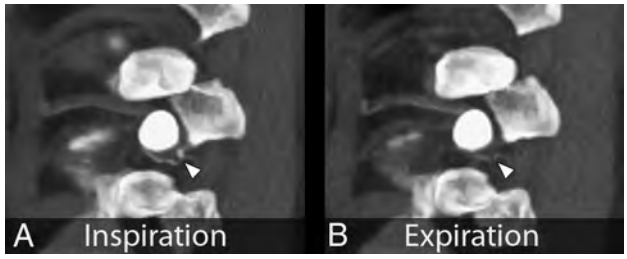

FIG 3. Parasagittal maximum-intensity-projection CT myelograms through the neuroforamen of a left T10 CSF–venous fistula. *A*, Image acquired during inspiration clearly captures contrast within the CSF–venous fistula (*arrowhead*). *B*, Image acquired during expiration. Note the markedly reduced conspicuity of the CSF–venous fistula (*arrowhead*).

decision to acquire the images depicted in this report. CVFs all originated from nerve root sleeves, consistent with previous reports, and were identified on the right at T9 and on the left at C8, T2, T8, and T10.[8]

Myelogram Findings

Images were acquired with breath-hold during various phases of the respiratory cycle, with the patient in the lateral decubitus position. Inspiratory imaging was compared with additional phases of respiration including expiration ($n = 3$), neutral breath hold ($n = 1$), and Valsalva ($n = 1$). In all 5 patients, the CVF was more conspicuous during the inspiratory phase (Figs 1–5).

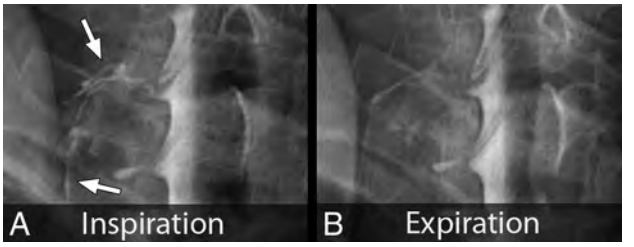

FIG 4. Spot-magnified radiographs of a left C8 CSF–venous fistula during an ipsilateral decubitus dynamic myelogram. *A*, Image acquired during inspiration demonstrates increased visibility and extent of the CSF–venous fistula (*arrows*). *B*, Image acquired during expiration leads to reduced visibility and extent of the CSF–venous fistula.

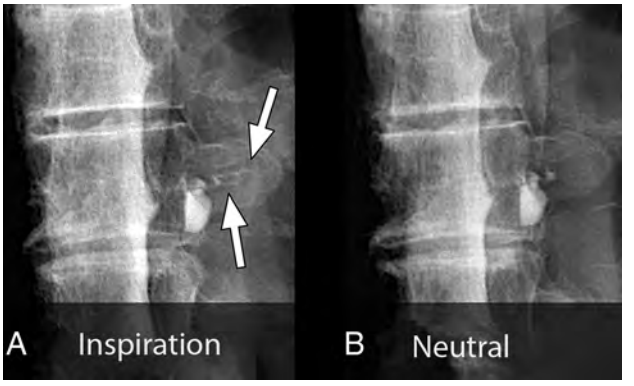

FIG 5. Spot-magnified radiographs of a left T8 CSF–venous fistula during an ipsilateral decubitus dynamic myelogram. *A*, Image acquired during inspiration demonstrates contrast opacification of the CSF–venous fistula extending out over the transverse process (*arrows*). *B*, Image acquired during quiet breath-hold during the mid-respiratory cycle. The CSF–venous fistula is no longer visible over the transverse process.

DISCUSSION

We found that the conspicuity of some CVFs varied during different phases of the respiratory cycle and that in all cases, they were most conspicuous during inspiration. This finding suggests that for patients with SIH, myelography performed during maximum inspiration may aid in the detection of CVFs, thereby improving the overall diagnostic yield.

It is well-known that venous return is highly dependent on the respiratory phase.[9] Inspiration results in descent of the diaphragm causing negative intrathoracic pressure as well as increased intraabdominal pressure. This result creates a pressure gradient driving blood from the inferior vena cava to the right atrium, increasing venous return to the heart.[10] This blood flow also results in decreased intravascular pressure within the inferior vena cava, which would produce a gradient of pressure between the higher pressure CSF and the lower pressure epidural venous plexus and paraspinal veins.

In the setting of a CVF, we hypothesize that this gradient would result in rapid unregulated egress of CSF back into the circulatory system, with resultant increased conspicuity on myelography.[11] Conversely, during a Valsalva maneuver, the intrathoracic and inferior vena cava pressure considerably increases. This increase markedly reduces venous return and also eliminates the aforementioned pressure gradient between the CSF and the infradiaphragmatic venous system, which we hypothesize would reduce flow through a CVF.[12]

Our findings suggest that in cases in which a CVF is suspected, the diagnostic yield of spinal imaging may increase if it is performed during inspiration. In our practice, we now routinely perform our initial image acquisitions in this manner. This modification to the myelography technique is broadly applicable across modalities and can be used even in centers without the resources and equipment necessary to perform digital subtraction myelography.

This investigation is limited by the small number of cases reported and by its retrospective nature, which introduces the potential for selection bias. Furthermore, in our practice, some patients with CVF have not demonstrated changes in imaging conspicuity that are dependent on the phase of respiration. The proportion of patients with CVFs that are affected by differences in respiration remains unknown. Effort to answer this question as well as to determine the factors predictive of CVFs that exhibit imaging changes dependent on respiration is a logical direction for future research. Additionally, there may be other unknown factors related to respiration that result in changes to CVF conspicuity. For example, it is possible that there is a threshold at which substantially increased rates of venous return to the heart would result in rapid washout of contrast from a CVF, paradoxically reducing its conspicuity during inspiration.

CONCLUSIONS

The conspicuity of CVFs is improved during inspiration in some cases. Further investigation into the improved diagnostic performance of myelography performed during inspiration is warranted.

Disclosures: Linda Gray—*UNRELATED*: *Board Membership*: Spinal CSF Leak Foundation.

REFERENCES

1. Amrhein TJ, Kranz PG. **Spontaneous intracranial hypotension: imaging in diagnosis and treatment.** *Radiol Clin North Am* 2019;57:439–51 CrossRef Medline
2. Wang TY, Karikari IO, Amrhein TJ, et al. **Clinical outcomes following surgical ligation of cerebrospinal fluid-venous fistula in patients with spontaneous intracranial hypotension: a prospective case series.** *Oper Neurosurg (Hagerstown)* 2020;18:239–45 CrossRef Medline
3. Kranz PG, Gray L, Malinzak MD, et al. **Spontaneous intracranial hypotension: pathogenesis, diagnosis, and treatment.** *Neuroimaging Clin N Am* 2019;29:581–94 CrossRef Medline
4. Schievink WI, Maya MM, Jean-Pierre S, et al. **A classification system of spontaneous spinal CSF leaks.** *Neurology* 2016;87:673–79 CrossRef Medline
5. Kranz PG, Gray L, Amrhein TJ. **Decubitus CT myelography for detecting subtle CSF leaks in spontaneous intracranial hypotension.** *AJNR Am J Neuroradiol* 2019;40:754–56 CrossRef Medline
6. Headache Classification Committee of the International Headache Society (IHS). **The International Classification of Headache Disorders, 3rd Edition (Beta Version).** *Cephalalgia* 2013;33:629–808 CrossRef Medline
7. Dobrocky T, Grunder L, Breiding PS, et al. **Assessing spinal cerebrospinal fluid leaks in spontaneous intracranial hypotension with a scoring system based on brain magnetic resonance imaging findings.** *JAMA Neurol* 2019;76:580–87 CrossRef Medline
8. Kranz PG, Amrhein TJ, Gray L. **CSF venous fistulas in spontaneous intracranial hypotension: imaging characteristics on dynamic and CT myelography.** *AJR Am J Roentgenol* 2017;209:1360–66 CrossRef Medline
9. Pinsky MR. **Cardiopulmonary interactions: physiologic basis and clinical applications.** *Ann Am Thorac Soc* 2018;15:S45–48 CrossRef Medline
10. Willeput R, Rondeux C, De Troyer A. **Breathing affects venous return from legs in humans.** *J Appl Physiol Respir Environ Exerc Physiol* 1984;57:971–76 CrossRef Medline
11. Kumar N, Neidert NB, Diehn FE, et al. **A novel etiology for craniospinal hypovolemia: a case of inferior vena cava obstruction.** *J Neurosurg Spine* 2018;29:452–55 CrossRef Medline
12. Laborda A, Sierre S, Malve M, et al. **Influence of breathing movements and Valsalva maneuver on vena caval dynamics.** *World J Radiol* 2014;6:833–39 CrossRef Medline

Celebrating 35 Years of the AJNR

September 1985 edition

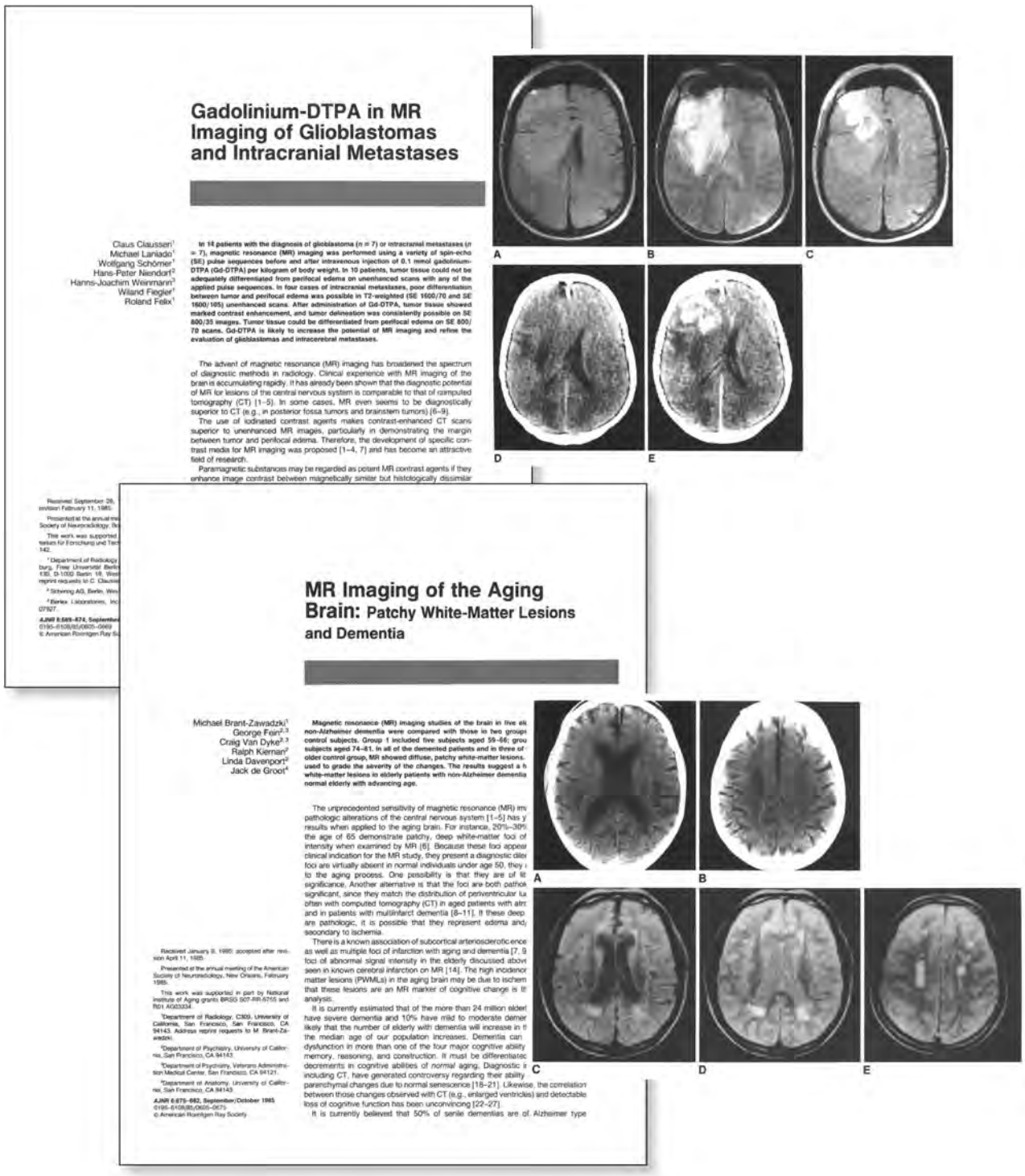

Gadolinium-DTPA in MR Imaging of Glioblastomas and Intracranial Metastases

Claus Claussen[1]
Michael Laniado[1]
Wolfgang Schörner[1]
Hans-Peter Niendorf[2]
Hanns-Joachim Weinmann[3]
Willand Fiegler[1]
Roland Felix[1]

In 14 patients with the diagnosis of glioblastoma (n = 7) or intracranial metastases (n = 7), magnetic resonance (MR) imaging was performed using a variety of spin-echo (SE) pulse sequences before and after intravenous injection of 0.1 mmol gadolinium-DTPA (Gd-DTPA) per kilogram of body weight. In 10 patients, tumor tissue could not be adequately differentiated from perifocal edema on unenhanced scans with any of the applied pulse sequences. In four cases of intracranial metastases, poor differentiation between tumor and perifocal edema was possible in T2-weighted (SE 1600/70 and SE 1600/105) unenhanced scans. After administration of Gd-DTPA, tumor tissue showed marked contrast enhancement, and tumor delineation was consistently possible on SE 800/35 images. Tumor tissue could be differentiated from perifocal edema on SE 800/70 scans. Gd-DTPA is likely to increase the potential of MR imaging and refine the evaluation of glioblastomas and intracerebral metastases.

The advent of magnetic resonance (MR) imaging has broadened the spectrum of diagnostic methods in radiology. Clinical experience with MR imaging of the brain is accumulating rapidly. It has already been shown that the diagnostic potential of MR for lesions of the central nervous system is comparable to that of computed tomography (CT) [1–5]. In some cases, MR even seems to be diagnostically superior to CT (e.g., in posterior fossa tumors and brainstem tumors) [6–9].

The use of iodinated contrast agents makes contrast-enhanced CT scans superior to unenhanced MR images, particularly in demonstrating the margin between tumor and perifocal edema. Therefore, the development of specific contrast media for MR imaging was proposed [1–4, 7] and has become an attractive field of research.

Paramagnetic substances may be regarded as potent MR contrast agents if they enhance image contrast between magnetically similar but histologically dissimilar

Received September 26, revision February 11, 1985.

Presented at the annual me... Society of Neuroradiology, Ba...

This work was supported ... Fellows für Forschung und Tec... 142.

[1]Department of Radiology ... burg, Freie Universität Berlin ... 130, D-1000 Berlin 18, West ... reprint requests to C. Clauss...

[2]Schering AG, Berlin, Wes...

[3]Berlex Laboratories, Inc... 07927.

AJNR 6:569–574, September/October 1985
0195-6108/85/0605-0569
© American Roentgen Ray So...

MR Imaging of the Aging Brain: Patchy White-Matter Lesions and Dementia

Michael Brant-Zawadzki[1]
George Fein[2,3]
Craig Van Dyke[2,3]
Ralph Kiernan[2]
Linda Davenport[2]
Jack de Groot[4]

Magnetic resonance (MR) imaging studies of the brain in five el... non-Alzheimer dementia were compared with those in two groups control subjects. Group 1 included five subjects aged 59–66; grou... subjects aged 74–81. In all of the demented patients and in three of ... older control group, MR showed diffuse, patchy white-matter lesions. ... used to grade the severity of the changes. The results suggest a h... white-matter lesions in elderly patients with non-Alzheimer dementia ... normal elderly with advancing age.

The unprecedented sensitivity of magnetic resonance (MR) ima... pathologic alterations of the central nervous system [1–5] has y... results when applied to the aging brain. For instance, 20%–30%... the age of 65 demonstrate patchy, deep white-matter foci of... intensity when examined by MR [6]. Because these foci appear... clinical indication for the MR study, they present a diagnostic dile... foci are virtually absent in normal individuals under age 50, they ... to the aging process. One possibility is that they are of lit... significance. Another alternative is that the foci are both pathol... significant, since they match the distribution of periventricular lu... often with computed tomography (CT) in aged patients with alzh... and in patients with multiinfarct dementia [8–11]. If these deep ... are pathologic, it is possible that they represent edema and/... secondary to ischemia.

There is a known association of subcortical arteriosclerotic ence... as well as multiple foci of infarction with aging and dementia [7, 9... foci of abnormal signal intensity in the elderly discussed above ... seen in known cerebral infarction on MR [14]. The high incidence ... matter lesions (PWMLs) in the aging brain may be due to ischem... that these lesions are an MR marker of cognitive change is th... analysis.

It is currently estimated that of the more than 24 million elderl... have severe dementia and 10% have mild to moderate demen... likely that the number of elderly with dementia will increase in t... the median age of our population increases. Dementia can ... dysfunction in more than one of the four major cognitive ability ... memory, reasoning, and construction. It must be differentiated ... decrements in cognitive abilities of *normal* aging. Diagnostic s... including CT, have generated controversy regarding their ability ... parenchymal changes due to normal senescence [18–21]. Likewise, the correlation ... between those changes observed with CT (e.g., enlarged ventricles) and detectable ... loss of cognitive function has been unconvincing [22–27].

It is currently believed that 50% of senile dementias are of Alzheimer type

Received January 9, 1985; accepted after revision April 11, 1985.

Presented at the annual meeting of the American Society of Neuroradiology, New Orleans, February 1985.

This work was supported in part by National Institute of Aging grants BRSG 507-RR-5755 and R01 AG03034.

[1]Department of Radiology, C359, University of California, San Francisco, San Francisco, CA 94143. Address reprint requests to M. Brant-Zawadzki.

[2]Department of Psychiatry, University of California, San Francisco, CA 94143.

[3]Department of Psychiatry, Veterans Administration Medical Center, San Francisco, CA 94121.

[4]Department of Anatomy, University of California, San Francisco, CA 94143.

AJNR 6:875–882, September/October 1985
0195-6108/85/0605-0875
© American Roentgen Ray Society

Missed Medium-Vessel Occlusions on CT Angiography: Make It Easier . . . Easily!

We read with great interest the article by Fasen et al,[1] which addresses an important and often underappreciated topic in radiology: diagnostic errors and, more specifically, missed large- and medium-vessel occlusions on CT angiography in patients with acute ischemic stroke. Little is known about the factors that lead to such errors, and the article adds important knowledge in this regard. Fasen et al found that a more distal occlusion location in the M2 segment in the middle cerebral artery (ie, medium-vessel occlusions [MeVOs][2]) was missed in 82% of cases at the time of the initial CTA evaluation, and M2 occlusion location was significantly associated with the initial missing of the occlusion. M2 occlusions are increasingly targeted with endovascular thrombectomy (EVT),[3] and it is, thus, crucial to accurately and reliably detect them. Fasen et al relied on axial single-phase CTA images to detect M2 occlusion, which is often challenging because the M2 segment is small in caliber and does not run horizontal to the axial plane.

Multiphase CTA (mCTA), which comprises 2 delayed phases in addition to the arterial phase with no additional contrast and minimal additional time and radiation dose,[4] was successfully used for large-vessel occlusion (LVO) detection and EVT patient selection in the Endovascular Treatment for Small Core and Proximal Occlusion Ischemic Stroke (ESCAPE) and Safety and Efficacy of NA-1 in Subjects Undergoing Endovascular Thrombectomy for Stroke (ESCAPE-NA1) trials[5,6] and MeVOs are much easier to catch on mCTA because a contrast hold-up is often seen in the downstream territory (Figure *A–C*). Recent advances in mCTA postprocessing have rendered real-time generation of color-coded mCTA maps possible, which facilitates detection of LVOs and particularly MeVOs even further (Figure *E*).[7] Lastly, mCTA can also be used to generate tissue-level perfusion maps just as CT perfusion does. In these maps, striking color changes in the downstream territory allow quick and easy detection of MeVOs (Figure *F*). We are convinced that the number of missed M2s would have been much lower had mCTA rather than single-phase CTA been used in the study of Fasen et al,[1] and we encourage the use of mCTA in the acute stroke setting to minimize the risk of missing potential EVT target occlusions, which dramatically impacts patient management and, ultimately, worsens patient outcomes.

Disclosures: Johanna M. Ospel—*UNRELATED*: *Grants/Grants Pending*: Julia Bangerter Rhyner-Stiftung Foundation, University of Basel Research Foundation, Freiwiliige Akademische Gesellschaft Basel, *Comments*: research scholarships. Wu Qiu—*UNRELATED*: *Employment*: University of Calgary. Mayank Goyal—*RELATED*: *Grant*: Stryker, Cerenovus*; *Consulting Fee or Honorarium*: Medtronic, Stryker, MicroVention, Mentice; *Other*: GE Healthcare, *Comments*: licensing agreement, systems of acute stroke diagnosis. *Money paid to the institution.

REFERENCES

1. Fasen B, Heijboer RJJ, Hulsmans FH, et al. **CT angiography in evaluating large-vessel occlusion in acute anterior circulation ischemic stroke: factors associated with diagnostic error in clinical practice.** *AJNR Am J Neuroradiol* 2020;41:607–11 CrossRef Medline
2. Goyal M, Ospel JM, Menon BK, et al. **MeVO: the next frontier?** *J Neurointerv Surg* 2020;12:545–47 CrossRef Medline
3. Almekhlafi M, Ospel JM, Saposnik G, et al. **Endovascular treatment decisions in patients with M2 segment MCA occlusions.** *AJNR Am J Neuroradiol* 2020;41:280–85 CrossRef Medline
4. Menon BK, d'Esterre CD, Qazi EM, et al. **Multiphase CT angiography: a new tool for the imaging triage of patients with acute ischemic stroke.** *Radiology* 2015;275:510–20 CrossRef Medline
5. Goyal M, Demchuk AM, Menon BK, et al; ESCAPE Trial Investigators. **Randomized assessment of rapid endovascular treatment of ischemic stroke.** *N Engl J Med* 2015;372:1019–30 CrossRef Medline
6. Hill MD, Goyal M, Menon BK, et al; ESCAPE-NA1 Investigators. **Efficacy and safety of nerinetide for the treatment of acute ischaemic stroke (ESCAPE-NA1): a multicentre, double-blind, randomised controlled trial.** *Lancet* 2020;395:878–87 CrossRef Medline
7. Ospel JM, Volny O, Qiu W, et al. **Displaying multiphase CT angiography using a time-variant color map: practical considerations and potential applications in patients with acute stroke.** *AJNR Am J Neuroradiol* 2020;41:200–05 CrossRef Medline

http://dx.doi.org/10.3174/ajnr.A6670

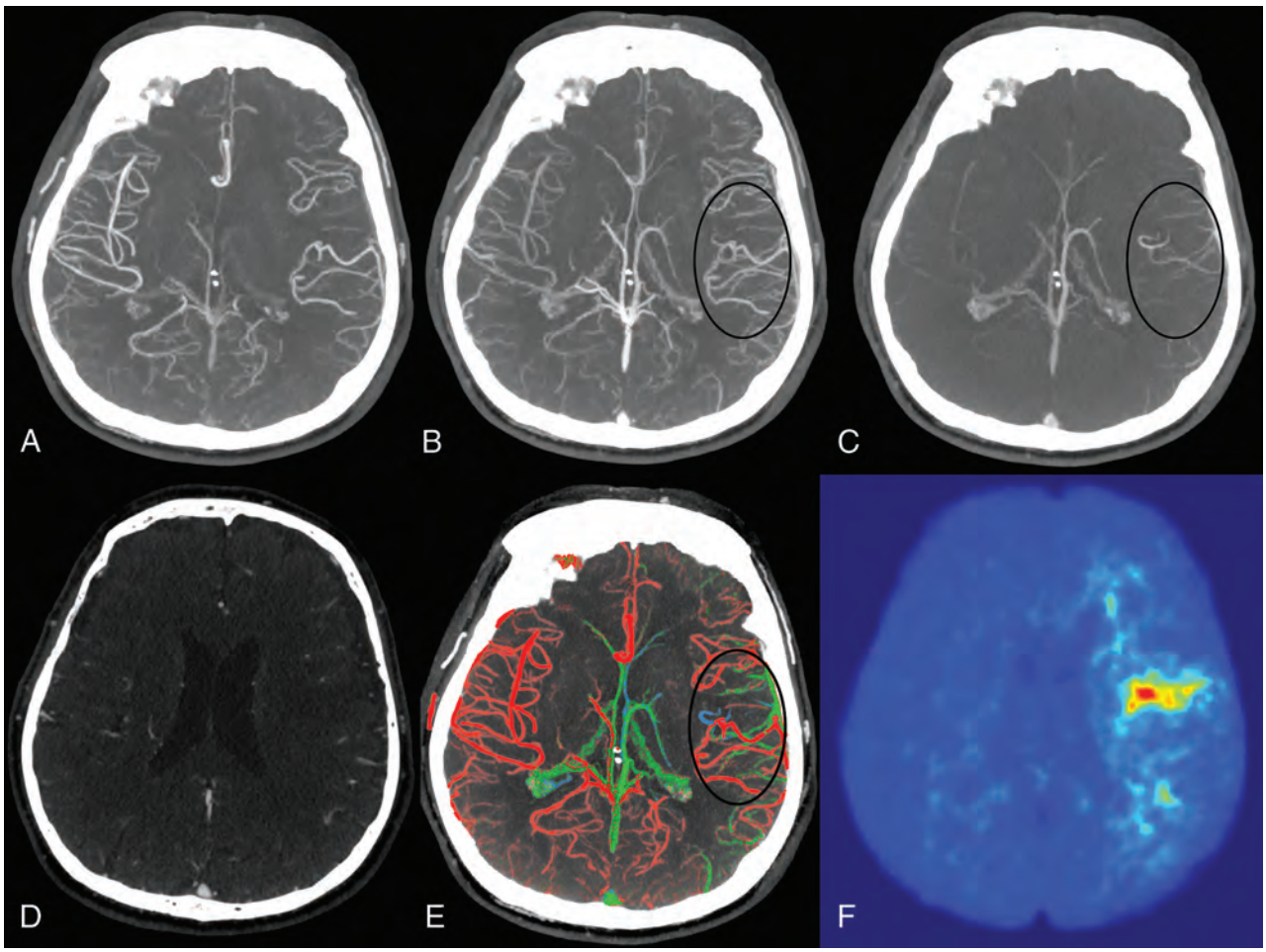

FIGURE. Patient with acute left-hemispheric symptoms (weakness of the right arm and aphasia). Multiphase CTA (arterial phase shown in *A*, peak-venous and late-venous phases shown in *B* and *C*) shows delayed contrast washout in the left peri-Sylvian region, which raises the suspicion of a medium-vessel occlusion. On single-phase CTA (*D*), it is very challenging to see the occlusion or any difference in collateral filling. Color-coded time-variant mCTA summation maps facilitate the diagnosis further because the abrupt change in vessel color on the mCTA summation map is more obvious than changes in enhancement on gray-scale images (color-coded mCTA summation map is shown in *E*, the *black circle* highlights the color changes caused by the medium vessel occlusion), vessels with maximum enhancement in the arterial phase are shown in red, those enhancing in the peak-venous and late-venous phases are shown in green and blue). The time-to-peak map derived from mCTA (*F*) shows a clear change of color in the affected parenchyma and is another possibility for fast and reliable detection of MeVOs.

J.M. Ospel
Department of Clinical Neurosciences
University of Calgary
Calgary, Alberta, Canada

Department of Radiology
University Hospital Basel, University of Basel
Basel, Switzerland

W. Qiu
Department of Clinical Neurosciences

M. Goyal
Departments of Clinical Neurosciences and Radiology
University of Calgary
Calgary, Alberta, Canada

REPLY:

We thank Ospel and colleagues for their interest in our article "CT Angiography in Evaluating Large-Vessel Occlusion in Acute Anterior Circulation Ischemic Stroke: Factors Associated with Diagnostic Error in Clinical Practice."[1]

In our study, we investigated the diagnostic performance of single-phase CTA, which is the minimum suggested imaging approach for patients with acute stroke with suspected large-vessel occlusion (LVO).[2] Single-phase CTA was also used for patient selection in the Multicenter Randomized Clinical Trial of Endovascular Treatment for Acute Ischemic Stroke in the Netherlands (MR CLEAN).[3] The CTA scans in our study were prospectively read in real-life clinical practice. This practice contrasts with most previous studies on CTA in patients with stroke, which are usually a retrospective review and may be performed in a calm research setting, which does not reflect a busy clinical practice setting.

As we have mentioned in the Discussion section of our article,[1] the use of advanced CTA techniques (including multiphase CTA) may help to improve detection of LVO, which we certainly encourage. However, before new techniques are widely applied in clinical practice or included in guidelines, we believe that it is necessary that their added value (in terms of improved diagnostic accuracy, higher interobserver agreement, increased reading speed, and so forth) is unequivocally supported by high-quality research, preferably by multiple independent studies. We welcome any such data that will improve the care of patients with acute stroke.

Although advanced CTA techniques could certainly be valuable, we want to emphasize that the value of noncontrast head CT should not be forgotten. Retrospective review of the 17 initially missed or misinterpreted LVOs in our study[1] showed that there were 4 patients with a calcified embolus, all visible on noncontrast head CT. In 7 of the other 13 patients, a dense artery sign was present on noncontrast head CT. Therefore, in 65% of the initially missed or misinterpreted LVOs, noncontrast head CT could have been helpful in making the correct diagnosis.

CT angiography has relatively recently become the standard of care for patients with acute stroke with suspected LVO after the results of randomized trials like the MR CLEAN trial[3] have been published. Consequently, the use of CTA and the workload for radiologists have dramatically increased.[4] Neuroradiologist coverage 24/7/365 is not feasible in many hospitals, including ours, because of staff shortages. Of interest, our study demonstrated that neuroradiologists were more accurate than non-neuroradiologists in detecting LVO, which can be explained by a difference in experience and training. Thus, we believe that non-neuroradiologists may benefit from training, which will hopefully further improve LVO detection and eventually the outcome of patients with acute ischemic stroke.

REFERENCES

1. Fasen B, Heijboer RJJ, Hulsmans FH, et al. **CT angiography in evaluating large-vessel occlusion in acute anterior circulation ischemic stroke: factors associated with diagnostic error in clinical practice.** *AJNR Am J Neuroradiol* 2020;41:607–11 CrossRef Medline
2. Almekhlafi MA, Kunz WG, Menon BK, et al. **Imaging of patients with suspected large-vessel occlusion at primary stroke centers: available modalities and a suggested approach.** *AJNR Am J Neuroradiol* 2019;40:396–400 CrossRef Medline
3. Berkhemer OA, Fransen PSS, Beumer D, et al; MR CLEAN Investigators. **A randomized trial of intraarterial treatment for acute ischemic stroke.** *N Engl J Med* 2015;372:11–20 CrossRef Medline
4. Fasen B, Heijboer RJJ, Hulsmans FH, et al. **Radiology workload in clinical implementation of thrombectomy for acute ischemic stroke: experience from the Netherlands.** *Neuroradiology* 2020 April 5. [Epub ahead of print] CrossRef Medline

B.A. Fasen
R.M. Kwee
Department of Radiology
Zuyderland Medical Center
Heerlen/Sittard/Geleen, the Netherlands

http://dx.doi.org/10.3174/ajnr.A6700

CT Fluid-Blood Levels in COVID-19 Intracranial Hemorrhage

We read with great interest the article by Professor Jain, "Evolving Neuroimaging Findings during COVID-19," which highlighted the published coronavirus 2019 (COVID-19) literature on ischemic strokes associated with a possible virus-induced prothrombotic state.[1] We agree that intracranial hemorrhage (ICH) associated with the pandemic may become more important, especially as therapeutic anticoagulation is initiated to treat thrombotic complications such as in deep vein thrombosis, pulmonary embolism, cardioembolic stroke, ischemic limb, and acute myocardial infarction.[1-3] Already, CT demonstrating hemorrhagic conversion of ischemic strokes and hemorrhagic strokes composes up to one-quarter of positive neuroimaging findings.[1,2] ICH secondary to anticoagulation therapy is an important iatrogenic complication that radiologists need to recognize as we aid our clinician counterparts in appropriate treatment and prognostication.

We recently observed such a situation in a 64-year-old male patient who was admitted to the intensive care unit with multiorgan failure secondary to severe COVID-19 pneumonia. He required extracorporeal membrane oxygenation (ECMO) support with protocolized anticoagulation therapy to prevent circuit clotting. The team had targeted and achieved a low activated partial thromboplastin time. However, on the second day, his consciousness level deteriorated, and his pupils became dilated and unresponsive. Urgent CT revealed bihemispheric multifocal intracranial hematomas, with multiple fluid-blood levels (Figure) and general sulcal and ventricular effacement. Our patient demonstrated the characteristic neuroimaging finding of intracranial hematomas containing horizontal menisci (caused by dependent separation of heavier, hyperattenuating blood from lighter, hypoattenuating serous fluid), which has a high specificity for patients who have been treated with anticoagulants.[4]

While ICH is a known complication of ECMO, in this patient, it represented an unexpected turn of events despite achieving low therapeutic anticoagulation. Currently, the interaction between coagulopathy and the effect of the Severe Acute Respiratory Syndrome coronavirus 2 (SARS-CoV-2) on the vascular endothelium is not well-studied.[3] Individualized risk stratification, with possible extended coagulation work-up, before and during anticoagulation therapy may be an important direction of research. Although COVID-19 infection may modify intracranial hemorrhage, it is hoped that prompt recognition and treatment of coagulopathy may help reduce mortality rates and improve clinical outcomes.[4] As neuroradiologists increasingly encounter and diagnose central nervous system complications of COVID-19 infection, we should recognize the characteristic finding of fluid-blood levels within the intracranial hematoma as associated with anticoagulation.

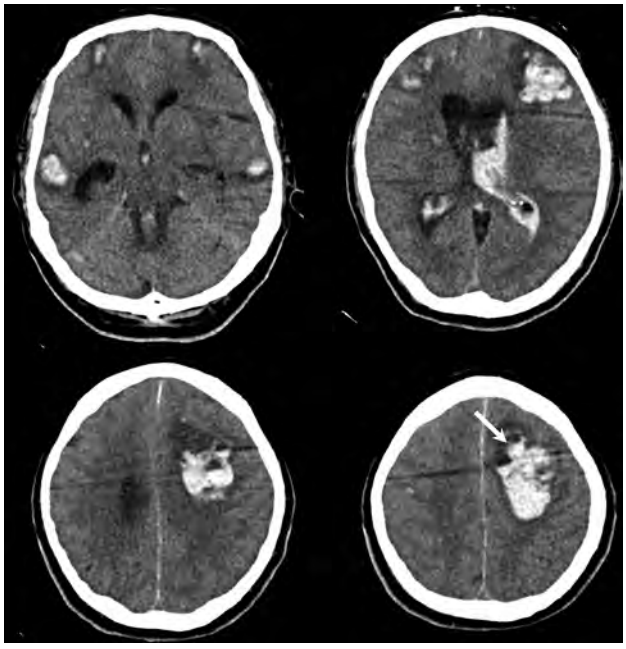

FIGURE. Unenhanced axial CT scan of the brain showing the presence of bihemispheric multifocal intracranial hematomas, with multiple fluid-blood levels (*arrow*) and general sulcal and ventricular effacement.

Disclosures: Yew Woon Chia—*UNRELATED: Employment*: Tan Tock Seng Hospital, Singapore.

REFERENCES

1. Jain R. **Evolving neuroimaging findings during COVID-19.** *AJNR Am J Neuroradiol* 2020;41 CrossRef

Indicates open access to non-subscribers at www.ajnr.org

http://dx.doi.org/10.3174/ajnr.A6672

2. Dogra S, Jain R, Cao M, et al. **Hemorrhagic stroke and anticoagulation in COVID-19.** *J Stroke Cerebrovasc Dis* 2020;28:104984 CrossRef
3. Klok FA, Kruip M, van der Meer NJ, et al. **Incidence of thrombotic complications in critically ill ICU patients with COVID-19.** *Thromb Res* 2020;191:145–47 CrossRef Medline
4. Pfleger MJ, Hardee EP, Contant CF, et al. **Specificity of fluid-blood levels for coagulopathy in acute intracerebral hematomas.** *AJNR Am J Neuroradiol* 1994;15:217–23 Medline

N.K. Wee
Department of Diagnostic Imaging

E.B. Fan
Department of Hematology
Tan Tock Seng Hospital
Singapore

K.C.H. Lee
Department of Respiratory and Critical Care Medicine
Singapore General Hospital
Singapore

Y.W. Chia
Department of Cardiology
Tan Tock Seng Hospital
Singapore

T.C.C. Lim
Department of Neuroradiology, National Neuroscience Institute
Duke-NUS Graduate Medical School, Singapore
Singapore

Neuro-Thoracic Radiologists "Corner": Incidental Pulmonary Findings on a Neck MRI Leading to the Diagnosis of COVID-19

We read with great interest the recently published article by Jain et al[1] in the July 2020 issue of the *American Journal of Neuroradiology*. In this article, the authors reported a cohort of 17 patients who presented to the emergency department with either trauma or stroke-like symptoms and underwent neuroimaging evaluation revealing incidental thoracic findings on a CTA of the neck or CT of the cervical/thoracic spine, suspicious for viral pneumonia, triggering testing for Severe Acute Respiratory Syndrome coronavirus 2 (SARS-CoV-2) with an eventual diagnosis of coronavirus disease 2019 (COVID-19). It is emphasized that neuroradiologists should be familiar with the imaging appearance of common thoracic and abdominal diseases that can be detected on neuroimaging studies and they should always carefully scrutinize the image "corners" or "blind-spots" to minimize perceptual diagnostic errors, the significance of which has never been more important. Similarly, as MR imaging outpatient volumes continue to return to normal levels as the country reopens, larger numbers of potentially infected-but-asymptomatic or paucisymptomatic patients will be coming to the radiology clinics each day, providing new opportunities for incidental detection of COVID-19 on routine MR neuroimaging. To date, there is a scarcity of reporting on the MR imaging appearance of the coronavirus disease,[2] which is not surprising given the overall reduced MR imaging volume and strict infection control measures taken during the lockdown.

We, therefore, report the following case of incidentally detected COVID-19 in a 43-year-old man undergoing MR imaging of the neck. He presented as an outpatient to his otorhinolaryngologist with chronic intermittent throat/neck and ear pain, excessive sputum production, and a history of prior tonsillectomy. Findings of physical examination, throat swab for *Streptococcus pyogenes*, and nasopharyngolaryngoscopy were negative. MR imaging of the neck was ordered, which showed no aerodigestive tract mass or cervical lymphadenopathy (Fig 1); however, slices through the lung apices showed bilateral, peripheral consolidation with rounded morphology, consistent with high confidence features of COVID-19 pneumonia (Fig 2). The consolidation was hyperintense on T2/STIR sequences and avidly enhanced on T1-weighted fast multiplanar spoiled gradient-echo sequences. These findings were urgently communicated to the ordering otorhinolaryngologist with a recommendation for SARS-CoV-2 testing. The patient tested positive the next day, and later remembered mild upper respiratory tract infection symptoms a few weeks prior. Retrospectively, the presenting symptoms may have been an atypical manifestation of COVID-19.

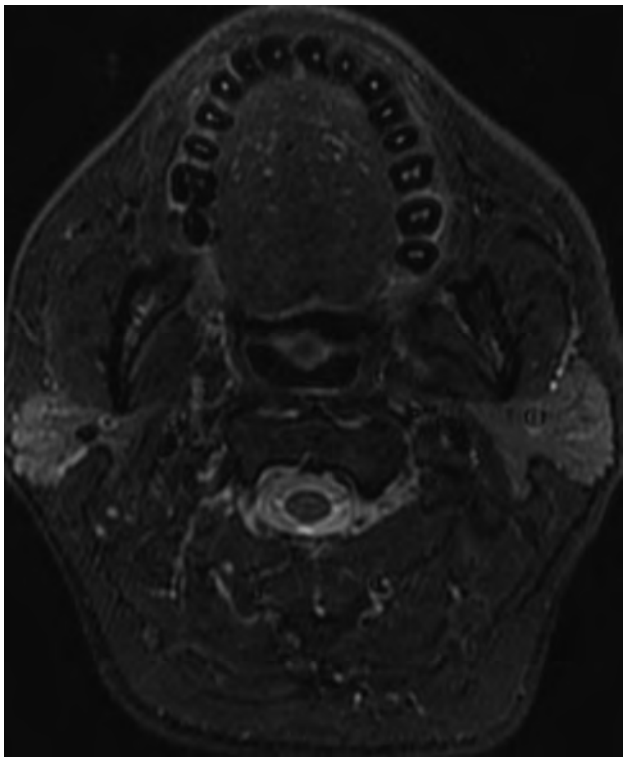

FIG 1. Axial STIR image, at the level of the oropharynx, demonstrating no oropharyngeal mass or abnormality at the site of prior tonsillectomy.

The cases highlighted by Jain et al[1] and our example above demonstrate that neuroradiologists can be the first to detect

Indicates open access to non-subscribers at www.ajnr.org

http://dx.doi.org/10.3174/ajnr.A6699

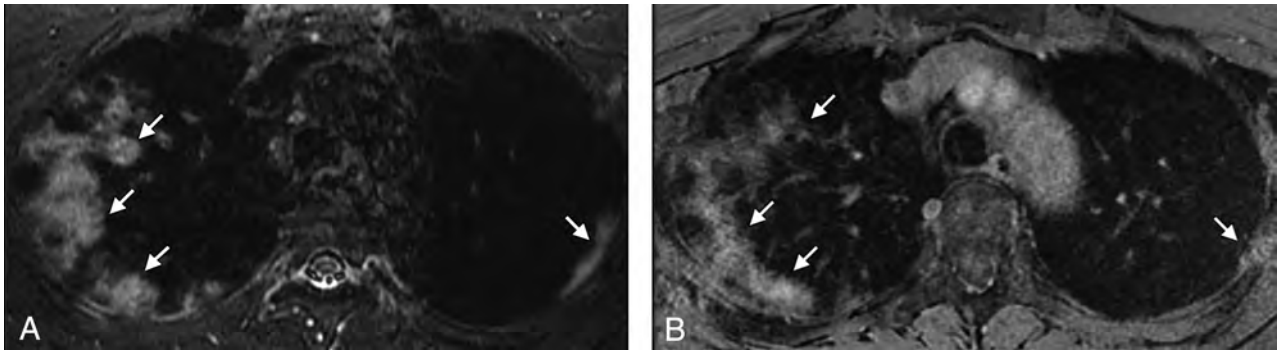

FIG 2. Axial STIR image (*A*) and axial postcontrast T1-weighted image obtained with a fast multiplanar spoiled gradient-echo sequence (*B*) through the lung apices demonstrating bilateral, peripheral consolidation with rounded morphology, consistent with high confidence features of COVID-19 pneumonia (*arrows*).

incidental pulmonary findings of major importance leading to an unsuspected diagnostic discovery. This detection is becoming even more relevant during the current coronavirus pandemic when many patients are presenting with atypical symptoms that prompt neurologic or body imaging studies on which incidental thoracic findings may yield an accurate and expedited diagnosis that could be lifesaving for patients and prevent spread of the disease. The role of neuroradiologists during this pandemic is evolving with detection of a spectrum of CNS abnormalities that were not previously known,[3] as well as heightened sensitivity for incidental pulmonary findings leading to an expanding repertoire of our specialty as neuro-thoracic radiologists.

Disclosures: Suyash Mohan—*UNRELATED*: *Consultancy*: Northwest Biotherapeutics, *Comment*: Money paid to individual; *Grants/Grants Pending*: Novocure, Galileo, *Comment*: Money paid to institution.

REFERENCES

1. Jain R, Young M, Dogra S, et al. **Surprise diagnosis of COVID-19 following neuroimaging evaluation for unrelated reasons during the pandemic in hot spots.** *AJNR Am J Neuroradiol* 2020 May 28. [Epub ahead of print] CrossRef Medline
2. Langenbach MC, Hokamp NG, Persigehl T, et al. **MRI appearance of COVID-19 infection.** *Diagn Interv Radiol* 2020 Apr 30. [Epub ahead of print] CrossRef Medline
3. Zubair AS, McAlpine LS, Gardin T, et al. **Neuropathogenesis and neurologic manifestations of the coronaviruses in the age of coronavirus disease 2019: a review.** *JAMA Neurol* 2020 May 29. [Epub ahead of print] CrossRef Medline

P. Smith
M. Bilello
S. Mohan
Department of Radiology
University of Pennsylvania Perelman School of Medicine
Philadelphia, Pennsylvania

The Development of Subcortical Gray Matter Atrophy in Multiple Sclerosis: One Size Does Not Fit All

Deep gray matter involvement is a relevant feature of multiple sclerosis.[1] Indeed, atrophy of subcortical structures, especially the thalamus, occurs in early phases and continues throughout the disease course,[2] showing a strong potential for the prediction of disability[3] and cognitive impairment.[4]

However, despite its pathophysiologic and clinical relevance, what drives this typical pattern of neurodegeneration in MS remains partially unclear, probably including a combination of primary local neuroinflammatory and neurodegenerative pathologic processes and secondary effects from remote injury in other parts of the brain (mainly white matter) via anterograde/retrograde degeneration and/or spreading of inflammation along axonal pathways.[5]

The study by Kalinin et al,[6] published in a recent issue of *the American Journal of Neuroradiology*, explores the impact of purely intracortical lesions compared with white matter lesions (WMLs) on the volumes of deep gray matter structures in a cohort of patients with relapsing-remitting MS (RRMS, $n = 54$), secondary-progressive MS (SPMS, $n = 12$), and primary-progressive MS (PPMS, $n = 5$). They found that patients with intracortical lesions had longer disease duration, greater disability, and more deep gray matter atrophy. WML burden was the main correlate of subcortical volume loss in patients with RRMS with a disease duration of <5 years and Expanded Disability Status Scale scores of <4.0, while a prominent impact of intracortical lesion volume on deep gray matter volumes, independent from WMLs, was found in patients with an SPMS course or longer disease duration and greater disability.

These results highlight an important point—namely that the relative weight of the different factors contributing to subcortical gray matter atrophy may vary with the disease phases and phenotypes. Indeed, if inflammation in the white matter, related to the formation of WMLs, is recognized as the major driving force for deep gray matter atrophy in early phases and a relapsing-remitting course,[7] less is known about the mechanisms sustaining the enduring subcortical volume loss in chronic disease stages and a progressive course, when neuroinflammation in the white matter becomes less pronounced, as well as its impact on subcortical atrophy and disease progression.[5]

In this light, the correlation between cortical lesions and deep gray matter atrophy, reported by Kalinin et al,[6] may reflect a second-order disconnection effect via thalamocortical radiations and corticothalamic tracts, and/or it may represent an epiphenomenon related to the prominent primary involvement of gray matter (both cortical and subcortical, simultaneously), which is known to characterize chronic disease stages and progressive phenotypes.[1]

Understanding the pathogenic processes underlying subcortical gray matter (primarily thalamic) atrophy in different phases of the disease would be critical in the determination of treatment strategies, potentially informing therapeutic choices with the aim of preventing the occurrence of thalamic damage and its detrimental consequences in terms of brain network economy and clinico-cognitive functioning.

To this end, recent multimodal MR imaging approaches combining the assessment of deep gray matter atrophy with the characterization of local microstructural properties, as inferred by diffusion imaging and susceptibility mapping, have yielded promising results, leading to the identification of new potential biomarkers of local pathology (eg, reduced susceptibility reflecting iron depletion in the thalamus) that may concur with, or even precede, the development of atrophy.[7,8]

For these reasons, we think that future longitudinal multimodal studies are strongly warranted, to unravel the causal relationship between deep gray matter atrophy and local and remote pathologic processes, as well as to understand how this complex interplay dynamically changes throughout the disease course. All along in this process, while adding pieces to the fascinating puzzle of MS pathophysiology, we should not forget John Wheeler's words of advice: "As our island of knowledge grows, so does the shore of our ignorance."

Disclosures: Maria Petracca—*UNRELATED*: *Travel/Accommodations/Meeting Expenses Unrelated to Activities Listed*: Novartis. Sirio Cocozza—*UNRELATED*: *Board Membership*: Amicus Therapeutics, *Comments*: Advisory Board; *Payment for Lectures Including Service on Speakers Bureaus*: Sanofi, Amicus Therapeutics.

REFERENCES

1. Geurts JJ, Barkhof F. **Grey matter pathology in multiple sclerosis.** *Lancet Neurol* 2008;7:841–51 CrossRef Medline
2. Azevedo CJ, Cen SY, Khadka S, et al. **Thalamic atrophy in multiple sclerosis: a magnetic resonance imaging marker of neurodegeneration throughout disease.** *Ann Neurol* 2018;83:223–34 CrossRef Medline

http://dx.doi.org/10.3174/ajnr.A6698

3. Eshaghi A, Prados F, Brownlee WJ, et al; MAGNIMS study group. **Deep gray matter volume loss drives disability worsening in multiple sclerosis.** *Ann Neurol* 2018;83:210–22 CrossRef Medline
4. Eijlers AJC, van Geest Q, Dekker I, et al. **Predicting cognitive decline in multiple sclerosis: a 5-year follow-up study.** *Brain* 2018;141:2605–18 CrossRef Medline
5. Calabrese M, Magliozzi R, Ciccarelli O, et al. **Exploring the origins of grey matter damage in multiple sclerosis.** *Nat Rev Neurosci* 2015;16:147–58 CrossRef Medline
6. Kalinin I, Makshakov G, Evdoshenko E. **The impact of intracortical lesions on volumes of subcortical structures in multiple sclerosis.** *AJNR Am J Neuroradiol* 2020;41:804–08 CrossRef Medline
7. Pontillo G, Cocozza S, Lanzillo R, et al. **Determinants of deep gray matter atrophy in multiple sclerosis: a multimodal MRI study.** *AJNR Am J Neuroradiol* 2019;40:99–106 CrossRef Medline
8. Zivadinov R, Tavazzi E, Bergsland N, et al. **Brain iron at quantitative MRI is associated with disability in multiple sclerosis.** *Radiology* 2018;289:487–96 CrossRef Medline

G. Pontillo
Department of Advanced Biomedical Sciences

M. Petracca
Department of Neurosciences and Reproductive and Odontostomatological Sciences

S. Cocozza
A. Brunetti
Department of Advanced Biomedical Sciences
University "Federico II"
Naples, Italy

Possible Acute Disseminated Encephalomyelitis Related to Severe Acute Respiratory Syndrome Coronavirus 2 Infection

As of June 1, 2020, there were 1.84 million confirmed cases of coronavirus disease 2019 (COVID-19) in the United States with more than 372,000 of the cases in New York City. Most of the clinical manifestations of the infection are related to the respiratory and gastrointestinal systems. Several neurologic manifestations of COVID-19 infection have also been documented, predominantly presenting as olfactory or gustatory dysfunction, encephalopathy, and cerebrovascular accidents. We present a less common neurologic symptom presumed to be acute disseminated encephalomyelitis (ADEM), presenting as transverse myelitis in an adult male patient with no preceding upper respiratory symptoms.

The patient is a 44-year-old healthy man who initially presented with urinary retention for 2 days with additional symptoms of bilateral lower extremity weakness and numbness and an inability to walk. There was no history of back trauma, only a history of back pain for which he had taken nonsteroidal anti-inflammatory drugs. There were no upper respiratory symptoms or fever. There was no known recent viral illness or vaccinations.

Initial examination was remarkable only for lethargy, dysarthria, bilateral arm ataxia, urinary retention, and weakness of both legs that was barely antigravity. Initial imaging work-up included a head CT and MR imaging of the lumbar spine. The head CT findings were normal.

The lumbar spine MR imaging demonstrated slight expansion of the conus medullaris with mild T2 hyperintensity and minimal foci of enhancement (Fig 1). The patient was admitted with an impression of transverse myelitis of unclear etiology.

Per hospital policy, every admitted patient was tested for Severe Acute Respiratory Syndrome coronavirus 2 (SARS-CoV-2) via a nasopharyngeal swab using a real-time reverse transcription polymerase chain reaction (RT-PCR) test, which resulted positively 1 day after admission.

Further imaging of the remainder of the brain and spinal axis demonstrated nonenhancing T2 hyperintense lesions throughout the cervical and thoracic spinal cord (Fig 2) and several periventricular and juxtacortical lesions within the brain (Fig 3). The inferior cervical lesion demonstrated slight associated cord expansion. There was homogeneous brisk enhancement associated with the dominant left parietal lobe juxtacortical/cortical

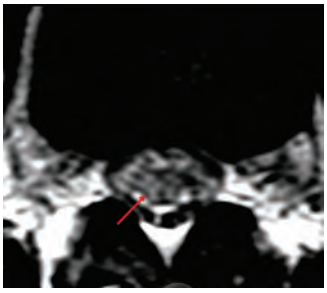

FIG 1. Axial T2 image through the conus demonstrating abnormally increased T2 signal (*arrow*) with slight expansion of the conus.

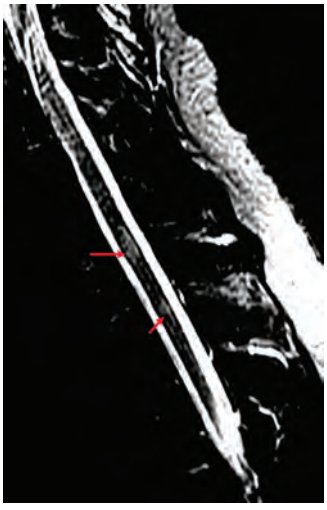

FIG 2. Sagittal inversion recovery sequence demonstrating abnormal T2 hyperintense lesions within the lower cervical and upper thoracic spinal cord (*arrows*).

Indicates open access to non-subscribers at www.ajnr.org

http://dx.doi.org/10.3174/ajnr.A6714

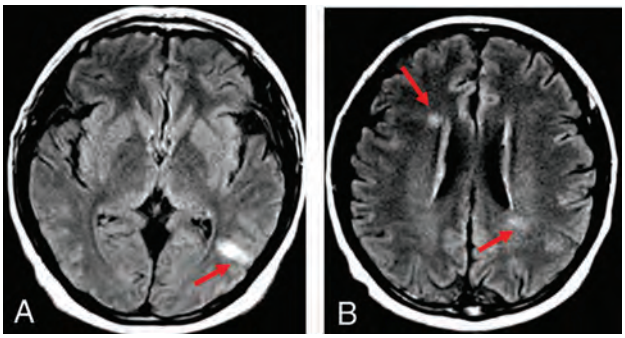

FIG 3. Axial FLAIR images of the brain demonstrating FLAIR hyperintense lesions (*arrows*) within the left posterior parietal lobe (*A*) and periventricular region (*B*).

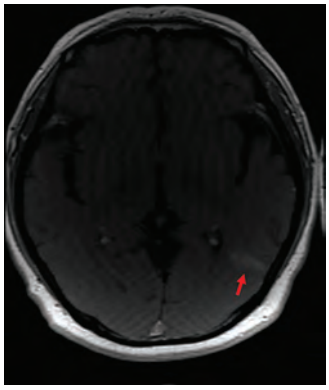

FIG 4. Axial T1 postcontrast image demonstrating brisk homogeneous enhancement of the dominant lesion (*arrow*).

lesion (Fig 4). A lumbar puncture was eventually performed because of ongoing and progressing symptoms.

The initial serum tests showed normal complete blood cell count, metabolic panel, urine studies, and inflammatory markers (sedimentation rate, C-reactive protein level) and were negative for HIV. D-dimer was 2.8 μg/mL FEU (reference range, $<$0.8 μg/mL FEU). Serum cardiolipin antibody immunoglobulin M was mildly elevated at 39 MPL (reference range, 0–12 mpl). Findings of other rheumatologic work-ups were unrevealing. There were no deficiencies in vitamin B_{12}, vitamin E, or copper. Serum protein electrophoresis, angiotensin-converting enzyme levels, and syphilis screen findings were normal.

The CSF profile was largely unremarkable, with white blood cells counts of 6/μL (0–5/μL), of which lymphocytes were 92%; protein 36. CSF bacterial and viral PCR studies were negative. Cytology and flow cytometry were also unrevealing. Oligoclonal bands were absent. The immunoglobulin G (IgG) index was normal. CSF PCR analysis for SARS-CoV-2 was initially questionably positive; however, it was eventually negative to date.

In this patient with unexplained acute encephalopathy and multifocal neurologic signs and symptoms, the constellation of imaging findings in this case is suggestive of ADEM, which may have been triggered by a SARS-CoV-2 infection. The brain lesions are within the periventricular or juxtacortical white matter, predominantly favoring a primary demyelinating process. None of the FLAIR hyperintense lesions in the brain showed hemorrhage as is commonly seen in cases of encephalitis; in addition, the results of the CSF bacterial and viral PCR tests were also negative, making the diagnosis of infectious encephalitis less likely. No T1 hypointense lesions were present. The diagnosis of a first multiple sclerosis attack was thought less likely because of the absence of oligoclonal bands, a normal IgG index, cortical gray matter involvement, and clinical features of encephalopathy.

ADEM is presumed to be a post- or parainfectious process. Typically, ADEM presents in children or adolescents, usually younger than 15 years of age, though cases have been reported in all ages. Approximately 75% of patients have a history of a recent upper respiratory infection or vaccination. Despite reports of the possible association between infection and ADEM, there is no clear understanding of the relationship between the infectious agent and the onset of demyelination. There is experimental evidence in mice for a relationship between coronavirus and CNS demyelination. The literature did report detection of coronavirus in the CNS of a 15-year-old adolescent, and most recently, there has been a report of acute myelitis in an older adult patient with known COVID-19 from Wuhan, China.[1-3] The pathophysiology remains uncertain. The patient was initially treated with IV methylprednisolone and subsequently IV immunoglobulin with modest improvement. At the time of this writing, the patient has been discharged to an acute rehabilitation facility.

Disclosures: Gul Moonis—*UNRELATED: Royalties:* Wolters Kluwer, approximately $150 for *Neuroradiology: A Core Review*.

REFERENCES

1. Ann Yeh E, Collins A, Cohen ME, et al. **Detection of coronavirus in the central nervous system of a child with acute disseminated encephalomyelitis.** *Pediatrics* 2004;113(1 Pt 1):e73–76 CrossRef Medline
2. Zhao K, Huang J, Dai D, et al. **Acute myelitis after SARS-CoV2 infection: a case report.** https://doi.org/10.1101/2020.03.16.20035105. Accessed June 1, 2020
3. **Acute disseminated encephalomyelitis (ADEM). Radiopaedia.org.** https://radiopaedia.org/cases/acute-disseminated-encephalomyelitis-adem. Accessed June 1, 2020

P.S. Utukuri
Department of Neuroradiology

A. Bautista
Department of Neurology

A. Lignelli
G. Moonis
Department of Neuroradiology
Columbia University Irving Medical Center
New York, New York

In the article "Ultra-High-Field Targeted Imaging of Focal Cortical Dysplasia: The Intracortical Black Line Sign in Type IIb" (*AJNR Am J Neuroradiol* 2019;40:2137–42), the institutional affiliations for M. Costagli were listed incorrectly. The correct affiliations are as follows:

- IMAGO7 Research Foundation, Pisa, Italy.
- Istituto Di Ricovero e Cura a Carattere Scientifico Fondazione Stella Maris, Pisa, Italy.

http://dx.doi.org/10.3174/ajnr.A6735